

Annual Report to



Development of Non-Contaminating Cryogenic Fracturing Technology for Shale and Tight Gas Reservoirs Project Number: 10122-20

February 27, 2016

PI: Dr. Yu-Shu Wu (ywu@mines.edu)

Completed by Yu-Shu Wu, Xiaolong Yin, Timothy J. Kneafsey, Jennifer L. Miskimins,
Lei Wang, Minsu Cha, Bowen Yao, Taylor W. Patterson, Naif B. Alqahtani

221 Marquez Hall, 1600 Arapahoe St.
Golden, CO 80401

Tel: 303-384-2093

<http://petroleum.mines.edu/research/emg/>

Petroleum Engineering Department
Colorado School of Mines

LEGAL NOTICE

This report was prepared by Yu-Shu Wu et al as an account of work sponsored by the Research Partnership to Secure Energy for America (RPSEA). Neither RPSEA, members of RPSEA, the National Energy Technology Laboratory, the U.S. Department of Energy, nor any person acting on behalf of any of these entities:

- a. MAKES ANY WARRANTY OR REPRESENTATION, EXPRESS OR IMPLIED WITH RESPECT TO ACCURACY, COMPLETENESS, OR USEFULNESS OF THE INFORMATION CONTAINED IN THIS DOCUMENT, OR THAT THE USE OF ANY INFORMATION, APPARATUS, METHOD, OR PROCESS DISCLOSED IN THIS DOCUMENT MAY NOT INFRINGE PRIVATELY OWNED RIGHTS, OR
- b. ASSUMES ANY LIABILITY WITH RESPECT TO THE USE OF, OR FOR ANY AND ALL DAMAGES RESULTING FROM THE USE OF, ANY INFORMATION, APPARATUS, METHOD, OR PROCESS DISCLOSED IN THIS DOCUMENT.

THIS IS A FINAL REPORT. THE DATA, CALCULATIONS, INFORMATION, CONCLUSIONS, AND/OR RECOMMENDATIONS REPORTED HEREIN ARE THE PROPERTY OF THE U.S. DEPARTMENT OF ENERGY.

REFERENCE TO TRADE NAMES OR SPECIFIC COMMERCIAL PRODUCTS, COMMODITIES, OR SERVICES IN THIS REPORT DOES NOT REPRESENT OR CONSTITUTE AN ENDORSEMENT, RECOMMENDATION, OR FAVORING BY RPSEA OR ITS CONTRACTORS OF THE SPECIFIC COMMERCIAL PRODUCT, COMMODITY, OR SERVICE.

ABSTRACT

This report presents the results of our research investigating cryogenic fracturing technology. While hydraulic fracturing technology has revolutionized the development of unconventional oil and gas reservoirs, waterless fracturing technologies are being continuously sought due to the concerns over formation damage, water consumption, and contamination risks. Liquid nitrogen fracturing has been attempted in field, but its processes, mechanisms, and effectiveness are not well understood due to very limited investigation. This study systematically investigated the feasibility of wellbore liquid nitrogen fracturing by creating a sharp thermal gradient which generated destructive tensile stresses in the near-field rock.

Over the duration of the project, we designed and built an integrated experimental system that consists of liquid nitrogen delivery, triaxial stress loading, parameter monitoring, and data acquisition systems to conduct cryogenic fracturing tests with and without triaxial stresses. With this equipment, experiments on different rocks, borehole injection pressure, different initial temperature, and varying triaxial stress conditions were conducted and monitored in real-time. With the system, the triaxial stresses can be applied up to 6500 psi vertically and 4500 psi horizontally on 8" × 8" × 8" rock blocks. In addition, a second smaller triaxial stress setup was used that allowed visualization of fracturing of blocks up to 4" × 4" × 4" in size with concurrent condition monitoring. CT scans, acoustic signals, pressure decay tests, and breakdown pressure measurements were used to characterize fractures before and after the experiments.

Different types of cryogenic stimulation tests were conducted on both artificial and natural rock samples, including acrylic, glass, concrete, sandstone, and shale. Transparent acrylic and glass samples enable us to directly observe cryogenic fracture initiation, propagation, and patterns under different conditions. Submersion tests performed on concrete samples have demonstrated the concept of cryogenic fracturing by sharp thermal gradient and allowed refined observation of fractured surfaces. Borehole thermal shock created by circulating liquid nitrogen into the borehole demonstrated that cryogenic stimulation is

capable of generating fractures emanating throughout the acrylic cylinders and concrete blocks from borehole wall. Borehole pressurization improves the penetration of liquid nitrogen into the cryogenically generated fractures and enlarges the cryogenic contact with rock, in turn boosting the evolution of the fracture network, indicated by the drop of breakdown pressure during or after the cryogenic stimulation. Stimulations with glass samples under triaxial stress loading revealed that cryogenic fractures partially close as temperature rises back to normal. This same phenomenon was observed for shale samples by pressure decay tests with and without triaxial stress loading.

Cryogenic fracturing processes depend on rock properties, water saturation, injection pressure, treatment time and cycles, and triaxial stress conditions. For concrete samples, longer curing time improves the rock strength, thus increasing the breakdown pressure, while liquid nitrogen injection pressure and number of cycles, and water saturation are negatively correlated with the breakdown pressure. On glass samples we determined that the cryogenic stresses must overcome the applied stresses to cause fractures in the medium. Combining tests on sandstone and shale samples, it is confirmed that liquid nitrogen stimulation reduces the breakdown pressures by generating fractures inside the rock blocks, and as temperature warms up, the fractures narrow. Multiple cycles of stimulation in shale samples indicate that greater permeability enhancement can be achieved after each cycle by creating new fractures and widening the existing ones. Optimized and improved CT scanning techniques empower visualization of micrometer fractures with high accuracy inside opaque shale samples. In addition, triaxial stress anisotropy has been demonstrated to be favorable for cryogenic fracture generation.

Finite element and finite difference modeling approaches successfully reproduced the observations and measurements from our laboratory experiments, confirming the great potential of liquid nitrogen in fracturing unconventional oil and gas reservoirs. On basis of the results from laboratory experiments and numerical simulation, we recommend testing cryogenic stimulation in shallow well groups or in real field wells.

TABLE OF CONTENTS

ABSTRACT.....	i
TABLE OF CONTENTS.....	iii
LIST OF FIGURES	vii
LIST OF SYMBOLS	xxvii
1. Introduction.....	1
1.1 Objectives	2
1.2 Major Achievements.....	3
2. Literature Review.....	5
2.1 Concerns with Hydraulic Fracturing.....	5
2.2 Waterless Fracturing Technologies	6
2.2.1 Explosive and Propellant Fracturing.....	6
2.2.2 Gelled Liquid Systems.....	7
2.2.3 Gas Fracturing.....	8
2.2.4 Supercritical CO ₂ Fracturing.....	8
2.3 Cryogenic Fracturing	9
3. Experimental Designs	12
3.1 Experimental Setup.....	12
3.1.1 Setup for Borehole Thermal Shock.....	13
3.1.2 Setup for Pressurized Borehole Stimulation	13
3.1.3 Triaxial Stress Loading System	16
3.1.4 Integrated Experimental System	19
3.1.5 Casing and Wellhead Installation	20
3.2 Experimental Procedure.....	21
3.2.1 Submersion Tests	21
3.2.2 Borehole Thermal Shock	22
3.2.3 Pressurized Borehole Stimulation.....	22
3.2.4 Borehole Stimulation with Triaxial Stresses.....	23
3.2.5 Pressure Decay Tests	23
3.2.6 Acoustic Measurements	23

3.2.7 CT Scan.....	25
3.3 Summary	26
4. Experimental Results and Analyses.....	28
4.1 Submersion Tests of Concrete	28
4.1.1 Semi-Submersion Test.....	28
4.1.2 Full-Submersion Test.....	30
4.2 Borehole Thermal Shock	33
4.2.1 Acrylic Cylinders	33
4.2.2 Concrete Samples.....	43
4.2.3 Sandstone Sample	72
4.3 Pressurized Borehole Stimulation.....	76
4.3.1 Concrete Samples.....	76
4.3.2 Sandstone Sample	116
4.4 Borehole Stimulation with Triaxial Stresses	136
4.4.1 Glass Samples	137
4.4.2 Concrete Samples.....	143
4.4.3 Sandstone Samples.....	165
4.4.4 Shale Samples	172
4.5 Summary	203
5. CT Imaging Techniques for Fracture Detection	206
5.1 X-Ray CT Scan of Sandstone and Shale Samples	206
5.1.1 Dry and Wet Sandstone Samples with Triaxial Stresses	206
5.1.2 Shale Samples with Triaxial Stresses	207
5.2 PET/CT Scan of Glass and Shale Samples	210
5.2.1 Glass Sample.....	210
5.2.2 Shale Sample.....	212
5.3 Optimization of CT Parameters and Method Improvement	213
5.3.1 Energies and Currents	214
5.3.2 Averaging Scans	218
5.3.3 Image Analysis Techniques	219
5.4 Micro-CT Sample Examination at the Advanced Light Source	223

5.5 Summary	223
6. Numerical Simulation	224
6.1 Finite Element Modeling	224
6.1.1 Theoretical Analysis	225
6.1.2 Problem Setup	228
6.1.3 Results	240
6.2 Finite Difference Modeling	284
6.2.1 Theoretical Analysis	284
6.2.2 Problem Setup	288
6.2.3 Results	293
6.3 Summary	313
7. Field Test Plan	315
7.1 Well Site	315
7.2 Well Pattern	316
7.3 Drilling and Completion	317
7.4 Wellhead Installation	319
7.5 LN ₂ Delivery System	320
7.6 Planned Experimental Procedure	320
7.6.1 Pre-Stimulation Wellbore Characterization	320
7.6.2 Cryogenic Stimulation	321
7.6.3 Post-Stimulation Well Characterization/Evaluation	321
7.7 Schedule	321
8. Conclusions and Recommendations	322
8.1 Conclusions	322
8.2 Recommendations	325
8.2.1 Field Tests	325
8.2.2 Larger Scale Laboratory Tests	325
8.2.3 Further Testing of Tight Sandstone	325
8.2.4 Permeability Enhancement by Cryogenic Seed Fractures	326
8.2.5 Development of Proppants for Cryogenically Induced Fractures	326
8.2.6 Improvement of LN ₂ Delivery System	326

8.2.7 Improvement in Cryogenically Induced Fracture Detection Techniques	326
REFERENCES	328
APPENDIX A: Master and PhD Theses.....	335
APPENDIX B: Presentations / Posters / Publications	336
APPENDIX C: Participating Researchers / Students	337

LIST OF FIGURES

Figure 3.1.1 Overall schematic drawing for cryogenic thermal shock experiments without borehole pressurization. Low pressure GN ₂ is used to force LN ₂ from the dewar.	14
Figure 3.1.2 Overall schematic drawing for cryogenic stimulation experiments with borehole pressurization. Low pressure GN ₂ is used to force LN ₂ from the dewar, high pressure GN ₂ is used for pressurization and fracturing.	15
Figure 3.1.3 Triaxial stress loading system designed for cryogenic fracturing experiments.	17
Figure 3.1.4 Three hydraulic air pumps.	18
Figure 3.1.5 Pistons in horizontal directions within the containment ring.	18
Figure 3.1.6 Vertical piston on rolling frame and the containment ring.	19
Figure 3.1.7 Integrated laboratory equipment for cryogenic fracturing experiments.	20
Figure 3.1.8 Packer installation using a confining structure.	21
Figure 3.2.1 Setup for semi-submersion tests.	22
Figure 3.2.2 The pulser and the digital oscilloscope used for acoustic measurements. ...	24
Figure 3.2.3 Experiment setup for acoustic measurements.	24
Figure 3.2.4 Typical input pulse and received signals from acoustic tests.	25
Figure 3.2.5 The CT scanner used in this study.	26
Figure 4.1.1 Subtracted before and after images of block sides after semi-submersion test. Top row-Top side; Middle row-four vertical faces from front turning to the right side; Bottom row-Bottom side. Cracks are indicated by the red arrows.	29
Figure 4.1.2 CT scan showing a vertical slice of the block from the semi-submersion test. Arrows point to fractures in the block resulting from cryogenic fracturing.	30
Figure 4.1.3 Top surface of the concrete block before and after the full-submersion test.	31
Figure 4.1.4 Images of the concrete block Face 1 after the full-submersion test show both the extension of existing fractures and the creation of large, new fractures.	31
Figure 4.1.5 Top surface of the wet concrete block after the full-submersion test.	32
Figure 4.1.6 Changes in P-wave velocities before and after the cryogenic test.	33
Figure 4.2.1 Acrylic Sample 1: (a) dimension, and (b) description of stainless steel casing and inlet tube.	34
Figure 4.2.2 Locations of thermocouples and temperature evolution during the experiment.	35

Figure 4.2.3 Borehole pressure and LN ₂ released during the test.....	35
Figure 4.2.4 Crack development. The steps shown above do not represent all the crack growth steps.	37
Figure 4.2.5 Crack morphology and driving thermal tensile stresses.....	38
Figure 4.2.6 Effect of crack propagation on surface temperature.....	38
Figure 4.2.7 Effect of borehole condition.....	39
Figure 4.2.8 Acrylic Sample 2: (a) dimension, and (b) description of stainless steel casing and inlet tube.....	40
Figure 4.2.9 Temperature evolution during the testing.....	41
Figure 4.2.10 Effect of crack propagation on surface temperature.....	41
Figure 4.2.11 Crack development.....	43
Figure 4.2.12 Effect of borehole condition.....	43
Figure 4.2.13 X-ray CT scan vertical cross section of the concrete block.	44
Figure 4.2.14 Experimental setup for test with unconfined packer.....	45
Figure 4.2.15 Cracks observed after the thermal shock (a) near the borehole, and (b) at the borehole surface.....	46
Figure 4.2.16 Pre-existing surface cracks, the superimposed lines are weighted according to the crack thickness.....	47
Figure 4.2.17 Surface cracks after the thermal shock. Note that the dark spots are stains from the couplant used for securely attaching the ultrasonic sensors.....	47
Figure 4.2.18 Locations of the thermocouples used in the temperature measurements. ..	48
Figure 4.2.19 Temperature evolution during thermal shock experiment.....	48
Figure 4.2.20 Temperature evolution during thermal shock experiment with more locations.....	49
Figure 4.2.21 Temperature evolution after the thermal shock experiment (up to 10 hours).....	49
Figure 4.2.22 Acoustic measurement locations before and after thermal shock.....	50
Figure 4.2.23 P and S wave arrivals before and after the thermal shock (compared with normalized amplitude.....	52
Figure 4.2.24 P and S wave amplitudes before and after the thermal shock.....	54
Figure 4.2.25 Global waveforms before and after the thermal shock.....	56
Figure 4.2.26 Experimental setup with “packer-confining structure”.....	57
Figure 4.2.27 Cracks at the borehole walls observed from the top and the borescope.....	58

Figure 4.2.28 Surface cracks after the second thermal shock-the superimposed lines are weighted according to the crack thickness.....	59
Figure 4.2.29 CT images: axis and direction.	59
Figure 4.2.30 The CT slide at 0.4" from the top surface.	60
Figure 4.2.31 The CT slide at 0.5" from bottom.....	60
Figure 4.2.32 The CT slide at the mid-height.	61
Figure 4.2.33 The CT slide at 0.5" away from Face 4.....	61
Figure 4.2.34 Locations of thermocouple tips.	63
Figure 4.2.35 Temperature vs. time during cryogenic stimulation.....	63
Figure 4.2.36 Synchronized plots of LN ₂ consumption, temperature, and pressure with time.	64
Figure 4.2.37 P and S wave arrivals before and after the thermal shock (compared with normalized amplitude).	66
Figure 4.2.38 P and S wave amplitudes before and after the thermal shock.	68
Figure 4.2.39 Global waveforms before and after the thermal shock.....	70
Figure 4.2.40 liquid nitrogen and gas nitrogen permeating through fractures.....	71
Figure 4.2.41 Cryogenic performance of surrounding materials.....	72
Figure 4.2.42 The locations of the thermocouples in the sandstone block tests. There are no external stresses and borehole pressure.	73
Figure 4.2.43 Temperature values during the first cryogenic test. The numbers (1-7) are the locations of the thermocouples. Red arrows in the figure mark the times when LN ₂ was poured.	74
Figure 4.2.44 Temperature values during the second cryogenic test. The numbers (1-7) are the locations of the thermocouples. Red arrows in the figure mark the times when LN ₂ was poured.	74
Figure 4.2.45 Constant pressure and flow rate are reached before shut-in for the gas leak-off test.	75
Figure 4.2.46 Epoxy was damaged by repeated exposures to the cryogenic temperature.....	75
Figure 4.3.1 Breakage points for dry Samples 1-3 using nitrogen gas.....	78
Figure 4.3.2 Pre-fracture pressure decay curves for Samples 2 and 3.....	79
Figure 4.3.3 Fracture profile of Sample 1.....	80
Figure 4.3.4 Fracture profile of Sample 2.....	81
Figure 4.3.5 Fracture profile of Sample 3.....	82

Figure 4.3.6 Pressure and temperature records during cryogenic treatment of Sample 5.	83
Figure 4.3.7 Pressure and temperature records during cryogenic treatment of Sample 6.	84
Figure 4.3.8 Pressure decay tests for dry concrete samples with liquid nitrogen treatments.	86
Figure 4.3.9 Observation of Joule-Thomson cooling effect during a pressure decay test.	86
Figure 4.3.10 Fracture profile of Sample 4.....	87
Figure 4.3.11 Fracture profile of Sample 5.....	88
Figure 4.3.12 Fracture profile of Sample 6.....	89
Figure 4.3.13 Pressure and temperature records during cryogenic treatment of Sample 7.	90
Figure 4.3.14 Pressure and temperature records during cryogenic treatment of Sample 8.	91
Figure 4.3.15 Pressure and temperature records during treatment of Sample 9.	92
Figure 4.3.16 Pressure decay curves for Samples 7, 8, and 9.....	93
Figure 4.3.17 Fracture profile of Sample 7.....	94
Figure 4.3.18 Fracture profile of Sample 8.....	95
Figure 4.3.19 Fracture profile of Sample 9.....	96
Figure 4.3.20 Pressure and temperature records during treatment of Sample 10.	97
Figure 4.3.21 Pressure and temperature records during treatment of Sample 11.	98
Figure 4.3.22 Pressure and temperature records during cryogenic treatment of Sample 12.	99
Figure 4.3.23 Fracture profile of Sample 10.....	100
Figure 4.3.24 Fracture profile of Sample 11.....	101
Figure 4.3.25 Fracture profile of Sample 12.....	102
Figure 4.3.26 Pressure decay tests for Samples 10, 11, and 12.	103
Figure 4.3.27 Pressure and temperature records during cryogenic treatment of Sample 13.	104
Figure 4.3.28 Pressure and temperature records during cryogenic treatment of Sample 14.	105
Figure 4.3.29 Pressure and temperature records during cryogenic treatment of Sample 15.	106
Figure 4.3.30 Pressure decay tests for Samples 13, 14, and 15.	107
Figure 4.3.31 Fracture profile of Sample 13.....	108

Figure 4.3.32 Fracture profile of Sample 14.....	109
Figure 4.3.33 Fracture profile of Sample 15.....	110
Figure 4.3.34 Breakage pressure of samples as a function of curing time.	112
Figure 4.3.35 Breakage pressure as a function of cycles of treatments.....	113
Figure 4.3.36 Experimental setup (the 1st thermal shock)	117
Figure 4.3.37 Pressure generated during nitrogen gas flow and LN ₂ consumption.	118
Figure 4.3.38 Locations of thermocouples. The dark spots are stains of the couplant used for the ultrasonic measurements.	119
Figure 4.3.39 Temperature during the 1 st thermal shock.....	119
Figure 4.3.40 Experimental setup for the 2 nd thermal shock.	120
Figure 4.3.41 Temperature profiles during the cryogenic treatment.	121
Figure 4.3.42 Frost attracted at the surfaces	122
Figure 4.3.43 Leakage and sealing integrity check of the packer.....	122
Figure 4.3.44 Gas pressure decay test.....	123
Figure 4.3.45 Pressure decay comparison.....	123
Figure 4.3.46 Temperature evolution during the 3 rd thermal shock.	124
Figure 4.3.47 Pressure and LN ₂ consumption vs. time of the 4 th thermal shock.....	125
Figure 4.3.48 Experimental setup for thermal shock and borehole pressurization (protection shields not shown in this picture).....	126
Figure 4.3.49 Experimental setup near the specimen and locations of thermocouples..	127
Figure 4.3.50 Two borehole pressurization schemes.....	127
Figure 4.3.51 Monitored LN ₂ consumption and borehole pressure.....	128
Figure 4.3.52 Temperature vs. time during the cryogenic stimulation.....	129
Figure 4.3.53 Leakage/permeation test by bubbles. (a) Leakage hole created at the packer/rock contact during the gas pressurization of the 4 th test, (b) localized air permeation observed at the top, and (c) local permeation at the side (Face 1).....	130
Figure 4.3.54 P and S wave arrivals before and after the cryogenic stimulation (compared with normalized amplitude).	132
Figure 4.3.55 P and S wave amplitudes before and after the cryogenic stimulation.....	134
Figure 4.3.56 Global waveforms before and after the cryogenic stimulation.	136
Figure 4.4.1 Triaxial stress frame and preliminary liquid nitrogen delivery system.....	138
Figure 4.4.2 Test G1 with stress applied in the z direction.....	139

Figure 4.4.3. 4-inch block with annular (red arrows), vertical (white arrow), and sub-horizontal (yellow arrows) fractures. Left-side view, Center-view along the borehole, Right-top view. 140

Figure 4.4.4 Views along the boreholes of cryogenically fractured 2-inch glass blocks. Left-uniaxial vertical stress ~190 psi, Center-triaxial 700:1050:1400 psi, Right-triaxial 2800:4200:5600 psi..... 140

Figure 4.4.5 View perpendicular to the borehole of cryogenically fractured 2-inch glass blocks. Left-uniaxial vertical stress, Center-Triaxial 700:1050:1400 psi, Right-triaxial 2800:4200:5600 psi..... 141

Figure 4.4.6 Final image from Test G5 after 12 minutes..... 141

Figure 4.4.7 Images collected of visibly observed fractures upon stress removal. Stress removal occurred 50 minutes after the application of cryogen was completed. From left to right, top to bottom: fully stressed, three-quarters stressed, one-half stressed, one-quarter stressed, and unstressed. 142

Figure 4.4.8 Fractures in vertical borehole with annular fractures suppressed. 143

Figure 4.4.9 Triaxial stresses applied to Sample 16. 144

Figure 4.4.10 Breakdown pressure for Sample 16 under triaxial stresses is 583 psi..... 145

Figure 4.4.11 Picture for Sample 16 (not the number marked on sample) after fracturing by GN₂. The created fracture seems to be a premature fracture perpendicular to the maximum horizontal stress, which is in y-axis direction applied on Faces 2 and 4. This might be because of the center dent leading to weakness in the area around the wellbore. 145

Figure 4.4.12 Triaxial stresses applied on Sample 17 (x = 500 psi, y = 750 psi, and z = 1000 psi)..... 146

Figure 4.4.13 Breakdown pressure for Sample 17 of 1180 psi under triaxial stress. 146

Figure 4.4.14 Picture of Sample 17 (not the number marked on sample) after fracturing by GN₂. The fractures propagate perpendicular to the minimum horizontal stress (x-axis). The black dots follow the fractures..... 147

Figure 4.4.15 Top view picture from inside the borehole of Sample 17 after fracturing by GN₂. The fractures propagate perpendicular to the minimum horizontal stress (x-axis). 147

Figure 4.4.16 Triaxial stresses applied on Sample 21 (x = 1000 psi, y = 1500 psi, and z = 2000 psi)..... 148

Figure 4.4.17 Breakdown pressure profile for Sample 21 under triaxial stresses. 149

Figure 4.4.18 Picture for Sample 21 (not the number marked on sample) after fractured by GN₂. 149

Figure 4.4.19 Triaxial stresses applied on Sample 18 ($x = 500$ psi, $y = 750$ psi, and $z = 1000$ psi). Red dots indicate when the fracture happened. 150

Figure 4.4.20 Temperature profiles from the start of injecting LN₂ until the end of the test showing the temperature at the borehole wall decreased fairly quickly to the LN₂ temperature. 151

Figure 4.4.21 Breakdown pressure profile for Sample 18 under triaxial stresses and right after the LN₂ treatment. Leaking sounds were heard when the pressure inside the wellbore reached 200 psi and became louder as the wellbore pressure increased. The major fracture happened at 685 psi..... 151

Figure 4.4.22 Picture for Sample 18 (not the number marked on sample) after fracturing by GN₂. The fractures propagated perpendicular to the maximum horizontal stress, which is in y-axis direction applied on Faces 2 and 4). The black dots follow the fractures..... 152

Figure 4.4.23 Temperature vs. time during the high pressure LN₂ treatment. Sample 19 was treated by three LN₂ cycles. 153

Figure 4.4.24 Breakdown pressure profile for Sample 19 under triaxial stress immediately after the LN₂ treatments. Leaking sounds were heard when the pressure inside the wellbore reached 400 psi and became louder as the wellbore pressure increased. The major fracture happened at 778 psi as noted on the figure. 153

Figure 4.4.25 Picture of Sample 19 after fracturing by GN₂. The fractures propagated perpendicular to the maximum horizontal stress which is in y-axis direction applied on Faces 2 and 4. The black dots follow the fractures..... 154

Figure 4.4.26 Locations of the acoustic measurements before and after the test. (a) The face number, and (b) the transducer locations on the sample Face 2. 155

Figure 4.4.27 P- and S-wave arrivals before (blue) and after (red) the LN₂ test along Faces 1-3 and 2-4. 157

Figure 4.4.28 Changes in the P-wave velocities before and after the cryogenic test, (a) Faces 1-3, and (b) Faces 2-4. 158

Figure 4.4.29 Temperature vs. time during three cycles of high pressure LN₂ treatment on Sample 20..... 159

Figure 4.4.30 Breakdown pressure profile for Sample 20 under triaxial stresses and right after the LN₂ treatment. Leaking sounds were heard when the pressure inside the wellbore reached 700 psi and became louder as the wellbore pressure increased. The major fracture happened at 759 psi..... 159

Figure 4.4.31 Picture for Sample 20 (not the number marked on sample) after being fractured by GN₂. The black lines follow the fractures. 160

Figure 4.4.32 Temperature profiles from the start of injecting the LN ₂ until the end of the test. GN ₂ fracturing attempts failed (red circles) because the sample was already fractured due to stress loading.....	161
Figure 4.4.33 GN ₂ fracturing attempts on Sample 22.....	161
Figure 4.4.34 Picture of Sample 22 (not the number marked on sample) after the GN ₂ fracturing attempts. The black dots follow the fractures.	162
Figure 4.4.35 Temperature vs. time during the high pressure LN ₂ treatment on Sample 23 with four LN ₂ cycles.	163
Figure 4.4.36 Breakdown pressure profile for Sample 23 by injecting GN ₂ after an LN ₂ treatment under triaxial stresses.....	163
Figure 4.4.37 Picture of Sample 23 (not the number marked on sample) after fracturing by GN ₂ . The black lines follow the fractures.....	164
Figure 4.4.38 Breakdown pressure values of intact and stimulated concrete samples. ..	165
Figure 4.4.39 Breakdown pressure for Sample SS2 by injecting only GN ₂	166
Figure 4.4.40 Sandstone Sample SS2 before (a) and after (b) the nitrogen gas fracturing. This block exhibited significant fracturing, as can be seen in (b) photos.....	167
Figure 4.4.41 Pressure decay tests under different loading conditions for Sample SS1.	169
Figure 4.4.42 Pressure decay tests before LN ₂ treatment on Sample SS1 and after each LN ₂ treatment cycle. All tests were conducted under triaxial stress loading. There is no significant difference in the pressure decay curves after each treatment cycle.	169
Figure 4.4.43 Pressure decay tests with different temperature conditions for Sample SS1.	170
Figure 4.4.44 Pressure decay test at the end of the experiment on SS1. During this step, the sample fractured at a very low pressure of 219 psi.....	170
Figure 4.4.45 Sandstone Sample SS1 before (a) and after (b) the fracturing. It appears that the created fractures follow the natural fractures.....	171
Figure 4.4.46 Breakdown pressure for Sample 4 using GN ₂	172
Figure 4.4.47 Shale Sample 4 after nitrogen gas fracturing.	173
Figure 4.4.48 Pressure decay test for shale Sample 1 before the LN ₂ test and with no stress loading ($\sigma_z = 60$ psi). It takes more time for the pressure to decay compared to concrete and sandstone samples.	174
Figure 4.4.49 Temperature profiles for shale Sample 1 from the start of injecting the LN ₂ until the end of the test.....	175
Figure 4.4.50 Temperature profile at early time of the shale Sample 1 tests giving a closer look at the temperature of the borehole wall.	175

Figure 4.4.51 Pressure decay tests for shale Sample 1 before and after the LN₂ test. 176

Figure 4.4.52 Locations of the acoustic measurements before and after the shale Sample 1 test. (a) The face numbers, and (b) the transducer locations numbered on the sample faces. 177

Figure 4.4.53 P-wave arrivals before (blue) and after (red) the LN₂ test for all side faces with the adjusted amplitude to compare changes in arrival time and wave forms. Faces 1 and 3 on top (a) and Faces 2 and 4 on bottom (b)..... 178

Figure 4.4.54 CT-scan images for shale Sample 1 before cryogenic treatment. The pictures on the right are the YZ-plane images and the pictures on the left are the XY-plane images. The red lines in the YZ-planes show the location of the XY-plane. The red circle shows the pre-existing fracture on the top surface of this shale block. 179

Figure 4.4.55 Pressure decay tests under different stress conditions for shale Sample 1. 181

Figure 4.4.56 Pressure decay tests before LN₂ treatment and after each LN₂ treatment cycle for shale Sample 1, all of them conducted under triaxial stress loading. Significant differences in the pressure decay curves after each treatment cycle indicate permeability enhancements. 181

Figure 4.4.57 Pressure decay tests with different temperature conditions for shale Sample 1..... 182

Figure 4.4.58 Pressure decay tests before and after the LN₂ test for shale Sample 1..... 182

Figure 4.4.59 Breakdown pressure for shale Sample 1 using GN₂..... 183

Figure 4.4.60 CT-scan images for shale Sample 1 after GN₂ fracturing. The pictures on the left are the XY-plane images and the pictures on the right are the YZ-plane images. The red lines in the YZ-planes show the location of the XY-plane. The red circle in XY-plane (a) shows the pre-existing fracture on the top surface of this shale block. The two red circles in XY-plane (c) show the created fractures at the bottom of the block. 184

Figure 4.4.61 Shale Sample 1 before (a) and after (b) LN₂ and GN₂ fracturing. The color change of the sample before and after the treatment is a result of illumination difference. 185

Figure 4.4.62 Pressure decay tests for Sample 2 with and without triaxial stress loading. 187

Figure 4.4.63 Pressure decay tests for Sample 2 before the LN₂ treatment and after each cycle of LN₂ treatment. There is a measurable increase in the pressure decay time after the first LN₂ cycle. The pressure decay tests after the second LN₂ cycle decreased, indicating enhancements in the permeability..... 187

Figure 4.4.64 Pressure decay tests with different temperature conditions for Sample 2.188

Figure 4.4.65 Pressure decay tests before and after the LN ₂ test on Sample 2.....	188
Figure 4.4.66 Pressure decay tests under different stress conditions before the second test on Sample 2.....	190
Figure 4.4.67 Pressure decay tests before LN ₂ treatment and after each LN ₂ treatment cycle for Sample 2. All of them conducted under triaxial stress loading. There is a significant difference in the pressure decay curves after each treatment cycle.	190
Figure 4.4.68 Pressure decay tests with different temperature conditions for the third test on Sample 2.....	191
Figure 4.4.69 Pressure decay tests before and after the second LN ₂ test on Sample 2...	191
Figure 4.4.70 P-wave arrivals before and after the second LN ₂ test for Faces 1 & 3 (a) and 2 & 4 (b) with the adjusted amplitude to compare changes in arrival time and wave forms.	192
Figure 4.4.71 Changes in P-wave velocities before and after the cryogenic test for Faces 1 and 3.....	193
Figure 4.4.72 Changes in P-wave velocities before and after the cryogenic test for Faces 2 and 4.....	193
Figure 4.4.73 Changes in P-wave velocities before and after the cryogenic test for Faces 5 and 6.....	194
Figure 4.4.74 Breakdown pressure profile for Sample 2 using GN ₂	195
Figure 4.4.75 Shale Sample 2 before (a) and after (b) the GN ₂ fracturing.	196
Figure 4.4.76 Fracture plane in shale Sample 2 after LN ₂ and GN ₂ fracturing.	196
Figure 4.4.77 Temperature profiles from the start of injecting LN ₂ till the end of the test for Sample 3.....	198
Figure 4.4.78 Pressure decay tests before and after the LN ₂ test for Sample 3.	198
Figure 4.4.79 P- and S-wave arrivals before and after the LN ₂ test on Sample 3 for all side faces with the adjusted amplitude to compare changes in arrival time and wave forms.	201
Figure 4.4.80 Breakdown pressure of Sample 3 using GN ₂ . This happened during the pressure decay test.	202
Figure 4.4.81 Shale Sample 3 fractured during pressure decay test.	202
Figure 5.1.1 Left: post-test CT scan of sandstone block, fractures would be shown as dark features in this image. Right: difference scan (140kV-120kV), fractures would be shown as light features in this image (see borehole for reference).	207
Figure 5.1.2 Initial scans of one of the Mancos shale blocks (typical). Left image adjusted to show fractures. Right image adjusted to show epoxy (see arrows). Note “X”-like artifacts resulting from block geometry.....	208

Figure 5.1.3 Shale sample borehole inspection and video recording using a fiberscope.	209
Figure 5.1.4 Post-test CT scan image. The borehole is black. The cross-cutting fracture (wavy black feature) was also present at the start of the test.....	209
Figure 5.2.1 PET/CT of 4-inch glass block: a to c are photos, d to f are images from first PET/CT, g to i are PET/CT images following injection of labeled fluid using a syringe.	212
Figure 5.2.2 PET/CT scan of 4-inch Mancos shale block: a to c are from X-ray CT scan (to show locations), d to f from PET/CT imaging.	213
Figure 5.3.1 CT scan of 4-inch Mancos shale block (left) and 4.5-inch diameter Mont Terri Opalinus shale with darker shades indicating fractures (examples indicated by yellow arrows).	213
Figure 5.3.2 Montage of a sequence of images of fractured Mancos shale at 120 kV and 300 mA.....	215
Figure 5.3.3 Average of 120 kV and 140 kV scans.....	217
Figure 5.3.4 Plotted Hounsfield unit values for the selected region of interest for the different scanning conditions.....	217
Figure 5.3.5 Five images averaged at 120 kV and 160 mA.....	218
Figure 5.3.6 Plotted Hounsfield unit values for the selected region of interest for the different scanning conditions.....	219
Figure 5.3.7 Left: Processed CT image showing fracture pattern in lighter colors. Center: CT cross section, right: fractures identified using Connected Component Analysis.	221
Figure 5.3.8 X-ray CT cross section of an 8-inch concrete block showing the “X” artifacts.	221
Figure 5.3.9 Left: initial image, center: fast Fourier transform of the initial image showing removed values, and right: inverted image. Note improvement of “X” artifacts, but loss of overall quality.	222
Figure 5.3.10 Left: 6061 aluminum “moons” around fractured glass sample, right: CT slice.	223
Figure 6.1.1 (a) Arbitrary curved boundary domain modeled using square elements. Grey areas are not included in the model. (b) Refined finite element mesh showing reduction of the area not included in the model on the left. Adapted from Hutton (2004).....	225
Figure 6.1.2 (a) A general two-dimensional domain of field variable. (b) A three-node finite element defined in the domain. (c) Additional element showing a partial finite element meshes of the domain. Adapted from Hutton (2004).	225

Figure 6.1.3 Flow chart for the FEM using COMSOL Multiphysics 3.5a software.	228
Figure 6.1.4 Model geometry for concrete and sandstone blocks with a 6-inch wellbore from COMSOL Multiphysics 3.5a. The scale is in feet.	231
Figure 6.1.5 Model geometry for concrete and sandstone blocks with a cased 6-inch wellbore from COMSOL Multiphysics 3.5a. The scale is in feet.	231
Figure 6.1.6 Model geometry for concrete and sandstone blocks with an 8-inch wellbore from COMSOL Multiphysics 3.5a. The scale is in feet.	232
Figure 6.1.7 Model geometry for multilayered shale block with a 6-inch wellbore from COMSOL Multiphysics 3.5a. The scale is in feet.	232
Figure 6.1.8 Model geometry for multilayered shale block with a cased 6-inch wellbore from COMSOL Multiphysics 3.5a. The scale is in feet.	233
Figure 6.1.9 Model geometry for multilayered shale block with an 8-inch wellbore from COMSOL Multiphysics 3.5a. The scale is in feet.	233
Figure 6.1.10 Multilayered shale block model (12 sublayers) constructed with alternating layers of siltstone, clay, and limestone.	234
Figure 6.1.11 Multilayered shale block model with a 6-inch cased wellbore with a “normal” size mesh from COMSOL Multiphysics 3.5a.	238
Figure 6.1.12 2D deformed shape plot for -321 °F borehole, no external stress applied and room temperature (70 °F) concrete block. More deformation was observed at the top side of the block and reducing the diameter of the wellbore (deformation is exaggerated for easy observation).	241
Figure 6.1.13 2D deformed shape plot for -321 °F borehole, unstressed and reservoir temperature (200 °F) concrete block. More deformation was observed at the top side of the block and reducing the diameter of the wellbore.	242
Figure 6.1.14 3D deformed shape plot for unstressed and reservoir temperature (200 °F) concrete block. More deformation was observed at the top side of the block, reducing the diameter of the wellbore. Also the centers of the block sides have been deformed and displaced inward to the center of the block.	242
Figure 6.1.15 2D shear stress plot on XY-plane for unstressed and room temperature (70 °F) concrete block. Most of the shear stress values concentrate around the wellbore circumference.	243
Figure 6.1.16 2D shear stress plot on XY-plane for unstressed and reservoir temperature (200 °F) concrete block. Most of the shear stress values concentrate around the wellbore circumference.	244

Figure 6.1.17 2D shear stress plot on XY-plane for concrete block with triaxial stresses at room temperature (70 °F). Most of the shear stress values concentrate around the wellbore circumference..... 244

Figure 6.1.18 2D shear stress plot on XY-plane for concrete block with triaxial stresses at reservoir temperature (200 °F). Most of the shear stress values concentrate around the wellbore circumference..... 245

Figure 6.1.19 2D radial stress plot on XY-plane for unstressed and room temperature (70 °F) concrete block. The radial stress values concentrate around the wellbore circumference with equal distribution. 246

Figure 6.1.20 2D tangential stress plot on XY-plane for unstressed and room temperature (70 °F) concrete block. The tangential stress values concentrate around the wellbore circumference with equal distribution. 246

Figure 6.1.21 2D radial stress plot on XY-plane for unstressed and reservoir temperature (200 °F) concrete block. The radial stress values concentrate around the wellbore circumference with equal distribution. 247

Figure 6.1.22 2D tangential stress plot on XY-plane for unstressed and room temperature (200 °F) concrete block. The tangential stress values concentrate around the wellbore circumference with equal distribution. 247

Figure 6.1.23 2D radial stress plot on XY-plane for concrete block under triaxial stresses at room temperature (70 °F). The radial stress values concentrate around the wellbore circumference, however, a lower radial magnitude is in the direction of maximum horizontal stress which is along the direction of fracture propagation. 248

Figure 6.1.24 2D tangential stress plot on XY-plane for concrete block under triaxial stresses at room temperature (70 °F). The tangential stresses values concentrate around the wellbore circumference, however, a lower tangential magnitude is in the direction of maximum horizontal stress which is along the direction of fracture propagation. 248

Figure 6.1.25 Time-dependent temperature of unstressed concrete sample with 6-inch wellbore. These slices in the XZ-plane plot the temperature distribution in °F with time. Figure 6.1.25a shows the temperature in °F after 1 minutes; Figure 6.1.25b after 5 minutes; Figure 6.1.25c after 12 minutes; and Figure 6.1.25d after 20 minutes. 249

Figure 6.1.26 Time-dependent radial stress distribution of unstressed concrete sample with 6” wellbore. These slices in the XZ-plane show radial stress variation with time as a result of changing temperature. The radial stress changes from the wellbore towards the boundary. Figure 6.1.26a shows the radial stress in psi after 1 min; Figure 6.1.26b after 5 minutes; Figure 6.1.26c after 12 minutes; and Figure 6.1.26d after 20 minutes. 250

Figure 6.1.27 2D temperature and deformed shape plot for unstressed concrete block at room temperature (70 °F). More deformation is observed on the area attached to the casing at the top side of the block and reduces the diameter of the wellbore. 251

Figure 6.1.28 2D radial stress plot on YZ-plane for unstressed concrete block at room temperature (70 °F). Since the stainless steel is present, it covers all the stress contrast and it is hard to see any stress variation around the wellbore. 252

Figure 6.1.29 2D log₁₀ radial stress plot on YZ-plane for unstressed concrete block at room temperature (70 °F). The radial stress development is seen around the wellbore and the magnitudes are in the range of 1.649 to 7.697 (log₁₀ psi)..... 252

Figure 6.1.30 2D log₁₀ tangential stress plot on YZ-plane for unstressed concrete block at room temperature (70 °F). The tangential stress development is seen around the wellbore and the magnitudes are in the range of 2.142 to 7.449 (log₁₀ psi). 253

Figure 6.1.31 The red line is the line cross section along x-axis and passes through the stainless steel casing. 254

Figure 6.1.32 Plot showing the radial stress value along the line cross section on the x-axis from Figure 6.1.31. 254

Figure 6.1.33 Plot showing the tangential stress value along the line cross section on the x-axis from Figure 6.1.31..... 255

Figure 6.1.34 2D one-level slice plot of the τ_{xy} shear stress in psi with the slice taken in the XY-plane for a cased concrete sample that was triaxially stressed at room temperature (70 °F). Shear stress magnitudes are in the range of 0 to 81,550 psi in opposite direction across the wellbore of the concrete sample..... 256

Figure 6.1.35 2D one-level slice plot of the τ_{yz} shear stress in psi with the slice taken in the YZ-plane for a cased concrete sample that was triaxially stressed at room temperature (70 °F). Shear stress magnitudes are in the range of 0 to 87,000 psi in the opposite direction across the wellbore of the concrete sample..... 256

Figure 6.1.36 2D one-level slice plot of the log₁₀ radial stress with the slice taken in the XY-plane for a cased concrete sample that was triaxially stressed at room temperature (70 °F). The radial stress development is seen around the casing and wellbore, and the magnitudes are in the range of 3.07 to 7.704 (log₁₀ psi)..... 258

Figure 6.1.37 2D one-level slice plot of the log₁₀ tangential stress with the slice taken in the XY-plane for a cased concrete sample that was triaxially stressed at room temperature (70 °F). The radial stress development is seen around the casing and the wellbore, the magnitudes are in the range of 2.775 to 7.388 (log₁₀ psi)..... 258

Figure 6.1.38 2D one-level slice of the radial stress in psi with the slice taken in the XY-plane in the open-hole part of the wellbore for a cased concrete sample that was triaxially

stressed at room temperature (70 °F). The radial stress development is seen around the wellbore, and the magnitudes are in the range of -10,050 to 10,050 psi. 259

Figure 6.1.39 2D one-level slice of the tangential stress in psi with the slice taken in the XY-plane in the open-hole part of the wellbore for a cased concrete sample that was triaxially stressed at room temperature (70 °F). The tangential stress development is seen around the wellbore, and the magnitudes are in the range of -10,000 to 10,000 psi. 259

Figure 6.1.40 2D one-level slice of the \log_{10} radial stress with the slice taken in the YZ-plane pass through the casing for a cased concrete sample that was triaxially stressed at room temperature (70 °F). The radial stress development is seen around the wellbore and the magnitudes are in the range of 3.07 to 7.704 (\log_{10} psi). 260

Figure 6.1.41 2D one-level slice of the \log_{10} tangential stress with the slice taken in the YZ-plane pass through the casing for a cased concrete sample that was triaxially stressed at room temperature (70 °F). The tangential stress development is seen around the wellbore and the magnitudes are in the range of 2.775 to 7.386 (\log_{10} psi) 260

Figure 6.1.42 The temperature in the YZ-plane with deformation plot of unstressed concrete sample and the outside boundary temperature is the room temperature (70 °F). 261

Figure 6.1.43 2D one-level slice plot of the τ_{yz} shear stress in psi with the slice taken in the YZ-plane for an unstressed concrete sample with the 8-inch wellbore during the cryogenic treatment when the wellbore temperature is -321 °F and the sample temperature is 70 °F. Shear stress magnitudes are in the range of 0 to 1400 psi, in the opposite directions across the wellbore (compressional and tensional forces). 262

Figure 6.1.44 2D one-level slice plot of the τ_{xy} shear stress in psi with the slice taken in the XY-plane for an unstressed concrete sample with the 8-inch wellbore during the cryogenic treatment when the wellbore temperature is -321 °F and the sample temperature is 70 °F. Shear stress magnitudes are in the range of 0 to 5300 psi in opposite directions across the wellbore (compressional and tensional forces). 262

Figure 6.1.45 The temperature and deformation plot in the YZ-plane of an unstressed sandstone sample when the outside boundary temperature is the room temperature (70 °F). 263

Figure 6.1.46 The temperature with deformation plot in the YZ-plane of an unstressed sandstone sample with the outside boundary temperature of 200 °F. 264

Figure 6.1.47 2D slice plot of the τ_{xy} shear stress in psi taken in the XY-plane for an unstressed sandstone sample at room temperature (70 °F). Shear stress magnitudes are in the range of 0 to 8831 psi in the opposite directions across the wellbore (compressional and tensional forces). 265

Figure 6.1.48 2D slice of the τ_{xy} shear stress in psi taken in the XY-plane for an unstressed sandstone sample at reservoir temperature (200 °F). Shear stress magnitudes are in the range of 0 to 11,000 psi in the opposite directions across the wellbore (compressional and tensional forces). 265

Figure 6.1.49 2D slice of the τ_{xy} shear stress in psi taken in the XY-plane for a sandstone sample that was triaxially stressed (x = 4000 psi, y = 6000 psi, and z = 8000 psi) at room temperature (70 °F). Shear stress magnitudes are in the range of 0 to 4400 psi in the opposite directions across the wellbore. 266

Figure 6.1.50 2D slice of the τ_{xy} shear stress in psi taken in the XY-plane for a sandstone sample that was triaxially stressed (x = 4000 psi, y = 6000 psi, and z = 8000 psi) at reservoir temperature (200 °F). Shear stress magnitudes are in the range of 0 to 7200 psi in the opposite directions across the wellbore. 266

Figure 6.1.51 2D slice of radial stress in psi taken in the XY-plane for unstressed sandstone sample at room temperature. The radial stress development is seen around the wellbore, and the magnitudes are in the range of -10,000 to 9000 psi. 267

Figure 6.1.52 2D slice of tangential stress in psi taken in the XY-plane for an unstressed sandstone sample at room temperature. The radial stress development is seen around the wellbore, and the magnitudes are in the range of -4230 to 17,100 psi. 268

Figure 6.1.53 2D slice of radial stress in psi taken in the XY-plane for an unstressed sandstone sample at reservoir temperature (200 °F). The radial stress development is seen around the wellbore, and the magnitudes are in the range of -23,000 to 12,000 psi. 268

Figure 6.1.54 2D one-level slice of tangential stress in psi with the slice taken in the XY-plane for an unstressed sandstone sample at reservoir temperature (200 °F). The radial stress development is seen around the wellbore, and the magnitudes are in the range of -5600 to 22,000 psi. 269

Figure 6.1.55 2D one-level slice of radial stress in psi with the slice taken in the XY-plane for triaxially stressed sandstone sample at room temperature (70 °F). The radial stress development is seen around the wellbore, and the magnitudes are in the range of -26,500 to 3820 psi. 270

Figure 6.1.56 2D one-level slice of tangential stress in psi with the slice taken in the XY-plane for triaxially stressed sandstone sample at room temperature (70 °F). The tangential stress development is seen around the wellbore, and the magnitudes are in the range of -11,500 to 8780 psi. 270

Figure 6.1.57 2D one-level slice plot of the τ_{xy} shear stress in psi taken in the XY-plane for a triaxially stressed sandstone sample at room temperature (70 °F). The shear stress development is seen inside the stainless steel casing and around the wellbore. Shear stress magnitudes are in the range of 0 to 125,000 psi in opposite directions across the wellbore. 271

Figure 6.1.58 2D one-level slice plot of the τ_{yz} shear stress in psi with the slice taken in the YZ-plane for a sandstone sample that was triaxially stressed at room temperature (70 °F). The shear stress development is seen at the edge of the casing and the wellbore. Shear stress magnitudes are in the range of 0 to 120,000 psi in opposite directions across the wellbore of the sandstone sample. 272

Figure 6.1.59 2D one-level slice of the \log_{10} radial stress with the slice taken in the XY-plane. The radial stress development is seen around the wellbore and the magnitudes are in the range of 3.206 to 7.682 (\log_{10} psi). 272

Figure 6.1.60 2D one-level slice of the \log_{10} tangential stress with the slice taken in the XY-plane. The tangential stress development is seen around the wellbore and the magnitudes are in the range of 2.775 to 7.388 (\log_{10} psi)..... 273

Figure 6.1.61 2D one-level slice of the \log_{10} radial stress with the slice taken in the YZ-plane pass through the casing. The radial stress development is seen around the wellbore, and the magnitudes are in the range of 3.206 to 7.682 (\log_{10} psi). 273

Figure 6.1.62 2D one-level slice of the \log_{10} tangential stress with the slice taken in the YZ-plane. The tangential stress development is seen around the wellbore, and the magnitudes are in the range of 2.635 to 7.532 (\log_{10} psi)..... 274

Figure 6.1.63 Temperature in °F with deformed shape in the YZ-plane for the unstressed multi-layered shale sample with the outside boundary temperature of 70 °F. 275

Figure 6.1.64 Temperature in °F with deformed shape in the YZ-plane for the unstressed shale and the outside boundary temperature is the reservoir temperature (200 °F). 275

Figure 6.1.65 2D slice plot of the τ_{xy} shear stress in psi taken in the XY-plane for an unstressed shale sample at the bottom side of the wellbore at room temperature (70 °F). The shear stress development is seen around the wellbore. Shear stress magnitudes are in the range of 0 to 2100 psi in opposite directions across the wellbore. 276

Figure 6.1.66 Line cross section plot of the τ_{xy} share stress in psi of the shale sample at 70 °F, with line taken in the z-axis (red line inside the block-top right illustration). The share stress development has different magnitudes for each layer. 276

Figure 6.1.67 Line cross section plot of the τ_{xy} share stress in psi of the shale sample at 200 °F, with line taken in the z-axis (red line inside the block-top right illustration). The share stress development has different magnitudes for each layer. 277

Figure 6.1.68 Line cross section plot of the τ_{xy} share stress in psi of the stressed shale block ($x = 4000$ psi, $y = 6000$ psi, and $z = 8000$ psi) at 70 °F, the line is taken in the z-axis (red line inside the block-top right illustration). The shear stress development is seen around the wellbore, and its magnitudes are from 0 to 4900 psi in opposite directions across the wellbore. The shear stress has different magnitudes for each layer. 277

Figure 6.1.69 2D one-level slice of the radial stress in psi with the slice taken in the YZ-plane to show the variation in radial stress for each layer. The radial stress development is seen around the wellbore, and the magnitudes are in the range of -3197 to 2640 psi. ... 278

Figure 6.1.70 2D one-level slice of the tangential stress in psi with the slice taken in the YZ-plane. The tangential stress development is seen around the wellbore, and the magnitudes are in the range of -1469 to 8470 psi. 278

Figure 6.1.71 2D one-level slice of the radial stress in psi taken in the YZ-plane during the cryogenic treatment of the unstressed shale sample with the wellbore temperature of -321 °F and the boundary temperature of 200 °F. The radial stress development is seen around the wellbore, and the magnitudes are in the range of -3686 to 3413 psi. 279

Figure 6.1.72 2D one-level slice of the radial stress in psi with the slice taken in the YZ-plane. The radial stress development is seen around the wellbore, and the magnitudes are in the range of -22,957 to 691 psi. 279

Figure 6.1.73 2D one-level slice of the radial stress in psi with the slice taken in the XZ-plane. The radial stress development is seen around the wellbore, and the magnitudes are in the range of -22,957 to 691 psi. 280

Figure 6.1.74 2D one-level slice plot of the τ_{xy} shear stress in psi with the slice taken in the XY-plane for a triaxially stressed shale sample at room temperature (70 °F). The shear stress development is seen inside the stainless steel casing and also around the wellbore next to the casing. Shear stress magnitudes are in the range of 0 to 93,000 psi in the opposite directions across the wellbore. 281

Figure 6.1.75 2D one-level slice plot of the τ_{yz} shear stress in psi with the slice taken in the YZ-plane for a triaxially stressed shale sample at room temperature (70 °F). The shear stress development is seen at the edge of the casing and between the first and second layers from the top around the wellbore. Shear stress magnitude are in the range of 0 to 56,000 psi in the opposite directions across the wellbore. 281

Figure 6.1.76 2D slice plots of radial stress during the cryogenic treatment of a triaxially stressed shale sample ($x = 4000$ psi, $y = 6000$ psi, and $z = 8000$ psi) when the wellbore temperature is -321 °F and the sample temperature is 70 °F. (a) shows a one-level slice of the \log_{10} radial stress with the slice taken in the YZ-plane. (b) shows a one-level slice of the \log_{10} radial stress with the slice taken in the XZ-plane. The radial stress develops around the wellbore with the magnitudes in the range of 2.803 to 7.574 (\log_{10} psi). 283

Figure 6.1.77 2D one-level slice plots of tangential stress during the cryogenic treatment of a triaxially stressed shale block ($x = 4000$ psi, $y = 6000$ psi, and $z = 8000$ psi) when the wellbore temperature is -321 °F and the shale sample temperature is 70 °F. (a) shows a one-level slice of the \log_{10} tangential stress with the slice taken in the YZ-plane. (b) shows a one-level slice if the \log_{10} tangential stress with slice taken in the XZ-plane. The magnitudes are in the range of 2.67 to 7.364 (\log_{10} psi). 284

Figure 6.2.1 Failure envelope of Mogi-Coulomb Criterion (Aadnoy and Looyeh, 2011).	288
Figure 6.2.2 Schematic drawing for modeled geometry.....	289
Figure 6.2.3 Work flow chart of the simulation tool.	292
Figure 6.2.4 Pressure decay tests for shale Sample 1.	294
Figure 6.2.5 Temperature distribution in shale Sample 1 after the first cryogenic treatment.	295
Figure 6.2.6 Fractured grids distribution in shale Sample 1 after the first treatment.	296
Figure 6.2.7 Pressure distribution in shale Sample 1 after the second cryogenic treatment.	297
Figure 6.2.8 Temperature distribution in shale Sample 1 after the second cryogenic treatment.	298
Figure 6.2.9 Fractured grids distribution in shale Sample 1 after the second treatment.	299
Figure 6.2.10 Pressure decay tests for shale Sample 2.	301
Figure 6.2.11 Fracture planes of shale Sample 2.	301
Figure 6.2.12 Pressure distribution in shale Sample 2 after the first high pressure cryogenic treatment.	303
Figure 6.2.13 Temperature distribution in shale Sample 2 after the first high pressure cryogenic treatment.....	304
Figure 6.2.14 Fractured grids distribution in shale Sample 2 after the first high pressure cryogenic treatment.....	305
Figure 6.2.15 Pressure distribution in shale Sample 2 after the second round of cryogenic treatment.	306
Figure 6.2.16 Temperature distribution in shale Sample 2 after the second round of cryogenic treatment.....	307
Figure 6.2.17 Fractured grids distribution in shale Sample 2 after the second round of cryogenic treatment.....	308
Figure 6.2.18 Pressure decay test for shale Sample 3.....	310
Figure 6.2.19 Breakdown pressure of shale Sample 4.....	311
Figure 6.2.20 Faces of shale Sample 4 after high pressure gas fracturing.....	311
Figure 6.2.21 Fracture distribution in shale Sample 4.....	312
Figure 7.1.1 Well site location from Google Maps and corresponding east-west geological cross section provided by CEMEX. The cross section has the same length scale but a different depth scale.....	316

Figure 7.2.1 Double five-spot pattern for wellbore layout. Wellbores 1 and 8 were to be fractured with liquid nitrogen. 317

Figure 7.3.1 Wellbore vertical sketch. 318

Figure 7.3.2 Mock-ups of top cap assembly (left), pant-leg hydraulic packer (center back), and PVC shoe (right) for casing..... 319

LIST OF SYMBOLS

A	Cross section area of the sample
B_i	Biot number of the rock
C_{al}	Heat capacity of the aluminum inner vessel of calorimeter
$c_{p-sample}$	Specific heat of the sample
c_{p-w}	Specific heat of water
D	Diameter of the sample
D_n^i	Displacement discontinuities in normal direction at the crack tip element
D_s^i	Displacement discontinuities in shear direction at the crack tip element
E	Young's Modulus
F	Mass or heat flux
G	Shear modulus
K	Bulk modulus
K_{Ic}	Critical stress intensity factor
K_I	Stress intensity factor in the normal direction
K_{II}	Stress intensity factor in the shear direction
k	Mogi-Coulomb intercept
L	Thickness of the specimen
M	Constraint modulus
m	Mogi-Coulomb slope
m_{sample}	Mass of the sample
m_w	Mass of water
n	Total number of grid blocks
P	Maximum applied load
P_b	Break down pressure of formation rock
P_p	Formation pore pressure
$P_{wf,r}$	Bottom-hole flowing pressure assuming radial injection
Q	Quantity represents mass or energy per volume
\dot{Q}_{avg}	Average heat loss rate
q	Sinks and sources

T	Temperature
T_o	Reference or original temperature
V_n	An arbitrary subdomain of the system under study
V_p	Compressional wave velocity
V_s	Shear wave velocity
x_f	Half-length of an internal crack
ΔT_w	Temperature change of water
ΔT_{sample}	Temperature change of the sample
Δt	Time used to reach equilibrium
β	Linear thermal expansion of the rock
k	Total number of component
ρ	Density
$\sigma^{\Delta T}$	Thermo-elastic stress
Γ_n	Closed surface by which the subdomain is bounded by
σ_c	Uniaxial compressive strength
σ_{cr}	Stress at which a crack starts to grow
σ_{Hmax}	Maximum horizontal principal stress
σ_{hmin}	Minimum horizontal principal stress
σ_{kk}	Normal stress in kk direction
σ_{oct}	Octahedral normal stress
σ_t	Splitting tensile strength
σ_{tip}	Reservoir stress at the fracture tip
σ_v	Vertical stress
τ_{oct}	Octahedral shear stress
ε_{kk}	Strain in kk direction
ν	Poisson's ratio
\mathbf{d}	Displacement vector
\mathbf{f}	Body-force vector per unit volume
\mathbf{I}	Identity matrix
$\boldsymbol{\sigma}$	Stress tensor

$\boldsymbol{\varepsilon}$ Strain tensor
 \mathbf{n} A normal vector on surface element $d\Gamma_n$ pointing inward into V_n

1. Introduction

Cryogenic fracturing is a new concept that looks to expand and improve upon traditional hydraulic fracturing technology. The concept rests on the idea that cryogenic fluids, or cryogenes can induce fractures when brought into contact with a much warmer rock under downhole conditions. When liquid nitrogen (LN_2), which normally boils at $-195.8\text{ }^\circ\text{C}$ is injected into a rock with much higher temperature, heat from the rock will quickly transfer to the LN_2 . This rapid heat transfer creates a drastic thermal shock that causes the surface of the rock to contract. Temperature gradients from the near-surface cooled rock to the inner and warmer part of the rock, may cause the rock surface to eventually fail due to sufficient tension, inducing fractures orthogonal to the contact plane of the cryogen and the rock. Furthermore, since liquid nitrogen has a liquid-gas expansion ratio of 1:694 under the ambient condition (1 atm, $20\text{ }^\circ\text{C}$), the vaporized gas should, in a confined space, create a high pressure environment helping to propagate the fractures.

As hydraulic fracturing has changed the development landscape of unconventional oil and gas resources, waterless fracturing technologies have been actively sought due to concerns arising from both heavy water usage and intractable formation damage. Cryogenic fracturing offers a solution to these issues, as well as supporting the oil and gas industry's quest to improve both the pace and efficiency of hydrocarbon recovery. This new technology could potentially increase the effectiveness of fracturing while decreasing cost, enabling more formations becoming economically viable. Cryogenic fracturing therefore has the potential to drastically increase recoverable oil and gas reserves.

This report consists of eight chapters. In this chapter (Chapter 1), we present the background, motivations, and objectives of this project, and summarize the major research activities during the past three+ years' period. In Chapter 2, we review the literature on waterless fracturing technologies with focus on the fundamentals of cryogenic fracturing and a few previous field tests in oil and gas industry. In Chapter 3, equipment setups established for these investigations are presented, along with the experimental procedures of a series of tests designed and carried out for quantitative assessment of cryogenic

treatments. In Chapter 4, we present the results and analyses of cryogenic fracturing treatments on artificial and natural rock samples, demonstrating the effectiveness of cryogenic fracturing. Then, in Chapter 5, we present the CT scan techniques we optimized and improved for fracture detection and imaging inside rock samples, which enable us to visualize the internal fractures created by cryogenic treatments. In Chapter 6, we present the finite element and finite difference schemes specifically modified for modeling the cryogenic fracturing processes and corresponding simulation results, achieving very good agreement with the experimental results. In Chapter 7, we present the design of small scale field pilot tests, located on a Niobrara shale outcrop. In Chapter 8, we conclude our findings from this project and recommend future research directions.

1.1 Objectives

The objective of the project is to study, test and develop an innovative cryogenic fracturing technology for enhanced gas recovery (EGR) from low-permeability shale gas and tight gas reservoirs. Specifically, our objective is to develop well stimulation techniques using cryogenic fluids, e.g. liquid nitrogen or liquid CO₂, to significantly increase permeability in a large reservoir volume by initiating and propagating fractures surrounding vertical and horizontal wells. The new waterless technology has the potential to reduce formation damage created by current water-based stimulation methods, as well as minimize or eliminate water usage and the potential for groundwater contamination by fracturing fluid additives.

The research project mainly consists of the following tasks:

1. Review and synthesize literature on waterless fracturing technologies across academia and industry to assess the state of the technology and understand the fundamentals of generating fractures using a cryogenic fluid;
2. Design and develop a triaxial stress loading system capable of testing LN₂ fracturing on artificial and natural rock block samples in the laboratory;

3. Conduct cryogenic fracturing tests on acrylic, glass, concrete, sandstone, and shale block samples under triaxial stress conditions to investigate and evaluate the effectiveness and feasibility of cryogenic fluid on rock samples and determine how cryogenically induced fractures initiate and propagate in unconventional reservoirs;
4. Build mathematical models to simulate the process of cryogenic fracturing, including finite element and finite difference schemes; and measure rock properties of block samples to provide input parameters for the mathematical models; and
5. After proof of concept and demonstration of the potential effectiveness of cryogenic fracturing technology at the lab-scale, demonstrate field implementation and assess permeability improvement.

1.2 Major Achievements

We designed and built an integrated laboratory system incorporating liquid nitrogen delivery, triaxial stress loading, and data acquisition systems for unstressed and stressed cryogenic stimulation tests on cubic rock samples as large as 8 inches. With this system and another smaller one, we carried out cryogenic stimulation tests with acrylic cylinders, glass cubes, concrete cubes, sandstone, and shale rock samples while varying operational parameters. It was found that a minimum threshold flow rate of cryogen is needed to create the necessary sharp temperature gradient in the borehole. With direct observations, bubble leakage tests, temperature and pressure monitoring, CT scans, acoustic measurements, and gas breakdown pressure tests, cryogenic fracture growth, morphology and stimulation efficacy inside the samples were analyzed and compared.

The results demonstrate that cryogenic stimulation can create fractures in all types of rock cubes and deteriorate rock properties. Also, it was found that the generation of fractures is dependent on rock material properties. In weak concrete samples after submersion tests, more cracks were created near the surface than internally. Borehole stimulation on concrete samples indicated that longer curing time increases breakdown pressure, higher LN₂

injection pressure and rate, and water saturation are favorable for cryogenic fracturing. Tests on sandstone and shale samples confirm that LN₂ stimulation reduces the breakdown pressure of gas nitrogen fracturing, and as temperature warms up, the fractures narrow. Multiple cycles of treatments in shale samples achieve greater permeability enhancement after each cycle by both widening the existing fractures and creating new ones. Optimized and improved CT scanning techniques empowered us to visualize 50 μm-scale fractures with reasonable accuracy inside opaque shale samples. The cryogenic tests in transparent glass cubes as well as CT scans of post-stimulated shale cubes demonstrated different fracture patterns under different stress conditions. Particularly, under isotropic stress condition, visual examination and permeation tests indicated that fractures were difficult to initiate.

We developed finite element and finite difference mathematical models to account for heat conduction, thermal expansion or contraction, fluid pressure change, external stress change, and cryogenic fractures during the stimulation process. Simulation results from finite difference and finite element modeling agree very well with cryogenic fracturing in rock cubes, in terms of temperature distribution, fracture generation, and permeability enhancements.

On the basis of observations and measurements from our laboratory experiments, results from numerical simulation, and geological analysis of the Niobrara shale outcrop, we pinpointed a site on Niobrara shale outcrop in Lyons, Colorado and designed a double 8-spot well pattern for cryogenic stimulation tests. Borehole characterization and target interval evaluation were to be carried out before and after cryogenic stimulation to evaluate its effectiveness in fracturing the shale gas formation. This small-scale field test was not implemented at the request of the funding agency.

2. Literature Review

Without a doubt hydraulic fracturing has revolutionized the exploitation of unconventional oil and gas resources in the United States and around the world. Hydraulic fracturing technology for developing reservoirs of micro- and nano-Darcy permeability pumps highly pressurized fracturing fluids at high flow rate to create fractures in reservoir rocks, as pumping stops, the proppants suspended in the fracturing fluid prop open the complex network of fractures. These popped fractures increase the contact area between the reservoir and the wellbore, serving as highly conductive pathways for reservoir fluids to flow into the wellbore and be produced. Hydraulic fracturing and its associating technologies have drastically increased the United States' oil and gas production (Steward, 2013).

2.1 Concerns with Hydraulic Fracturing

Modern hydraulic fracturing technology is being applied world-wide in field, more than 90% of gas wells and 70% of oil wells drilled have been hydraulically fractured in recent years (Brannon, 2010). Hydraulic fracturing relies on water-based fracturing fluids, e.g. nowadays the most popular slick water, due to the general availability and low cost of water as well as its compatibility for proppants transport; however, a dependence upon water presents several major shortcomings. First, water can cause significant formation damage, which can occur as capillary end effects/relative permeability decrease and clay swelling stemming from imbibition and hydration, respectively. Formation damage mechanisms inhibit hydrocarbon flow from rock matrix into fracture network and thus impair production rates and recovery efficiency. Second, water use in large quantities may place significant stresses upon local water resources, especially for areas experiencing serious drought, as well as the local environments. For example, hydraulic fracturing of a horizontal well generally requires at least 2 million gallons of water (DOE, 2009), diverting water supply away from other purposes. Transportation of such huge amount of water to well sites on road infrastructure that was not designed for high traffic volumes, or construction activities associated with pipeline development can all have great impacts on

the surrounding community. Third, the high pressure downhole injection along with the chemical additives in water-based fracturing formulas (Sun, 2014), including slickwater and gel-based fracturing treatments, leads to contentious public concerns and political climate over induced seismicity and groundwater contamination. Finally, after fracturing treatment, large amount of flow back of fracturing fluids containing high concentration of suspended solids, salts, and hydrocarbons, etc. needs to be properly treated in order to avoid environmental pollution, which again lifts the cost of implementing hydraulic fracturing treatments (Hayes et al. 2014). All of these water related issues necessitate the research and development of waterless fracturing technologies.

2.2 Waterless Fracturing Technologies

A few waterless fracturing technologies have been developed and tested during the past several decades. Oil based/emulsion fracturing fluids are expensive and hard to be disposed, thus nowadays it is rarely used. Foams, by stabilizing CO₂, N₂ or their combination in liquid with the aid of surfactants, have been used since late 1960s for fracturing to reduce water usage and formation damage. The volume of gas in the foam system varies in the range of 53-95%, and its subsequent expansion during flow back would assist and accelerate the cleaning up of the liquid phase from rock matrix (Gupta, 2005). Generally, the higher the density and viscosity of foam, the better it carries proppants and the deeper it can be applied. However, foam is sensitive and fragile to high temperature, high salinity, and oil/condensate presence, therefore its efficacy is restrained by the reservoir conditions. Besides, foam fracturing is not completely waterless, it mitigates instead of eliminates the water related issues.

2.2.1 Explosive and Propellant Fracturing

One of those earliest explosive fracturing technologies focusing on stimulating low permeability gas reservoirs is the nuclear fracturing detonated in New Mexico and Colorado from 1967 to 1974 (Stosur, 1977). Tens of nuclear explosions for stimulating oil and gas wells were also carried out by USSR during that period. These peaceful nuclear attempts, though proved to be very successful in increasing natural gas production, were

abandoned due to prohibitive radioactivity accompanying the gas production. Starting in 1964 (Miller and Johansen, 1976), a series of explosive fracturing using nitroglycerin and TNT had been tested in small and shallow 5-spot well patterns to fragment oil shale formations for following in-situ retorting in Wyoming. Extensive fractures to a radius of 90 feet and significant airflow enhancement up to 800% were measured for different field tests by various evaluation techniques. Afterwards, Sandia National Laboratory carried out a series of high energy gas fracturing experiments by burning or deflagrating propellant in boreholes, aiming to fracture oil, gas, and geothermal wells. Multiple fractures have been obtained in wellbores with perforations (Warpinski et al. 1980; Cuderman et al. 1982; 1986). Rather than generating compressive shock wave, propellant deflagration rives rock matrix by producing slower propagating pressure peaks. Propellant fracturing is not capable of carrying proppants into fractures, instead, shear slippage or spalling of the fracture planes might provide support for fracture openings (Page and Miskimins, 2009).

2.2.2 Gelled Liquid Systems

Non-aqueous liquids, such as alcohol and liquefied petroleum gas (LPG), have long been recognized as promising fluids for fracturing unconventional reservoirs. Laboratory studies and field application of crosslinked gelled methanol-based fracturing fluid demonstrated higher regained permeability than crosslinked water-based gel and gelled oil (Thompson et al. 1992). Infinite solubility in water and favorable interfacial tension help achieve more efficient cleaning up and recovery of the flow back, thus increasing the permeability of the gas phase. In spite of these advantages, high safety risks are associated with methanol-based fracturing fluid operations due to its unfavorable properties, including low flash point of 11°C, wide explosive limits ranging from 6.7% to 35%, and higher specific gravity of the vapor phase (Hernandez et al. 1994). More recently, gelled liquefied petroleum gas has been gelled for efficient fracturing treatment and proppants transport, consistently demonstrating complete recovery of the fluid from the invaded zone after gel breaking. Also, superior to gas fracturing, gelled LPG has been applied to stimulate formations of a larger depth range from 750 feet to 11,500 feet (Tudor et al. 2009). Compared with water-based fluid, gelled LPG fracturing generated longer effective fracture half lengths and higher gas production rate due to much better clean up performance and much shorter flow

back period of less than 20 days (LeBlanc et al. 2011). Similar to methanol, LPG has potential safety risks with much lower flash point of $-104\text{ }^{\circ}\text{C}$, explosive limits of 2.37-9.5%, and larger specific gravity.

2.2.3 Gas Fracturing

Formation can be fractured by injecting a gas at pressures high enough to split the rock matrix, the most widely available and economical gas species is gaseous nitrogen (Freeman et al. 1983). In field application, nitrogen is first delivered as liquid, after heating up, gaseous is pumped into the wellbore. Shallow well stimulations using gaseous nitrogen had been conducted in Devonian shale formation in Ohio (Gottschling et al. 1985), about 60% of the injection was pure nitrogen for fracture propagation, then the latter 40% was mixing with sands to pop up the fractures generated. Since gas is of low density and high compressibility, gaseous nitrogen fracturing is primarily used in shallow unconventional oil and gas reservoirs less than 5,000 feet deep (Rogala et al. 2013). Besides, low density and viscosity limit the capability of nitrogen fracturing to transport proppants. Although self-propping by rubbing fracture surfaces is considered as a contribution for fracture opening at shallow depths, this possibility is wiped off for deep formations of tight cementation. Recently, in pace with the development of ultralight weight proppants, hundreds of gas fracturing jobs have been successfully performed in the Montney and Cardium plays in Canada (Canyon Technical Service, 2016). Without issues related to water usage and chemical additives, the economics and applicability of gaseous nitrogen fracturing has been well justified, as compared to foam and hydraulic fracturing (Kothare, 2013).

2.2.4 Supercritical CO₂ Fracturing

Reservoir temperature and pressure are normally higher than the critical temperature $31\text{ }^{\circ}\text{C}$ and pressure 7.38 MPa of CO₂ (Suehiro et al, 1996), hence CO₂ is supercritical while being used for fracturing oil and gas reservoirs. As compared to hydraulic fracturing, CO₂ is believed to be capable of creating more complex and extensive fracture networks due to its low viscosity, also CO₂ can hardly be trapped and poses no damage threat to formations, attributing to its miscibility with hydrocarbons (Middleton et al. 2015). In addition,

attraction between CO₂ molecules and the organic matter is stronger than that between methane molecules and the organic matter, which could result in enhanced desorption of methane during CO₂ injection into the shale formation (Cracknell et al. 1996). This preferential adsorption behavior and large adsorption capacity offers additional potential for CO₂ sequestration in fractured shale reservoirs during enhanced gas recovery or after the depletion of the reservoirs. To efficiently transport proppants into the fracture network, attempts of adding CO₂-philic solvents or creating gelled systems were tried and several successful formulas have been found (Enick, 1998). Several drawbacks are associated with CO₂ fracturing, such as searching for proper CO₂ sources and transportation, and post-stimulation separation of CO₂ from hydrocarbon stream.

2.3 Cryogenic Fracturing

Cryogenic fracturing is not a new emerging concept in petroleum industry, although not much research has been done in this area. King (1983) used gelled liquid carbon dioxide to stimulate tight gas sand formations instead of conventional fracturing fluids, such as water or oil. His primary motivation for using liquid carbon dioxide as stimulation fluid is to eliminate the effects of residual fluid in the stimulation of low permeability reservoirs, especially, for the low fluid return problem. After the liquid carbon dioxide treatment, the carbon dioxide would evaporate and return to the surface under controlled rates as a gas, resulting in a more rapid cleanup. Since the liquid carbon dioxide is gelled, it has enough capability for bringing proppants into the fractures to hold them open. He used this technique to treat several wells in field, all of which showed increased production rate after treatment. Unfortunately, there is no post fracturing production data over a long period available for these wells. Although the field tests showed successful results in King's research, the laboratory experiments were absent. The field test results cannot address whether the fractures are generated due to hydraulic effect or thermal effect from the gelled liquid carbon dioxide.

To further address the fracturing mechanism, McDaniel et al. (1997) conducted several laboratory liquid nitrogen submersion tests on coal samples to prove that cryogenic

fracturing may have an advantageous effect on gas production from tight, low-rate coal-bed methane wells. The coal samples experienced significant shrinkage during the submersion tests with creation of micro-fractures orthogonal to the surfaces which were exposed to cryogen. After further multi-cycle cryogen submersion tests, the coal samples were shattered into small pieces. After three cycles of submersion in liquid nitrogen and warming up to the ambient temperature, the coal samples were reduced to grain size particles. This research shows that cryogenic fracturing can effectively increase the production in coal-bed methane formation and may also have a promising effect on other rock formations. Besides the laboratory experiments, McDaniel et al. also applied cryogenic fracturing to 5 wells for field tests. However, the results from these wells were mixed: three of them experienced increased production rate, one experienced equivalent production and one experienced decreased production. Among the three wells with increased production, two of them had long term increment in production.

Grundmann et al. (1998) later conducted a cryogenic fracturing treatment in a Devonian shale well with liquid nitrogen. The well showed an 8% increment in the initial production rate when compared to a nearby offset well that underwent a traditional nitrogen gas fracturing treatment. However, there was no subsequent production information available for this well due to a logistical shut in. Although the result from this well may result from various reasons, such as anisotropic stress conditions and heterogeneous reservoir conditions over short distances, it showed no drawback with cryogenic fracturing technology as opposed to conventional hydraulic fracturing.

Although the reported field tests have shown some promising benefits from cryogenic fracturing, they did not identify the fracturing mechanisms at work in downhole conditions. In addition, there are also some concerns about the effectiveness of cryogenic fracturing, such as equipment used for injection cryogenic fluids and proppant carrying capability. Liquid nitrogen and carbon dioxide lack significant viscosity for carrying proppants into fractures at downhole conditions (Rudenko et al. 1934; Fenghour et al. 1998), which may lead to inadequate proppants in fractures to hold them open. Gupta and Bobier (1998) concluded that it is possible for cryogenic carbon dioxide to transport adequate amount of

proppants by increasing the velocity of the fluid. The turbulence accompanied by the high velocity permitted proppants to be carried efficiently from the wellbore to the perforations or even to the fractures. In addition, with the rubblization effect discovered in the research from McDaniel et al. (1997), the rock formations treated with cryogenic fluid may undergo a self-propping process. The rubblized rock may enable the fractures to stay open against in-situ stress after cessation of treatment pressure. Most of the work performed to date on cryogenic fracturing was simple laboratory or field work that does not show consistent results. Besides, none of the previous work actually reflects the fracture initiation by cryogenic fracturing under different states of stress and temperature. Therefore, there is a need to define the fracture mechanisms presented during the cryogenic fracturing processes under such conditions.

Without the issues associated with use of water-based fracturing fluids, cryogenic fracturing offers potentially greater fracturing capabilities. As for formation damage, there are completely no concerns for cryogenic fracturing, since nitrogen will not react with minerals inside the formation, neither as liquid nor as gas. In addition, there is also no liquid flowback after cryogenic fracturing for nitrogen gas is miscible with natural gas and has little retention when displaced by liquid hydrocarbons inside the formation. After cryogenic treatment, the formation can be regarded as intact from any kind of water or drilling fluid. Cryogenic fracturing can also minimize water consumption in stimulation process, which will save millions of gallons of water compared to traditional hydraulic fracturing operations. Once massively deployed, liquid nitrogen can be obtained by separating and compressing nitrogen gas from air by commercial air separation equipment at operation sites, which also minimizes the cost for transportation or pipeline development.

3. Experimental Designs

For cryogenic stimulation tests, there are multiple types of fracturing mechanisms and a few variable parameters to investigate and analyze. Thus, it is vital that all samples tested are similar to each other. To ensure this, most of the artificial and natural rock samples to be tested are processed into 8" × 8" × 8" blocks, an intermediate scale between cores and reservoirs. The types of artificial and natural rock samples tested include concrete, acrylic, glass, tight sandstone, and shale. Concrete samples were prepared by mixing Portland cement (commercial grade Portland Cement Quikrete Type I/II #1124) with coarse sand (**Table 3.1**) and water. The sand/cement and water/cement ratios are 2.5 and 0.55, respectively. They were frequently used in liquid nitrogen injection tests in view of the controllable mechanical properties based on numerous variables, such as material ratios, curing time, and the curing environment. We carried out different types of cryogenic stimulations by varying operational factors and experimental conditions.

Table 3.1 Sieve analysis of sand used for concrete preparation

Sand Mesh Size	Percentage
4	100.0
8	99.4
16	86.8
30	58.4
50	27.6
100	6.9
200	2.4

3.1 Experimental Setup

We considered two cryogenic stimulation plans: borehole thermal shock and thermal shock combined with borehole pressurization. In both plans, LN₂ is injected into 1" diameter boreholes, which are drilled 6 inches deep from the center of a face into the 8" cubic samples. Fracturing by borehole thermal shock only uses tensile stress resulting from sharp thermal gradient to initiate fractures. Additional borehole pressurization may keep cryogenic fractures open and help propagate fractures further into the rock matrix. We have designed and built an integrated heavy-duty experimental system, which empowers us to conduct borehole stimulation tests with and without pressurization, and borehole

stimulation tests with and without confining stress conditions that uses a triaxial loading system. These setups and the integrated equipment are presented below.

3.1.1 Setup for Borehole Thermal Shock

In this test setup, we are mainly concerned about cooling the borehole as rapidly as possible to maximize the thermal gradient across the contact surface. This is done by flowing LN₂ continuously through the borehole without pressurization. The basic scheme is illustrated in **Figure 3.1.1**. In this lab-scale experiment, LN₂ is pumped from the Dewar by pressure difference using a liquid nitrogen withdrawal device. LN₂ is transported by a vacuum-jacketed hose to the specimen, and injected into the borehole and then directed to an outlet at atmospheric pressure. A pressure transducer is attached to monitor the borehole pressure. In this thermal shock setup, pressure inside the borehole is approximately the same as the release pressure from the Dewar. Because this scheme does not generate much pressure, it can be applied to both stressed and unstressed samples. This experimental equipment employs specialized cryogenic-rated transport, control, and measurement systems. We have set up real-time monitoring and logging of various parameters inside the borehole including pressure, LN₂ consumption, temperature, and acoustic signals. For moderate increases in pressure, a structure that confines a packer in place was built to prevent LN₂ leakage through the packer.

3.1.2 Setup for Pressurized Borehole Stimulation

This system in **Figure 3.1.2** was designed and built for applying an increased injection pressure in the borehole to enhance the fractures initiated by thermal shock either during or after the LN₂ injection. The scheme used to force fluids into a borehole is connecting the system with a high pressure nitrogen gas (GN₂) cylinder. Also, the high pressure GN₂ cylinder can be switched between LN₂ dewar and the wellhead for pressurized LN₂ and GN₂ injection. The pressure release valve installed over the wellhead was set to help maintain a constant pressure inside the borehole. The LN₂ dewar was chosen for high pressure purpose as well. This system is applicable for both unconfined rock samples and confined ones with triaxial stress loading. In addition, the real-time monitoring and data acquisition system is completely compatible with this setup.

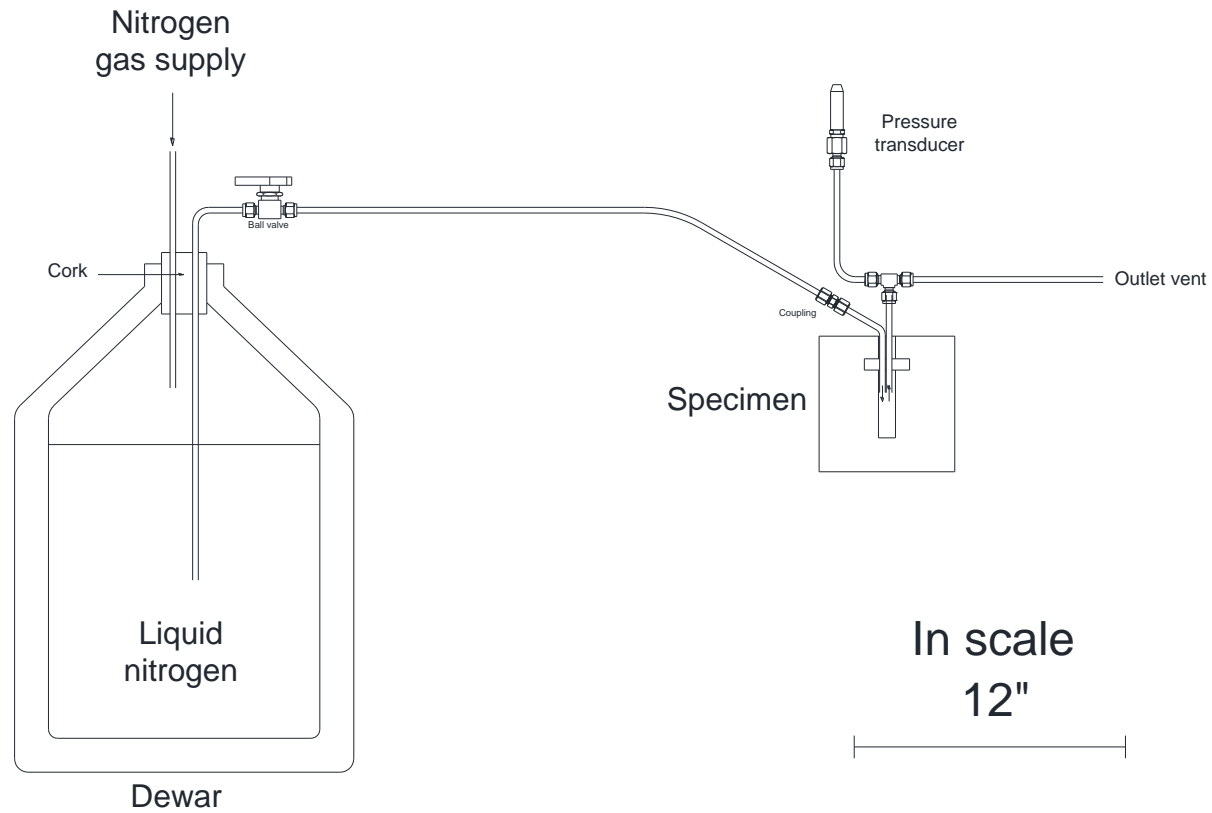


Figure 3.1.1 Overall schematic drawing for cryogenic thermal shock experiments without borehole pressurization. Low pressure GN₂ is used to force LN₂ from the dewar.

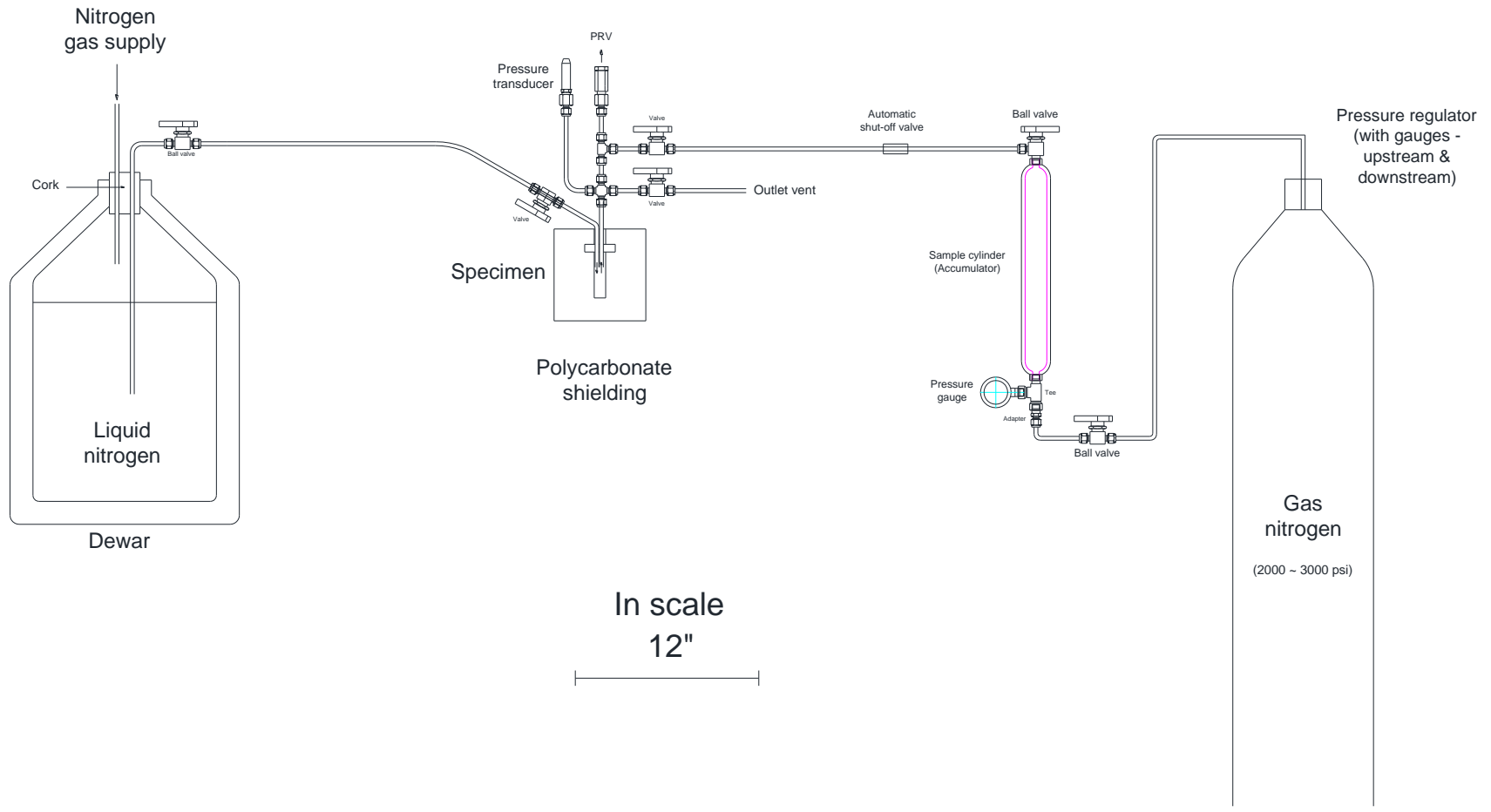


Figure 3.1.2 Overall schematic drawing for cryogenic stimulation experiments with borehole pressurization. Low pressure GN₂ is used to force LN₂ from the dewar, high pressure GN₂ is used for pressurization and fracturing.

3.1.3 Triaxial Stress Loading System

We built a triaxial stress loading system to simulate in situ reservoir confining stress conditions. The system operates a press and two hydraulic cylinders to load up to 6500 psi vertically and 4500 psi horizontally on 8" × 8" × 8" blocks (**Figure 3.1.3**). By controlling the hydraulic air pumps for vertical and horizontal loading (**Figure 3.1.4**), quasi-constant stresses can be kept during the cryogenic stimulation tests. The triaxial stress loading system at LBNL applies constant stress to smaller samples, however has custom platens even allowing visualization through as many as two faces.

Most other commercially available triaxial loading rigs use membrane packs that are connected to the hydraulic power system, and are closed systems where the confining structure and loading pad, or piston, encloses the specimen. Our equipment is a straightforward open system where all three loading drivers and the specimen blocks are exposed and assembled inside the containment ring (**Figure 3.1.5** and **Figure 3.1.6**). In addition, three heavy-duty ratchet tie-down straps (5000 lbs. each) surround the containment for extra safety. This open system is versatile, because it is easier to observe internal processes during the experiment and we can act immediately upon an accidental internal problem, e.g. cryogen spill. This also makes the system much less expensive than hydraulic power systems contained by flexible membrane bladder. The simple, yet flexible design can also easily be converted for hydraulic fracturing experiments.

One expected disadvantage of this system is that it is not ideal for rock specimens with uneven surfaces or tilted surfaces, although the pistons can accommodate limited tilt. Uneven surfaces or significantly tilted surfaces will create uneven stress distribution. At high stress, this may fracture the rock. While we are trying to prepare even and untilted specimens as much as possible, the effect of uneven and/or tilted surfaces can be alleviated by inserting flexible rubber pads to evenly distribute stresses. The other disadvantage that both the CSM and LBNL triaxial stress setups have is the inability to apply a pore pressure. Few systems exist that allow realistic pore pressures, temperatures, stresses, and the application of a cryogen at this moment.

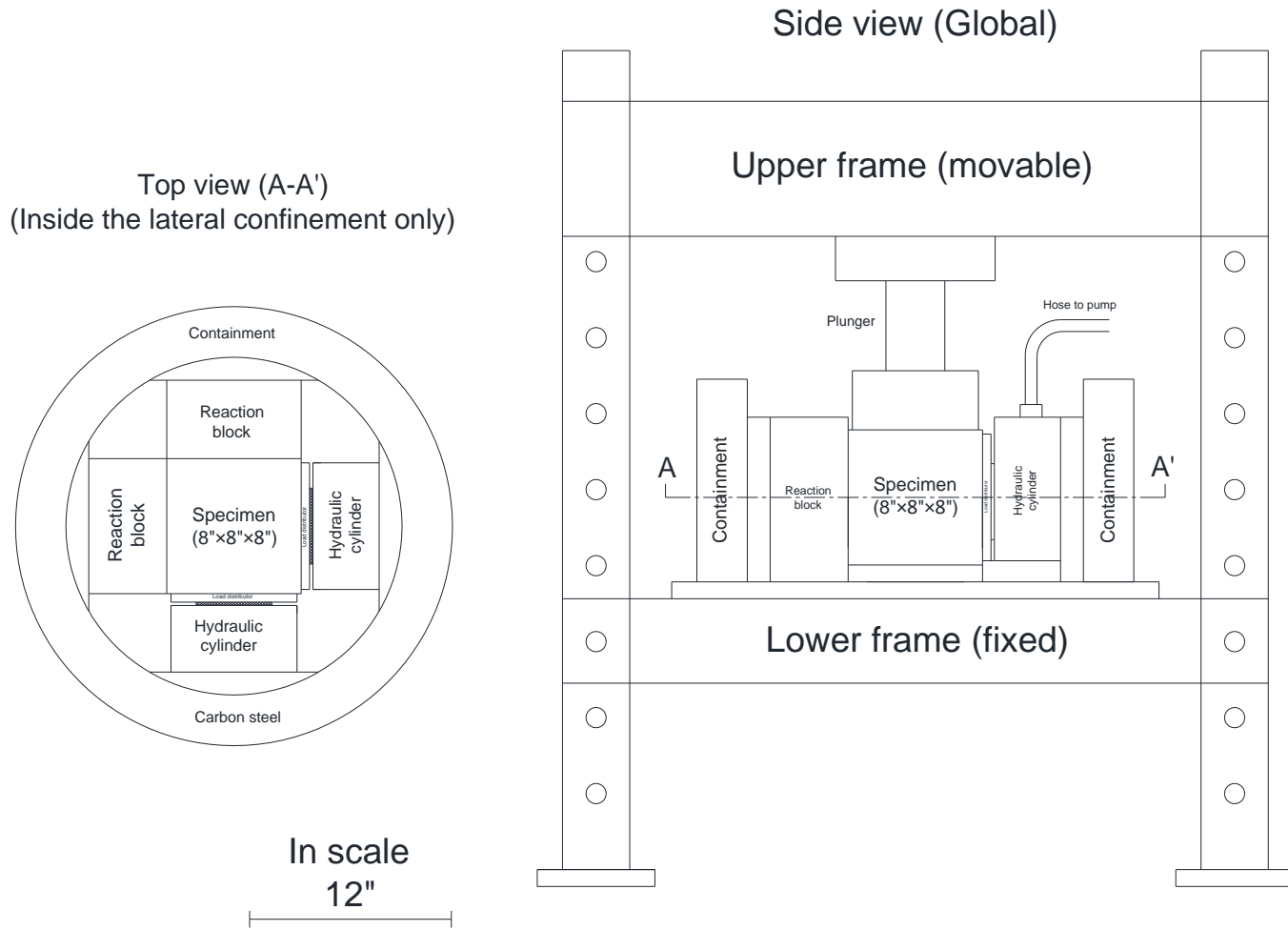


Figure 3.1.3 Triaxial stress loading system designed for cryogenic fracturing experiments.

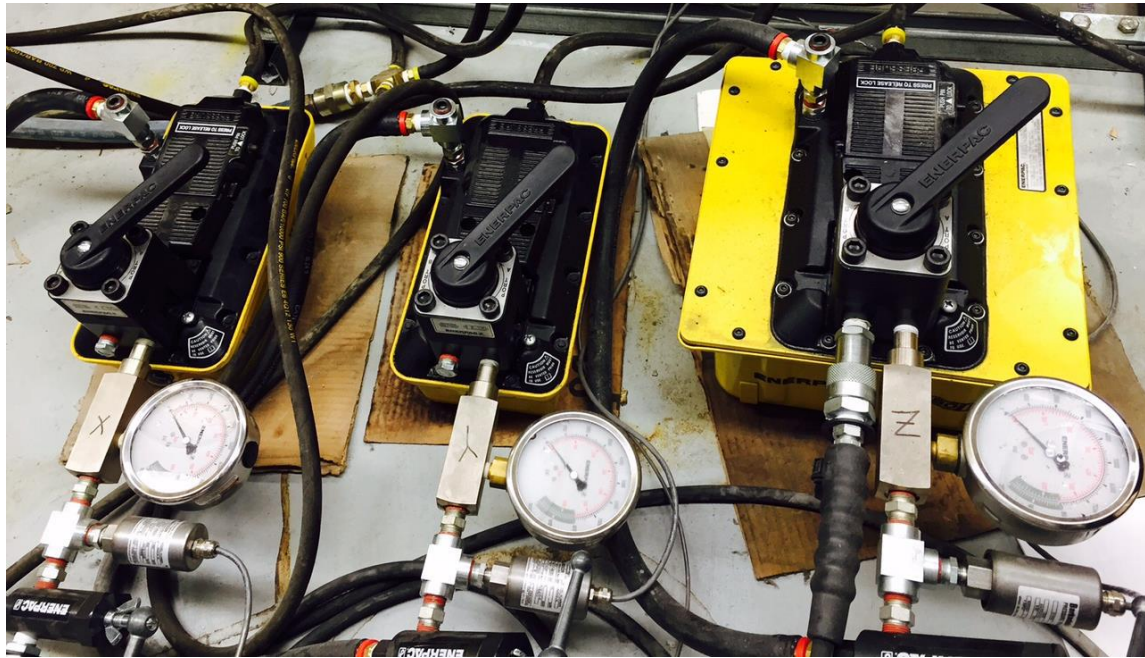


Figure 3.1.4 Three hydraulic air pumps.

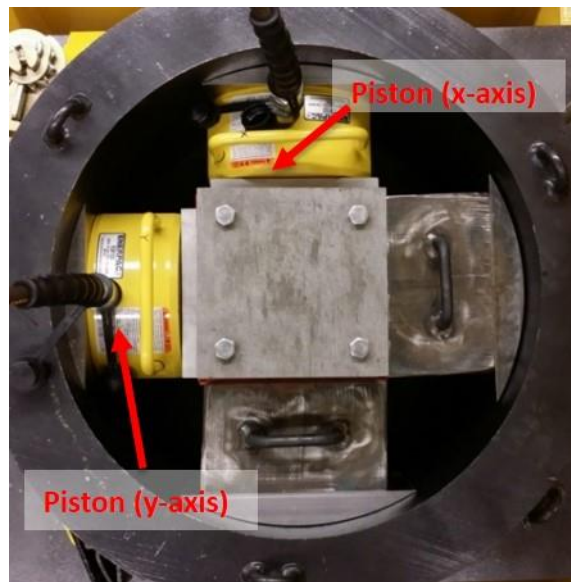


Figure 3.1.5 Pistons in horizontal directions within the containment ring.



Figure 3.1.6 Vertical piston on rolling frame and the containment ring.

3.1.4 Integrated Experimental System

The abovementioned borehole LN₂ injection system was integrated with the triaxial stress loading system, meanwhile a real-time temperature and pressure monitoring capability was built by installing a data logger with temperature sensors and pressure transducers. **Figure 3.1.7** shows a complete view of the entire equipment. One practical advantage of our system is that the vertical loading frame can be easily removed by rolling it away after unlocking it from the bed. This ability provides a user with space to work on specimens and inside the containment.

The boiling point of liquid nitrogen at atmosphere is $-195.8\text{ }^{\circ}\text{C}$ ($-320.4\text{ }^{\circ}\text{F}$), and the gas nitrogen used was always stored in cylinders at room temperature ($\sim 21.1\text{ }^{\circ}\text{C}$ or $70\text{ }^{\circ}\text{F}$). Therefore, temperature sensors chosen for our experiments are Type T thermocouples, which are made of copper and constantan and suited for temperature measurement in the range of -200 to $350\text{ }^{\circ}\text{C}$ (-380 to $392\text{ }^{\circ}\text{F}$). There are up to ten thermocouples that can be used depending on different experiments. Generally, one thermocouple is attached to the borehole wall inside wellbore in samples. A second one is suspended inside wellbore. The others are attached to the surface of samples or are used for additional temperature data collection at flexible positions.

Pressure transducers are used to monitor pressure inside wellbore of samples, and injection gas pressure in a gas accumulator. The pressure transducers used are rated up to 3000 psi and connected to the data acquisition system, which can provide real-time reading or monitoring while testing. The pressure transducer connected to wellbore is placed about 5 inches higher than the top surface of the rock sample, to avoid liquid nitrogen contacting it thus resulting in inaccurate reading.

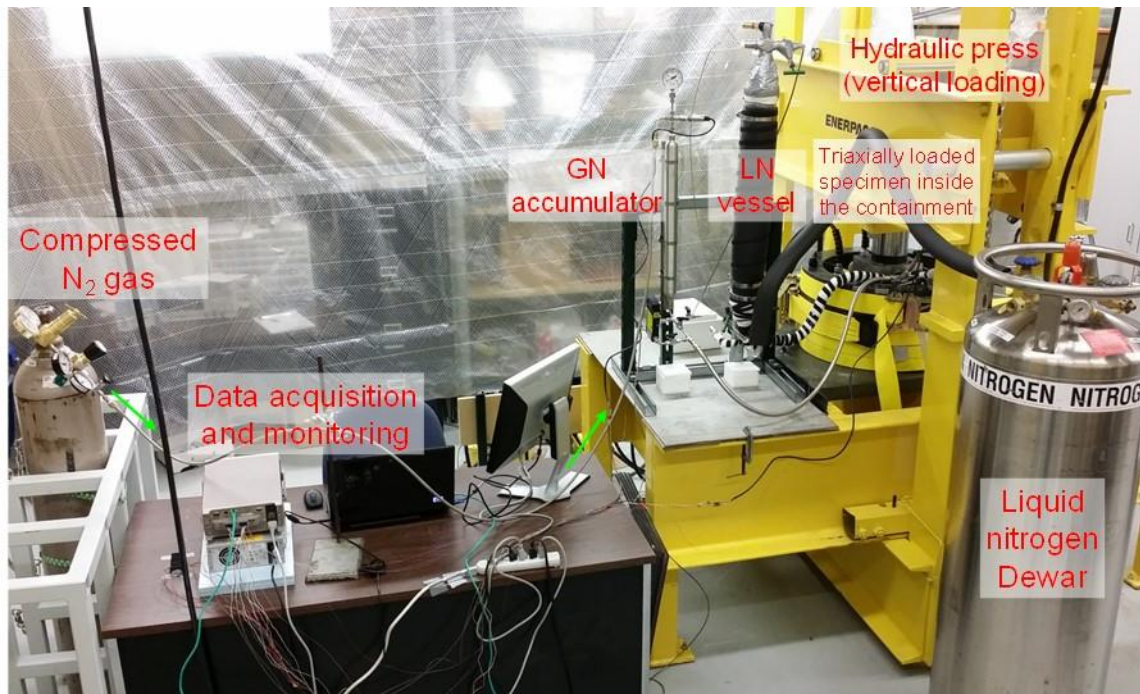


Figure 3.1.7 Integrated laboratory equipment for cryogenic fracturing experiments.

3.1.5 Casing and Wellhead Installation

With the exception of submersion tests, stainless steel casing was cemented to the borehole to facilitate LN₂ injection and vertical stress loading. The annulus between the borehole and the casing is filled with epoxy, leaving 2" open hole section at the bottom of the 6-inch deep borehole. Then, a packer was designed and assembled to accommodate inlet and outlet tubings and seal the casing from the outside. Keeping the casing in place is important in our fracturing experiment. At low borehole pressure conditions in unstressed rock specimens, a packer-confining structure can be readily applicable (**Figure 3.1.8**). A packer can be attached to the top of a borehole with epoxy and then slight loading can be applied by the confining

device. The degree of confining depends on the expected level of pressure inside the borehole. This device has been used for unconfined specimens and has been controllable and repeatable. To adapt to the triaxial loading system where the existence of an external rig is undesirable due to loading drivers, we designed and manufactured a recoverable wellhead coupling the inlet and outlet tubings.

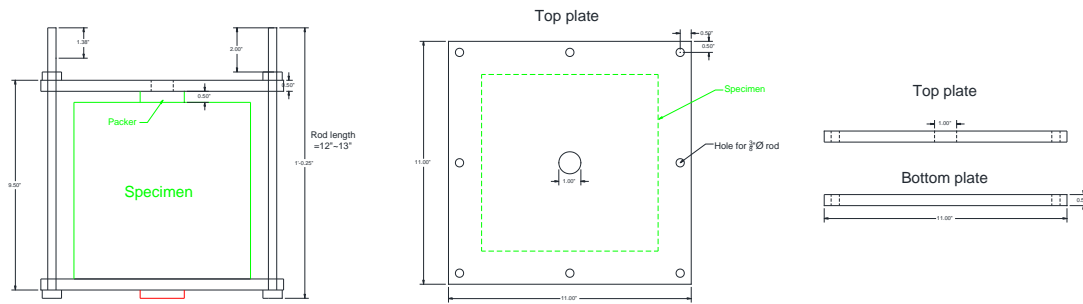


Figure 3.1.8 Packer installation using a confining structure.

3.2 Experimental Procedure

To investigate the fracturing mechanisms and characteristics of cryogenic stimulation, we proposed different types of experiments to investigate the effect of varying experimental parameters and conditions on the fracturing processes. Additionally, to better evaluate and illustrate the efficacy of cryogenic fracturing, we established several kinds of measurement methods, including the pressure decay test, acoustic measurements, and CT scanning.

3.2.1 Submersion Tests

As preliminary tests, the setup of semi-submersion and full-submersion experiments is quite simple. To apply a strong constant temperature gradient across a rock block, an 8" cubic concrete block was set on supports in an open-top insulated enclosure, as shown in

Figure 3.2.1. The enclosure was filled with liquid nitrogen up to the midline of the concrete block. The liquid nitrogen level was maintained for 30 minutes and then allowed to boil off. In the full-submersion, one dry and one wet 2.7" × 2.5" × 1.5" concrete blocks were completely immersed into the liquid nitrogen in an insulating container for 50 minutes. The blocks were not removed until they equilibrated thermally with ambient temperature. Each

side was labeled and photographed at high resolution before and after the test. The images were carefully aligned and digitally subtracted from one another to highlight the differences.

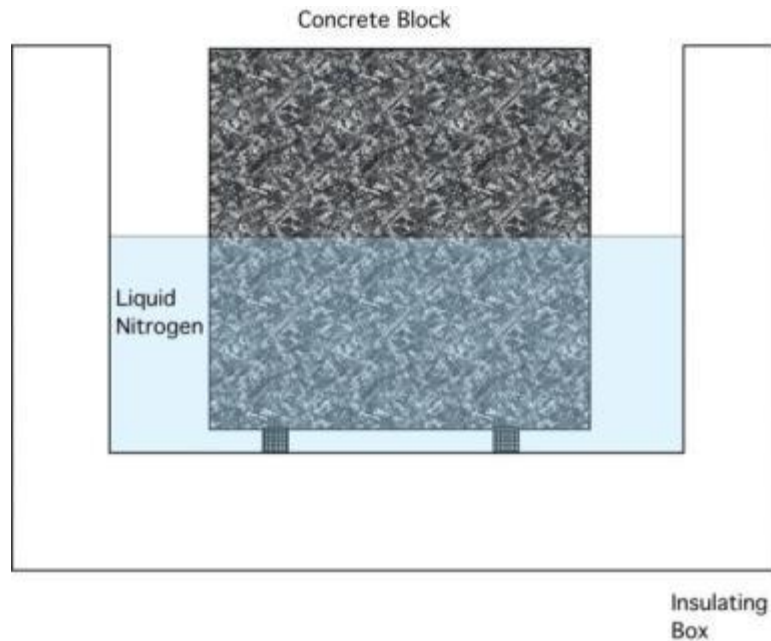


Figure 3.2.1 Setup for semi-submersion tests.

3.2.2 Borehole Thermal Shock

With the outlet open to atmosphere, we cool the borehole as rapidly as possible by flowing LN_2 continuously through the borehole. LN_2 is pumped out of the storage dewar by pressure difference using a liquid nitrogen withdrawal device. Then it is transported through a vacuum-jacketed hose to the specimen, and injected into the borehole and then directed to an outlet open to the atmosphere. A pressure transducer is attached to the wellhead to monitor the borehole pressure, which is approximately the same as the release pressure of the dewar. During the thermal shock tests, several thermocouples were attached to the inlet, borehole, outlet, and sample surface to monitor the dynamic evolution of temperatures. Before and after the test, the dewar was weighed for LN_2 consumption, and acoustic signals were measured for quantitative evaluation of fracture generation inside the blocks.

3.2.3 Pressurized Borehole Stimulation

To enhance the fractures created by thermal shock, we applied pressure to the borehole during and/or after the LN_2 injection. During LN_2 injection, GN_2 of constant pressure was used to

drive the LN₂ from dewar to the borehole. While after LN₂ injection, high pressure GN₂ is directly injected into the borehole. Borehole pressurization was applied for both unconfined and confined cubic rock samples stressed by the triaxial loading system. Unconfined specimens cannot sustain much borehole pressure, as fissures were observed in weak concrete due to pressurization at pressures lower than ~100 psi.

3.2.4 Borehole Stimulation with Triaxial Stresses

Borehole stimulation tests with triaxial stresses were conducted with our integrated experimental setup described in **Sections 3.1.2** and **3.1.3**. The 8” cubic rock samples are first placed in the containment, with stainless steel blocks and rubber/teflon pads placed between the cube faces and the pump piston. Then, on top of the rock sample, steel blocks manufactured to fit the wellhead are placed. By gradually increasing the hydraulic air pumps, desired stresses in x, y, and z axes can be achieved. Next, cryogenic stimulation tests with or without pressurization can be carried out by operating the LN₂ delivery system. At the same time, temperature, pressure and stresses are logged and displayed as curves. Before and after the cryogenic stimulation tests, pressure decay tests are conducted for quantitative permeability comparison.

3.2.5 Pressure Decay Tests

The pressure decay tests are performed to evaluate the permeability of rock samples. We performed a pre-stimulation pressure decay test on all samples and for each experiment in which rock samples were not broken or shattered during liquid nitrogen treatment, we performed a post-stimulation pressure decay test. These tests provide the rate of pressure decay, indicating the changes in effective air permeability of the sample in the vicinity of the borehole. Pressure decay tests were performed by pressurizing the borehole to 175 psi, shutting in the wellbore, and allowing the pressure to slowly draw down.

3.2.6 Acoustic Measurements

Acoustic measurements give the velocity of compressional and shear waves inside various materials. By comparing these velocities before and after performing the LN₂ treatment, the existence of fractures within the rock sample medium can be qualitatively proven.

Additionally, with known rock density, the dynamic elastic modulus (Young's modulus) and Poisson's ratio can be calculated from these two velocities. The equipment used here was an OLYMPUS pulser and a DSO-X 2004A digital oscilloscope (**Figure 3.2.2**). **Figure 3.2.3** shows a schematic of the experimental setup for acoustic measurement, **Figure 3.2.4** shows the typical waveform that is captured in the acoustic tests (Cha and Cho, 2007).

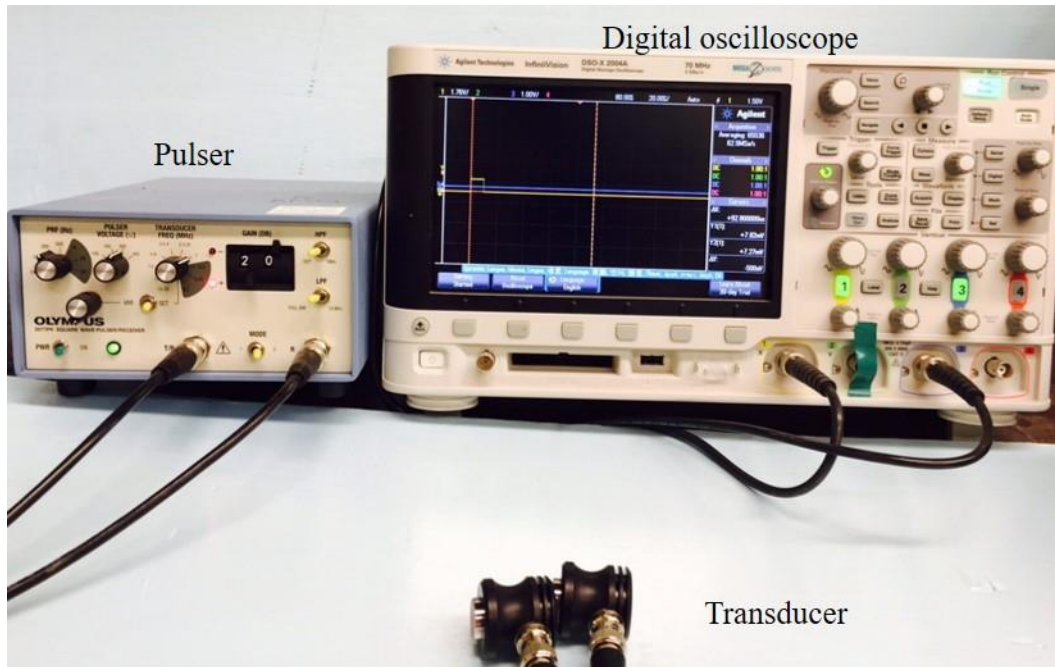


Figure 3.2.2 The pulser and the digital oscilloscope used for acoustic measurements.

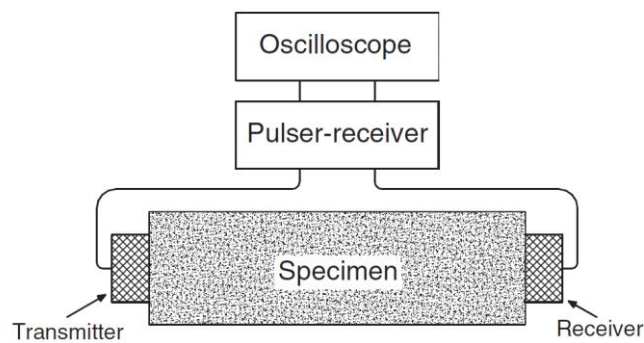


Figure 3.2.3 Experiment setup for acoustic measurements.

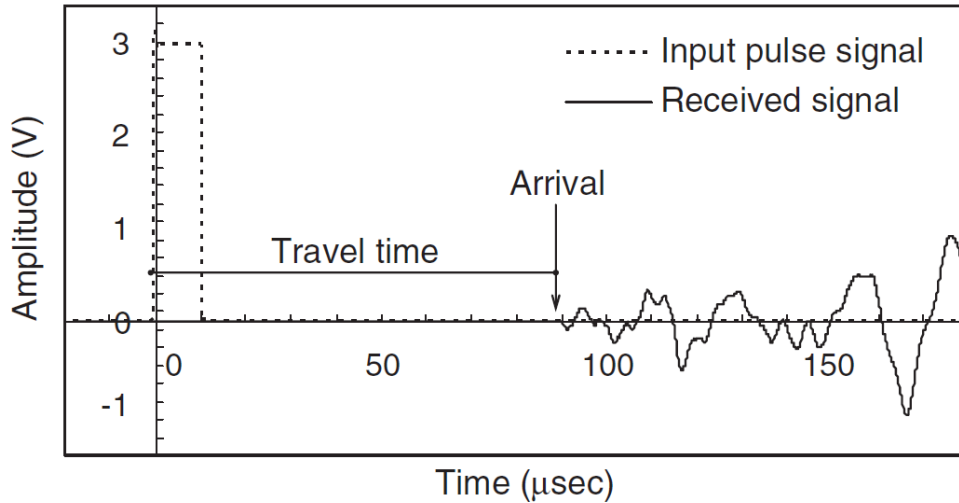


Figure 3.2.4 Typical input pulse and received signals from acoustic tests.

3.2.7 CT Scan

Computed tomography (CT) uses X-rays to image details of the structures inside rock samples. This instrument has been used for many years in the medical, scientific, and industrial fields to obtain three dimensional images of the internal structure of people or objects. CT scanning demonstrates value as a reliable tool in analyzing natural fractures (Bergosh et al. 1985). The scanner consists of a rotating X-ray source and rows of detectors which circle the block sample lying on a moveable table. **Figure 3.2.5** shows the CT scanner used at CSM that was provided by Weatherford Laboratory in Golden, Colorado.

The major advantage of the CT scanner in detecting fractures is that it's non-destructive. However, for the 8" cubic rock samples used in this study, this type of conventional CT scanner encountered difficulties in detecting thermally induced fractures, due to its low resolution around 0.3 mm. The minimum fracture aperture detectable is smaller than this however. Additionally, the size and the shape of the block, as well as the steel casing cemented in the rock block could have some negative effects on the scan.

In consideration of the limitations of conventional CT scanners, we tried to optimize the operational parameters and integrated new techniques into it to improve its capability in

imaging microscale cryogenic fractures inside rock samples, which were mainly done at LBNL. These are explained in details in Chapter 5.



Figure 3.2.5 The CT scanner used in this study.

3.3 Summary

Starting from submersion tests of concrete samples into liquid nitrogen, we continued to simply pour liquid nitrogen into boreholes drilled in the concrete samples to observe cryogenic fractures. With positive observations, we further extended the borehole thermal shock tests to mimic the possibilities in field application by circulating liquid nitrogen in and out, and injecting liquid nitrogen into the borehole under increased pressures. Then, considering the in-situ stress conditions in real reservoirs, we designed and built a heavy-duty triaxial stress loading system to apply analogous stresses to rock samples. By incorporating the liquid nitrogen delivery, triaxial stress loading, and real-time data acquisition systems, we eventually established an integrated experimental system that is suitable for conducting various cryogenic fracturing tests with and without triaxial stresses on 8” cubic rock blocks. In addition, at LBNL, we designed and built a similar but smaller equipment consisting of liquid nitrogen delivery and triaxial stress loading systems. This

equipment has an observation port, which allows us to directly see the cryogenic fracturing processes in transparent samples (acrylic and glass) under triaxial stress conditions.

With the integrated equipment, we formulated procedures for a variety of experiments conducted on different types of rocks, borehole injection pressure, initial temperature, water saturation, and triaxial stress conditions. To characterize the cryogenic fractures generated inside the rock samples, we adopted CT scans, pressure decay tests, acoustic measurements, and breakdown tests and modified them for better qualitative and quantitative evaluation of the cryogenic fracturing efficacy. All of these evaluation methods are capable of detecting cryogenic fractures created in the rock samples after liquid nitrogen treatments.

4. Experimental Results and Analyses

Numerous tests have been conducted on different types of artificial and natural rock: concrete, acrylic, glass, sandstone, and shale. The concrete samples were made in the laboratory, transparent acrylic and glass samples are commercial products, while sandstone and shale samples are acquired from mining companies. **Table 4.1** shows generic values of the available mechanical and thermal properties of the samples.

These samples are tested under different stresses and temperature scenarios including unconfined and confined tests. More test details are presented later in this section. Cryogenic stimulations carried out on transparent acrylic and glass samples enable us to visualize the fracture morphology and its relation to stress conditions, as are also reported in the following sections.

Table 4.1 Mechanical and thermal properties of rock samples

Rock type \ Properties	Concrete	Sandstone	Shale
Density (gm/cc)	2.24-2.4	2.2-2.8	2.4-2.8
Compressive strength (psi)	2900-5800	2900-25,000	720-14,000
Tensile strength (psi)	290-720	580-3600	290-1400
Young's modulus (10^6 psi)	2-6	0.15-3	0.15-10
Poisson's ratio	0.20-0.21	0.21-0.38	0.20-0.40
Shear strength (psi)	870-2500	1200-5800	440-4400
Specific heat capacity (kJ/kg·K)	0.75	0.92	0.88-1.09

4.1 Submersion Tests of Concrete

We conducted two types of submersion tests. One is semi-submersion, where liquid nitrogen is filled up to the midline of the concrete block; the other is full-submersion, in which a smaller concrete sample is completely immersed into the liquid nitrogen.

4.1.1 Semi-Submersion Test

Figure 4.1.1 shows the results of subtracting the before and after images (difference images). The differences for the top and bottom (shown at the top and bottom) do not show any apparent fractures. The four vertical faces that were semi-submerged show a fracture along the center all the way around the block (light shaded crack). This indicates that the block was

fractured due to the application of the thermal gradient. No obvious indication of block fracturing was observed during the 30-minute test and no obvious cracking sound was heard.

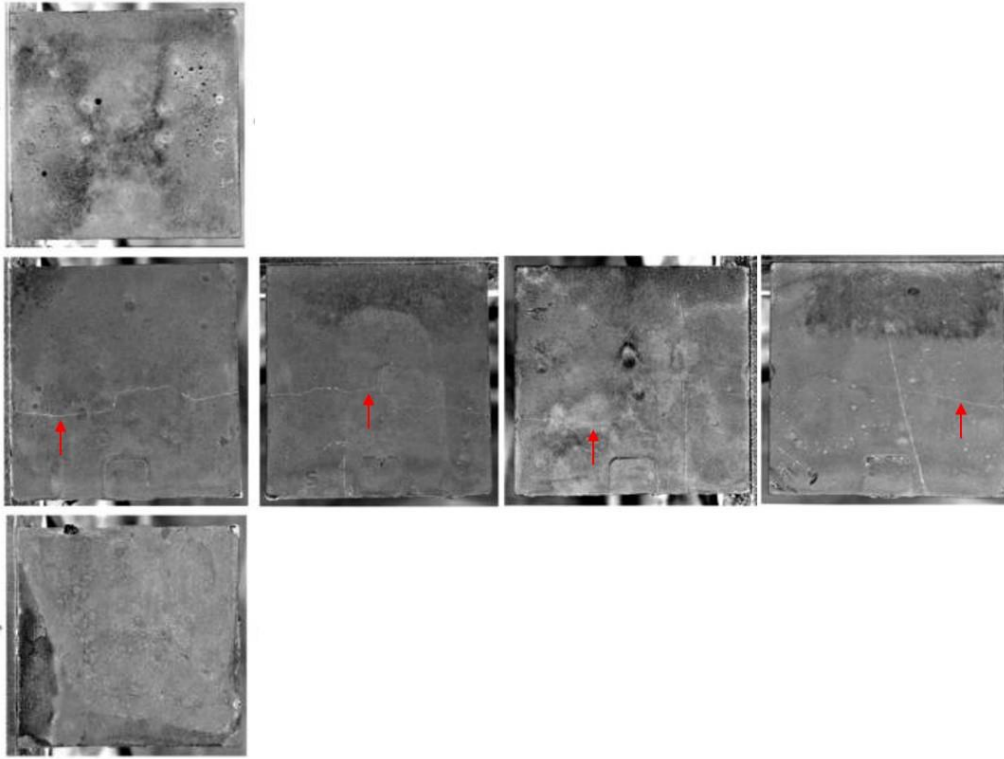


Figure 4.1.1 Subtracted before and after images of block sides after semi-submersion test.
Top row-Top side; Middle row-four vertical faces from front turning to the right side;
Bottom row-Bottom side. Cracks are indicated by the red arrows.

Following the semi-submersion test, the block was CT scanned using a modified G.E. LightSpeed 16 medical CT scanner. **Figure 4.1.2** shows a vertical cross section indicating the presence of a fracture (darker) emanating from both sides and progressing towards the center of the block.

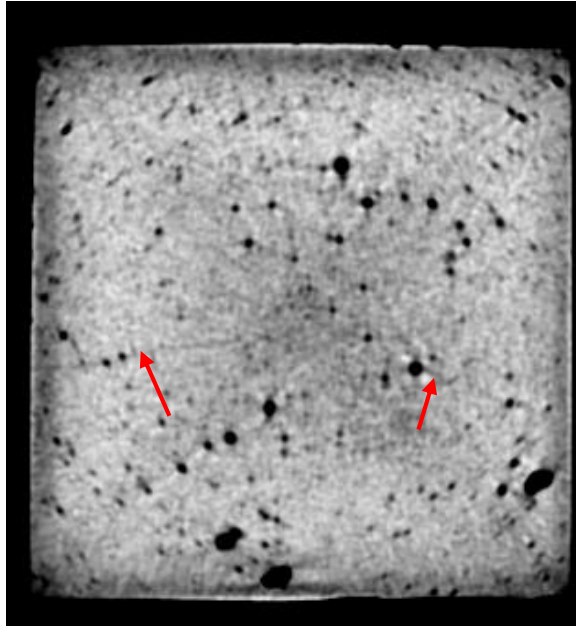


Figure 4.1.2 CT scan showing a vertical slice of the block from the semi-submersion test. Arrows point to fractures in the block resulting from cryogenic fracturing.

4.1.2 Full-Submersion Test

The dry concrete sample was immersed in LN₂ for 50 minutes, the sample was then left for 4 hours to finish evaporating and equilibrate with room temperature. The concrete block tested showed apparent shrinkage while immersed. After the test, the main fractures formed polygonal shapes around the exterior of the dry sample. This behavior indicates that the block was fractured due to the application of the thermal gradient.

Figure 4.1.3 shows the images of the top side of the dry concrete block before and after the submersion test. The image marked as “after” was taken immediately after the cryogenic test when the fractures were clear and easily observed by the naked eye. The induced fractures formed a polygonal network. Since there are no stresses applied during this test, the block was fractured purely due to the application of the thermal shock. All faces of the block had newly created fractures and/or extensions of existing fractures. **Figure 4.1.4** shows a new fracture on face (1). Next to it is a pre-existing fracture that was extended vertically. The scale of these pictures is 1 mm. After the sample rose back to the room temperature, some fractures were observed to close.

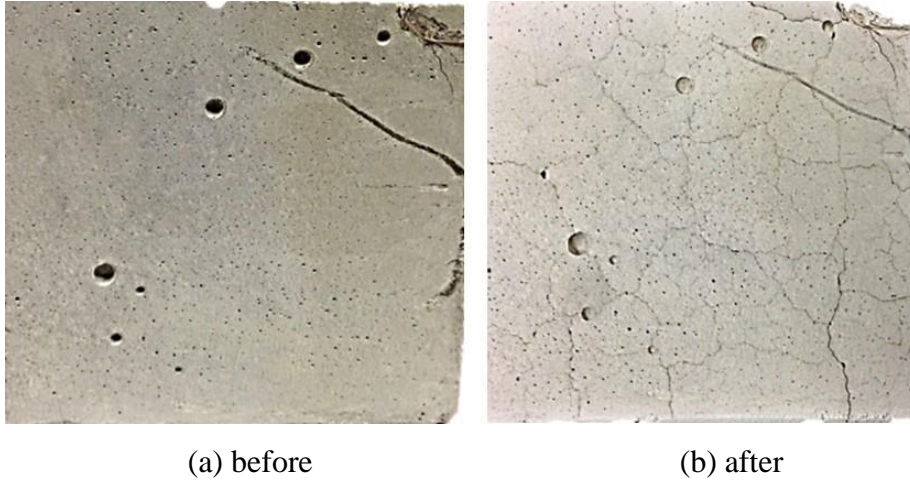


Figure 4.1.3 Top surface of the concrete block before and after the full-submersion test.



Figure 4.1.4 Images of the concrete block Face 1 after the full-submersion test show both the extension of existing fractures and the creation of large, new fractures.

Another wet concrete block, cured in the same environment with the dry one, was placed in water for one week. Then it was immersed into liquid nitrogen for 50 minutes and left for 4 hours to finish evaporating and equilibrate with room temperature. As was seen with the dry sample, the concrete block tested showed apparent shrinkage while cold and several new fractures were identified, and similar fractures were formed with polygonal shapes around the exterior of the block. However, these polygonal shapes were bigger in size compared to those on the dry sample.

Figure 4.1.5 shows the before and after images of the top side of the wet concrete block. The pictures of the block were taken immediately after the cryogenic test. Fractures were created extensively in big polygonal shapes, and as before in the case of the dry sample, due to the absence of other applied stresses these fractures had to be created from thermal shock. When comparing the samples, the dry sample has more fractures that propagate away from the block edges, while the fractures on the wet sample were created near the edges. This may have been due to the effect of ice formation in the pores of the wet sample. Ice formation would only occur in the pores on the outer layer of the sample, causing additional stress on the block. The freezing of outer layer caused lateral expansion, resulting in shear fractures parallel to the exposed surfaces (Kneafsey et. al. 2011).

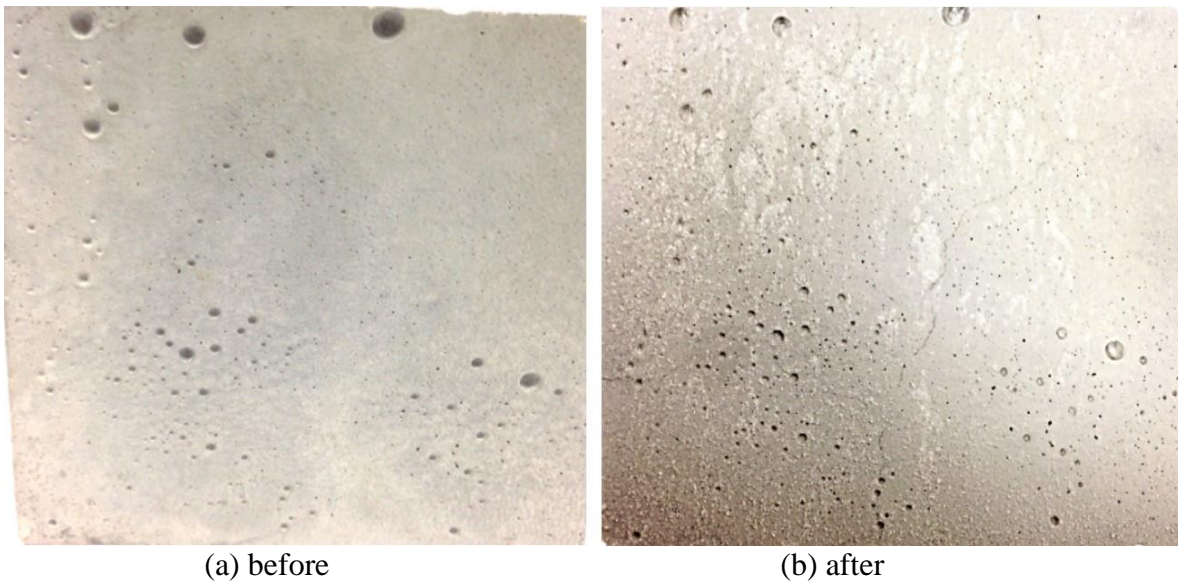


Figure 4.1.5 Top surface of the wet concrete block after the full-submersion test.

Acoustic measurements were conducted on the dry concrete samples used in the submersion tests to see the changes in acoustic velocities after the cryogenic treatment. The location of the acoustic sensors was in the center of each block face. **Figure 4.1.6** shows P-wave velocities before and after putting the sample inside the LN₂ container. The decrease in P-wave velocity indicates that fractures were created by the cryogenic treatment since the wave takes a longer time when traveling through any air gap.

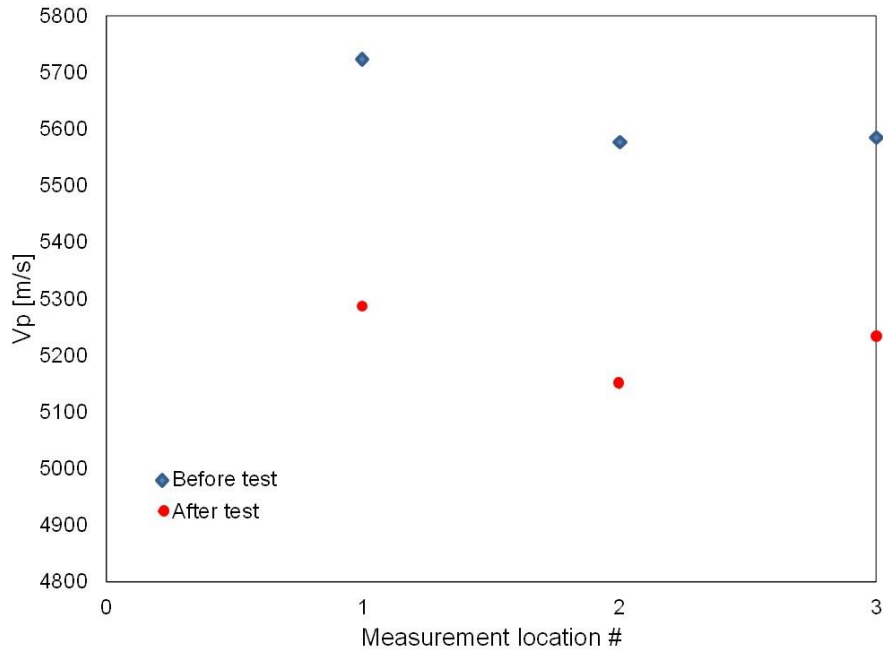


Figure 4.1.6 Changes in P-wave velocities before and after the cryogenic test.

4.2 Borehole Thermal Shock

We conducted cryogenic stimulation tests by circulating LN₂ in and out of the borehole drilled in artificial and natural rock blocks at low pressure. Since the outlet is open to atmosphere, the fluid pressure in borehole is not considered as a contributing factor for propagating cryogenic fractures, i.e. the sharp thermal gradient from LN₂ injected into the borehole is the only driving force for fracture generation inside the rock blocks.

4.2.1 Acrylic Cylinders

Experiments are performed to observe and study the development and morphology of cracks generated from cryogenic thermal shock at the borehole geometry. Acrylic specimens are chosen because they are transparent, and relatively brittle, which is one of the important characteristics of rocks.

4.2.1.1 Sample 1

The dimensions of the acrylic Sample 1 are illustrated in **Figure 4.2.1**. The acrylic cylinder is 4" in diameter and 9.1" in height and the borehole is 7" deep and 0.5" in diameter. A 0.5"

stainless steel tube is inserted and attached to the borehole wall to the depth of 2.5". LN₂ inlet tubing is inserted to 2.25" below the casing end.

Taking advantage of the sample being transparent, we observed the flow characteristics inside the borehole. Upon the start of the experiment, nitrogen inside the borehole was flown initially as a gas state (for about 1~2 minutes), and then flown as a gas mixed with droplets of liquid, and finally flown in a more continuous phase of liquid with still a significant amount of gas phase intermixed.

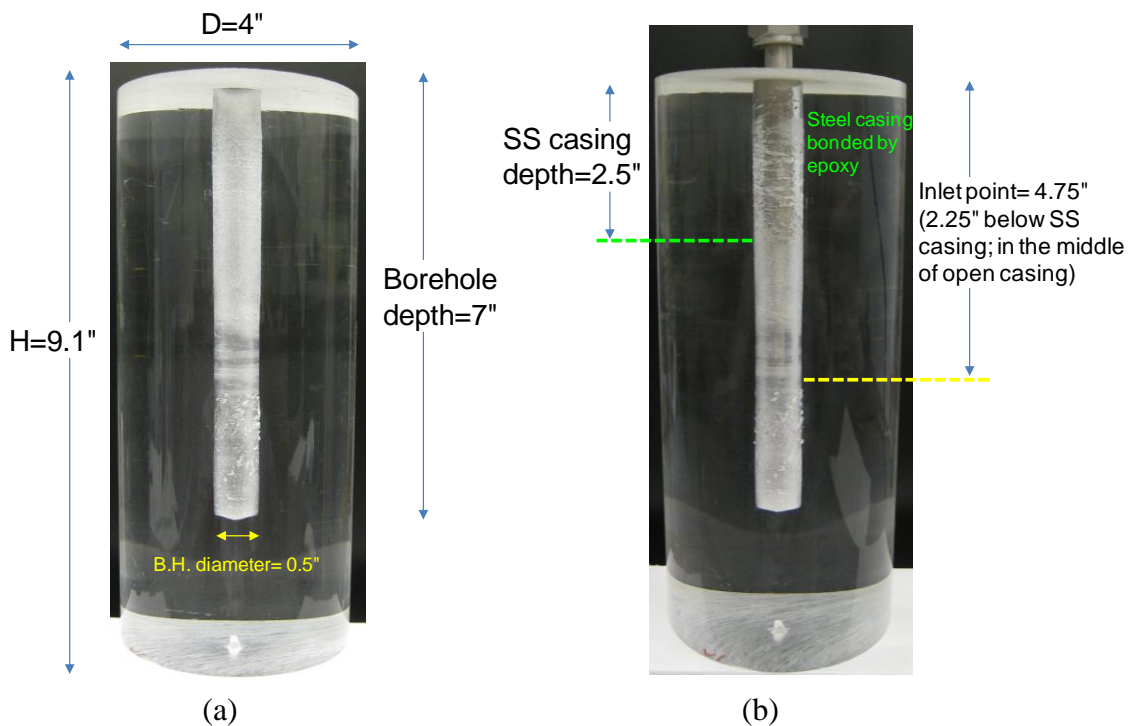


Figure 4.2.1 Acrylic Sample 1: (a) dimension, and (b) description of stainless steel casing and inlet tube.

4.2.1.1.1 Temperature, pressure, and LN₂ consumption

Temperature decreased fairly rapidly compared to the previous experiments, potentially aided by improved and more efficient tube connections and insulations. Although a large volume of LN₂ (20kg) was used, most of the fractures occurred at an early stage (within 20 minutes). The Dewar lever was opened fully during releasing LN₂ without any partial or full closure.

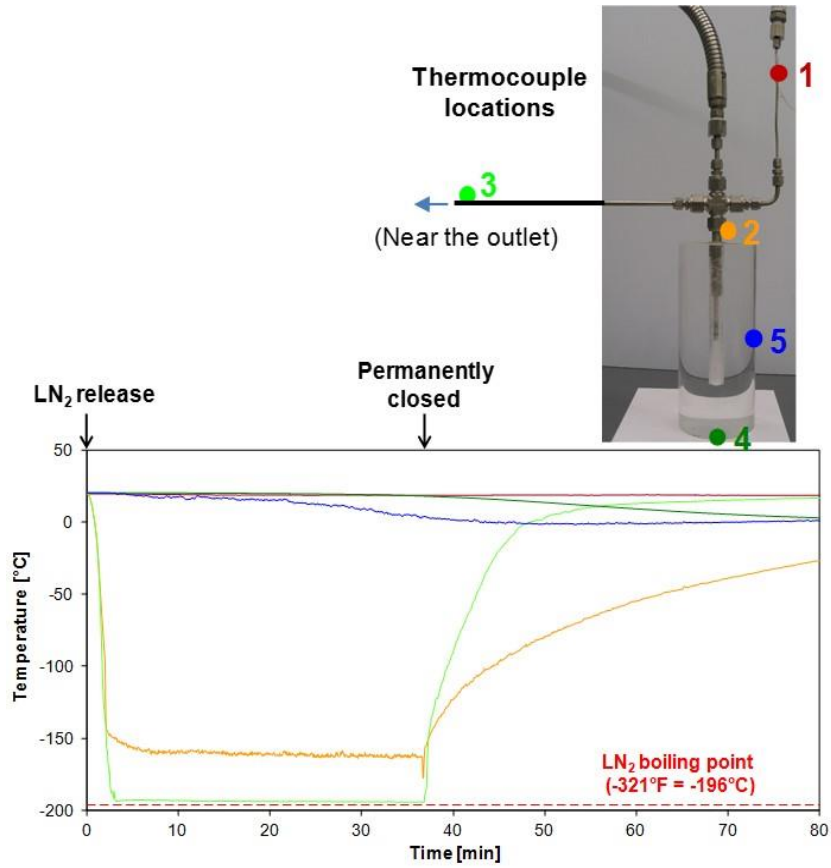


Figure 4.2.2 Locations of thermocouples and temperature evolution during the experiment.

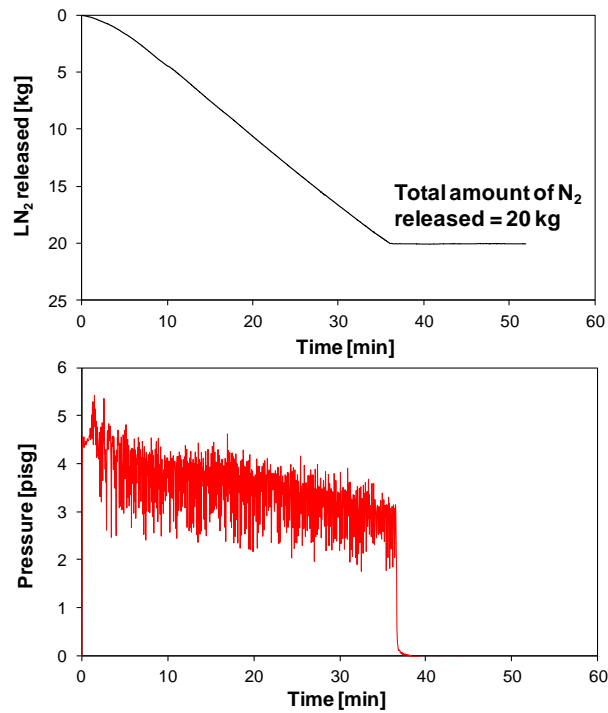


Figure 4.2.3 Borehole pressure and LN₂ released during the test.

4.2.1.1.2 Crack development

Images of the acrylic cylinder are captured in a time-lapse manner throughout the experiment, as shown in **Figure 4.2.4**. It is observed that fracture growth is not continuous, but rather jumpy and instantaneous. It emits clear audible sounds, when the fracture jumps to grow. The magnitude/amount of jump (or instantaneous growth) tends to decrease as the fracture grows larger. Most of the cracks occurred within 20 minutes.

The dominant pattern of crack morphology is a horizontal, planar, radial propagation. Each of such cracks is created, spaced by a certain length (exclusion distance). This can be explained by the fact that the specimen is cylindrical with a borehole height greater than the diameter, which makes the amount of thermal contraction greater in the longitudinal direction. An exclusion distance exists because a set of cracks cannot be created closer than a certain length due to a limited amount of thermal contraction (**Figure 4.2.5**).

The circumferential thermal contraction does generate vertical cracks, though they are smaller and fewer than the horizontal fractures. The vertical tension cracks tend to initiate from or form between the existing horizontal radial cracks, bridging between the radial cracks, presumably because it takes lower energy to start from pre-existing defects (i.e., the horizontal radial crack) and propagate toward an existing defect (**Figure 4.2.4-Figure 4.2.5**). At the end of the experiment, the specimen shows complex fracture morphology created by interplay between longitudinal and circumferential thermal contraction (**Figure 4.2.4**).

Temperature distribution at the surface is also affected by the location of cracks. In fact, free movement of the liquid nitrogen was observed inside the cracks. This may help a crack to further propagate. **Figure 4.2.6** show that some cracks approached the surface at a later stage of the experiment, and the temperature near the crack is readily affected by the proximity to the cracks.



Figure 4.2.4 Crack development. The steps shown above do not represent all the crack growth steps.

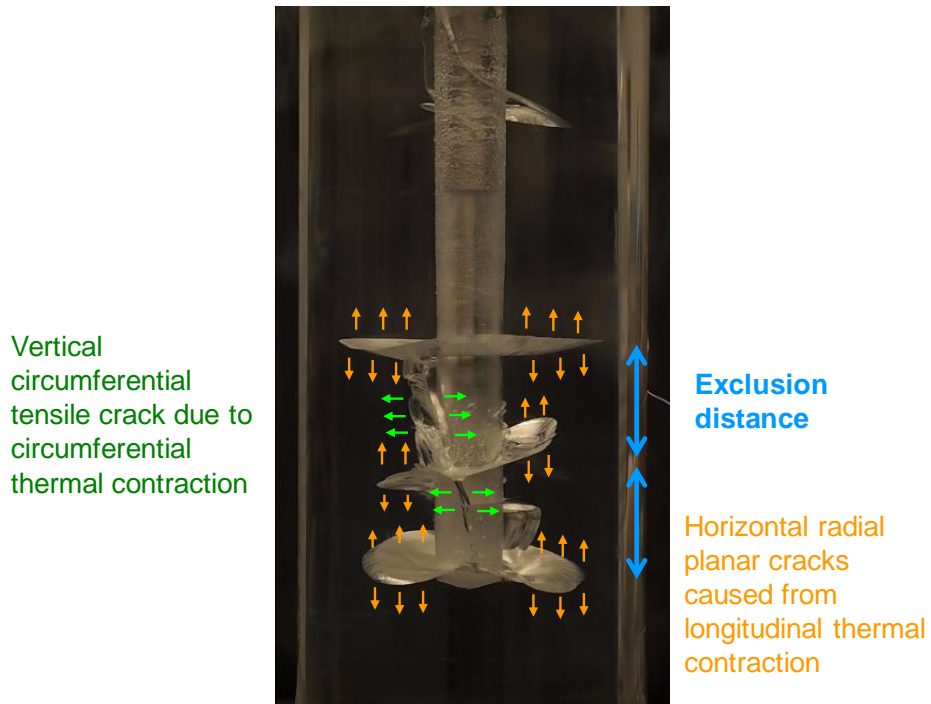


Figure 4.2.5 Crack morphology and driving thermal tensile stresses.

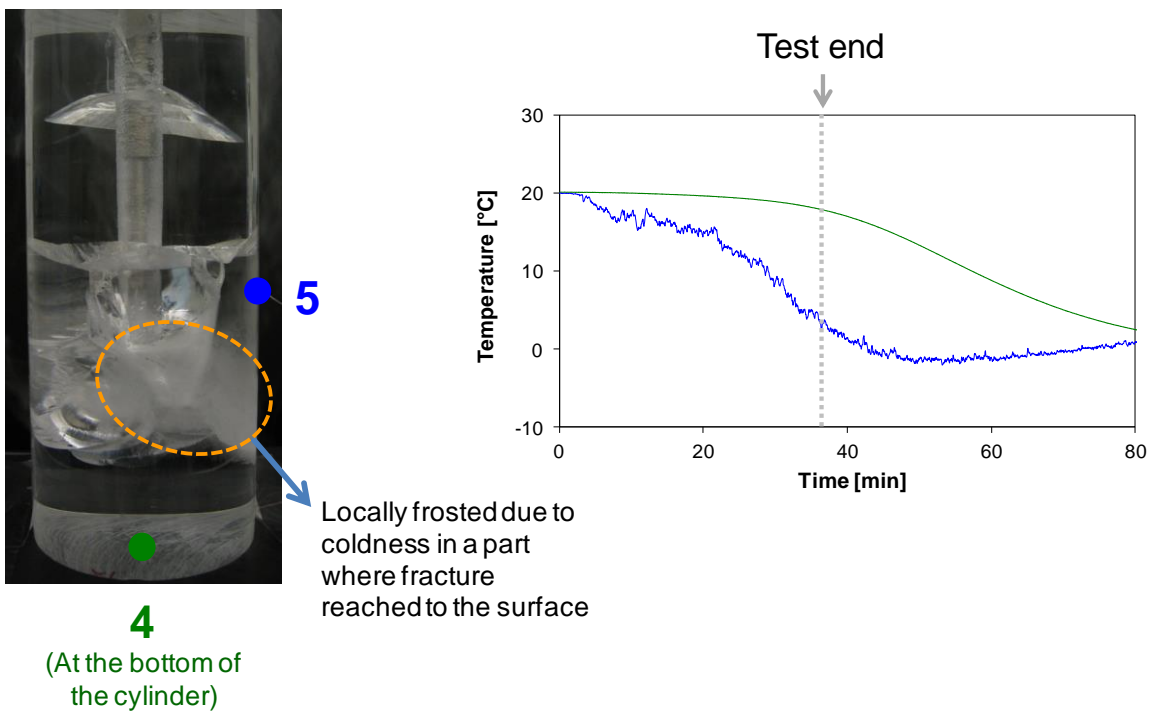


Figure 4.2.6 Effect of crack propagation on surface temperature.

4.2.1.1.3 Effect of borehole condition

One major planar radial crack occurred in the steel casing area at an early stage. This is likely due to the presence of the steel casing, which has a high heat conductivity and will have shorter period of Leidenfrost effect (Liquid nitrogen vaporizes at the solid surface, generating a nitrogen gas cushion, which has a much lower thermal conductivity than the LN₂). However, further growth is limited because LN₂ cannot flow into the generated crack (**Figure 4.2.7**).

We have noticed that the distribution of cryogenic temperature inside the borehole is affected by the location of the injection point. Cracks are mainly generated near and right in front of the injection point, which suggests a temperature differential in the borehole due to colder temperatures near the inlet (**Figure 4.2.7**).

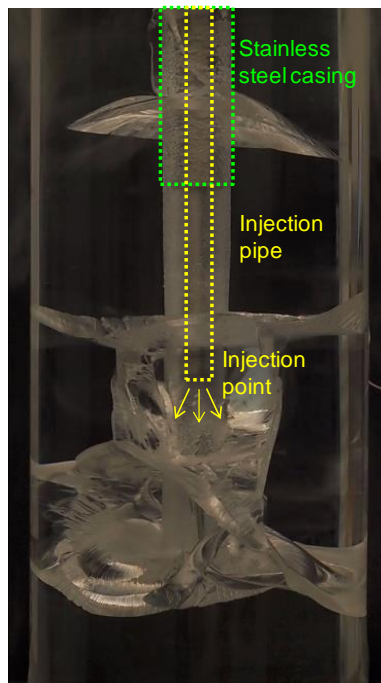


Figure 4.2.7 Effect of borehole condition.

4.2.1.2 Sample 2

The dimensions of Sample 2 are the same as those of the Sample 1. In this experiment however, both the steel casing and the inlet point are 1.5” in depth. The injection point is purposely located higher than the previous test for the Sample 1 to see the effect of the

location of injection point (**Figure 4.2.8**). The duration of the experiment is 11 minutes and the amount of liquid nitrogen consumption is 7.6 kg.

4.2.1.2.1 Temperature

Temperatures at the side (TC #2, TC #4, and TC #5) dropped by measurable amounts shortly after the end of the test as shown in **Figure 4.2.9** and **Figure 4.2.10**. It is probably due to the pressure drop at the borehole. The temperature distribution at the surface is also dependent on the proximity to the cracks (**Figure 4.2.10**).

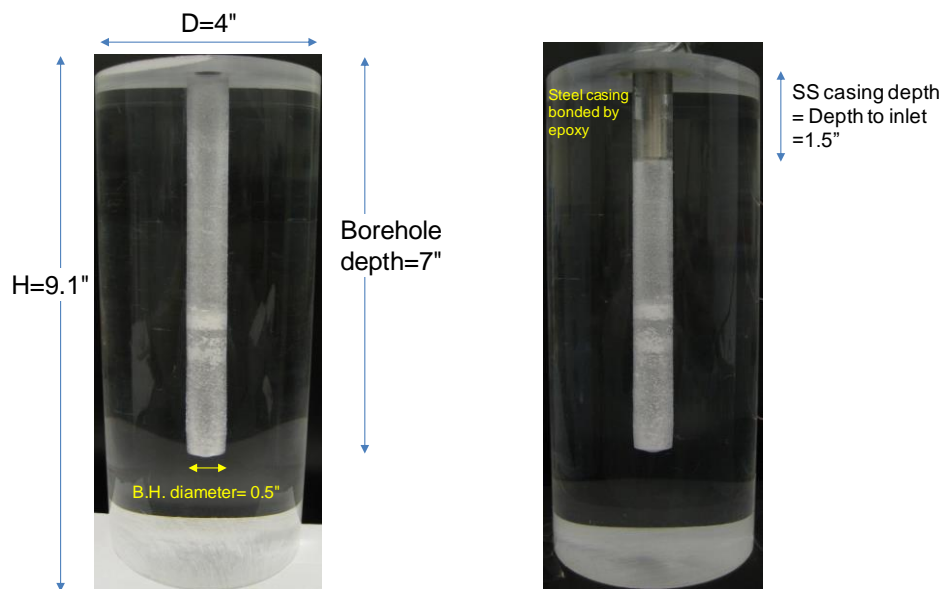


Figure 4.2.8 Acrylic Sample 2: (a) dimension, and (b) description of stainless steel casing and inlet tube.

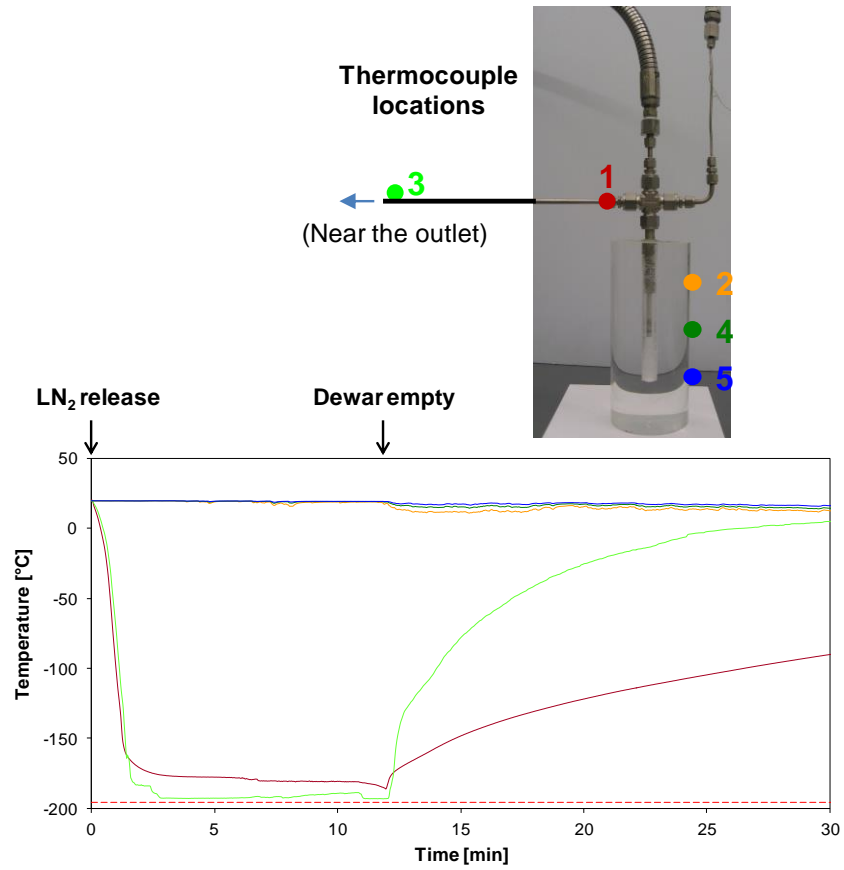


Figure 4.2.9 Temperature evolution during the testing.

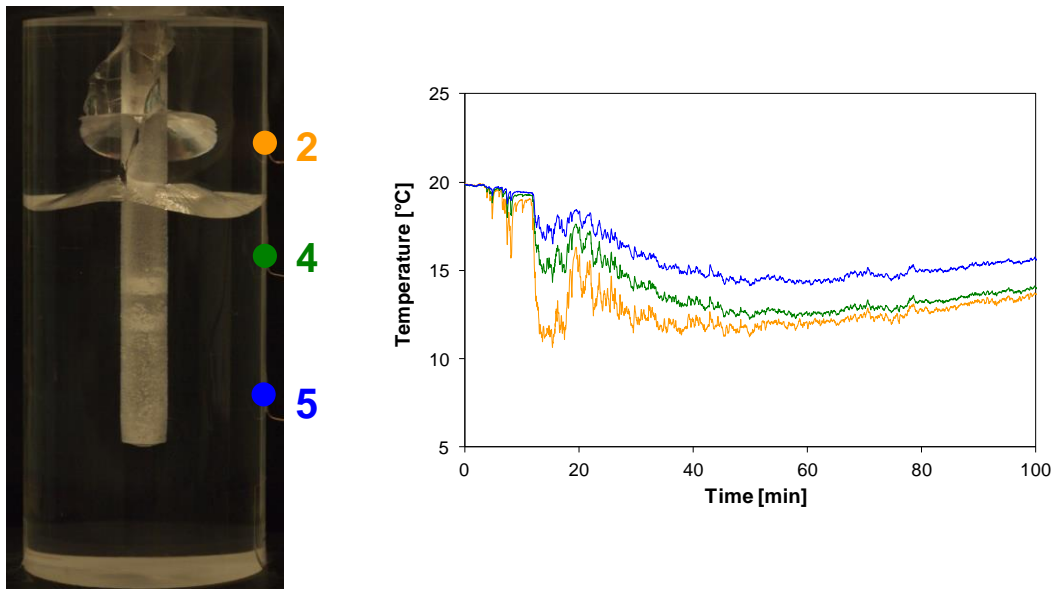


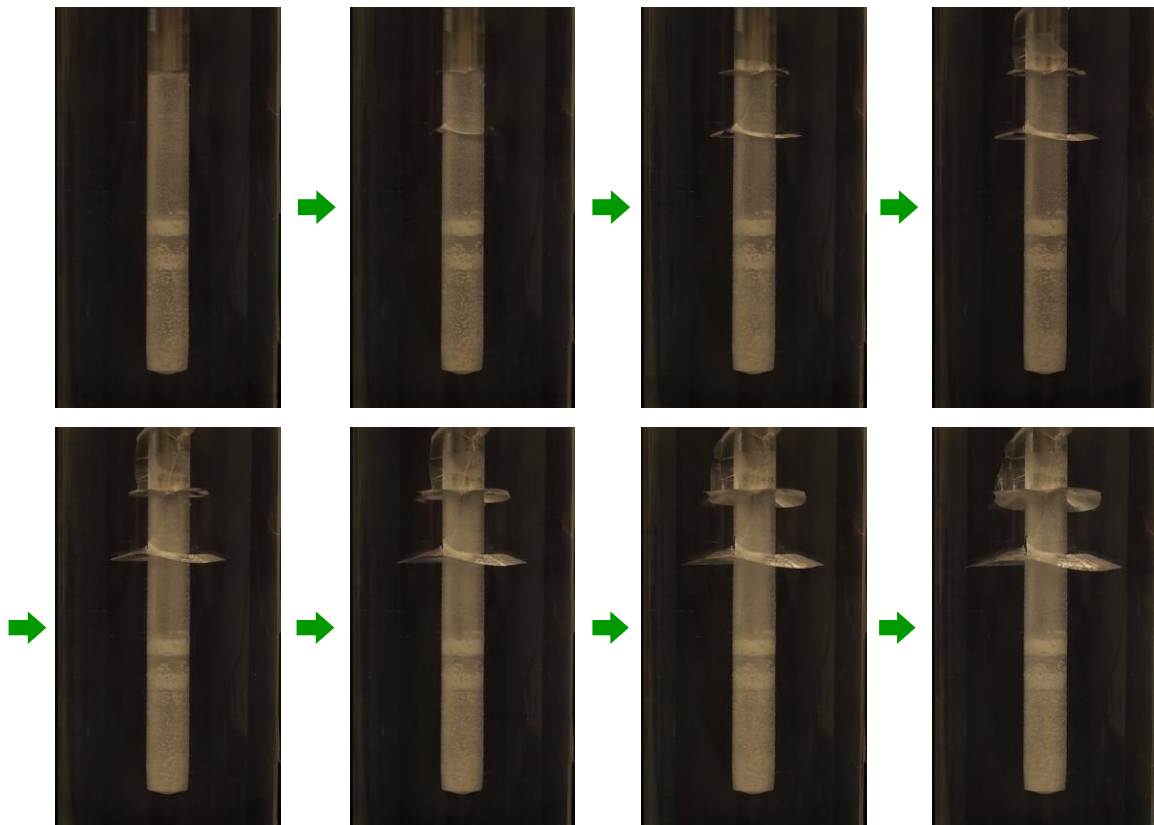
Figure 4.2.10 Effect of crack propagation on surface temperature.

4.2.1.2.2 Crack development

Two cracks are started as the horizontal radial pattern: one in the steel casing part and the other right in front of the inlet port (**Figure 4.2.11**). Later on, vertical cracks are created and bridges the radial cracks.

As observed and explained for the Sample 1 test, the cracks at the steel casing are aided by the efficient propagation of the cryogenic temperature from the casing, and the radial growth of the crack in the steel casing is limited by the lack of LN₂ supply to the generated crack (**Figure 4.2.11** and **Figure 4.2.12**).

Similar to the Sample 1 test, the crack in the uncased part is located close to the inlet port. In this test; however, only one big radial wing is created (compared to the three in the previous test), which means that there was not enough driving contraction to generate more cracks. The lack of thermal driving could be due to shorter stimulation time (smaller amount of LN₂ applied).



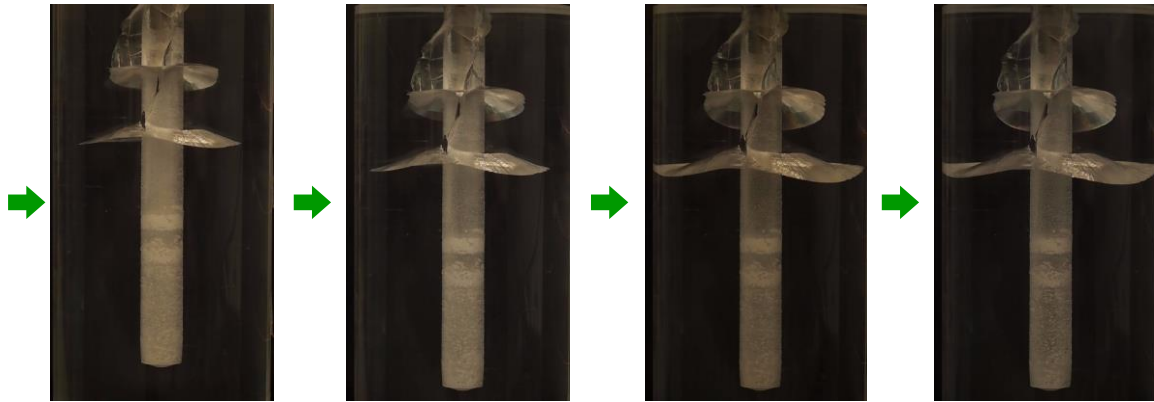


Figure 4.2.11 Crack development.

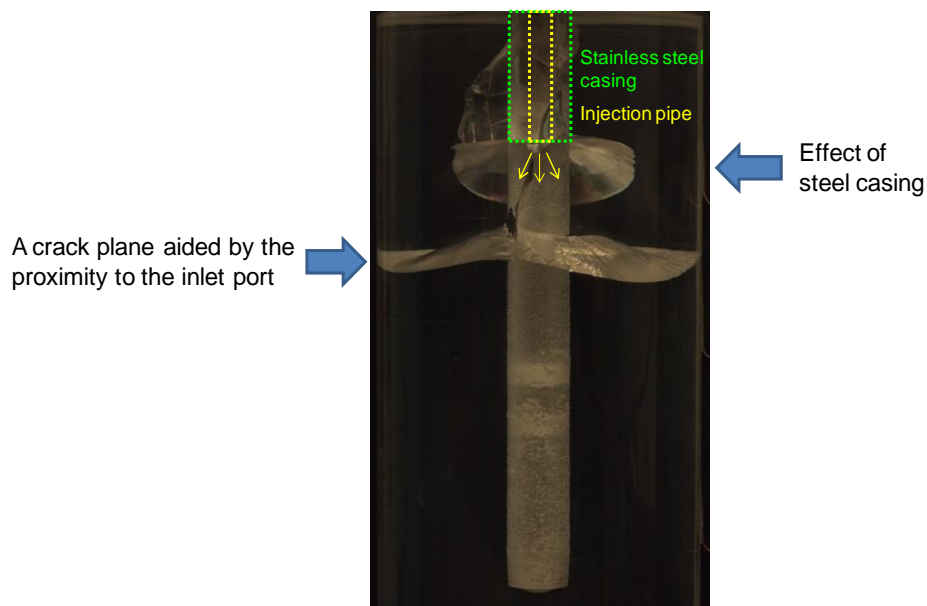


Figure 4.2.12 Effect of borehole condition.

4.2.2 Concrete Samples

Liquid nitrogen was brought into the open borehole in the center of concrete samples in two ways. One is simply pouring LN₂ into the borehole, the other is injecting LN₂ into the borehole by setting a packer on top of it.

4.2.2.1 Pouring LN₂ into Open Borehole

As a first-step experiment, a cement concrete specimen with 8" × 8" × 8" dimension are made and a 6" deep borehole with diameter of 0.75" is drilled at the center of the top surface. Liquid nitrogen is poured into the open borehole using a portable liquid nitrogen bottle. We observed rapid vaporization of liquid nitrogen with Leidenfrost effect.

After pouring of liquid nitrogen into the borehole, the concrete block was imaged using X-ray computed tomography (CT) scan to look for fractures resulting from the cryogenic treatment. Note that no pre-treatment CT scan was done for this block. Scanning was performed using a modified Siemens Somatom HiQ medical X-ray CT scanner. The block was scanned in two orientations to provide orthogonal views of the inside of the block.

Figure 4.2.13 shows a vertical cross section through the borehole in the center of the block. Fracture density would be expected to be highest near the borehole where temperature gradients are highest. The lighter shades in CT scan indicate higher density and the darker shades indicate lower density. Fractures, if seen, would show up as darker features most likely emanating from the borehole. A number of features are visible in **Figure 4.2.13**. One is an “X”-shaped pattern across the block. This is an artifact of scanning a rectangular block. The second feature is a series of concentric circles in the upper third of the image. This is an artifact of non-uniform response of a series X-ray detector. The third feature is dark lines extending from the bottom of the borehole, which are X-ray scanning artifacts since they are not seen in the perpendicular scan. Numerous voids are visible (dark patches) from air entrained in the block formation process. No fractures are observed in this set of scans, which is consistent with visual observations as well.

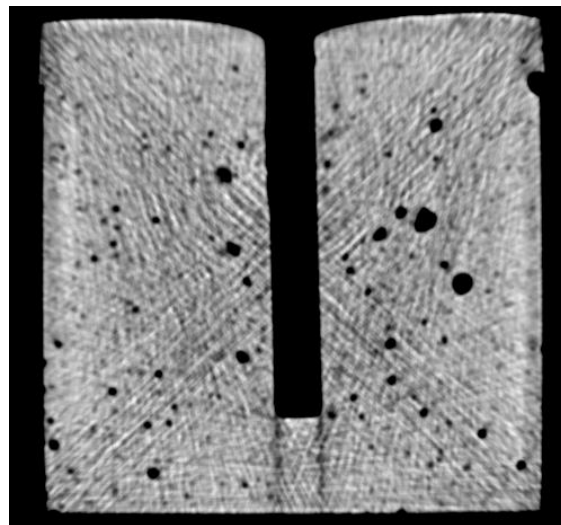


Figure 4.2.13 X-ray CT scan vertical cross section of the concrete block.

4.2.2.2 Injecting LN₂ with Packers

Thermal shock experiments were carried out on a concrete sample without forced pressurization in the borehole. The block was air-cured for 5 weeks after contained in the mold for 24 hours, resulting in relatively low strength (both compressive and tensile).

4.2.2.2.1 Test with an Unconfined Packer

Figure 4.2.14 shows the experimental setup that was used for the thermal shock experiment on concrete by flowing LN₂ in the borehole. A spray-type insulation is applied for heat insulation as well as packer sealing. The packer is loosely sitting on top of the borehole. LN₂ is released from the Dewar and flows to the sample borehole through the vacuum jacketed tube and insulated stainless steel tubes. The borehole is open to the air through a vent and warmed GN₂ flows freely into the atmosphere. Low pressure about 5~10 psi was generated due to rapid vaporization of LN₂ inside the borehole and along the transport lines. During the LN₂ injection, leakage was observed at the packer/block interface and out of the insulation.

A set of S-wave acoustic sensors are mounted at a location on Face 2 and 4 to monitor the wave signatures. An oscilloscope and a pulser are used to generate and record signals.

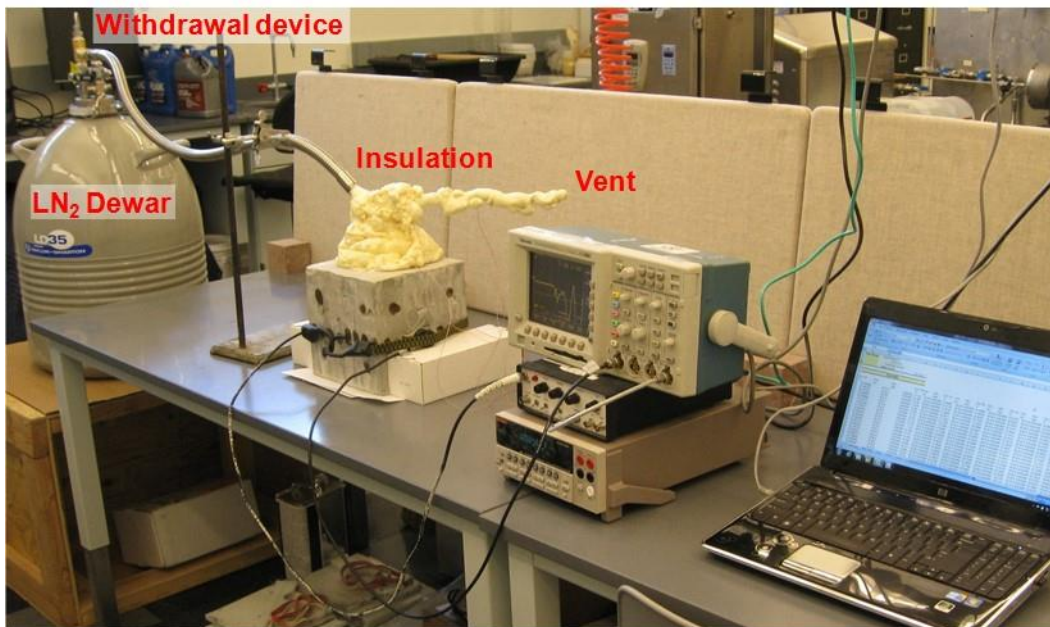


Figure 4.2.14 Experimental setup for test with unconfined packer.

Cracks

Before the thermal shock, no visible cracks near or inside the borehole existed. Several noticeable cracks are found near and inside the borehole after the thermal shock (**Figure 4.2.15**).

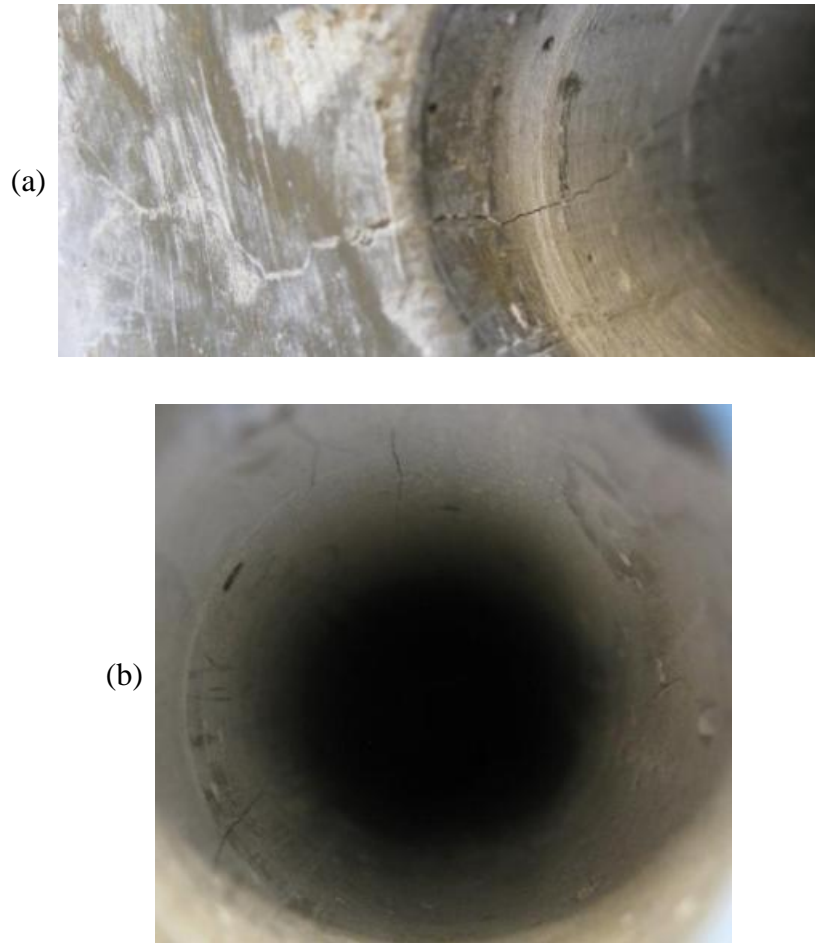


Figure 4.2.15 Cracks observed after the thermal shock (a) near the borehole, and (b) at the borehole surface.

However, there were some pre-existing micro-cracks even before the thermal shock at the block surfaces due to the natural shrinkage of concrete (**Figure 4.2.16**). The dark spots are stains from the couplant used for securely attaching the ultrasonic sensors.

After the testing (**Figure 4.2.17**), not only new cracks were generated, but the existing cracks were widened. Particularly, there were virtually no cracks at the bottom face before applying cryogen, some major cracks are generated after the cryogenic stimulation.

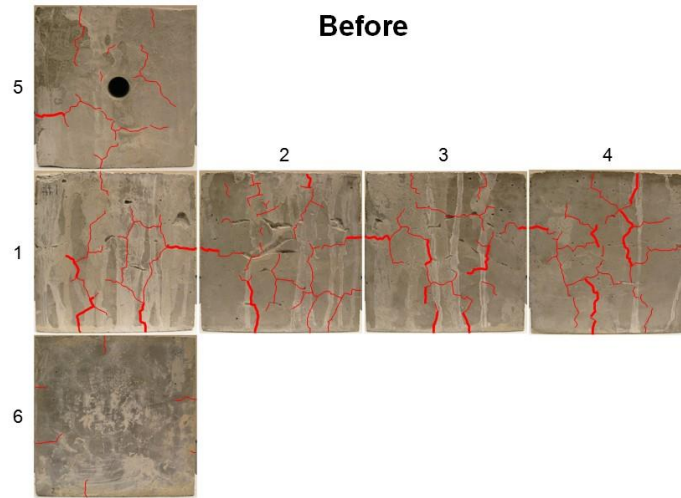


Figure 4.2.16 Pre-existing surface cracks, the superimposed lines are weighted according to the crack thickness.

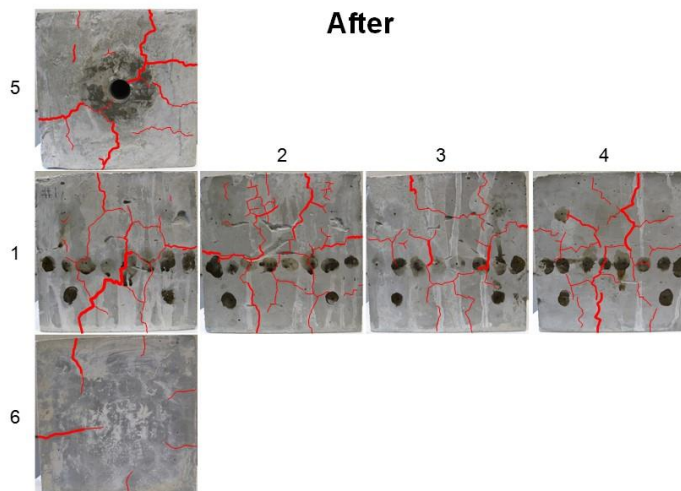


Figure 4.2.17 Surface cracks after the thermal shock. Note that the dark spots are stains from the couplant used for securely attaching the ultrasonic sensors.

Temperature

Thermocouples are used to measure temperatures at various locations in the experiment. Location 2 (black) is hung inside the borehole (**Figure 4.2.18**).

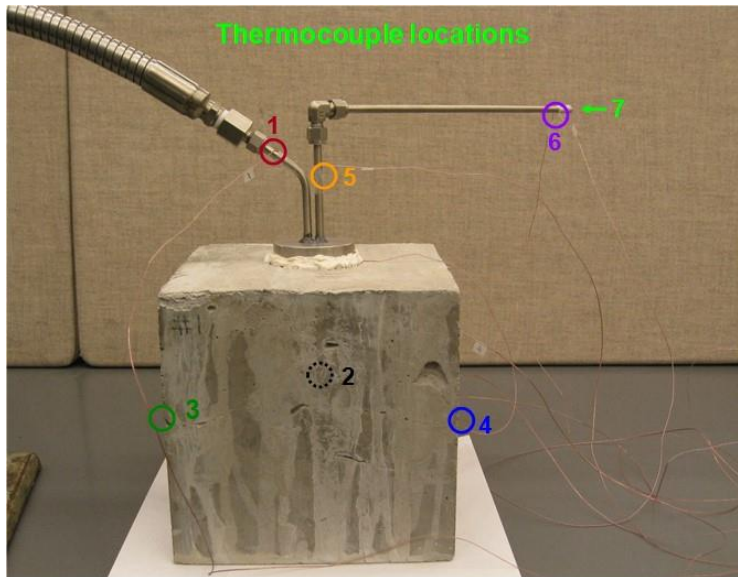


Figure 4.2.18 Locations of the thermocouples used in the temperature measurements.

The spikes shown in the plots in **Figure 4.2.19**, **Figure 4.2.20** and **Figure 4.2.21** are where the LN₂ is closed temporarily to reduce pressure inside the borehole, as the packer is not confined. LN₂ starts to leak from the packer toward the right surface at some point. This lowers the temperature at the right surface as shown in the plot. Throughout the test, the temperature differences between inside the borehole and the block faces are observed to be large, which are distinguishable even after 10 hours.

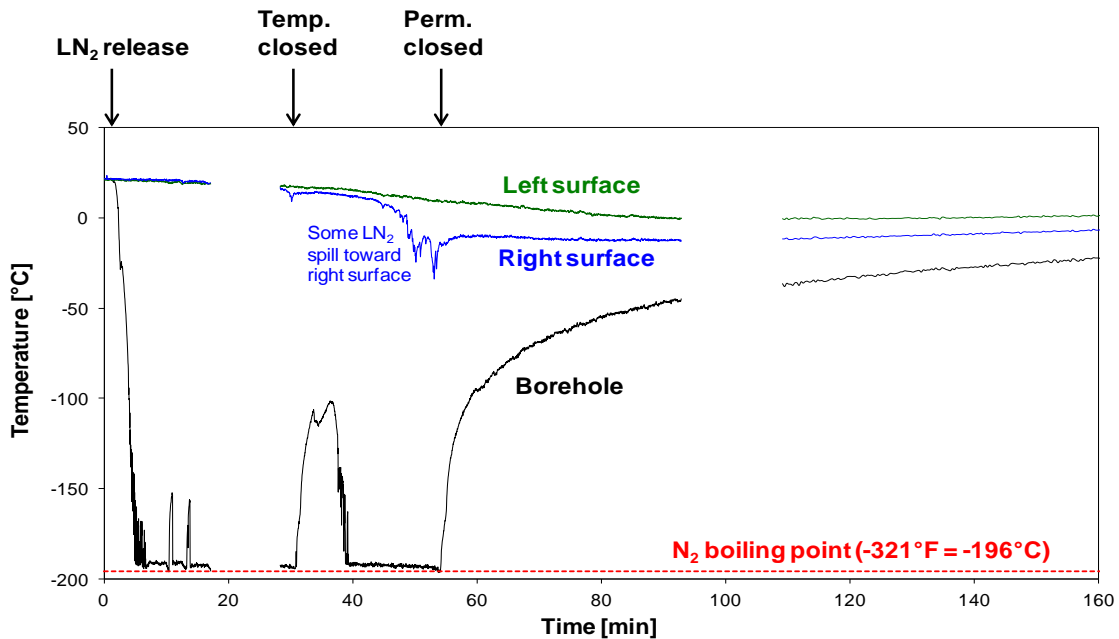


Figure 4.2.19 Temperature evolution during thermal shock experiment.

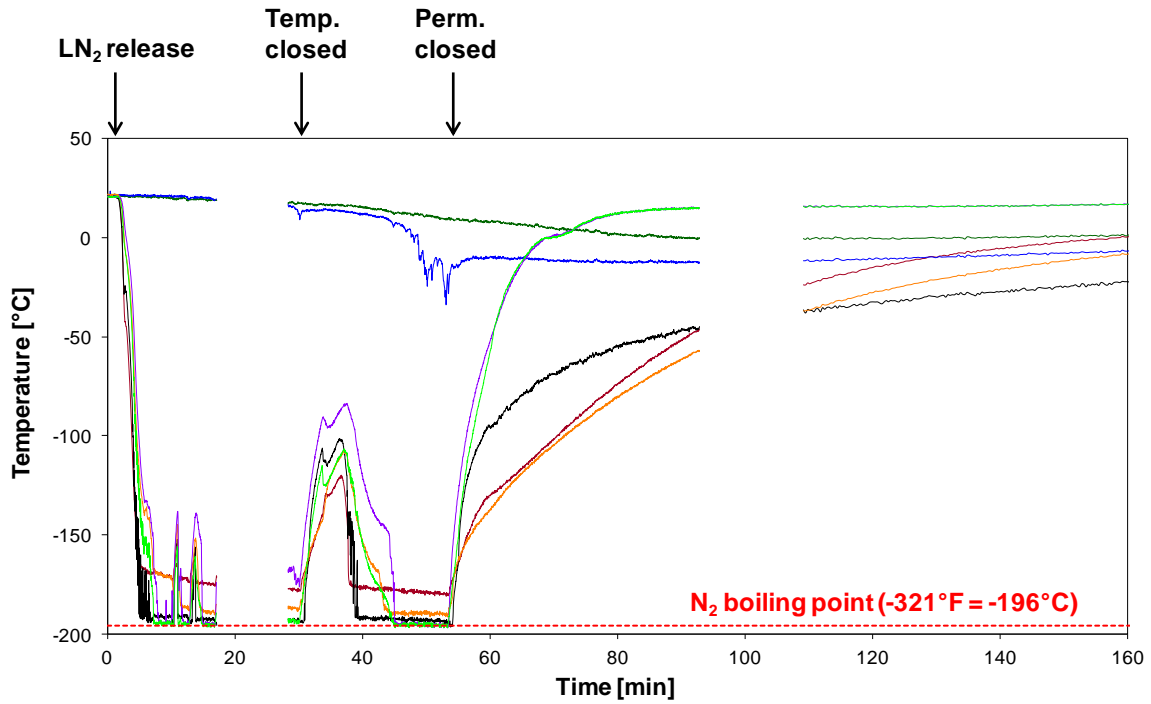


Figure 4.2.20 Temperature evolution during thermal shock experiment with more locations.

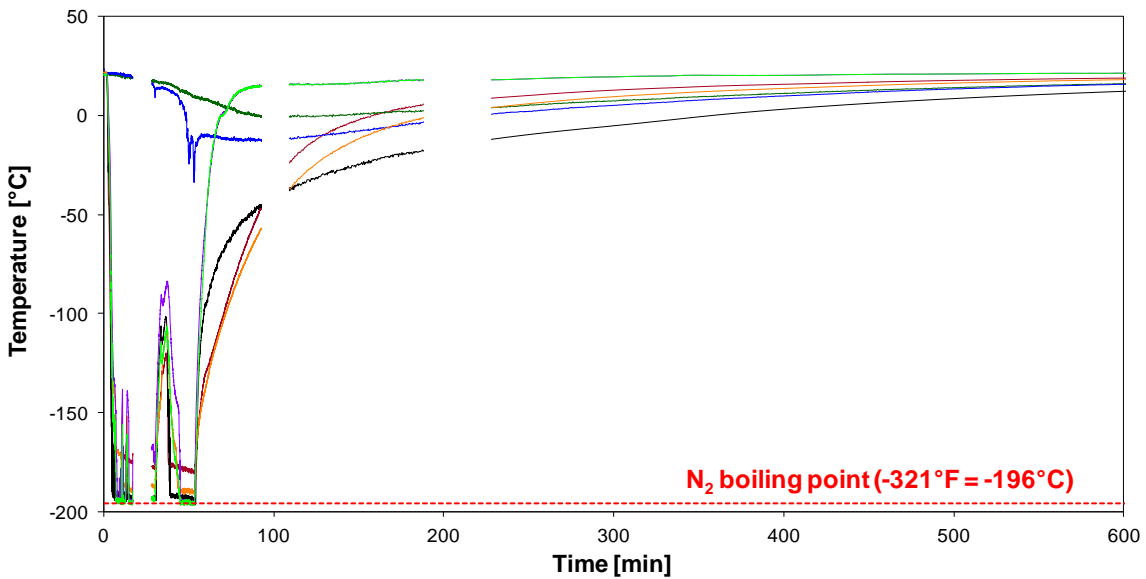


Figure 4.2.21 Temperature evolution after the thermal shock experiment (up to 10 hours).

Acoustic signatures

The characteristics of acoustic waves propagating through the medium depend on the mechanical properties of the medium. We would like to know the differences in the acoustic signatures before and after the cryogenic stimulation. Acoustic measurements were

conducted before and after the test using S and P ultrasonic transducers. Acoustic waves were also monitored during the cryogenic stimulation by mounting the S transducer acoustic sensors to the sample surfaces.

Figure 4.2.22 shows the locations for the acoustic measurements before and after the cryogenic stimulation. Acoustic signals were measured along Faces 1&3 and 2&4. For each pair of faces, the acoustic measurements were conducted at 12 locations. We are mainly interested in P and S wave velocities and amplitudes.

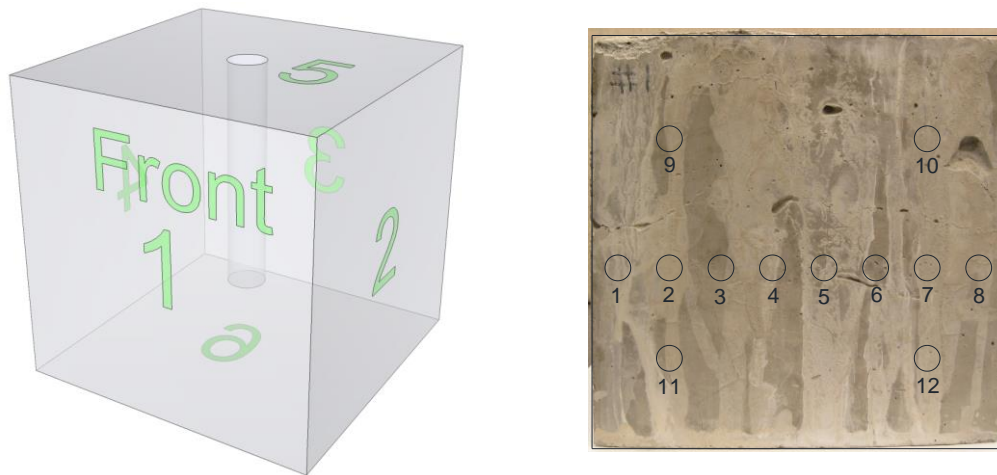
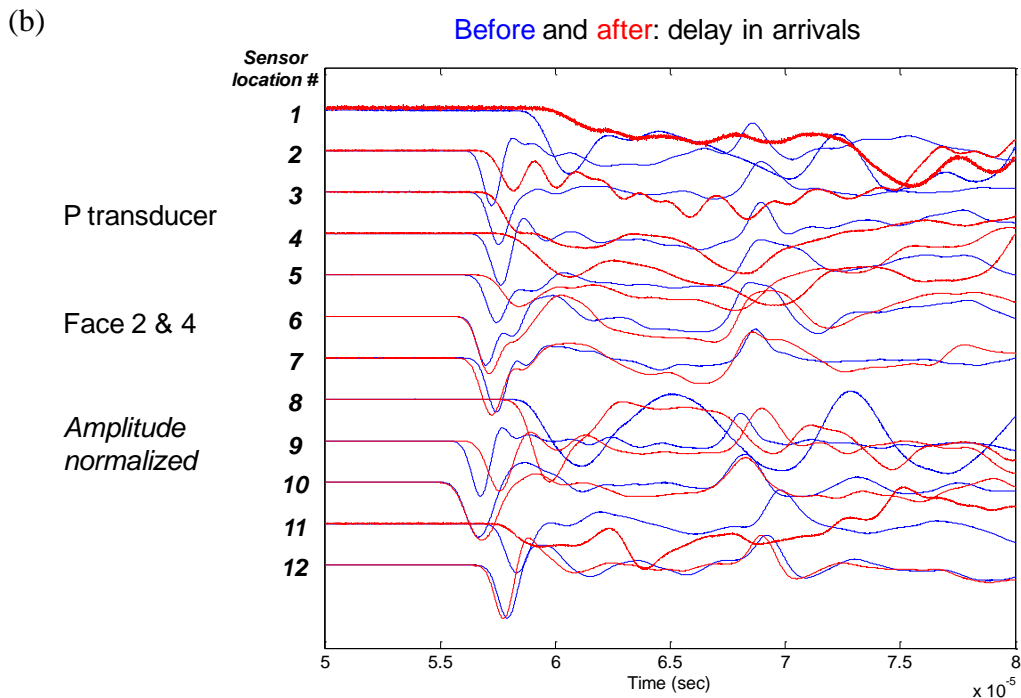
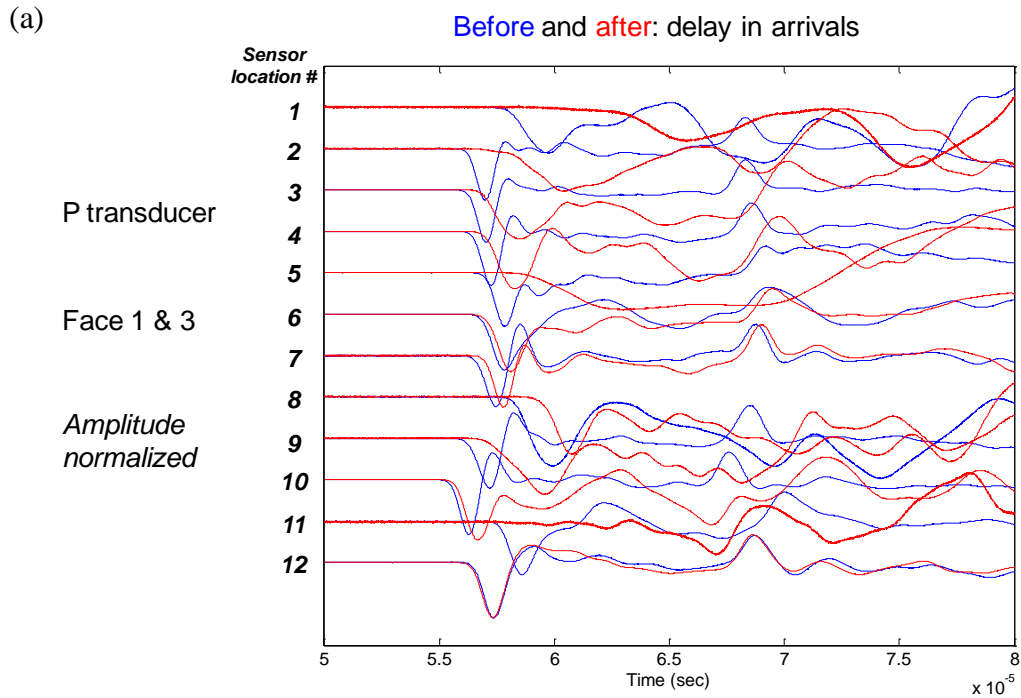


Figure 4.2.22 Acoustic measurement locations before and after thermal shock.

In **Figure 4.2.23**, early arrival parts of elastic wave signals are presented with the normalized amplitude to compare changes in arrival time and waveforms. At most measurement locations, arrivals are delayed and waveforms have changed significantly. The characteristics of acoustic signatures approximately correspond to the surface cracks. For example, the acoustic signals at location 12 is the least changed in terms of arrival time, and we also observed that the surface around location 12 is the least cracked due to the thermal shock.

In **Figure 4.2.24**, the signals are still early parts near the arrivals. However, the original amplitude is kept to compare changes in the amplitudes of the P and S waves. The amplitude measured at most locations for both P and S wave decreased significantly after the thermal shock (except for the location 12).

Finally, all signals are presented with their full range and original amplitude to compare global waveforms (**Figure 4.2.25**). It is observed that global amplitude is reduced and the global frequency of the signals is lowered.



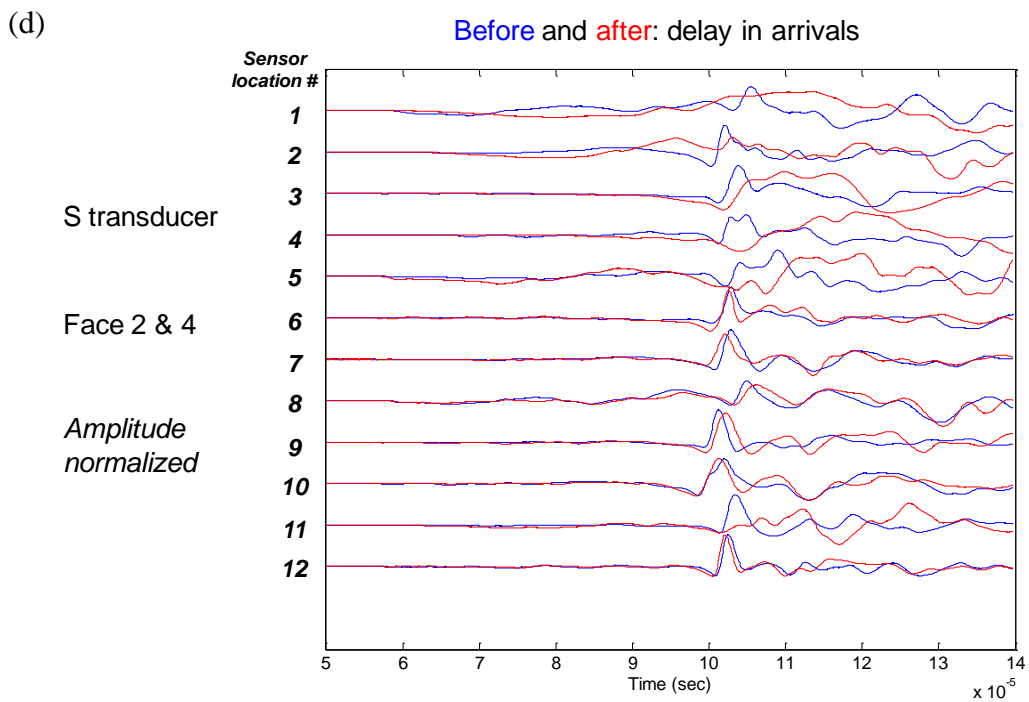
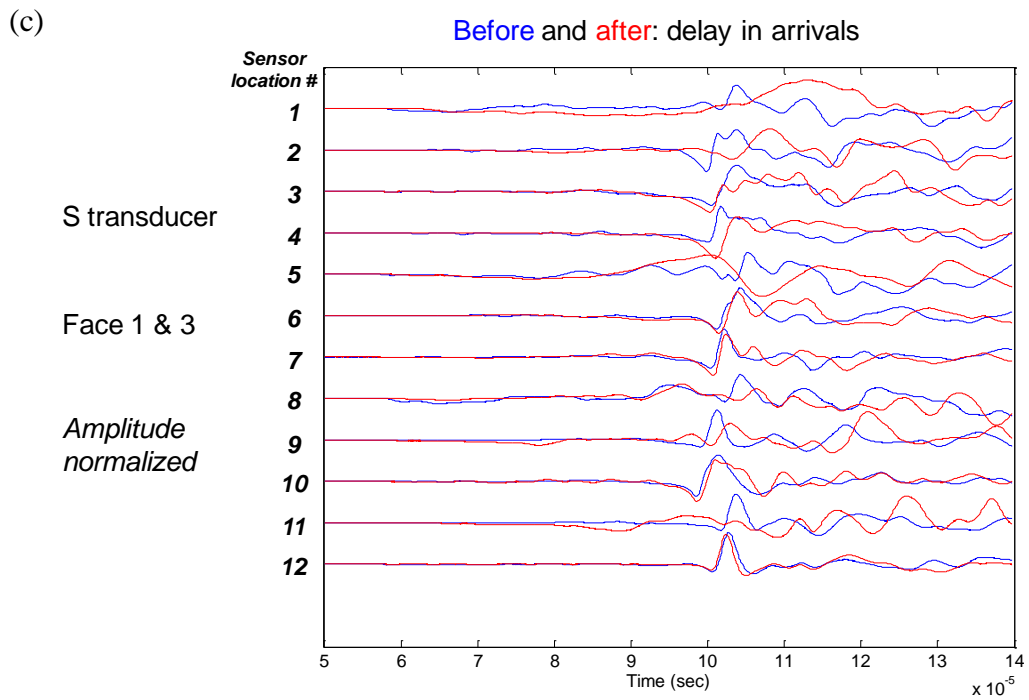
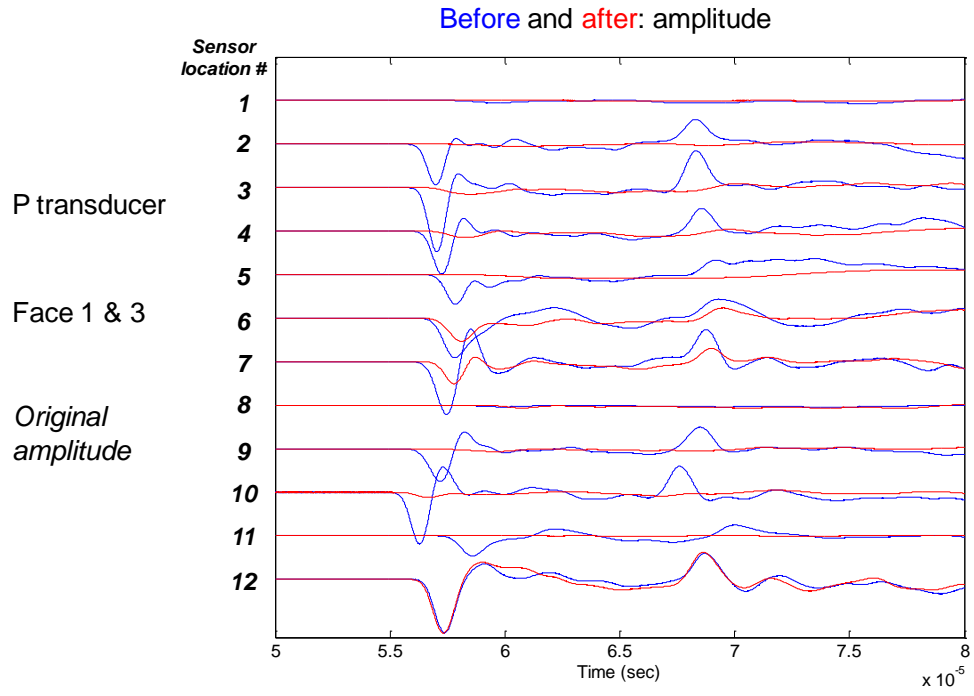
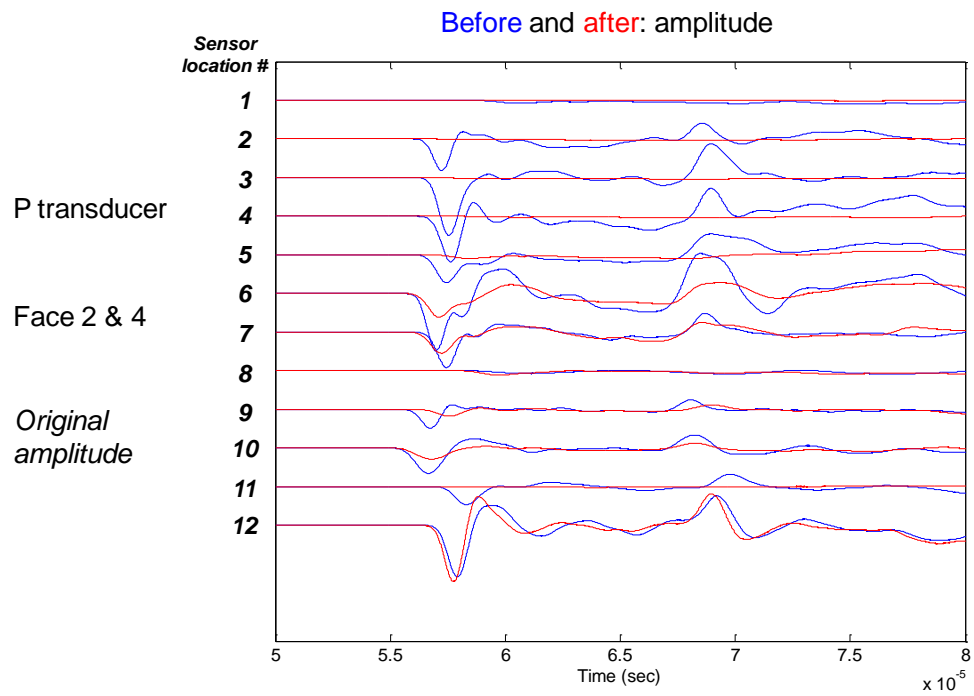


Figure 4.2.23 P and S wave arrivals before and after the thermal shock (compared with normalized amplitude)

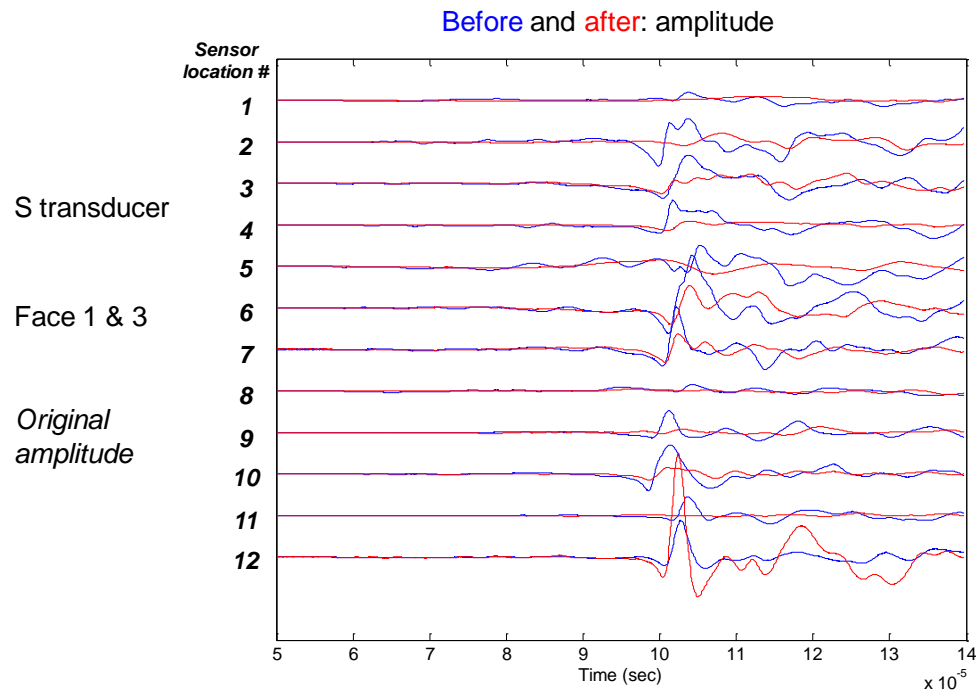
(a)



(b)



(c)



(d)

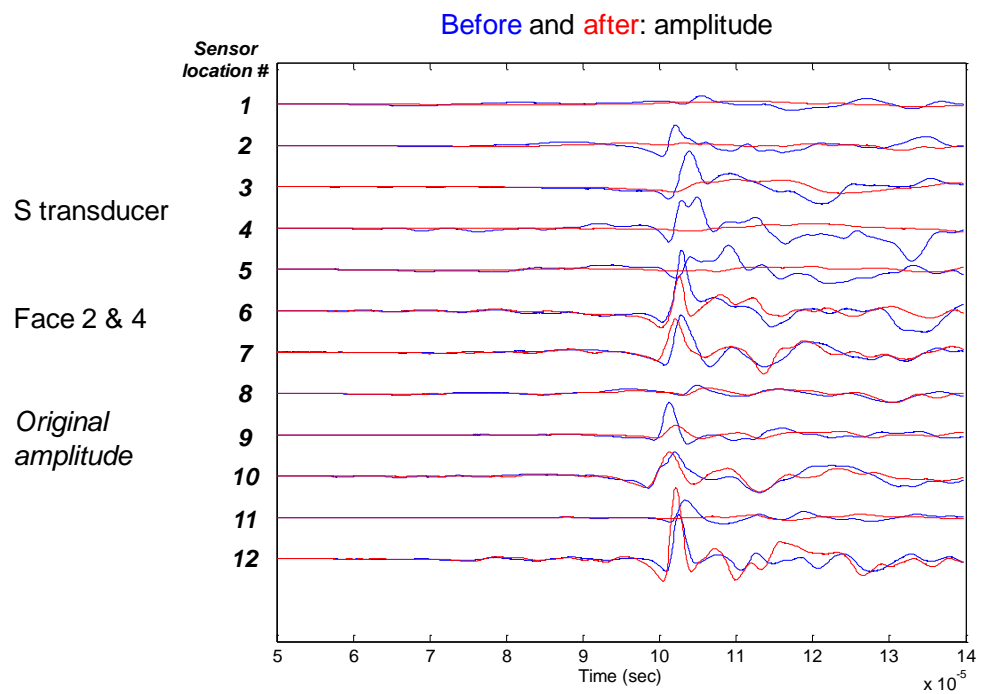
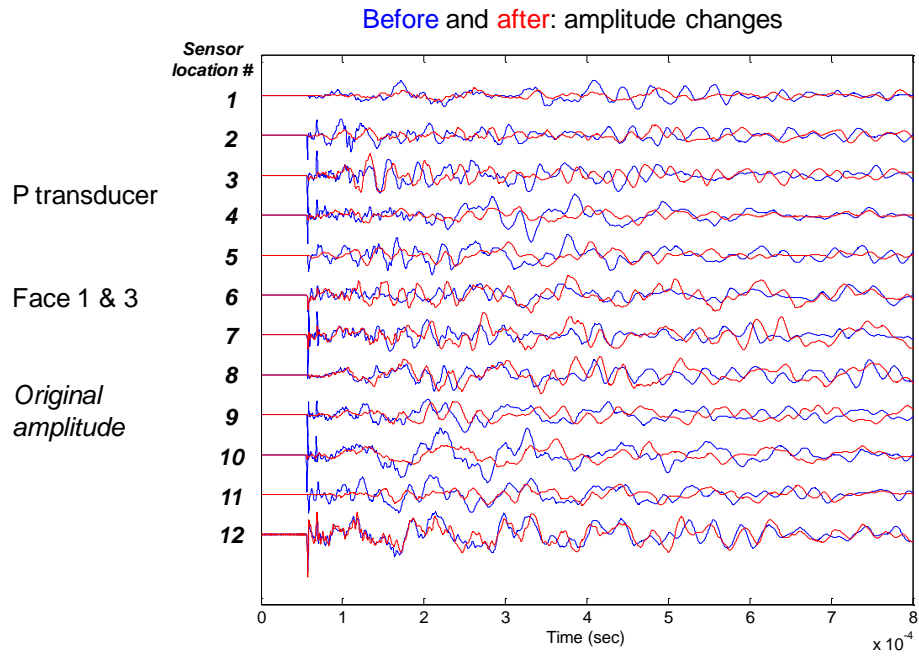
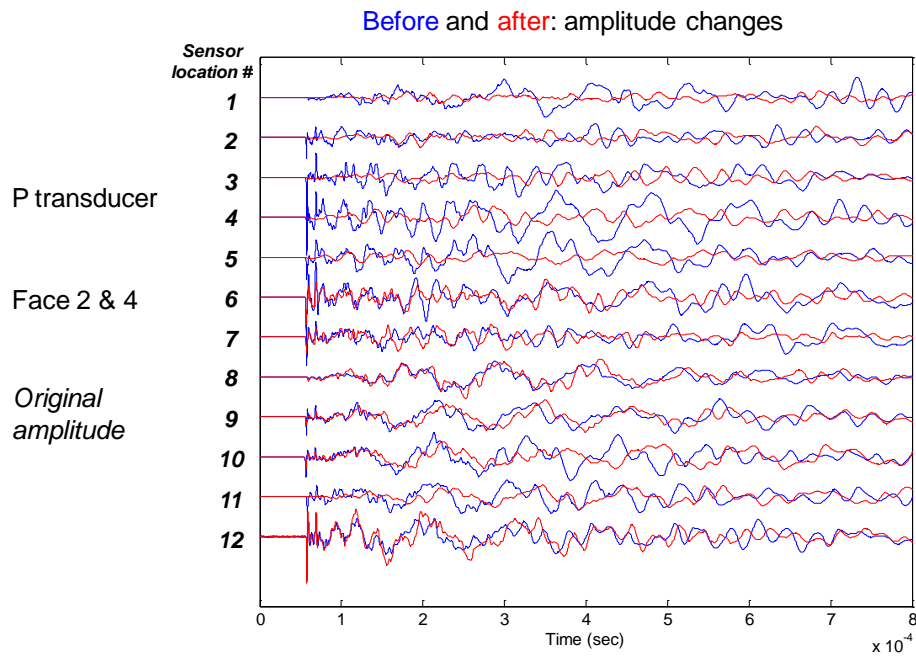


Figure 4.2.24 P and S wave amplitudes before and after the thermal shock.

(a)



(b)



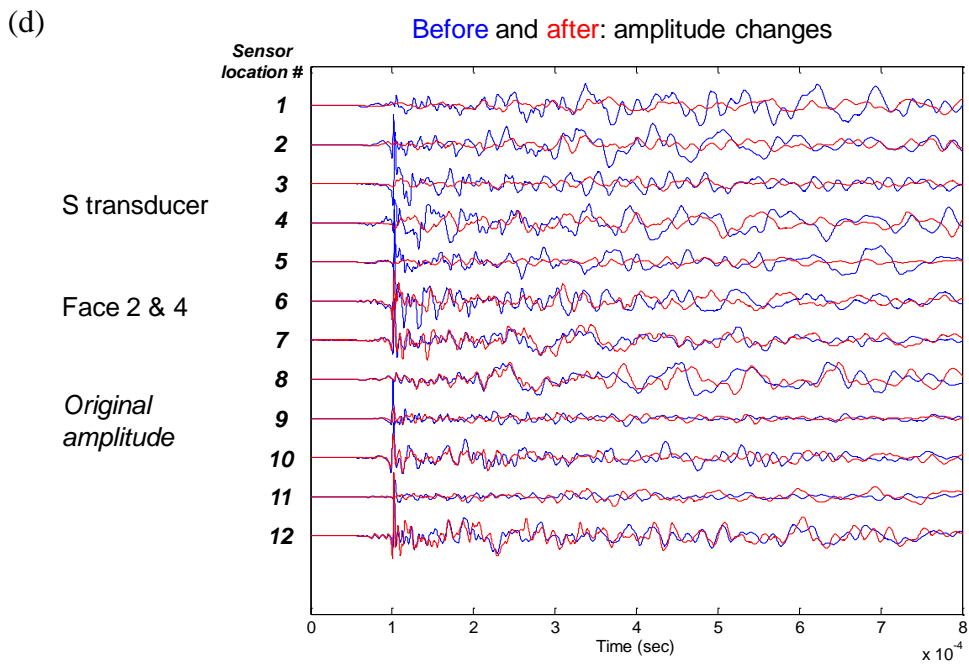
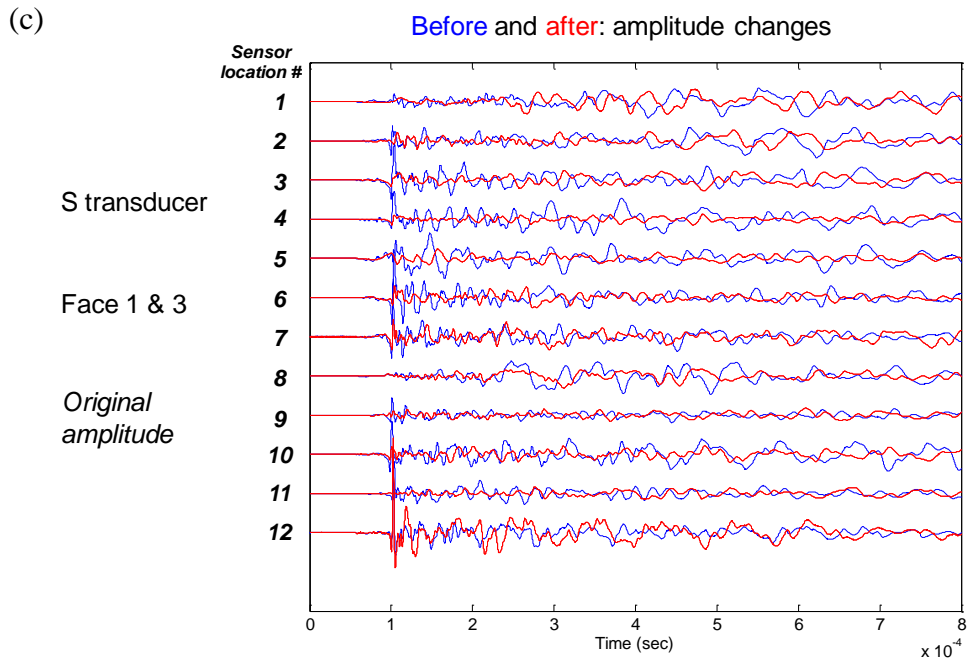


Figure 4.2.25 Global waveforms before and after the thermal shock.

4.2.2.2.2 Test with a Confined Packer

In this test, we used the same concrete block that was used for the 1st concrete test described in **Section 4.2.1.1**. For this experiment, a special structure is designed and fabricated to withstand some borehole pressure caused by vaporization (~10 psi) and subsequent application of borehole pressurizations (up to ~500 psi). A pressure transducer is attached to monitor borehole pressure, and a scale is used to record LN₂ consumption. For safety, we made sure that top and bottom plates which are made of carbon steel are not subjected to temperatures lower than -20 °C so that it does not reach the brittle-ductility transition point.

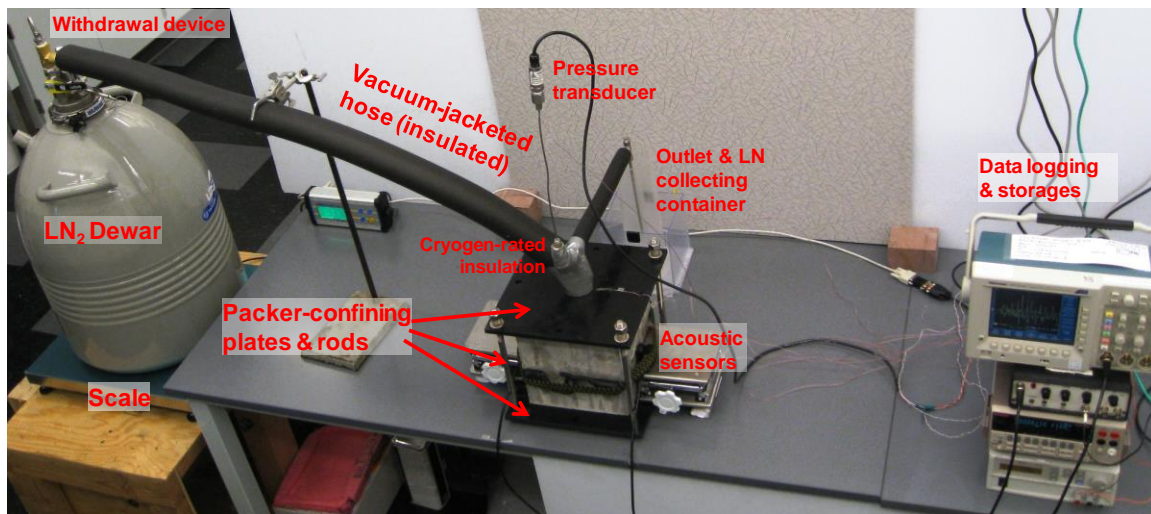


Figure 4.2.26 Experimental setup with “packer-confining structure”.

Cracks

Major cracks were visible from the top of the borehole (**Figure 4.2.27**). However, there has been no noticeable change from the 1st thermal shock. Cracks on the borehole wall were visible from the borescope. On the other hand, new cracks were generated on the block surfaces, and the existing cracks were a bit widened (**Figure 4.2.28**). There were relatively a small number of cracks at the bottom before applying the cryogen (after the 1st stimulation); however, many new cracks were created after the 2nd cryogen application.

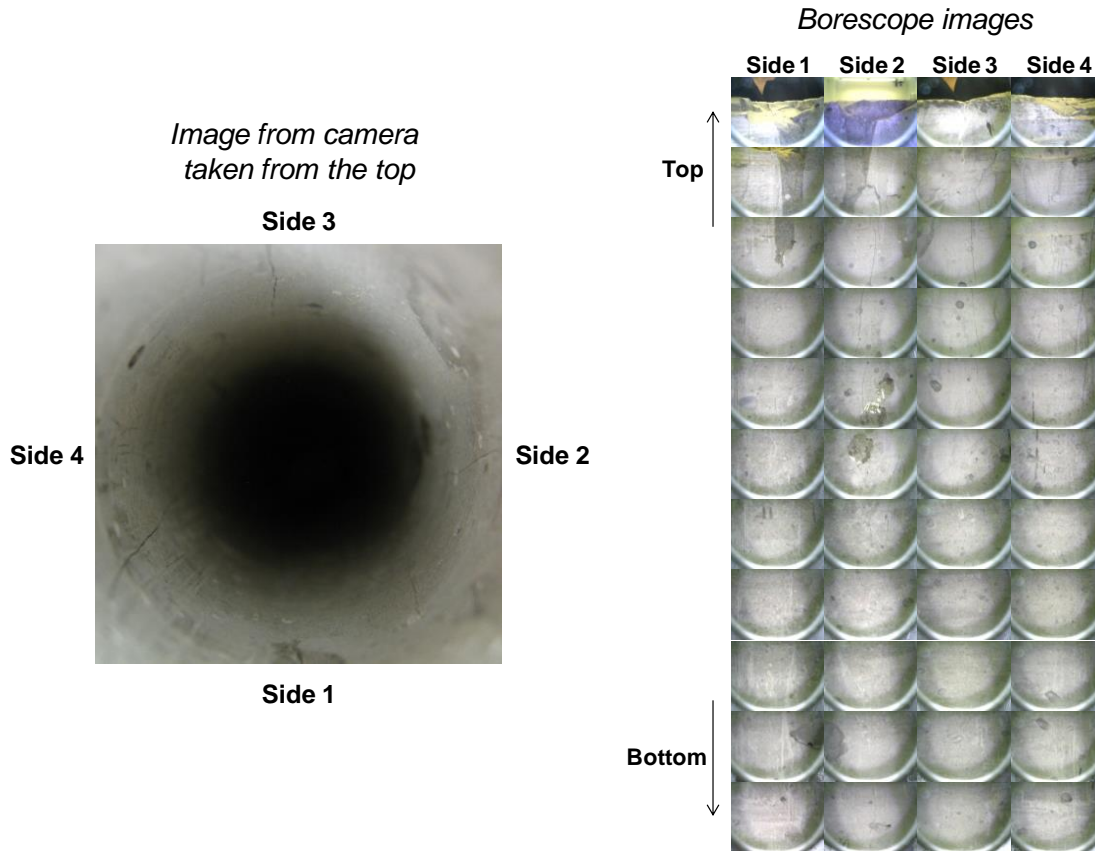


Figure 4.2.27 Cracks at the borehole walls observed from the top and the borescope.

The sample was scanned using X-ray CT at the Weatherford Lab at Golden, Colorado. The maximum resolution of the images from the scanner (Toshiba Aquilion 64) is 0.3mm×0.3mm×0.3mm. Thus, the CT images from the scanner show only major cracks. Unfortunately, micro cracks were invisible from these scanned images. The X-ray images at the front and back of the sample experienced artifacts called beam hardening as the cubic sample enters and exits the X-ray field (**Figure 4.2.29**).

The CT images show that there are more fractures near the surfaces than inside. The animation of X-ray slides from one surface to another shows that the cracks distributed near the surfaces diminish as they move inside, although a few independent cracks exist internally.

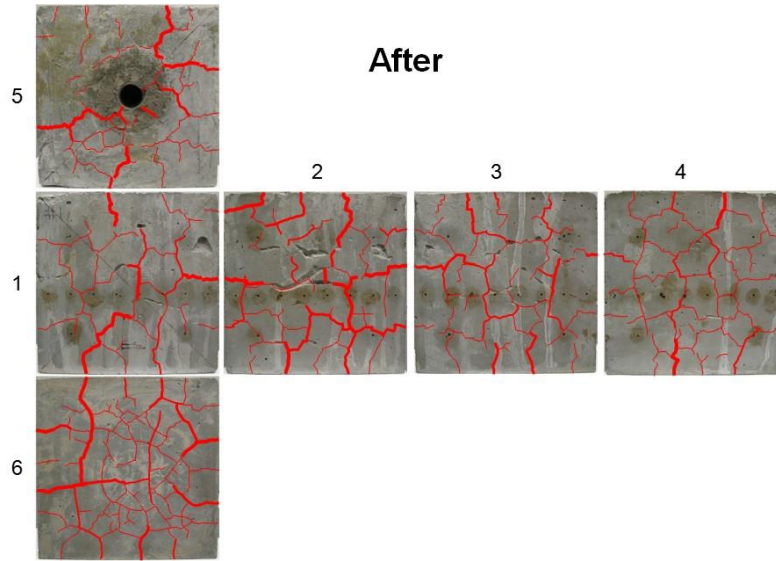
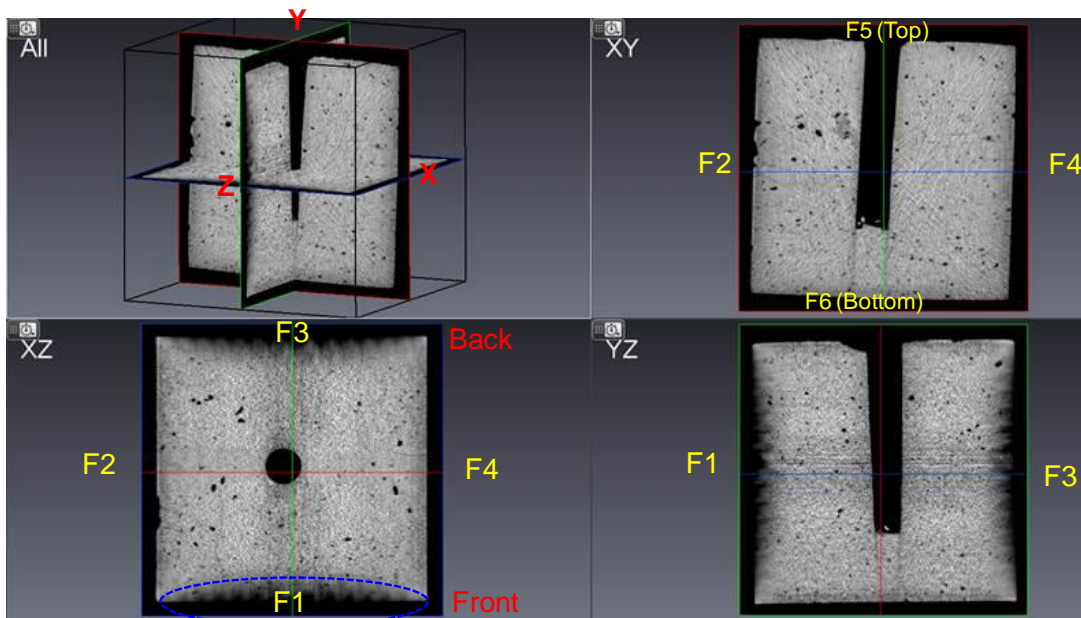


Figure 4.2.28 Surface cracks after the second thermal shock-the superimposed lines are weighted according to the crack thickness.



Beam hardening
or "cupping"

Figure 4.2.29 CT images: axis and direction.

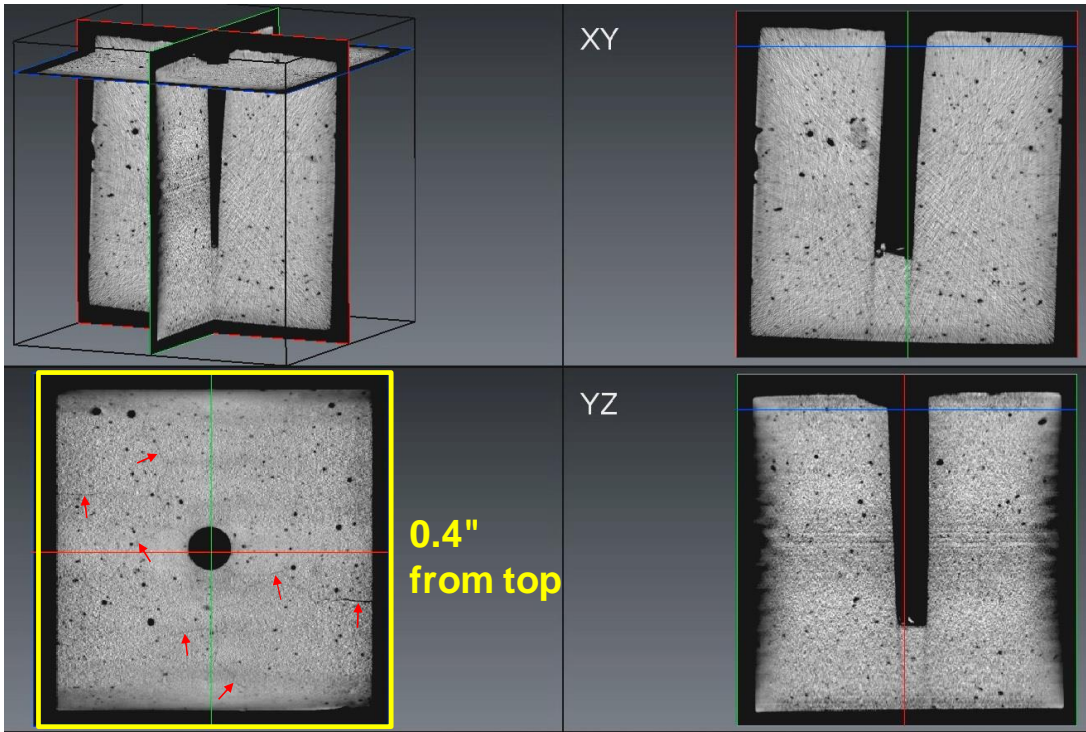


Figure 4.2.30 The CT slide at 0.4" from the top surface.

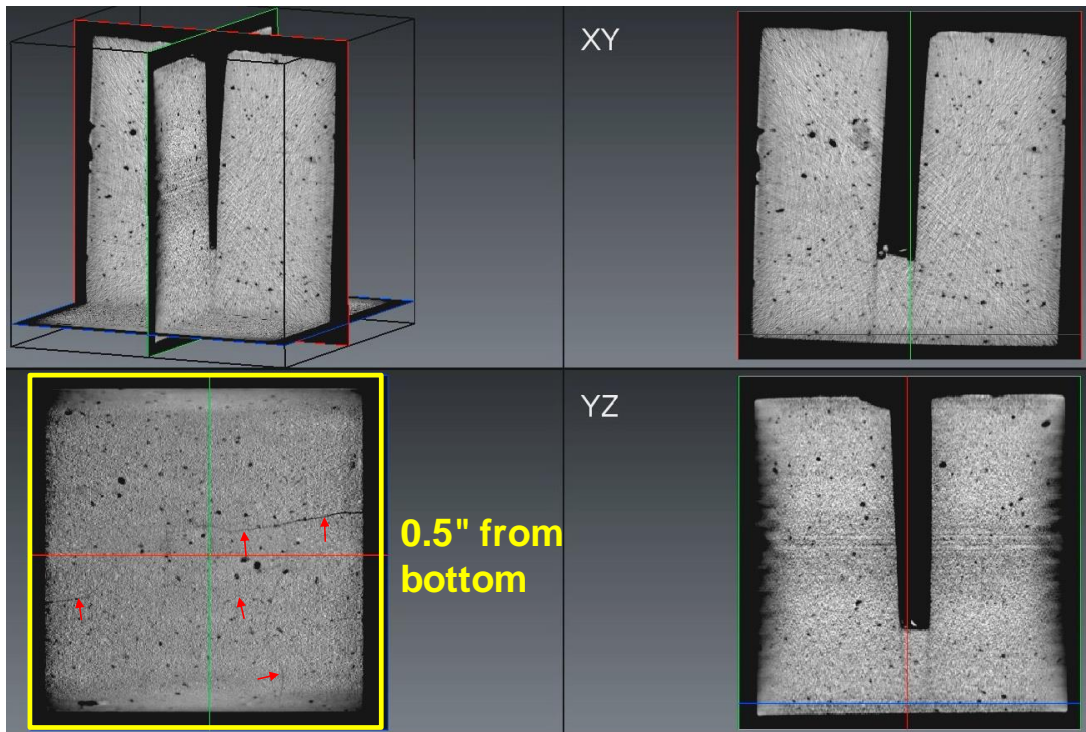


Figure 4.2.31 The CT slide at 0.5" from bottom.

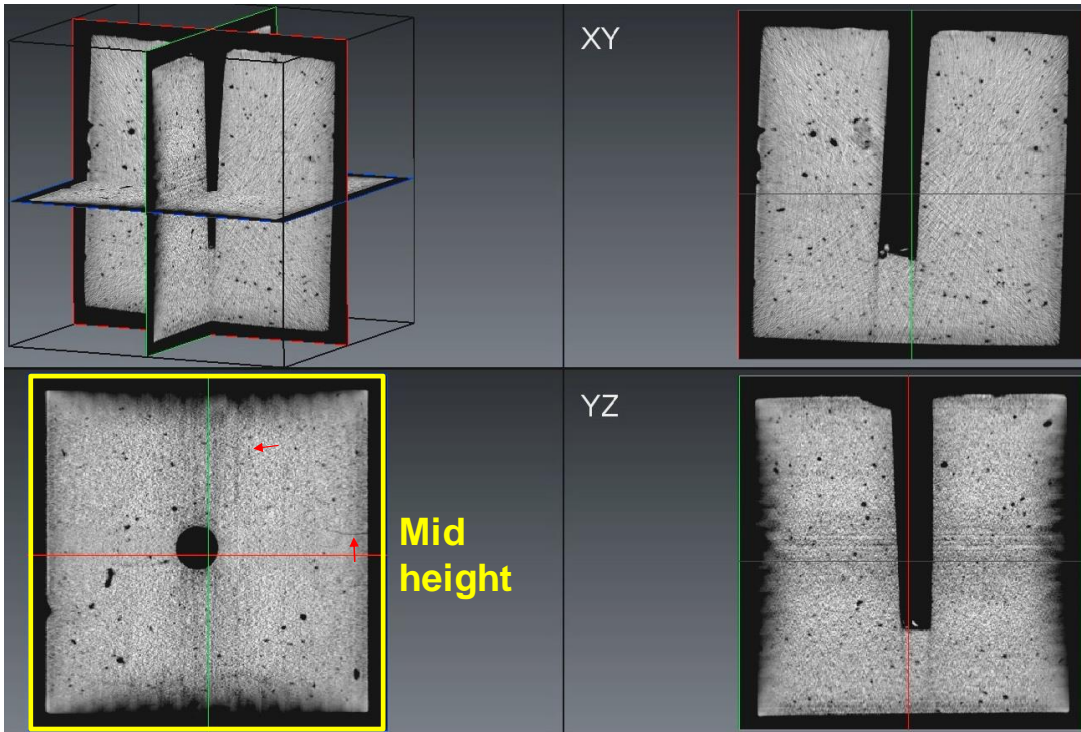


Figure 4.2.32 The CT slide at the mid-height.

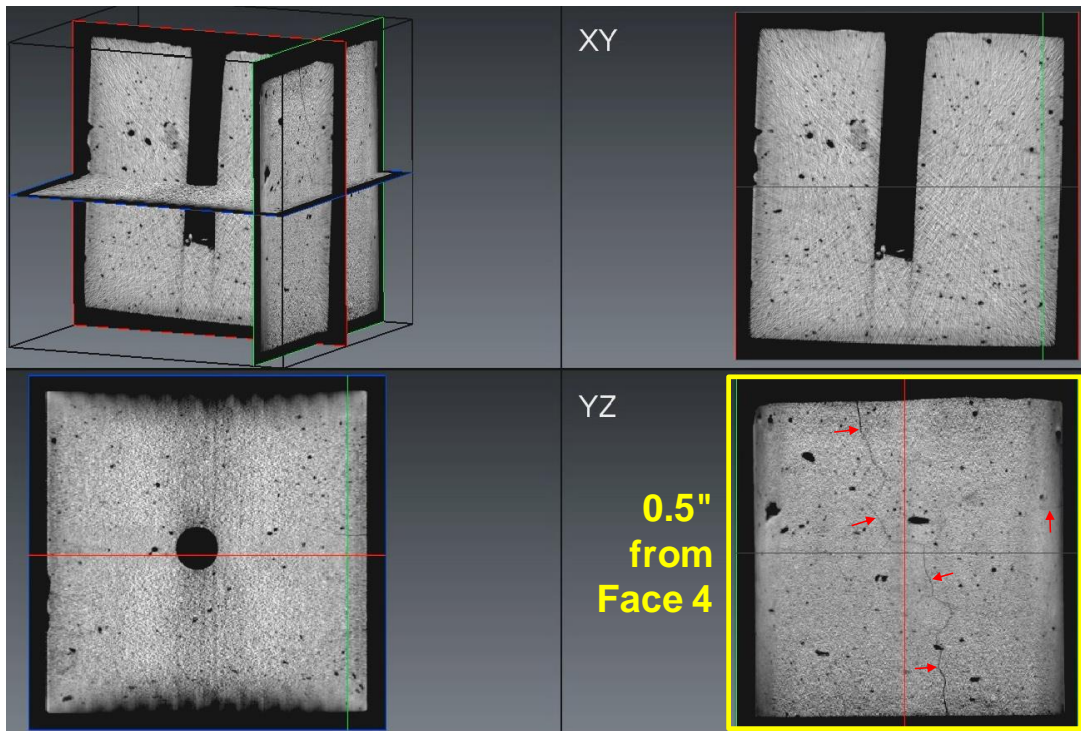


Figure 4.2.33 The CT slide at 0.5" away from Face 4.

Temperature, pressure, and liquid nitrogen consumption

Figure 4.2.34 shows the seven locations of the thermocouples (TC) where temperature is measured. TC #2 is hanging in the air inside the borehole, while TC #1 is attached to the borehole wall. Temperatures at the carbon steel plate (TC #4) and near the pressure transducer (TC #3) are monitored to protect the plates and the sensor.

The temperature evolution during the experiment at the seven locations is plotted in **Figure 4.2.35**. Throughout the test, the temperature difference between the inside of the borehole and the block face is observed to be large. It is observed that cooling at the borehole surface is slower. This is due to the insulating nature of the Leidenfrost effect resulting from very large temperature difference between the surface of the rock and LN₂. We had to repeat partially closing and opening the Dewar lever to control the amount of GN₂ & LN₂ leaking out through fractures and at the outlet as well for safety (Note that the top surface of the block had some fractures from the 1st thermal shock). It is observed that the temperature inside the borehole is sensitive to lever operations.

To obtain more accurate LN₂ delivery rates, the amount of LN₂ flowed out of Dewar was monitored using a scale. The initial part of the nonlinear curve of LN₂ consumption vs. time before the first partial closure shows that more vaporization occurred at the beginning and as LN₂ continued flowing, the flow rate of liquid nitrogen that came out of the Dewar increased (**Figure 4.2.36**). The pressure is generated due to rapid vaporization at the borehole and along transport lines. The changes in pressure clearly correspond to the Dewar lever operation.

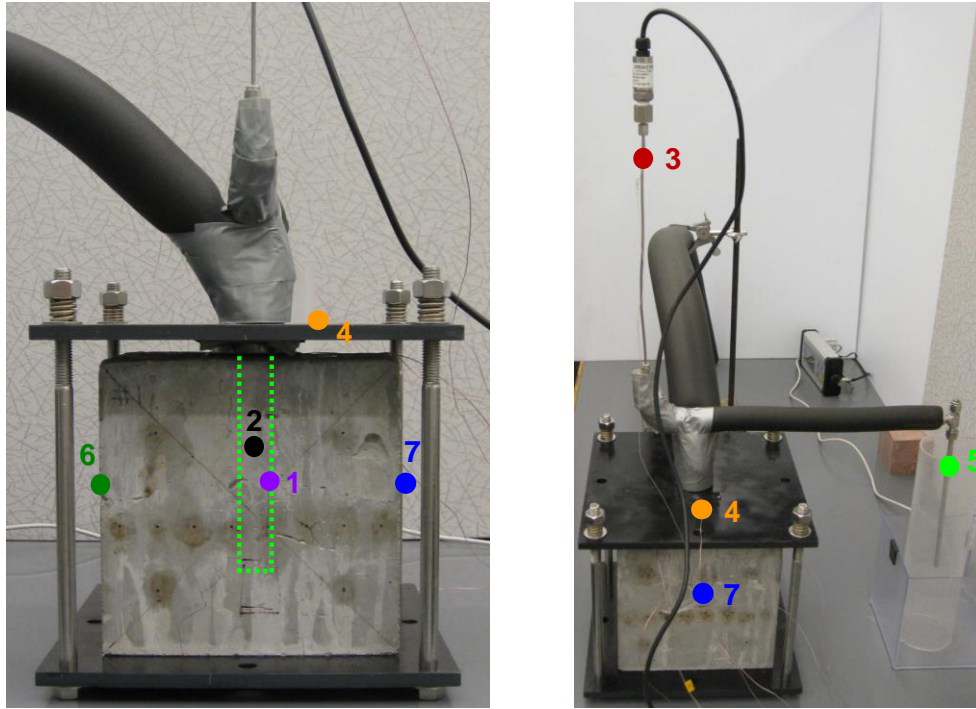


Figure 4.2.34 Locations of thermocouple tips.

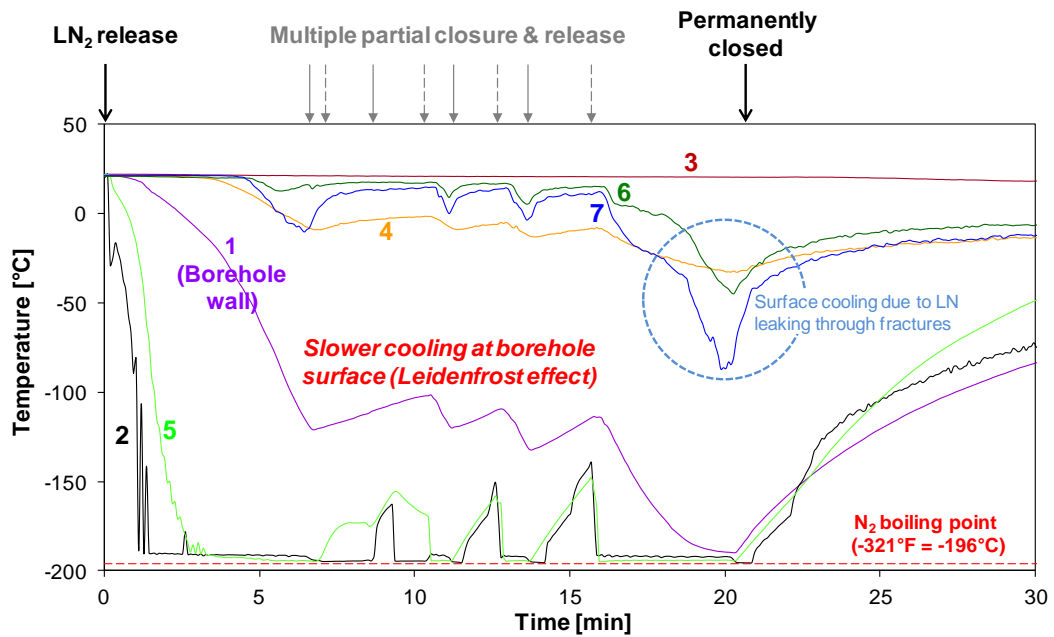


Figure 4.2.35 Temperature vs. time during cryogenic stimulation.

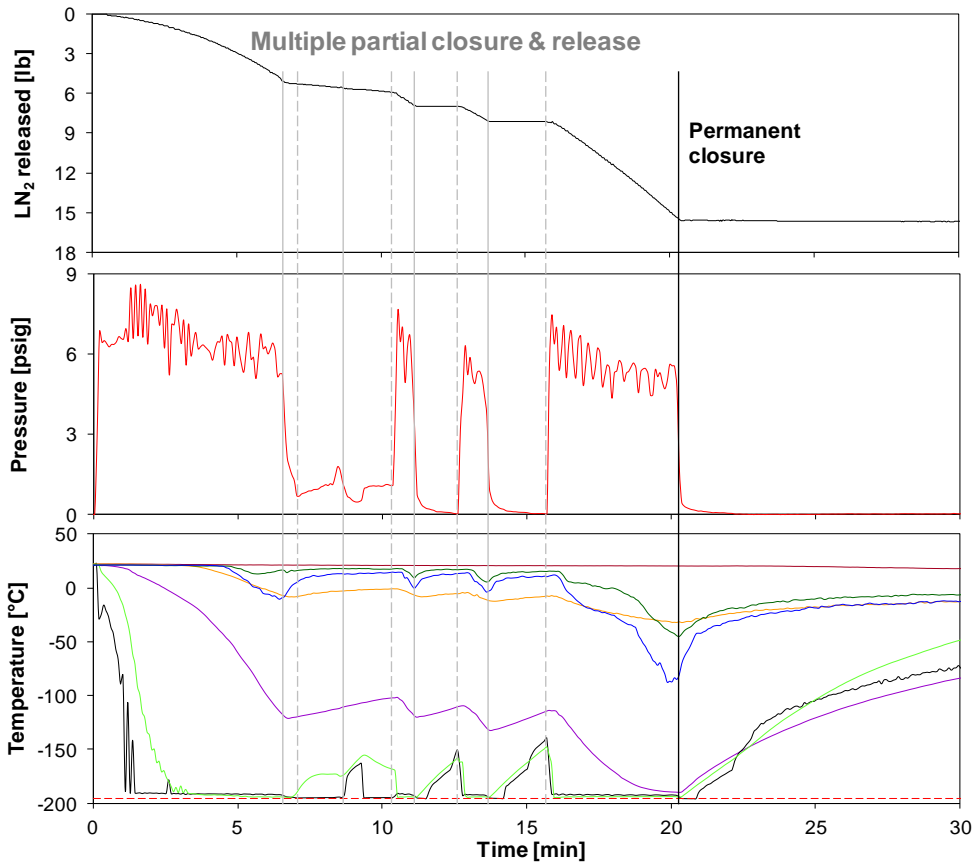
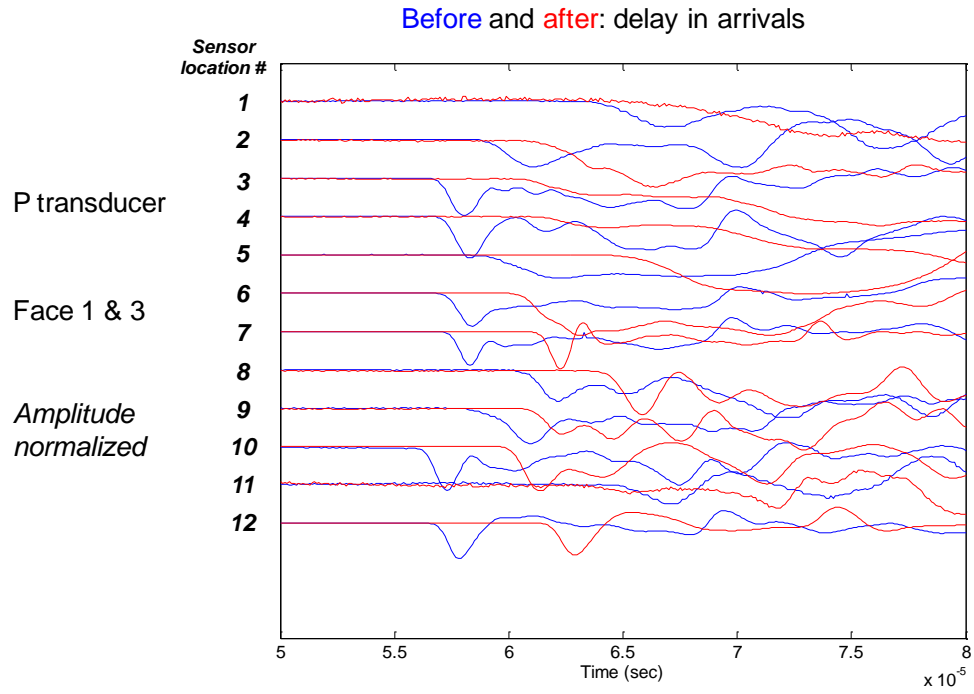


Figure 4.2.36 Synchronized plots of LN₂ consumption, temperature, and pressure with time.

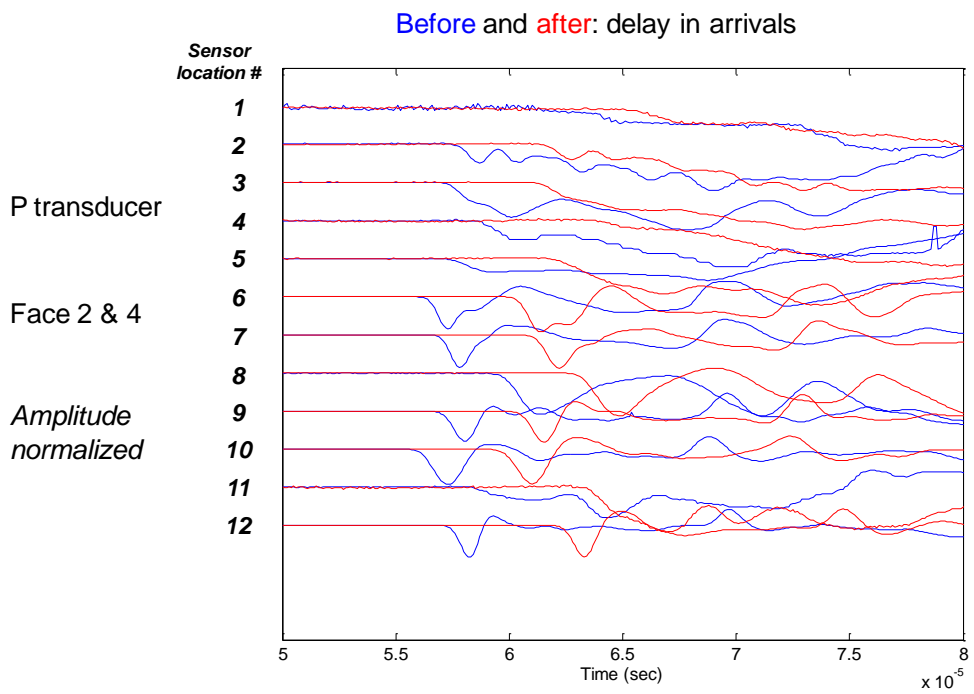
Acoustic signatures

Similar to the case of the 1st thermal shock, in all locations, the P and S wave velocity decreased after the cryogenic stimulation (**Figure 4.2.37**). Wave amplitudes reduced significantly (**Figure 4.2.38**), and global wave amplitudes were reduced (**Figure 4.2.39**) after the cryogenic fracturing in most locations. Higher frequency contents are more filtered after the stimulation.

(a)



(b)



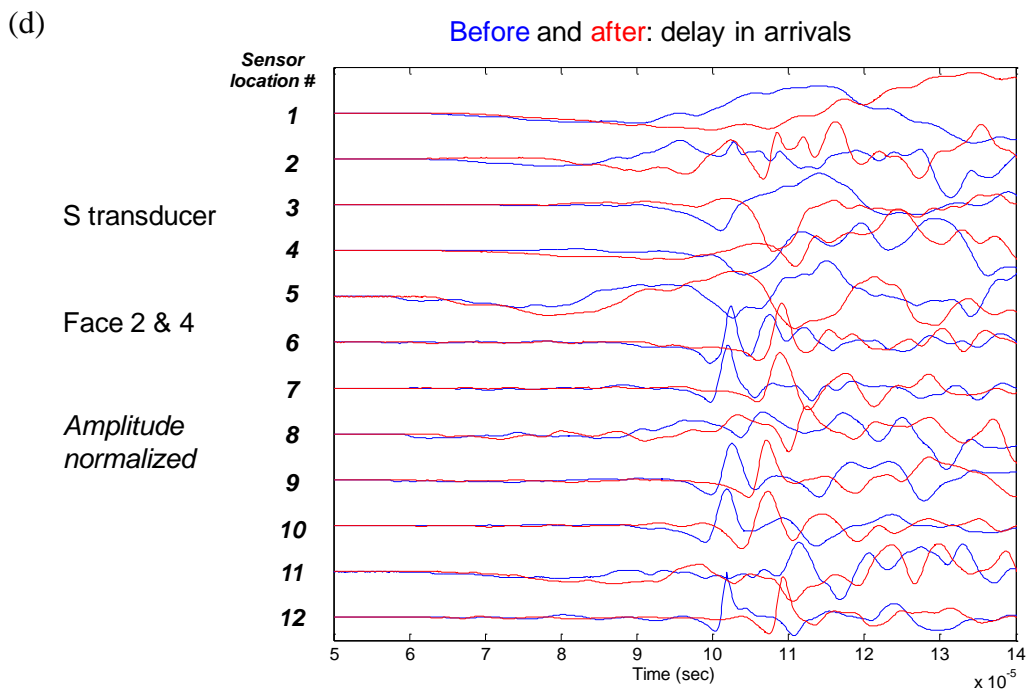
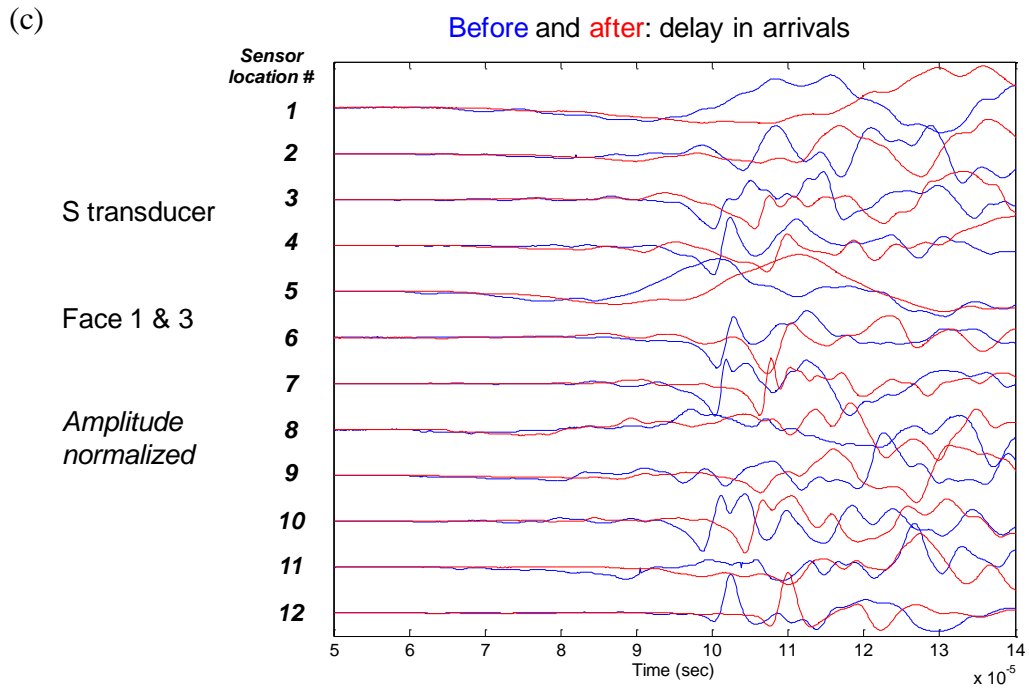
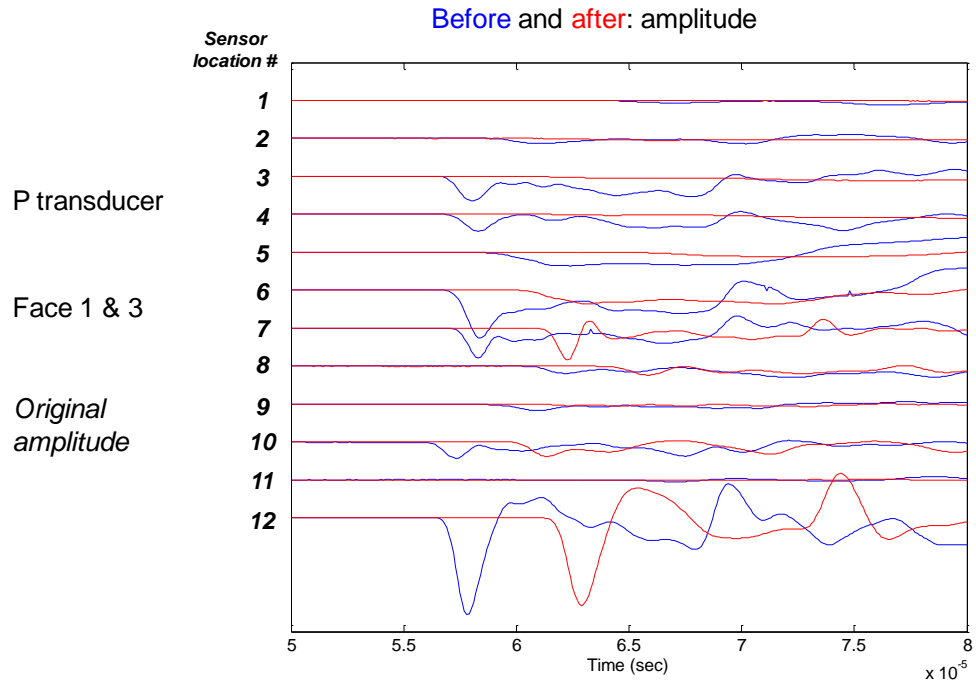
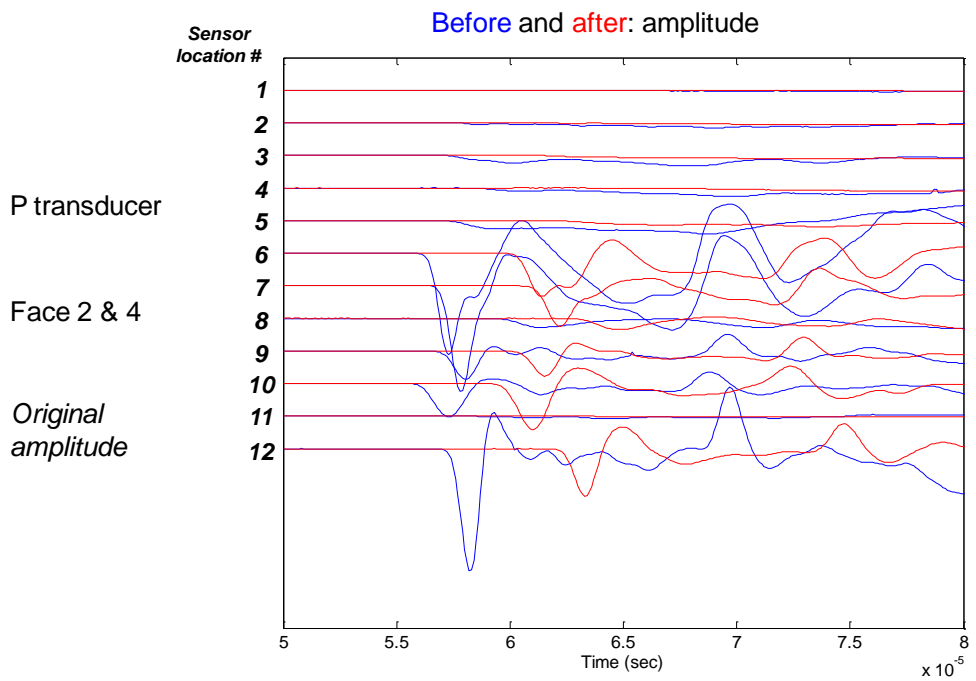


Figure 4.2.37 P and S wave arrivals before and after the thermal shock (compared with normalized amplitude).

(a)



(b)



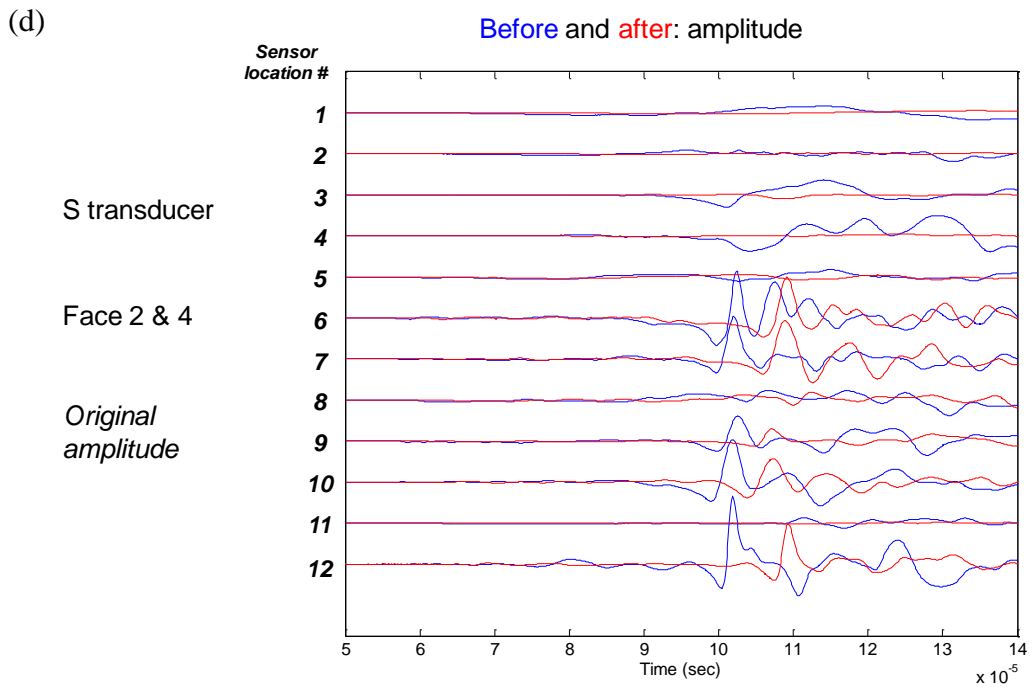
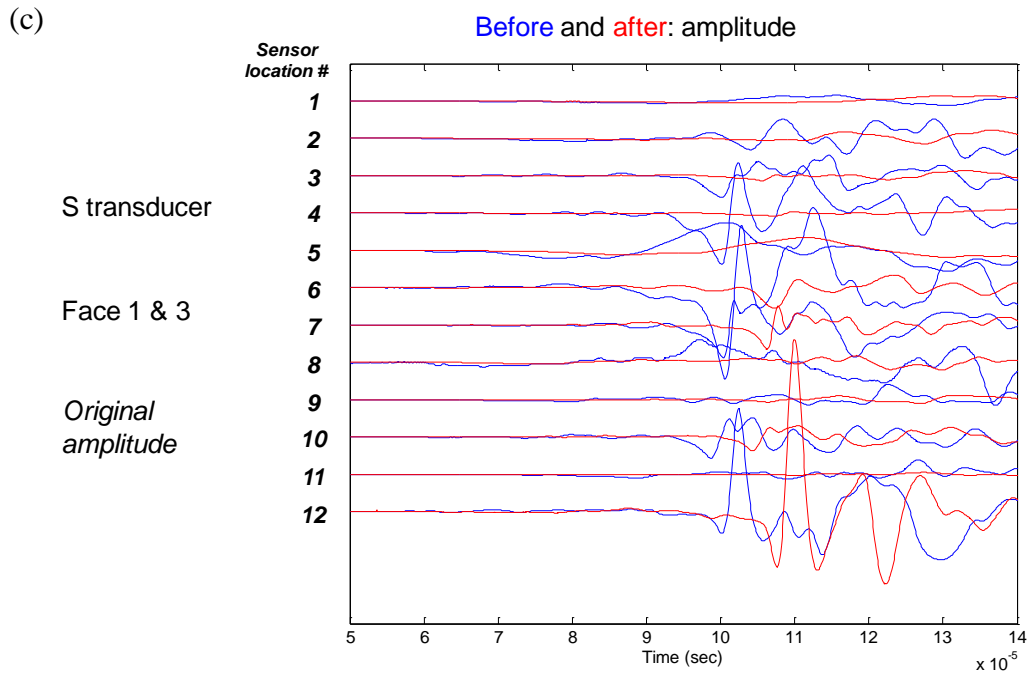
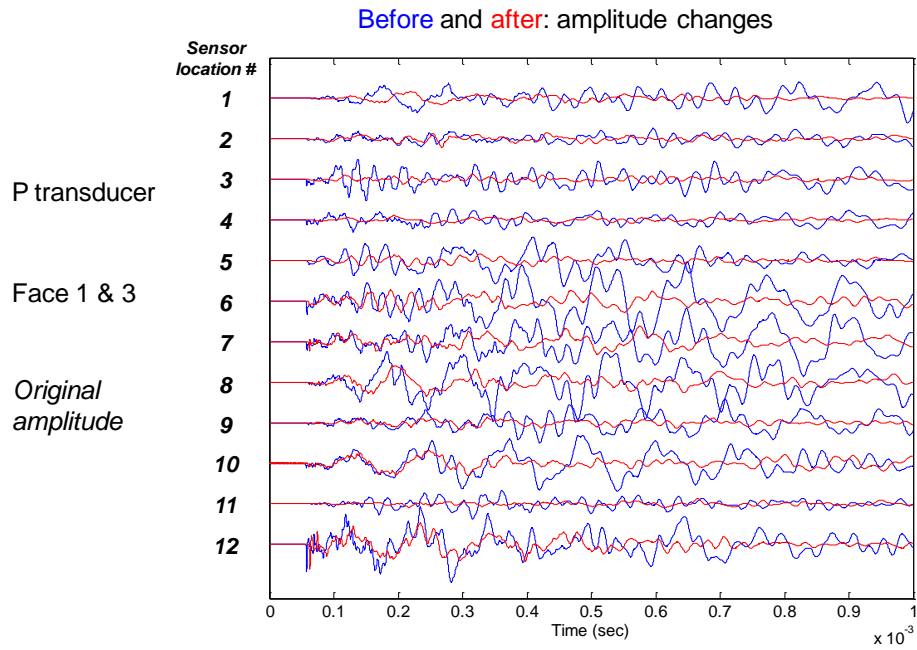
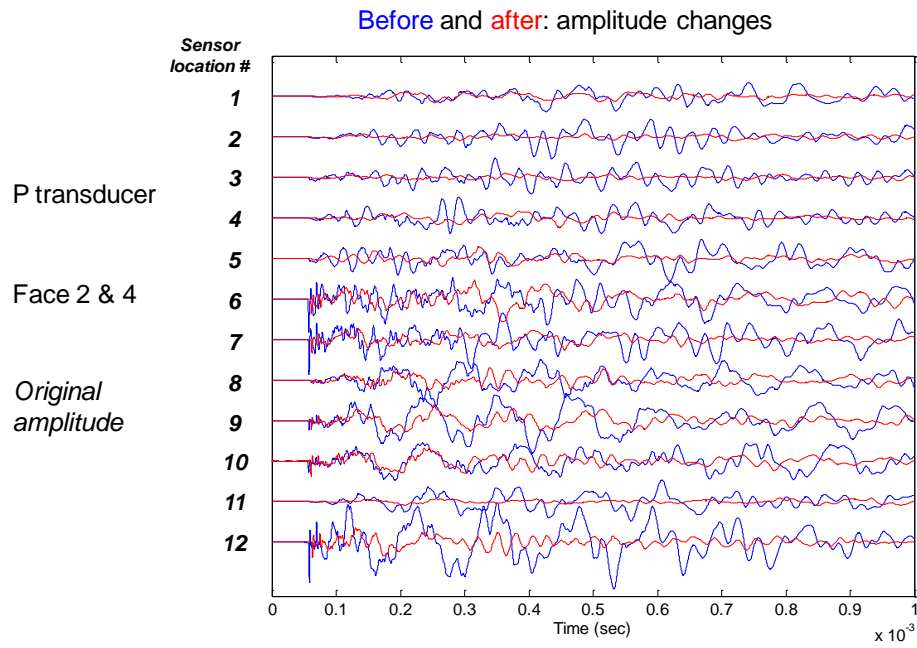


Figure 4.2.38 P and S wave amplitudes before and after the thermal shock.

(a)



(b)



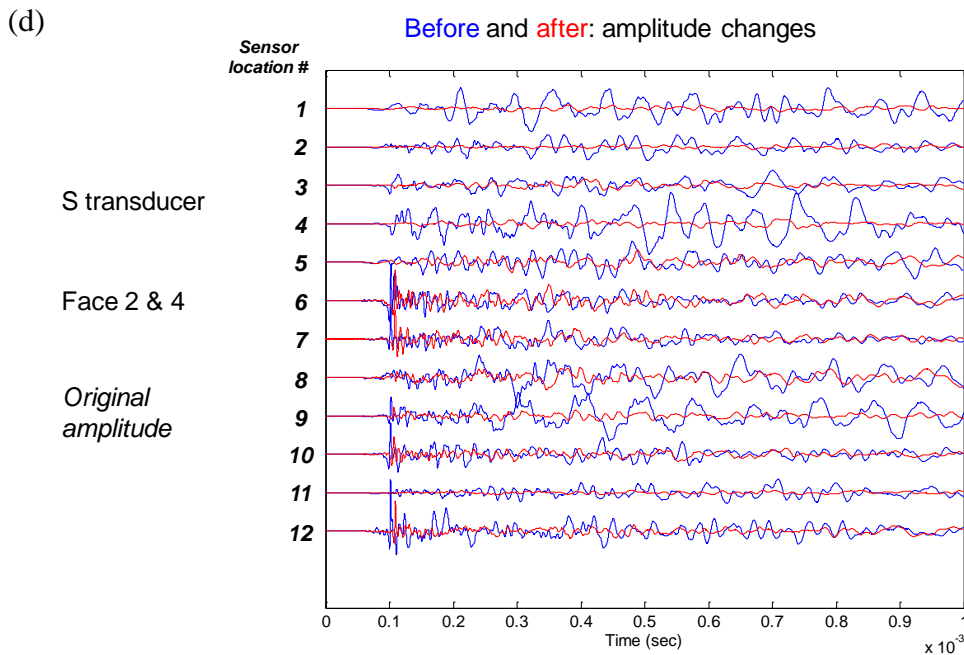
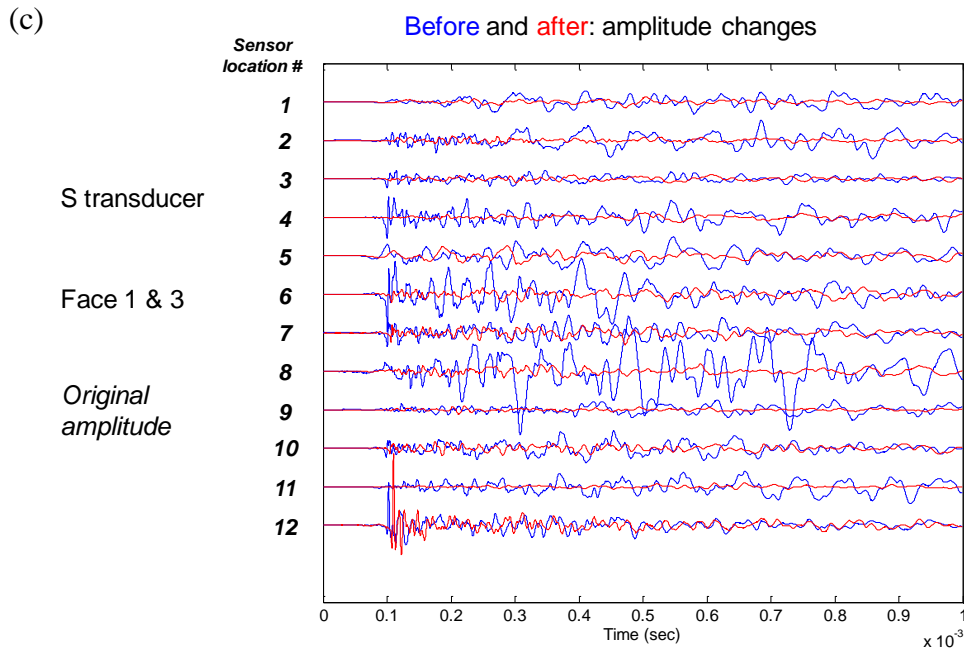


Figure 4.2.39 Global waveforms before and after the thermal shock.

Some other observations

The concrete specimen was already slightly cracked at the surfaces of the borehole and the block due to the 1st thermal shock. At the later stage of the experiment, fractures might have been opened up more, allowing significant nitrogen permeation. It is observed that the matrix

became highly permeable to liquid nitrogen and gas through the fractures (**Figure 4.2.40**). The amount of leaking also depended on the release rate from the Dewar.

There were no leakages through the packer/rock interface. The epoxy seal and stainless steel packer with tubes connected all remained intact under the cryogenic temperature and the pressure conditions (**Figure 4.2.41**). The cryogen-rated insulation and plastic container remained functional. The upper plate (carbon steel) survived at low temperatures ($\sim -30\text{ }^{\circ}\text{C}$). One of the reasons why these are undamaged is that, unlike the borehole environment, temperature propagation is slower in the surrounding environment. Another reason could be that small volume of LN_2 does not create enough contraction to fail the materials and/or interfaces. The thermocouple's plastic insulation coat remained functional throughout the experiment. The block surfaces started to form frost once the temperature of the surface decreased below the water-freezing point.

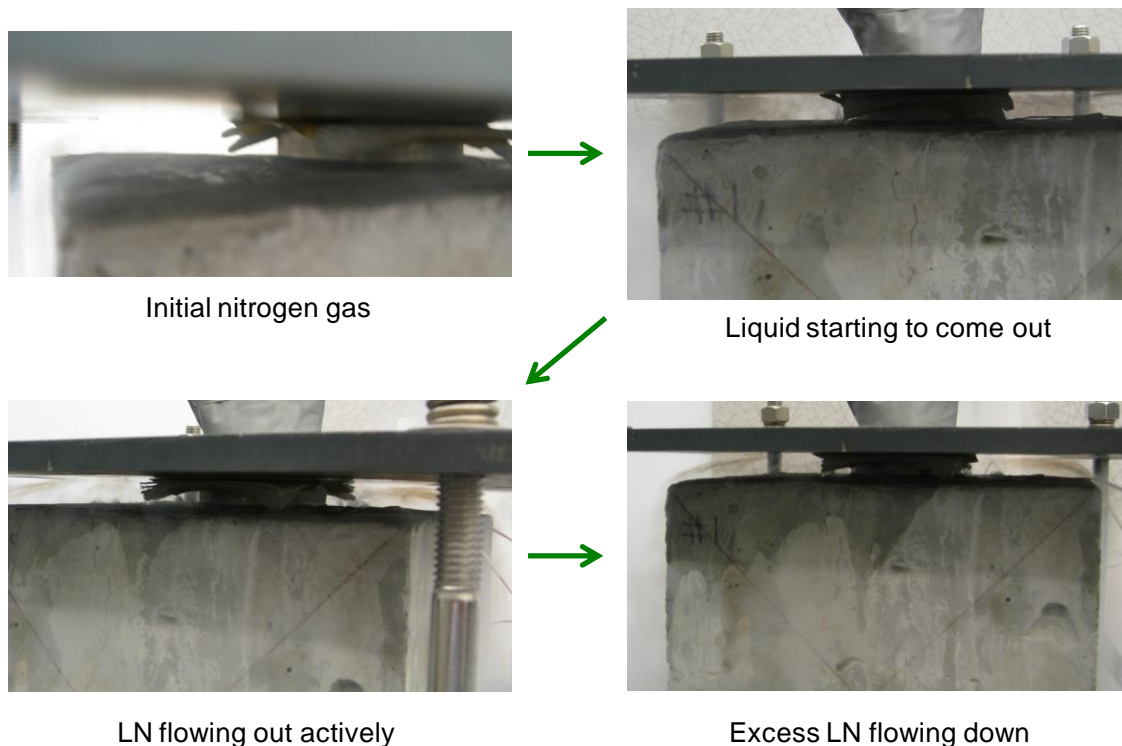


Figure 4.2.40 liquid nitrogen and gas nitrogen permeating through fractures



(a) Epoxy and stainless steel packer

(b) Insulations and carbon steel plates

Figure 4.2.41 Cryogenic performance of surrounding materials.

4.2.3 Sandstone Sample

The sandstone samples were collected from the outcrop of Williams Fork formation, which is a tight gas reservoir producing from fluvial deposits consisting of discontinuous sandstones, siltstones, shales, and coals in Rifle County in the northwest of Colorado (Pranter et al. 2008). This Late Cretaceous unit is found within the greater Mesaverde Group, which is estimated to contain as much as 423 TCF of natural gas, trapped in the sandstone lenses and sealed by impermeable shale layers (Law 2002).

In the experiment, LN₂ was poured into the borehole through a funnel into the 8" × 8" × 8" sandstone block (**Figure 4.2.42**). The LN₂ volume poured each time was about 350 inch³. **Figure 4.2.43** and **Figure 4.2.44** show the results of two consecutive cryogenic tests applied to the same sandstone sample. The blue line is the temperature at the top of the block sample, the red arrows mark the times when the LN₂ was poured. The temperature of the borehole wall (#1) did not reach the boiling point of LN₂ (#2), indicating that the Leidenfrost effect prevented the liquid to be in contact with formation. Thus, a ventilation setup should be added to this setup to remove the vapor cushion resulting in the Leidenfrost effect, or, a pressure may be applied on the LN₂ to reduce the Leidenfrost barrier for heat transfer.

To measure the effectiveness of the cryogenic treatment, pre-stimulation and post-stimulation gas leak-off tests were performed. This is done by pressurizing the specimen with GN₂ at a constant pressure (~100 psi) and flow rate (~600 mL/min) and shutting it in, which is shown schematically in **Figure 4.2.45**. Before the cryogenic test, the pressure inside the wellbore took 47 minutes to decay; after the cryogenic test, the decay time was 39 minutes. This change clearly indicates permeability enhancements due to cryogenic fracturing.

Even though we did not use a packer, the epoxy used to attach the casing to the sample withstood the thermal shock during our first two tests. However, on the third test, the epoxy was damaged (**Figure 4.2.46**).

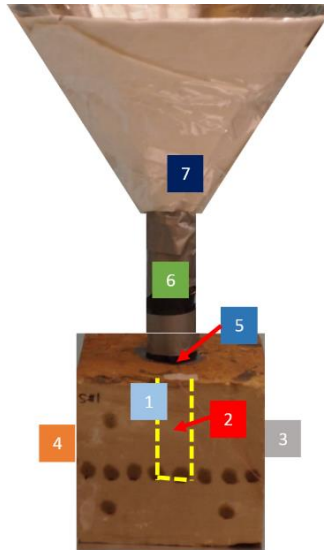


Figure 4.2.42 The locations of the thermocouples in the sandstone block tests. There are no external stresses and borehole pressure.

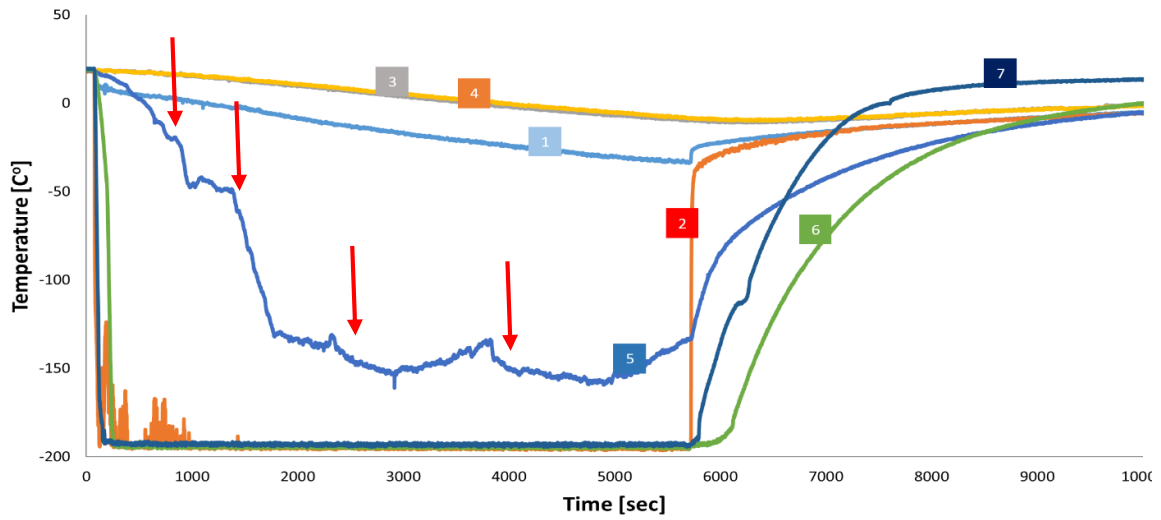


Figure 4.2.43 Temperature values during the first cryogenic test. The numbers (1-7) are the locations of the thermocouples. Red arrows in the figure mark the times when LN₂ was poured.

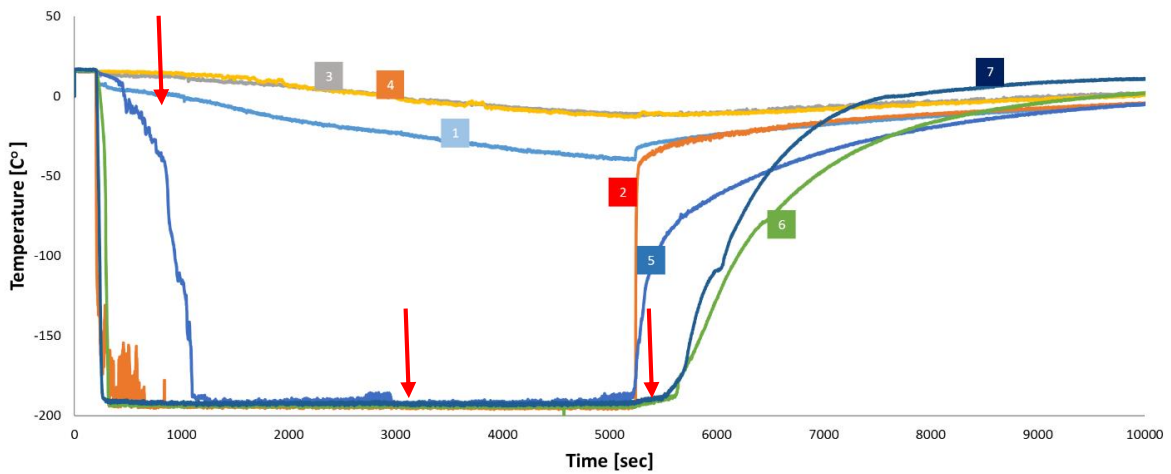


Figure 4.2.44 Temperature values during the second cryogenic test. The numbers (1-7) are the locations of the thermocouples. Red arrows in the figure mark the times when LN₂ was poured.

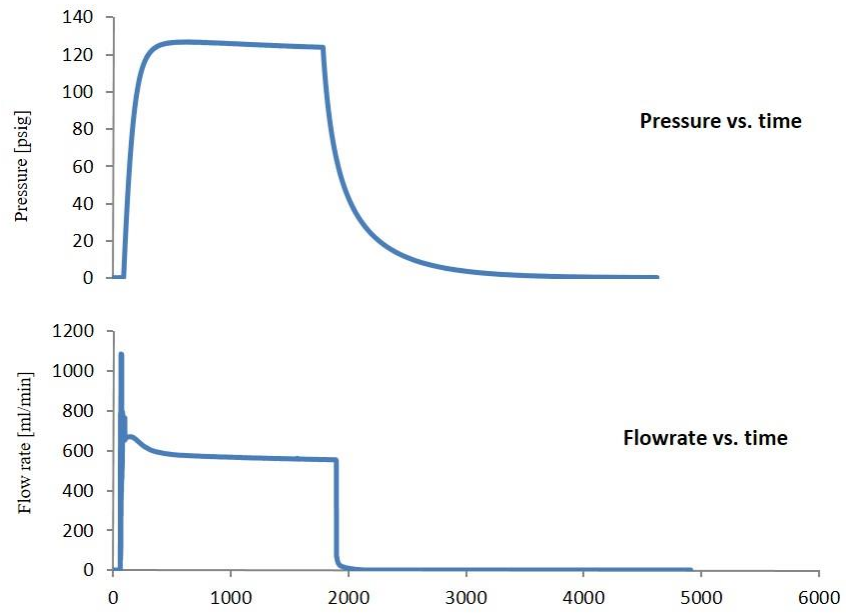


Figure 4.2.45 Constant pressure and flow rate are reached before shut-in for the gas leak-off test.



Figure 4.2.46 Epoxy was damaged by repeated exposures to the cryogenic temperature.

4.3 Pressurized Borehole Stimulation

Borehole thermal shock experiments in the previous section were conducted without external stresses at low borehole pressure, which was mainly caused by rapid vaporization of LN₂. In this section, the borehole stimulation experiments, using either GN₂ or LN₂, were carried out by pressurizing the fracturing fluids into the borehole.

4.3.1 Concrete Samples

For each type of tests, the concrete samples were prepared following different procedures. The specifics of the concrete samples used in this section are summarized in **Table 4.1**.

For the tests involving oven-dried samples, all samples were placed in a Quincy Lab Oven at 65 °C for 10 days. After 10 days of drying, the changes in weights from day to day measured by an Adams Scale (CPWplus-75) with a readability of 0.05 pounds were insignificant; therefore, all of the oven-dried samples were heated for 10 days before they were tested. The samples were then taken out of the oven and allowed to cool to a room temperature of 20 °C before tests.

The saturated samples were prepared by completely submerging oven-dried samples in a bin filled with tap water at the room temperature of 20 °C. They were submerged for 3 days to allow water to completely permeate the samples. Then, the samples were taken out and tested. On average, the samples weighed approximately 1kg more after saturation. Once the samples were fully saturated they were taken out of the water bin, sponged of any excess water on the surface, and tested immediately.

The dry high-temperature samples were prepared similar to the oven-dried samples, except they were not allowed to cool back down to the room temperature. These samples, with a temperature of 65 °C, were taken out of the oven and a pressure decay test was performed on them. Since the pressure decay test takes time, the samples would cool down significantly. They were then placed in the oven overnight to allow the temperature of the sample to increase back to 65 °C and tested the next day.

The last type of test was a combination of high temperature testing while the sample was saturated with water. For these experiments the samples were prepared by placing them in a large plastic bin filled with water. The bin was then covered to reduce evaporation, and placed in the oven at 65 °C. It was left in the oven for 3 days to allow for full saturation and to allow adequate time for the sample to reach the desired temperature.

Table 4.1 Specifics of concrete samples

Sample #	Experiment type	Saturated weight (kg)	Dry weight (kg)	Borehole creation	Curing time (days)
1	Oven-dried, GN ₂	17.62	17.02	Mold	143
2	Oven-dried, GN ₂	17.68	17.10	Mold	67
3	Oven-dried, GN ₂	17.58	16.98	Mold	96
4	Oven-dried, LN ₂	17.88	17.16	Mold	148
5	Oven-dried, LN ₂	17.64	16.78	Mold	75
6	Oven-dried, LN ₂	17.86	16.96	Mold	96
7	Saturated, LN ₂	17.92	×	Drilled	52
8	Saturated, LN ₂	17.84	×	Drilled	45
9	Saturated, LN ₂	17.86	×	Drilled	45
10	Dried, high T, LN ₂	17.78	17.04	Drilled	55
11	Dried, high T, LN ₂	17.98	17.10	Drilled	115
12	Dried, high T, LN ₂	17.82	16.98	Drilled	118
13	Saturated, high T, LN ₂	17.92	×	Drilled	104
14	Saturated, high T, LN ₂	17.84	×	Drilled	66
15	Saturated, high T, LN ₂	17.80	×	Drilled	67

4.3.1.1 Nitrogen Gas Fracturing

The following experiments were all performed on oven-dried concrete samples. Nitrogen gas fracturing was an attempt to determine a baseline to compare subsequent tests. As seen below in **Figure 4.3.1** the breakage points for the three samples were 909 psi, 566 psi, and 491 psi, respectively. Sample 1 has a much higher breakdown pressure than Samples 2 and 3 because it had a much longer curing time.

Figure 4.3.2 shows the pressure decay tests for Samples 2 and 3. The experiment on Sample 1 was performed before deciding to do pressure decay tests on all samples therefore pressure decay data were not collected. It can be observed that Sample 2 has a faster decay and

therefore higher permeability. These two tests were performed with an initial pressure of 175 psig at a room temperature of 20 °C.

Figure 4.3.3, Figure 4.3.4, and Figure 4.3.5 show the GN₂ fracture profiles of Samples 1, 2, and 3. For each tested sample, the fracture profiles on six sample faces and the internal faces are presented. The purpose of this is to draw parallels between different samples and fracturing conditions and see if there is a correlation by which the sample fractures. It can be observed from these three figures that Sample 1 and 2 developed vertical fractures that are parallel to the axis of the borehole, whereas Sample 3 developed a fracture that is almost perpendicular to the borehole. For unconfined samples, direction of the fracture can be arbitrary, depending on the locations of weaknesses.

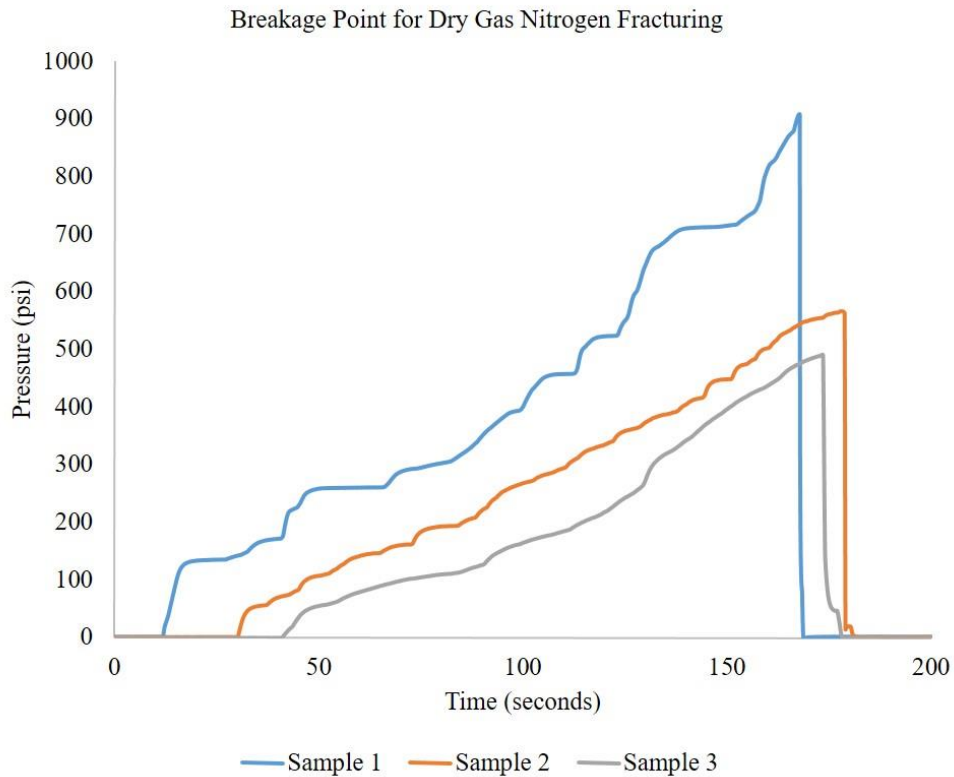


Figure 4.3.1 Breakage points for dry Samples 1-3 using nitrogen gas.

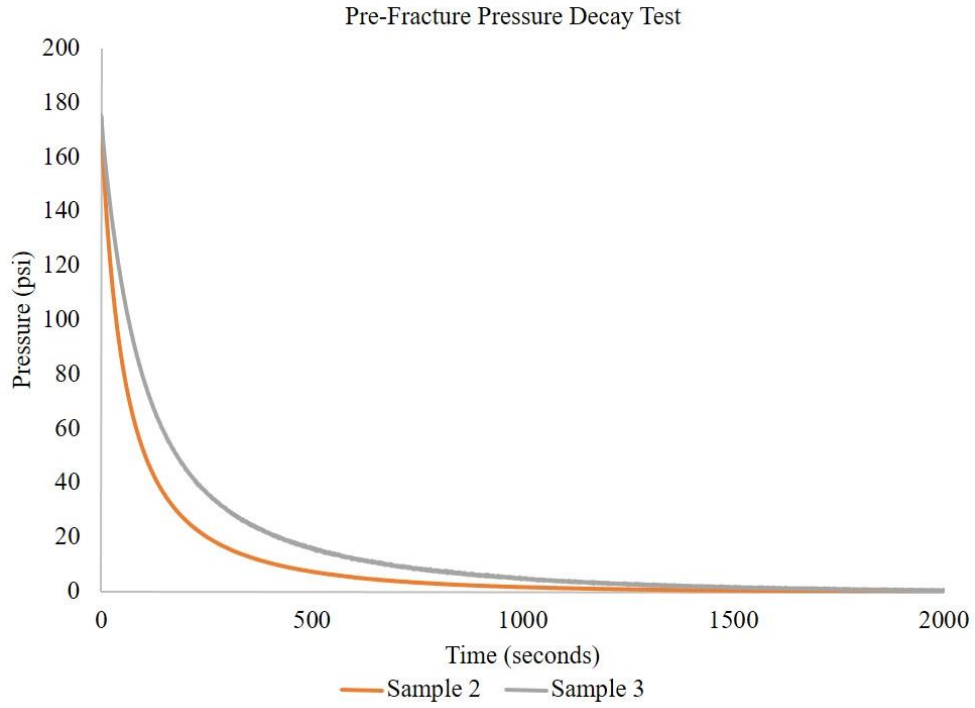


Figure 4.3.2 Pre-fracture pressure decay curves for Samples 2 and 3.

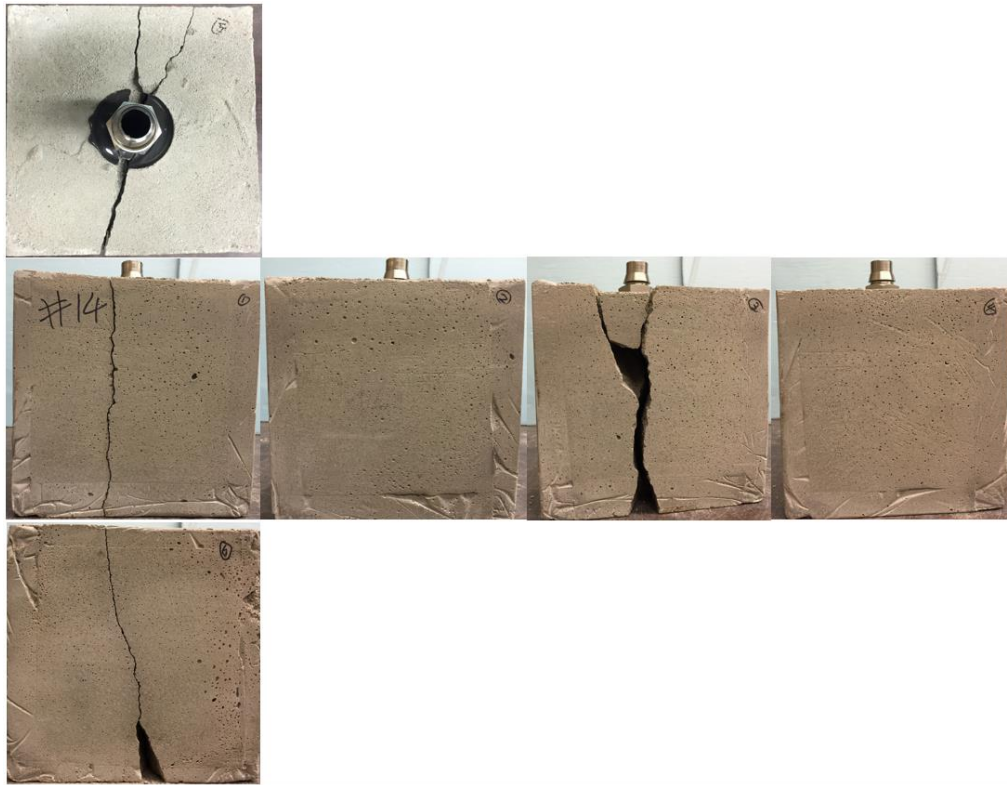




Figure 4.3.3 Fracture profile of Sample 1.





Figure 4.3.4 Fracture profile of Sample 2.

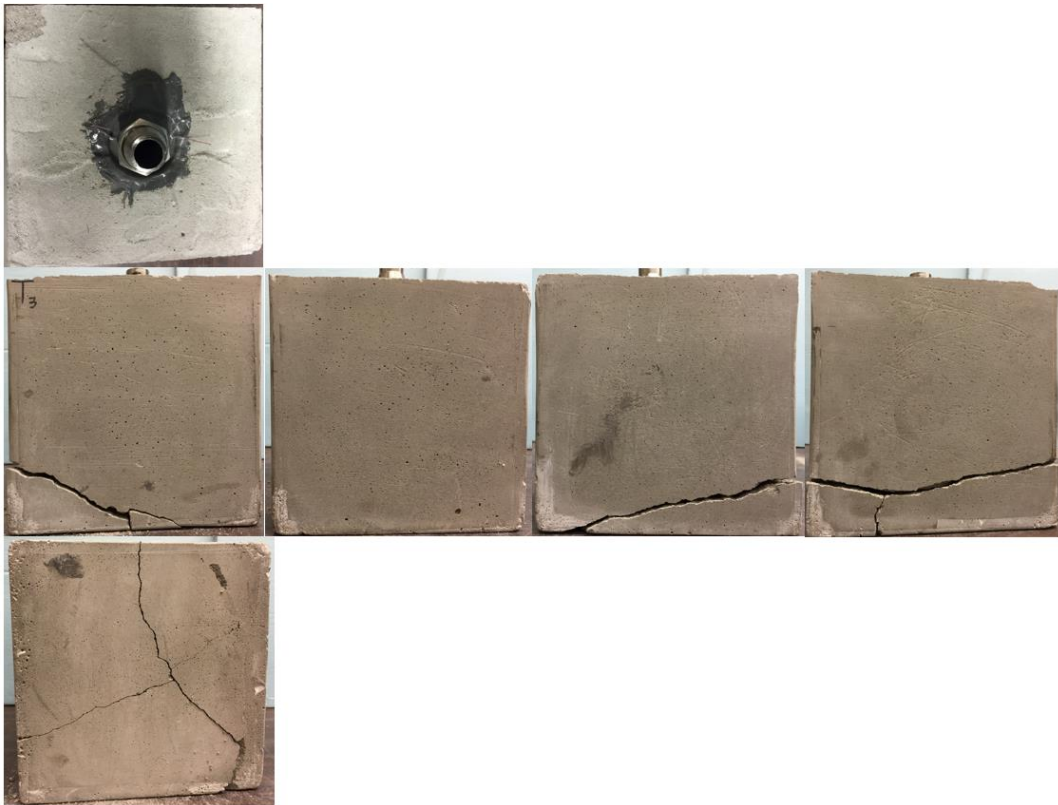




Figure 4.3.5 Fracture profile of Sample 3.

4.3.1.2 LN₂ Stimulating Dry Samples

The following experiments were all performed on concrete samples by injecting liquid nitrogen. Samples 4, 5 and 6 were oven-dried concrete samples. Sample 4 was performed while the testing procedure was still being fine-tuned; therefore, the data for Sample 4 are rather sparse, inconclusive, and different from the other two samples. The data acquisition system also failed during the testing of Sample 4, so some of the data gathered were lost. In addition, Sample 4 was treated with liquid nitrogen at 15 psi for 30 minutes, allowed to warm back up to room temperature, and then fractured with gas nitrogen; Samples 5 and 6, on the other hand, were treated with liquid nitrogen pressurized to 305 psi and 320 psi, respectively. After Samples 5 and 6 warmed back to the room temperature, they were also fractured by gas nitrogen. Shown below in **Figure 4.3.6** and **Figure 4.3.7** are the results from injecting liquid nitrogen into Sample 5 and 6, respectively. For Sample 5, at $t = 2290$ (all time units are in second) the valve from the liquid nitrogen accumulator into the borehole was opened, allowing liquid nitrogen to flow into the wellbore. At $t = 2550$ the liquid nitrogen in the accumulator was depleted. As a result, the temperature in the borehole began to rise back to the room temperature. For Sample 6, there are two distinct decreases in temperature during the experiment. The first occurred at $t = 2290$, while the cryogen outlet valve was not completely opened. The second temperature drop, at $t = 2505$, occurred after the outlet was

opened more. There is a distinct pressure difference in the accumulator and the sample when the outlet was opened more, because the nitrogen gas has to pressurize both the nitrogen gas accumulator and the liquid nitrogen accumulator, both of which have relatively large volumes in comparison with the deliverability of the tubing that supplies the gas nitrogen. Another observation is the temperature change in the liquid nitrogen accumulator. The liquid nitrogen supply was turned on at $t = 285$, leading to the decrease of accumulator temperature. The temperature decreased linearly until $-70\text{ }^{\circ}\text{C}$, when there was a noticeable change in the cooling rate of the accumulator. Then the temperature of the accumulator continued to decrease linearly but at a much slower rate. This trend was seen for all of the tests performed.

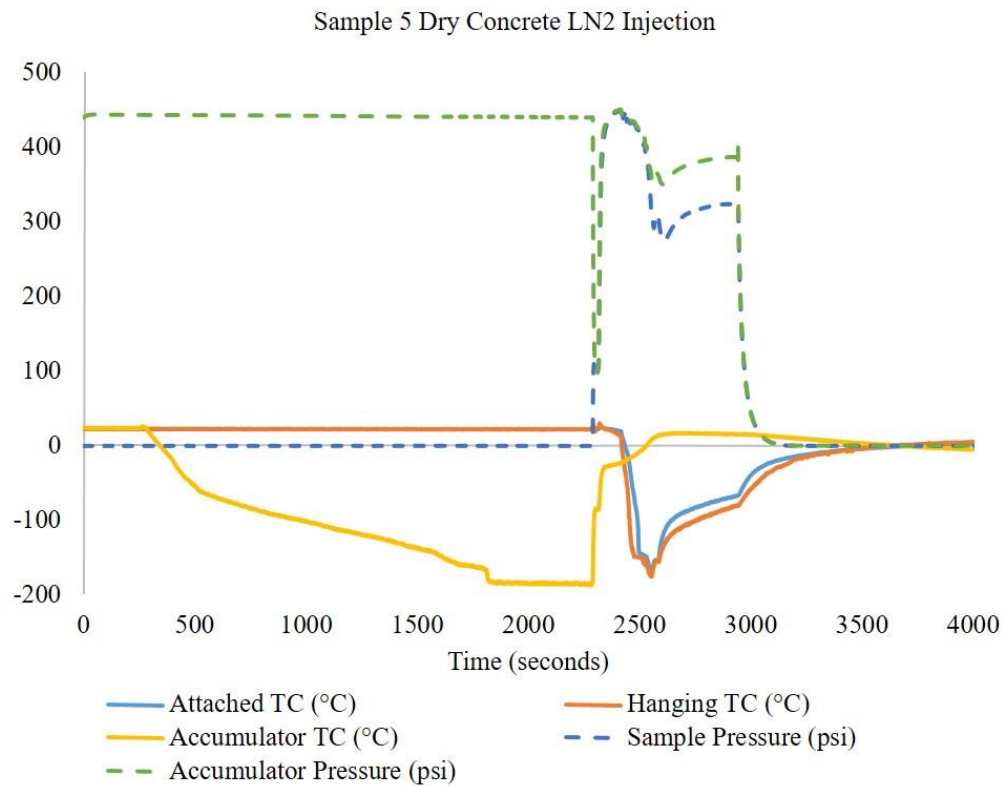


Figure 4.3.6 Pressure and temperature records during cryogenic treatment of Sample 5.

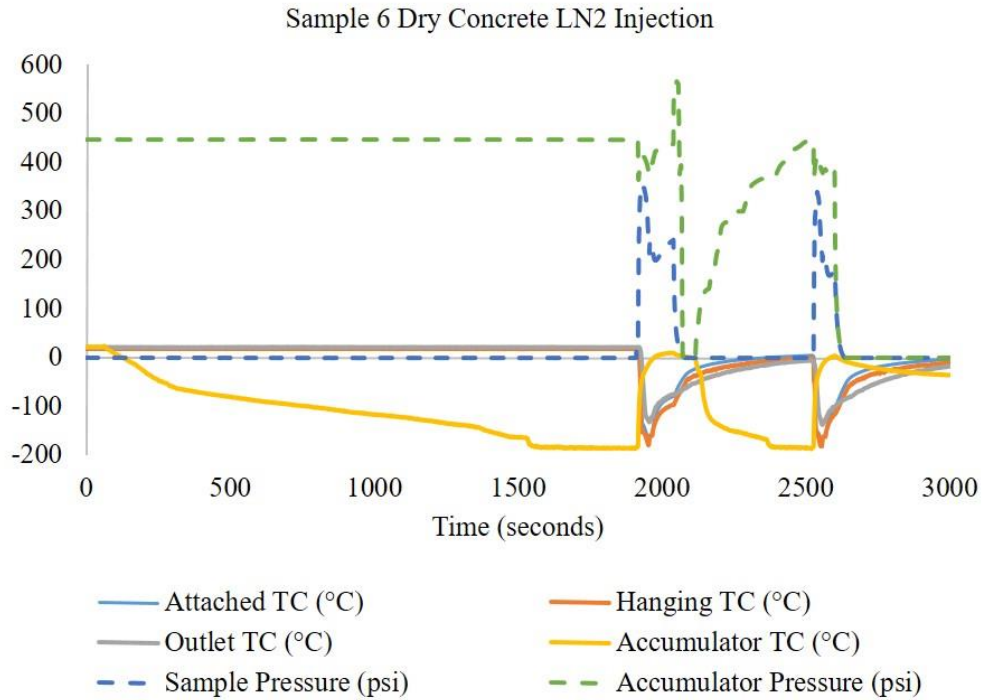


Figure 4.3.7 Pressure and temperature records during cryogenic treatment of Sample 6.

Compared to Sample 5, which was treated with liquid nitrogen only once, Sample 6 was treated twice, as indicated by the two separate major temperature drops in the borehole in **Figure 4.3.7**. The specific list of events done is as follows: liquid nitrogen began filling the accumulator at $t = 67$; the first treatment started at $t = 1917$; the first treatment completed and the accumulator started to refill at $t = 2117$; the second treatment began at $t = 2528$ and completed at $t = 2636$. As seen in this figure, the injection pressure of LN₂ was not a constant, but varied with the temperature and pressure conditions in the borehole and the accumulator. This is a limitation of the design, as we do not have a liquid nitrogen pump, the maximum volume of liquid nitrogen that can be discharged from the accumulator per treatment is one liter, and it is difficult to have consistent pressure as the process was manually controlled by a valve.

Shown below in **Figure 4.3.8** are the results of pre- and post-treatment pressure decay tests for Samples 5 and 6. It appears that Sample 5 had a significant increase in gas permeability. It should also be noted that there was practically no change between pre- and post-treatment

pressure decay data for Sample 6. Pressure decay tests should only be compared between pre- and post-treatment on the same sample. It was noticed that not every sample formed a perfect seal. Depending on how much epoxy was used, air leaking was audibly heard and physically felt through the concrete around the epoxy near the borehole. At times, hissing sound indicating leak was also heard through the thermocouple lines. **Table 4.2** summarizes the results from the liquid nitrogen experiments on dry concrete samples.

In addition to the pre-stimulation and post-stimulation pressure decay rates, we wanted to show a phenomenon present in all of the pressure leak-off tests. In the previous pressure decay tests, the temperature data were omitted and the test began exactly when the pressure in the sample is shut-in at 175 psi. Below in **Figure 4.3.9** is a complete pre-stimulation pressure leak-off test on Sample 6 with temperature data. Notice how the temperature changed with the pressure. This is an observation of the Joule-Thomson effect which occurs when a gas expands under adiabatic conditions. As shown in this case, as pressure increases, temperature increases, and as the pressure is relieved, the temperature decreases. This was observed in all pressure decay tests. However, only this instance is shown here. It is an indication that in order to precisely match the pressure decay, we may need to use a non-isothermal reservoir simulator. **Figure 4.3.10** to **Figure 4.3.12** shown on the following page are the fracture profiles of Samples 4, 5, and 6.

Table 4.2 Summary of dry concrete liquid nitrogen injection tests

Summarization of dry concrete liquid nitrogen injection tests				
Sample	Breakdown pressure (psi, nitrogen gas)	Injecting pressure at lowest temperature(psi)	Minimum temperature in borehole (°C)	Cycles of treatments
4	580	×	×	1
5	352	305	-176	1
6	822	320	-182	2

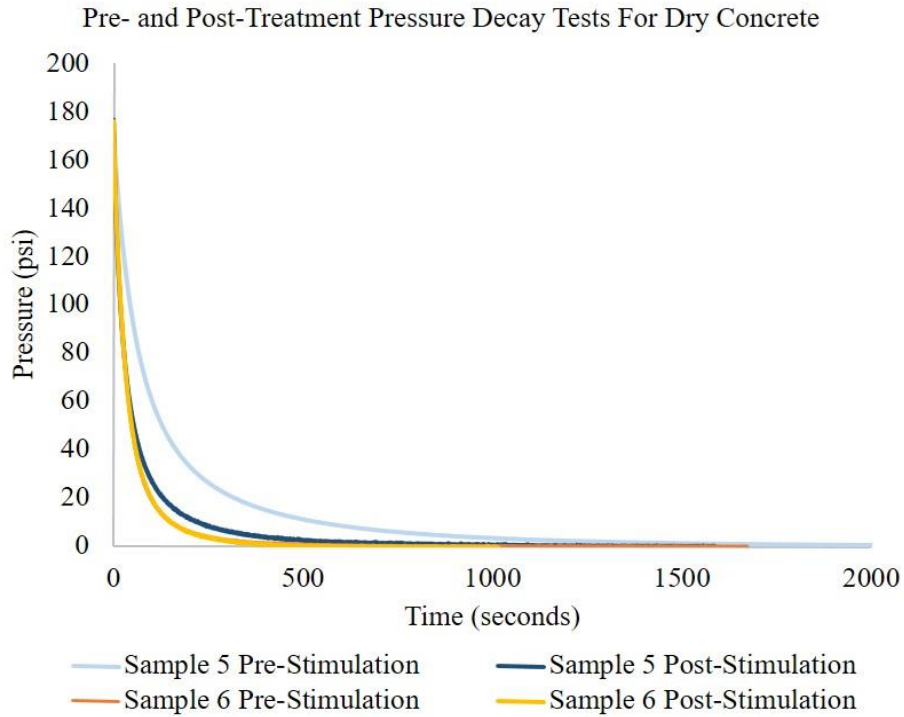


Figure 4.3.8 Pressure decay tests for dry concrete samples with liquid nitrogen treatments.

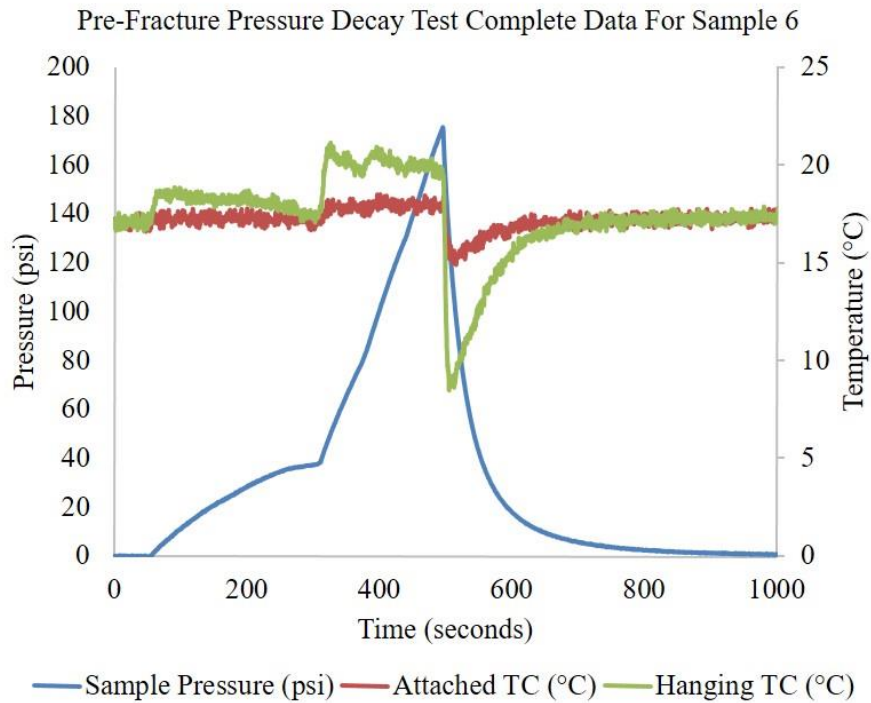


Figure 4.3.9 Observation of Joule-Thomson cooling effect during a pressure decay test.

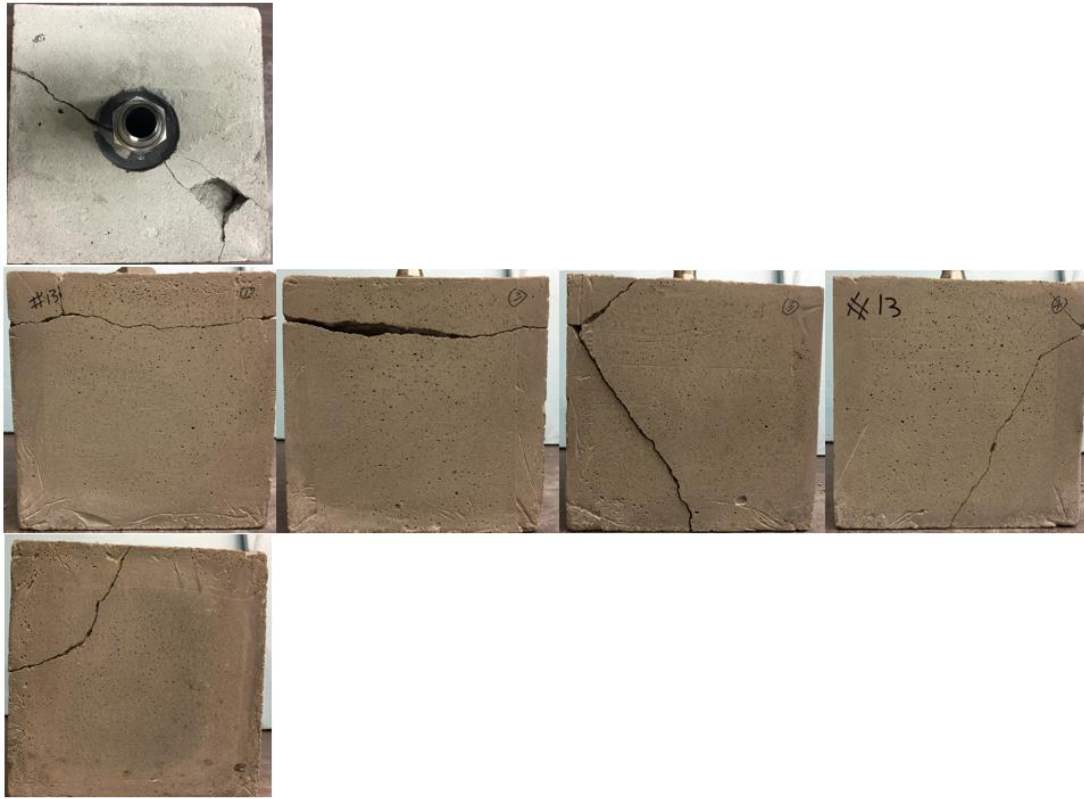


Figure 4.3.10 Fracture profile of Sample 4.



Figure 4.3.11 Fracture profile of Sample 5.



Figure 4.3.12 Fracture profile of Sample 6.

4.3.1.3 LN₂ Stimulating Saturated Samples

The following experiments were all performed on fully saturated concrete samples. As detailed previously, the samples were all submerged in water for an ample amount of time until fully water saturated. **Figure 4.3.13-Figure 4.3.15** show the liquid nitrogen injection results for Samples 7, 8, and 9.

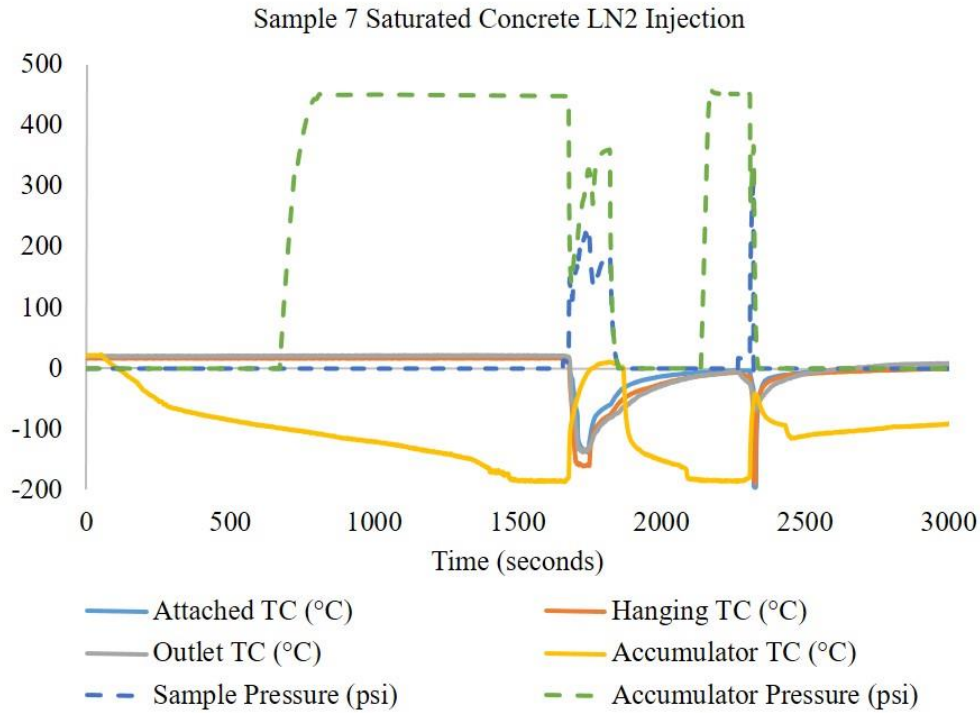


Figure 4.3.13 Pressure and temperature records during cryogenic treatment of Sample 7.

Sample 7 was exposed to liquid nitrogen twice and was fractured during the second stimulation. The specific list of events in **Figure 4.3.13** is as follows: liquid nitrogen began filling the accumulator at $t = 55$; the first treatment started at $t = 1679$; the first treatment completed and the accumulator started to refill at $t = 1849$; the second treatment began at $t = 2309$ and completed at $t = 2321$ when the specimen fractured. It was also during this experiment that an important feature was noticed about the experiment. The orifice size of the outlet plays a crucial role in controlling the injecting pressure and flow rate of the liquid nitrogen. It was noticed that if the orifice was opened too much, with the limited cryogen supply used in these experiments, the liquid nitrogen would quickly escape the system and dissipate into the atmosphere without pressurizing or cooling the wellbore sufficiently. On the contrary, if the outlet orifice were too small, not enough liquid nitrogen would flow into

the wellbore to adequately cool the borehole to generate cryogenic fractures. To measure the opening of the outlet orifice for each experiment, we considered fully closing the valve being 0% open and fully opening the valve being 100% open. When fully opened the outlet ID is 0.1785 inches. We then precisely measured the percent of the orifice being opened for each cryogenic stimulation based on how far the valve was opened. For Sample 7, the first cryogenic stimulation was 20% open and the second stimulation was 8% open. This was not realized until this experiment, so the outlet orifice size was not measured in previous experiments.

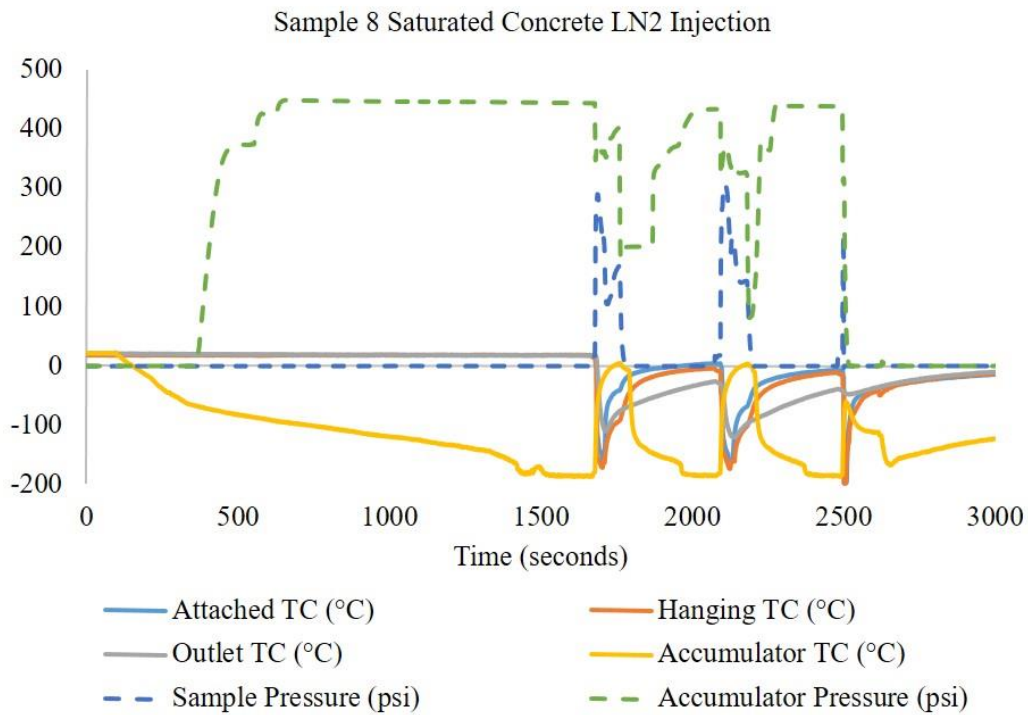


Figure 4.3.14 Pressure and temperature records during cryogenic treatment of Sample 8.

Sample 8 experienced three thermal shocks and was fractured during the third test. The specific list of events in **Figure 4.3.14** is as follows: liquid nitrogen began filling the accumulator at $t = 100$; the first treatment started at $t = 1679$ with the outlet opened to 18%; the first treatment completed and the accumulator started to refill at $t = 1783$; the second treatment began at $t = 2094$ with the outlet opened to 18%, and completed at $t = 2201$; the third treatment began at $t = 2496$ with the outlet opened to 8%, and ended at $t = 2502$ when the sample broke.

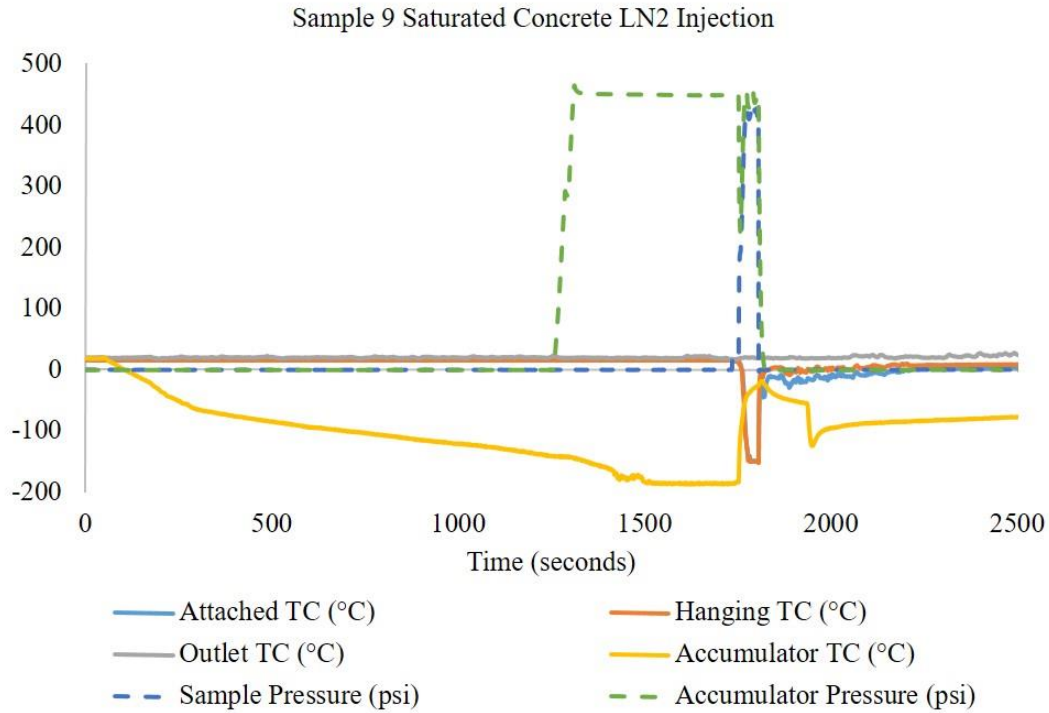


Figure 4.3.15 Pressure and temperature records during treatment of Sample 9.

As shown above in **Figure 4.3.15**, Sample 9 was fractured with only one stimulation treatment. The specific list of events done is as follows: liquid nitrogen began filling the accumulator at $t = 53$; the first treatment started at $t = 1753$ with the outlet opened to 5%; the first treatment completed at $t = 1807$ when the sample fractured. Notice that at this opening level, the borehole was not sufficiently cooled as the temperature did not reach the boiling point of LN_2 .

Figure 4.3.16 presents the pre-stimulation pressure decay tests for Samples 7, 8, and 9. There does not seem to be a correlation between the original permeability of the sample and the number of stimulations needed to fracture them.

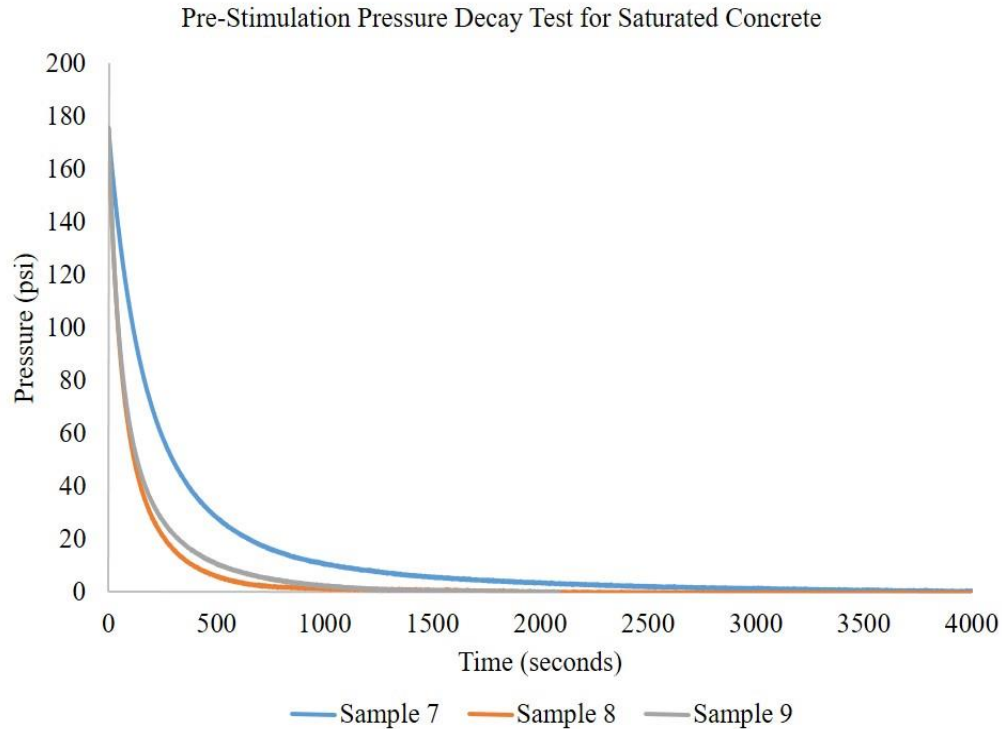


Figure 4.3.16 Pressure decay curves for Samples 7, 8, and 9.

Table 4.3 summarizes the stimulation results of water saturated concrete samples (7, 8, and 9) with liquid nitrogen. Compared with Samples 5 and 6, liquid nitrogen directly fractured the samples. This observation, though preliminary, indicates that water saturation helps to reduce the breakdown pressure during cryogenic treatment. This may occur because as the water freezes in the sample it will expand. This expansion introduces an additional stress on the surface of the rock face. **Figure 4.3.17-Figure 4.3.19** show the fracture profiles for the saturated concrete samples fractured using liquid nitrogen.

Table 4.3 Summarization of cryogenic stimulation results of water saturated samples

Sample	Breakdown pressure (psi)	Temperature at breakdown point (°C)	Δ Temperature at breakdown point (°C)	Cycles of treatments
7	308	-73	90	2
8	224	-38	56	3
9	416	-150	168	1



Figure 4.3.17 Fracture profile of Sample 7.

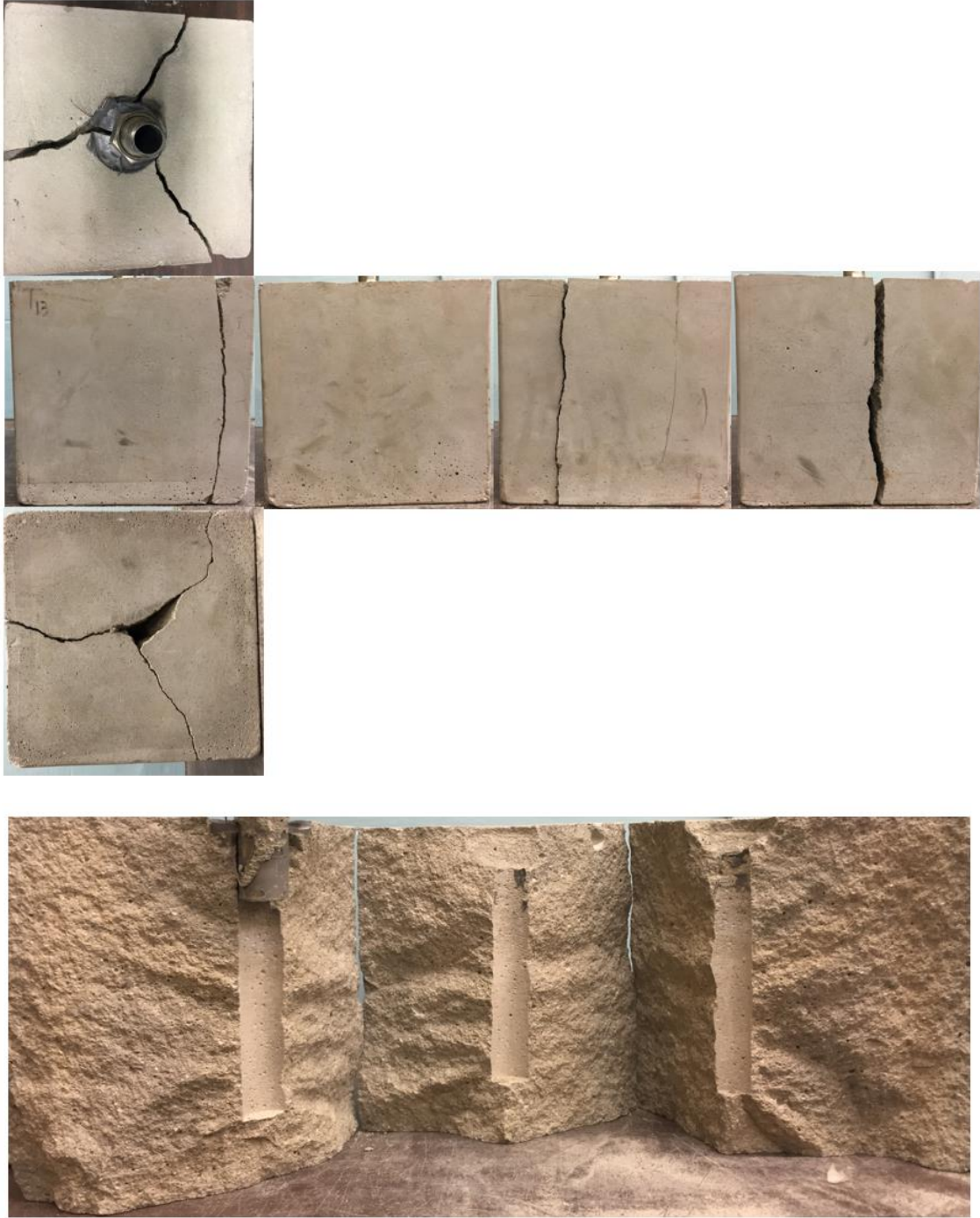


Figure 4.3.18 Fracture profile of Sample 8.



Figure 4.3.19 Fracture profile of Sample 9.

4.3.1.4 LN₂ Stimulating Dry Heated Samples

The following experiments were all performed on dry heated concrete samples. As previously stated, the samples were dried and heated to 65 °C for testing. The initial thermocouple readings in these experiments are a little less than 65 °C because of the time it took to move

the sample out of the oven and prepare it for testing. **Figure 4.3.20-Figure 4.3.22** shown below are the stimulation results for Samples 10, 11, and 12.

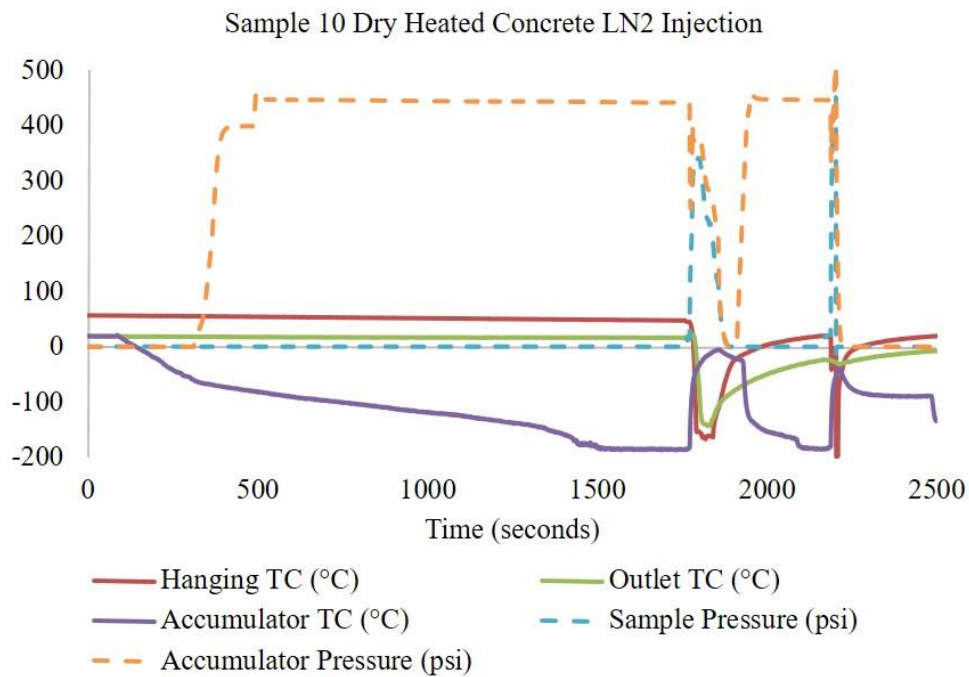


Figure 4.3.20 Pressure and temperature records during treatment of Sample 10.

As shown above in **Figure 4.3.20**, there were a total of two treatments performed on Sample 10. The specific list of events done is as follows: liquid nitrogen began filling the accumulator at $t = 88$; the first treatment started at $t = 1772$ with the outlet opened to 12%; the first treatment completed and the accumulator started to refill at $t = 1886$; the second treatment began at $t = 2188$ with the outlet opened to 8%, and completed at $t = 2204$ when the specimen fractured. Since the thermocouple attached to the borehole failed during this experiment, only the temperature data from the hanging thermocouple are presented.

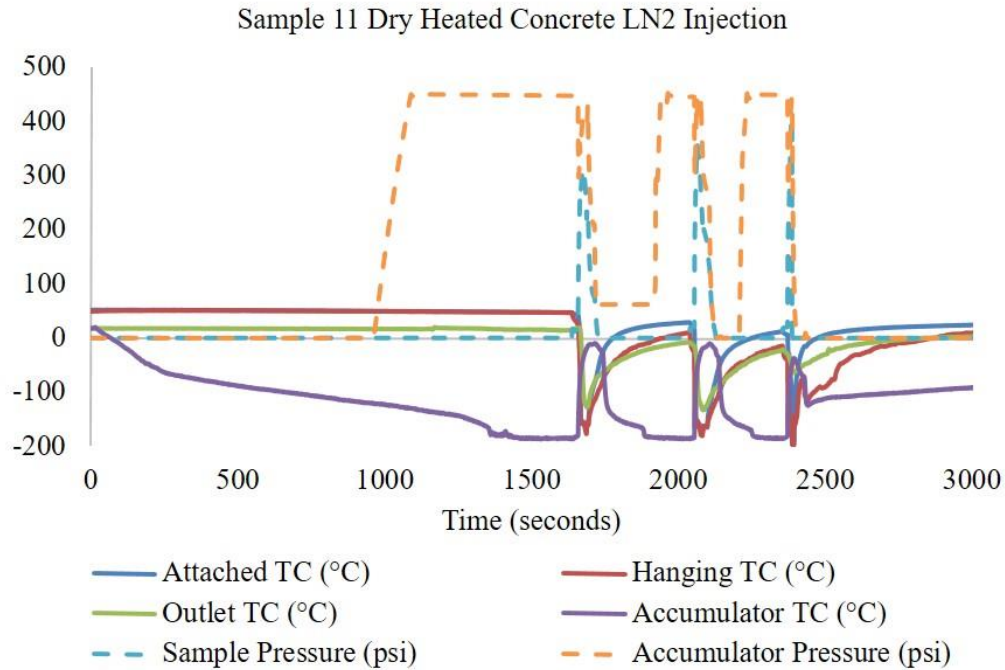


Figure 4.3.21 Pressure and temperature records during treatment of Sample 11.

For Sample 11, three separate stimulation treatments were conducted before the sample was fractured. The specific list of events in **Figure 4.3.21** is as follows: liquid nitrogen began filling the accumulator at $t = 18$; the first treatment started at $t = 1660$ with the outlet opened to 12%; the first treatment completed and the accumulator started to refill at $t = 1730$; the second treatment began at $t = 2056$ with the outlet opened to 12% and completed at $t = 2129$; the third treatment began at $t = 2373$ with the outlet opened to 8% and ended at $t = 2388$ when the specimen fractured. The fracture profiles for Samples 10, 11, and 12 are shown below in **Figure 4.3.23-Figure 4.3.25**. The pressure decay test is shown in **Figure 4.3.26**.

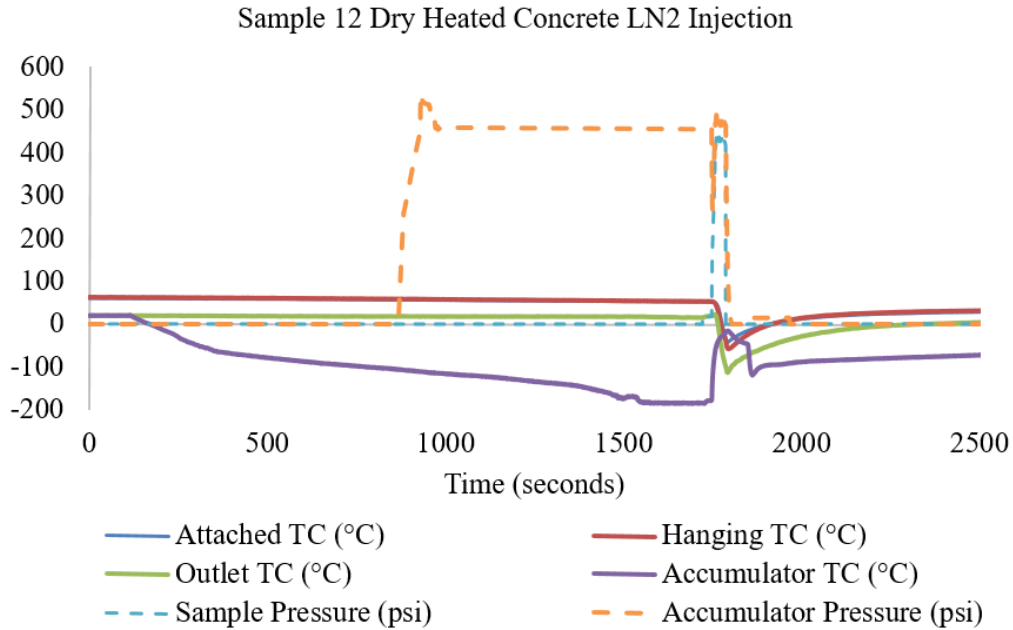


Figure 4.3.22 Pressure and temperature records during cryogenic treatment of Sample 12.

For Sample 12 shown above in **Figure 4.3.22** there was only one cryogenic treatment. The specific list of events is as follows: liquid nitrogen began filling the accumulator at $t = 115$; the first treatment started at $t = 1748$ with the outlet opened to 8%; the first treatment completed at $t = 1788$ when the sample fractured.

Table 4.4 summarizes the breakdown data for Samples 10, 11, and 12.

Table 4.4 Summarization of stimulation results for dry heated concrete samples

Sample	Breakdown pressure (psi)	Temperature at breakdown point (°C)	Δ Temperature at breakdown point (°C)	Cycles of treatments
10	484	-2	56	2
11	408	-150	196	3
12	416	-37	97	1

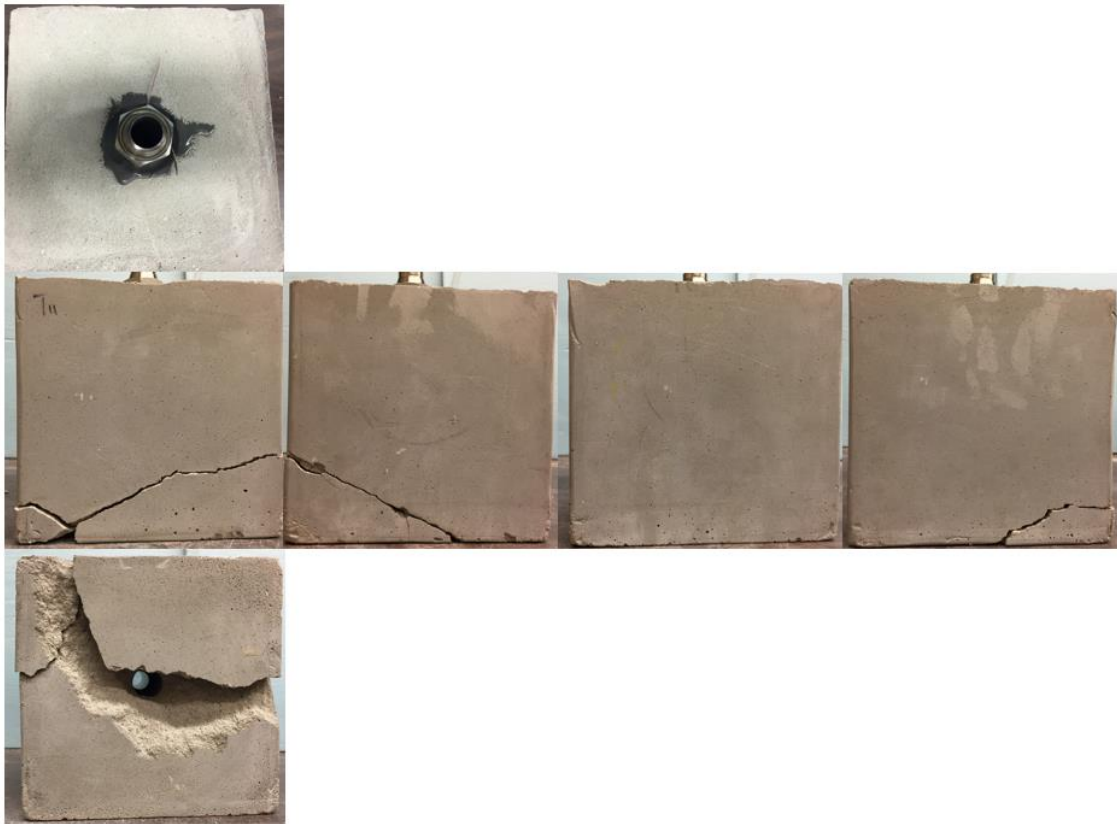


Figure 4.3.23 Fracture profile of Sample 10.



Figure 4.3.24 Fracture profile of Sample 11.



Figure 4.3.25 Fracture profile of Sample 12.

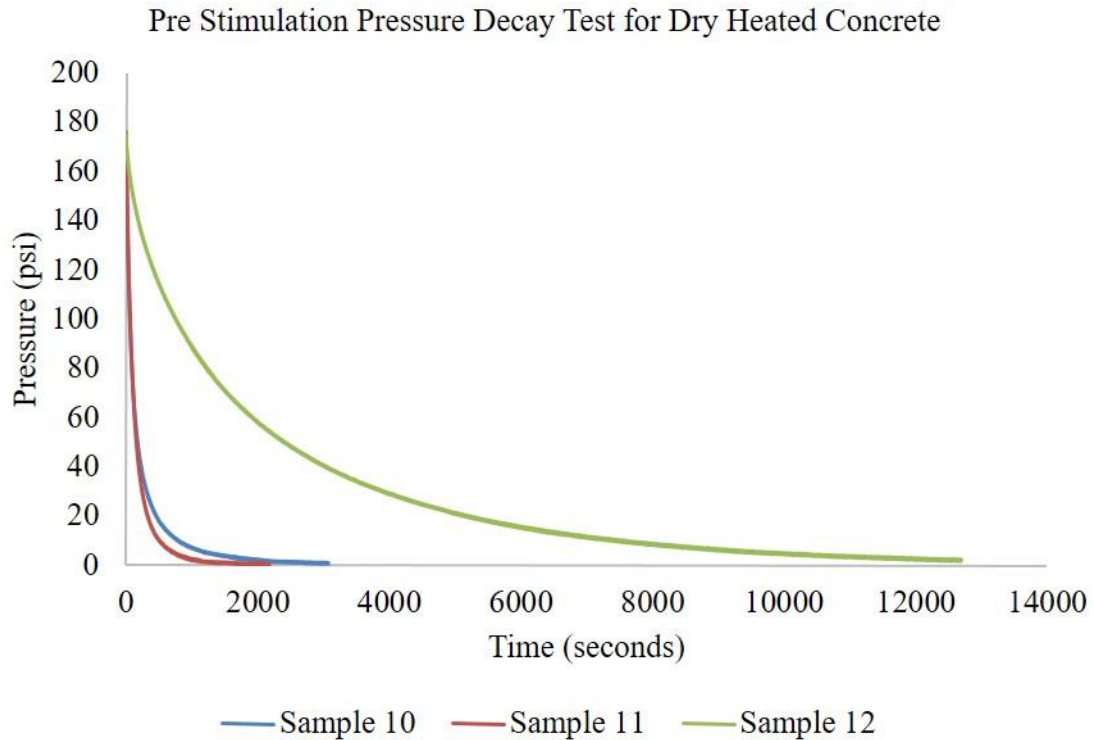


Figure 4.3.26 Pressure decay tests for Samples 10, 11, and 12.

Until Sample 12, most pressure leak-off tests lasted about 1500-2500 seconds. Sample 12, as seen above, lasted for nearly 13,000 seconds until the pressure fully drew down. This sample was prepared following the identical procedures. It is not clear why the decay for Sample 12 was so much longer than other samples, but we speculate that the seal, for whatever reason, was much better than previous samples. Also, there must have been negligible pressure leaking through the thermocouples, which presented in some of the previous samples.

4.3.1.5 LN₂ Stimulating Saturated Heated Samples

The following experiments were all performed on saturated heated concrete samples, numbered as 13, 14, and 15. As previously stated, the samples were placed in a covered water bath and heated to 65 °C for three days before cryogenic stimulation.

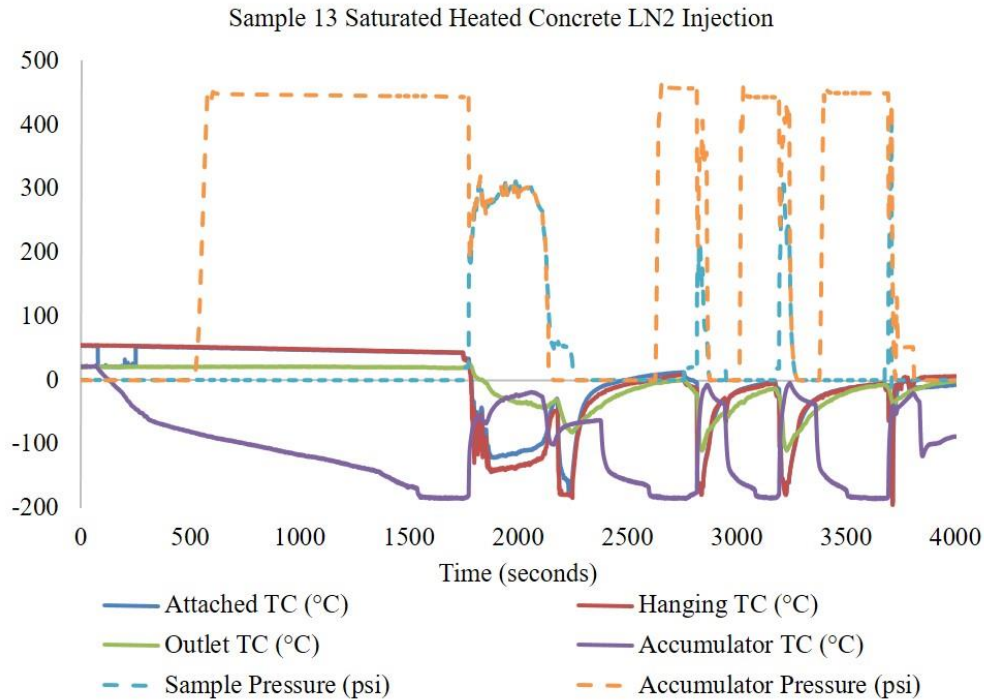


Figure 4.3.27 Pressure and temperature records during cryogenic treatment of Sample 13.

For Sample 13, four separate stimulation treatments were conducted before the sample was fractured. The specific list of events in **Figure 4.3.27** is as follows: liquid nitrogen began filling the accumulator at $t = 76$; the first treatment started at $t = 1774$ with the outlet opened to 5%; after noticing that the outlet was not opened enough, the outlet was adjusted to 20% at $t = 1854$ and then 100% at $t = 2190$; the first treatment completed and the accumulator started to refill at $t = 2380$; the second treatment began at $t = 2818$ with the outlet opened to 20% and completed at $t = 2877$; the third treatment began at $t = 3195$ with the outlet opened to 15% and ended at $t = 3276$; the fourth treatment began at $t = 3694$ with the outlet opened to 8% and ended at $t = 3709$ when the sample was fractured. During the first treatment it appears that the water from the sample froze in the tubing and blocked the nitrogen gas from escaping. Even after opening up the outlet to 20% the line still appeared to be clogged. It was not fully unclogged until the outlet was fully open.

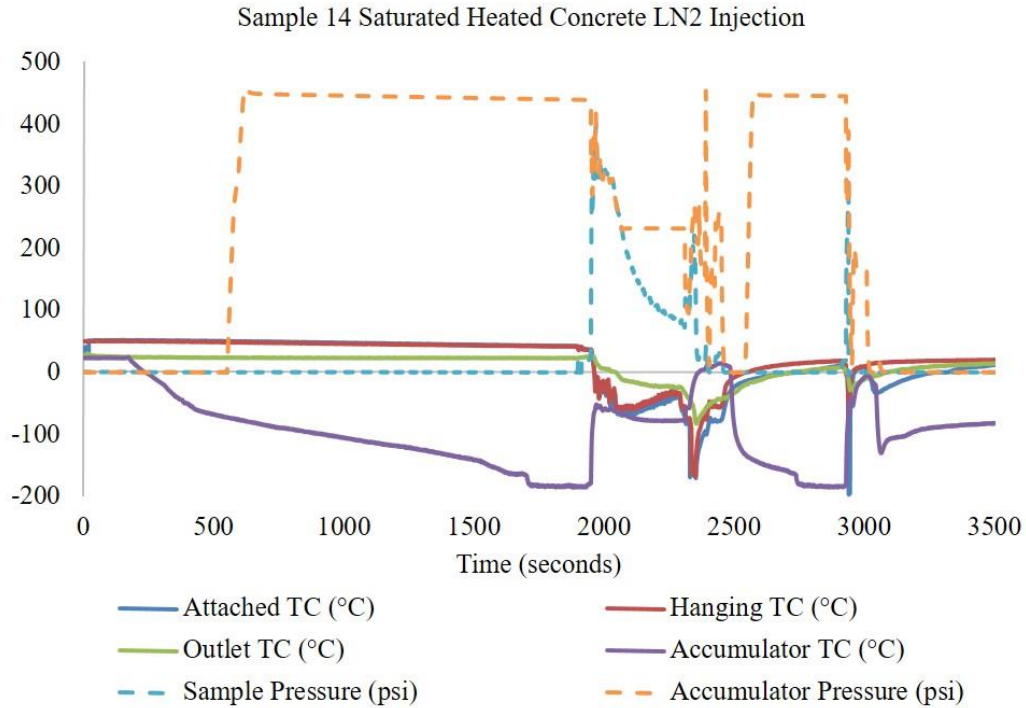


Figure 4.3.28 Pressure and temperature records during cryogenic treatment of Sample 14.

For Sample 14, two separate stimulation treatments were conducted before the sample was fractured. And again, it appears that water froze in the tubing, blocking the nitrogen gas from escaping. The specific list of events in **Figure 4.3.28** is as follows: liquid nitrogen began filling the accumulator at $t = 176$; the first treatment started at $t = 1951$ with the outlet opened to 8%; the outlet seemed to be clogged so the outlet was opened to 20% at $t = 2311$; the first treatment completed and the accumulator started to refill at $t = 2403$; the second treatment began at $t = 2931$ with the outlet opened to 8% and completed at $t = 2940$ when the specimen was fractured at 313 psi. When the tubing becomes clogged with ice, both the pressure and temperature deviate from what is expected. This should be taken into consideration when performing field tests. This will be further elaborated on in the discussion section.

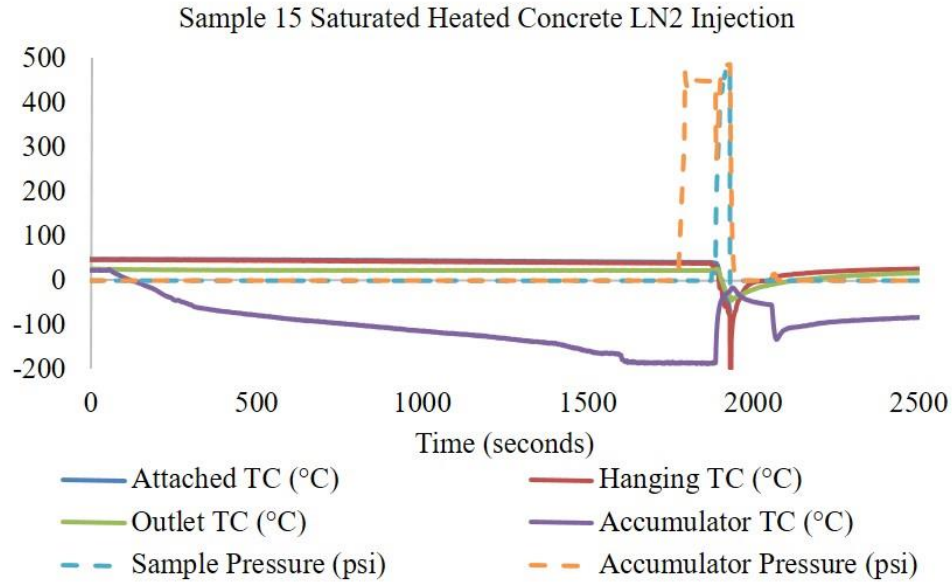


Figure 4.3.29 Pressure and temperature records during cryogenic treatment of Sample 15.

For Sample 15, only one stimulation treatment was conducted before the sample was fractured. The specific list of events in **Figure 4.3.29** is as follows: liquid nitrogen began filling the accumulator at $t = 60$; the first treatment started at $t = 1887$ and the outlet was opened to 8%; the first treatment completed at $t = 1930$ when the specimen was fractured.

Table 4.5 summarizes the results for Samples 13, 14, and 15. **Figure 4.3.30** shows the pressure decay tests for Samples 13, 14, and 15. There is no significant difference among the three samples in the pressure decay data. Since all of the samples were fractured during the cryogenic treatments, there are no post-fracture data to compare to. **Figure 4.3.31-Figure 4.3.33** show the fracture profiles for Samples 13, 14, and 15.

Table 4.5 Summarization of stimulation results for saturated heated concrete samples

Sample	Breakdown pressure (psi)	Temperature at breakdown point (°C)	Δ Temperature at breakdown point (°C)	Cycles of treatments
13	400	-50	104	4
14	313	-84	134	2
15	471	-80	127	1

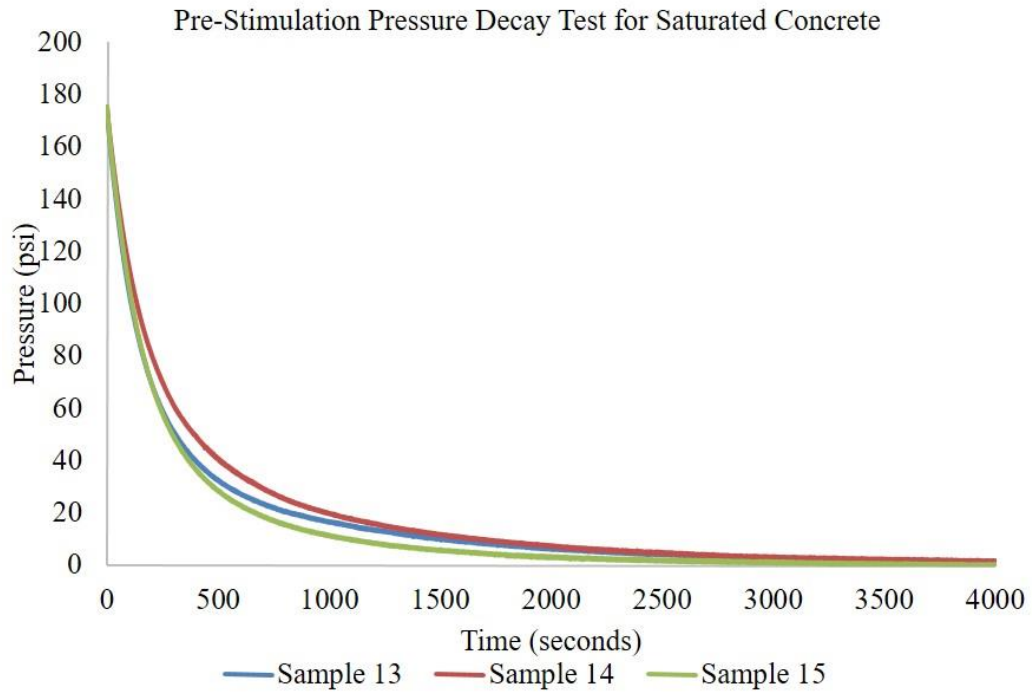


Figure 4.3.30 Pressure decay tests for Samples 13, 14, and 15.





Figure 4.3.31 Fracture profile of Sample 13.





Figure 4.3.32 Fracture profile of Sample 14.





Figure 4.3.33 Fracture profile of Sample 15.

4.3.1.6 Results Comparison and Analysis

When comparing results from experiments, there are numerous factors to look at that may have influenced the pressure at which the samples were fractured. **Table 4.6** summarizes these factors that are critical in influencing the breakdown pressures. These factors are the temperature at which the sample fractures, the differential temperature ΔT between the starting temperature and that at the actual breakage point, the number of cryogenic treatment cycles performed on the sample, and the amount of time allotted for the samples to cure. One critical factor that is not presented in this table is the opening size of the outlet orifice. Since this variable changes for each individual treatment, it could not be summarized in a simple table; however, it will be discussed in detail later in this chapter.

As a reminder, the first 3 samples were fractured using nitrogen gas on dried concrete specimens at 20 °C, Samples 4-6 were dried concrete specimens treated with liquid nitrogen and fractured with nitrogen gas at 20 °C, Samples 7-9 were saturated concrete samples at 20 °C and fractured with liquid nitrogen, Samples 10-12 were dry concrete samples heated to 65 °C and fractured with liquid nitrogen, and Samples 13-15 were water saturated samples heated to 65 °C and fractured with liquid nitrogen. Temperature data of Samples 4-6 were intentionally left off of this table because, unlike the other samples, these samples were

treated with liquid nitrogen but then fractured with gas nitrogen after their temperatures returned to the room temperature.

Table 4.6 Summarization of stimulation results for Samples 1-15

Sample	Breakdown pressure (psi)	Temperature at breakdown point (°C)	ΔT at breakdown point (°C)	Cycles of treatments	Curing time (days)
1	909	19	0	0	143
2	566	20	0	0	67
3	491	20	0	0	96
4	580	×	×	1	148
5	352	×	×	1	75
6	822	×	×	2	96
7	308	-73	90	2	52
8	224	-38	56	3	45
9	416	-150	168	1	45
10	484	-2	56	2	55
11	408	-150	196	3	115
12	416	-37	97	1	118
13	400	-50	104	4	104
14	313	-84	134	2	66
15	471	-80	127	1	67

Based on the data, it can be deduced that the strength of the concrete increases as the curing time increases. This is evident in the positive correlation between the curing time and the breakdown pressure, as shown in **Figure 4.3.34**. Despite this correlation, there are other factors that may have influenced each sample's testing condition; these factors are presented in **Figure 4.3.34**.

The breakage pressure and the cycles of treatments for each sample also seem to have a correlation. **Figure 4.3.35** shows the breakage pressure as a function of treatments. Although not strongly correlated, **Figure 4.3.35** suggests that more treatments weaken the specimen, subsequently resulting in a lower fracturing pressure. This increase of the likelihood of failure with more treatments can be explained by thermal shock. As the surface of the borehole rapidly cools, the thermal expansion coefficient of the sample dictates how much the surface

of the specimen will shrink. This shrinkage subjects the surface of the specimen to a tensile stress. If the thermal gradient between the cooled surface and the relatively warm interior is great enough, the rock sample will fail in tension. An increase in the number of cryogenic treatments increases the likelihood that the sample would fail due to small fractures that have formed during each treatment, which, when added up, significantly weakened the sample.

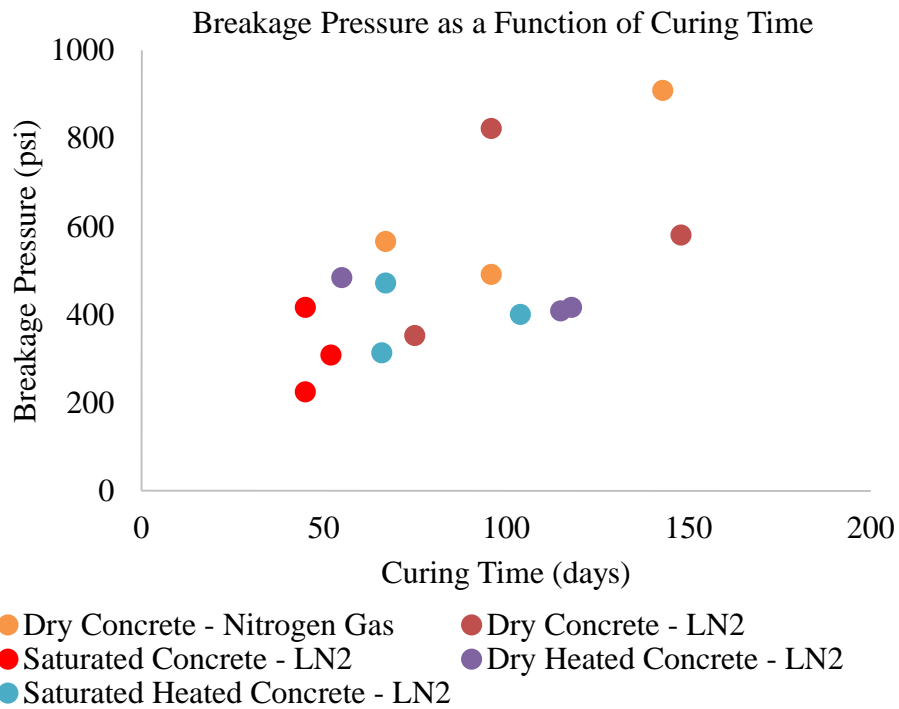


Figure 4.3.34 Breakage pressure of samples as a function of curing time.

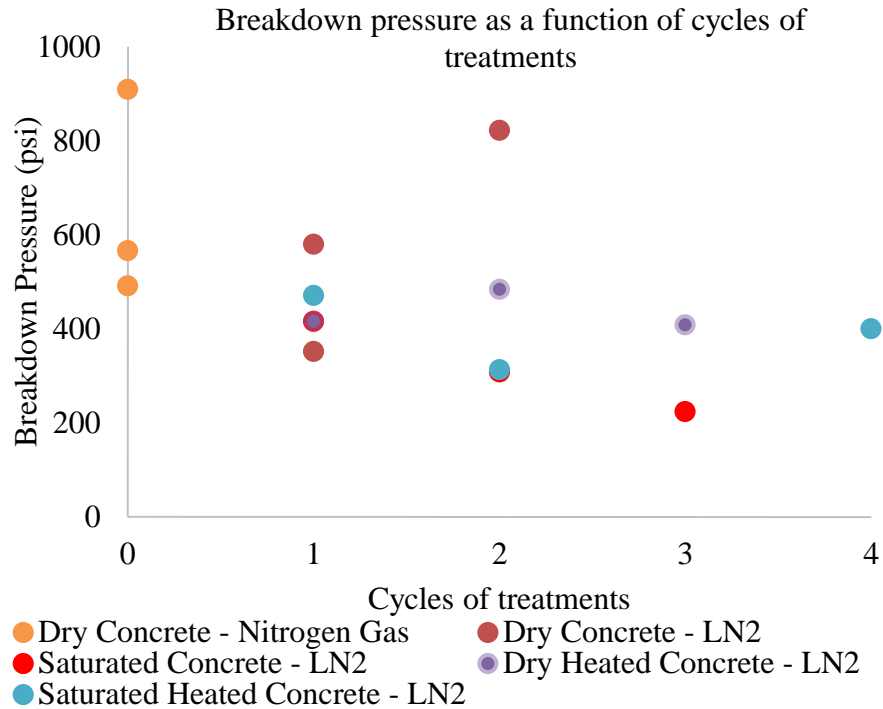


Figure 4.3.35 Breakage pressure as a function of cycles of treatments.

Because the samples were tested at unstressed conditions, the fracturing profiles are somewhat random. Even so, we listed descriptions of the generated fractures in **Table 4.7**, as an attempt to characterize and compare the fracture profiles.

The fracture complexity is an index that is developed to help categorize the fractures. It places the fractures formed in a category from 1-5, with 1 being the simplest type of fracture and 5 being the most complex. The goal was to see if more or less complex fractures would form at certain conditions. Based on the table, the fracture complexity has no correlation with the type of experiment being performed or the pressure at which the sample broke. The only similarities found between similar treatments are that dry samples, at room temperature or heated, tend to form horizontal fractures that broke off the bottom of the specimen and saturated samples tend to form three vertical fractures spaced approximately 120° apart.

Table 4.7 Characterization of fracture profiles

Sample	Fracturing pressure (psig)	Fracture description	Fracture complexity (1-5)
1	909	Two vertical fractures	1
2	566	Three vertical fractures	2
3	491	Horizontal fractures, bottom broken off	2
4	580	Vertical and horizontal fractures	3
5	352	Three vertical fractures	2
6	822	Four vertical and horizontal fractures	5
7	308	Two vertical fractures	1
8	224	Three vertical fractures	2
9	416	Three vertical fractures	4
10	484	Horizontal fractures, bottom broken off	2
11	408	Horizontal fractures, bottom broken off	2
12	416	Vertical fracture	1
13	400	Three vertical fractures	3
14	313	Numerous vertical and horizontal Fractures	5
15	471	Three vertical fractures	2

Based on the experimental results, it seems that cryogenic treatment of water saturated samples resulted in the lowest breakdown pressures. Intuitively, this is logical. In addition to the stresses generated from the pressurization of the borehole and the thermal stress generated from the liquid nitrogen, the water frozen inside the formation is expanding, offering an additional stress to fracture the specimen.

An important aspect of this experiment that is hard to capture in tables and figures is the outlet orifice opening percentage. Unfortunately, this parameter was not realized until mid-testing of Sample 7. It was experimentally found that if the orifice was “too open” the pressure inside the borehole was too low for fracturing and the liquid nitrogen was not

making adequate contact with the borehole for enough heat transfer. If we had a larger supply of pressurized liquid nitrogen, this would greatly reduce the heat transfer problem. Similarly, if the orifice was “too closed”, vapor would not escape the borehole easily; instead, it accumulates in the borehole and insulates the borehole surface from liquid nitrogen, again preventing effective heat transfer. Based on the experimental data, it seems that when the orifice was set to 5% open or less it was “too closed”, but 10% open or higher was “too open”. An 8% orifice opening seems to be the ideal situation for fracturing for this experimental setup. This concept is important for upscaling and transferring this study into field testing. The bottom line is that the liquid nitrogen must adequately flow through the wellbore in order to maximize the temperature differential that creates the necessary thermal stresses. Ultimately, in this experiment, the orifice outlet opening is part of a function that determines the pressure of the sample, the flowrate of the liquid nitrogen, and the temperature of the borehole.

By considering other important factors from this study, we can better design and conduct field tests. Although only two pressure decay tests, pre-treatment and post-treatment data, were measured in this study, they are important in determining if the liquid nitrogen would increase permeability. It can be determined that in Sample 5 there is clear indication that the liquid nitrogen treatment increased the permeability of the sample as the pressure decay test took significant less time than that before treatment. The pressure decay tests also help verify that the Joule-Thomson cooling effect occurred during the test. This is important for future modelling of the experiments as non-isothermal reservoir simulations may be required.

In some fracture tests, it was observed that the sample pressure would initially go above that at which the sample ultimately broke. The sample would not fracture at this pressure because the liquid nitrogen had not sufficiently cooled the sample allowing the thermal stresses to occur. In Sample 12, for example, the fracture occurred at 416 psi; however, before fracturing, while the pressure was still varying, the sample pressure once reached as high as 449 psi. At this pressure, the temperature of the borehole was 30 °C and just started to drop quickly. The sample eventually broke when the temperature of the borehole reached -37 °C at a pressure of 416 psi. The sample’s initial temperature was 63°C. This experiment proves that the

thermal stress generated in the borehole by the liquid nitrogen is a significant addition to the bore hole pressure when it comes to fracture initiation.

While performing a cryogenic treatment on saturated heated concrete Sample 13, it was observed that the water from the sample frozen by the liquid nitrogen clogged the outlet line. During the experiment, sputtering was initially heard from the outlet valve and then it was almost completely clogged as only a small amount of gas was flowing through the outlet valve even though the outlet was fully open. This observation should be taken into consideration when performing field tests.

4.3.2 Sandstone Sample

Cryogenic stimulation experiments were performed on a sandstone sample. Multiple cycles of thermal shock and pressurization were applied to the sandstone due to its more resistance to thermal shock than the previous concrete samples.

- a. The 1st thermal shock-cold nitrogen gas (4.3.2.1)
- b. The 2nd thermal shock-cold nitrogen gas (4.3.2.2)
- c. The 3rd thermal shock-liquid nitrogen (4.3.2.3)
- d. The 4th thermal stimulation-liquid nitrogen + pressurization (4.3.2.4)

Note that in the 1st and 2nd thermal shocks, cold nitrogen gas was used for the thermal shock. It was not our intention, but rather due to a malfunction of the withdrawal device, which resulted in cold nitrogen gas instead of liquid nitrogen released during thermal shock. This problem was improved from the 3rd thermal shock.

4.3.2.1 Thermal Stimulation with Cold GN₂

Acoustic measurements were not conducted for this test during the cryogenic stimulation due to risk of damage to the sensors.



Figure 4.3.36 Experimental setup (the 1st thermal shock)

Temperature, pressure, and LN₂ consumption

The pressure inside the borehole is similar to the pressure inside the Dewar (the pressure inside the borehole is slightly less by about 1 psi). In this test, the Dewar was opened completely until the end of the test without partial or temporal closure in the middle. The high-frequency fluctuation of borehole pressure as shown in **Figure 4.3.37** was qualitatively confirmed during the experiment in the laboratory by oscillating sounds coming from the outlet.

Due to the malfunctioning of the withdrawal device, nitrogen existed as gas in the borehole throughout the test. This is also indicated by temperatures and the outlet flow stream (no droplet of LN₂ observed throughout the test) in **Figure 4.3.39**. The temperature in the borehole is significantly higher than LN₂ boiling point. There seems to be no indication of the Leidenfrost effect according to the temperature data.

At the end of the test, no noticeable cracks were found at the block surfaces by visible examination. In consideration of the inefficiency of the first thermal shock, we performed the 2nd cycle of thermal shock.

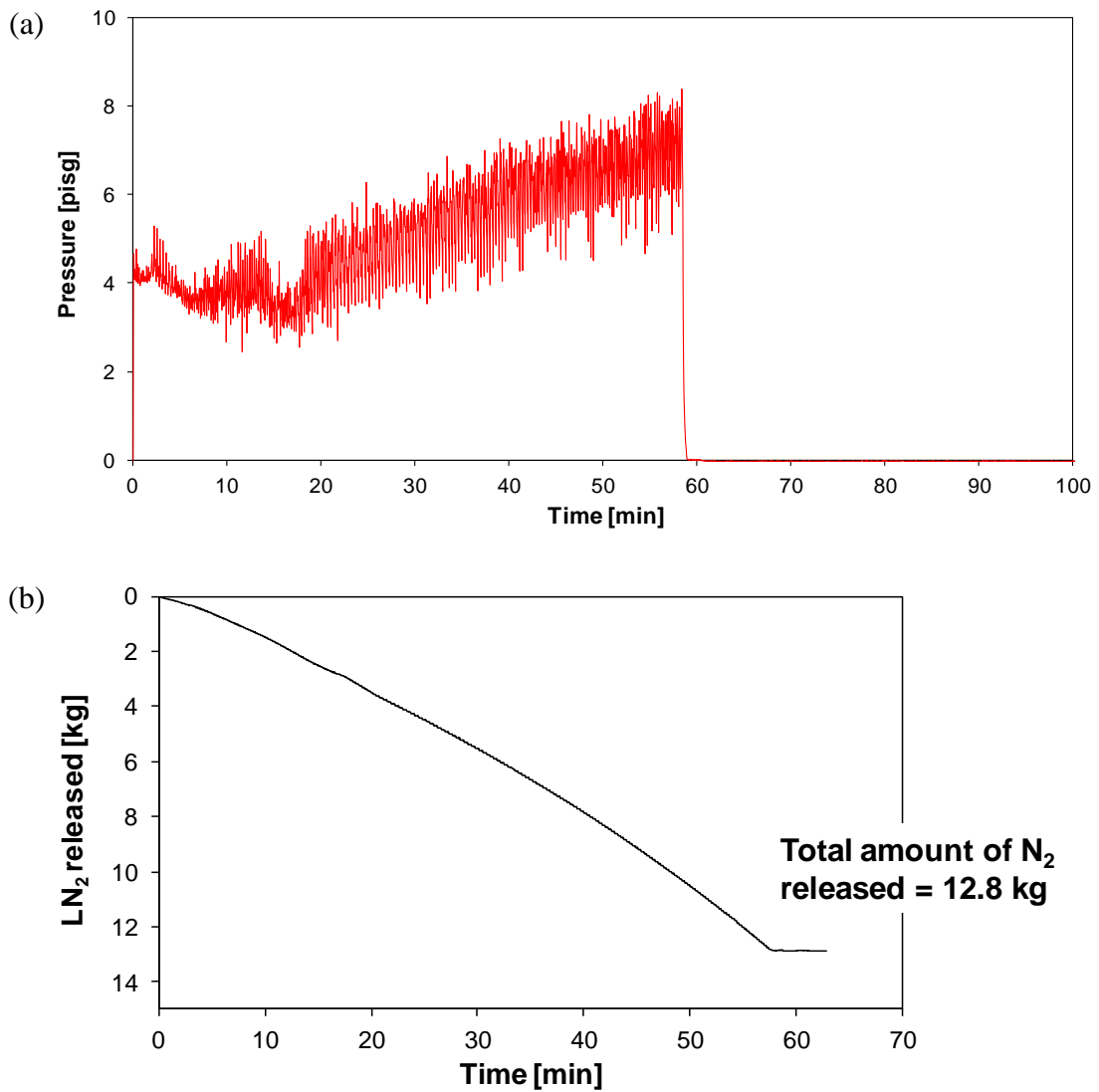


Figure 4.3.37 Pressure generated during nitrogen gas flow and LN₂ consumption.

Thermocouple locations

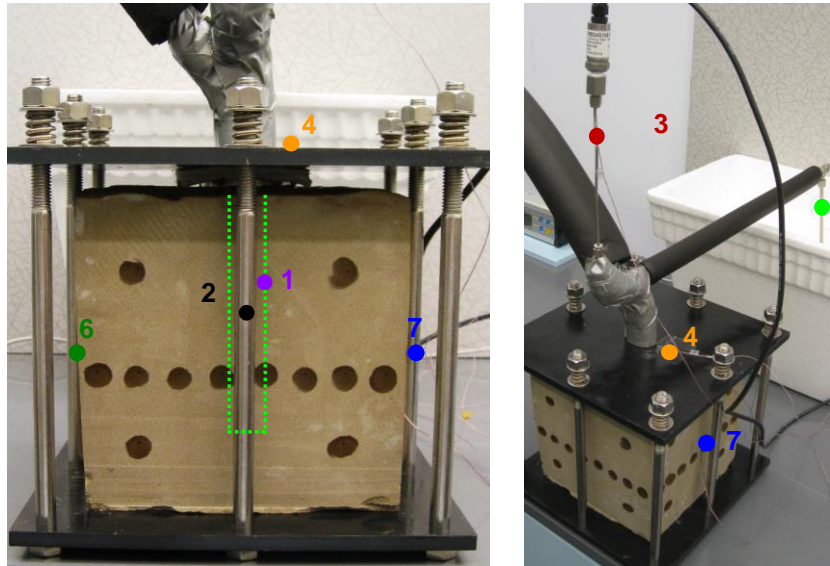


Figure 4.3.38 Locations of thermocouples. The dark spots are stains of the couplant used for the ultrasonic measurements.

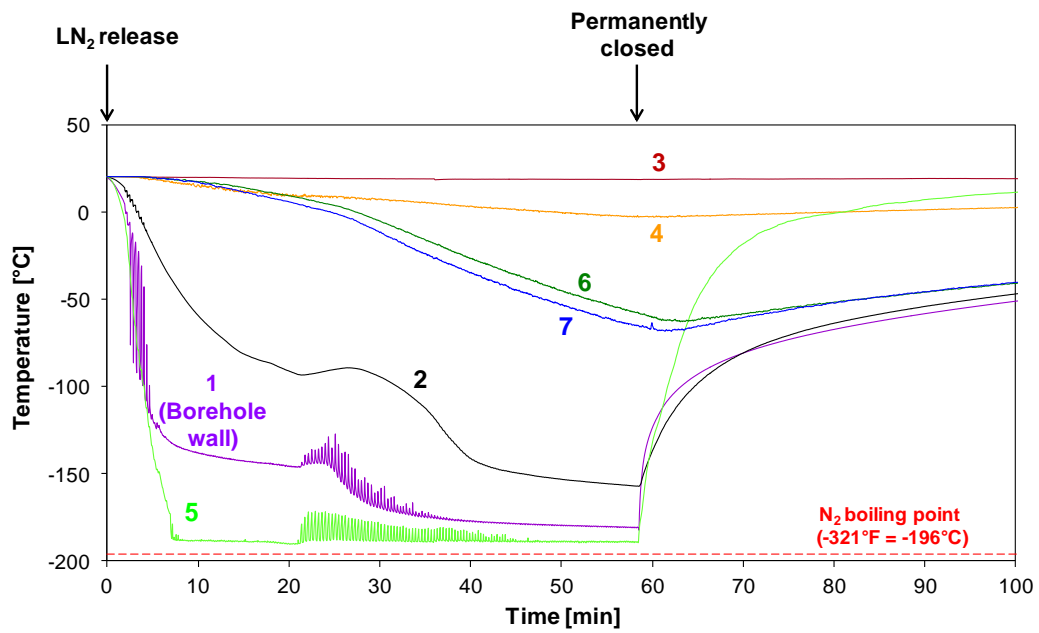


Figure 4.3.39 Temperature during the 1st thermal shock.

4.3.2.2 Thermal Stimulation with Cold GN₂

In the 2nd thermal shock, the outlet is moved further back to prevent any accidental leakage from the outlet tank and to keep cold vapor from influencing the experiment (**Figure 4.3.40**). Again, due to malfunctioning of the withdrawal device, cold nitrogen gas instead of liquid nitrogen was released during the thermal shock. The pressure and nitrogen consumption follow similar trends as the previous test and thus are omitted here.



Figure 4.3.40 Experimental setup for the 2nd thermal shock.

Temperature and crack examination

Due to the lengthy duration of the experiment (75 minutes), even the surface of the rock reached very low temperature (as low as -70 °C) (**Figure 4.3.41**). The high-frequency fluctuation of the temperature data (in TC #1, 2, 5) also appears to be indicated by a flow sound at the outlet and oscillating pressure changes in the borehole.

No noticeable cracks are generated after the two cycles of thermal shock, possibly due to slower dropping of temperature (causing lower thermal gradient), higher final temperature, and also the lower brittleness and the higher strength of the sandstone block.

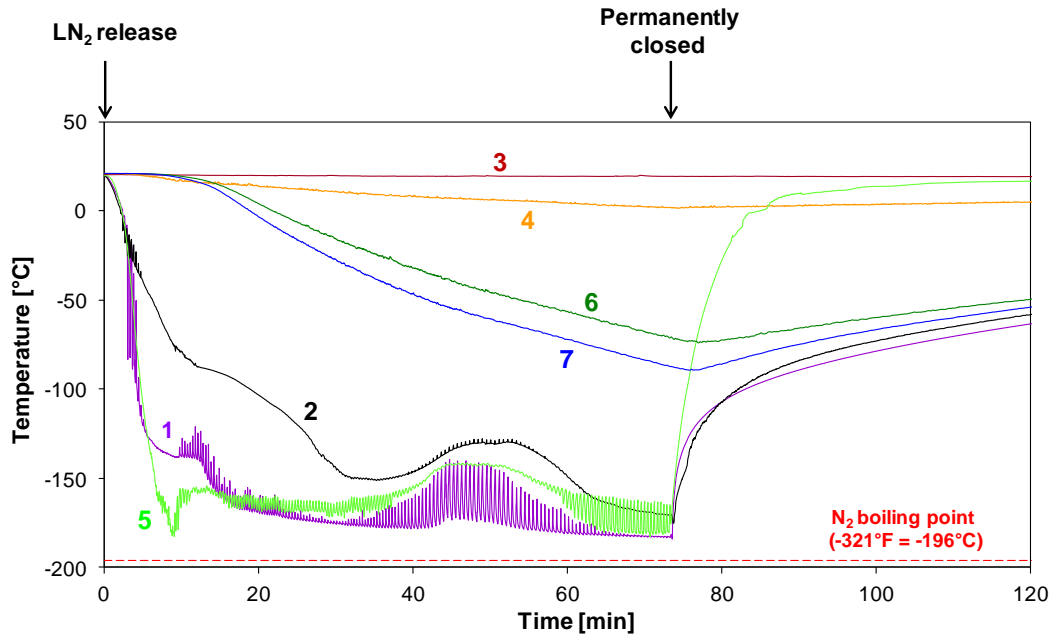


Figure 4.3.41 Temperature profiles during the cryogenic treatment.

Other observations

A significant amount of frost formed on the surface of the rock towards the end of the test (**Figure 4.3.42**). The frost was first noticed at the top and side faces of the specimen, which are closer to the borehole.

After the 2nd thermal shock, the packer is examined and then dismantled to check its integrity in sealing. We confirmed that the sealing is good and the nitrogen flow passage was not interrupted (**Figure 4.3.43**).

At the end of test



3 hours after the test

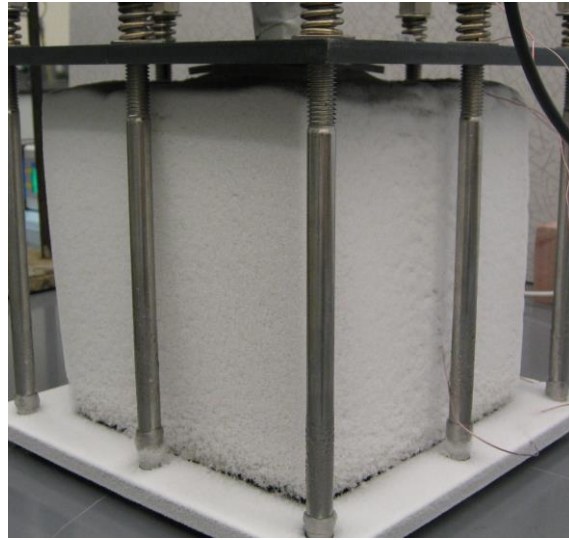


Figure 4.3.42 Frost attracted at the surfaces

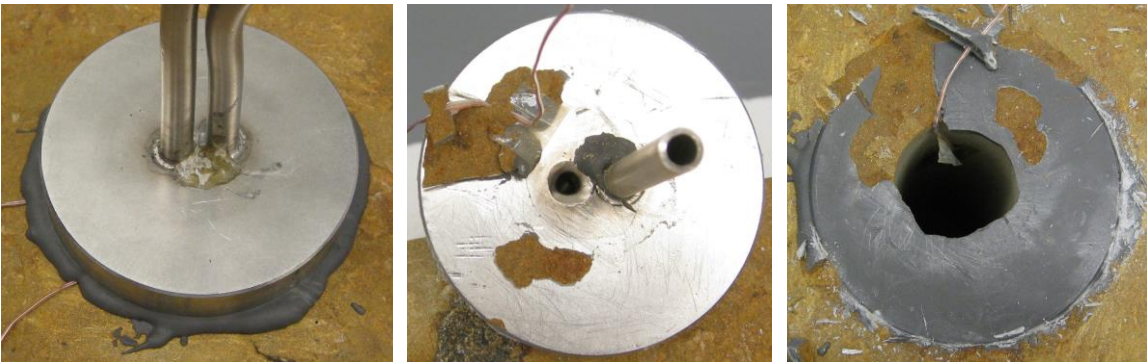


Figure 4.3.43 Leakage and sealing integrity check of the packer.

Pressure decay test

The pressure decay over time can be a qualitative measurement of gas permeability of the sandstone sample before and after cryogenic treatment. Before any thermal shock, and after the 1st and 2nd thermal shocks, bulk gas permeation tests were performed. Gas pressure is applied to the borehole and the valve is closed to record the pressure decay over time using a pressure transducer (**Figure 4.3.44**). We have noticed only minute changes in the decay profile (**Figure 4.3.45**) after the first two cycles of thermal shock.



Figure 4.3.44 Gas pressure decay test.

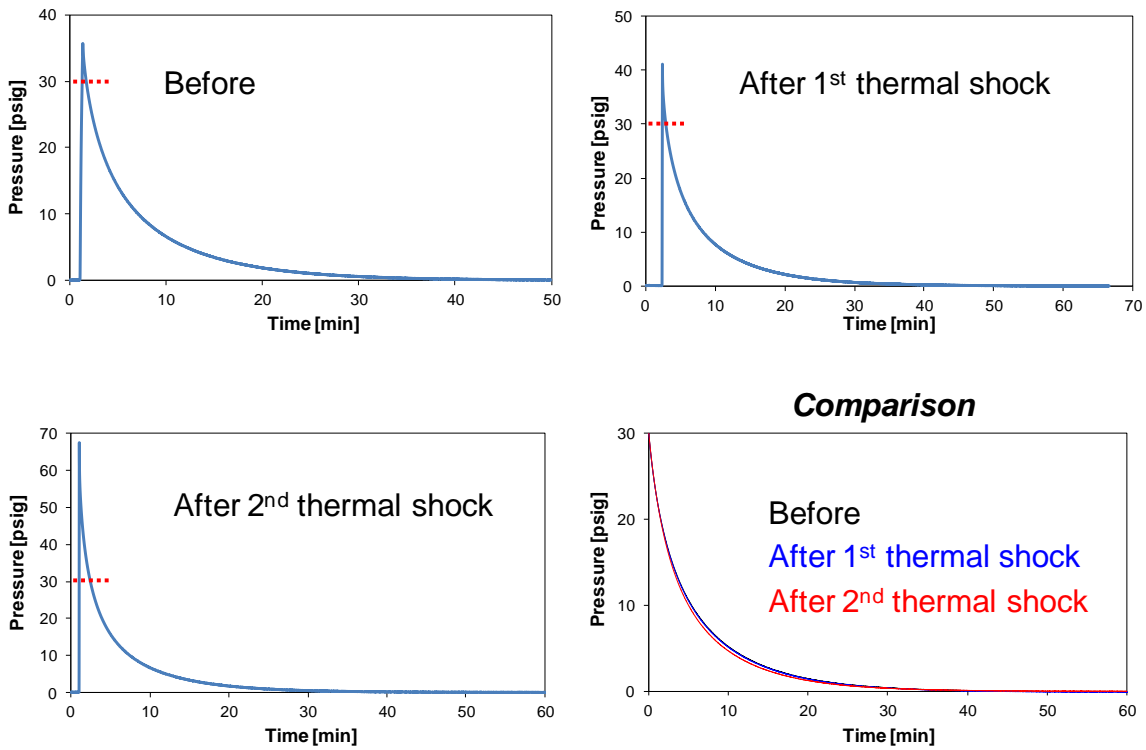


Figure 4.3.45 Pressure decay comparison.

4.3.2.3 The Third Stimulation with LN₂

Immediate liquid nitrogen flooding is important to make sure the borehole is cooled as quickly as possible. The efficient transport of LN₂ depends on the amount of leakage from the Dewar (affecting pressure inside the Dewar) and the condition of the withdrawal device. On this 3rd attempt, the device was improved and liquid nitrogen was successfully transferred to the borehole. The 3rd thermal shock test was finished by the depletion of LN₂ in the Dewar (Figure 4.3.46-Figure 4.3.47). Acoustic measurements were performed after the 3rd thermal shock to monitor material deterioration due to the thermal shocks. The acoustic signals are compared later.

Temperature, pressure, and LN₂ consumption

The temperature curve shows much more immediate temperature decrement compared with the two previous experiments. It also shows the Leidenfrost effect, which is another indication that LN₂ exists in the borehole. In Figure 4.3.47, the pressure plot shows a steady increase in the pressure until the end of test. While not knowing the cause of this increase, the temperature curve (Curve 2 in Figure 4.3.46) matches this trend by showing a steady increase of temperature.

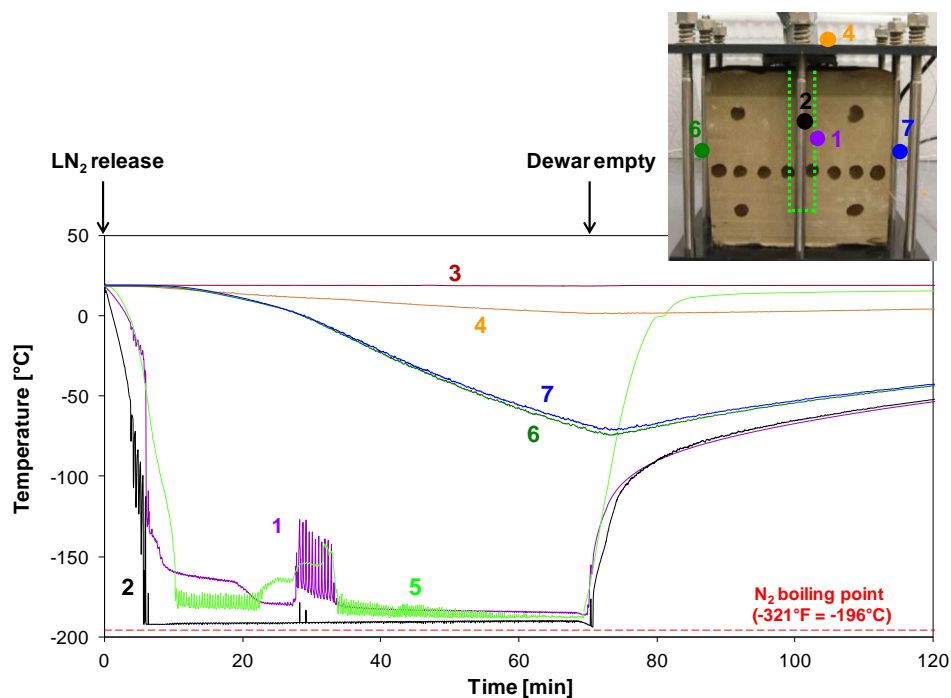


Figure 4.3.46 Temperature evolution during the 3rd thermal shock.

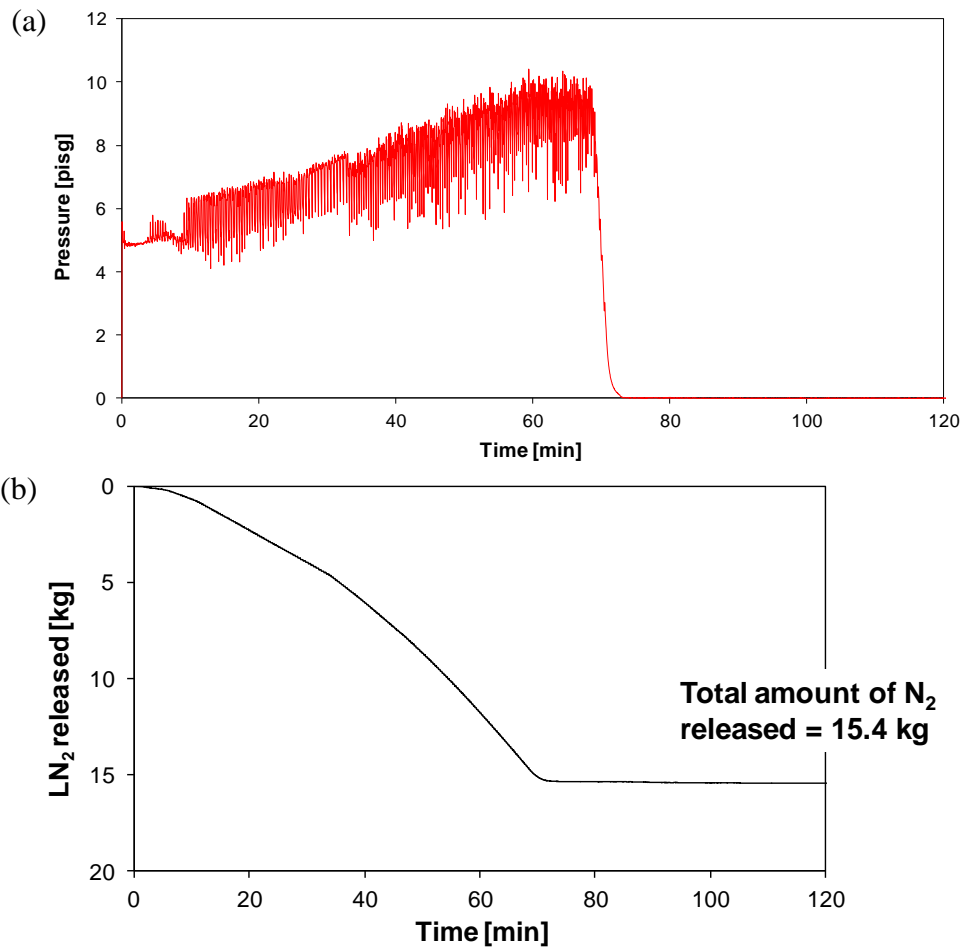


Figure 4.3.47 Pressure and LN₂ consumption vs. time of the 4th thermal shock.

4.3.2.4 The Fourth Pressurized Stimulation with LN₂

In the 4th cryogenic test, cryogenic-rated valves, a cryogenic pressure relief valve (burst pressure 275 psi), an accumulator (sample cylinder), and a compressed nitrogen cylinder were installed to enable pressurization of the borehole.

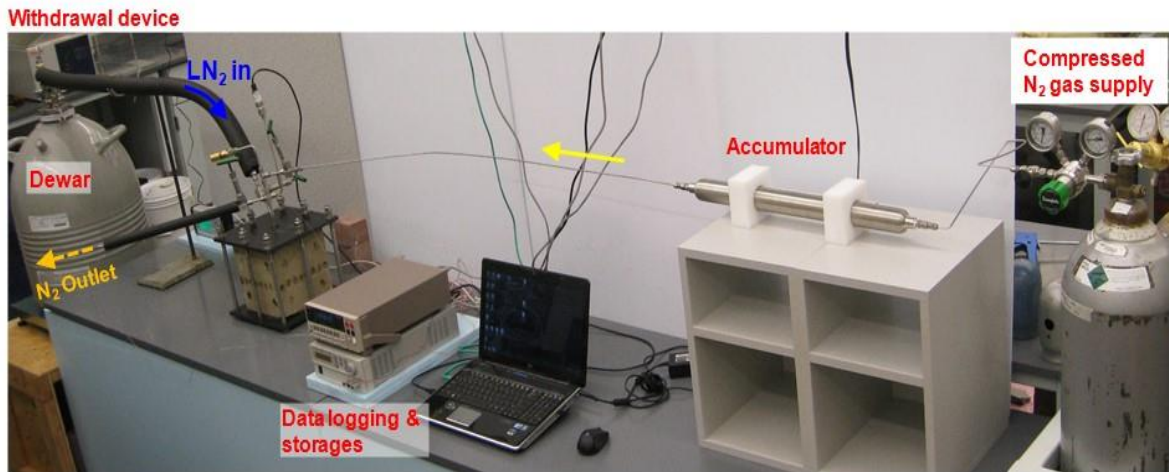


Figure 4.3.48 Experimental setup for thermal shock and borehole pressurization (protection shields not shown in this picture).

Pressure, temperature, and LN₂ consumption

The pressure transducer limit is 300 psi and the cryogenic relief valve limit is 275 psi, both of which will limit the pressure for borehole injection. Furthermore, unconfined specimens cannot sustain much pressure because geomaterials are generally weak at tensile stress.

After a thermal shock, two different borehole pressurizations are attempted. One is by natural vaporization of liquid nitrogen in a closed system. The other is pressurizing the borehole by supplying compressed nitrogen gas (**Figure 4.3.50**). It is observed that LN₂ vaporization causes the pressure to increase up to only 250 psi and thus the pressure relief valve was never operated (**Figure 4.3.51**). This means that nitrogen (most probably as a gas state) at the borehole was lost at a fairly high rate by permeation through the rock. This fast permeation rate is also hinted by the gas permeability tests done in the previous tests.

The temperature inside the borehole increases rapidly as the borehole is pressurized in both forced pressurization and self-pressurization (**Figure 4.3.52**), as a negative aspect of borehole pressurization according to gas law. The temperature keeps increasing after the LN₂ supply discontinues.

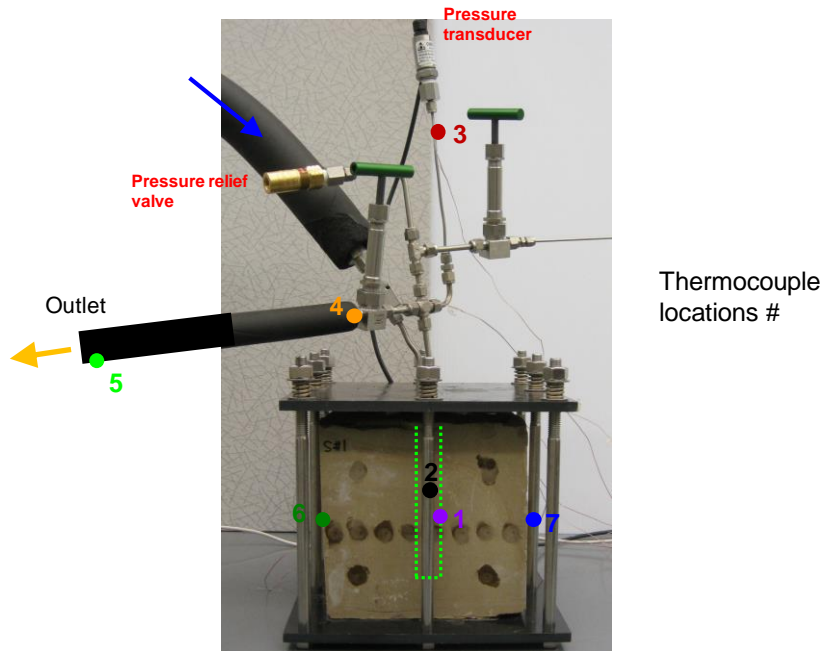


Figure 4.3.49 Experimental setup near the specimen and locations of thermocouples.

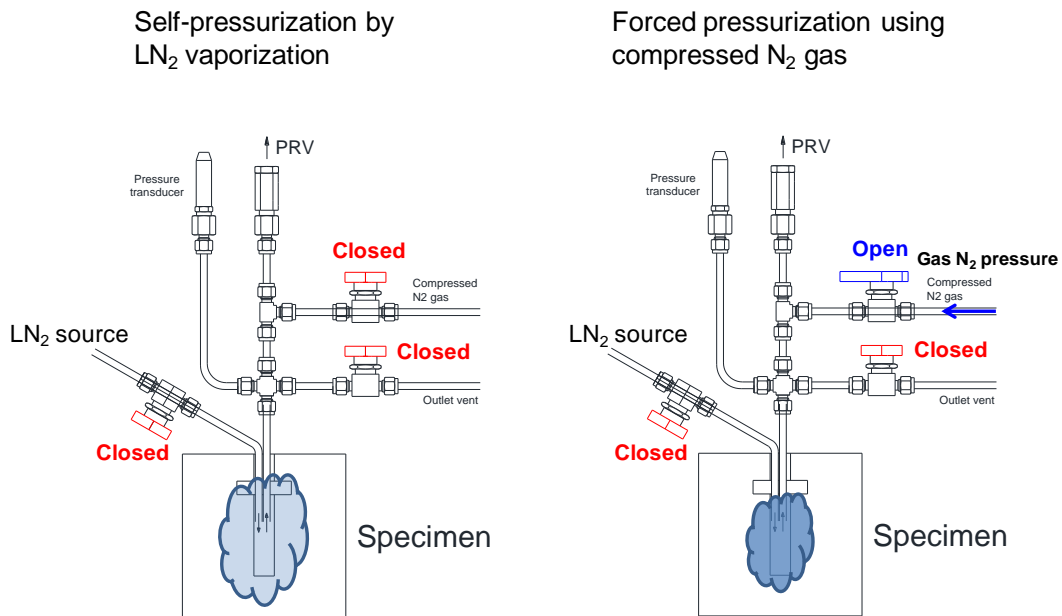


Figure 4.3.50 Two borehole pressurization schemes.

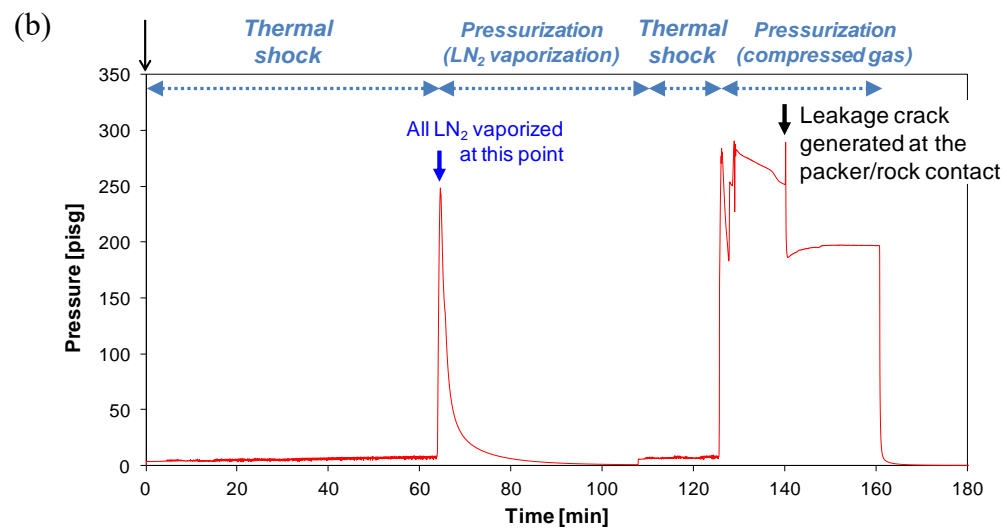
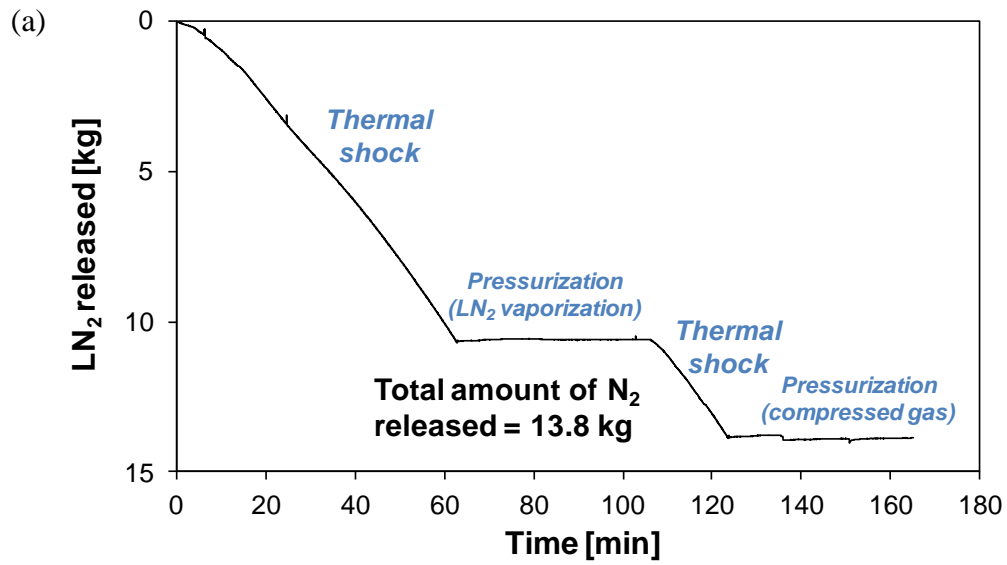


Figure 4.3.51 Monitored LN₂ consumption and borehole pressure.

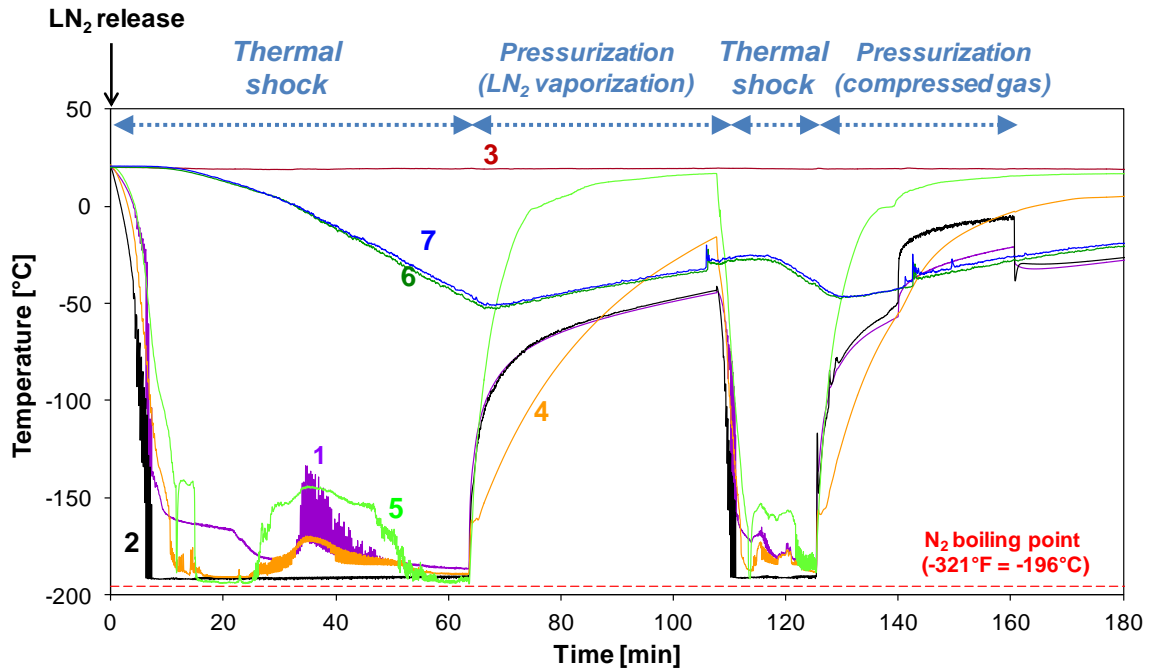


Figure 4.3.52 Temperature vs. time during the cryogenic stimulation.

Bubble leakage test

During the experiment, we observed that a leak hole/crack was generated after the 2nd pressurization (force pressurization) at the packer/rock interface, indicated by sound as well as pressure data.

After the test, a bubble agent is used to detect the leak crack. In order to do this, the borehole is pressurized to about 50 psi by air. The liquid that was used for the bubble tests is specially designed for sensitive leak tests in pressurized equipment such as Dewar or gas tank. A leak hole that was created during the cryogenic experiment is located from the massive bubble generation (**Figure 4.3.53a**). Then the bubble agent is applied all over the top surface and Face 1 to observe permeation pattern at the block surfaces. We observed that there are several localized permeation spots (or “leaking holes”) as shown in **Figure 4.3.53b** and c.

The bubble leakage test shows that permeation through the stone is not homogeneous; there are invisible path (cracks, holes, or simply less tight zone) that allows more permeation of air/fluid. We are not sure the holes/cracks are particularly due to the cryogenic stimulations because we did not compare before and after.

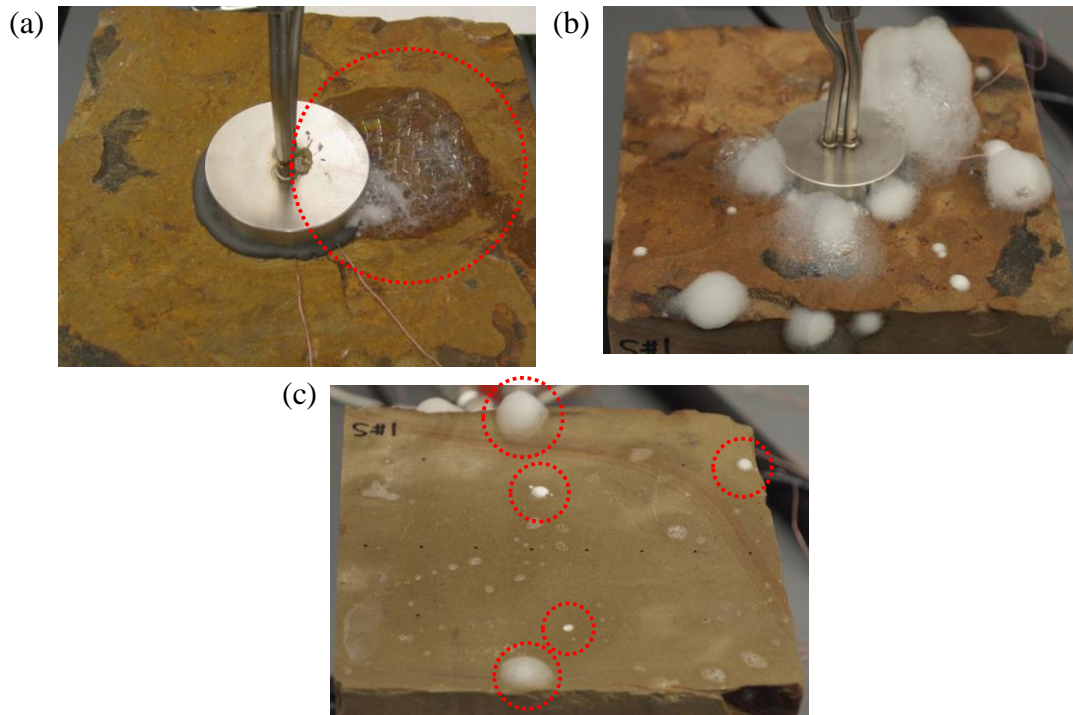
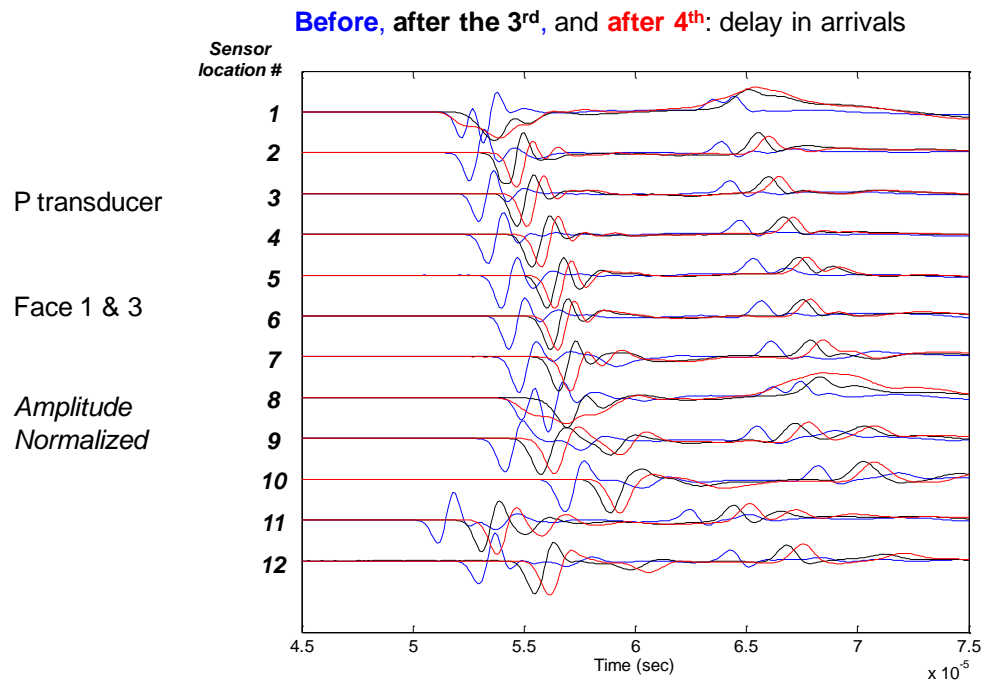


Figure 4.3.53 Leakage/permeation test by bubbles. (a) Leakage hole created at the packer/rock contact during the gas pressurization of the 4th test, (b) localized air permeation observed at the top, and (c) local permeation at the side (Face 1).

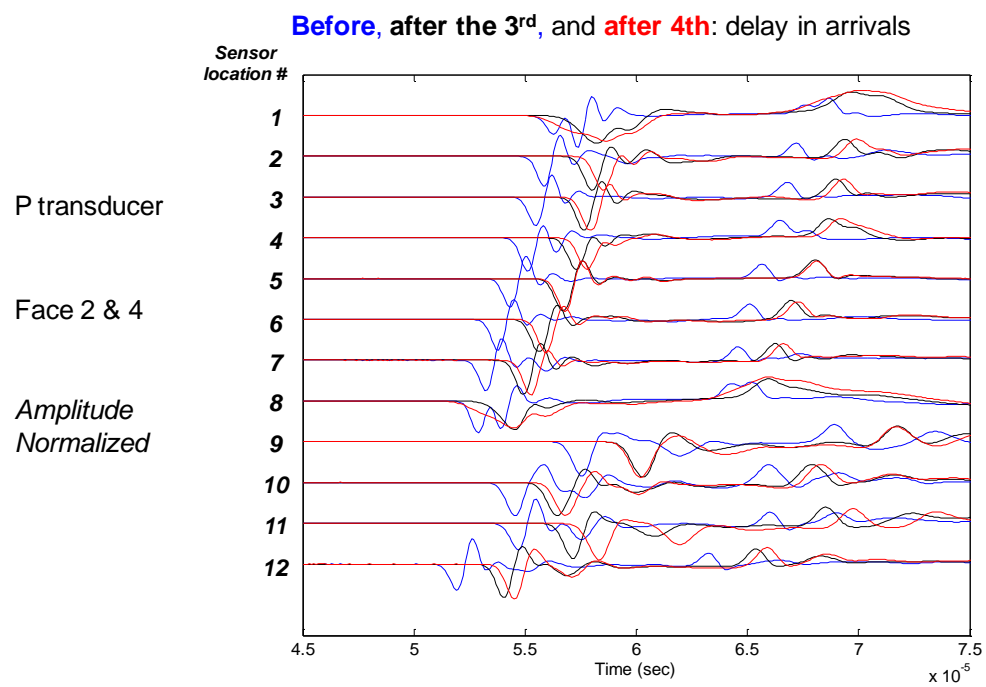
Acoustic measurements

The P and S wave signatures before any thermal shock, after the 3rd thermal shock, and after the 4th thermal shock are compared. The velocities and amplitudes clearly changed, but in relatively small magnitude considering the number of stimulations performed. This shows that sandstone is relatively resistant to cryogenic stimulations compared to the concrete samples. The decreasing or increasing velocities as the sensor location moves along the surface seems to be a result of both changing travel distance (due to uneven cut) as well as the internal rock properties.

(a)



(b)



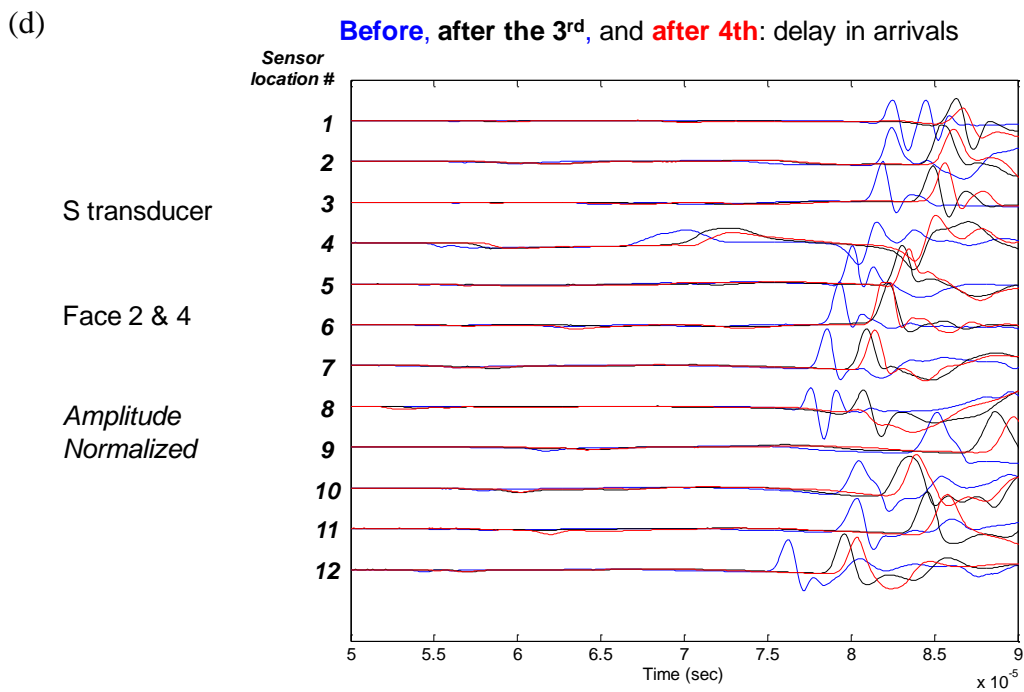
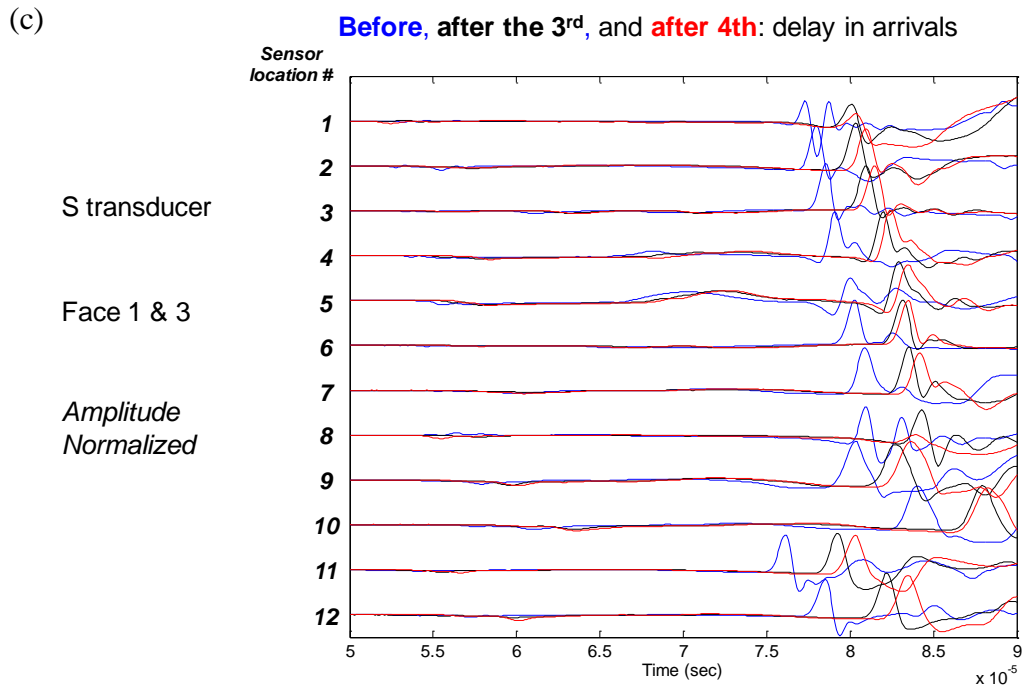
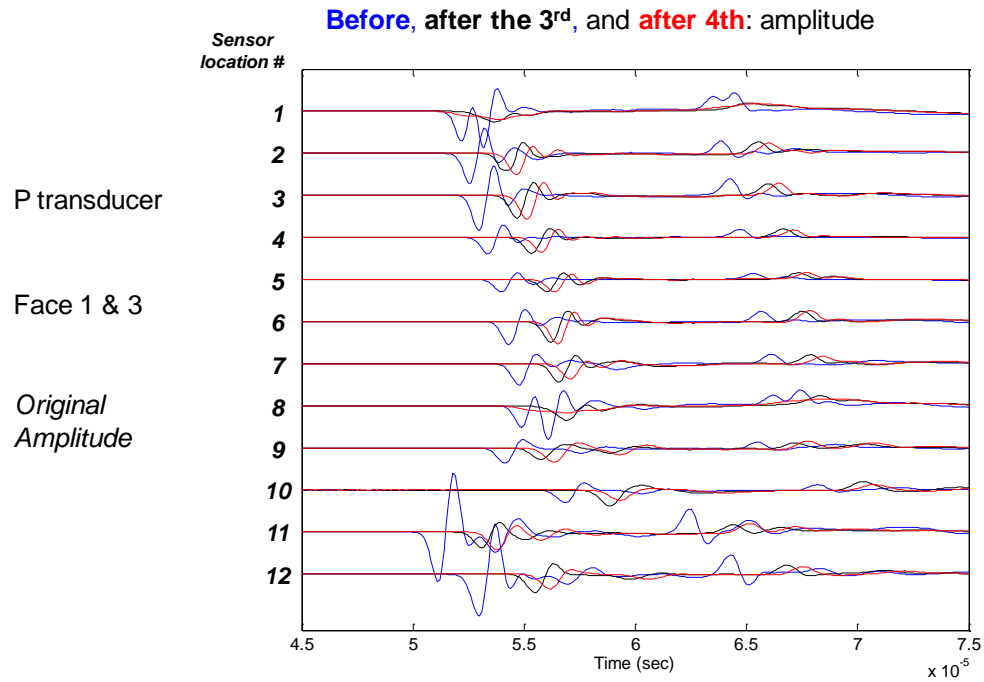
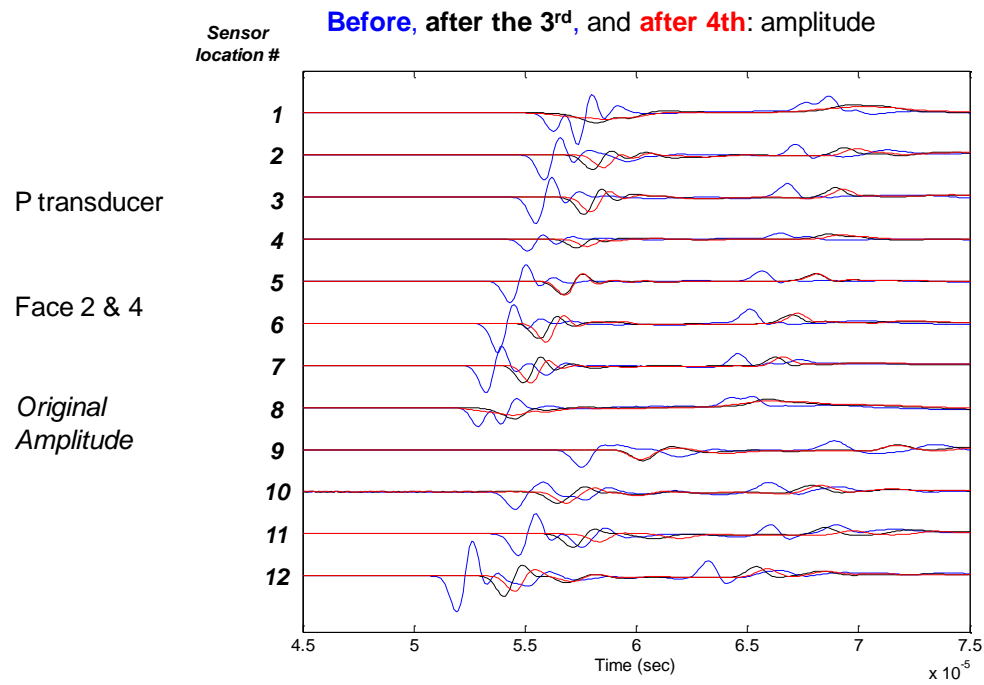


Figure 4.3.54 P and S wave arrivals before and after the cryogenic stimulation (compared with normalized amplitude).

(a)



(b)



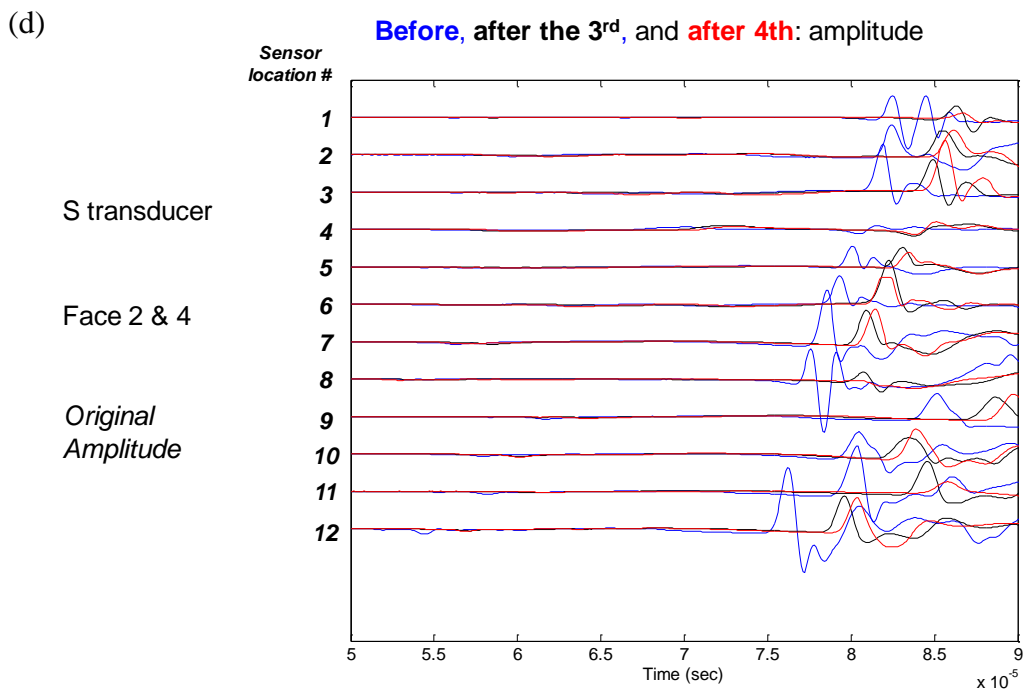
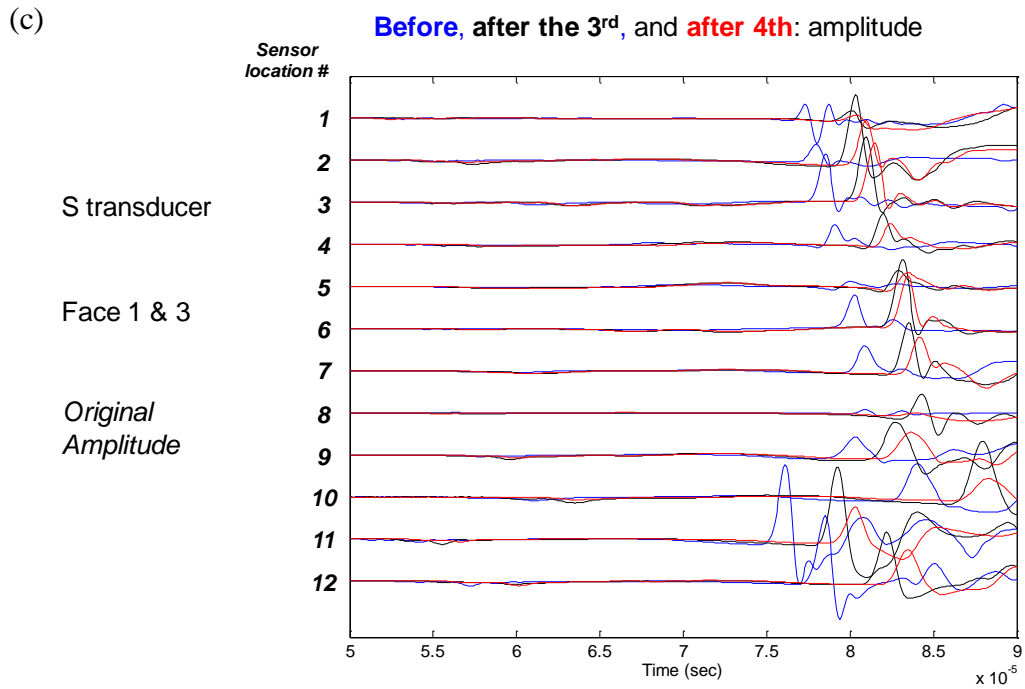
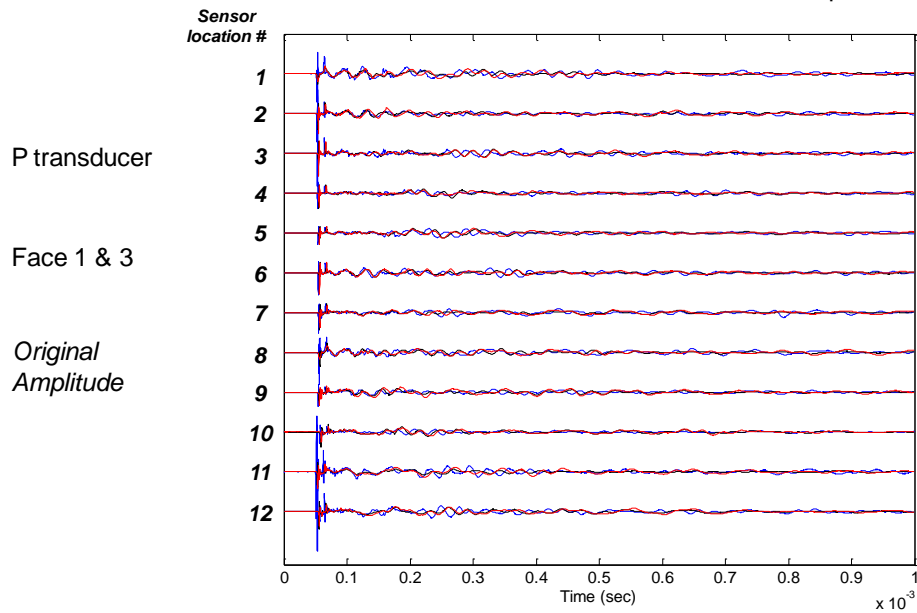


Figure 4.3.55 P and S wave amplitudes before and after the cryogenic stimulation.

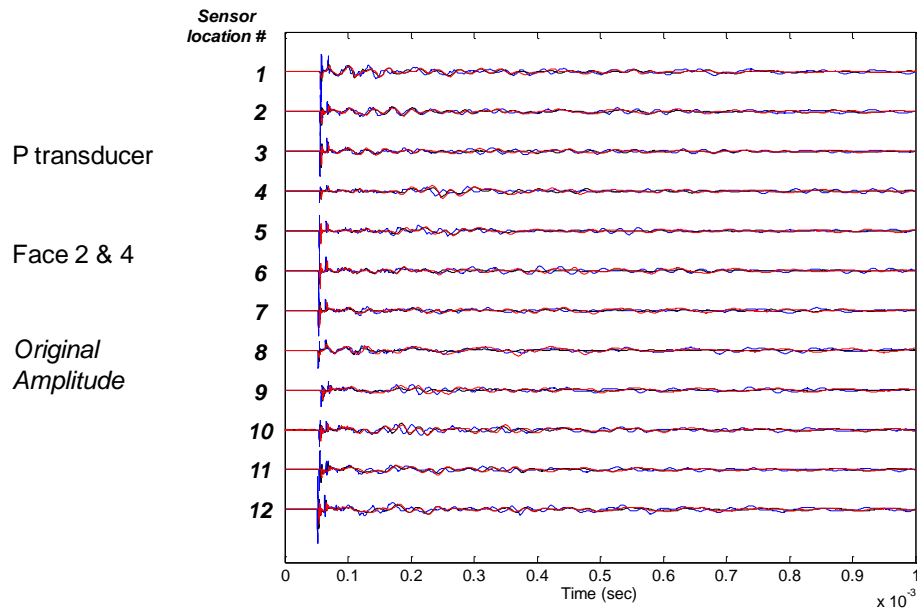
(a)

Before, after the 3rd, and after 4th: waveforms & amplitude



(b)

Before, after the 3rd, and after 4th: waveforms & amplitude



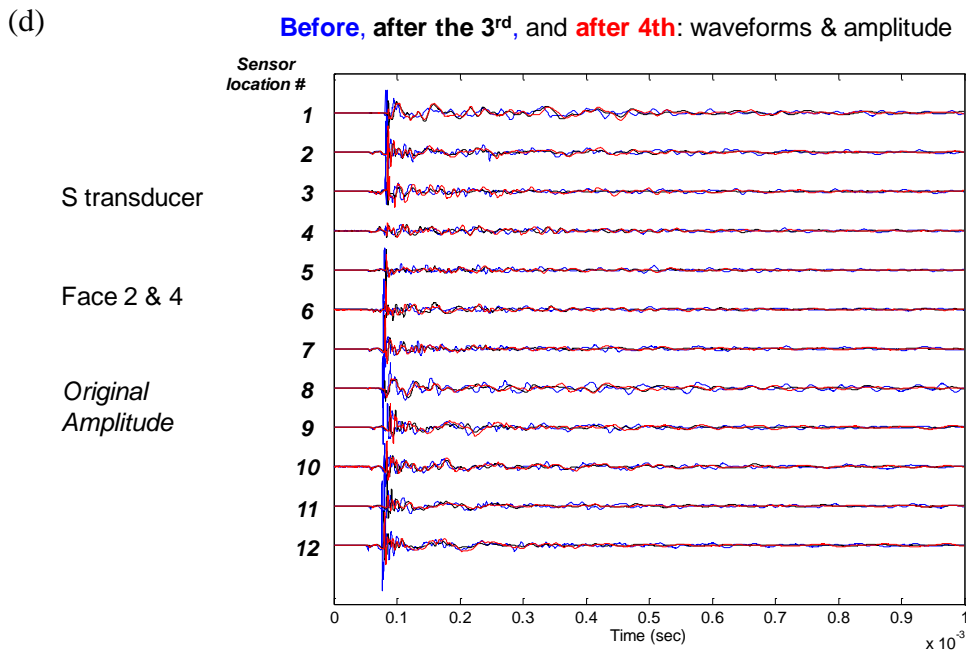
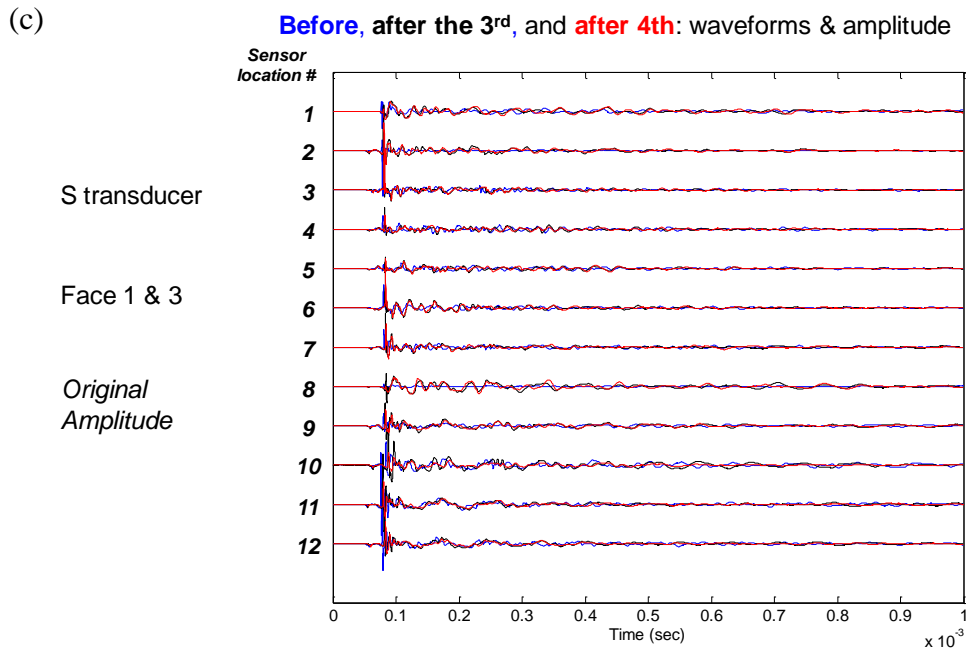


Figure 4.3.56 Global waveforms before and after the cryogenic stimulation.

4.4 Borehole Stimulation with Triaxial Stresses

Stimulation of artificial and natural rock samples under triaxial stress conditions was conducted to create fractures by injecting LN₂ into the boreholes drilled in the center. The

effects of stress levels and stress anisotropy on the characteristics of cryogenic fracturing were investigated using the triaxial stress loading system. The measurements included pressure, temperature, acoustic, and CT scanning; and the specimens were photographed before and after the test. The specifics and experimental conditions for these rock samples are summarized in **Table 4.8**.

Table 4.8 Rock specifics and experimental conditions for stressed borehole stimulation

Sample type	Sample #	Stresses (psi) and tests	Size (inch)
Glass	1	z=190, horizontal borehole, LN ₂	2
Glass	2-3	x:y:z=700:1050:1400, horizontal borehole, LN ₂	2 and 4
Glass	4	x:y:z=700:1050:1400, vertical borehole, LN ₂	2
Glass	5	x:y:z=2800:4200:5600, horizontal borehole, LN ₂	2
Concrete	16-17	x:y:z=500:750:1000, GN ₂ fracturing	8
Concrete	18	x:y:z=500:750:1000, LN ₂ under low pressure + GN ₂ fracturing	8
Concrete	19-20	x:y:z=500:750:1000, 3 cycles of LN ₂ under high pressure + GN ₂ fracturing	8
Concrete	21	x:y:z=1000:1500:2000, GN ₂ fracturing	8
Concrete	22-23	x:y:z=1000:1500:2000, Cyclic LN ₂ under high pressure + GN ₂ fracturing	8
Sandstone	1	Z=60, break down by GN ₂	8
Sandstone	2	x:y:z=1000:1500:2000, LN ₂ injection at 450 psi	8
Shale	1	x:y:z=1000:1500:2000, break down by GN ₂	8
Shale	2	x:y:z=1000:1500:2000, cyclic LN ₂ injection at ~450 psi + GN ₂ fracturing	8
Shale	3	x:y:z=1000:3000:4000, cyclic LN ₂ injection at ~450 psi + GN ₂ fracturing	8
Shale	4	x:y:z=1000:1500:2000, LN ₂ injection at low pressure 40 mins + GN ₂ fracturing	8

4.4.1 Glass Samples

Five cryogenic fracturing tests have been performed on transparent glass cubes. These glass cubes are high-quality soda lime glass used in laser engraving. The cubes had beveled for general handling without specialized gloves. For these tests, glass cubes were prepared by carefully coring out a 0.25-inch borehole that partially or fully penetrated the cube about $\frac{3}{4}$ of the side length. The cube was installed in the load frame (**Figure 4.4.1**) and stresses applied

in the ratio of 1:1.5:2 (horizontal along the borehole: horizontal perpendicular to the borehole: vertical). Two sizes of blocks have been used-2” and 4” cubes.



Figure 4.4.1 Triaxial stress frame and preliminary liquid nitrogen delivery system.

4.4.1.1 Uniaxial Stress, Horizontal Borehole

In test G1, only a small vertical stress (~190 psi in vertical direction) was applied to the 2” glass cube. A video camera was set up, and video monitoring was performed along the borehole axis through a hole in the x-axis resistance plate. Liquid nitrogen was added through a funnel system attached to the side of the cube. Fractures initiated at the bottom and end of the horizontal borehole, with annular fractures growing with time outward from the borehole. As the test progressed, a vertical fracture extended in the direction of maximum principal stress (vertical), finally surpassing the extent of the annular fractures. During the test, it appeared that liquid nitrogen momentarily imbibed into fractures, or that the aperture of the fractures widened and narrowed over time. The duration of this test was less than 2 minutes, and the resulting fracture pattern is shown in **Figure 4.4.2** and shows that the vertical fracture

parallel to the borehole propagated in the direction of maximum principal stress, and several annular fractures with somewhat uniform spacing resulted from tension along the borehole.

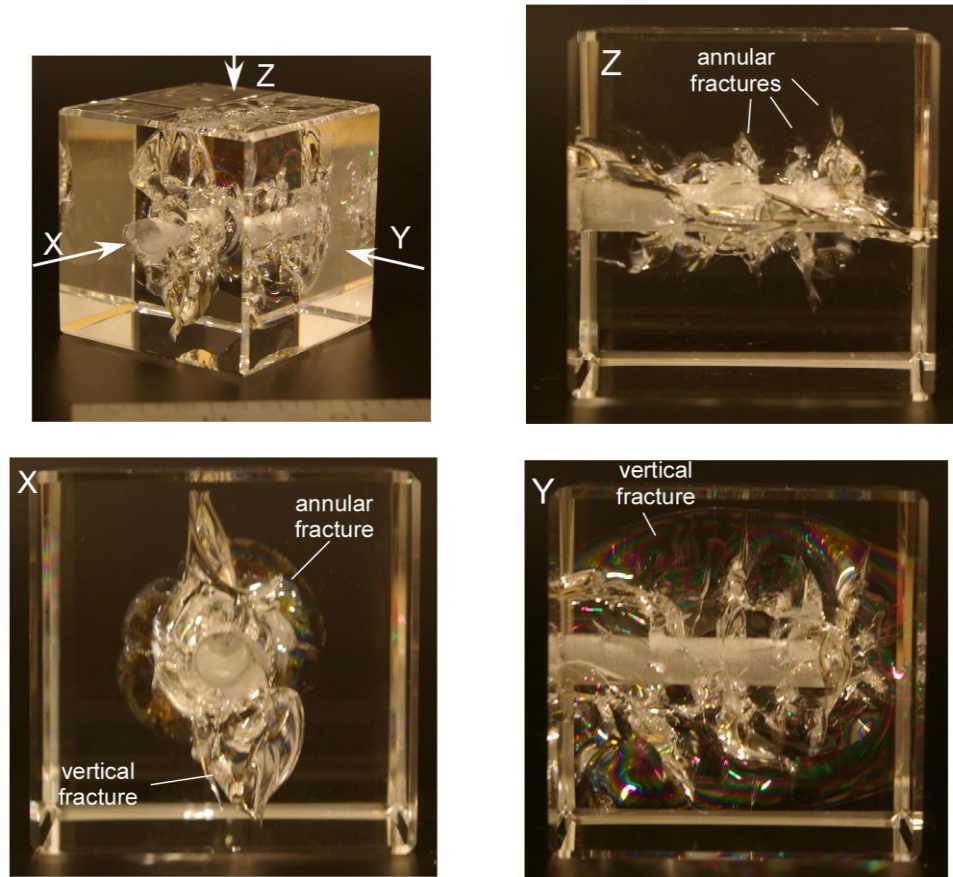


Figure 4.4.2 Test G1 with stress applied in the z direction.

4.4.1.2 Triaxial Stresses, Horizontal Borehole

Test G2 was performed on a 4-inch glass cube with x-y-z stresses of 700:1050:1400 psi (**Figure 4.4.3**). The same general behavior was observed with fractures starting at the bottom of the horizontal borehole from the liquid nitrogen. In this case, instead of a vertical propagating fracture beneath the borehole, two fractures propagated in sub-horizontal directions. Glass fracture surface temperatures were also monitored in this test. These temperatures are directly affected by the temperature of the glass block surface, and the temperatures of the supporting platens. The test was run for about 20 minutes.

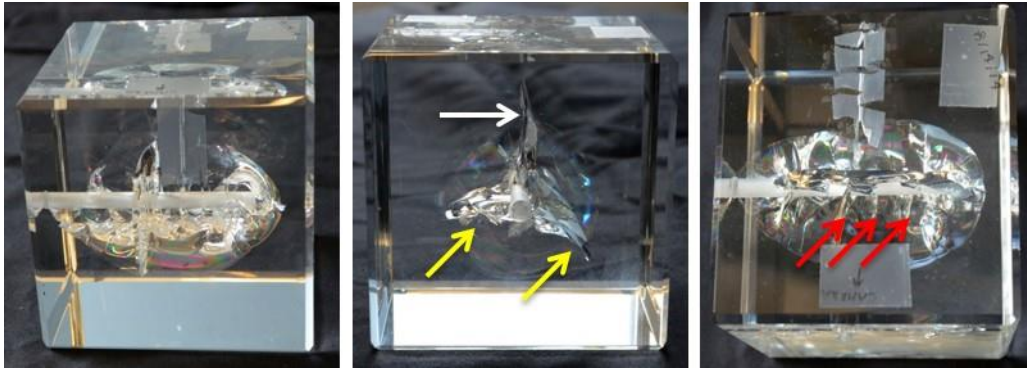


Figure 4.4.3. 4-inch block with annular (red arrows), vertical (white arrow), and sub-horizontal (yellow arrows) fractures. Left-side view, Center-view along the borehole, Right-top view.

4.4.1.3 Triaxial Stresses, 1x and 4x Comparison

Test G3 was performed with the same stress distribution as Test G2. Test G5 was performed with the stresses increased by a factor of 4. The images show a clear impact of the effect of stress. The fractures in the uniaxial case (left in **Figure 4.4.4** and **Figure 4.4.5**) are clearly more extensive than those in the triaxially-stressed cube (center in **Figure 4.4.4** and **Figure 4.4.5**), while the fractures in the 4x triaxial case (right in **Figure 4.4.4** and **Figure 4.4.5**) are far less extensive. This is because to fracture a stressed cube, the tension generated from the application of the cryogen must first overcome the compressive stresses, then overcome the tensile strength of the glass and the increased stresses provide a larger barrier to fracturing.



Figure 4.4.4 Views along the boreholes of cryogenically fractured 2-inch glass blocks. Left-uniaxial vertical stress ~190 psi, Center-triaxial 700:1050:1400 psi, Right-triaxial 2800:4200:5600 psi.

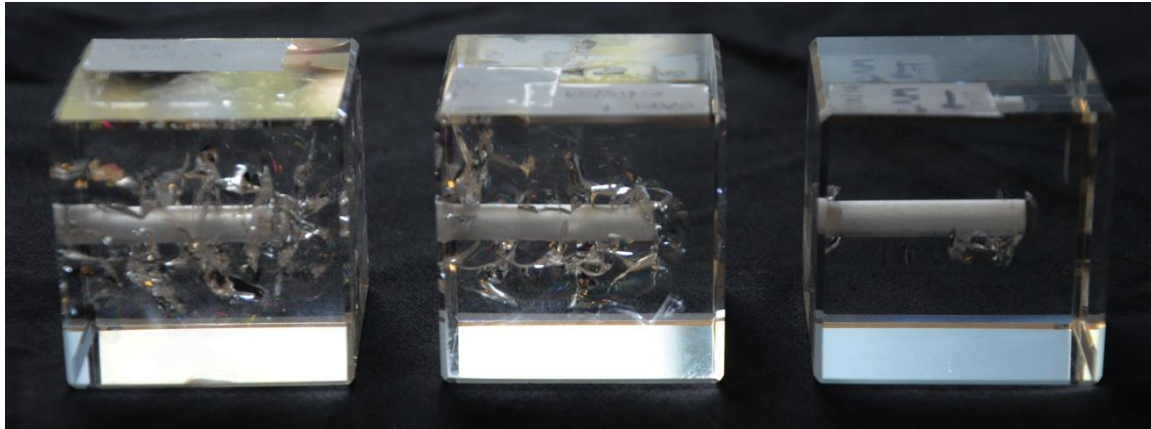


Figure 4.4.5 View perpendicular to the borehole of cryogenically fractured 2-inch glass blocks. Left-uniaxial vertical stress, Center-Triaxial 700:1050:1400 psi, Right-triaxial 2800:4200:5600 psi.

Two things should be noted about the high stress case. The first is that the fractures observed in **Figure 4.4.4** and **Figure 4.4.5** do not show the extent of fracturing due to fracture closing. For reference, see the final image collected in Test G5 (**Figure 4.4.6**).

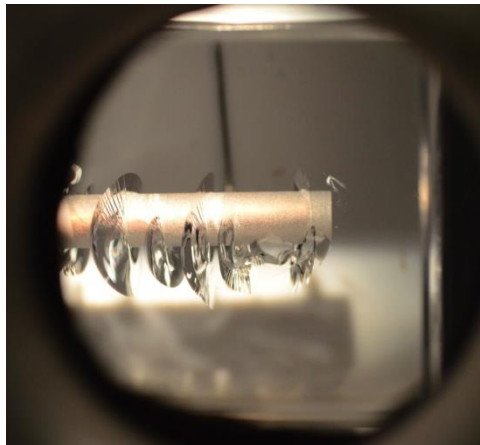


Figure 4.4.6 Final image from Test G5 after 12 minutes.

The other thing to note is the progression of fracture opening upon removal of the stress. Fifty minutes after the completion of cryogen addition, stress was removed from the block in a stepwise manner. Fractures that had appeared to close while the block warmed under stress opened again when stress was removed (**Figure 4.4.7**). Some of these fractures partially closed as the block fully returned to room temperature and that is the condition shown in **Figure 4.4.4** and **Figure 4.4.5**.

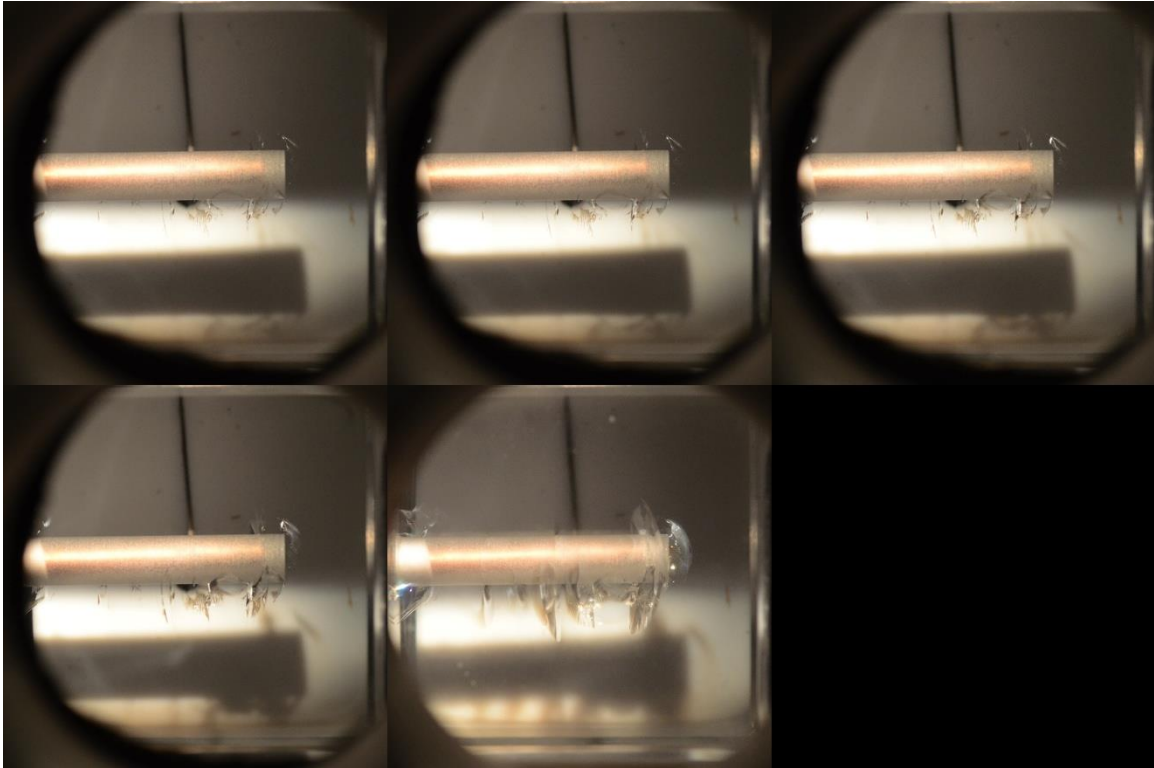


Figure 4.4.7 Images collected of visibly observed fractures upon stress removal. Stress removal occurred 50 minutes after the application of cryogen was completed. From left to right, top to bottom: fully stressed, three-quarters stressed, one-half stressed, one-quarter stressed, and unstressed.

4.4.1.4 Triaxial Stresses, Vertical Borehole

In this test the maximum principal stress was oriented parallel to the borehole in contrast to the other tests, where the maximum principal stress was oriented perpendicular to the borehole. Because of the orientation of the stresses in this test, annular fractures were suppressed as was expected, and vertical fractures propagated outward from the borehole (**Figure 4.4.8**). As in Test G2, three major fractures propagated, with the orientation of the major fractures either propagating in the direction of the maximum principal stress, or sub-perpendicular to it. Further analysis is required to understand this phenomenon.

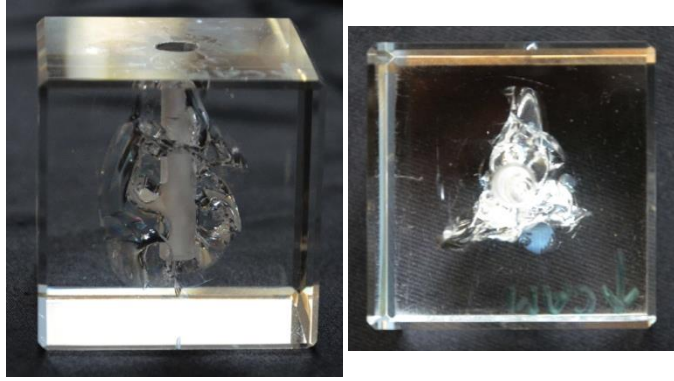


Figure 4.4.8 Fractures in vertical borehole with annular fractures suppressed.

4.4.2 Concrete Samples

Eight concrete samples, numbering from 16 to 23, were tested under different elevated triaxial stress conditions and with different LN₂ treatment procedures.

4.4.2.1 GN₂ Fracturing

Samples 16, 17, and 21 were dry concrete samples that were stimulated with GN₂ at room temperature. In these tests, the GN₂ was injected into the borehole with increasing pressure to fracture the stressed samples and the breakdown pressures were recorded. These breakdown pressure values are compared with values for samples that were treated with LN₂ in different situations.

Samples 16 and 17 were cured under water for about three months, then left at ambient conditions to dry for five months. Both samples had a little dent around the top part of the wellbore. **Figure 4.4.9** shows the triaxial stress profiles that were applied to Sample 16 ($x = 500$ psi, $y = 750$ psi, and $z = 1000$ psi). **Figure 4.4.10** shows that the breakdown pressure of Sample 16 is 583 psi while under triaxial stresses; **Figure 4.4.11** shows a picture of Sample 16 after it was fractured by GN₂. The fractures on Sample 16 seem to be a premature fracture perpendicular to the maximum horizontal stress (y -axis) that might be due to the center dent leading to a weakness in the area around the wellbore. Also the wellhead of the sample was in contact with the top machine block, adding more stress onto the stainless steel casing.

Due to these issues with Sample 16, a different approach was tried with Sample 17 before the Sample 16 test procedure was repeated. The dent around the wellbore was filled with epoxy, and the wellhead was shortened as to prevent it from hitting the top block. Therefore, in this case the stresses were distributed equally on the top side of the block, as well as, the other sides. **Figure 4.4.12** shows the triaxial stress profiles that were applied to Sample 17 ($x = 500$ psi, $y = 750$ psi, and $z = 1000$ psi). It is clear from this figure that the x-axis responded with the highest value (800 psi) at the time of fracture happening indicating that the fracture opened in a plane perpendicular to the minimum horizontal stress. **Figure 4.4.13** shows the breakdown pressure of 1180 psi for Sample 17 under triaxial stresses. **Figure 4.4.14** shows the picture of Sample 17 after being fractured with GN_2 . **Figure 4.4.15** shows the fracture at the wellbore bottom. The fracture direction in this sample matches the hydraulic fracturing theory when the x-axis is the minimum horizontal stress and y-axis is the maximum horizontal stress.

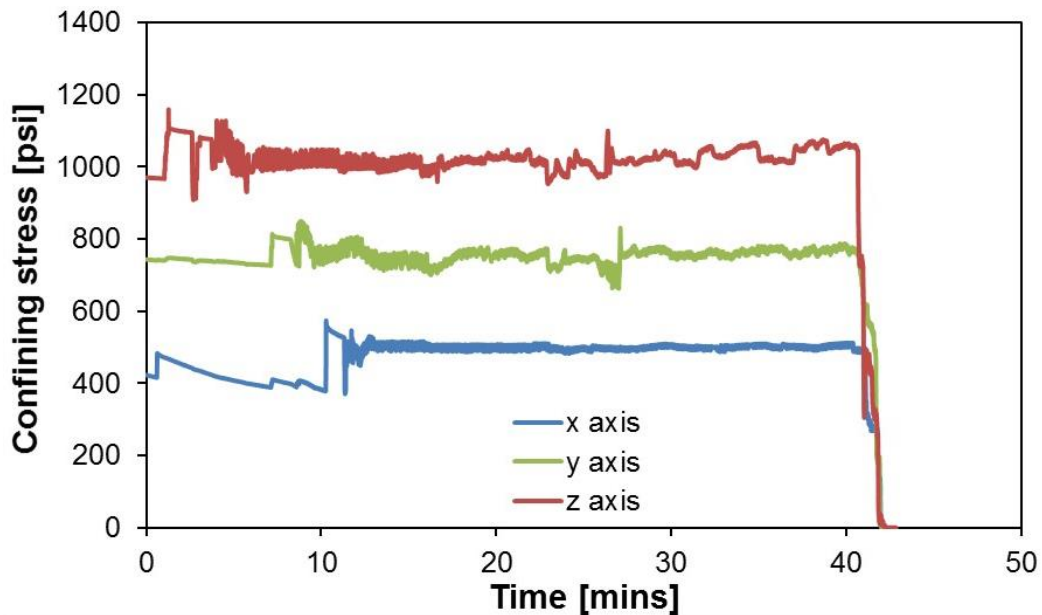


Figure 4.4.9 Triaxial stresses applied to Sample 16.

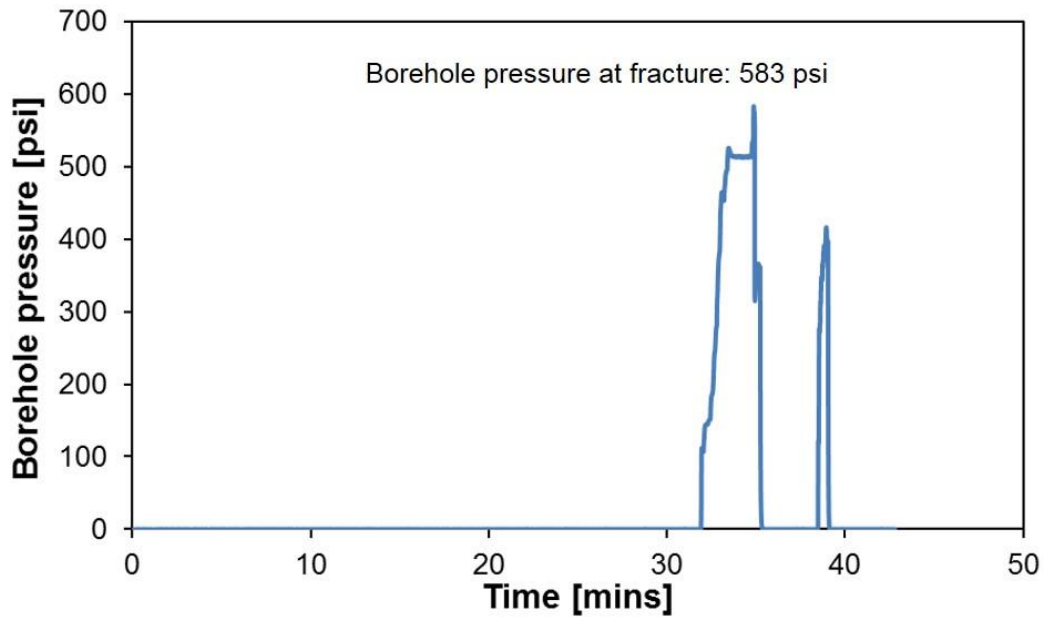


Figure 4.4.10 Breakdown pressure for Sample 16 under triaxial stresses is 583 psi.

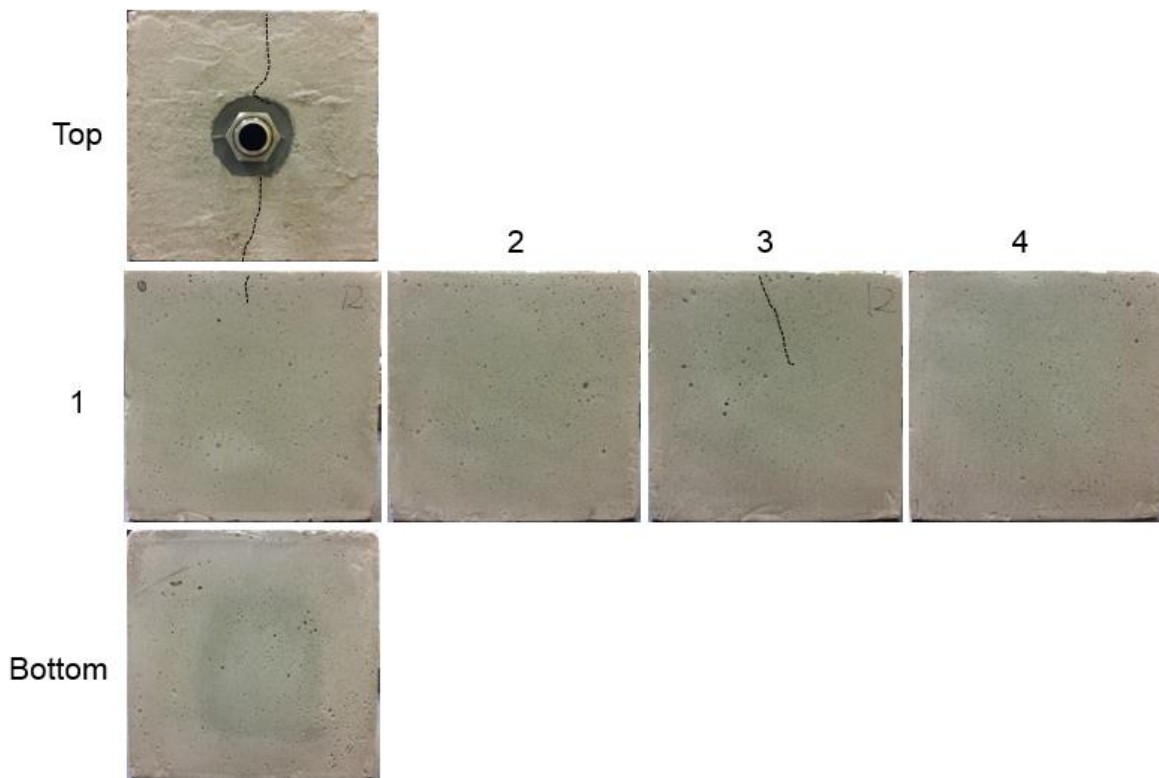


Figure 4.4.11 Picture for Sample 16 (not the number marked on sample) after fracturing by GN_2 . The created fracture seems to be a premature fracture perpendicular to the maximum horizontal stress, which is in y-axis direction applied on Faces 2 and 4. This might be because of the center dent leading to weakness in the area around the wellbore.

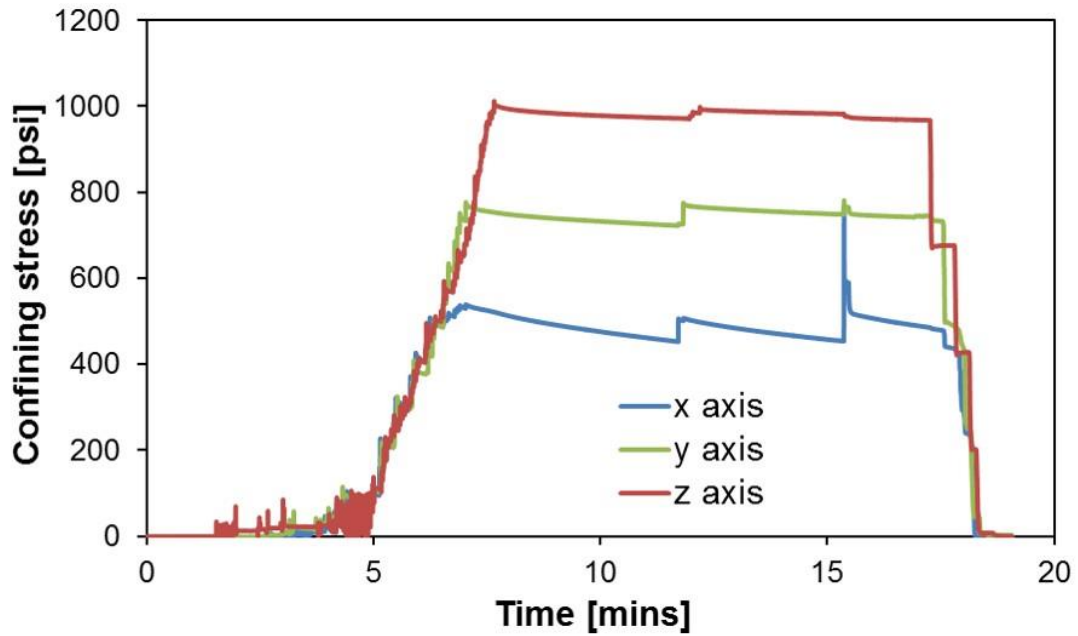


Figure 4.4.12 Triaxial stresses applied on Sample 17 (x = 500 psi, y = 750 psi, and z = 1000 psi).

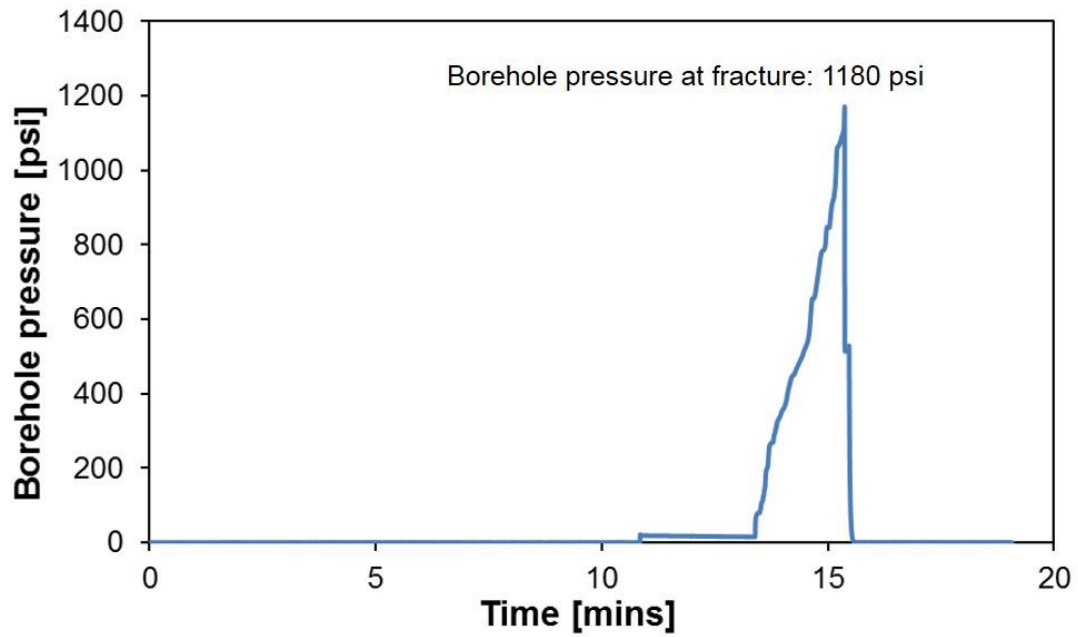


Figure 4.4.13 Breakdown pressure for Sample 17 of 1180 psi under triaxial stress.

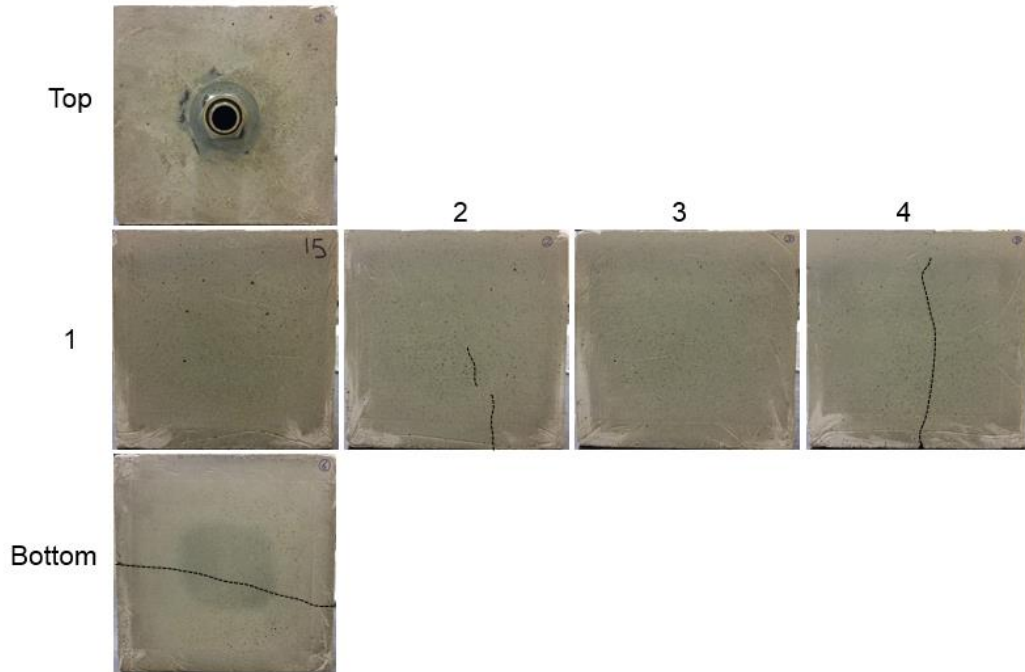


Figure 4.4.14 Picture of Sample 17 (not the number marked on sample) after fracturing by GN_2 . The fractures propagate perpendicular to the minimum horizontal stress (x-axis). The black dots follow the fractures.

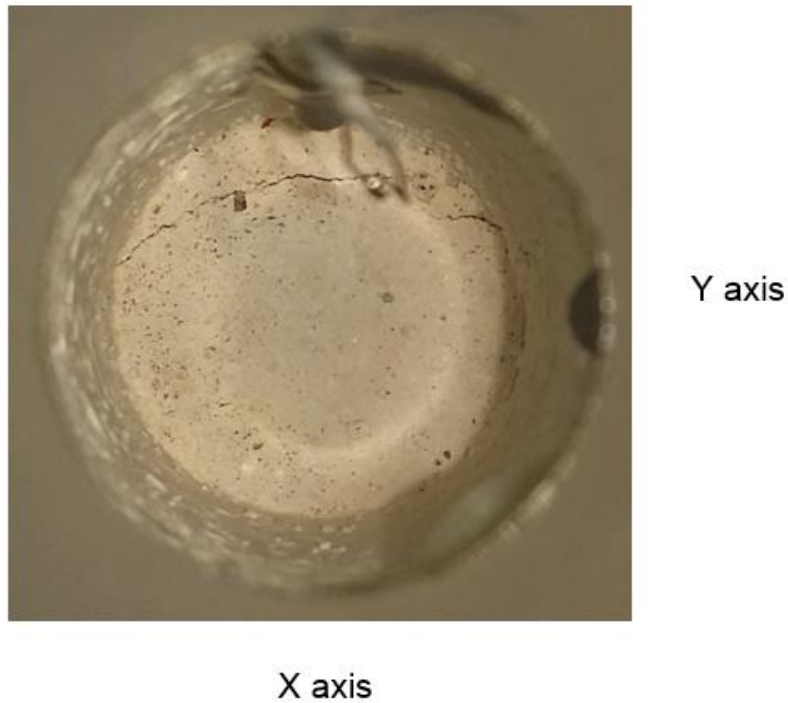


Figure 4.4.15 Top view picture from inside the borehole of Sample 17 after fracturing by GN_2 . The fractures propagate perpendicular to the minimum horizontal stress (x-axis).

Sample 21 was cured under water for five weeks then left at ambient conditions to dry for two months. It was stimulated by GN₂ with triaxial stresses of x = 1000 psi, y = 1500 psi, and z = 2000 psi. In this test, the GN₂ was injected into the sample until it fractured at the breakdown pressure, which serves as the reference for comparison with the other values of samples treated with LN₂ at the same triaxial stresses (Samples 22 and 23). **Figure 4.4.16** shows the triaxial stresses applied on Sample 21 (x = 1000 psi, y = 1500 psi, and z = 2000 psi). **Figure 4.4.17** shows the breakdown pressure of 1317 psi for Sample 21 under triaxial stresses. **Figure 4.4.18** shows a picture of Sample 21 after fracturing by GN₂. The fracture in Sample 21 propagated perpendicular to the minimum horizontal stress (x-axis) as expected.

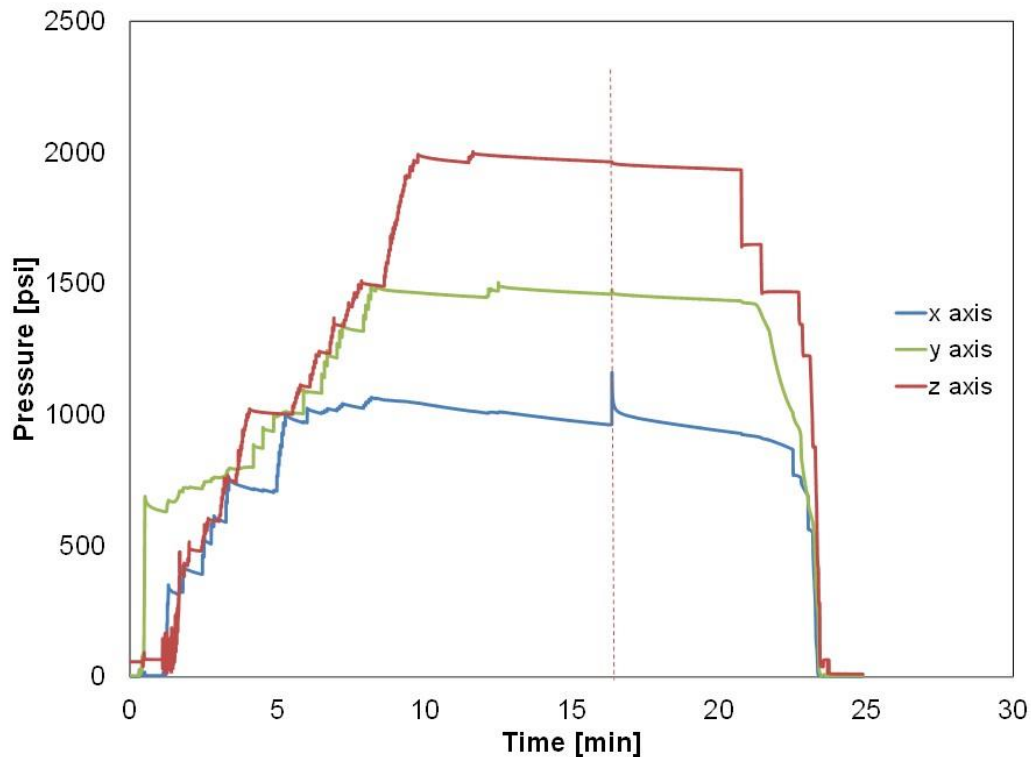


Figure 4.4.16 Triaxial stresses applied on Sample 21 (x = 1000 psi, y = 1500 psi, and z = 2000 psi).

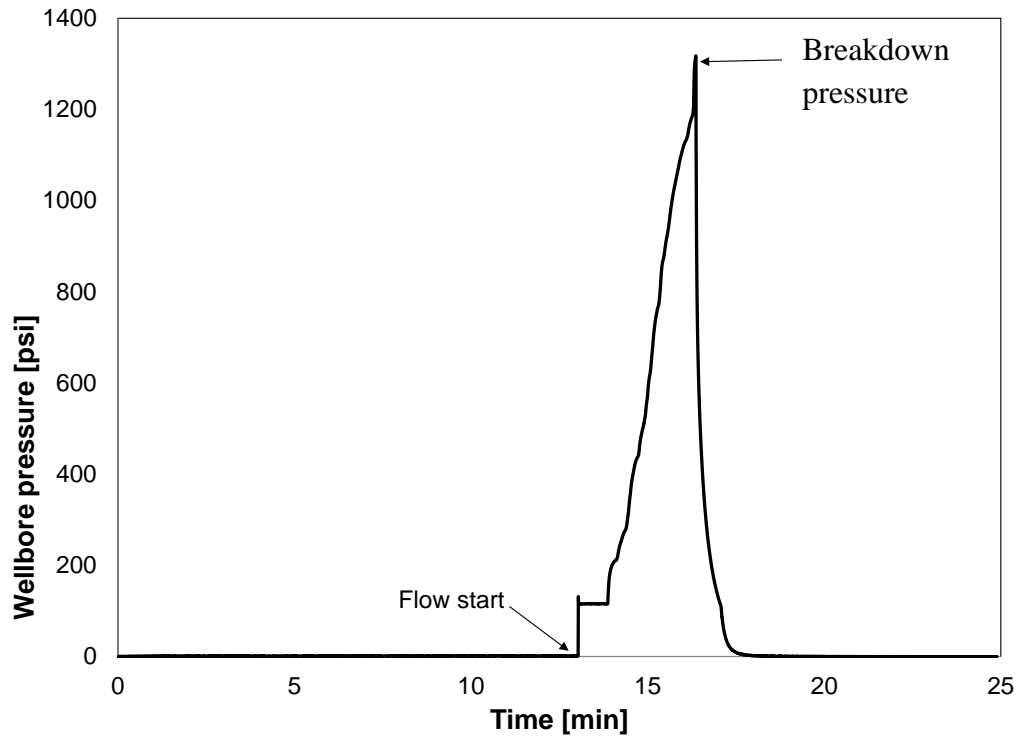


Figure 4.4.17 Breakdown pressure profile for Sample 21 under triaxial stresses.

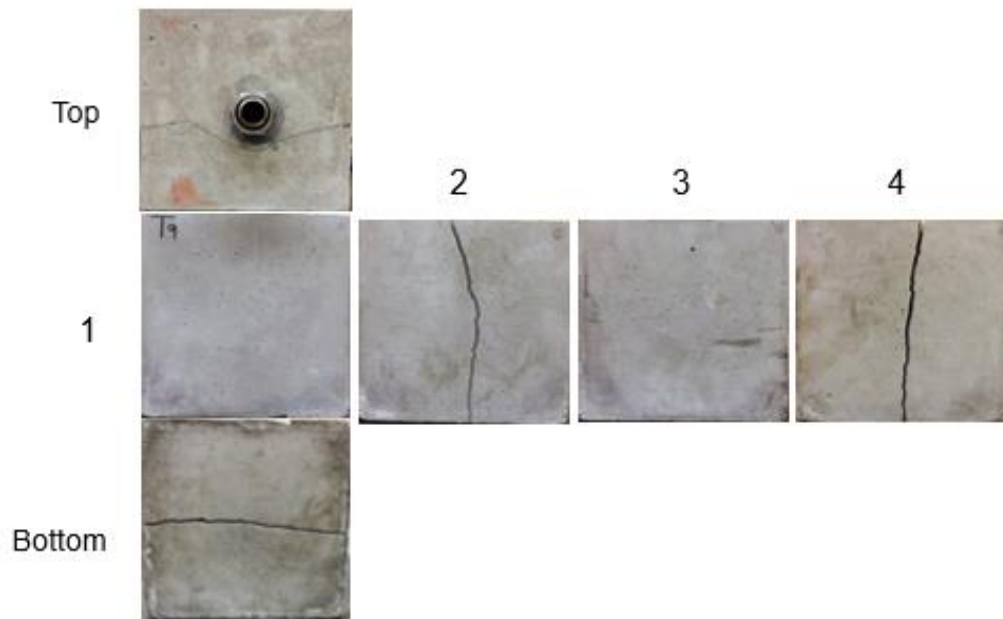


Figure 4.4.18 Picture for Sample 21 (not the number marked on sample) after fractured by GN_2 .

4.4.2.2 LN₂ Stimulation and GN₂ Fracturing

Sample 18 was cured under water for two months then left at ambient conditions to dry for seven weeks. It was treated with LN₂, which was flowed into the wellbore under 15 psi for 26 minutes. Then GN₂ was injected into the wellbore until the sample fractured. **Figure 4.4.19** shows the stress profiles for Sample 18 when applying the triaxial stresses ($x = 500$ psi, $y = 750$ psi, and $z = 1000$ psi). **Figure 4.4.20** presents the temperature profiles from the start of injecting LN₂ until the end of the test, showing that the temperature at the borehole wall decreased fairly fast to the LN₂ boiling point temperature. **Figure 4.4.21** shows the breakdown pressure for Sample 18 while it was under the triaxial stresses and right after the LN₂ treatment. Leaking sounds were heard when the pressure inside the wellbore reached 200 psi and became louder as the borehole pressure increased. This suggests a progressive failure, with the major fracture occurring at 685 psi. Both the x- and y-axis pistons responded at the same time when the major fracture happened as shown in **Figure 4.4.19** (red dashed line) which may indicate fracturing in both directions. **Figure 4.4.22** shows a picture of Sample 18 after fracturing with GN₂.

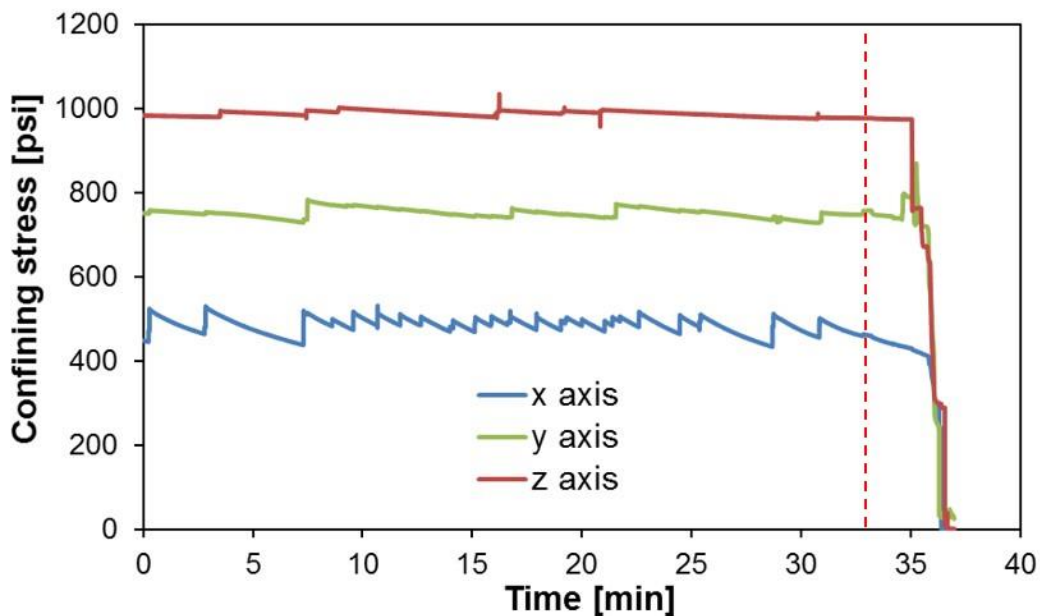


Figure 4.4.19 Triaxial stresses applied on Sample 18 ($x = 500$ psi, $y = 750$ psi, and $z = 1000$ psi). Red dots indicate when the fracture happened.

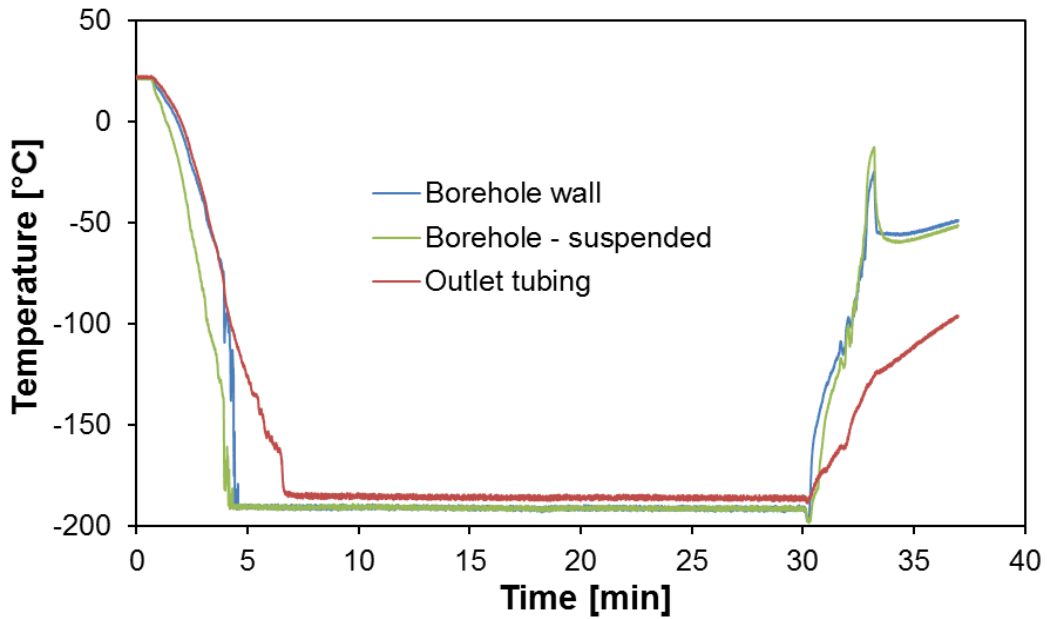


Figure 4.4.20 Temperature profiles from the start of injecting LN₂ until the end of the test showing the temperature at the borehole wall decreased fairly quickly to the LN₂ temperature.

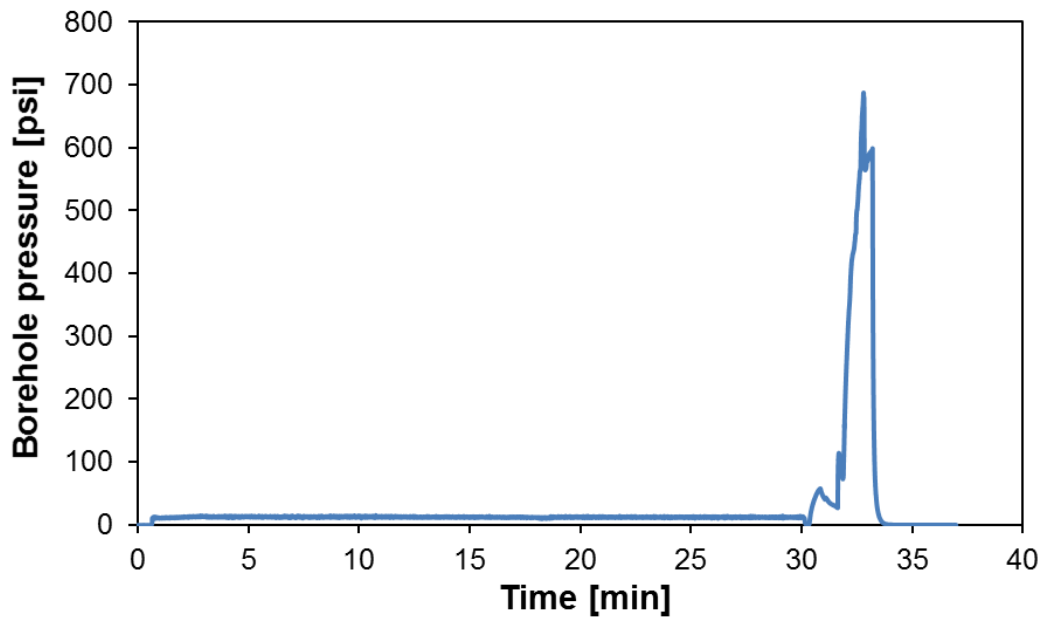


Figure 4.4.21 Breakdown pressure profile for Sample 18 under triaxial stresses and right after the LN₂ treatment. Leaking sounds were heard when the pressure inside the wellbore reached 200 psi and became louder as the wellbore pressure increased. The major fracture happened at 685 psi.

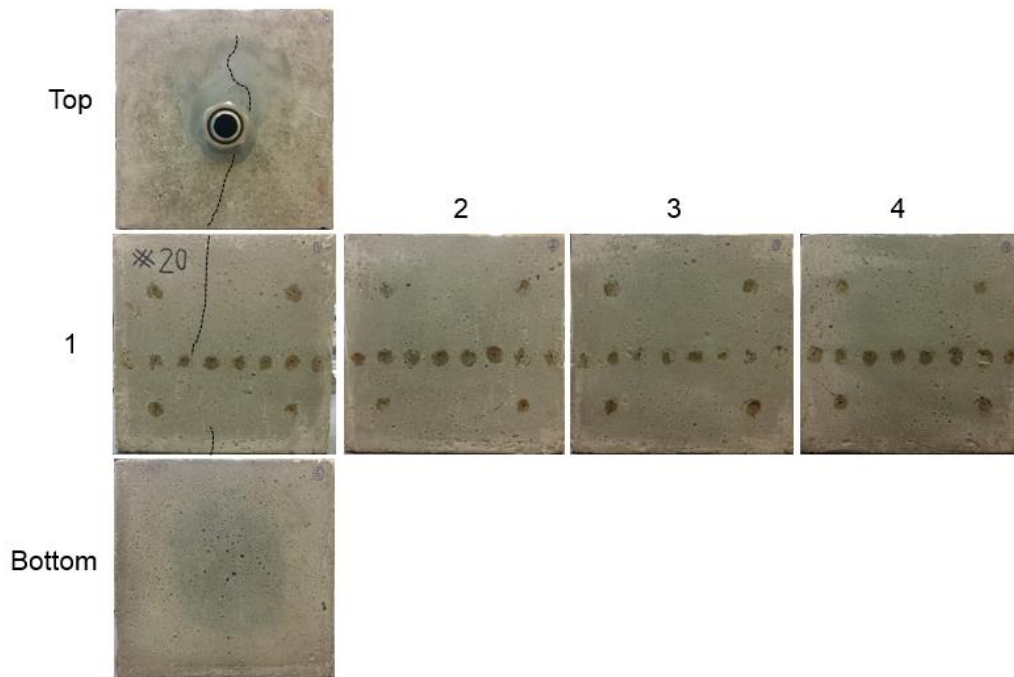


Figure 4.4.22 Picture for Sample 18 (not the number marked on sample) after fracturing by GN₂. The fractures propagated perpendicular to the maximum horizontal stress, which is in y-axis direction applied on Faces 2 and 4). The black dots follow the fractures.

Sample 19 was cured under water for two months then left at ambient conditions to dry for seven weeks. It was treated with high pressure LN₂ and was exposed for three LN₂ cycles, as shown in **Figure 4.4.23**. Sample 19 was fractured after the LN₂ treatment by injecting GN₂. **Figure 4.4.24** shows the breakdown pressure profile. Also in this sample, leaking sounds were heard when the pressure inside the wellbore reached 400 psi and it became louder as the wellbore pressure increased, indicating a progressive failure. The major fracture happened at 778 psi. **Figure 4.4.25** shows a picture of Sample 19 after fracturing by GN₂. The fracture deviated from the cased wellbore and opened in a plane perpendicular to the maximum horizontal stress (y-axis) which is the opposite direction from expected.

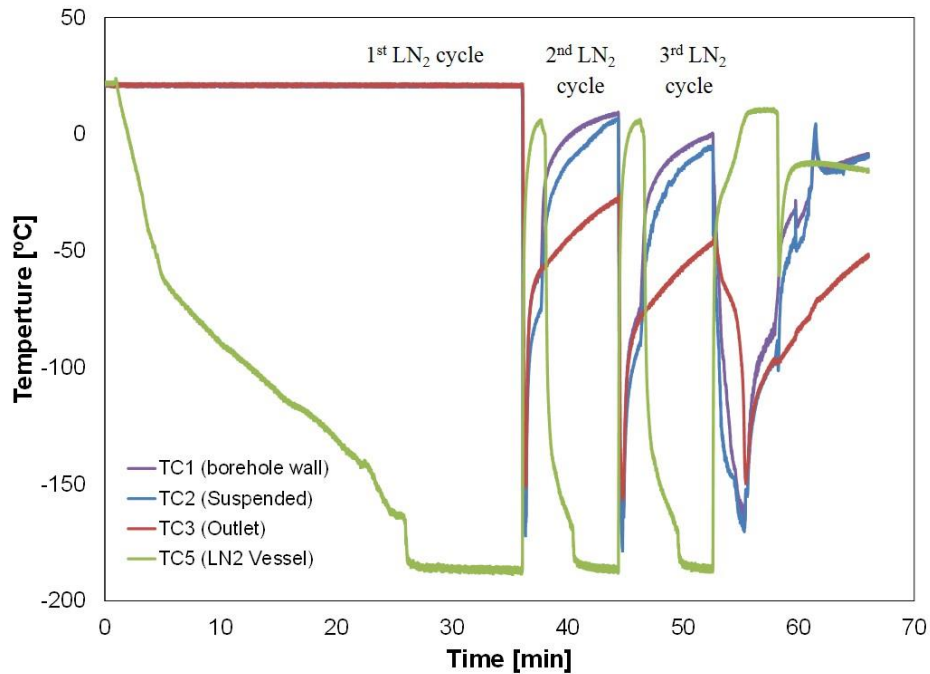


Figure 4.4.23 Temperature vs. time during the high pressure LN₂ treatment. Sample 19 was treated by three LN₂ cycles.

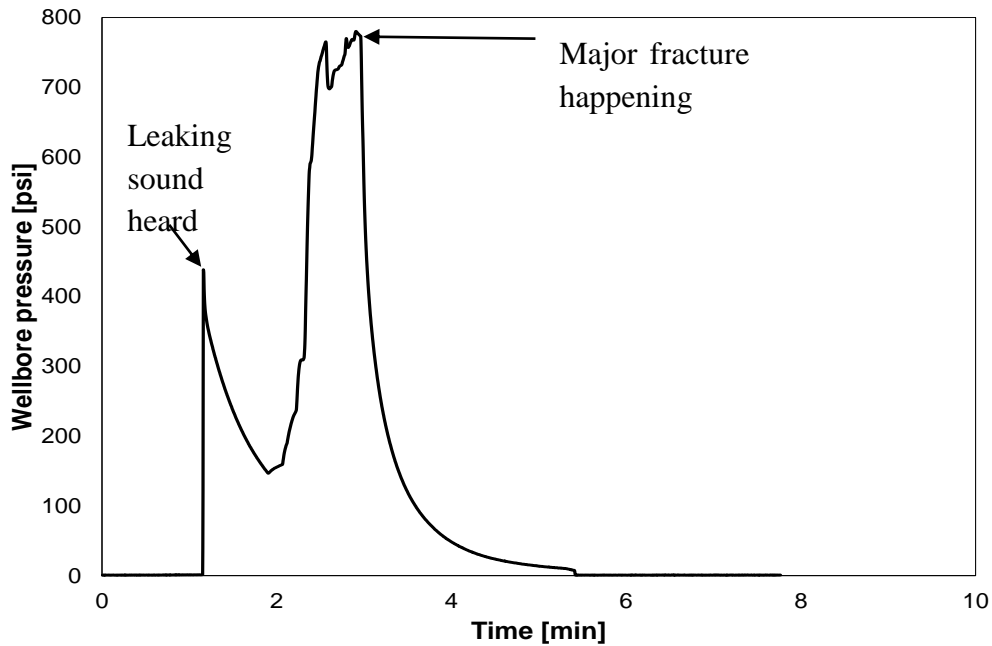


Figure 4.4.24 Breakdown pressure profile for Sample 19 under triaxial stress immediately after the LN₂ treatments. Leaking sounds were heard when the pressure inside the wellbore reached 400 psi and became louder as the wellbore pressure increased. The major fracture happened at 778 psi as noted on the figure.

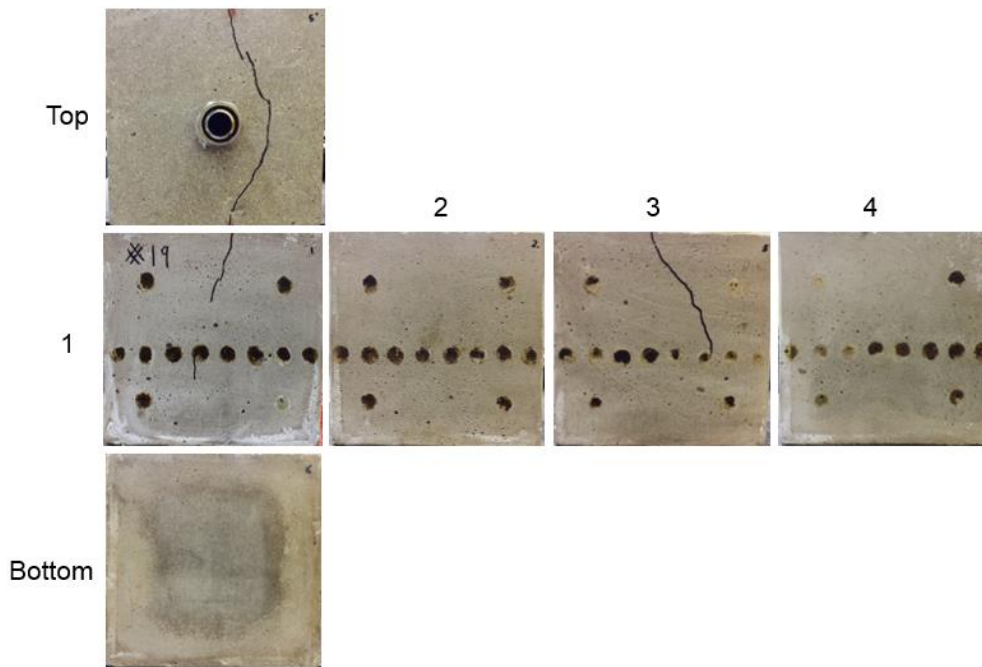


Figure 4.4.25 Picture of Sample 19 after fracturing by GN_2 . The fractures propagated perpendicular to the maximum horizontal stress which is in y-axis direction applied on Faces 2 and 4. The black dots follow the fractures.

Acoustic measurements were conducted before and after the LN_2 test for Sample 19 using P and S ultrasonic transducers. **Figure 4.4.26** shows the locations of the acoustic measurements. Signals were measured along Faces 1-3 and 2-4. **Figure 4.4.27** shows P- and S-wave arrivals before and after the LN_2 test for all faces with the adjusted amplitudes. **Figure 4.4.27** b and d show that there are delays in the arrival time of the acoustics waves especially at locations 5-10 (red circles) along Faces 2-4. Since the waves (after LN_2 test) took more time to reach the receivers, indicating there are fracture planes generated perpendicular to Faces 2-4, which is the y-axis direction. By comparing with the sample picture in **Figure 4.4.25**, the acoustic measurement results agree with the fracture profiles of Sample 19.

Figure 4.4.28 shows P-wave velocities before and after conducting the LN_2 test on this sample. The delays of wave velocities after stimulation indicate that fractures developed after the cryogenic treatment.

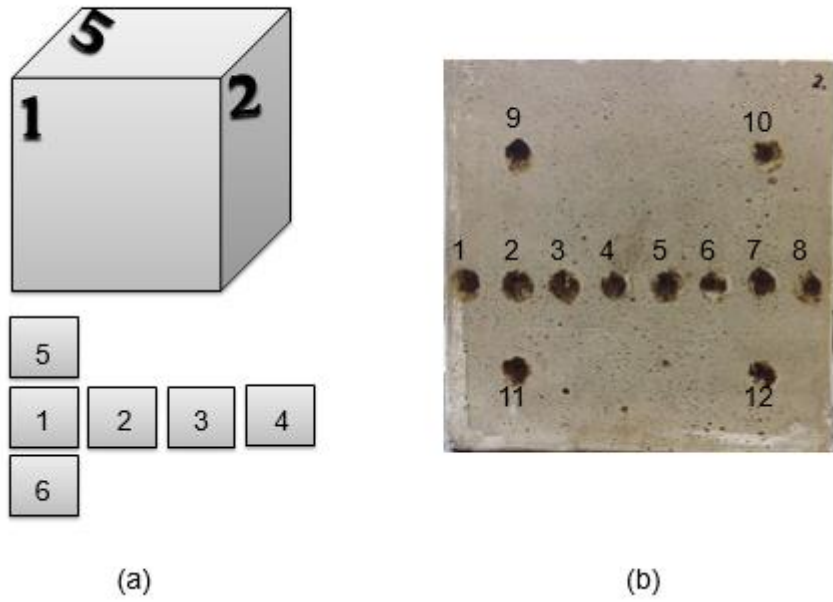
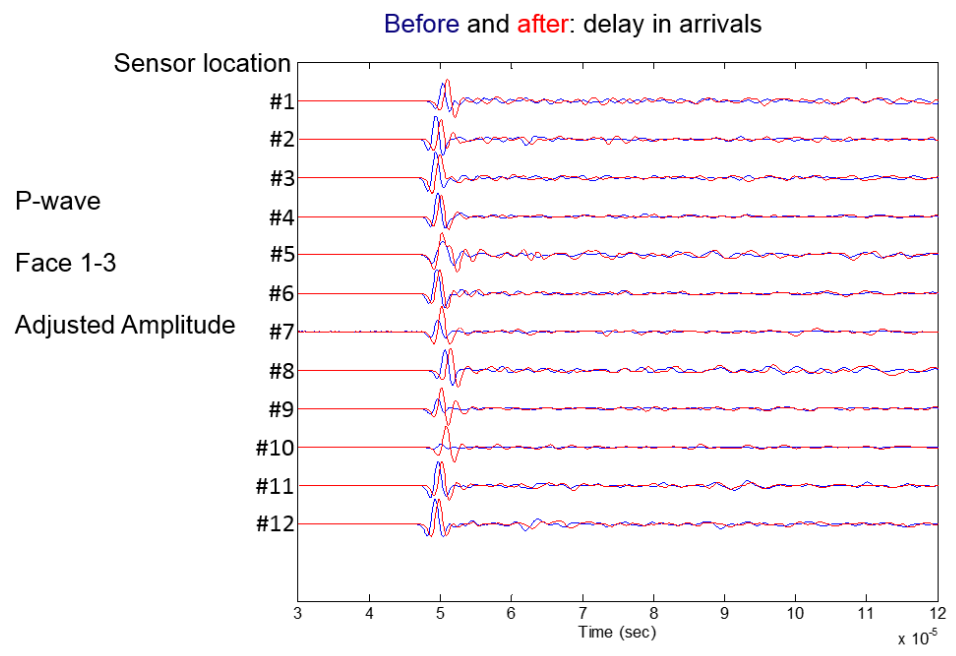
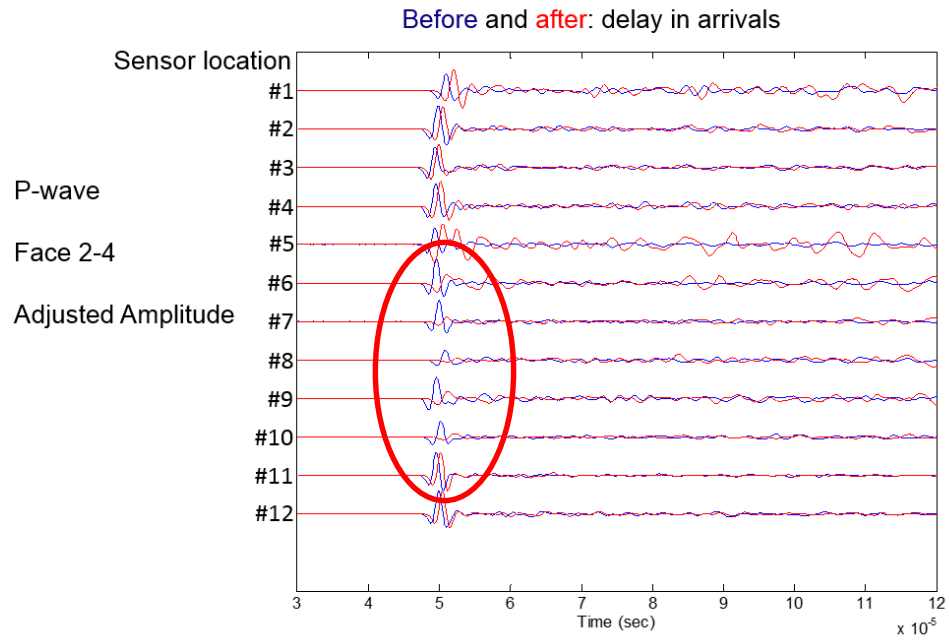


Figure 4.4.26 Locations of the acoustic measurements before and after the test. (a) The face number, and (b) the transducer locations on the sample Face 2.

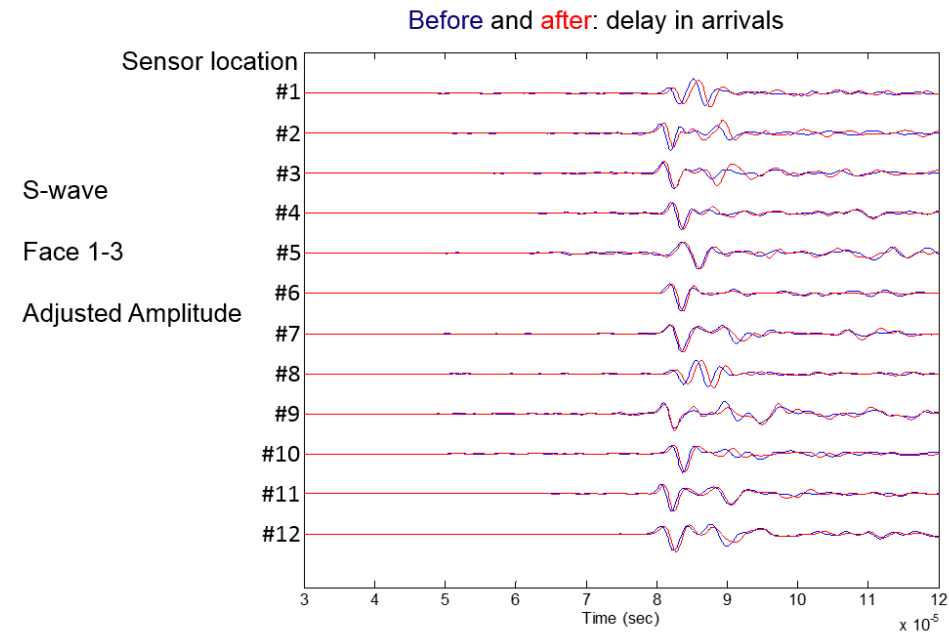
(a)



(b)



(c)



(d)

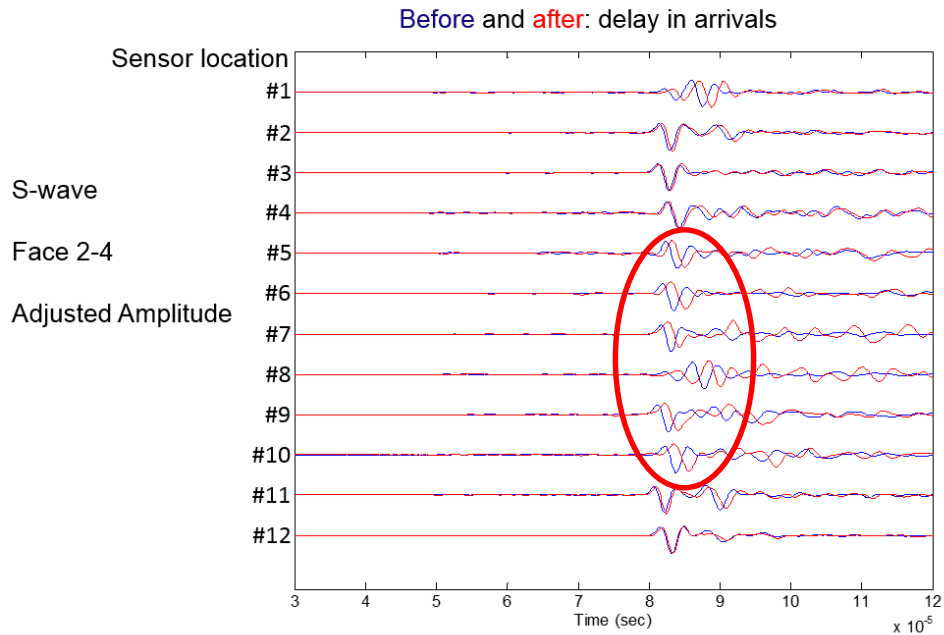
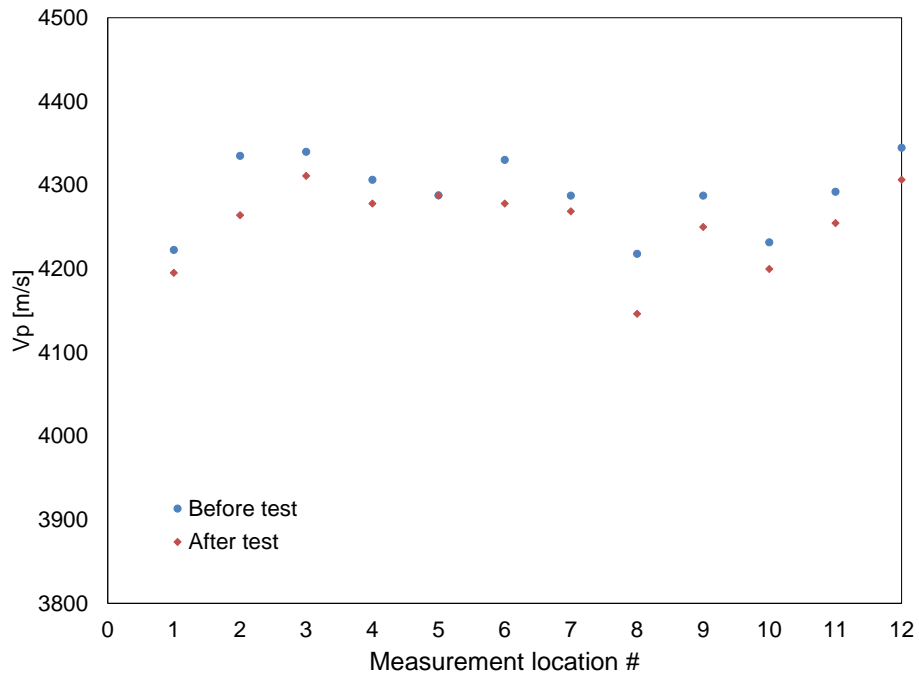


Figure 4.4.27 P- and S-wave arrivals before (blue) and after (red) the LN₂ test along Faces 1-3 and 2-4.

(a) Faces 1-3



(b) Faces 2-4

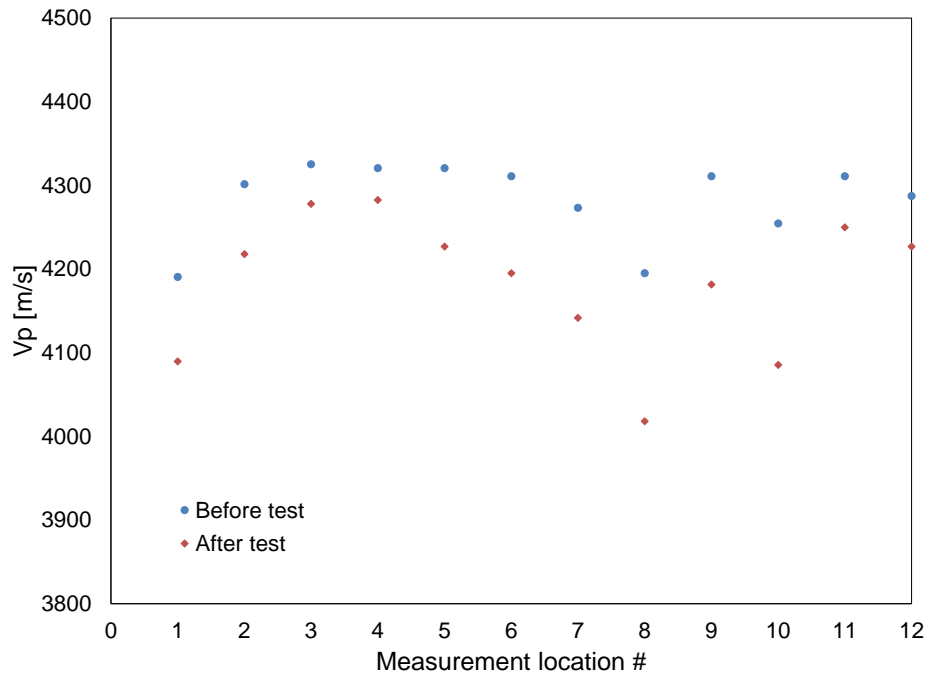


Figure 4.4.28 Changes in the P-wave velocities before and after the cryogenic test, (a) Faces 1-3, and (b) Faces 2-4.

Sample 20 was cured under water for seven weeks then left at ambient condition to dry for seven weeks. It was first treated with high pressure LN₂ for three cycles as shown in **Figure 4.4.29**. Then it was fractured by injecting GN₂ and the breakdown pressure profile is shown in **Figure 4.4.30**. Leaking sounds were heard when the pressure inside the wellbore reached about 700 psi and became louder as the wellbore pressure increased. The major fracture happened at 759 psi. **Figure 4.4.31** shows a picture of Sample 20 after fracturing by GN₂. Sample 20 was under triaxial stresses ($x = 500$ psi, $y = 750$ psi, and $z = 1000$ psi) during both the LN₂ treatment and gas fracturing test. The fracture opened in a half wing configuration along the minimum horizontal stress direction and another fracture wing along the maximum horizontal stress direction.

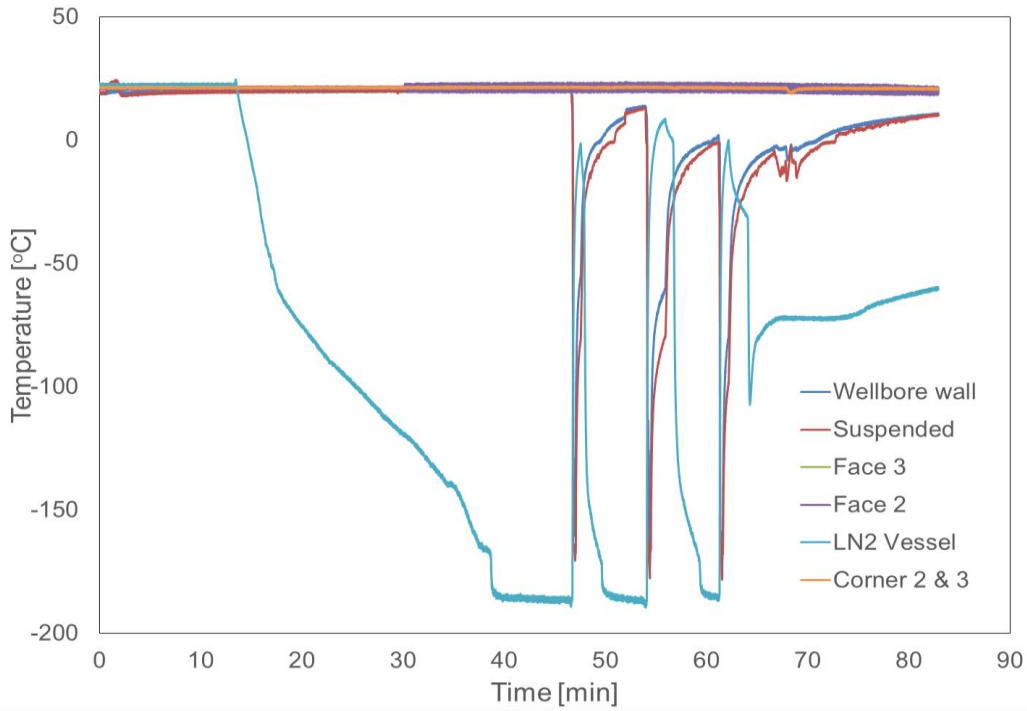


Figure 4.4.29 Temperature vs. time during three cycles of high pressure LN₂ treatment on Sample 20.

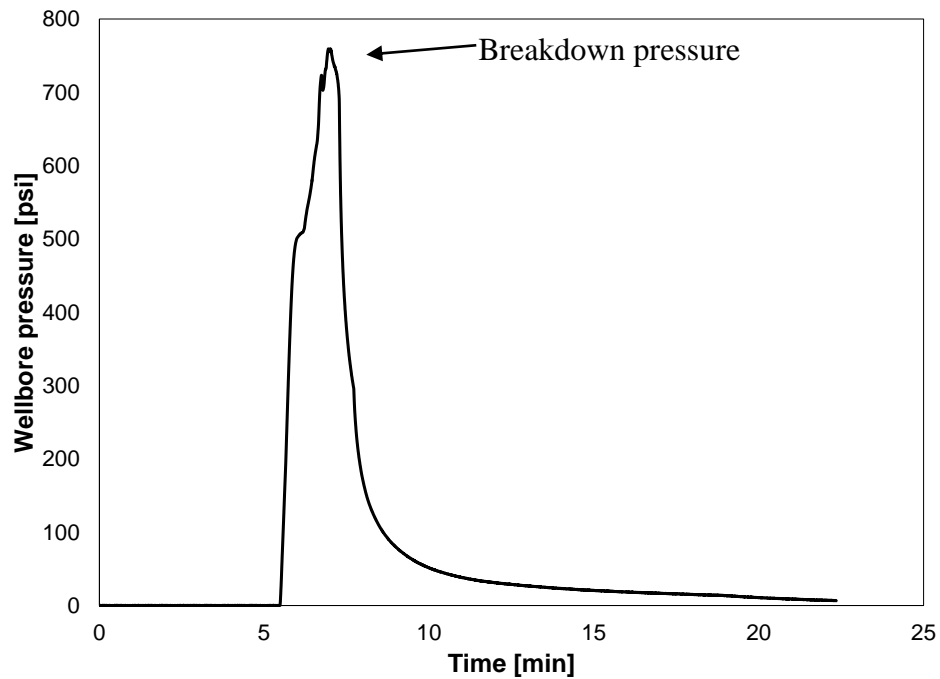


Figure 4.4.30 Breakdown pressure profile for Sample 20 under triaxial stresses and right after the LN₂ treatment. Leaking sounds were heard when the pressure inside the wellbore reached 700 psi and became louder as the wellbore pressure increased. The major fracture happened at 759 psi.

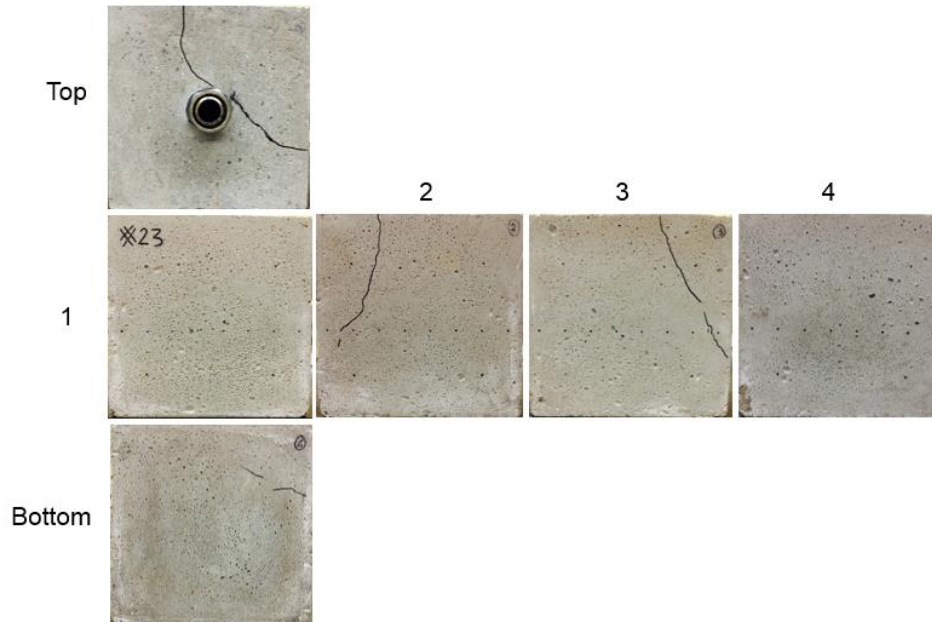


Figure 4.4.31 Picture for Sample 20 (not the number marked on sample) after being fractured by GN₂. The black lines follow the fractures.

Sample 22 was cured under water for four weeks then left at ambient conditions to dry for two months. It was treated with low pressure LN₂, which was flowed inside the wellbore at 15 psi for 28 minutes. Then GN₂ was injected into the wellbore. This time the triaxial stresses were increased to make the stress difference between the x- and y-axis more pronounced. **Figure 4.4.32** shows the temperature profiles from the start of injecting the LN₂ until the end of the test, the temperature at the borehole wall decreased fairly fast to the LN₂ temperature. This behavior was noticed for most of the confined tests. On one hand, it might be because when the sample is subjected under triaxial stresses, the circumference of the wellbore decreases, which may detach the thermocouples from the wellbore wall; on the other hand, LN₂ injection in these cases are more turbulent, mitigating the Leidenfrost effect on the borehole wall. Because the sample fractured earlier than planned, GN₂ fracturing attempts failed, during which loud sound indicated significant leaking. The sample might be fractured due to stress loading. **Figure 4.4.33** shows the attempts of GN₂ fracturing. **Figure 4.4.34** shows the picture of Sample 22 after the test.

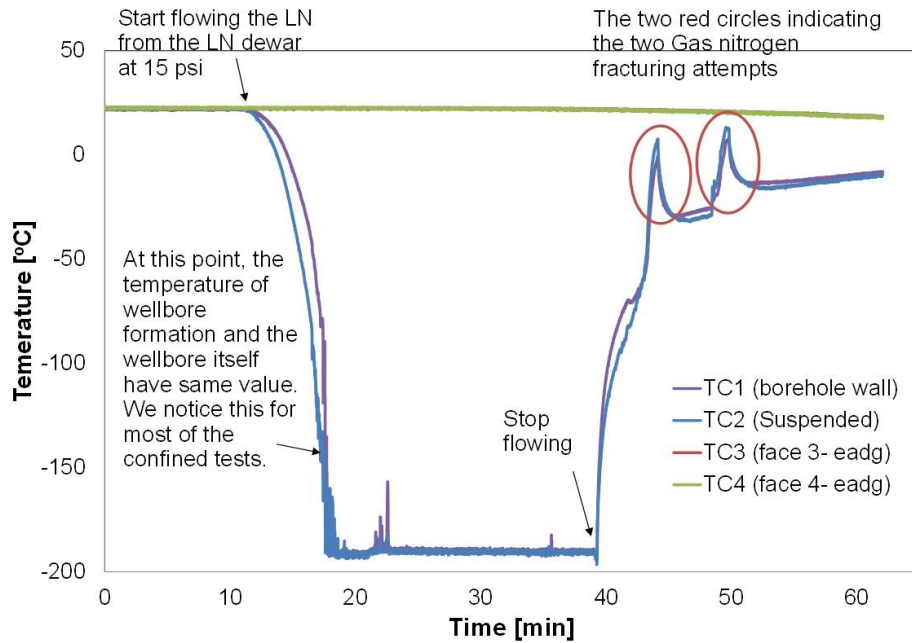


Figure 4.4.32 Temperature profiles from the start of injecting the LN₂ until the end of the test. GN₂ fracturing attempts failed (red circles) because the sample was already fractured due to stress loading.

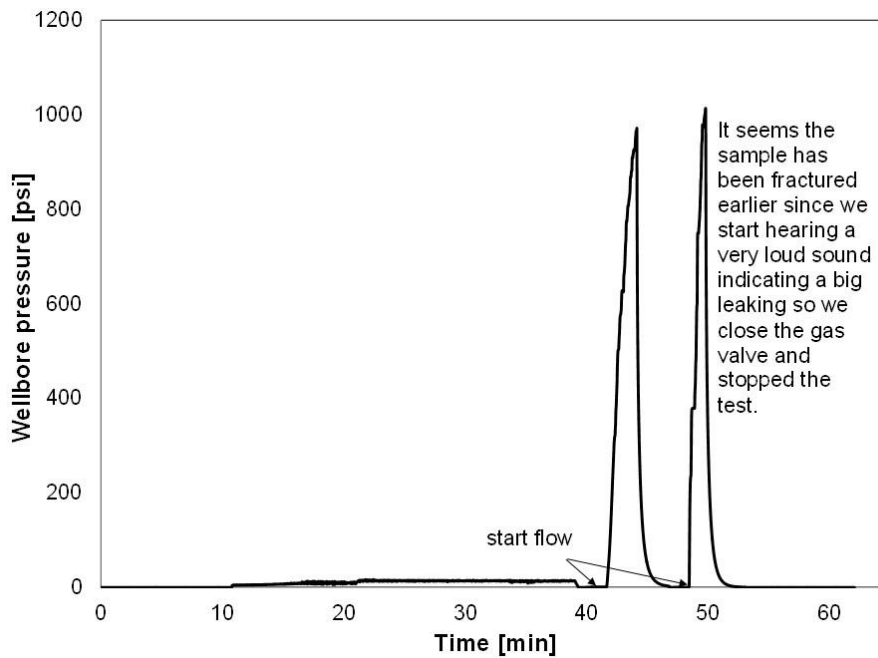


Figure 4.4.33 GN₂ fracturing attempts on Sample 22.

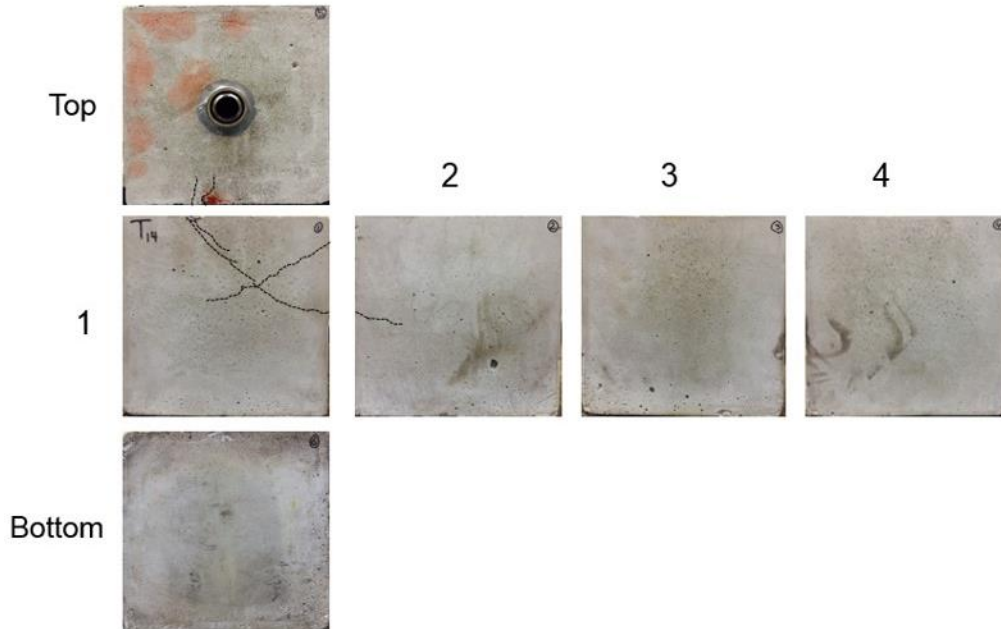


Figure 4.4.34 Picture of Sample 22 (not the number marked on sample) after the GN₂ fracturing attempts. The black dots follow the fractures.

Sample 23 was cured under water for six weeks then left at ambient conditions to dry for seven weeks. It was treated with high pressure LN₂ for four cycles, as shown in **Figure 4.4.35**. Sample 23 was fractured by injecting GN₂ after the LN₂ treatment. **Figure 4.4.36** shows the breakdown pressure profile. Leaking sounds were heard when the pressure inside the wellbore reached 550 psi and became louder as the wellbore pressure was increased, indicating progressive failure. The major fracture happened at 1094 psi. **Figure 4.4.37** shows a picture of the sample after the test. The main fracture was generated around the wellbore.

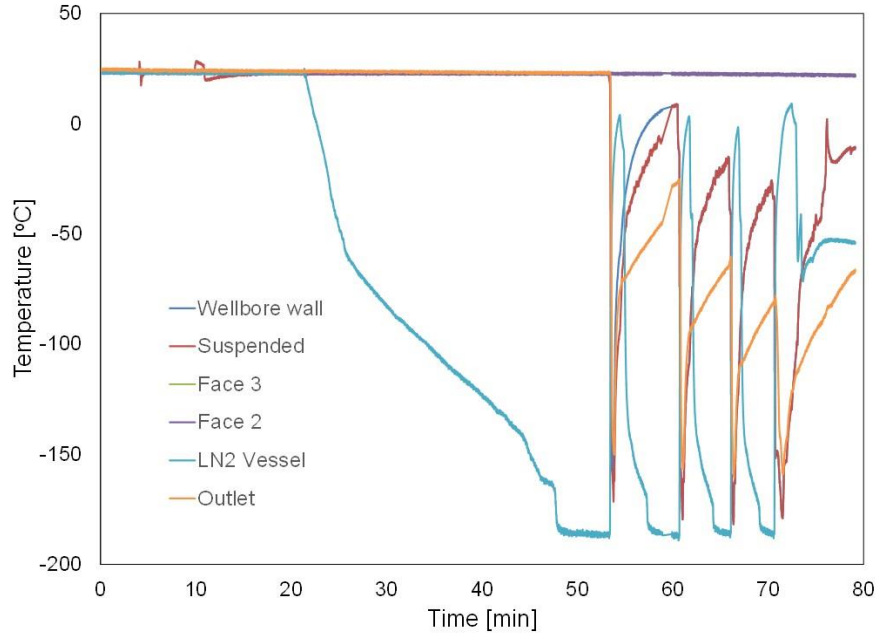


Figure 4.4.35 Temperature vs. time during the high pressure LN₂ treatment on Sample 23 with four LN₂ cycles.

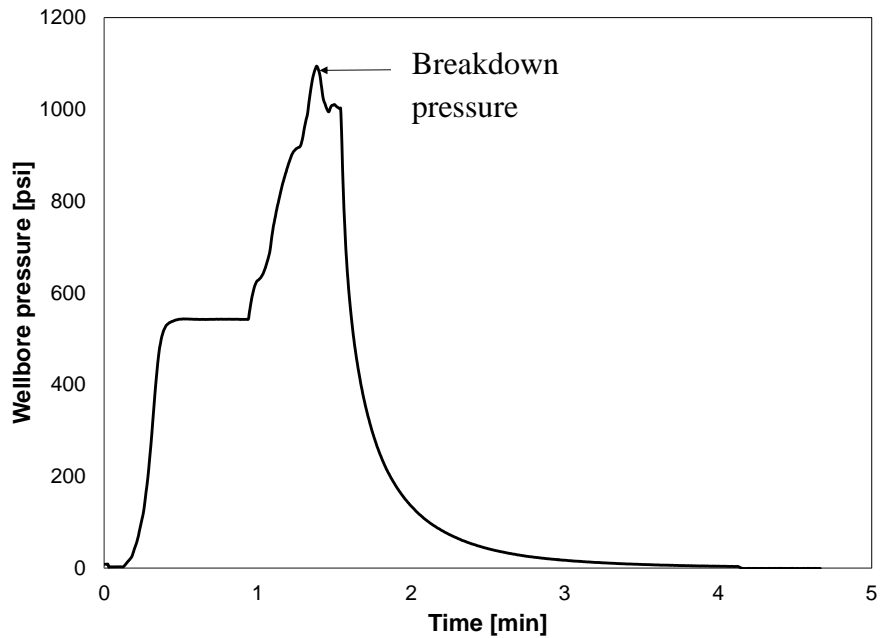


Figure 4.4.36 Breakdown pressure profile for Sample 23 by injecting GN₂ after an LN₂ treatment under triaxial stresses.

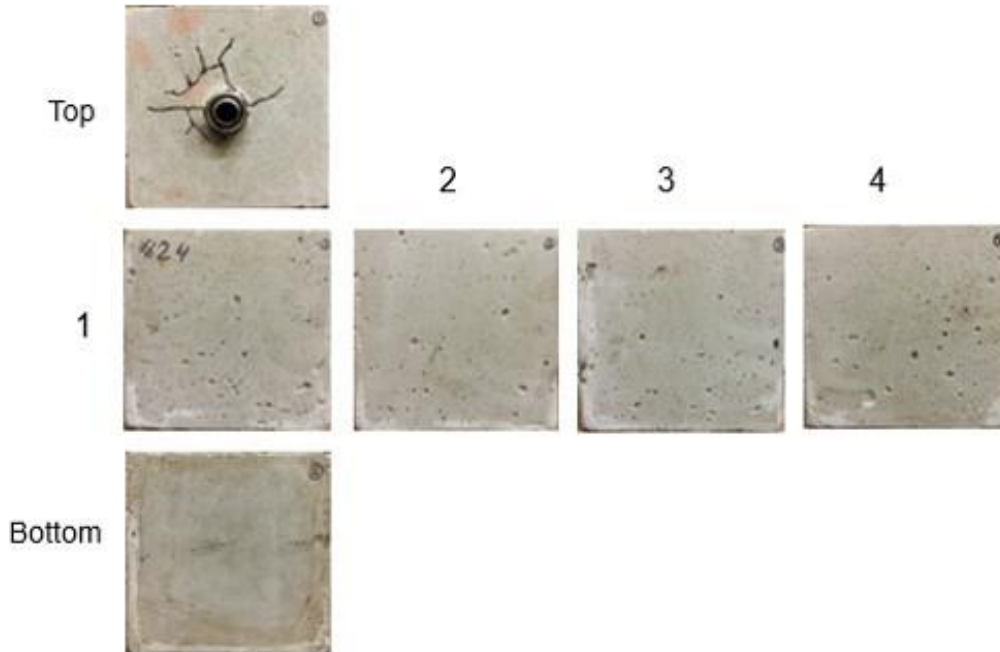


Figure 4.4.37 Picture of Sample 23 (not the number marked on sample) after fracturing by GN_2 . The black lines follow the fractures.

4.4.2.3 Breakdown Pressure Comparison

The breakdown pressure values of the intact and stimulated concrete samples under triaxial stress conditions are summarized in **Figure 4.4.38**. The data points in the yellow circle were acquired from experiments done with triaxial stresses of $x: y: z = 500: 750: 1000$ psi. Those in the black diamond were obtained from experiments with triaxial stresses of $x: y: z = 1000: 1500: 2000$ psi. It can be seen that as the triaxial stresses doubled, the breakdown pressure of the samples was elevated, which is reasonable. Since, the fracturing fluid must first overcome the confining stresses, then conquer the tensile strength of the concrete to split it. Also, for each triaxial stress loading condition, there is a negative correlation suggesting that LN_2 treatments weaken the rock strength, though one of the intact concrete samples deviates.

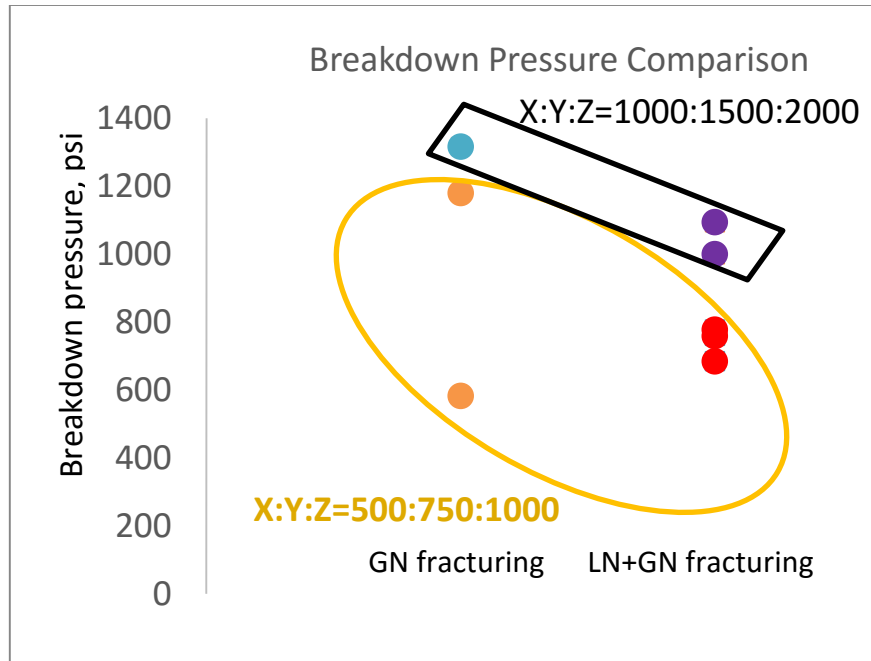


Figure 4.4.38 Breakdown pressure values of intact and stimulated concrete samples.

4.4.3 Sandstone Samples

Two sandstone samples, SS1 and SS2, were stimulated under triaxial stresses using GN₂ and LN₂, respectively.

4.4.3.1 GN₂ Fracturing (SS2)

Sample SS2 was directly fractured with GN₂. The intent with this sample was to find the breakdown pressure value and compare it with the breakdown pressure of Sample SS1 which was fractured under no loading ($\sigma_z = 60$ psi) with LN₂. **Figure 4.4.39** shows that the breakdown pressure for SS2 is 689 psi. This sample exhibited a higher breakdown pressure than Sample SS1 (described below). **Figure 4.4.40** shows pictures of SS2 before and after the gas fracturing.

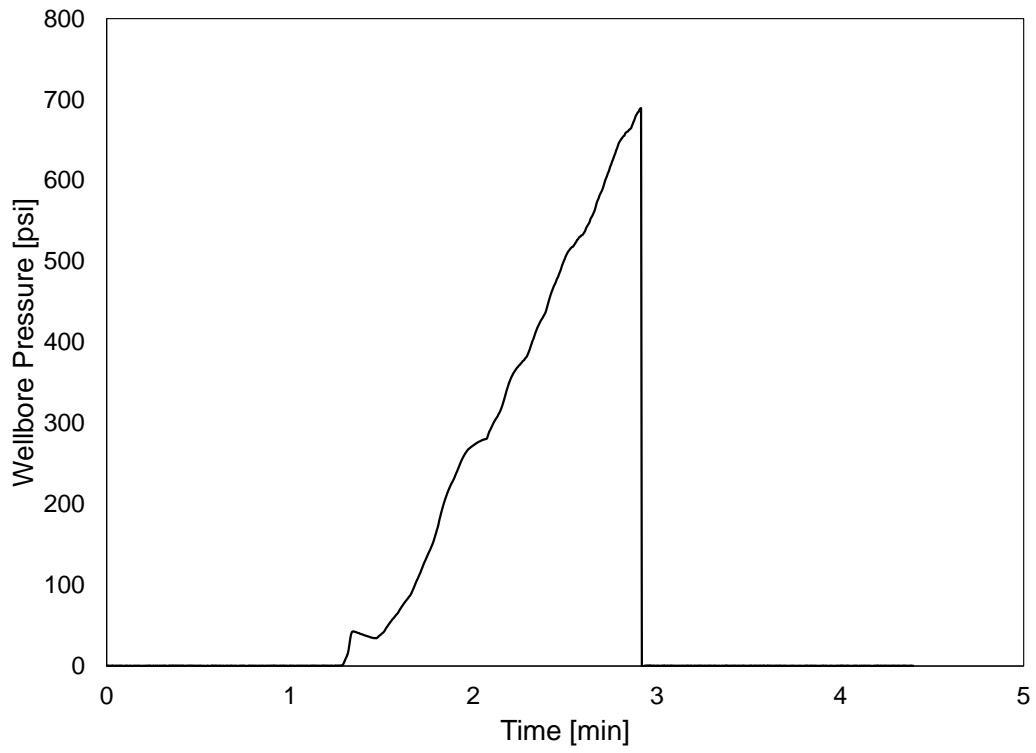
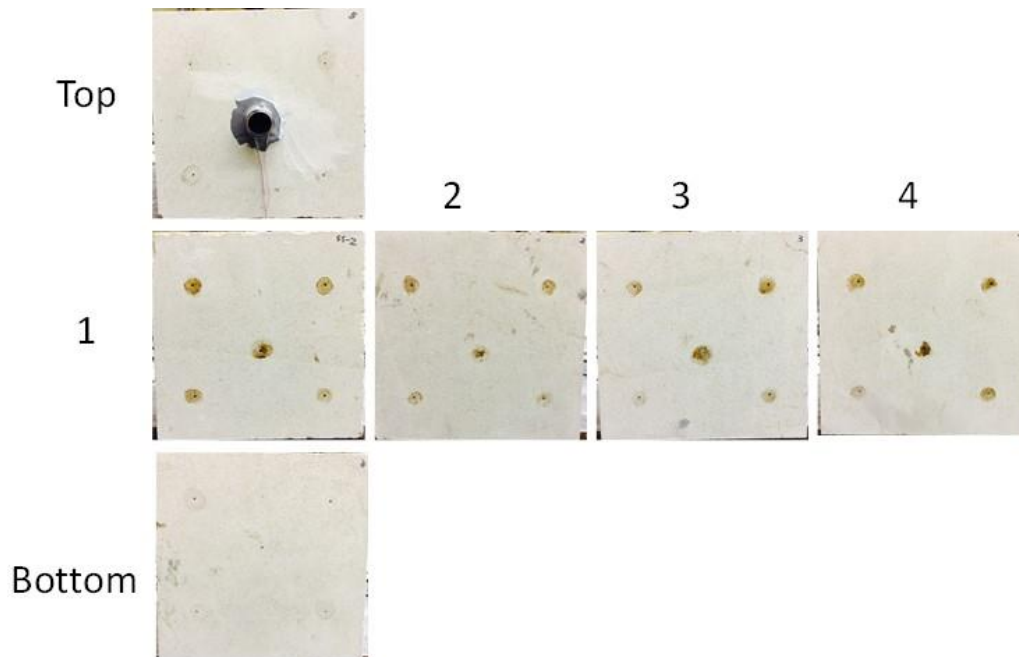


Figure 4.4.39 Breakdown pressure for Sample SS2 by injecting only GN₂.

(a)



(b)

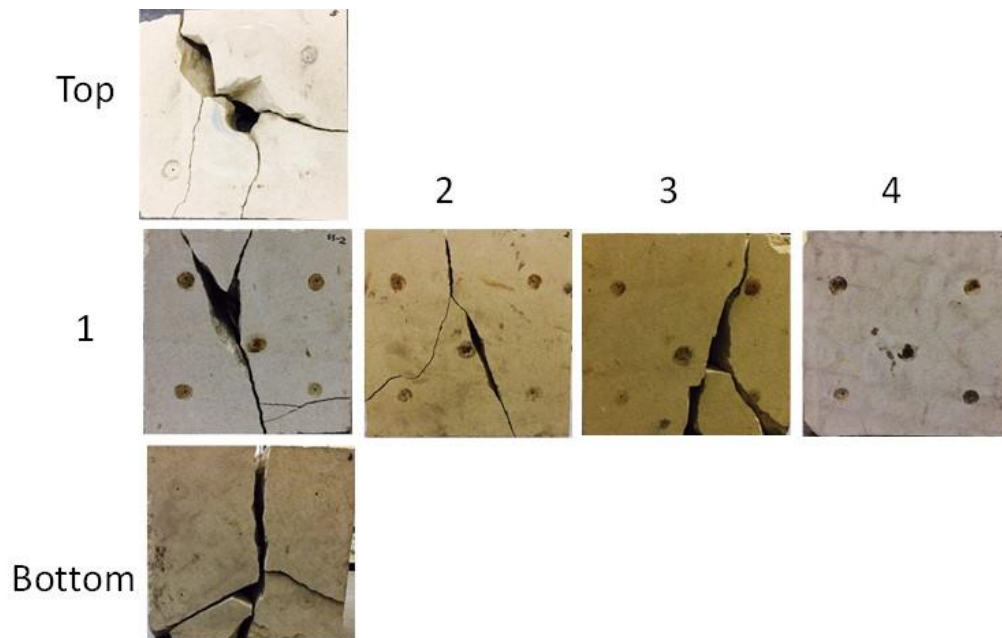


Figure 4.4.40 Sandstone Sample SS2 before (a) and after (b) the nitrogen gas fracturing. This block exhibited significant fracturing, as can be seen in (b) photos.

4.4.3.2 LN₂ Stimulation (SS1)

Sample SS1 was a dry sandstone at room temperature that was treated by LN₂. The procedures were as follows:

1. A pressure decay test was performed when 60 psi was applied to the top of the block ($\sigma_z = 60$ psi). However, we consider this step as a no stress condition;
2. A pressure decay test was performed under triaxial stress loading ($x = 1000$ psi, $y = 1500$ psi, and $z = 2000$ psi);
3. The 1st cycle of LN₂ injection was performed under high pressure (~450 psi);
4. Pressure decay test was performed after the 1st cycle and under triaxial stresses;
5. The 2nd cycle of LN₂ treatment was performed under high pressure (~450 psi);
6. Pressure decay test was performed after the 2nd cycle and under triaxial stresses;
7. The 3rd cycle of LN₂ treatment was applied under high pressure (~450 psi);
8. Pressure decay test was performed after the 3rd cycle and under triaxial stresses;
9. Pressure decay test was performed after the sample returned to the room temperature under triaxial stresses; and

10. Pressure decay test under no stress ($\sigma_z = 60$ psi) was performed to compare with the first pressure decay test.

Pressure decay test provides the rate of gas leak-off which is an indication of the gas permeability. The pressure decay test was performed by pressurizing the wellbore of the sample up to about 175 psi. After that the borehole was shut in, allowing the nitrogen gas in the wellbore to leak off.

Figure 4.4.41 shows the pressure decay tests from Steps 1 and 2 with different triaxial stress conditions. The permeability decreased when the sample was placed under stress loading. **Figure 4.4.42** shows the pressure decay tests for this sandstone sample before LN₂ treatment and after each LN₂ treatment cycle, all of them were conducted under triaxial stresses. It indicates that there is no difference in the pressure decay curves after each LN₂ treatment cycle. This could be because sandstone has a much higher permeability than the concrete and shale ($k_{\text{sandstone}} = 0.349$ mD, $k_{\text{concrete}} = 0.009$ mD, and $k_{\text{shale}} = 0.001$ mD) and also there were numerous natural fractures present in the sample.

Figure 4.4.43 shows the pressure decay tests with different temperature conditions while the sample was still under triaxial stress conditions. The permeability increased when the sample returned to the room temperature. At low temperature, the sandstone matrix was under thermal contraction and consequently, the pore sizes were reduced. Also, perhaps the natural fractures width was smaller until they relax and return to original room temperature. It appears there are no cryogenically generated fractures in Sample SS1. **Figure 4.4.44** shows the Step 10, which is the pressure decay test at the end of the experiment with no triaxial stress loading. During this step, the sample fractured at a very low pressure of 219 psi, so there was no way to acquire the pressure decay curve for this step. **Figure 4.4.45** shows the sandstone Sample SS1 before and after the fracturing. It seems that the created fractures follow the paths of the natural fractures.

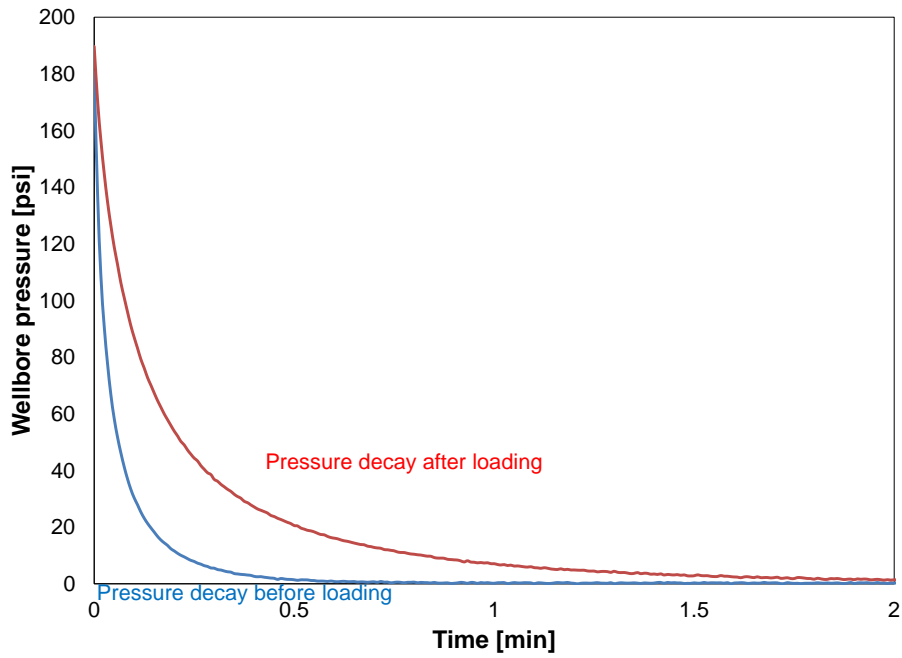


Figure 4.4.41 Pressure decay tests under different loading conditions for Sample SS1.

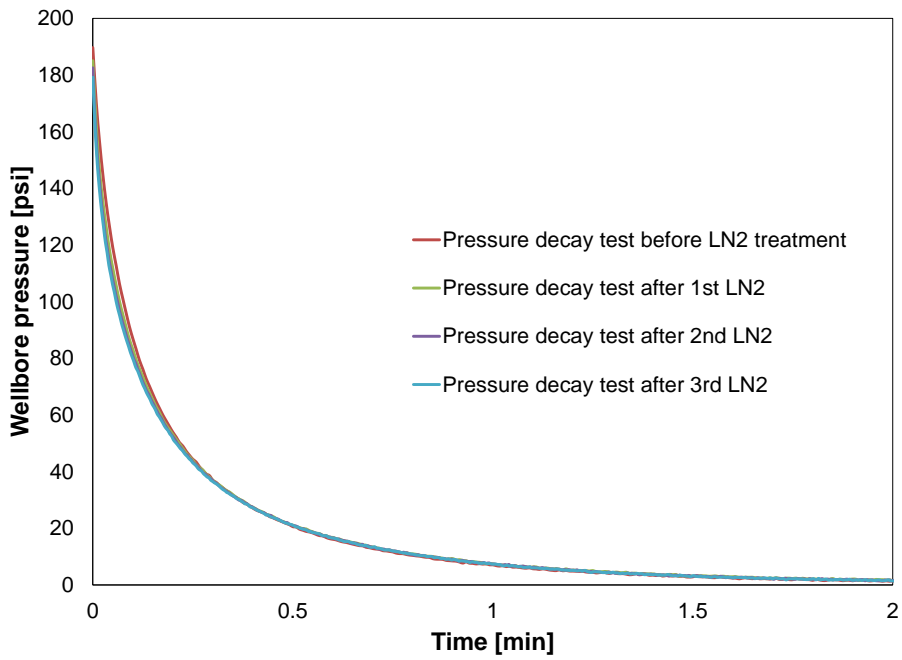


Figure 4.4.42 Pressure decay tests before LN₂ treatment on Sample SS1 and after each LN₂ treatment cycle. All tests were conducted under triaxial stress loading. There is no significant difference in the pressure decay curves after each treatment cycle.

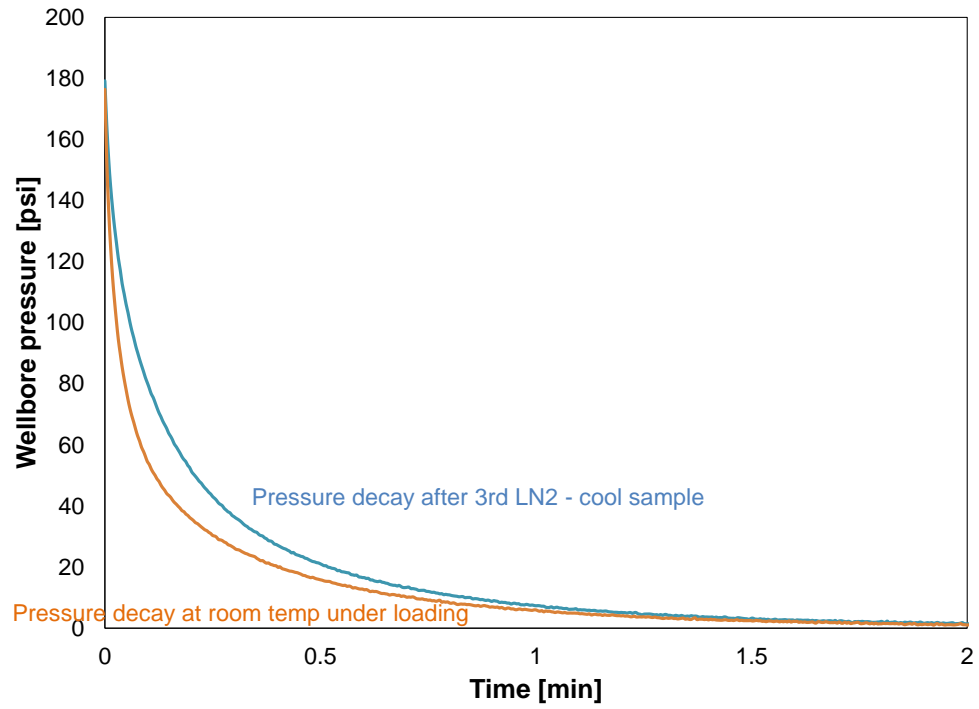


Figure 4.4.43 Pressure decay tests with different temperature conditions for Sample SS1.

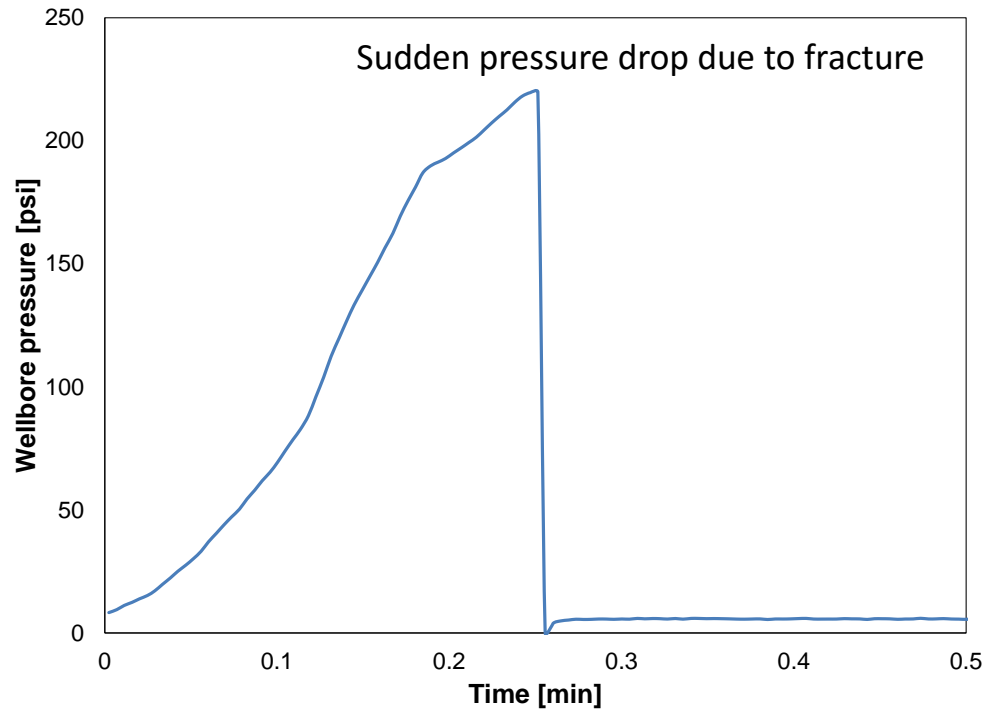


Figure 4.4.44 Pressure decay test at the end of the experiment on SS1. During this step, the sample fractured at a very low pressure of 219 psi.

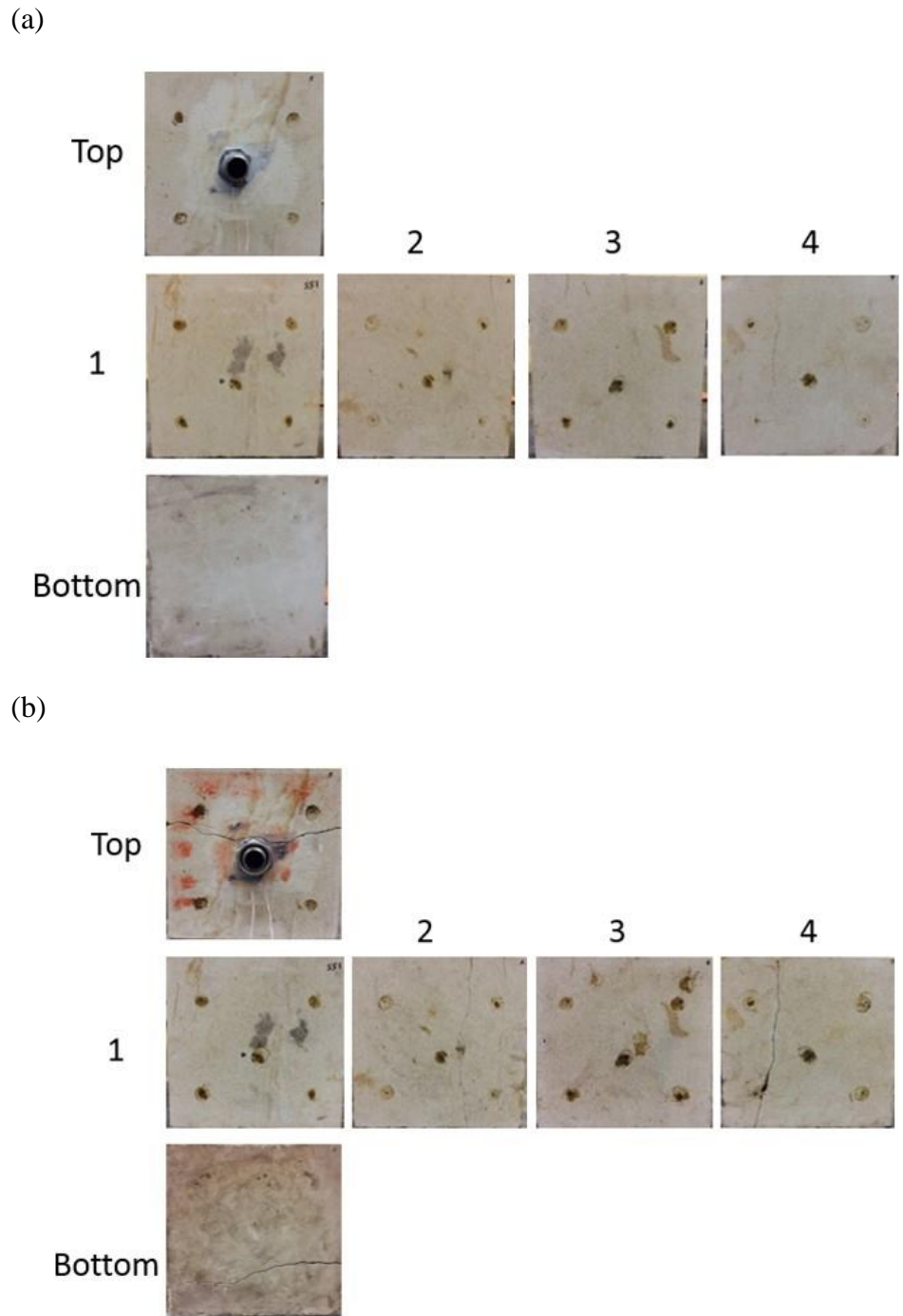


Figure 4.4.45 Sandstone Sample SS1 before (a) and after (b) the fracturing. It appears that the created fractures follow the natural fractures.

4.4.4 Shale Samples

Four shale samples (# 4, 1, 2, 3) were stimulated under different elevated triaxial stress conditions with different LN₂ treatment procedures, and one sample is directly fractured by GN₂ to measure the breakdown pressure for comparison. Shale sample availability was very limited, therefore, multiple tests were completed on each sample with different LN₂ treatment procedures. After each treatment procedure, any enhancements in the permeability were tested for comparison and any created fractures were observed and recorded.

4.4.4.1 GN₂ Fracturing (Sample 4)

Sample 4 was dry shale at room temperature and was fractured with GN₂. Triaxial stresses were applied as (x = 1000 psi, y = 1500 psi, and z = 2000 psi). The intent here was to find the breakdown pressure reference and compare it with the breakdown pressure of shale Sample 1, which was fractured by LN₂ under triaxial stress conditions in the next section. **Figure 4.4.46** shows the breakdown pressure for Sample 4 is 2439 psi. **Figure 4.4.47** shows the pictures of shale Sample 4 after GN₂ fracturing.

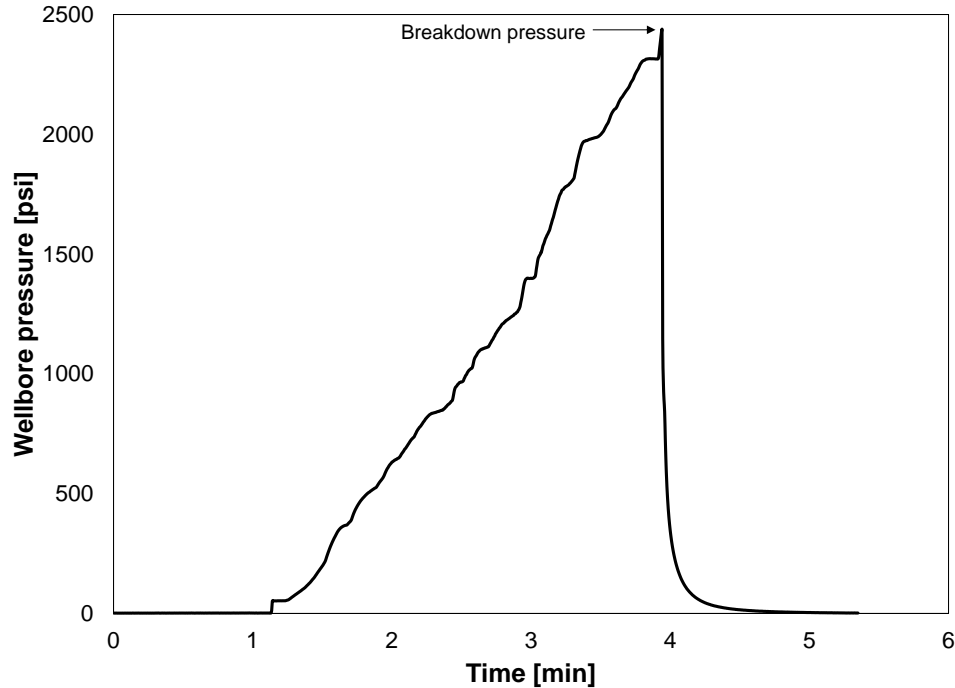


Figure 4.4.46 Breakdown pressure for Sample 4 using GN₂.

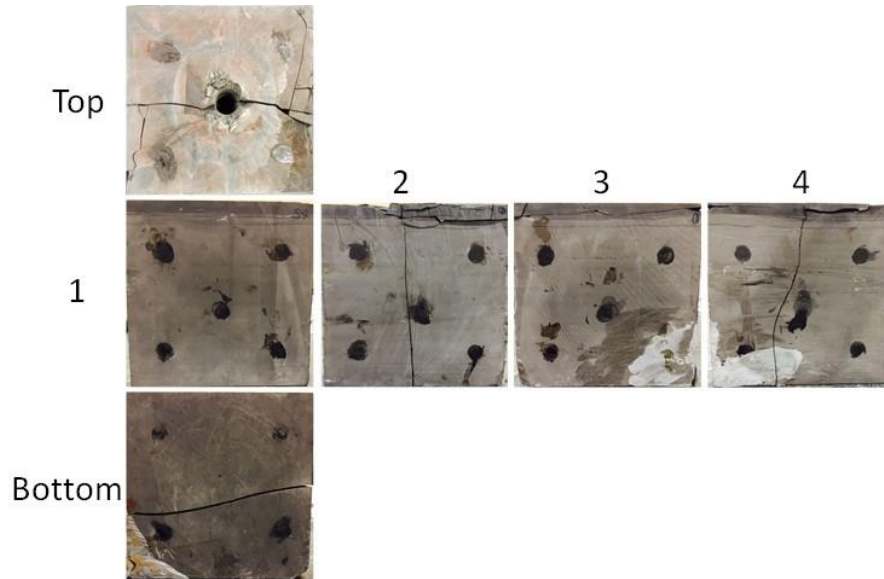


Figure 4.4.47 Shale Sample 4 after nitrogen gas fracturing.

4.4.4.2 LN₂ Stimulation and GN₂ Fracturing

Shale Samples 1 and 2 were first stimulated with multiple cycles of LN₂ under triaxial stress conditions, and finally fractured by GN₂. Sample 3 was fractured when we tried to conduct the high pressure LN₂ treatment, and broke down during the pressure decay test.

4.4.4.2.1 Sample 1

Sample 1 was dry shale at room temperature and was treated twice with LN₂. The first treatment was low pressure LN₂ treatment. Acoustic measurements and CT-scans were taken before conducting this test. The procedure for the low pressure LN₂ application was to start with a pressure decay test with no stress loading ($\sigma_z = 60$ psi) as shown in **Figure 4.4.48**. Then the triaxial stresses were applied gradually on the sample to these levels: $x = 1000$ psi, $y = 1500$ psi, and $z = 2000$ psi. Then the LN₂ was flowed into the wellbore under low pressure (~15 psi) (dewar pressure) for about 40 minutes. **Figure 4.4.49** shows the temperature changing with time during the LN₂ injection test. **Figure 4.4.50** shows the temperature versus time at early time. It can be observed that at early time, the temperature of borehole wall dropped quickly to the boiling point of LN₂. As mentioned before, this behavior might be due to the detachment of the thermocouples from the borehole wall. When the sample is subjected to the triaxial stresses, the circumference of the wellbore could change dimension,

causing the thermocouples to detach from the borehole wall as well as differential contraction of the thermocouple, adhesive, and rock. After flowing the LN₂, the stress loading was removed and the sample returned to stress-free conditions. A pressure decay test was conducted with no stress loading ($\sigma_z = 60$ psi) right after the test while the sample was still cold. Then, another pressure decay test was conducted one day later after the sample returned to room temperature to compare with the previous pressure decay tests. **Figure 4.4.51** shows the pressure decay tests before and after the LN₂ test. Pressure decay accelerated due to enhanced permeability.

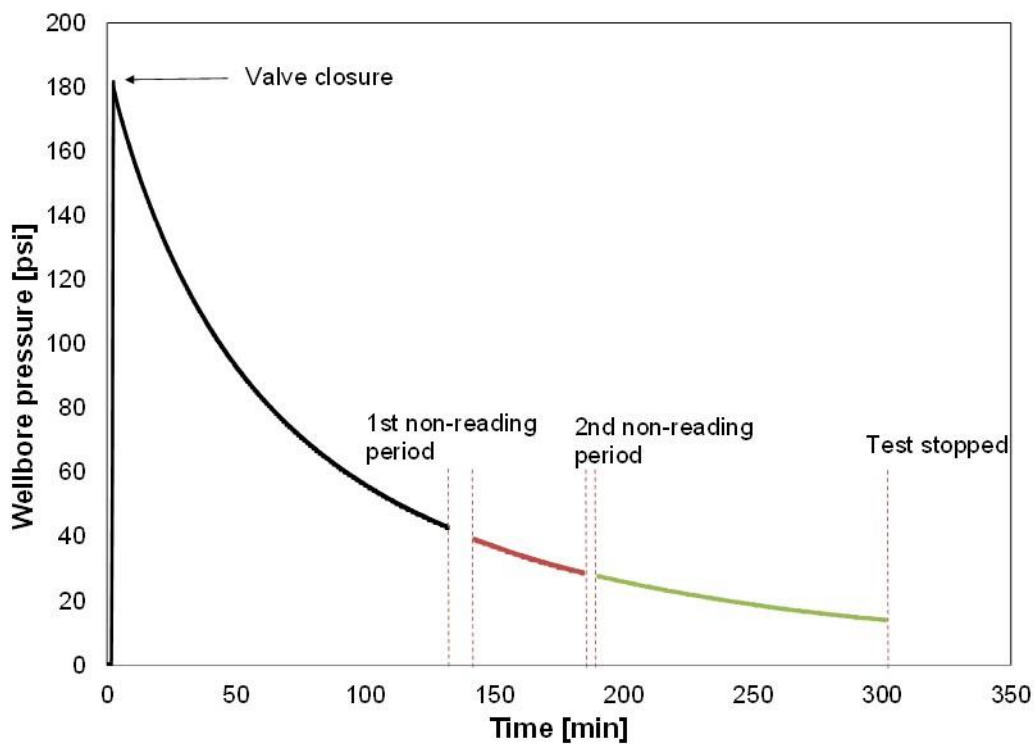


Figure 4.4.48 Pressure decay test for shale Sample 1 before the LN₂ test and with no stress loading ($\sigma_z = 60$ psi). It takes more time for the pressure to decay compared to concrete and sandstone samples.

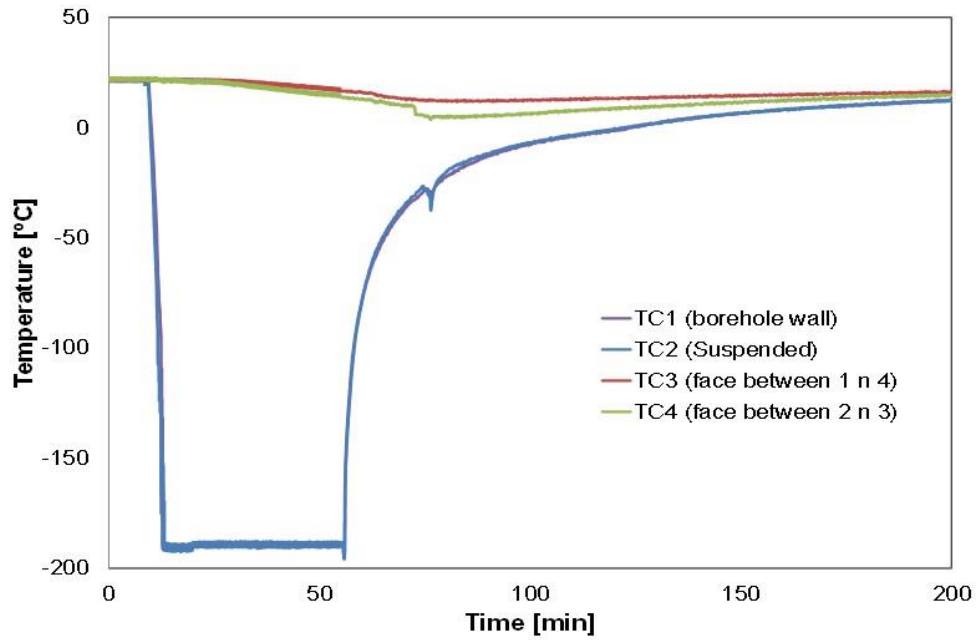


Figure 4.4.49 Temperature profiles for shale Sample 1 from the start of injecting the LN₂ until the end of the test.

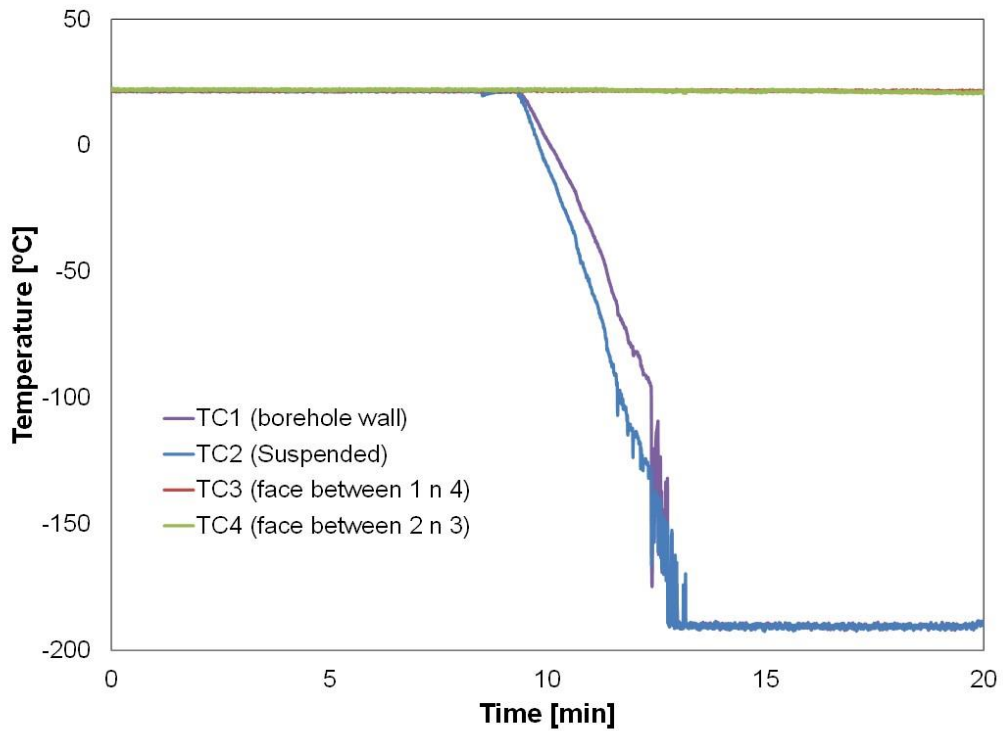


Figure 4.4.50 Temperature profile at early time of the shale Sample 1 tests giving a closer look at the temperature of the borehole wall.

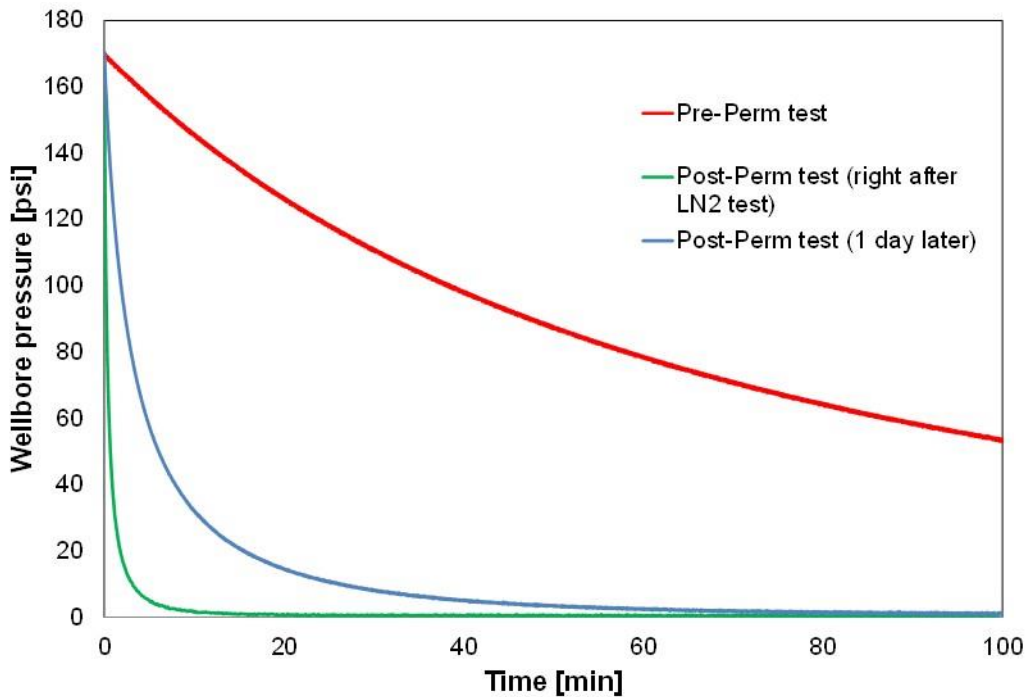


Figure 4.4.51 Pressure decay tests for shale Sample 1 before and after the LN₂ test.

Acoustic measurements were conducted before and after the LN₂ test for Sample 1 using P and S ultrasonic transducers. **Figure 4.4.52** shows the locations for the acoustic measurements before and after the test. The signals were measured across Faces 1 & 3 and 2 & 4. The interest here is in wave velocities and amplitudes. **Figure 4.4.53** shows P-wave arrivals before and after the LN₂ test for all side faces with the adjusted amplitude to compare changes in arrival time and wave forms. Location number 10 on Faces 1 and 3 (red circle - **Figure 4.4.53a**) has a delay in time arrivals indicating a new fracture created in the wave pathway.

Shale Sample 1 was also CT-scanned before and after the LN₂ treatment test. **Figure 4.4.54** shows the CT-scan images for the sample before the test. The CT-scan after the low pressure LN₂ test is identical to the scan before. The issue with CT-scanning is that the sample is very big and has a stainless steel casing that affects the quality of the picture. However, no fractures were seen in the surface of the sample or in the CT-scan images at this point of the test except a pre-existing fracture on the top surface of this shale block, as can be seen in **Figure 4.4.54a**.

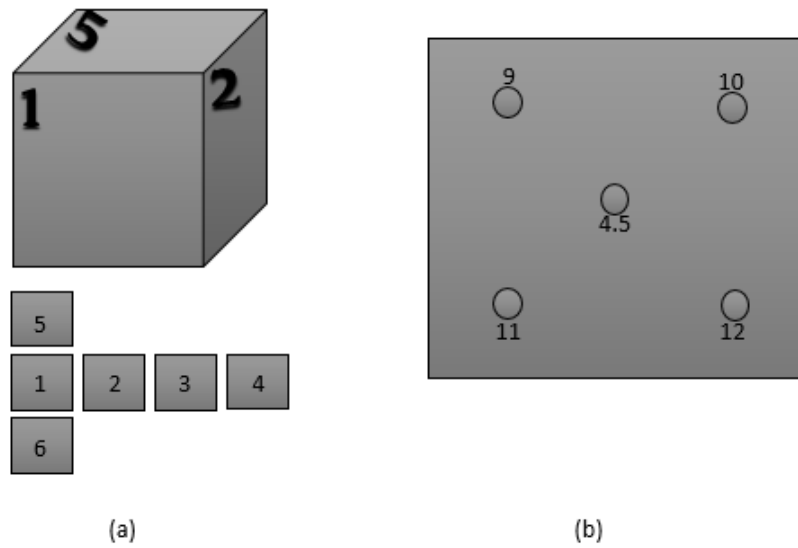
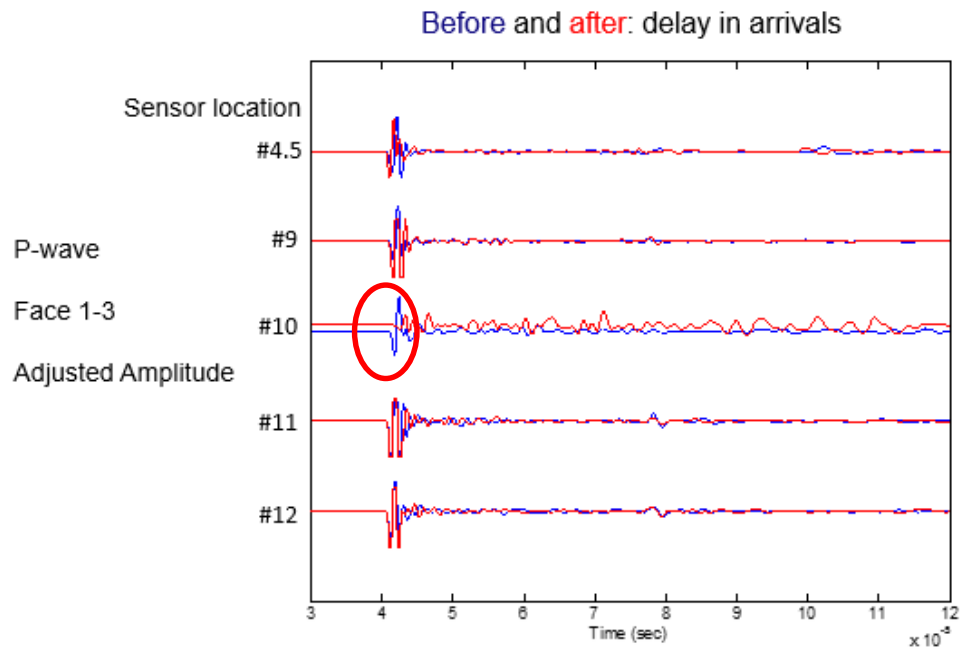


Figure 4.4.52 Locations of the acoustic measurements before and after the shale Sample 1 test. (a) The face numbers, and (b) the transducer locations numbered on the sample faces.

(a)



(b)

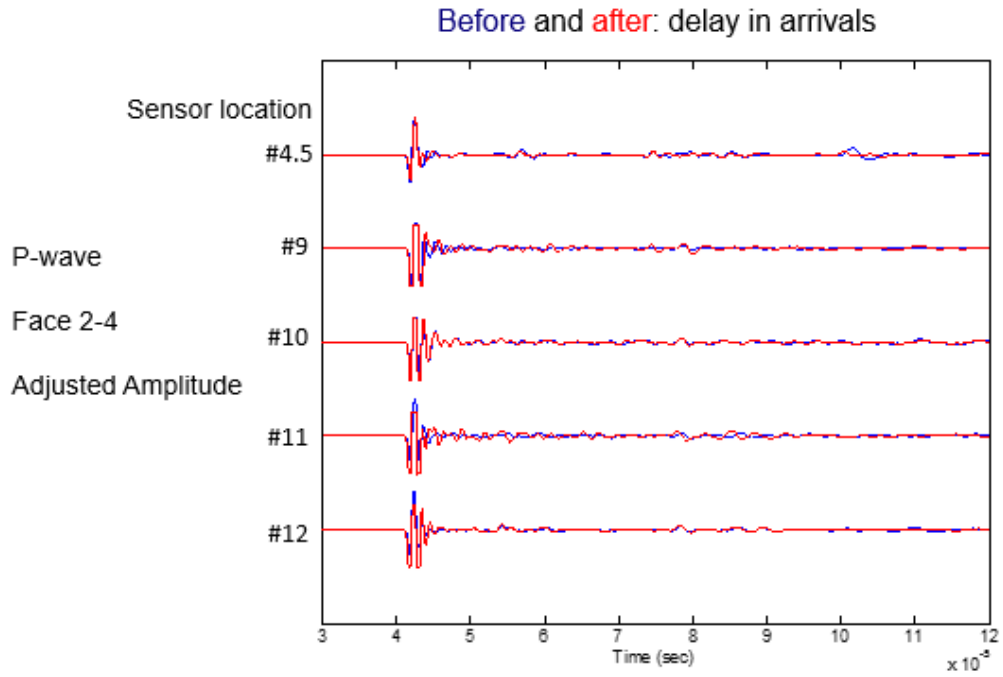
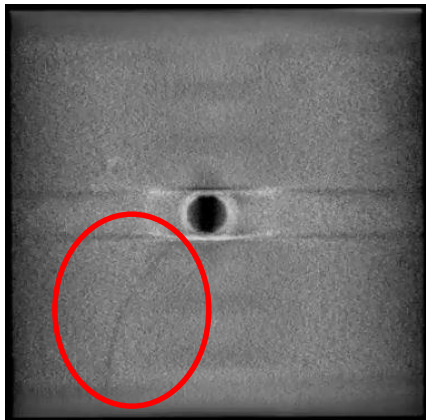
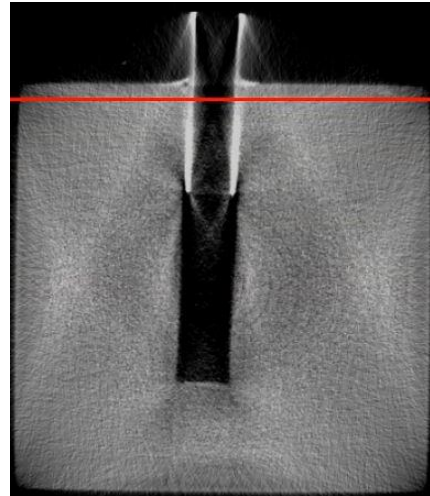


Figure 4.4.53 P-wave arrivals before (blue) and after (red) the LN₂ test for all side faces with the adjusted amplitude to compare changes in arrival time and wave forms. Faces 1 and 3 on top (a) and Faces 2 and 4 on bottom (b).



(a)



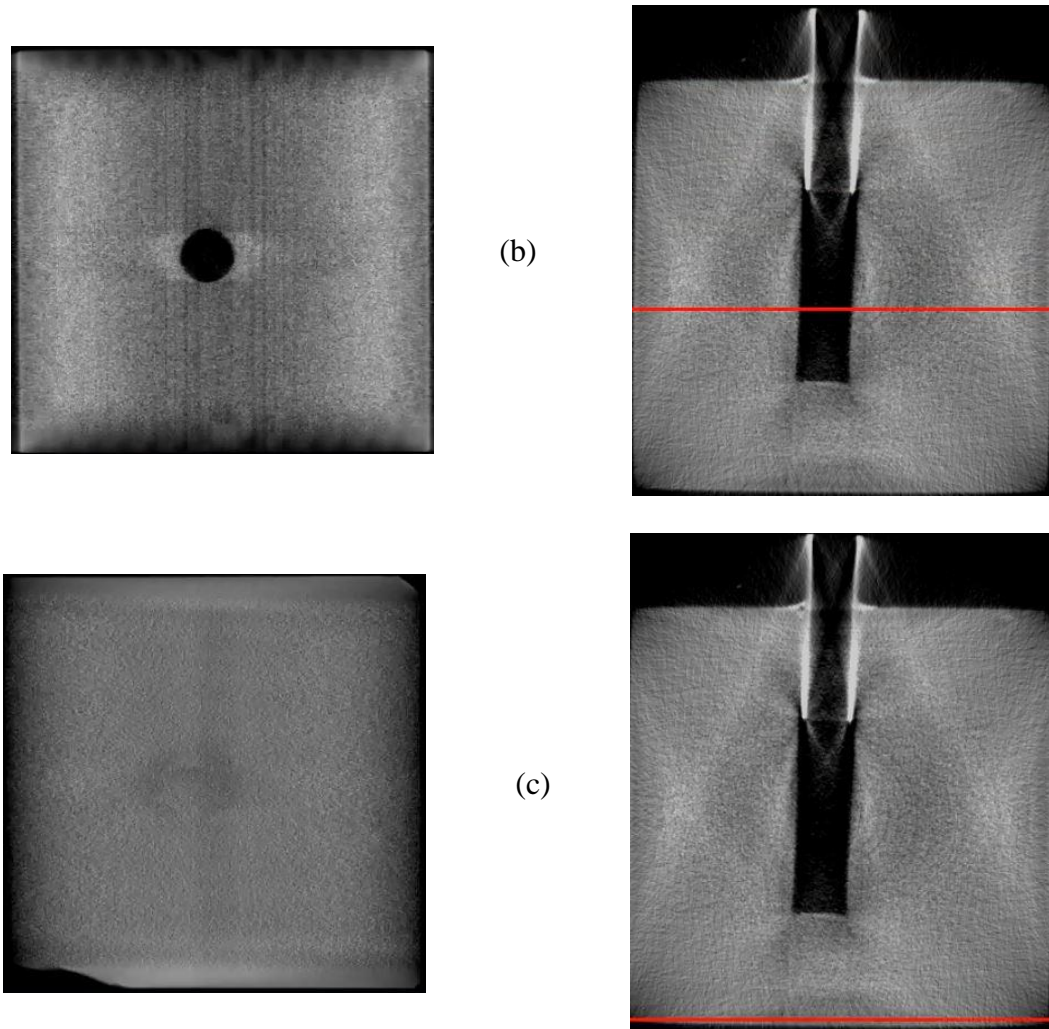


Figure 4.4.54 CT-scan images for shale Sample 1 before cryogenic treatment. The pictures on the right are the YZ-plane images and the pictures on the left are the XY-plane images. The red lines in the YZ-planes show the location of the XY-plane. The red circle shows the pre-existing fracture on the top surface of this shale block.

Shale Sample 1 was then stimulated with a high pressure LN₂ treatments. The procedures are listed as follows:

1. Pressure decay test under no stress loading ($\sigma_z = 60$ psi);
2. Pressure decay test with stress loading ($x = 1000$ psi, $y = 1500$ psi, $z = 2000$ psi);
3. The 1st cycle of LN₂ injection under high pressure (~450 psi);
4. Pressure decay test after the 1st cycle and under triaxial stresses;
5. The 2nd cycle of LN₂ treatment under high pressure (~450 psi);
6. Pressure decay test after the 2nd cycle and under triaxial stress loading;

7. The 3rd cycle of LN₂ treatment under high pressure (~450 psi);
8. Pressure decay test after the 3rd cycle and under stress loading;
9. Pressure decay test after the sample returned to room temperature and still under triaxial stress loading; and,
10. Pressure decay test under no stress loading ($\sigma_z = 60$ psi), to compare with the previous pressure decay tests.

Figure 4.4.55 shows the pressure decay tests with different triaxial stress conditions from test Steps 1 and 2. The permeability decreased when the sample was placed under triaxial stress loading. **Figure 4.4.56** displays the pressure decay tests for this shale sample before the LN₂ treatment and after each LN₂ treatment cycle, all of them were conducted under identical triaxial stress conditions. It is obvious that there is significant reduction in the pressure decay time after each treatment cycle, indicating permeability enhancements from the cryogenic treatments. **Figure 4.4.57** shows the pressure decay tests with different temperature conditions (Steps 8 and 9) while the sample was still under triaxial stress loading. The permeability decreased when the sample returned to room temperature, a different behavior from that of the **sandstone Sample SS1**. While under low temperature, it might be that the shale sample is under thermal contraction and fractures remain open around the wellbore. As the sample warms up, the sample relaxes and fractures close. This phenomenon was also observed in previously presented glass samples. **Figure 4.4.58** shows Step 10, which is the pressure decay test at the end of the experiment with no stress loading ($\sigma_z = 60$ psi). The acoustic measurements and CT scan did not show any significant changes before and after the high pressure LN₂ test. After two different LN₂ treatment procedures, shale Sample 1 was fractured by injecting GN₂ under triaxial stress loading. The sample was then CT scanned after the GN₂ fracturing test. **Figure 4.4.59** shows the breakdown pressure for Shale Sample 1 is 1394 psi. **Figure 4.4.60** shows the CT scan images after the GN₂ fracturing. **Figure 4.4.61** shows pictures of the shale Sample 1 before and after the LN₂ and GN₂ treatments.

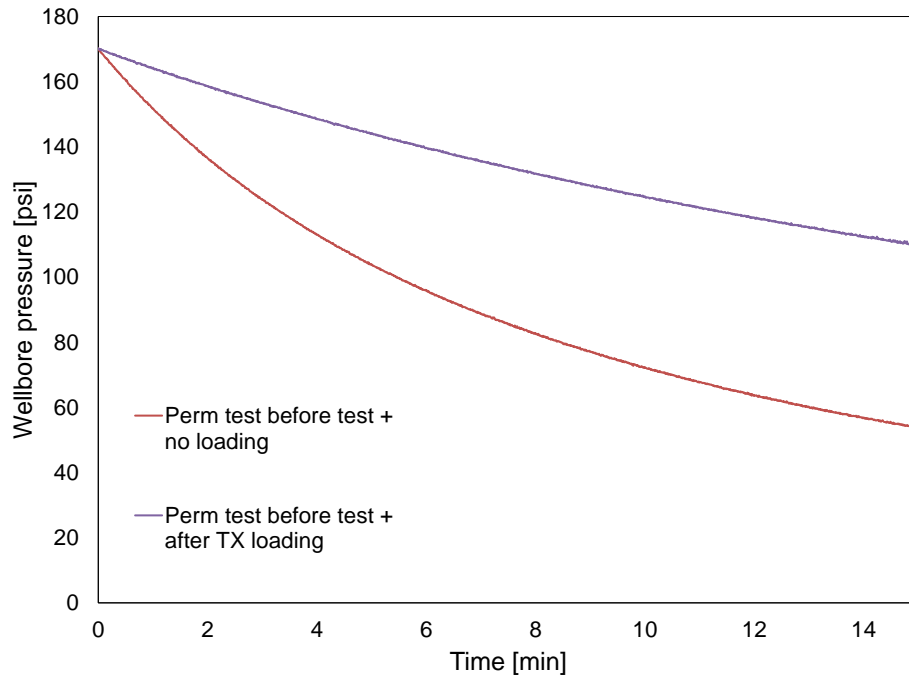


Figure 4.4.55 Pressure decay tests under different stress conditions for shale Sample 1.

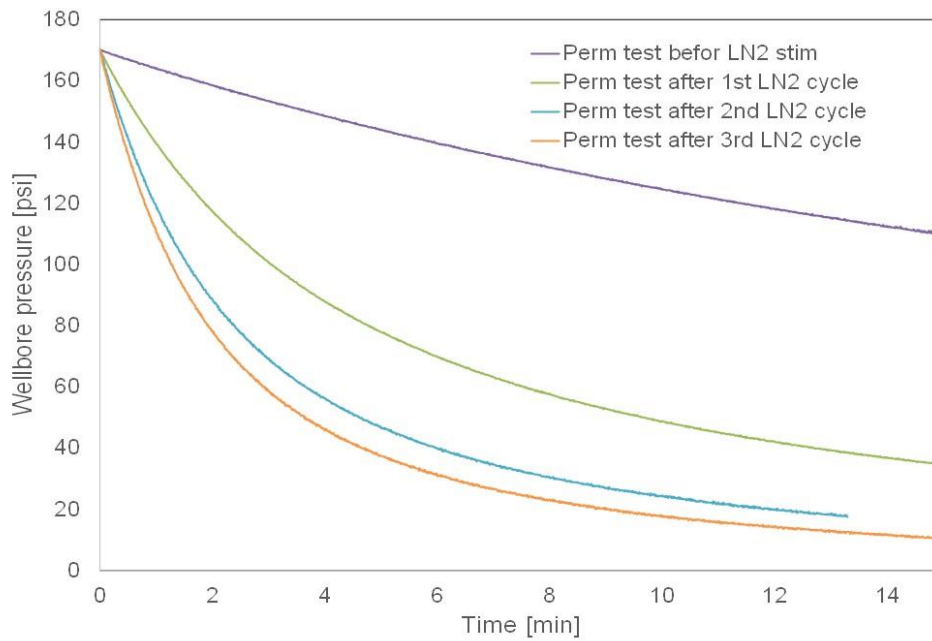


Figure 4.4.56 Pressure decay tests before LN₂ treatment and after each LN₂ treatment cycle for shale Sample 1, all of them conducted under triaxial stress loading. Significant differences in the pressure decay curves after each treatment cycle indicate permeability enhancements.

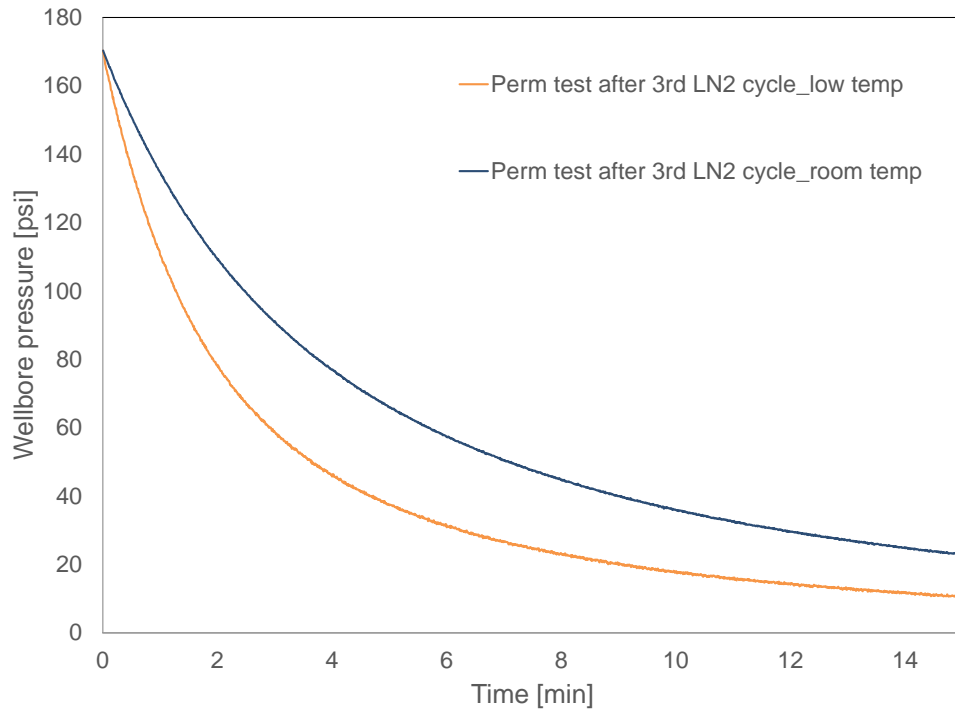


Figure 4.4.57 Pressure decay tests with different temperature conditions for shale Sample 1.

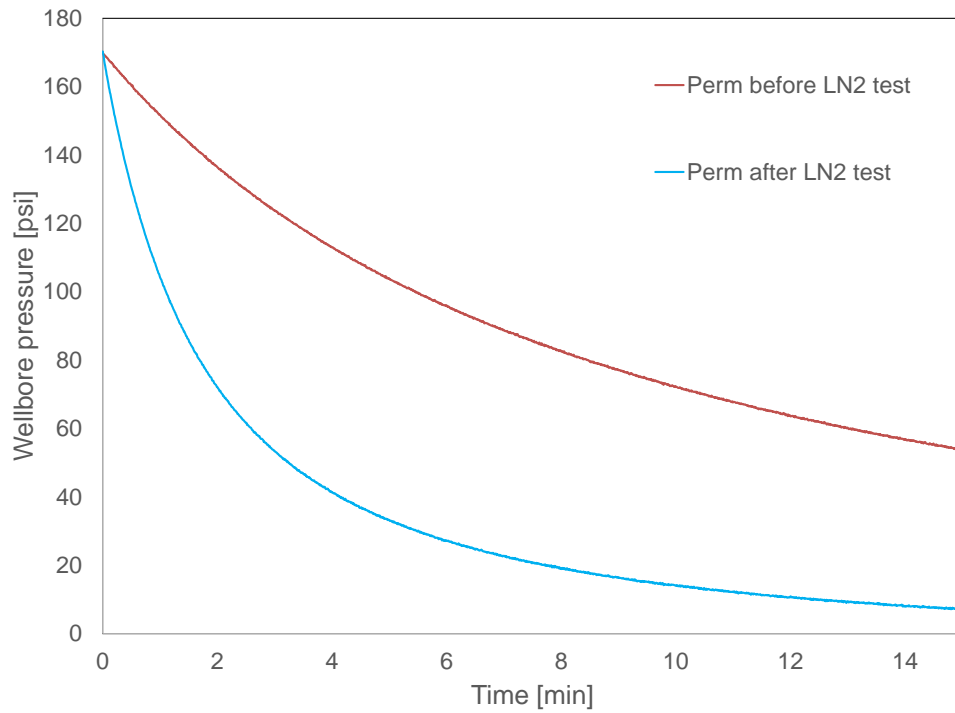


Figure 4.4.58 Pressure decay tests before and after the LN₂ test for shale Sample 1.

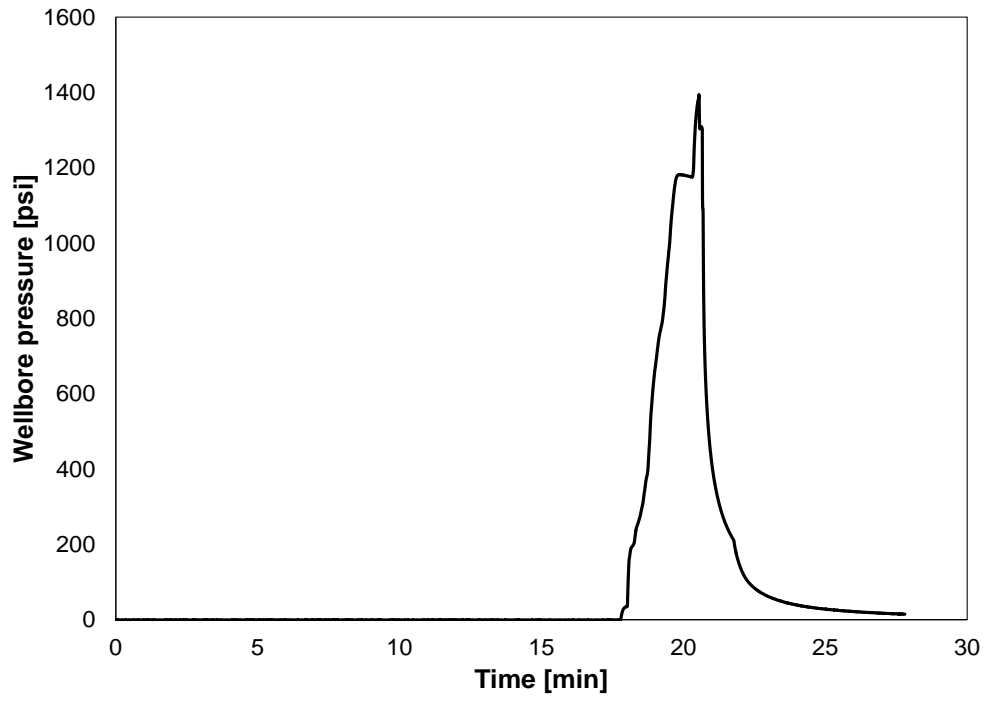
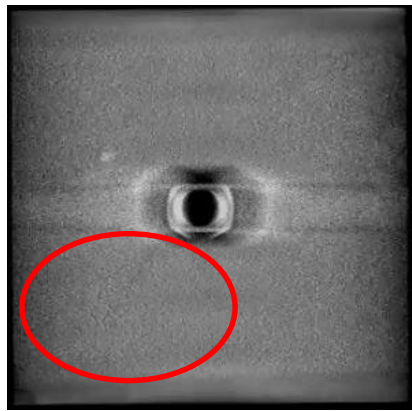
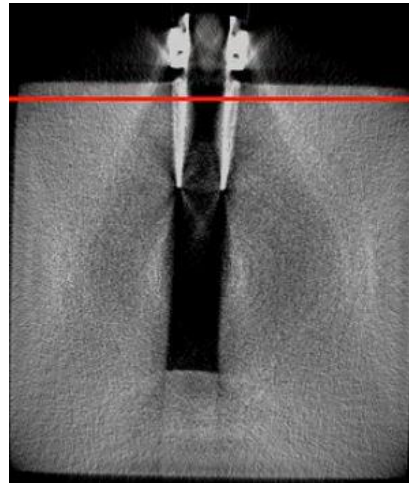


Figure 4.4.59 Breakdown pressure for shale Sample 1 using GN₂.



(a)



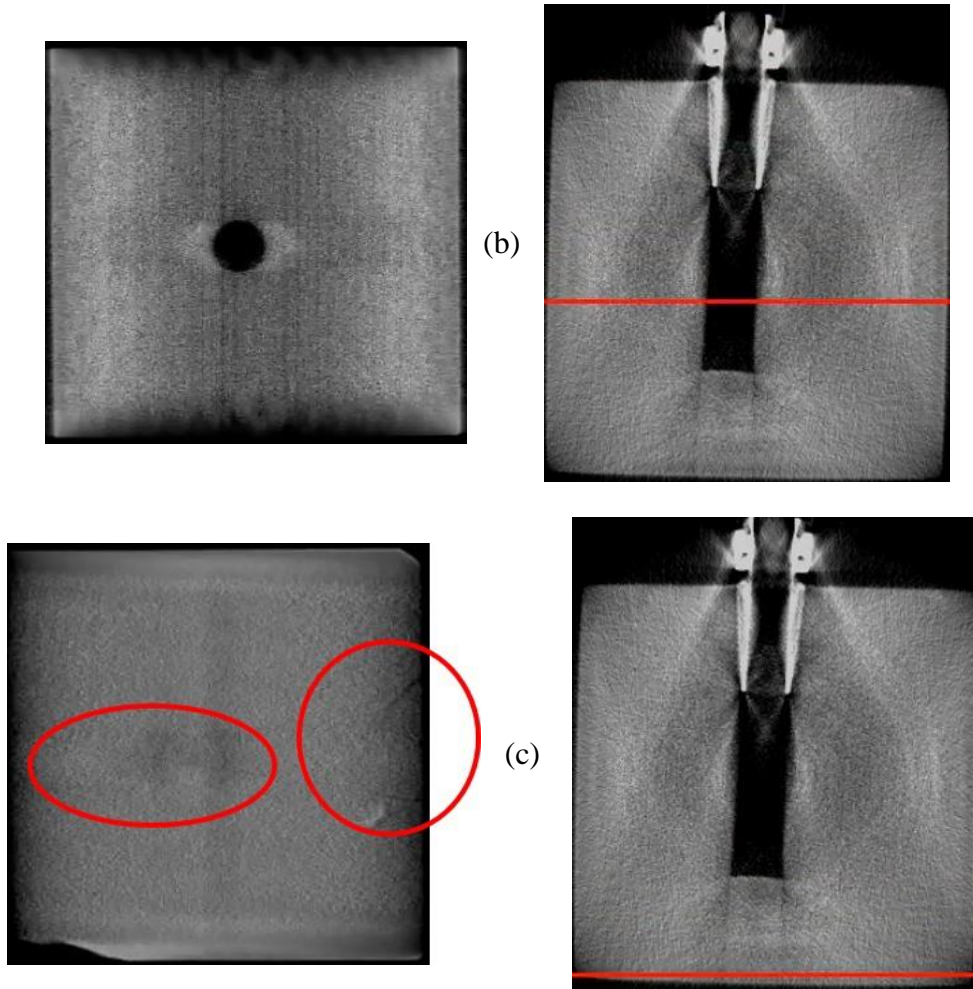


Figure 4.4.60 CT-scan images for shale Sample 1 after GN_2 fracturing. The pictures on the left are the XY-plane images and the pictures on the right are the YZ-plane images. The red lines in the YZ-planes show the location of the XY-plane. The red circle in XY-plane (a) shows the pre-existing fracture on the top surface of this shale block. The two red circles in XY-plane (c) show the created fractures at the bottom of the block.

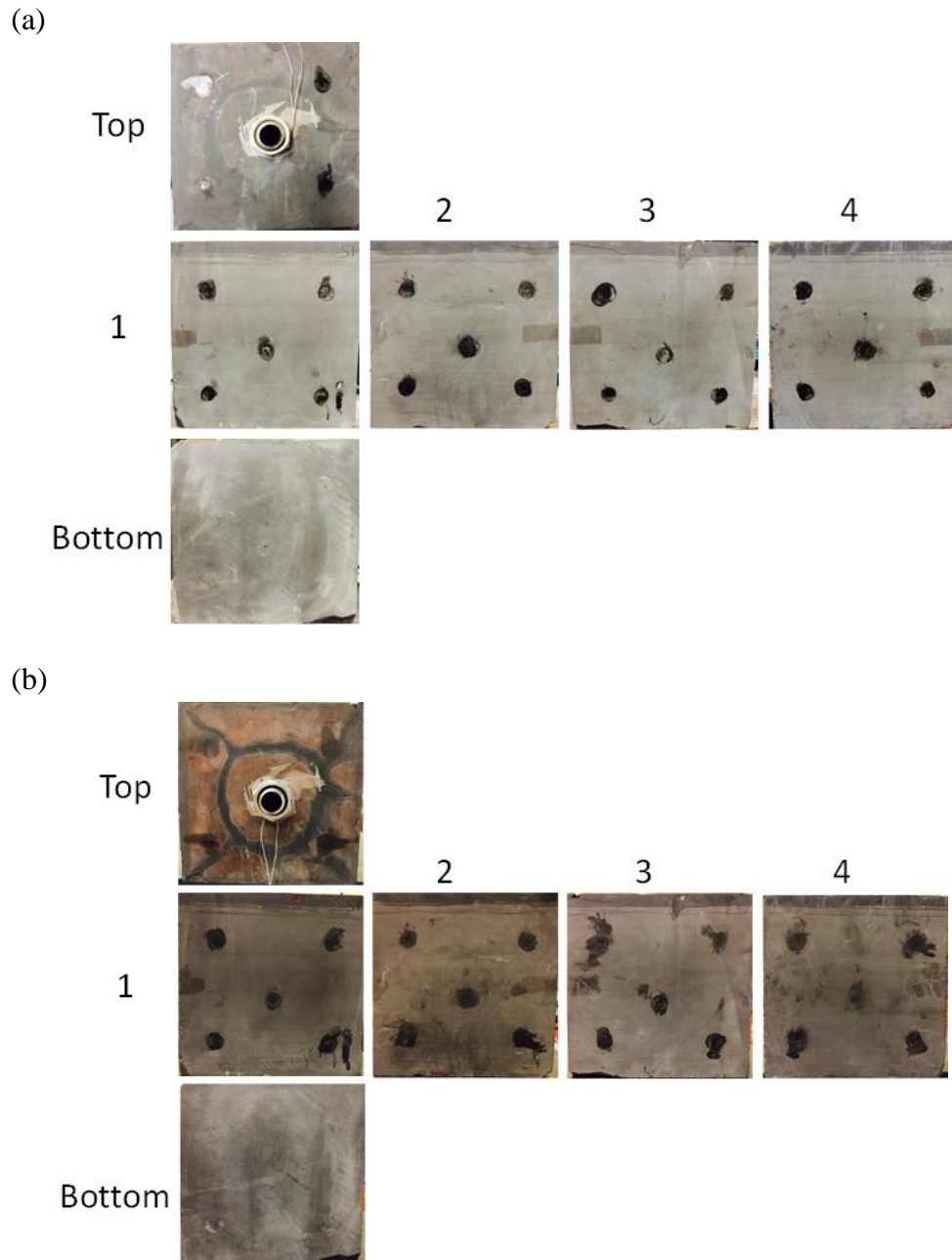


Figure 4.4.61 Shale Sample 1 before (a) and after (b) LN₂ and GN₂ fracturing. The color change of the sample before and after the treatment is a result of illumination difference.

4.4.4.2.2 Sample 2

Sample 2 was a dry shale that was treated three times by high pressure LN₂ at the room temperature. The reason for doing three cycles was that the drop in the pressure decay curves was small, so more LN₂ cycles were needed to achieve fast dropping pressure decay curves.

Triaxial stresses applied were $x = 1000$ psi, $y = 3000$, and $z = 4000$ psi. For both treatments, the high pressure LN₂ test procedure was as follows:

1. Pressure decay test under no stress loading ($\sigma_z = 60$ psi);
2. Pressure decay test under triaxial stresses ($x = 1000$ psi, $y = 3000$ psi, $z = 4000$ psi);
3. The 1st cycle of LN₂ injection under high injection pressure (~450 psi);
4. Pressure decay test after the 1st cycle and under triaxial stress loading;
5. The 2nd cycle of LN₂ treatment under high injection pressure (~450 psi);
6. Pressure decay test after the 2nd cycle and under triaxial stress loading;
7. The 3rd cycle of LN₂ treatment under high injection pressure (~450 psi);
8. Pressure decay test after the 3rd cycle and under triaxial stress loading;
9. Pressure decay test after the sample returned to room temperature and still under triaxial stress loading; and,
10. Pressure decay test under no stress loading ($\sigma_z = 60$ psi), to compare with the first pressure decay test from Step 1.

Figure 4.4.62 shows the pressure decay tests with different triaxial stress conditions from Steps 1 and 2, comparing the effect of applied stresses on pressure decay curves. The permeability decreased when the sample was placed under stress loading. **Figure 4.4.63** shows the pressure decay tests for shale Sample 2 before the LN₂ treatment and after each cycle of LN₂ treatment, and all of them were conducted under triaxial stresses. There is a significant increase in the pressure decay time after the first LN₂ cycle. However, the pressure decay tests after the second LN₂ treatment decreased, indicating an increase in the permeability. **Figure 4.4.64** shows the pressure decay tests with different temperature conditions while the sample was still under triaxial stresses. The permeability decreased when the sample returned to room temperature. While at lower temperature, it might be that the shale sample is under thermal contraction and fractures around the wellbore remain open. As the sample warms up, the sample relaxes and fractures close. **Figure 4.4.65** shows the results of Step 10, the pressure decay test at the end of the experiment with no stress loading ($\sigma_z = 60$ psi), demonstrating significant permeability enhancement after three cycles of LN₂ treatment.

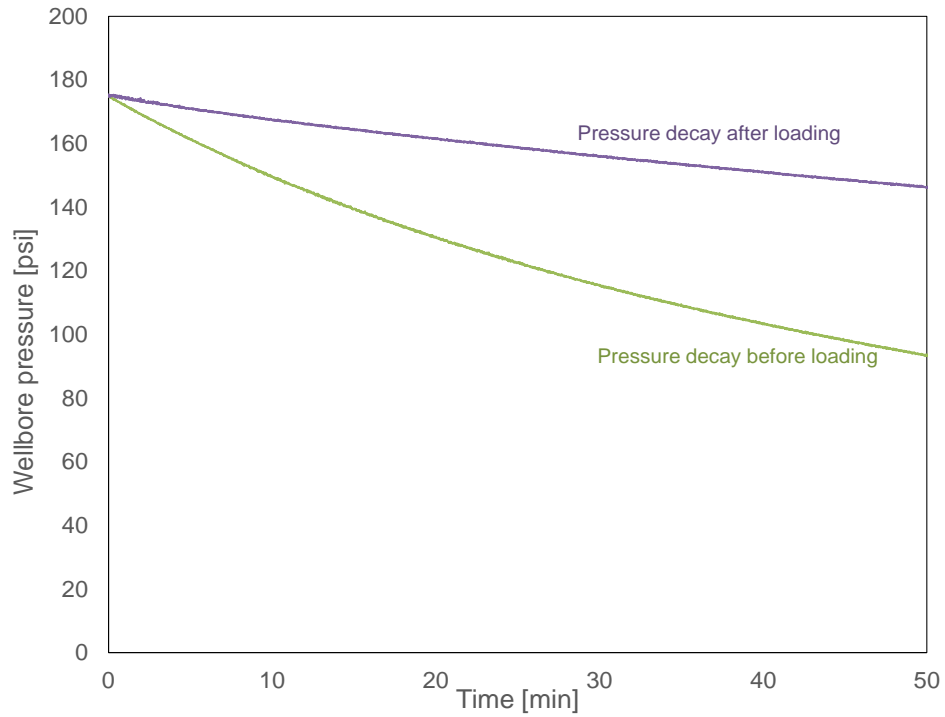


Figure 4.4.62 Pressure decay tests for Sample 2 with and without triaxial stress loading.

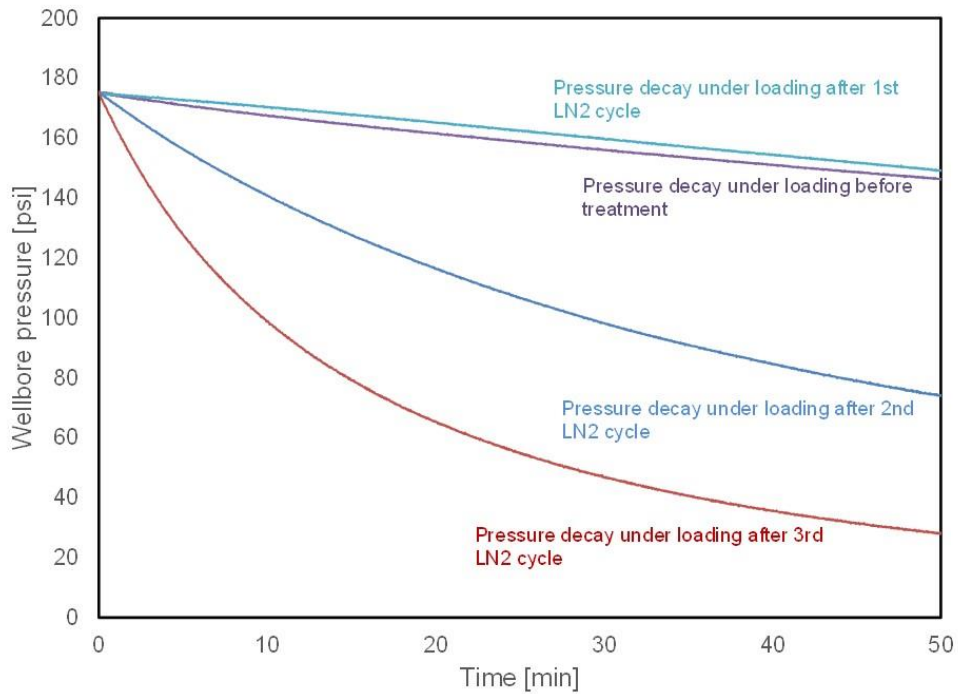


Figure 4.4.63 Pressure decay tests for Sample 2 before the LN₂ treatment and after each cycle of LN₂ treatment. There is a measurable increase in the pressure decay time after the first LN₂ cycle. The pressure decay tests after the second LN₂ cycle decreased, indicating enhancements in the permeability.

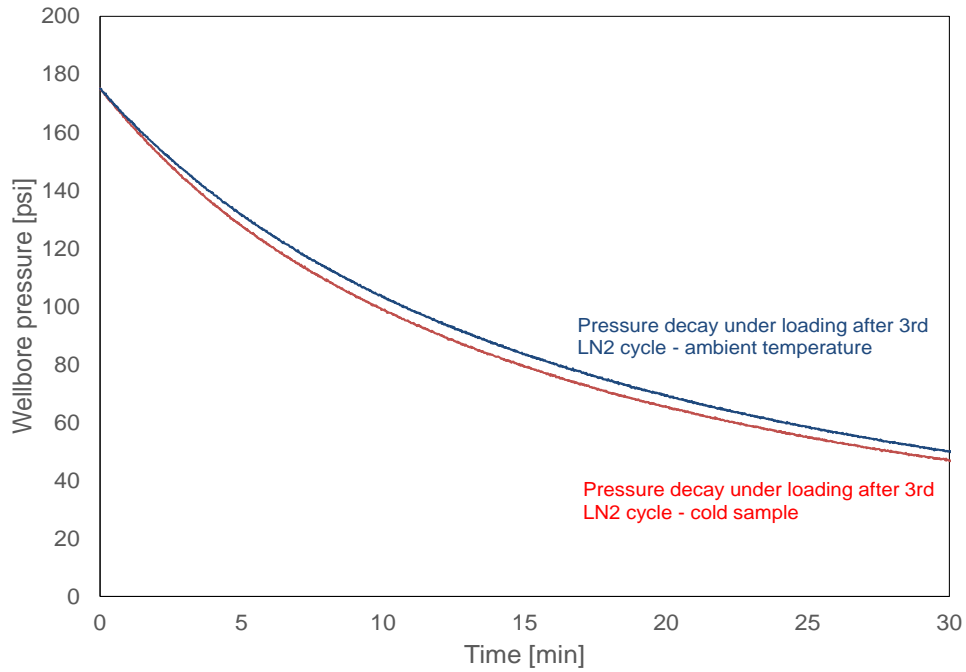


Figure 4.4.64 Pressure decay tests with different temperature conditions for Sample 2.

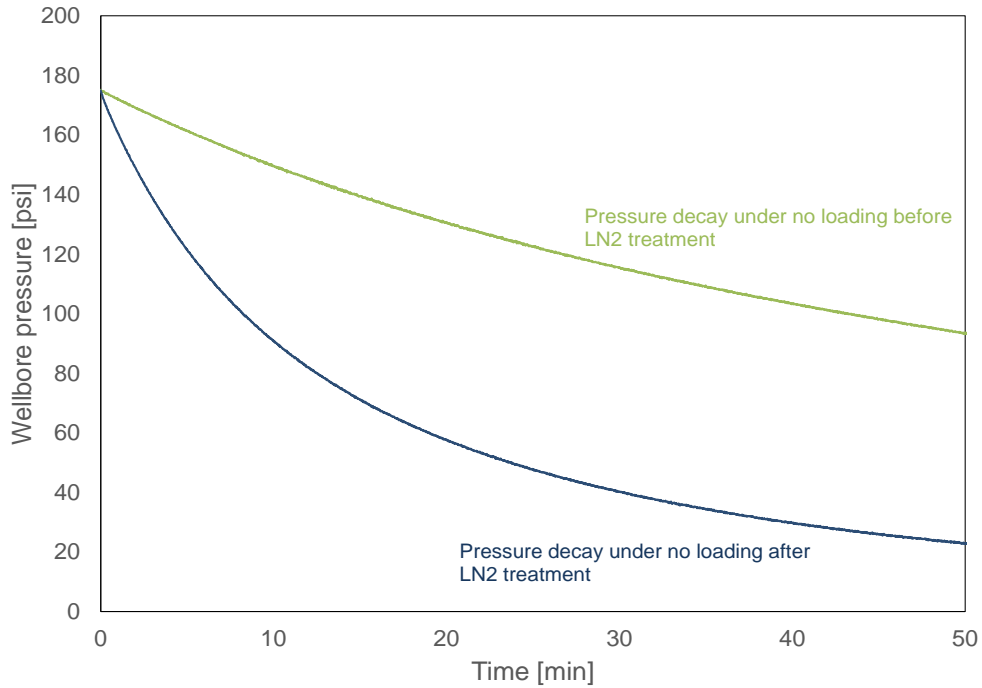


Figure 4.4.65 Pressure decay tests before and after the LN₂ test on Sample 2.

A second round of high pressure LN₂ test was conducted on Sample 2. **Figure 4.4.66** shows the pressure decay tests with different stress conditions before this second test. The pressure decay is affected by the stresses applied on the sample, and the permeability decreased when

the sample was placed under stress loading. **Figure 4.4.67** shows the pressure decay tests for this shale sample before LN₂ treatment and after each LN₂ treatment cycle, all of them again were conducted under triaxial stress loading, displaying significant reduction in the pressure decay time after each treatment cycle. **Figure 4.4.68** shows the pressure decay tests with different temperature conditions while the sample was still under triaxial stress loading. The permeability again decreased when the sample returned to room temperature, similar to the previous test. **Figure 4.4.69** shows test Step 10, the pressure decay test at the end of the experiment with no stress loading ($\sigma_z = 60$ psi), demonstrating permeability enhancement after three cycles of LN₂ treatment.

Acoustic measurements were conducted before and after the LN₂ test for Sample 2 using P and S ultrasonic transducers. The signals were measured along Faces 1 & 3, and 2 & 4. **Figure 4.4.70** shows P-wave arrivals before and after the LN₂ test for all side faces with the adjusted amplitude to compare changes in arrival time and wave forms. **Figure 4.4.71** to **Figure 4.4.73** show the P-wave velocities before and after the LN₂ test on this sample for Faces 1 & 3, 2 & 4, and 5 & 6, respectively, proving a decrease in the velocity due to fractures created during the cryogenic treatments since the wave will take a longer time traveling through any air gaps.

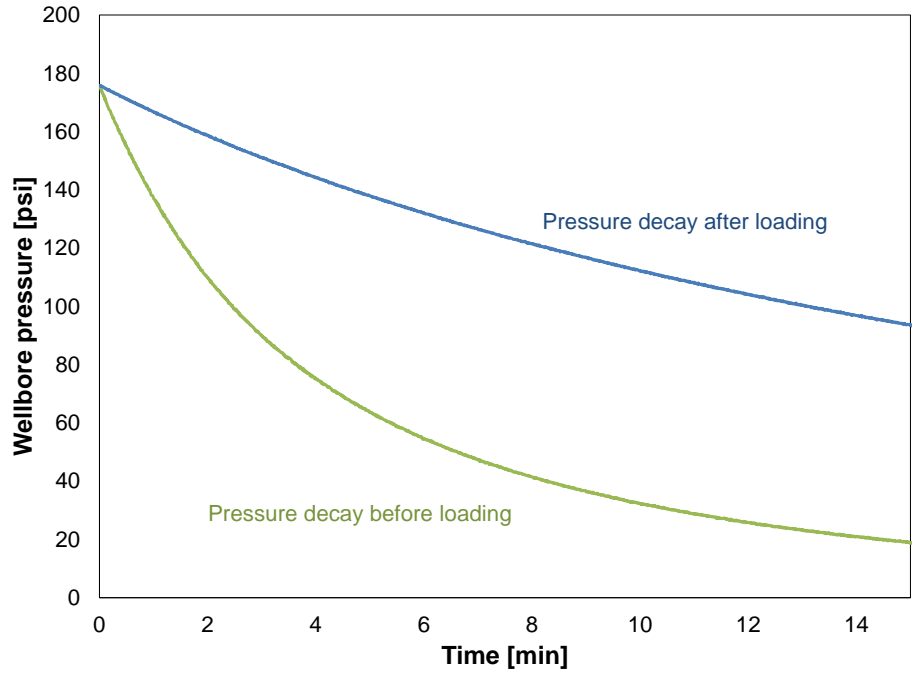


Figure 4.4.66 Pressure decay tests under different stress conditions before the second test on Sample 2.

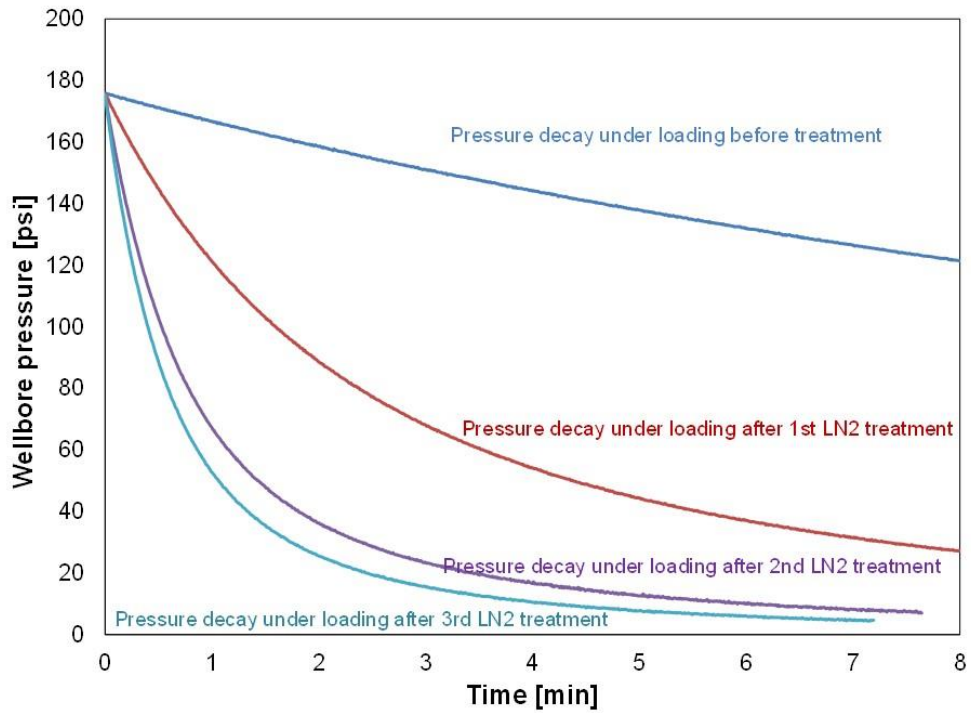


Figure 4.4.67 Pressure decay tests before LN₂ treatment and after each LN₂ treatment cycle for Sample 2. All of them conducted under triaxial stress loading. There is a significant difference in the pressure decay curves after each treatment cycle.

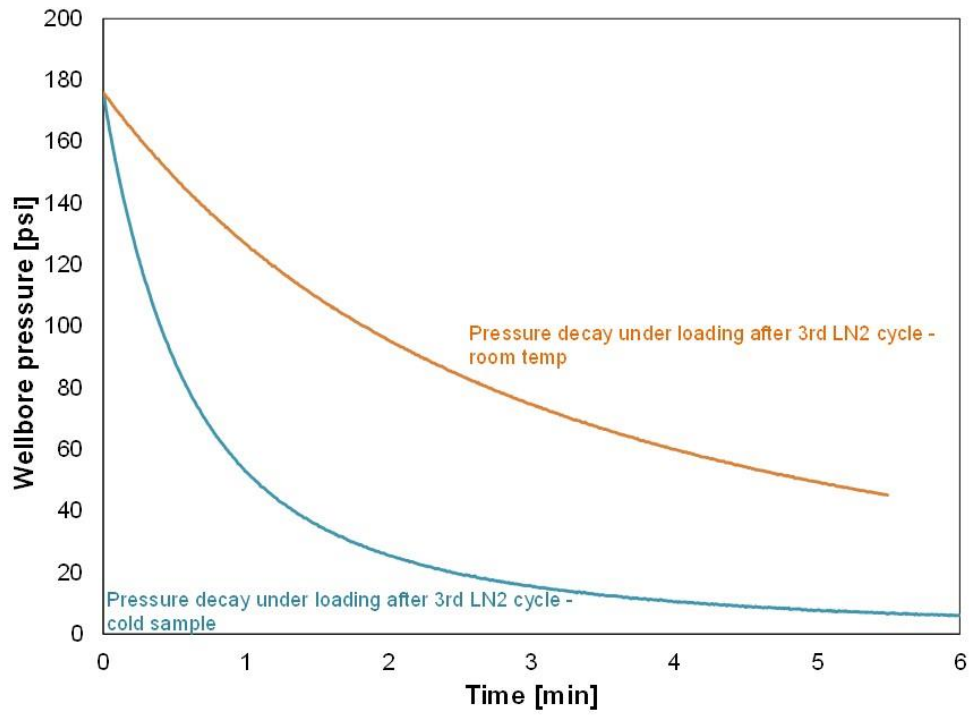


Figure 4.4.68 Pressure decay tests with different temperature conditions for the third test on Sample 2.

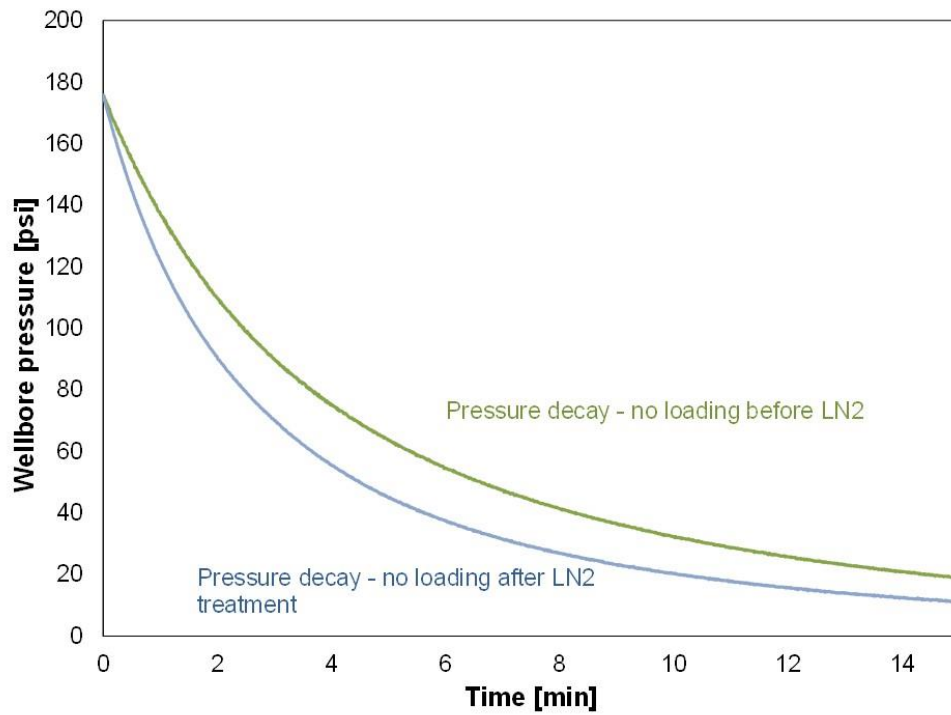
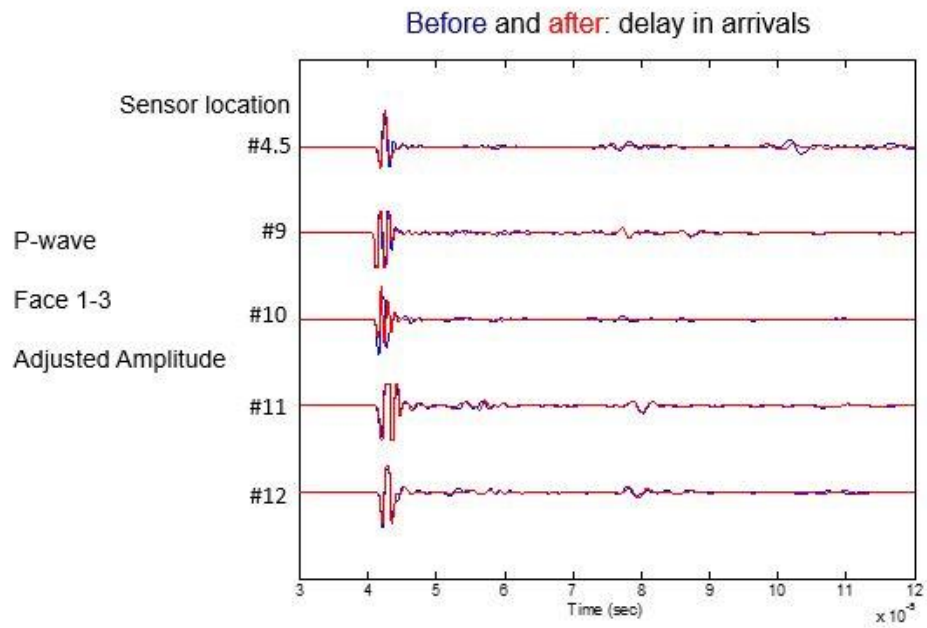


Figure 4.4.69 Pressure decay tests before and after the second LN₂ test on Sample 2.

(a)



(b)

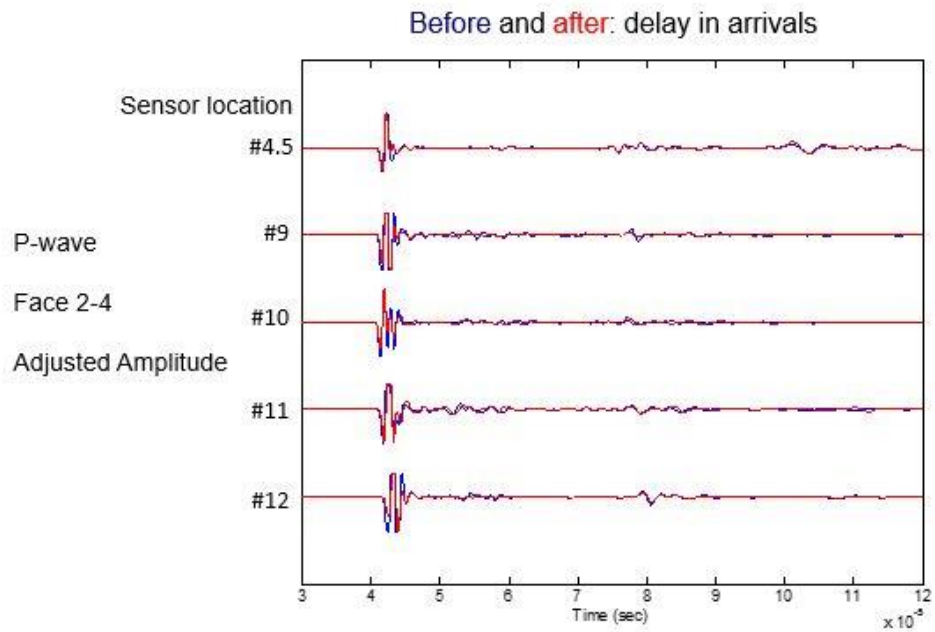


Figure 4.4.70 P-wave arrivals before and after the second LN₂ test for Faces 1 & 3 (a) and 2 & 4 (b) with the adjusted amplitude to compare changes in arrival time and wave forms.

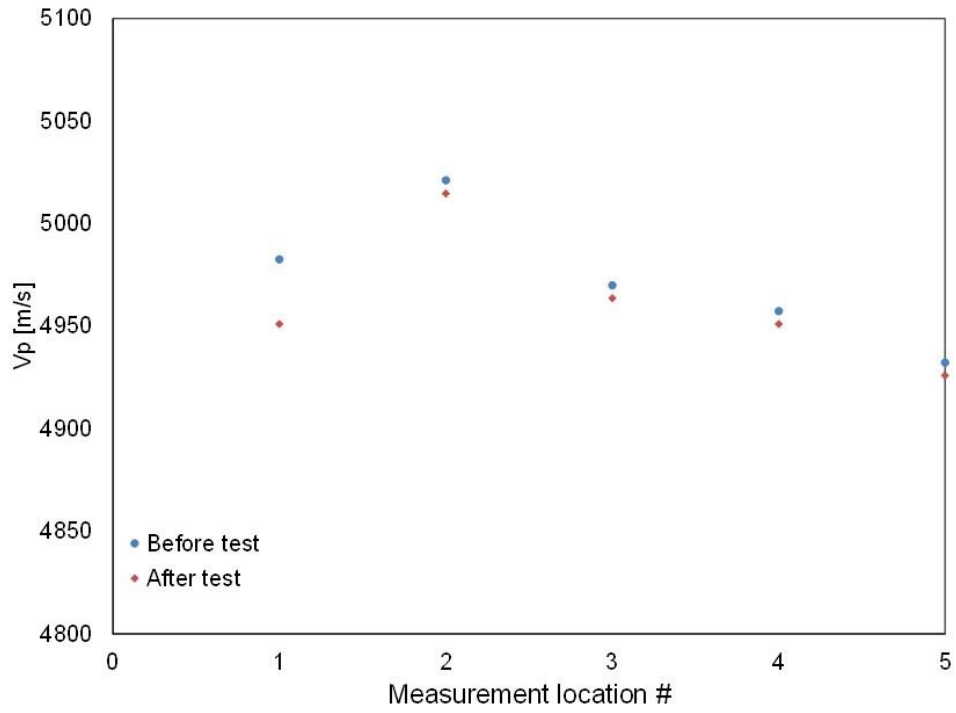


Figure 4.4.71 Changes in P-wave velocities before and after the cryogenic test for Faces 1 and 3.

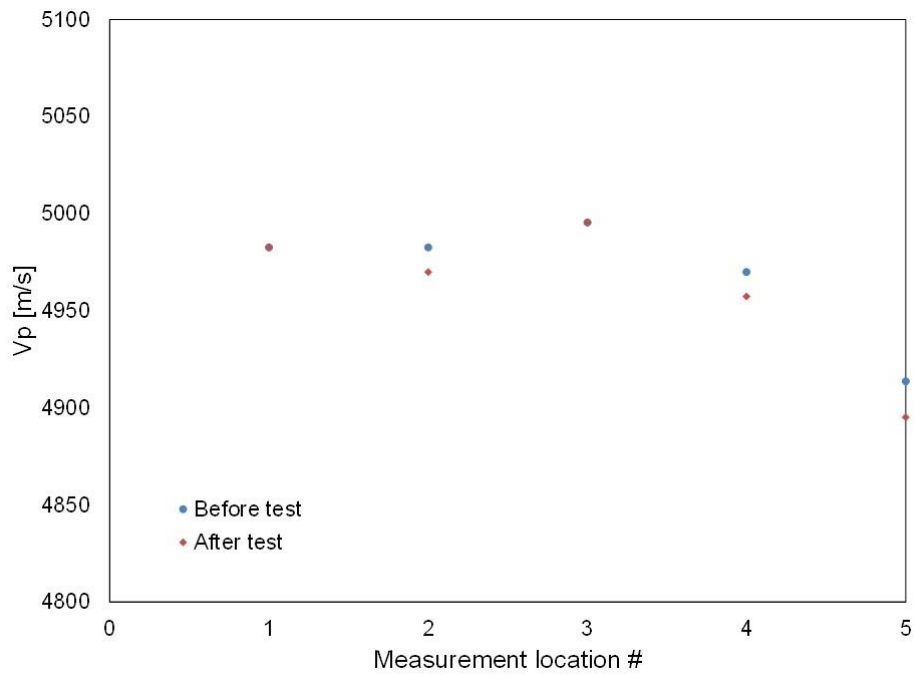


Figure 4.4.72 Changes in P-wave velocities before and after the cryogenic test for Faces 2 and 4.

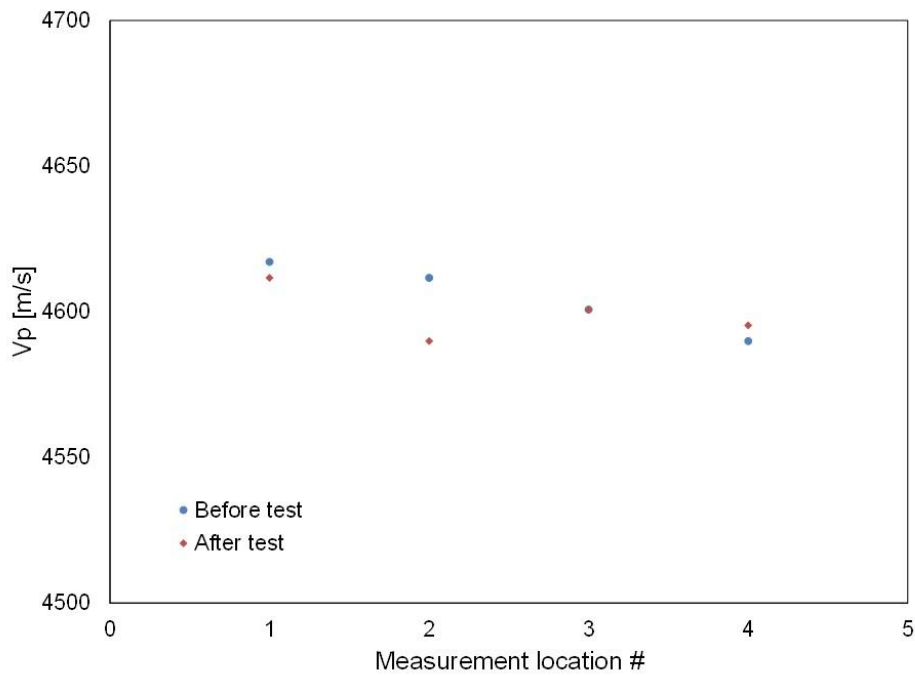


Figure 4.4.73 Changes in P-wave velocities before and after the cryogenic test for Faces 5 and 6.

Sample 2, after two high pressure LN₂ treatments with triaxial stresses (x = 1000 psi, y = 3000 psi, and z = 4000 psi), was fractured by injecting GN₂ under stress loading. **Figure 4.4.74** shows the breakdown pressure for shale Sample 2 is 1417 psi. **Figure 4.4.75** shows the picture of Sample 2 before and after the LN₂ and GN₂ treatments. The fracture propagated along the maximum horizontal stress, which is in y-axis direction. **Figure 4.4.76** shows the pictures of the fracture plane in shale Sample 2 after the LN₂ and GN₂ treatments. The fracture growth direction was deviated from the wellbore with an angle of 12°, which was only observed in LN₂ treated samples.

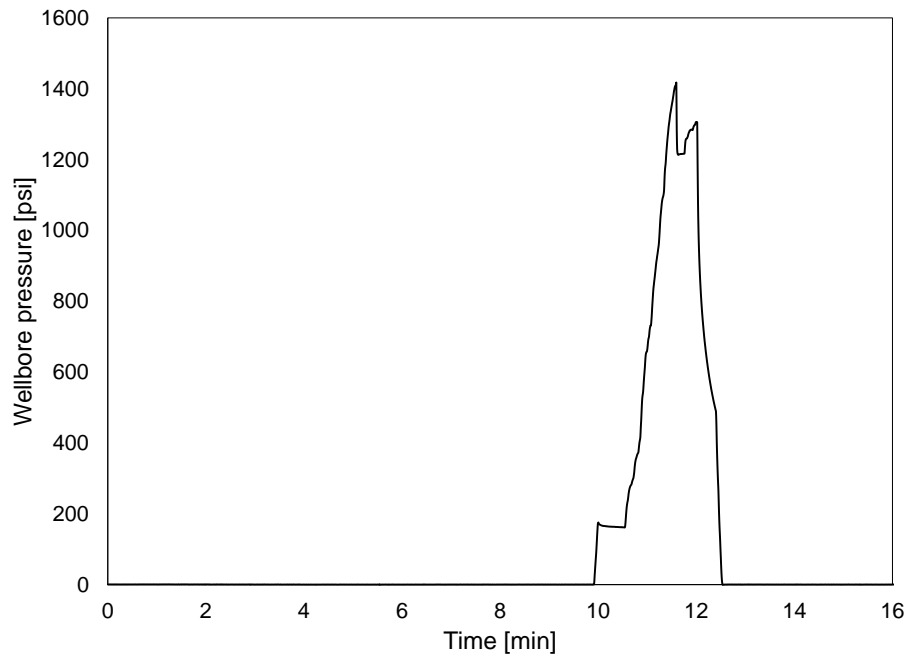
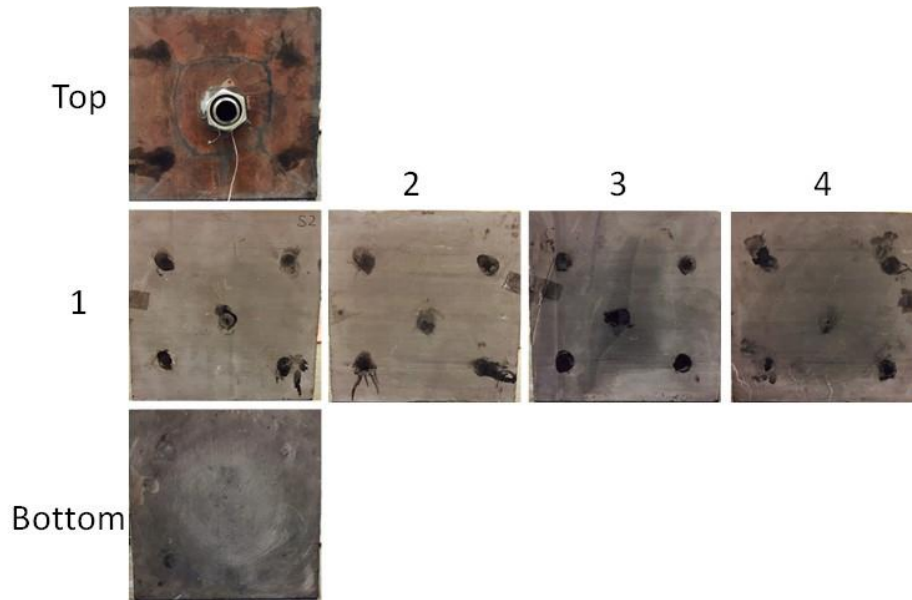


Figure 4.4.74 Breakdown pressure profile for Sample 2 using GN₂.

(a)



(b)

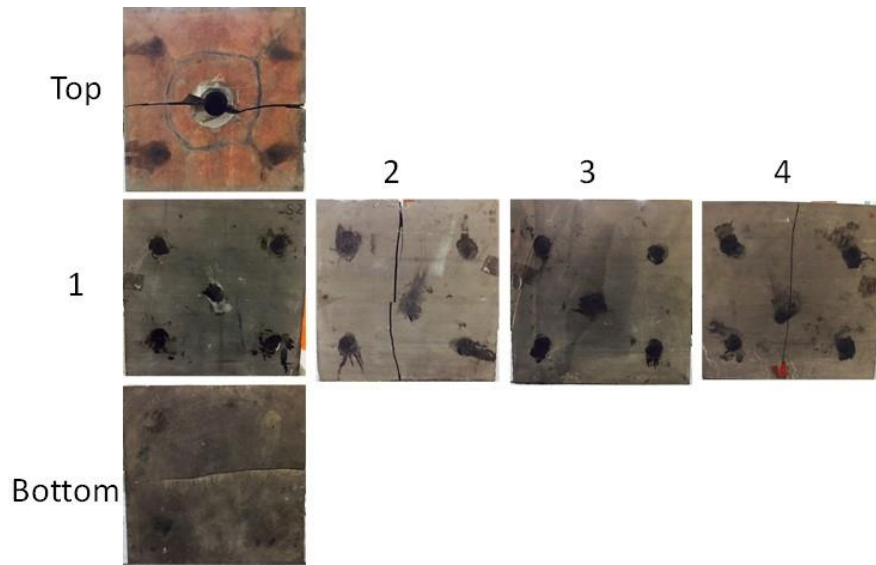


Figure 4.4.75 Shale Sample 2 before (a) and after (b) the GN₂ fracturing.



Figure 4.4.76 Fracture plane in shale Sample 2 after LN₂ and GN₂ fracturing.

4.4.4.2.3 Sample 3

Sample 3 was a dry shale and the same procedure used with shale Sample 1 was applied at the room temperature. The procedure started with conducting the pressure decay test before LN₂ injection with no stress loading ($\sigma_z = 60$ psi). Then triaxial stresses were applied gradually on the sample as ($x = 1000$ psi, $y = 1500$ psi, and $z = 2000$ psi). After that, LN₂

was flowed into the wellbore under low pressure (~15 psi) for about 40 minutes. **Figure 4.4.77** shows the temperature changing with time during the LN₂ injection on Sample 3. After the LN₂ injection, the stress loading was removed and the sample returned to the free stress condition. Then pressure decay test was conducted with no stress loading ($\sigma_z = 60$ psi) while the sample was still cold. **Figure 4.4.78** shows the pressure decay curves before and after the LN₂ stimulation.

Acoustic measurements were carried out before and after the LN₂ tests. **Figure 4.4.79** shows P-wave and S-wave arrivals before and after the LN₂ test for all side faces with the adjusted amplitude to compare changes in arrival time and wave forms. The acoustic results show that there is a planar fracture along the XY-plane (red circles in **Figure 4.4.79c** and **f**) at sensor locations #11 and #12 on Faces 5 and 6.

Shale Sample 3 was fractured when we attempted to do LN₂ treatments. The shale sample fractured at 168 psi during the pressure decay test under no loading ($\sigma_z = 60$ psi). **Figure 4.4.80** shows the breakdown pressure for Sample 3.

Figure 4.4.81 shows the picture of the shale sample after fracturing during the previous step. The fracture pattern corresponds with the acoustic results.

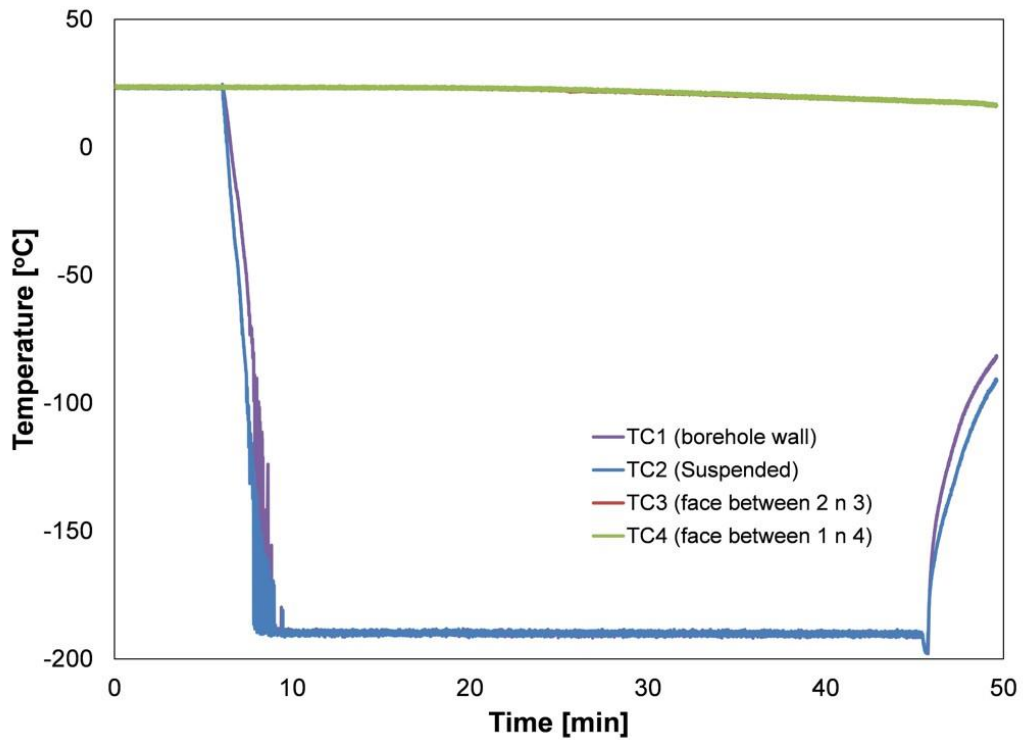


Figure 4.4.77 Temperature profiles from the start of injecting LN₂ till the end of the test for Sample 3.

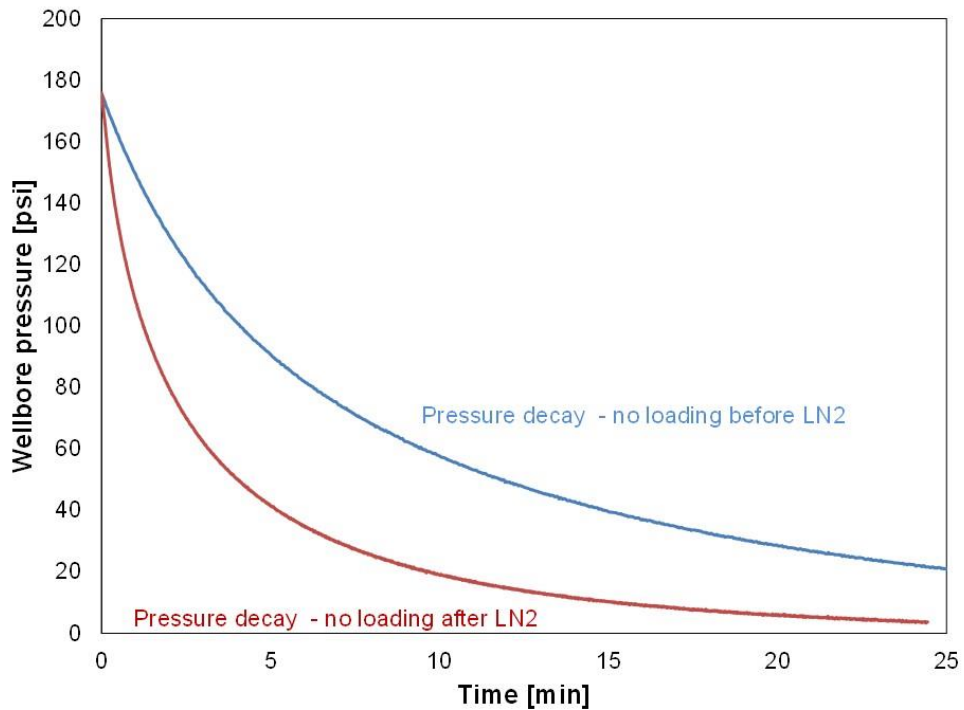
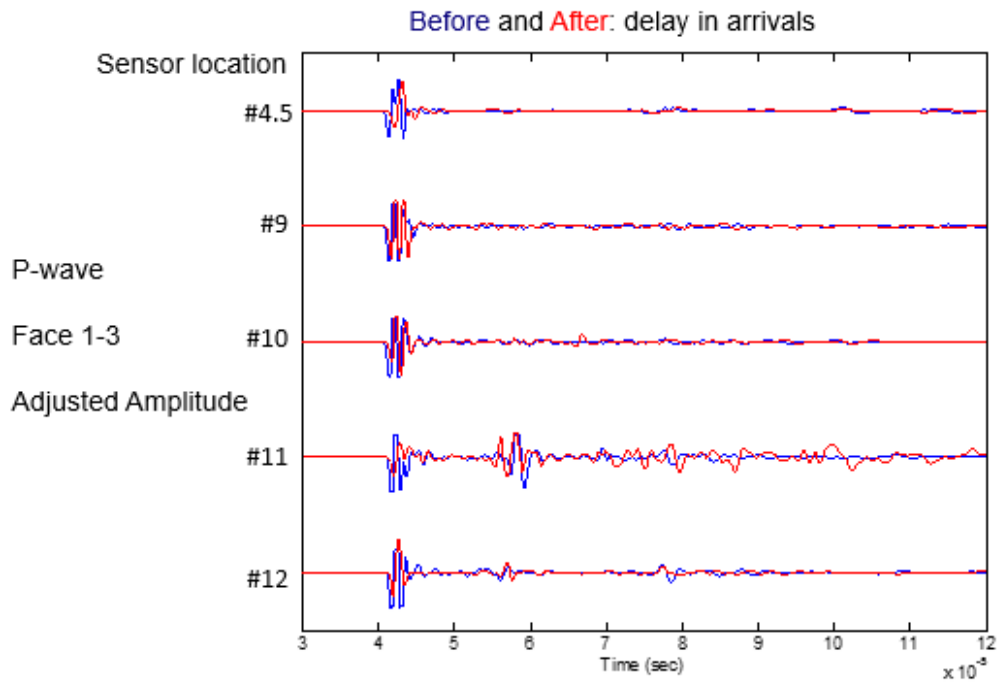
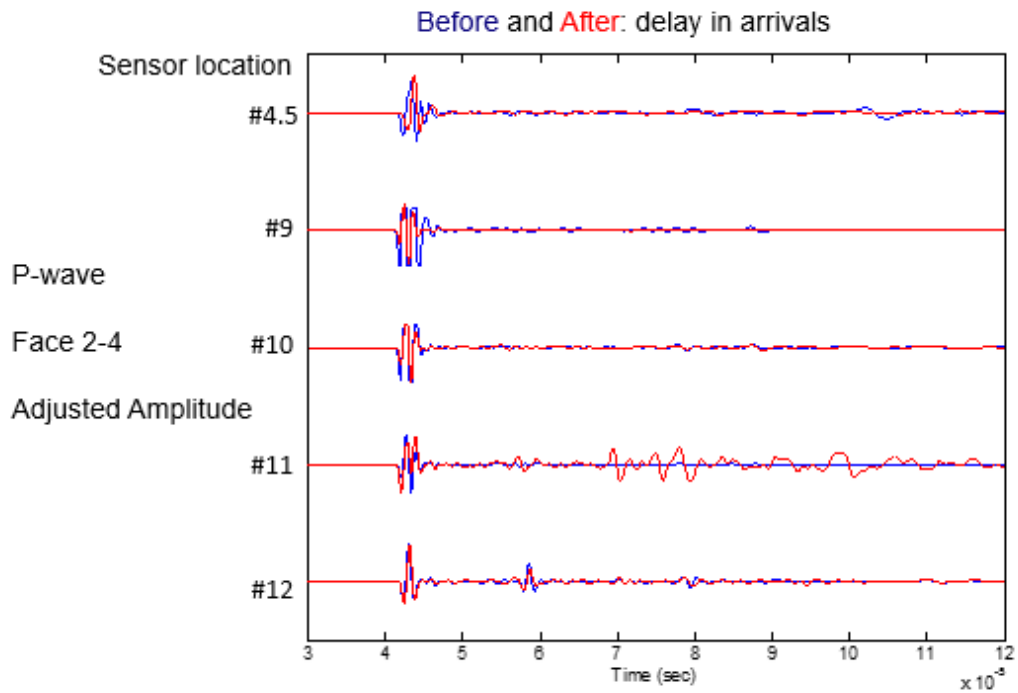


Figure 4.4.78 Pressure decay tests before and after the LN₂ test for Sample 3.

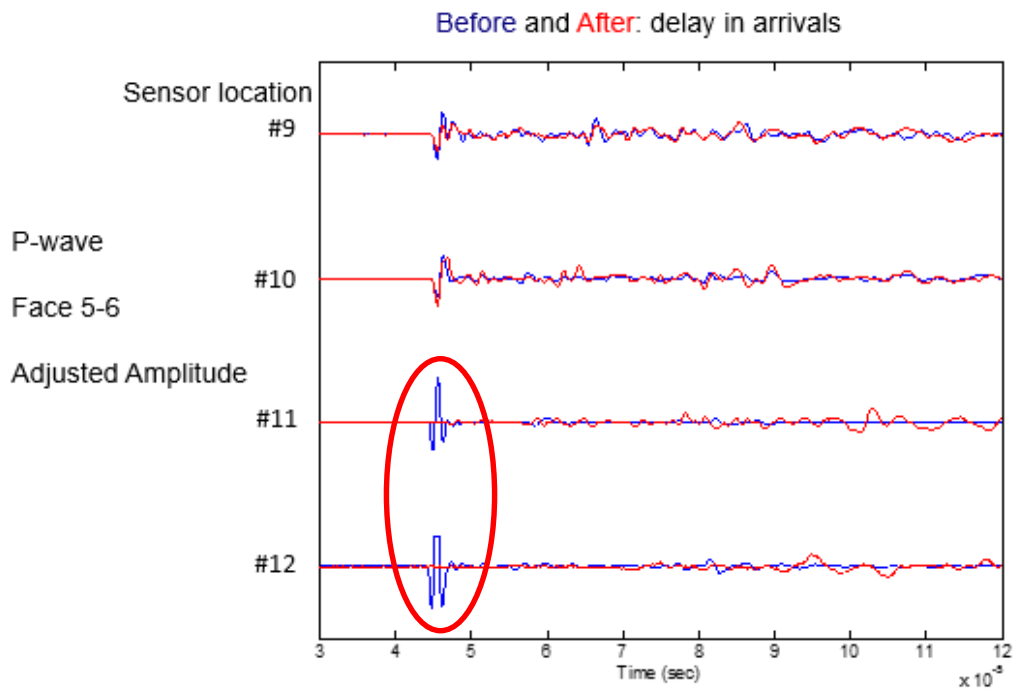
(a)



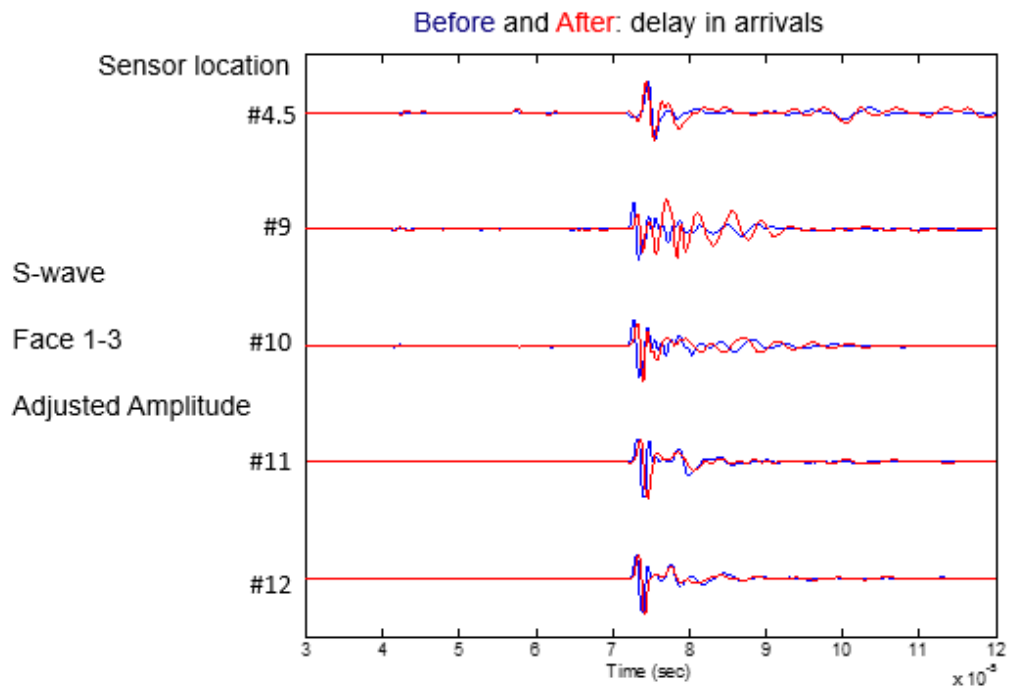
(b)



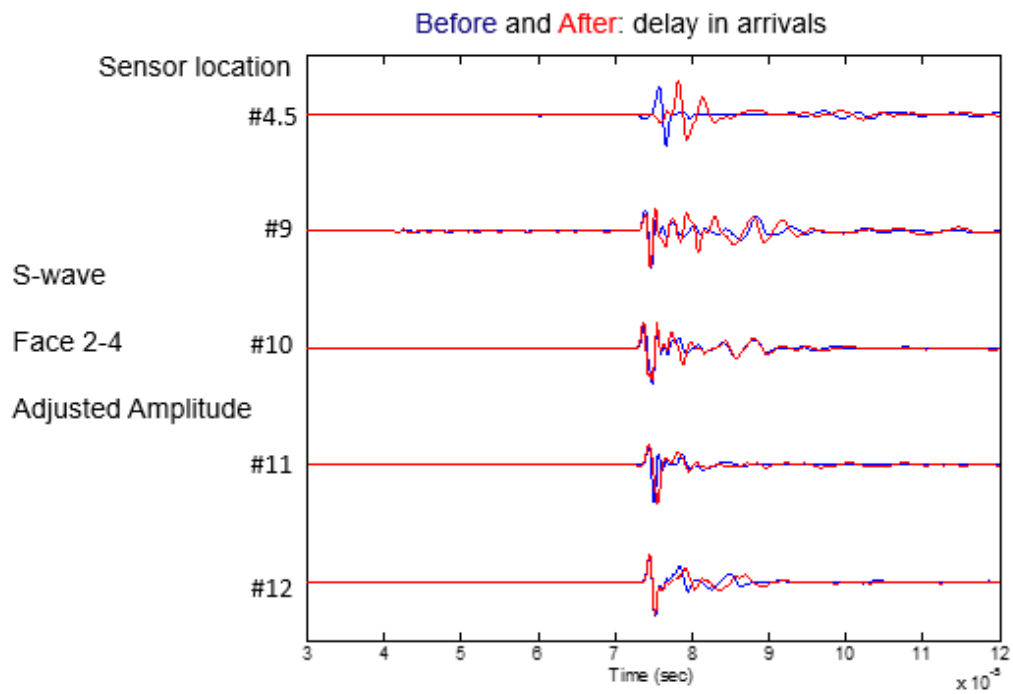
(c)



(d)



(e)



(f)

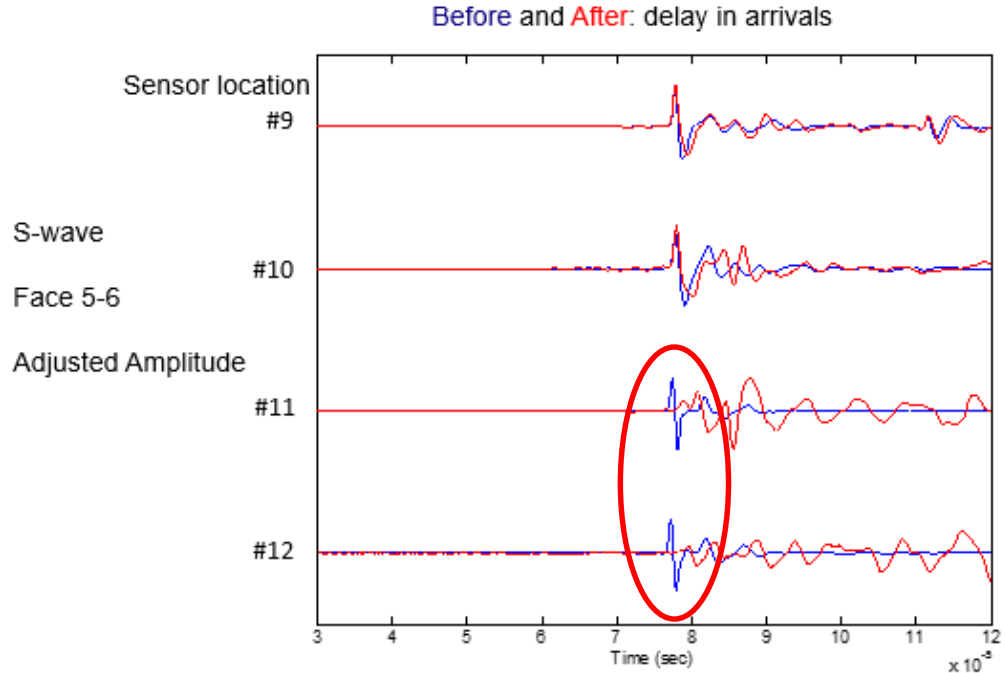


Figure 4.4.79 P- and S-wave arrivals before and after the LN₂ test on Sample 3 for all side faces with the adjusted amplitude to compare changes in arrival time and wave forms.

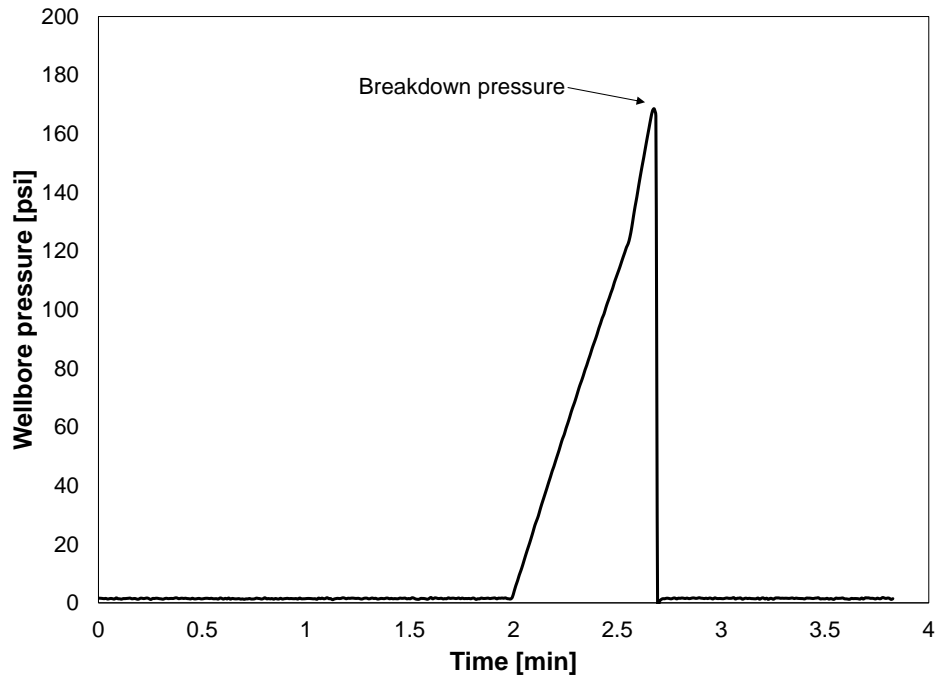


Figure 4.4.80 Breakdown pressure of Sample 3 using GN₂. This happened during the pressure decay test.

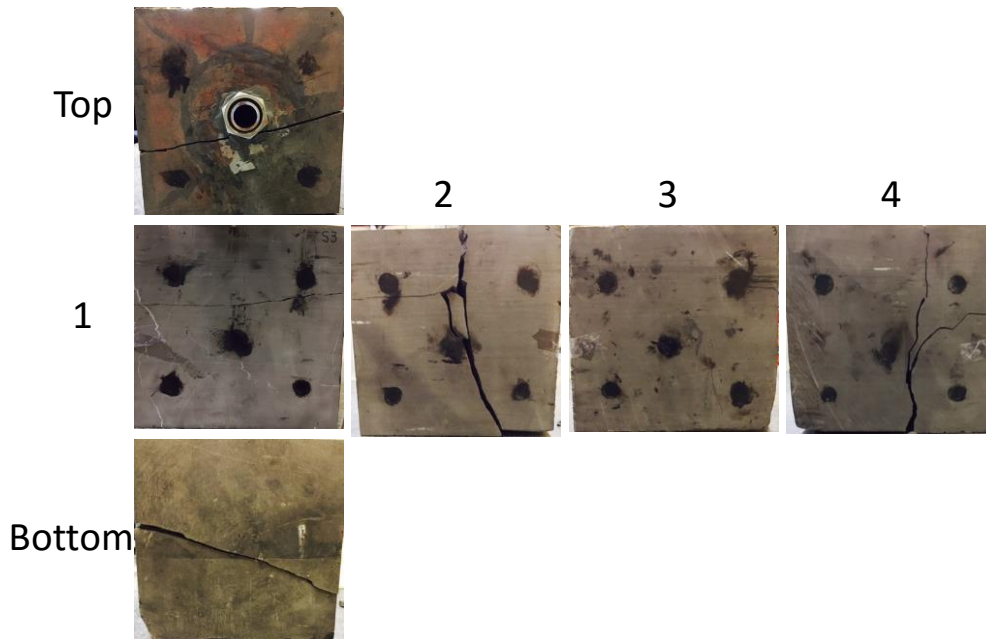


Figure 4.4.81 Shale Sample 3 fractured during pressure decay test.

4.5 Summary

Submersion of concrete samples into liquid nitrogen extended existing fractures and created new cryogenic fracture networks on the contact surface and inside the blocks. Since there are no stresses involved during the experiments, these new fractures are purely induced by the sharp thermal gradient caused by liquid nitrogen. It is also observed that, as the concrete samples warmed up, some minor fractures closed.

Borehole liquid nitrogen treatments of transparent acrylic cylinders showed that major cryogenic fractures initiated around the tip of the injection tubing, due to the most rapid cooling down at the direct contact point of LN₂. Borehole treatments of concrete samples demonstrated visible cryogenic fractures on both the borehole wall and the surface. Additionally, CT scan proved the development of fractures throughout the whole block from borehole to surface.

By pressurizing the liquid nitrogen into the borehole of concrete samples, we investigated the effect of concrete curing time, water saturation, initial sample temperature, and number of treatment cycles on the liquid nitrogen stimulation efficacy. The strength of concrete increases with increasing curing time, thus exhibiting high breakdown pressure. Compared to dry concrete samples, water saturation in wet concrete samples helps to reduce the breakdown pressures after liquid nitrogen treatments. Given more cycles of liquid nitrogen treatments, the concrete strength tends to become lower and lower, indicating existing fractures are extended and new fractures are created after each cycle of treatment. This accumulative fracturing process increases the likelihood of the tensile failure inside the concrete samples.

Under varying triaxial stress loading, we stimulated glass, concrete, sandstone, and shale samples using liquid nitrogen or/and gas nitrogen. Similar to acrylic samples, cryogenic fractures in glass cubes started growing from the liquid nitrogen contact point as well. Major fractures propagated in the direction of the maximum principal stress, as expected by the fracturing principles. Besides, as the triaxial stresses were doubled, the extension of the

fractures was confined. This is reasonable since the tensile stress created by LN₂ must first counterbalance the compressive stresses, then overcome the glass tensile strength to induce fractures. Also, some fractures partially closed as the cubes warmed up, but again opened when stresses were removed.

By keeping the triaxial stress ratio constant, the breakdown pressure of the concrete samples increases for both intact and LN₂ treated samples with increasing triaxial stress loading. As compared with intact samples, the breakdown pressure of LN₂ treated samples decreases, suggesting that LN₂ treatments weaken the rock strength under triaxial stress conditions.

The permeability of tested sandstone samples is 0.349 mD on average, two orders of magnitude larger than those of concrete and shale samples, showing high compressibility. Although pressure decay tests indicated that there are no obvious permeability enhancements after three cycles of LN₂ treatments for the sandstone samples, the breakdown pressure of the LN₂ treated sample is much lower than that of the intact sample. Also, it is observed that as the sandstone returned to room temperature, its permeability slightly increases. It is speculated that LN₂ partially destroyed the cement structure among the framework grains, contributing to lower breakdown pressure but not much permeability under quasi-static triaxial stress conditions. As the temperature rose up, the slightly shifted gains and cement expanded and self-propped the minor apertures around, preventing their closure.

Under triaxial stress loading, shale samples after LN₂ treatments demonstrated as much as 40% reduction in breakdown pressure. All pre- and post-measurements indicated permeability enhancements and fracture generation of the shale samples, including pressure decay, acoustic signatures, CT scans and GN₂ fracturing profiles. Specifically, pressure decay time is reduced due to enhanced permeability after each cycle of LN₂ treatment. Acoustic velocity is retarded because of fractures generated after the LN₂ treatments. In addition, CT scans showed observable cryogenic fractures generated inside the shale blocks. The major cryogenic fractures propagated along the maximum horizontal stress, after gas fracturing, the cryogenic fracture profile, which looks like an eggplant encircling the borehole, can be easily identified.

Results in this chapter deliver the milestones of this project. Major factors affecting the cryogenic fracturing processes, for the first time, are investigated and understood. These investigations not only provide us with conclusive remarks and conjectures, but also motivate our research plans for the next step.

5. CT Imaging Techniques for Fracture Detection

We have attempted many CT and image-processing techniques to detect and describe the cryogenic fractures generated in concrete, sandstone, shale, and glass blocks. These techniques include X-ray CT scanning at various energies and different scanning currents, the use of Positron Emission Tomography scanning in combination with X-ray CT scanning, and synchrotron micro-computed tomography at Beamline 8.3.2 at the Advanced Light Source at Lawrence Berkeley National Laboratory. In addition, numerous imaging-processing techniques have been attempted and screened for use. A summary of these investigations is presented below.

5.1 X-Ray CT Scan of Sandstone and Shale Samples

Two 2.5-inch cubes of a permeable sandstone with 0.5-inch boreholes were selected for the cryogenic fracturing tests. Prior to testing, the blocks were scanned using X-ray CT. For scanning, the blocks were submerged in sand in a cylindrical holder to reduce “X” artifacts in the CT data from the geometry of the samples. Before assembling into the triaxial test apparatus, one sample was saturated with water by evacuating the sample and allowing water to imbibe as the submerged sample returned to atmospheric pressure. The other sample was room dry. As with the glass cube tests, LN₂ was applied to the borehole and the temperature of the external block surface was monitored. Following the tests, the blocks were similarly CT scanned to look for fractures.

5.1.1 Dry and Wet Sandstone Samples with Triaxial Stresses

No fractures were identified comparing pre- and post-test scans (**Figure 5.1.1**) of either sandstone samples. These blocks were scanned at multiple energies. While the combination of energies selected for post-test scanning is not optimum for differencing (120 kV and 140kV-a larger difference in energies would be desirable), these energies were required for sufficiently illuminating the sample. The lack of fracture identification is not conclusive, however, the CT scanning was not able to identify fine fractures in the glass blocks either. Cryogenic fracturing tests on other sandstone blocks discussed above indicated changes in

the block permeability likely induced by breaking down the intergranular cements, but not indicative of larger-scale fracturing.

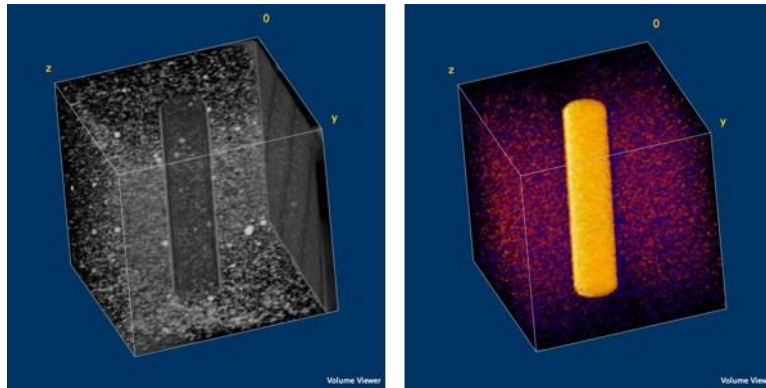


Figure 5.1.1 Left: post-test CT scan of sandstone block, fractures would be shown as dark features in this image. Right: difference scan (140kV-120kV), fractures would be shown as light features in this image (see borehole for reference).

5.1.2 Shale Samples with Triaxial Stresses

Three cubes of Mancos shale (4 inches on a side) were procured from Kocurek Industries (Caldwell, TX). Initial CT scanning showed numerous natural fractures in the blocks, and that the blocks had an epoxy-like material at the outer reaches of some of the larger fractures (**Figure 5.1.3**). As with the glass blocks, one-quarter inch boreholes were placed about three-quarters of the way through the block, using tap water as a cutting fluid. Two of the blocks were then painted with epoxy and epoxy was forced into the borehole. After the epoxy set, the borehole was drilled out. This was done to contain the injected liquid nitrogen to the borehole. The blocks were CT scanned again in a cylindrical holder surrounded by sand to decrease geometric artifacts (see “X” artifacts in **Figure 5.1.2**), and a fiberscope (**Figure 5.1.3**) was run through the borehole providing video images of the initial borehole condition. As with the glass blocks, the shale blocks were placed in the triaxial load frame and triaxial stresses were applied (first two tests 700 psi horizontal parallel to the borehole, 1050 psi horizontal perpendicular to the borehole, and 1400 psi vertical), and tests similar to the glass block tests were performed. Temperatures of the external block sides were recorded over time. Unlike the glass blocks, there was no direct visual or aural indication of fracturing during the tests.

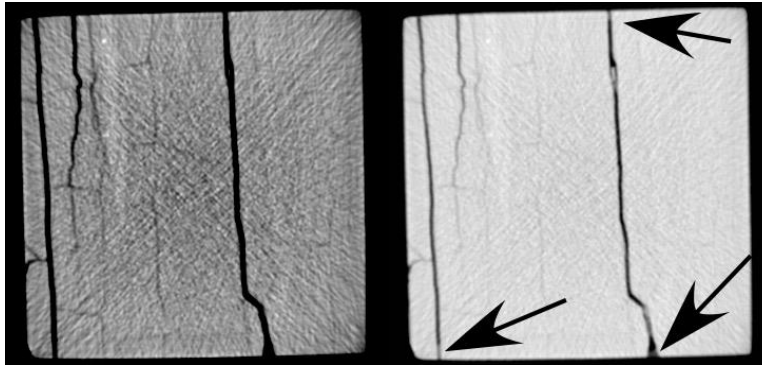


Figure 5.1.2 Initial scans of one of the Mancos shale blocks (typical). Left image adjusted to show fractures. Right image adjusted to show epoxy (see arrows). Note “X”-like artifacts resulting from block geometry.

Post-test analysis included CT scanning (**Figure 5.1.4**) and borehole inspection using the fiberscope. Techniques such as pre- and post-test flow resistance (indicative of permeability changes) and pre- and post-test acoustics (indicative of changes in the mechanical structure of the blocks) were not performed because of the presence of large fractures at the start of the test. These fractures in the block intersecting the borehole would already have high permeability, and these fractures would strongly affect the mechanical properties and acoustic signals. Post-test CT and borehole imaging did not show a significant change in the nature of the blocks. However, this neither confirms nor denies the occurrence of cryogenically induced fractures. Based on CT scanning and borescopic observations in glass blocks, cryogenic fractures may have small apertures beneath the noise level for the CT and borescope images.

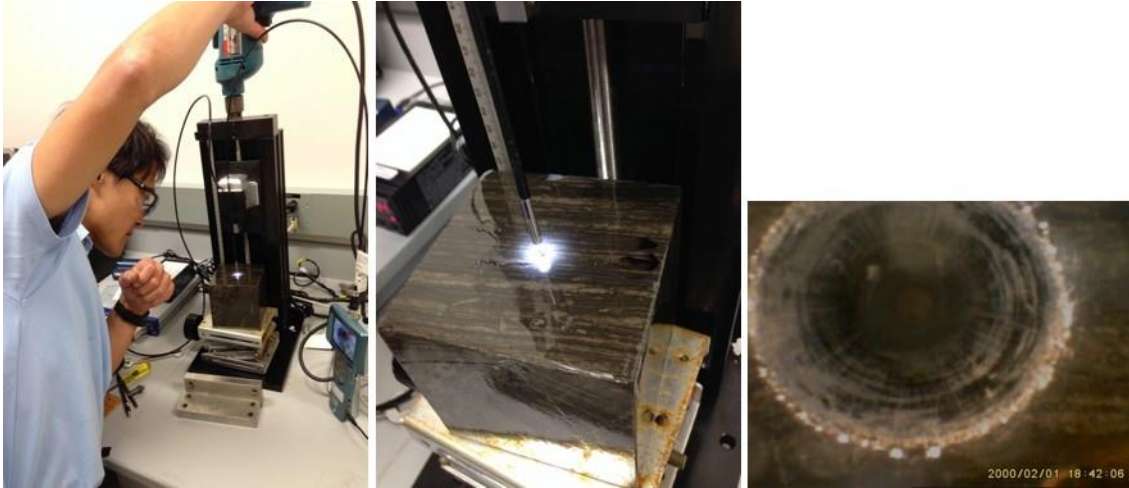


Figure 5.1.3 Shale sample borehole inspection and video recording using a fiberscope.

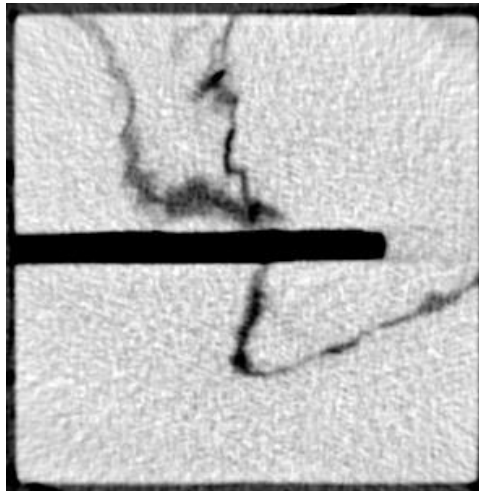


Figure 5.1.4 Post-test CT scan image. The borehole is black. The cross-cutting fracture (wavy black feature) was also present at the start of the test.

Quantifying the effects of cryogenic fracturing in opaque, heterogeneous, anisotropic media is challenging. Many of the fractures formed in the glass blocks are below the resolution of the medical CT scanners so it is expected that fractures in shale might be below the resolution of the CT scanner as well. A number of techniques can be used to help identify fractures. Conventionally, a dense enhancing agent is introduced, typically dissolved in fluid. Our cryogen limits our choices for injection during the test. A possible solution is to place a dense powder, such as barium chloride in the borehole, as it may be dragged into fractures as liquid nitrogen is imbibed. Liquid nitrogen, however, has a viscosity about one-sixth of water and

may be ineffective at dragging a proppant into the fractures. CT scanning would show where the dense powder was placed by the flowing cryogen if enough was placed.

Another technique would be to inject liquid metal (e.g. Galinstan) into the fractures following the test. This technique was attempted on both fractured glass blocks and fractured shale blocks. Like other liquid metals, Galinstan has a high surface tension (about 10 times that of the air-water interface). It will wet a mineral when unoxidized, but oxidizes rapidly and becomes nonwetting. Because of that, it may rapidly imbibe into a fracture and then drain as the wettability changes. A consideration for X-ray CT is density. A voxel having a fracture in it will have a lower density than an unfractured voxel all else being equal. Thus the X-ray attenuation will be lower for the fractured voxel. Adding some high-density liquid metal reverses this. Partial-filling of a voxel can mask the presence of the fracture.

5.2 PET/CT Scan of Glass and Shale Samples

Because of the difficulty in detecting fractures using X-ray CT, we attempted to use positron emission tomography (PET) scanning in combination with X-ray CT. In positron emission scanning, a labeled radioactive material is injected into the sample. When positrons are emitted, they meet electrons and annihilate each other releasing a pair of antiparallel gamma rays at a specific energy. The technique detects the gamma rays and then determines the locations from which the gamma rays are being emitted. In our case, a radio-labeled bicarbonate solution was placed in the sample. The instrument is coupled to an X-ray CT scanner to locate features. The X-ray CT scanner used with the PET scanner has a lower resolution than the scanner used in the previously mentioned studies.

5.2.1 Glass Sample

In our first PET/CT test, we used a fractured glass sample because we can see the fractures and thus have a basis for comparison. Panels *a* through *c* of **Figure 5.2.1** show photographic images of the glass block, which was previously cryogenically fractured using LN₂. Panels *d* through *f* show three views from the three-dimensional PET/CT data set. Brighter regions show regions containing more of the radioactive bicarbonate fluid. In this test, the borehole was not rinsed out prior to scanning, thus a very bright region is shown there. The fluid was

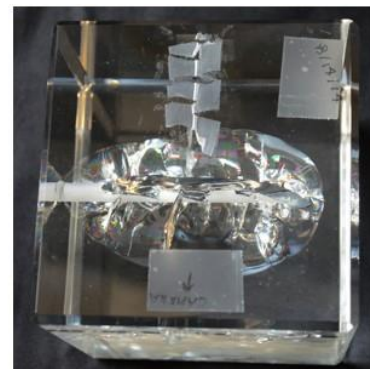
imbibed into the larger fractures as well, however the smaller fractures were not detected in the imaging. This imaging technique identified fractures where the X-ray CT did not. In an attempt to force fluid into smaller fractures, a hand-operated syringe was used to inject the fluid into the borehole while the block was under the unstressed condition. This had the dual impacts of forcing the labeled fluid into the fractures, but also of extending the fractures because of 1) the extremely high stress concentration at the fracture tips (indicating the imparting of seed fractures using cryogenic techniques), and 2) the presence of water which has long been known to affect glass fracturing. Some of the extended fractures penetrated through the outer edges of the block. The remaining labeled fluid in the borehole was rinsed out prior to scanning. Panels *g* through *i* show the results of the PET/CT under these conditions. The brightest locations are primarily on the outside of the block, and comparing *d* to *f*, it is clear that the major fractures have been extended as well.



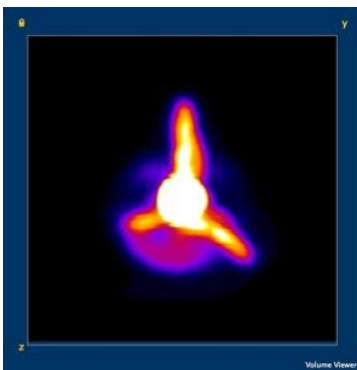
a.



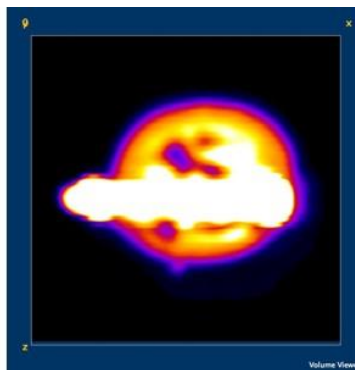
b.



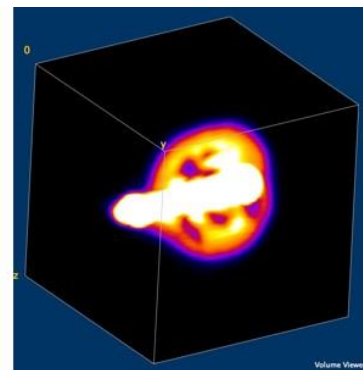
c.



d.



e.



f.

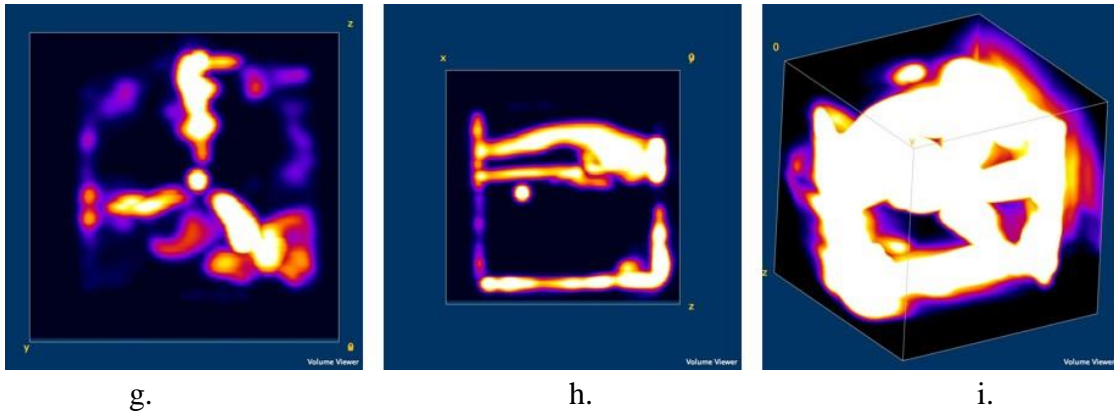


Figure 5.2.1 PET/CT of 4-inch glass block: a to c are photos, d to f are images from first PET/CT, g to i are PET/CT images following injection of labeled fluid using a syringe.

5.2.2 Shale Sample

A cryogenic fracturing test was performed on a 4-inch Mancos shale cube under triaxial stresses. The borehole in the sample was wet-cored before the cryogenic test, so although the block was not vacuum-saturated, it was not completely dry either. Vacuum saturation was not performed, as the process depends on sample permeability and the Mancos shale matrix permeability is very low. Pre- and post-test X-ray CT scans were compared to look for induced fractures. Fractures that were initially present in the shale were clearly observed after the test as well, however no new fractures resembling those in the glass cubes were observed.

PET/CT was used to scan the shale block following cryogenic stimulation. Panels *a* through *c* of **Figure 5.2.2** show X-ray CT projection views from three angles. It is clear that the block is fractured, however these fractures were present prior to the cryogen treatment. Panels *d* through *f* of **Figure 5.2.2** show the PET/CT views for the shale block. The concentrated labeled fluid is located in the borehole, but very little fluid is located outside the borehole, thus little of the radioactive tracer entered any fractures.

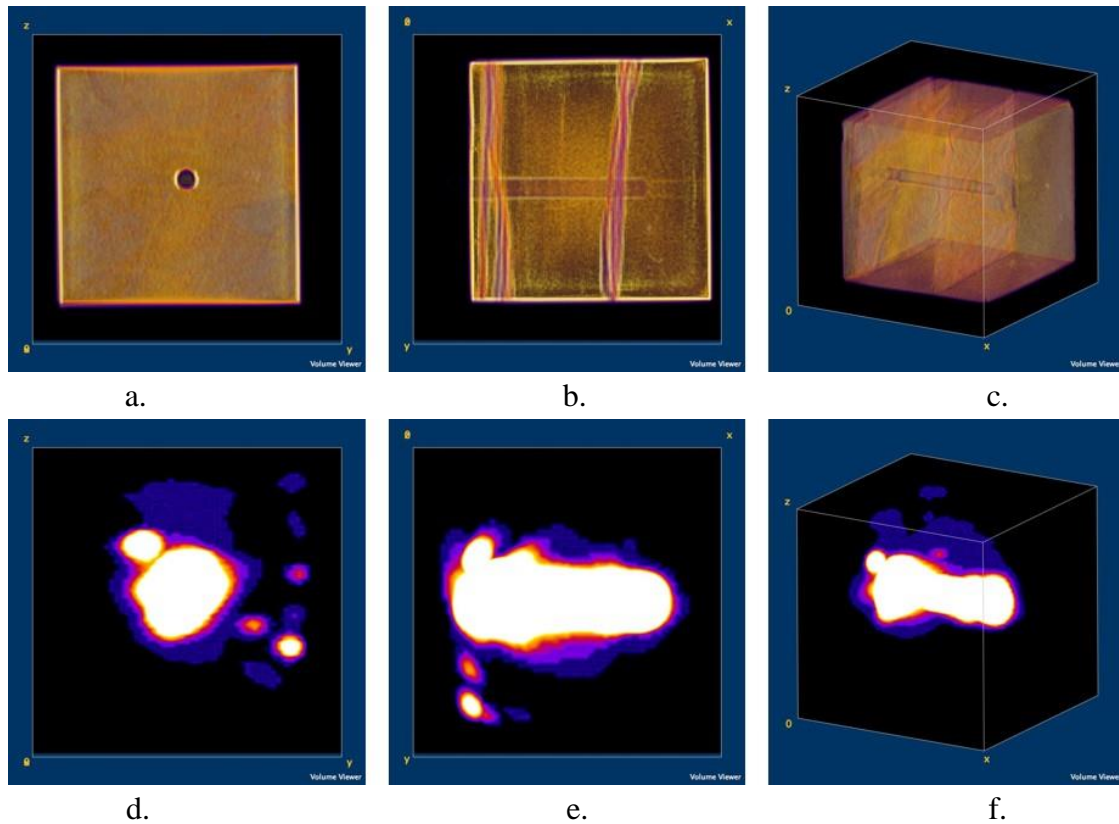


Figure 5.2.2 PET/CT scan of 4-inch Mancos shale block: a to c are from X-ray CT scan (to show locations), d to f from PET/CT imaging.

5.3 Optimization of CT Parameters and Method Improvement

We had expected to use X-ray CT (CT) to identify fractures in our shale and sandstone blocks, but initial tests did not show the thermally induced fractures. Fractures in the received shale and in many of our tests are often readily detectable by CT (**Figure 5.3.1**).

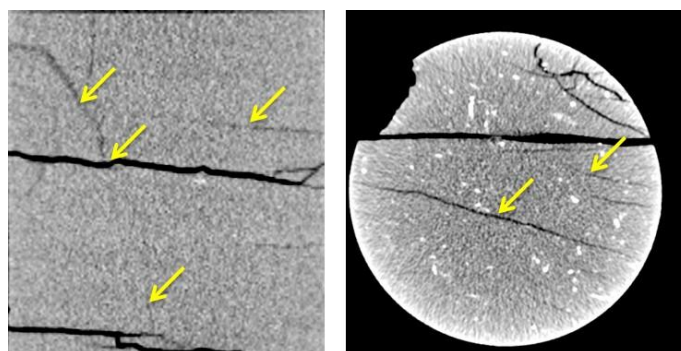


Figure 5.3.1 CT scan of 4-inch Mancos shale block (left) and 4.5-inch diameter Mont Terri Opalinus shale with darker shades indicating fractures (examples indicated by yellow arrows).

In collaboration with (and co-funded by) other projects needing similar information, we attempted many CT and imaging and image processing techniques to find fractures in glass blocks. The reason for using glass blocks is that fractures in glass are readily apparent, thus identifying the features to look for in the CT data in the natural samples. To optimize the CT parameters, a parametric study was performed. Scanning was performed at multiple energies, to identify differences between scans at different energies that would help identify the fractures. Scanning was performed in a sand-filled Styrofoam cylinder to minimize geometric “X” artifacts.

5.3.1 Energies and Currents

A 4-inch Mancos shale cube was placed in a cylindrical low-density Styrofoam holder and the four moon-shaped segments between the block and the cylinder were filled with silica sand (grain density 2.65 g/cm^3) in bags so that the sand was not in direct contact with the shale. X-rays at higher energies tend to penetrate denser objects better. Thus it is advantageous to increase X-ray flux through the object, however, higher energies can be less sensitive to sample density changes for the same reason. Current indicates the “brightness” of the X-rays. Brighter is better, but it comes at the cost of higher stress on the X-ray tube, which is a large fraction of the cost of a medical scanner-thus optimization is required. A 2-cm long region of the post-cryogenic fracturing tested shale block containing a known fracture set was scanned at 80 kV, 100 kV, 120 kV, and 140 kV at 200 mA current. In addition, the region was scanned at 120 kV energy at 160 mA, 240 mA, and 300 mA currents. A montage of 32 sequential 0.625-mm thick slices is shown in **Figure 5.3.2**, where the dark indicates low density, such as open space (fracture). A region of interest, the same for each set of scanning parameters, was selected and extracted from each data set, and each image brightness and contrast was set automatically resulting in the same gray distribution in each image. **Table 5.1** shows the images from the same location from each set of scans. This image corresponds to the third image down on the left in **Figure 5.3.2**.

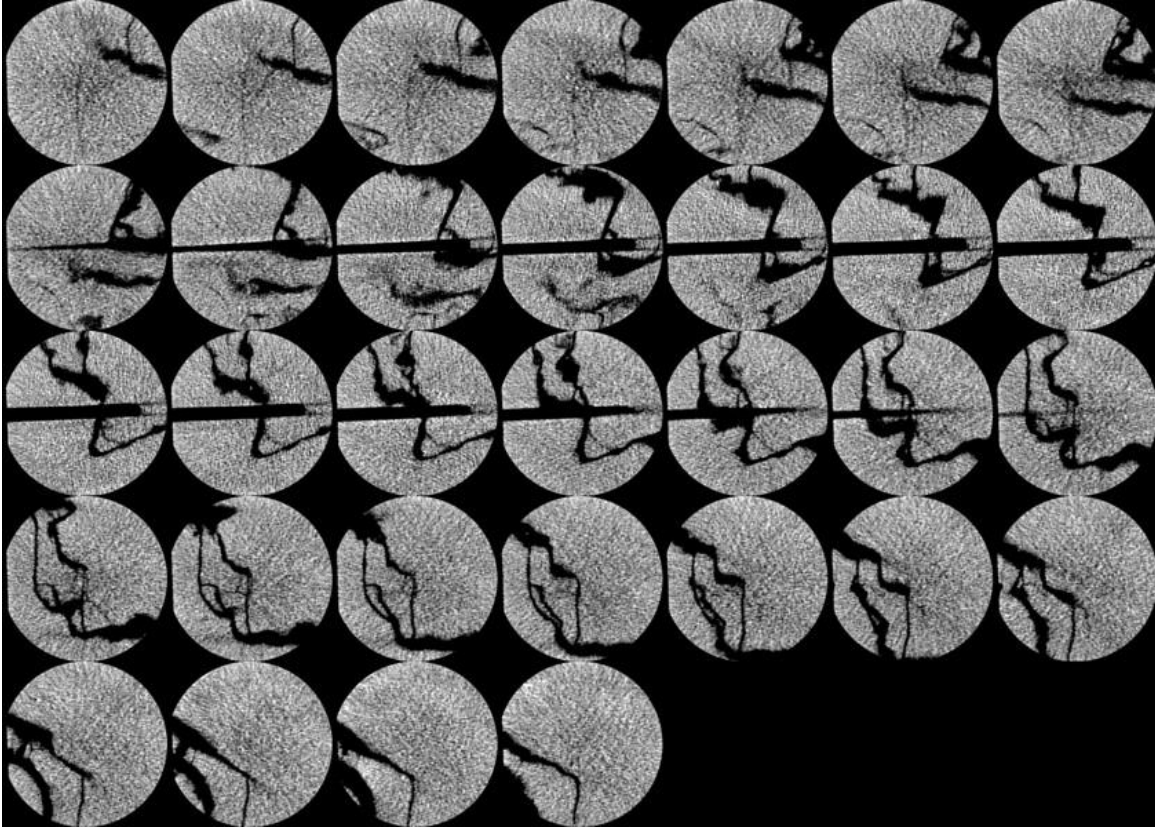


Figure 5.3.2 Montage of a sequence of images of fractured Mancos shale at 120 kV and 300 mA.

Looking across the second row from left to right in **Table 5.1** shows an increase in image quality from 80 to 120 kV. Over this range, the spatial scale of the noise decreases, making smaller features increasingly visible. There is a slight decrease in image quality from 120-140 kV (see fractures in lower right quadrant). Averaging the 120 kV and 140 kV scans yields a better image than either of the two individual images (**Figure 5.3.3** and **Figure 5.3.4**).

Images from top to bottom in **Table 5.1** (increasing current = increasing “brightness”) show an increase in image quality from 160 to 200 mA, and additional small gains with further current increases. Extracted numerical values (in Hounsfield units—each Hounsfield unit is about 0.001 g/cm^3) from the same region in the lower left unfractured portion of each image are presented in **Table 5.2**. As expected, the mean CT values decrease with increasing energy (increasing kV). This results in a slight reduction of the range of the measurements.

Additionally, the standard deviations decrease with increasing energy indicating less impact of the noise, but decreased sensitivity.

Table 5.1 CT slices of the same region under different energies (kV) and currents

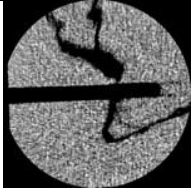
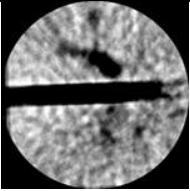
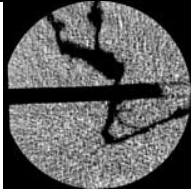
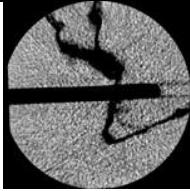
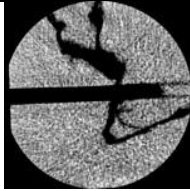
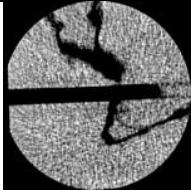
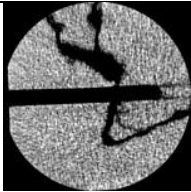
	80 kV	100 kV	120 kV	140 kV	Average 120 and 140 kV
160 mA					
200 mA					
240 mA					
300 mA					

Table 5.2 Numerical values from a region in the lower left of each image

Operating conditions	Mean	Standard deviation	Mode	Min	Max
80kV 200 mA	2128.157	160.578	2164	1639	2658
100kV 200 mA	1937.424	99.334	1924	1520	2310
120kV 200 mA	1777.722	85.579	1769	1489	2135
140kV 200 mA	1668.645	71.657	1675	1380	1960
120kV 160 mA	1761.479	91.785	1755	1443	2144
120 kV 240 mA	1759.094	73.233	1747	1460	2047
120 kV 300 mA	1761.697	63.164	1760	1521	2072
Average 120 kV and 140 kV 200 mA	1723.183	56.177	1721.285	1531.500	1941.500

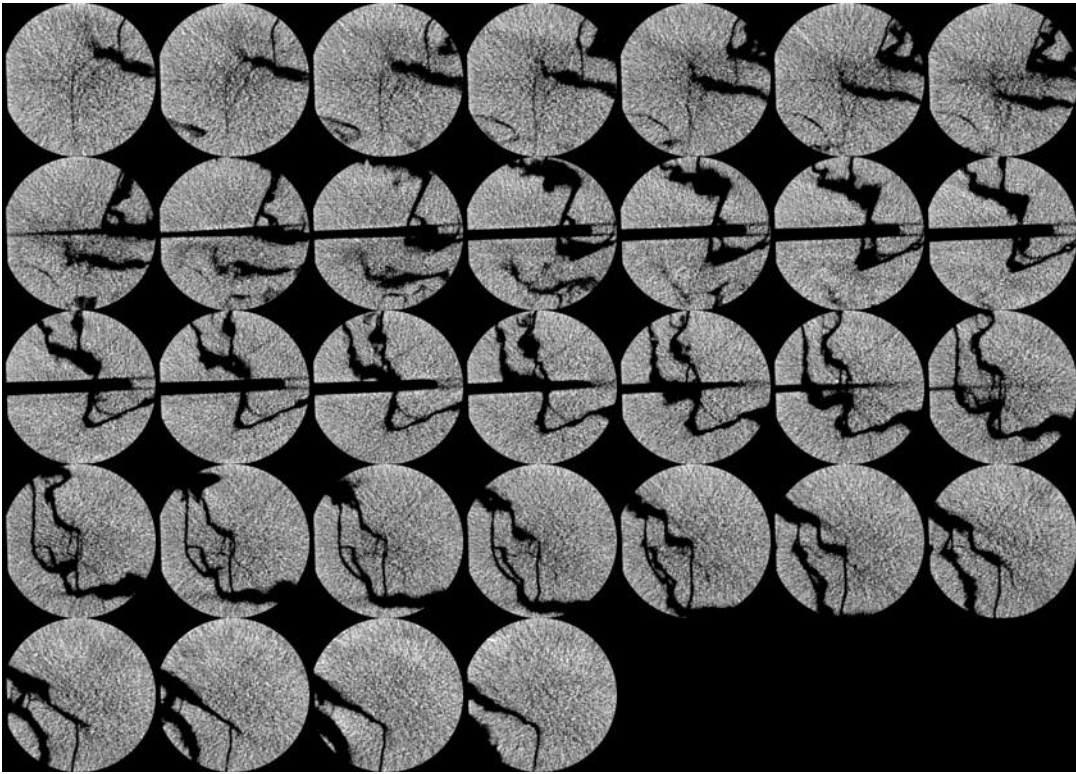


Figure 5.3.3 Average of 120 kV and 140 kV scans.

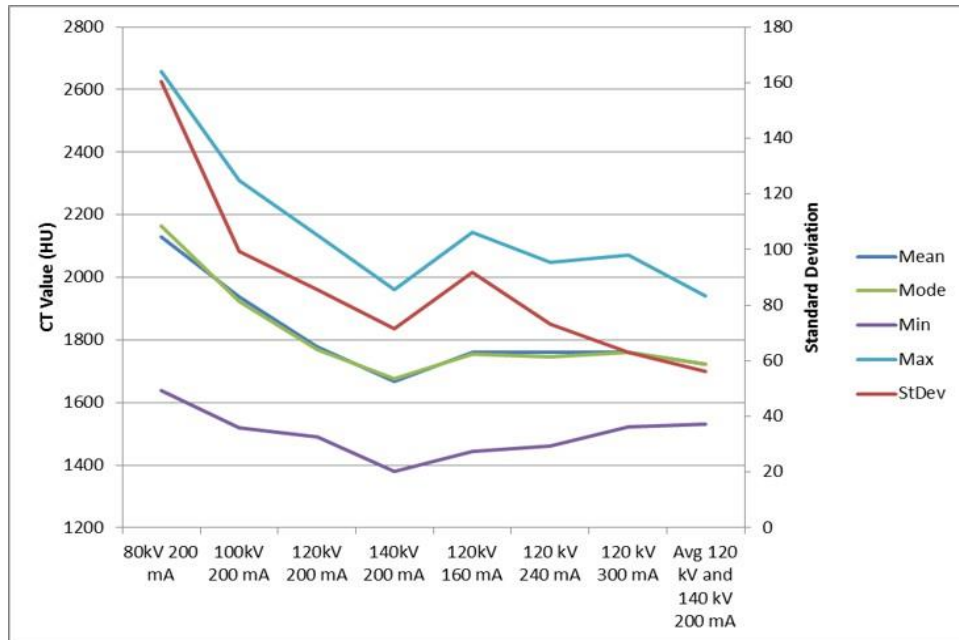


Figure 5.3.4 Plotted Hounsfield unit values for the selected region of interest for the different scanning conditions.

5.3.2 Averaging Scans

A region of the same shale block was scanned at 120kV and 160 mA for 5 times. The successive scans were then averaged and presented below (**Figure 5.3.5**, **Table 5.3** and **Figure 5.3.6**). A gray region in the lower left unfractured region was selected for analysis.

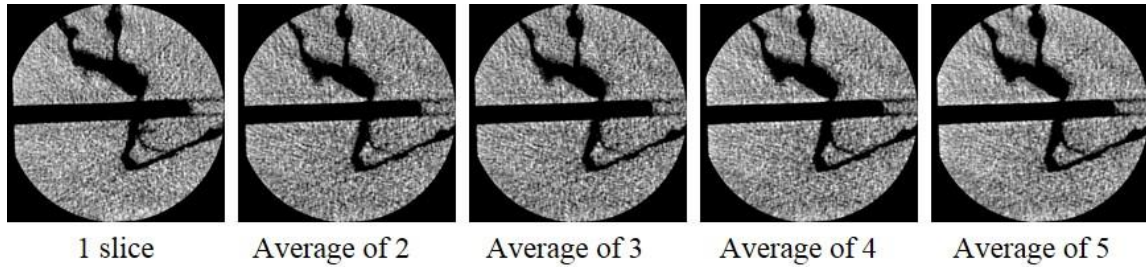


Figure 5.3.5 Five images averaged at 120 kV and 160 mA.

Table 5.3 Mean and standard deviation of the same region in the lower left of the images

Slice	Mean	Standard deviation
21-1	1760.401	97.416
21-2	1764.446	95.365
21-3	1761.414	98.269
21-4	1761.260	96.300
21-5	1763.618	99.920
Average 1-2	1762.424	68.493
Average 1-3	1762.087	57.444
Average 1-4	1761.880	49.887
Average 1-5	1762.228	45.171

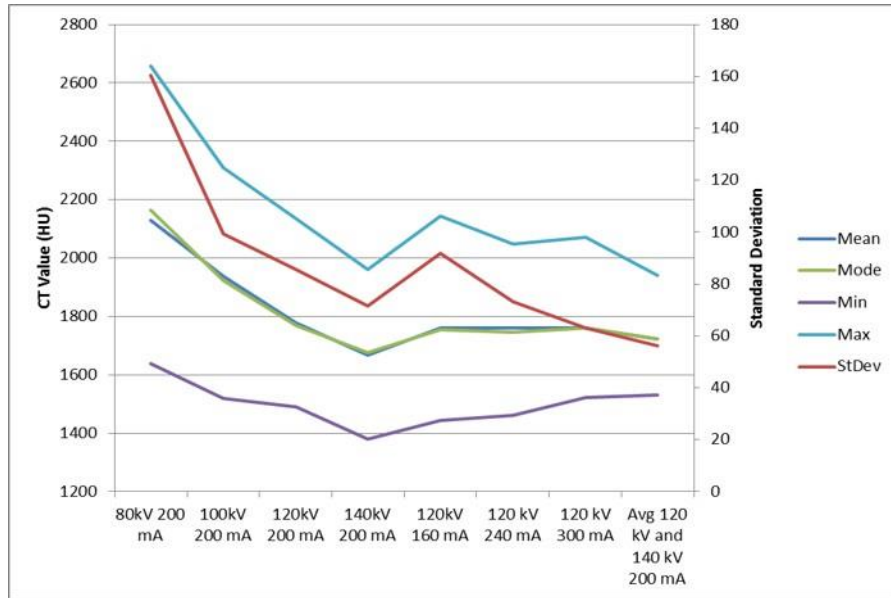


Figure 5.3.6 Plotted Hounsfield unit values for the selected region of interest for the different scanning conditions.

From these analyses, we learned that averaging scans reduces standard deviation improving image quality. In spite of that, the best resolutions from visual inspection were from the 120 kV/300 mA scan (brightest), and the average of the 120 kV/200 mA and the 140 kV/200 mA scans, with the latter being superior in detail and lowest in noise, and the average of multiple scans. Statistically, the resulting image from three averaged scans at 120 kV/160 mA was slightly superior to the average of the 140 kV and 120 kV scans, which was superior to the 120 kV/300 mA scan. In terms of X-ray tube use, however, the 120 kV/300 mA scan consumes fewer milliamp-seconds, and is likely more gentle on the tube for the quality of image.

5.3.3 Image Analysis Techniques

We performed a large number of analyses of CT data to identify fractures that were visible in the glass blocks. The objective was to identify visible fractures in the CT data, and translate the method to use with rock samples.

To progress with the analysis, we estimated the minimum aperture of a fracture that should be theoretically visible above the image noise. For a single set of scans at 120 kV and 200 mA, with voxel spacing of 200 microns (reasonable scanning parameters), we should be able

to detect 50 micron-wide fracture. In accepting that as a reasonable minimum, there have been instances where phase contrast and diffraction have identified much smaller apertures, although we have had difficulty quantifying them.

Numerous image-processing techniques were applied on many thermally fractured glass blocks (e.g. **Figure 5.3.7**). A number of blocks were fractured by pre-heating to a specified temperature and then rapidly quenching to room temperature. These blocks were fractured for another project, however are applicable to this project due to the thermal nature of fracturing. Some blocks were then brought to above the softening point reclosing some fractures and then allowed to cool slowly to room temperature. We also used laser-etched blocks and attempted to locate weakness plains in a number of blocks that had laser-induced internal fractures and fracture patterns. Because the laser-induced fracture patterns (similar to patterns in trophy glass) were emplaced as an assembly of tiny fractures composing planes of weakness, these did not significantly change the density of the glass in the location of the fracture, thus we could not locate them in the CT scans. Blocks with resealed fractures were also challenging, however larger fractures were still visible.

The inability to locate the thermally induced fractures in some samples is indicative of the apertures generated. For glass blocks, if a few fractures are formed and they are purely tensile with no shear displacement, closure of the fractures would be expected upon returning to normal conditions. Shear displacement would tend to keep the fractures open. From the thermally fractured glass blocks, some of which were fractured under the same temperature difference as cryogenic fracturing tests, many fractures were generated and fracture patterns were formed polygonal, similar to those in **Figure 4.1.3**. Because of the number of fractures formed and the polygonal geometry (e.g. **Figure 5.3.7**), the fractures remained open and were detectable by CT scanning. This helps to explain why multiple cryogenic treatments tend to result in higher permeability in rewarmed blocks as discussed in Section 4. The multiple treatments increased the fracture density, inducing some shear displacement between fracture surfaces keeping the fractures open.

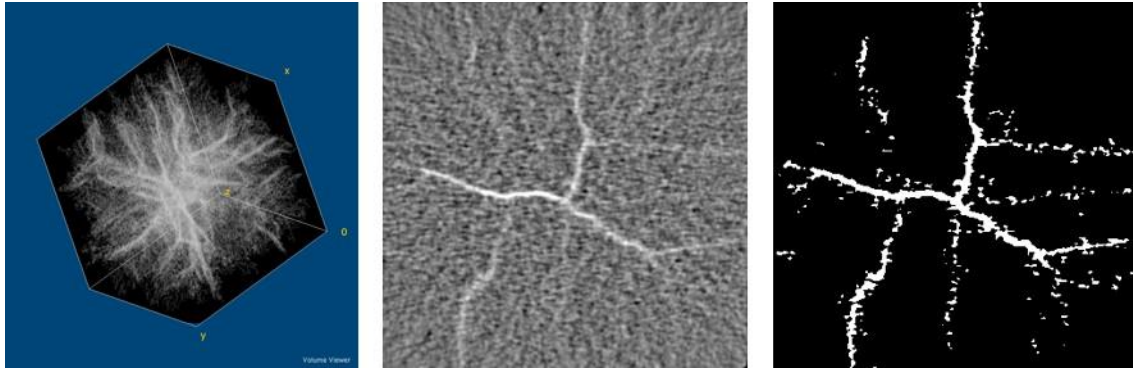


Figure 5.3.7 Left: Processed CT image showing fracture pattern in lighter colors. Center: CT cross section, right: fractures identified using Connected Component Analysis.

Most of our experiments use cubic samples, which typically have “X” artifacts in X-ray CT scanning (**Figure 5.3.8**). We have used four techniques to minimize these artifacts. The first technique is the data processing. After registering (aligning) the data stacks (a compilation of CT slices) so that the interesting portions of each image are properly aligned, a number of slices are averaged. It is desirable that these slices do not contain the features of interest, or the features are averaged out. This “average” slice is normalized, and then subtracted from the entire three-dimensional data set on a slice-by-slice basis. While this conceptually makes sense, some artifacts like the “X” artifacts have a random component, thus only a small improvement is made by subtracting out the averaged scan, but at the cost of some image clarity. This also applies to heterogeneity artifacts if the averaged slice still contains features; for example, a void in one slice will be averaged, but this average is carried through to slices without the void by the subtraction.

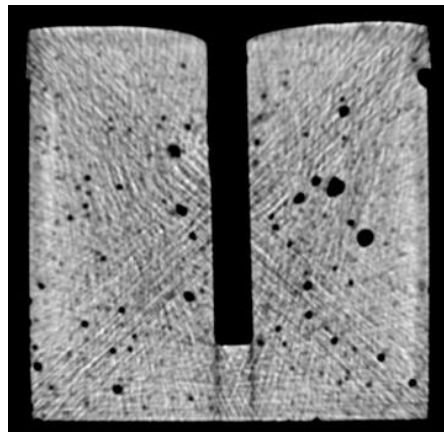


Figure 5.3.8 X-ray CT cross section of an 8-inch concrete block showing the “X” artifacts.

Another processing technique was used as well, in which the fast Fourier transform is taken of each image. Regions from the diagonals are cleared from the transformed image, and the inverse transform is applied (**Figure 5.3.9**). This method helps a little with these artifacts, but degrades the image because some good data are removed in the process.

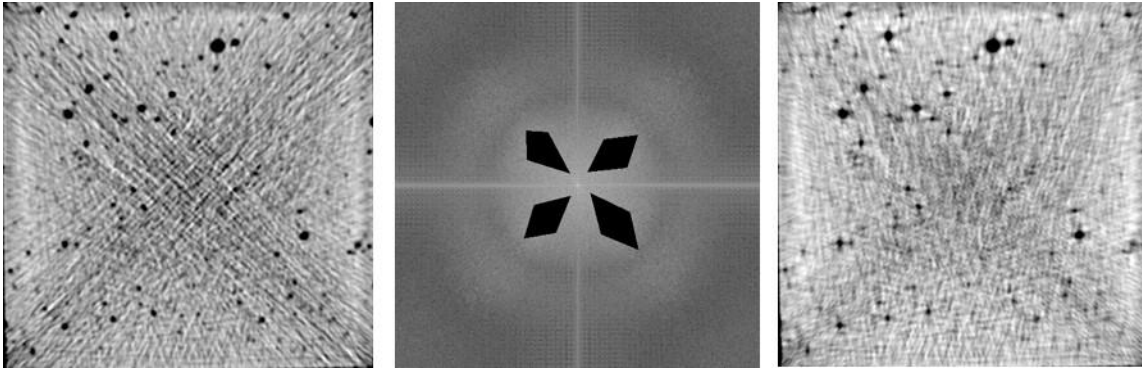


Figure 5.3.9 Left: initial image, center: fast Fourier transform of the initial image showing removed values, and right: inverted image. Note improvement of “X” artifacts, but loss of overall quality.

Data quality was improved by modifying the geometry of the sample. Since rectangular parallelepiped samples are required in our physical tests and cylindrical samples are optimal for CT scanning, two techniques have been used to “round” our samples. In the first technique, the sample is placed in a cylindrical low-density container. Plastic bags are placed in the interstitial segments between the block and the container, and they are filled with silica sand. This technique greatly improves the “X” artifacts. A second technique is to use “moon”-shaped pieces on four sides matching the sides of the block (**Figure 5.3.10**). Moons made from materials having similar density to the rock or glass also greatly reduce the “X” artifacts. Both of these techniques also reduce the X-ray flux through a sample at the cost of some image quality.

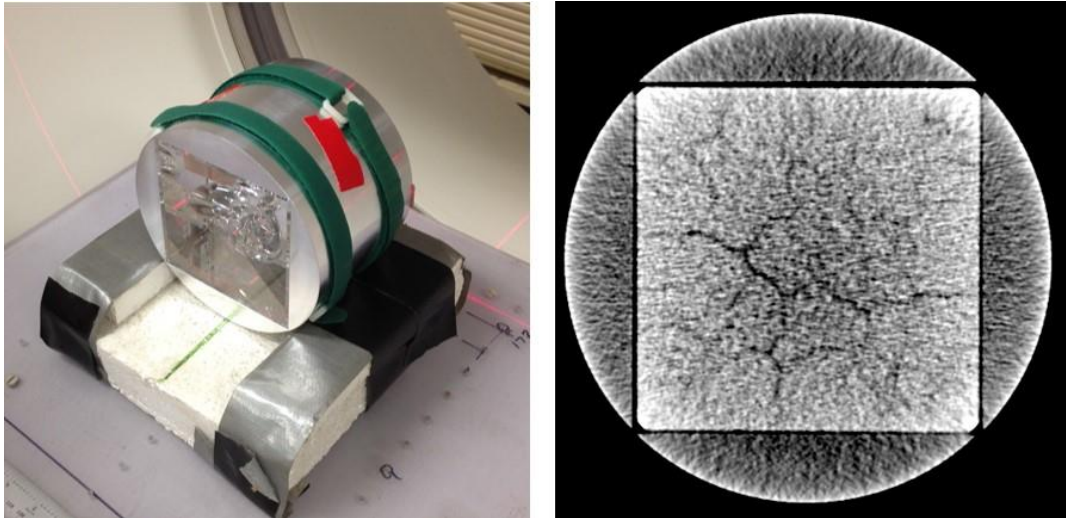


Figure 5.3.10 Left: 6061 aluminum “moons” around fractured glass sample, right: CT slice.

5.4 Micro-CT Sample Examination at the Advanced Light Source

Examination of fractures in glass blocks using synchrotron micro-computed tomography (Beamline 8.3.2. at the Advanced Light Source at Lawrence Berkeley National Laboratory) was attempted because voxel sizes as small as 0.5 microns on a side are achievable there, and the synchrotron provides a bright medium energy (~20-30 kV) X-ray source. Imaging was attempted using a 2-inch cryo-fractured glass block with known fractures. In spite of the bright X-rays, the imaging was unsuccessful because not enough X-ray flux passed through the sample to obtain a reasonable image. Typical samples imaged with this instrument are on the order of 1 cm diameter or less. The combination of large sample size and lower energy compared to the medical CT scanner reduced the effectiveness of the technique.

5.5 Summary

By optimizing the energies and currents of CT scanning, we determined optimized operation parameters for fracture detection in shale samples. These parameters enable us to detect 50-micron wide fractures. Improvements have been made in our X-Ray CT scan techniques and image processing to better characterize the fracture morphology in glass and shale samples by effectively reducing the CT artifacts.

6. Numerical Simulation

Numerical simulations for the cryogenic fracturing processes were conducted based on different numerical methods with different focuses on the physical processes involved. The finite element modeling uses COMSOL™ to evaluate the effect of thermal stresses during the cryogenic fracturing treatment. The finite difference modeling modifies TOUGH2-EGS (Enhanced Geothermal System) to simulate cryogenic fracture distribution along with fluid and heat flow under different stress conditions (Wu et al., 2014, Zhang et al., 2012a, 2012b, 2016). By combining the results from both approaches, the mechanisms of cryogenic fracturing can be more clearly demonstrated.

6.1 Finite Element Modeling

The finite element method (FEM) is a numerical technique for finding approximate but reasonably accurate solutions of boundary value practical engineering problems. A boundary value problem (sometimes referred to as a field problem) is a mathematical problem where one or more dependent variables (are referred to as field variables) must fulfill a differential equation within the domain of independent variables that are already known and also fulfill a specific condition on the boundary of that domain (Hutton 2004).

In FEM, the physical domain is divided into elements, which are generally geometric shapes such as squares, triangles, quadrilaterals, tetrahedrons, etc. This process is known as “meshing”. The mesh size affects the accuracy of the post-processing in terms of the converging of the finite element solution to the exact solution. Such a situation is shown in **Figure 6.1.1a**, where a curved boundary domain is meshed coarsely using square elements. A refined mesh for the same domain is shown in **Figure 6.1.1b**, using smaller, more numerous elements of the same shape (Hutton 2004).

The finite elements will then be reconnected at nodes which are the points at which the value of the field variable is to be explicitly calculated. The exterior nodes are located at the boundaries of the finite element and they connect an element to the adjoining finite elements;

while the interior nodes do not depend on the element boundaries and cannot be connected to any of the other elements (**Figure 6.1.2**).

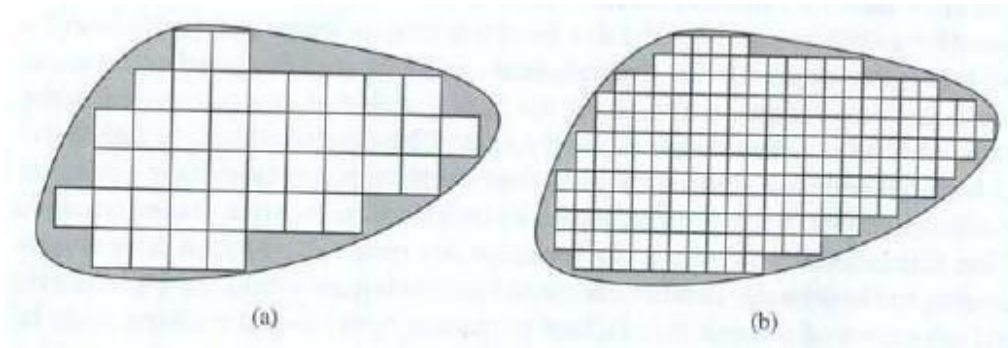


Figure 6.1.1 (a) Arbitrary curved boundary domain modeled using square elements. Grey areas are not included in the model. (b) Refined finite element mesh showing reduction of the area not included in the model on the left. Adapted from Hutton (2004).

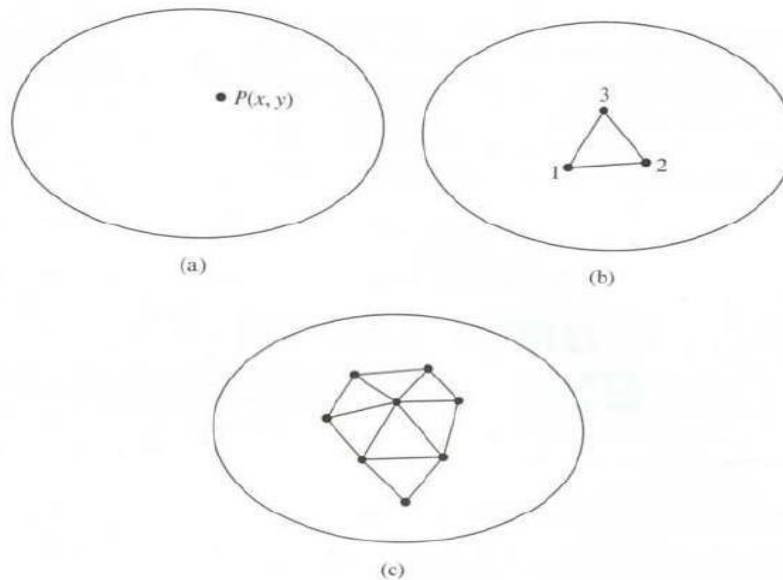


Figure 6.1.2 (a) A general two-dimensional domain of field variable. (b) A three-node finite element defined in the domain. (c) Additional element showing a partial finite element meshes of the domain. Adapted from Hutton (2004).

6.1.1 Theoretical Analysis

There are a number of approaches to solve linear and non-linear boundary value problems ranging from completely analytical to numerical as follows:

- 1) Direct integration;
- 2) Approximate solutions, including: power series, method of weighted residuals (MWR), Ritz method, and FEM.

For a few problems, it is possible to obtain an exact solution by direct integration of the differential equation. This can be accomplished by an obvious separation of variables or by applying a transformation that makes the variables separable and leads to a similarity solution. However, Fourier and Laplace transformations of differential equations can lead to exact solutions (Huebner et al. 2001).

The Ritz method and the MWR are common methods for getting the approximate solutions to the boundary value problems. Ritz method has been used to derive the equations of the FEM to find solutions to variational problems. However, in many practical problems, the classical variational principles are unknown and hence the MWR is used in many applications where FEM is the chosen numerical technique for general procedures (Huebner et al. 2001).

The MWR is an approximation technique for solving the partial differential equations. It uses trial functions that satisfy the boundary conditions for the model domain. The method is applied as follows (Hutton, 2004):

General form of a differential equation is,

$$D[y(x), x] = 0, \quad a < x < b$$

The boundary conditions are,

$$y(a) = y(b) = 0$$

MWR looks for approximation solution for the differential equation,

$$y^*(x) = \sum_{i=1}^n c_i N_i(x)$$

Where y^* is the approximate solution to the boundary value problem and $N_i(x)$ is the trial functions. However, this equation does not give any exact solution. By substitution of assumed solution into the general form of the differential equation, residual error $R(x)$ is,

$$R(x) = D[y^*(x), x] \neq 0$$

$R(x)$ is also a function of c_i . The unknown parameter c_i will be evaluated as it is required for MWR,

$$\int_a^b w_i(x) R(x) dx = 0, \quad i = 1, n$$

Where w_i is a weighting function.

The MWR issues many variations, and techniques differ in how weighting factors are selected. Galerkin's method is the most common technique used to select or determine the weighting factors (Hutton 2004).

In this method, the weighting functions are chosen to be similar to the trial functions,

$$w_i(x) = N_i(x), i = 1, n$$

As a result, the unknown parameters can be solved,

$$\int_a^b w_i(x)R(x)dx = \int_a^b N_i(x)R(x)dx = 0$$

which results in "n" algebraic equations for estimating all the unknowns (Hutton 2004).

Specific steps in formulating a finite element analysis of a physical problem are common to all such analyses, whether structural, heat transfer, fluid flow, or some other problems. The steps are pre-processing, solution, and post-processing.

The pre-processing (defining the model) includes these components (After Hutton 2004):

- Define the geometric domain of the problem;
- Define the element types to be used;
- Define the material properties of the elements;
- Define the geometric properties of the elements;
- Define the element connectivity;
- Define the physical constraints; and,
- Define the loadings.

To search for the solution, the finite element software assembles all the governing equations in a matrix form then computes the unknown values of the field variables. Then the computed values will be used by back substitution to compute additional derived variables (Hutton 2004).

Post-processing software has a complex procedure to evaluate the solution results from the previous step. This complex procedure was used for organizing and plotting the selected results. An example of operations that can be done include (Hutton 2004):

- Sort element stresses in order of magnitude;
- Check equilibrium;
- Calculate factors of safety;
- Plot deformed structural shape; and,
- Animate dynamic model behavior.

After the post-processing, the key is applying the engineering judgment to evaluate if the results solved are reasonable or not (Hutton 2004).

6.1.2 Problem Setup

This section describes defining the physics of the various block models in COMSOL Multiphysics 3.5a, constructing the model, the input parameters and boundary conditions, creating the finite element mesh, and solving the problem. The methodology for performing the FEM study is given in the flow chart shown in **Figure 6.1.3**.

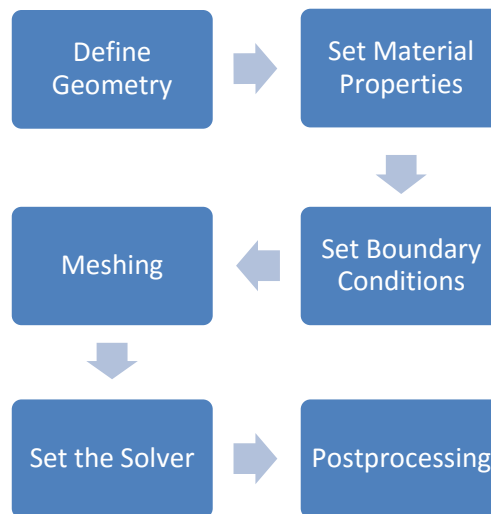


Figure 6.1.3 Flow chart for the FEM using COMSOL Multiphysics 3.5a software.

6.1.2.1 Geometry

To initiate the study, nine basic block systems were created and included a single layer homogeneous concrete, with a 6-inch long wellbore, cased 6-inch long wellbore, and an 8-inch long wellbore (Systems 1-3); a single layer homogeneous sandstone, with a 6-inch long

wellbore, cased 6-inch long wellbore, and an 8-inch long wellbore (Systems 4-6); and a multilayered system, such as a shale system, with a 6-inch long wellbore, cased 6-inch long wellbore, and an 8-inch long wellbore (Systems 7-9). For the multilayered system, a composite geometry object was created by joining together the layers. These base models were built using the Structural Mechanics module with Thermal Expansion in the COMSOL software, which combines solid, stress-strain with heat transfer by conduction, and also includes thermal expansion in the structural loads using the temperature field. This model can simulate the laboratory conditions during the cryogenic tests. The details of each different rock type are summarized in **Table 6.1**. There are three different types of wellbore. The open hole is assumed to be without casing attached to the rock media in the wellbore, as shown in **Figure 6.1.4** and **Figure 6.1.7**. The cased hole is cased with 2" long and 0.083" thick stainless steel at the top of the wellbore, as shown in **Figure 6.1.5** and **Figure 6.1.8**. The through borehole is an 8" long wellbore completely going through the rock sample, as shown in **Figure 6.1.6** and **Figure 6.1.9** show. The shale sample is designed to simulate layered, heterogeneous nature of the shale rocks. There are 12 layers in vertical direction (z-direction), consisting siltstone, clay, and limestone, as shown in **Figure 6.1.7-Figure 6.1.10**. **Table 6.2** lists all input data for material properties of all rock block models.

Table 6.1 Rock block model input parameters for different rock types

Rock type	Dimensions	Wellbore properties		
		Open hole	Cased hole	Through borehole
Concrete	x = 8", y = 8", z = 8"	r = 1", length = 6"	r = 1", length = 6", length of casing = 2" (from the top), thickness 0.083"	r = 1", length = 8"
Sandstone	x = 8", y = 8", z = 8"	r = 1", length = 6"	r = 1", length = 6", length of casing = 2" (from the top), thickness 0.083"	r = 1", length = 8"
Shale	x = 8", y = 8", z = 12 sublayers × 8/12"	r = 1", length = 6"	r = 1", length = 6", length of casing = 2" (from the top), thickness 0.083"	r = 1", length = 8"

Table 6.2 Input data for material properties of all rock block models

Material Type	Material Properties
Concrete	E = 3,625,943 psi
	$\nu = 0.33$
	$\rho = 2.3 \text{ gm/cc}$
	$\alpha = 5.556 \times 10^{-6} \text{ 1/ }^\circ\text{F}$
	$k = 1.8 \text{ W/(m}\cdot\text{K)}$
	$C_p = 4950.4 \text{ (lbf}\cdot\text{ft)/(slug}\cdot\text{ }^\circ\text{F)}$
Sandstone	E = 6,279,966 psi
	$\nu = 0.2$
	$\rho = 2.6 \text{ gm/cc}$
	$\alpha = 6.3 \times 10^{-6} \text{ 1/ }^\circ\text{F}$
	$k = 4.2 \text{ W/(m}\cdot\text{K)}$
	$C_p = 5507.7 \text{ (lbf}\cdot\text{ft)/(slug}\cdot\text{ }^\circ\text{F)}$
Siltstone	E = 1,015,258 psi
	$\nu = 0.2$
	$\rho = 2.24 \text{ gm/cc}$
	$\alpha = 5 \times 10^{-6} \text{ 1/ }^\circ\text{F}$
	$k = 2.8 \text{ W/(m}\cdot\text{K)}$
	$C_p = 5507.7 \text{ (lbf}\cdot\text{ft)/(slug}\cdot\text{ }^\circ\text{F)}$
Clay	E = 5,511,434 psi
	$\nu = 0.4$
	$\rho = 2.13 \text{ gm/cc}$
	$\alpha = 3.3 \times 10^{-6} \text{ 1/ }^\circ\text{F}$
	$k = 1.9 \text{ W/(m}\cdot\text{K)}$
	$C_p = 5507.7 \text{ (lbf}\cdot\text{ft)/(slug}\cdot\text{ }^\circ\text{F)}$
Limestone	E = 4,351,276 psi
	$\nu = 0.25$
	$\rho = 2.72 \text{ gm/cc}$
	$\alpha = 4.4 \times 10^{-6} \text{ 1/ }^\circ\text{F}$
	$k = 3.0 \text{ W/(m}\cdot\text{K)}$
	$C_p = 5428.8 \text{ (lbf}\cdot\text{ft)/(slug}\cdot\text{ }^\circ\text{F)}$
Stainless steel (316) casing	E = 28,644,950 psi
	$\nu = 0.27$
	$\rho = 8.03 \text{ gm/cc}$
	$\alpha = 29.7 \times 10^{-6} \text{ 1/ }^\circ\text{F}$
	$k = 15.0 \text{ W/(m}\cdot\text{K)}$
	$C_p = 2302.28 \text{ (lbf}\cdot\text{ft)/(slug}\cdot\text{ }^\circ\text{F)}$

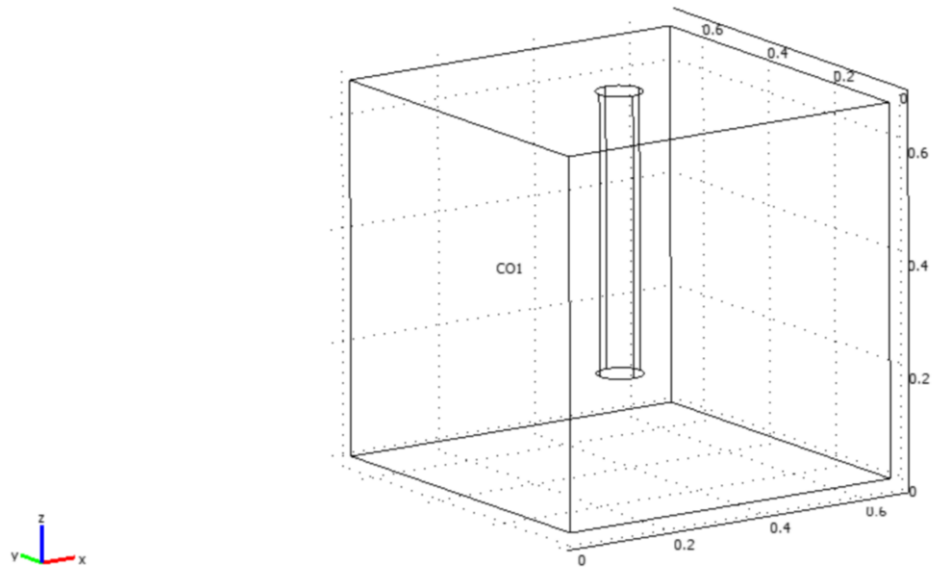


Figure 6.1.4 Model geometry for concrete and sandstone blocks with a 6-inch wellbore from COMSOL Multiphysics 3.5a. The scale is in feet.

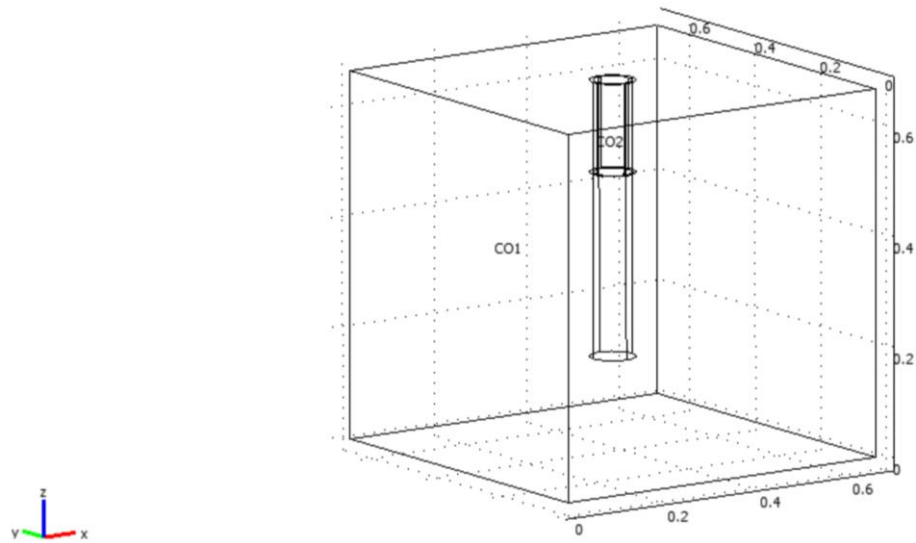


Figure 6.1.5 Model geometry for concrete and sandstone blocks with a cased 6-inch wellbore from COMSOL Multiphysics 3.5a. The scale is in feet.

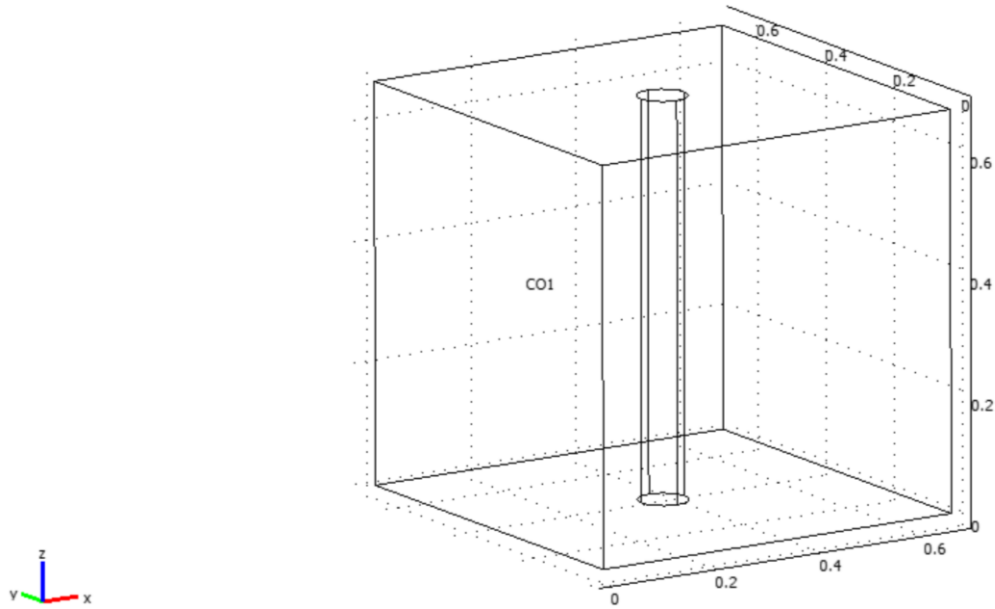


Figure 6.1.6 Model geometry for concrete and sandstone blocks with an 8-inch wellbore from COMSOL Multiphysics 3.5a. The scale is in feet.

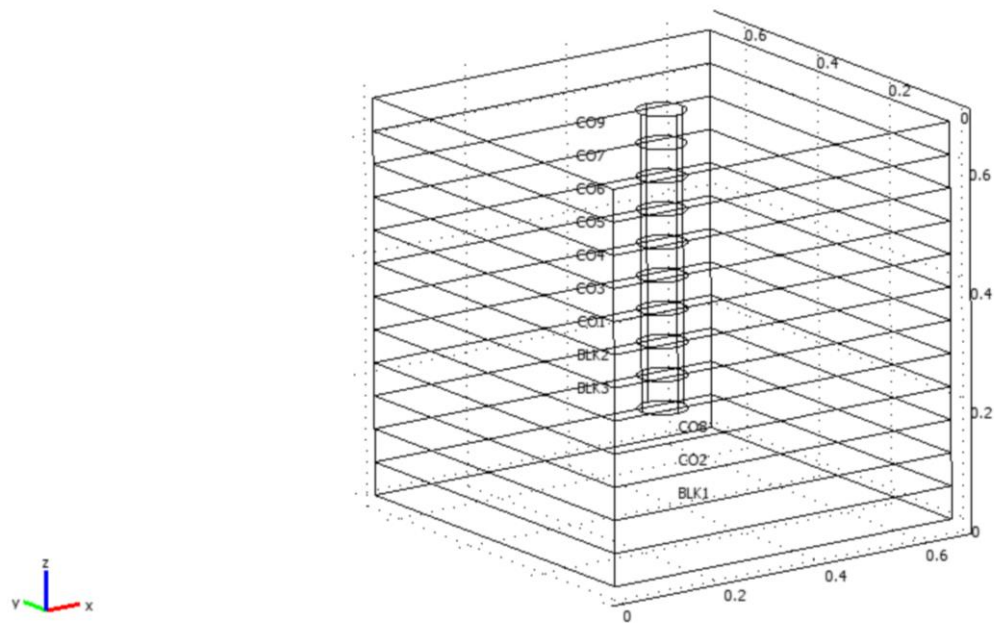


Figure 6.1.7 Model geometry for multilayered shale block with a 6-inch wellbore from COMSOL Multiphysics 3.5a. The scale is in feet.

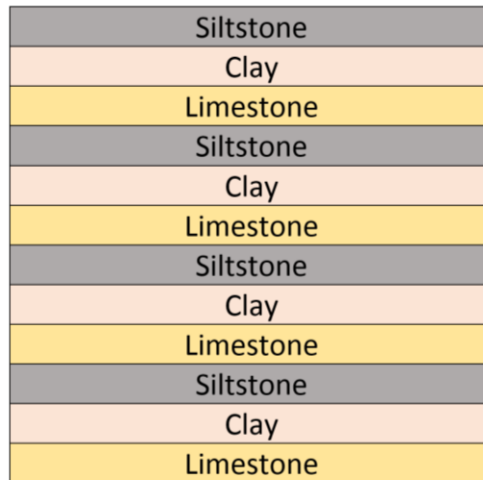


Figure 6.1.10 Multilayered shale block model (12 sublayers) constructed with alternating layers of siltstone, clay, and limestone.

6.1.2.2 Boundary Conditions

Table 6.3 shows the different boundary conditions that have been used in COMSOL Multiphysics 3.5a for various models (English unit system). It is worth mentioning that the stresses in this software called σ_1 , σ_2 , and σ_3 are equal to σ_x , σ_y , and σ_z , respectively. The equations for radial and tangential stresses were manually input into the model. The σ_x , σ_y , and σ_z values for the different test conditions were then used to find and plot the magnitude variations of radial and tangential stresses using the COMSOL model. These eight boundary conditions include:

- 1) All faces of a block model are free except the bottom of the block is roller boundary condition. The wellbore temperature is the LN₂ boiling point (-321 °F) and the outer faces are room temperature (70 °F). The intent is to see how this affects the results such as the principal stresses or displacement values.

- 2) Identical to Case 1, except the outer faces are reservoir temperature (200 °F). The intent is to see how this affects the results such as the principal stresses or displacements values by increasing the value of the temperature gradient.

3) All faces of a block model are constrained except for the top of the block, with 2000 psi applied as an overburden stress. As in Case 1, the wellbore temperature is the LN₂ boiling point (-321 °F) and the outer faces are room temperature (70 °F). The intent of this case is to calculate the second and third principal stresses (σ_2 and σ_3) and how they will be affected by introducing the thermal stresses.

4) Same conditions as Case 2, but all faces of a block model are constrained except the top of the block. The intent of this case is to calculate the second and third principal stresses (σ_2 and σ_3) and how they will be affected by introducing the thermal stresses and increasing the temperature gradient.

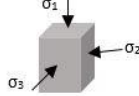
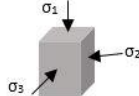
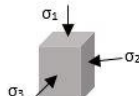
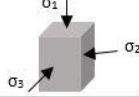
5) This case represents 3D triaxial stresses ($\sigma_1 \neq \sigma_2 = \sigma_3$). Stresses are applied on opposite faces of each of the three directions. The wellbore temperature is the LN₂ boiling point (-321 °F) and the outer faces are room temperature (70 °F).

6) Same as Case 5, except the outer faces are reservoir temperature (200 °F).

7) This case represents 3D triaxial stresses ($\sigma_1 \neq \sigma_2 \neq \sigma_3$). Stresses are applied on opposite face of each of the three directions. The wellbore temperature is the LN₂ boiling point (-321 °F) and the outer faces are room temperature (70 °F).

8) Same as Case 7, except the outer faces are reservoir temperature (200 °F).

Table 6.3 Summary of cases run, stresses applied and temperature

Cases		Concrete			Sandstone			Shale			Drawing
		6 in	Cased 6 in	8 in	6 in	Cased 6 in	8 in	6 in	Cased 6 in	8 in	
1	No applied stresses (Room temperature)	X	X	X	X	X	X	X	X	X	$\sigma_1 = \sigma_2 = \sigma_3 = 0$ psi $T = 70$ °F 
2	No applied stresses (Reservoir temperature)	X	X	X	X	X	X	X	X	X	$\sigma_1 = \sigma_2 = \sigma_3 = 0$ psi $T = 200$ °F 
3	Uniaxial stresses (Room temperature)	X	X	X	X	X	X	X	X	X	$\sigma_1 = 1000$ psi $\sigma_2 = \sigma_3 = 0$ psi $T = 70$ °F 
4	Uniaxial stresses (Reservoir temperature)	X	X	X	X	X	X	X	X	X	$\sigma_1 = 1000$ psi $\sigma_2 = \sigma_3 = 0$ psi $T = 200$ °F 
5	Triaxial stresses (Room temperature)	X	X	X	X	X	X	X	X	X	$\sigma_1 = 2500$ psi $\sigma_2 = \sigma_3 = 1000$ psi $T = 70$ °F 
6	Triaxial stresses (Reservoir temperature)	X	X	X	X	X	X	X	X	X	$\sigma_1 = 2500$ psi $\sigma_2 = \sigma_3 = 1000$ psi $T = 200$ °F 
7	Polyaxial stresses (Room temperature)	X	X	X	X	X	X	X	X	X	$\sigma_1 = 8000$ psi $\sigma_2 = 6000$ psi $\sigma_3 = 4000$ psi $T = 70$ °F 
8	Polyaxial stresses (Reservoir temperature)	X	X	X	X	X	X	X	X	X	$\sigma_1 = 8000$ psi $\sigma_2 = 6000$ psi $\sigma_3 = 4000$ psi $T = 200$ °F 

6.1.2.3 Meshing

The process of representing a physical domain with finite elements is called “meshing”. Since most of the commonly used mesh element geometries have straight edges, it is impossible to include the entire physical domain in the element mesh if the domain includes curved boundaries.

In such a situation, where the physical domain is meshed rather coarsely, mesh refinement is needed, i.e. smaller but more numerous elements of the same type are used. A refined mesh includes more of the physical domain in the finite element representation and boundaries are more closely approximated. As the number of elements is increased and the physical dimensions of the elements are decreased, the finite element solution changes incrementally. The incremental changes decrease with the mesh refinement process and approach or converge to the exact solution (Hutton 2004). A refined mesh will more closely represent the exact solution, but initially some limitations are faced due to the increasing associated time and computer memory requirements for solving the problem.

All the models were meshed using a “normal” mesh size. Sometimes we face some problems with the memory size of the computer that was used in this study. However, one way to get around the memory utilization problem is to use a different type of solver. For this study, linear type analysis, COMSOL Multiphysics 3.5a offers various types of solvers which are explained in the next section.

In COMSOL Multiphysics 3.5a, one can choose from a variety of mesh sizes: extra coarse, coarser, coarse, normal, fine, finer, and extra fine. There are two major modes of mesh generation, which are “mapped meshing” and “free meshing”. Mapped meshing provides great flexibility in element selection as well as control over mesh density. Free meshing permits mesh generation within any random shape but one has to give up on solution accuracy. Free meshing was used for this study with the meshing element being a tetrahedron for the layer subdomain (inside body) and triangles for the layer faces (boundaries). **Figure 6.1.11** shows the free meshed block for the shale block model with a cased wellbore.

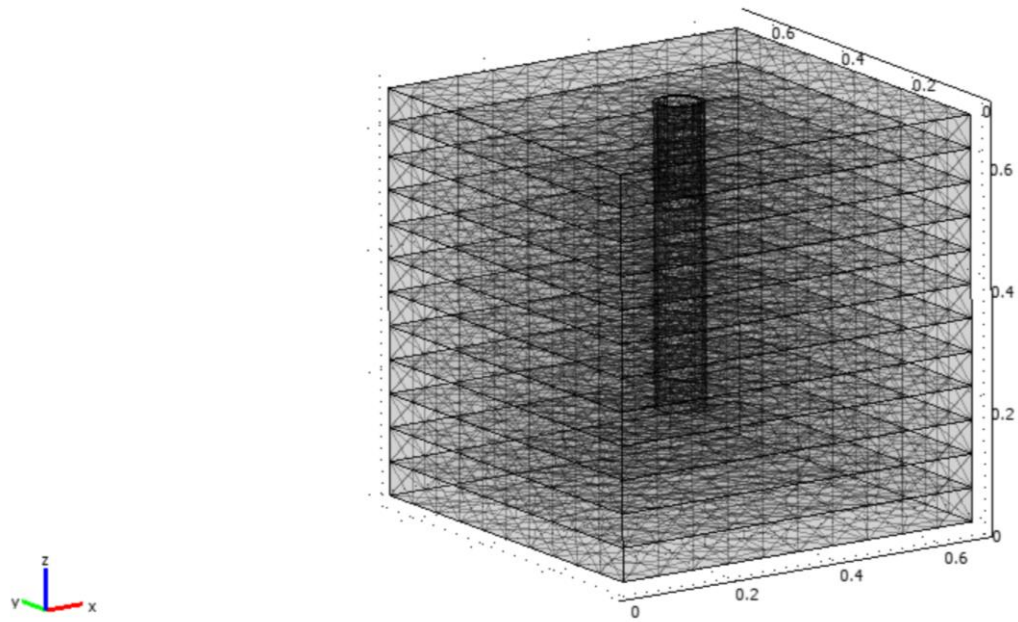


Figure 6.1.11 Multilayered shale block model with a 6-inch cased wellbore with a “normal” size mesh from COMSOL Multiphysics 3.5a.

6.1.2.4 The Solver

The solver technique used for this study was linear type analysis. COMSOL Multiphysics 3.5a offers various types of solvers which are considered as direct solvers. Direct solvers are often fast, but require more computer memory.

COMSOL Multiphysics 3.5a has many different direct linear system solvers, including Direct (UMFPACK), Direct (SPOOLES), Direct (PARDISO), Direct (PARDISO out of core), Direct Cholesky (TAUCS), GMRES, FGMRES, Conjugate gradients, BiCGStab, and Geometric multigrid. These linear solvers range from easy to complex, which will affect the time to solve these problems and require different computer memory sizes. On the other hand, mesh size will also impact the choice of the appropriate linear system solver.

For this study, “Direct (UMFPACK)” and “Direct (SPOOLES)” were used as linear system solvers for all stationary and time-dependent problems. The analysis types for Solid, Stress-Strain and General Heat Transfer are on the Transient mode.

6.1.2.5 Post-Processing

After drawing the block model, defining the problem, inputting the material properties and boundary conditions, and applying the appropriate mesh, the solver parameters were set to solve the problem. After an iterative process of choosing various combinations of mesh type and solvers, a “normal” mesh size and a direct linear system solver (type: Direct “UMFPACK” or “SPOOLES”) gave a converged solution, and the computer did not run out of memory while solving the problem. The models were reset every time after the solver solved the problem to obtain a new set of results. The results of the simulations were then analyzed using numerous 3D post-processing and visualization tools available in COMSOL Multiphysics 3.5a.

The following plots are available for post-processing and visualization for 3D problems which can be selected from the post-processing plot parameters window in COMSOL Multiphysics 3.5a:

- Slice
- Isosurface
- Subdomain
- Boundary
- Edge
- Arrow
- Streamline
- Particle tracing
- Max/min marker
- Deformed shape
- Geometry edges
- Combination of above

Cross section plots can be used to visualize a quantity as a family of plots in a plane, line or in a set of points in time along a parametric solution. In addition, animation can be used to provide a very clear picture for the time-dependent problems, showing how all different principal stresses change with time.

6.1.3 Results

This section presents the results and observations obtained for different models that were investigated using the COMSOL Multiphysics 3.5a simulator. The rock geometry models investigated consist of a one-layer cement block, a one-layer sandstone block, and a twelve-layer shale block model. The simulation results for various cases are presented.

To analyze the temperature, stress, and displacement for various cases, cross section, slice, subdomain, deformed shape and animation plots were used since they are optimal in terms of visualizing stress contrasts, deformed geometry and displacement in the stressed homogenous and layered rock blocks. The pre-defined quantities used for plotting and post-processing as part of the structural mechanics-solid stress and heat transfer by conduction modules, include (a) x, y and z displacements, (b) total displacement, (c) σ_x , σ_y and σ_z principal stresses, (d) τ_{xy} , τ_{yz} , and τ_{xz} shear stresses, (e) temperature, and (f) radial and tangential stresses, and (g) radial and tangential stresses. Several single and multiple slice plots were taken in 2D planes parallel to either the XY, XZ, or YZ-plane to help visualize the stresses inside the blocks with the defined loading and constraints on the boundaries.

6.1.3.1 Concrete Samples

In this section, the results and the observations for the homogeneous block models of concrete, with 6-inch open and cased wellbores, and an 8-inch open hole are presented.

6.1.3.1.1 Concrete Sample with a 6-inch Open Hole

Figure 6.1.12 shows the total displacement on the YZ-plane when there are no stresses applied and the outside boundary temperature is the room temperature and the wellbore temperature for all cases is -321 °F. Displacement in the deformed shape are in inches. The block deformed inward toward the center causing the top part of the wellbore to be smaller and tighter than the rest of the wellbore.

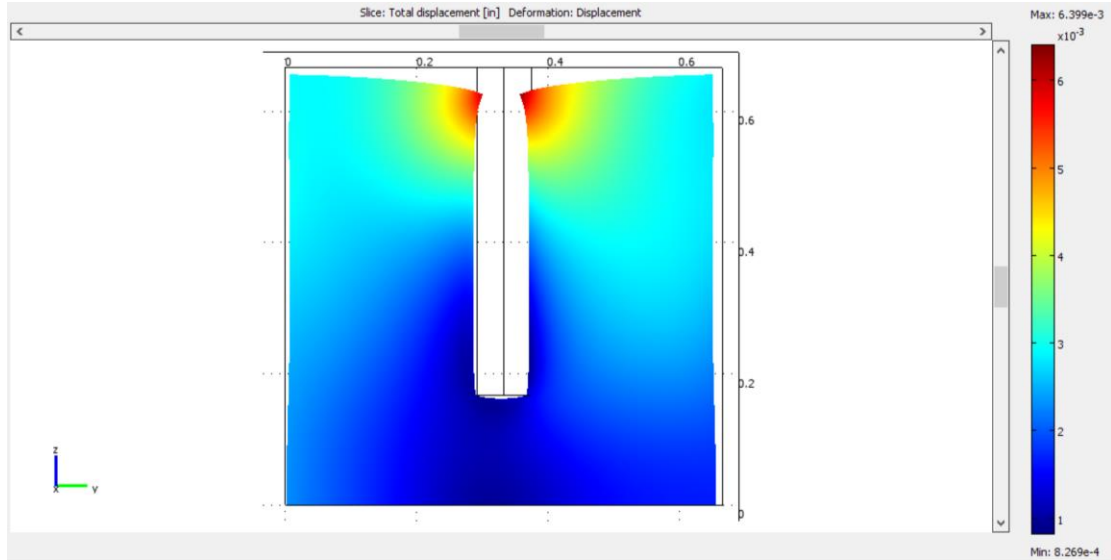


Figure 6.1.12 2D deformed shape plot for -321 °F borehole, no external stress applied and room temperature (70 °F) concrete block. More deformation was observed at the top side of the block and reducing the diameter of the wellbore (deformation is exaggerated for easy observation).

Figure 6.1.13 again shows the total displacement on YZ-plane as in **Figure 6.1.12**, when the outside boundary temperature of the reservoir has been increased to 200 °F. As before, the block deformed inward toward the center. However, in comparison with the room temperature example, the outside boundary is expanding due to the heat and the wellbore is shrinking due to the cryogenic temperature.

Figure 6.1.14 shows the 3D deformed shape plot for unstressed and reservoir temperature (200 °F) concrete block. More deformation was observed at the top side of the block, reducing the diameter of the wellbore. Also, the centers of the block sides have been deformed and displaced inward to the center of the block.

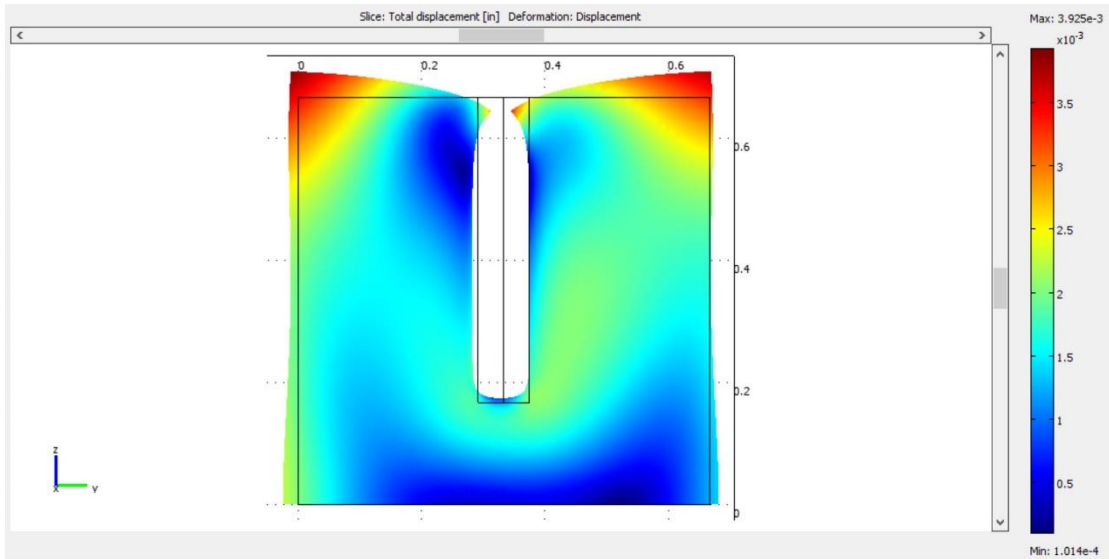


Figure 6.1.13 2D deformed shape plot for -321 °F borehole, unstressed and reservoir temperature (200 °F) concrete block. More deformation was observed at the top side of the block and reducing the diameter of the wellbore.

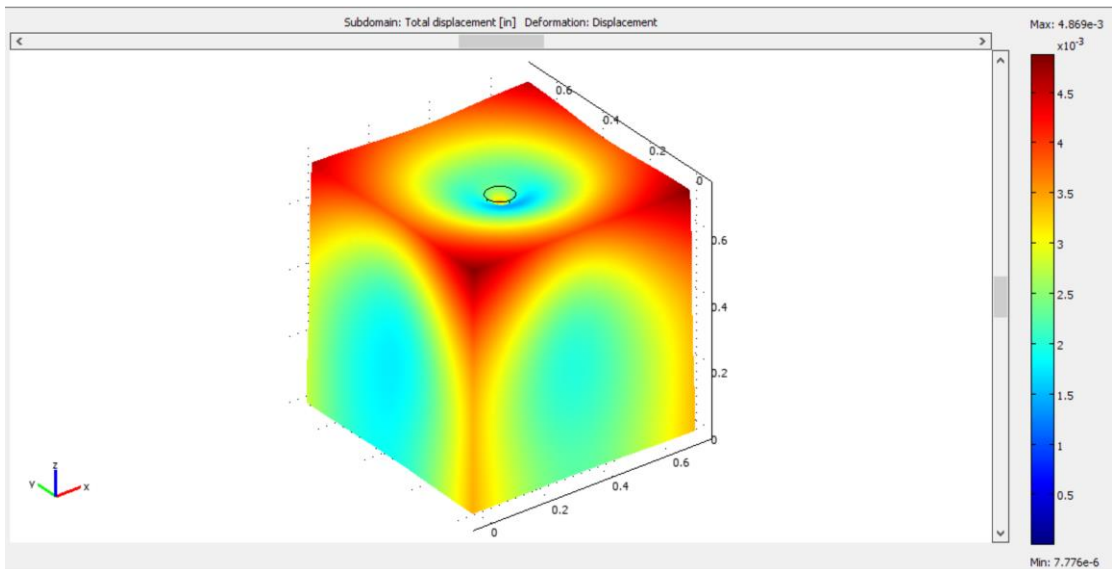


Figure 6.1.14 3D deformed shape plot for unstressed and reservoir temperature (200 °F) concrete block. More deformation was observed at the top side of the block, reducing the diameter of the wellbore. Also the centers of the block sides have been deformed and displaced inward to the center of the block.

Figure 6.1.15 to **Figure 6.1.18** show one-level slice plots of the τ_{xy} shear stress in psi with the slice taken in the XY-plane from a concrete sample. In all plots, the shear stress development is seen across the wellbore in opposite directions of the concrete sample

(compressional and tensional forces). **Figure 6.1.15** has not been triaxially stressed and was maintained at 70 °F. Shear stress magnitudes are in the range of 0 to 5384 psi. **Figure 6.1.16** also has not been triaxially stressed but the block is at reservoir temperature (200 °F). The shear stress increases in range from 0 to 7174 psi.

In **Figure 6.1.17**, the concrete block has been triaxially stressed ($x = 4000$ psi, $y = 6000$ psi, and $z = 8000$ psi) while at 70 °F. Shear stress magnitudes are in the range of 0 to 1467 psi. **Figure 6.1.18** shows the same triaxially stressed block at reservoir temperature (200 °F), showing shear stress magnitudes in the range of 0 to 2847 psi. These results indicate that increasing initial formation temperature results in increasing shear stress magnitudes around the wellbore.

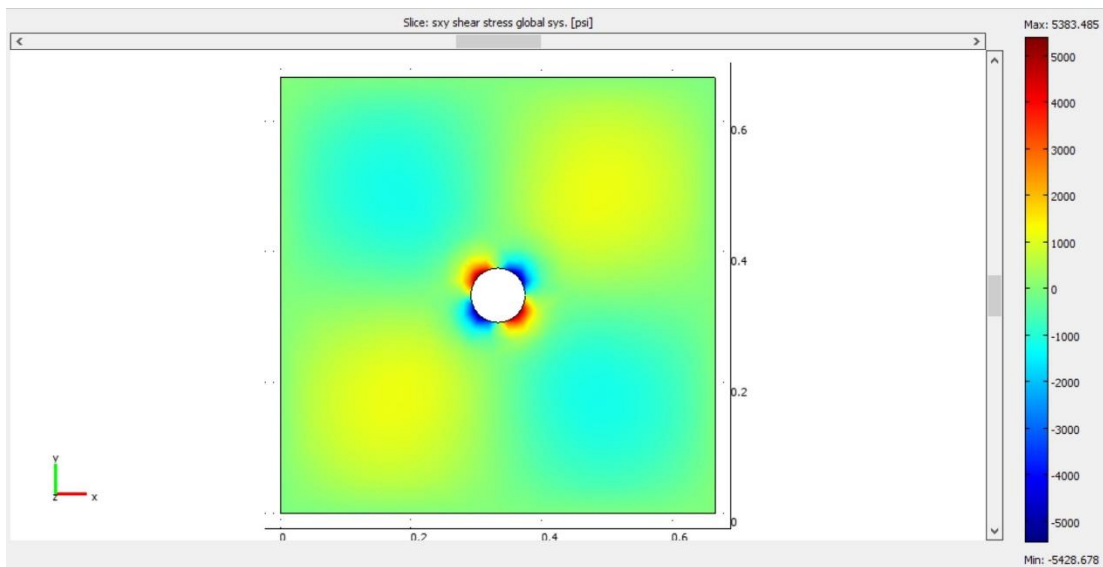


Figure 6.1.15 2D shear stress plot on XY-plane for unstressed and room temperature (70 °F) concrete block. Most of the shear stress values concentrate around the wellbore circumference.

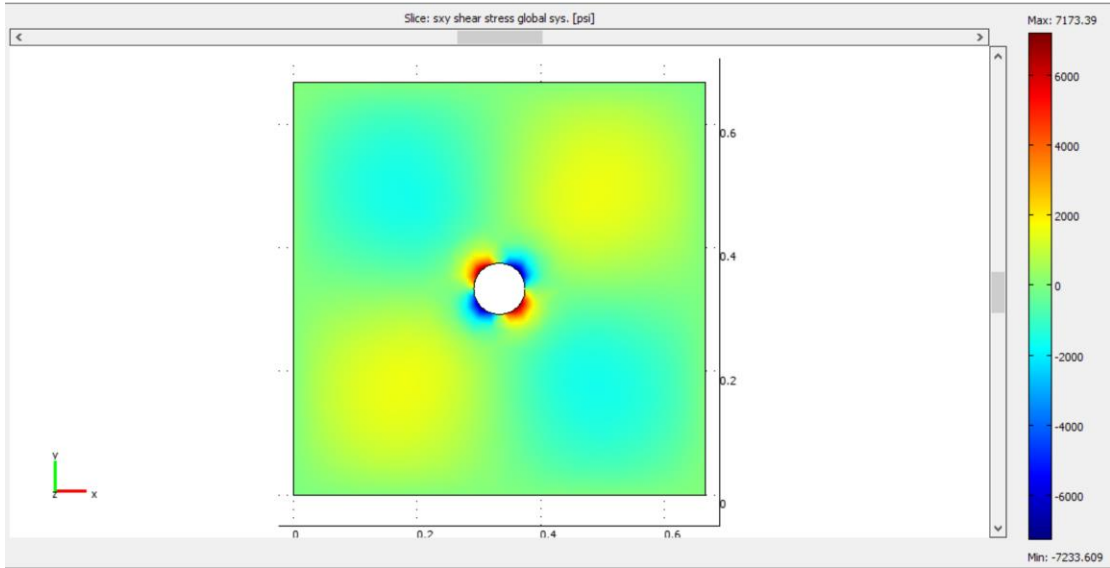


Figure 6.1.16 2D shear stress plot on XY-plane for unstressed and reservoir temperature (200 F) concrete block. Most of the shear stress values concentrate around the wellbore circumference.

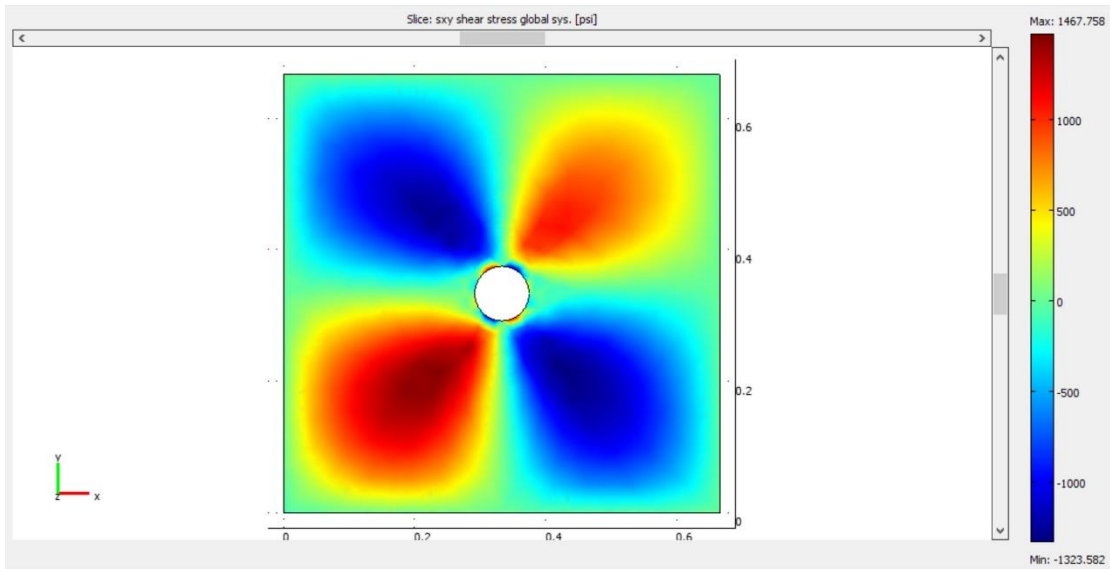


Figure 6.1.17 2D shear stress plot on XY-plane for concrete block with triaxial stresses at room temperature (70 F). Most of the shear stress values concentrate around the wellbore circumference.

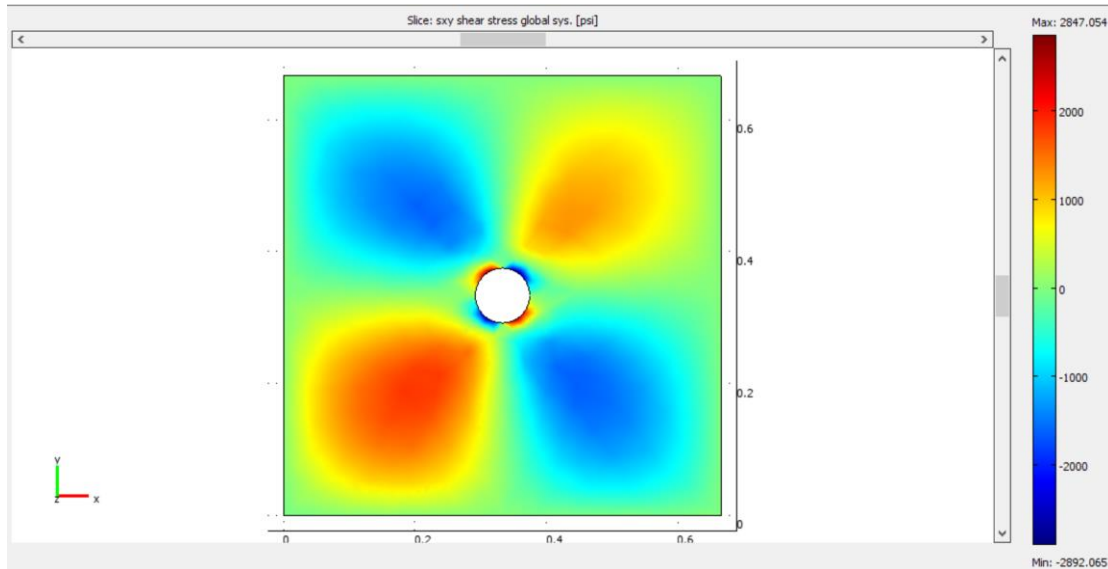


Figure 6.1.18 2D shear stress plot on XY-plane for concrete block with triaxial stresses at reservoir temperature (200 °F). Most of the shear stress values concentrate around the wellbore circumference.

Figure 6.1.19 through **Figure 6.1.24** show one-level slices of the radial and tangential stresses in psi for cryogenic treatment with and without external stress loading. For all conditions, thermal stress is applied with a wellbore temperature of -321 °F. **Figure 6.1.19** shows the concrete sample with unstressed condition at the temperature of 70 °F. The radial stress development is seen around the wellbore, and the magnitudes are in the range of -5000 to 5652 psi. **Figure 6.1.20** shows the tangential stress development for the same condition around the wellbore and the magnitudes are in the range of -3000 to 11,600 psi.

To see the effect of increased sample temperature, **Figure 6.1.21** and **Figure 6.1.22** show similar plots with the unstressed sample temperature increased to 200 °F. In **Figure 6.1.21** the radial stress ranges from -8000 to 7530 psi. In **Figure 6.1.22** the tangential stress ranges from -4000 to 16,600 psi. Clearly the radial and tangential stress values increased with increasing sample temperature.

To see the effect of triaxial stress loading, **Figure 6.1.23** and **Figure 6.1.24** show the radial and tangential stress plots from concrete samples with a temperature of 70 °F and with triaxial stresses applied as: $x = 4000$ psi, $y = 6000$ psi, and $z = 8000$ psi. **Figure 6.1.23** shows radial stress development in the range of -14,000 to 623 psi. The tangential stress in

Figure 6.1.24 is in the range of -9500 to 2231 psi. The lower radial and tangential magnitude is in the direction of maximum horizontal stress which is along the direction of fracture propagation.

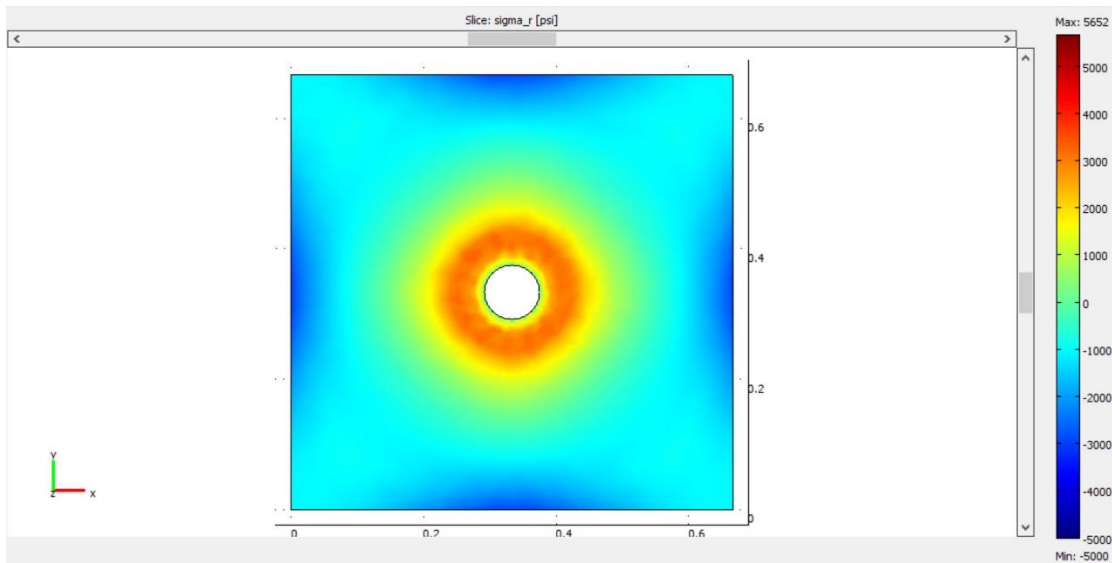


Figure 6.1.19 2D radial stress plot on XY-plane for unstressed and room temperature (70 F) concrete block. The radial stress values concentrate around the wellbore circumference with equal distribution.

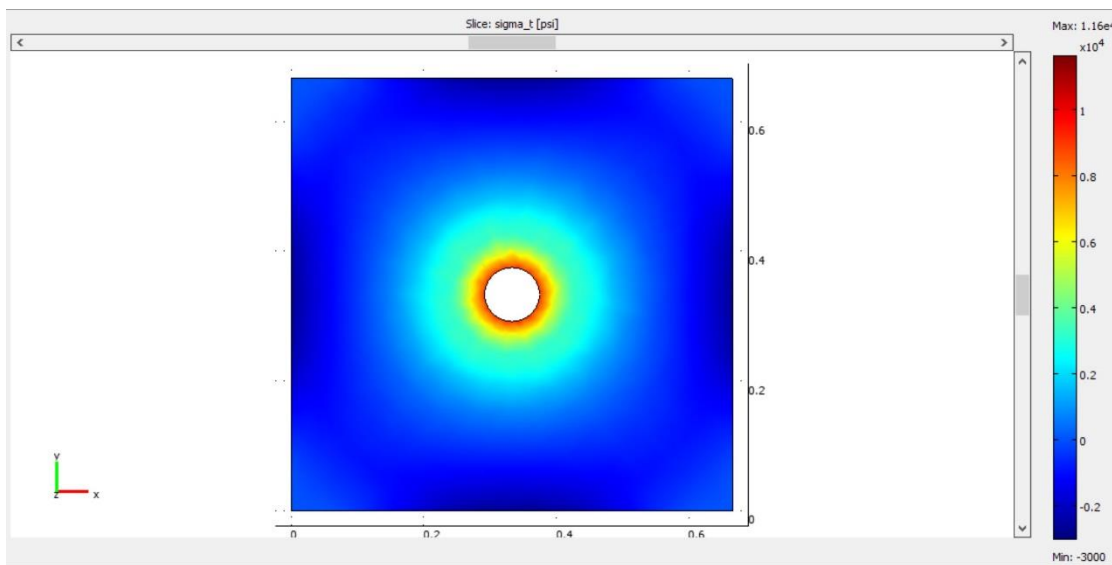


Figure 6.1.20 2D tangential stress plot on XY-plane for unstressed and room temperature (70 F) concrete block. The tangential stress values concentrate around the wellbore circumference with equal distribution.

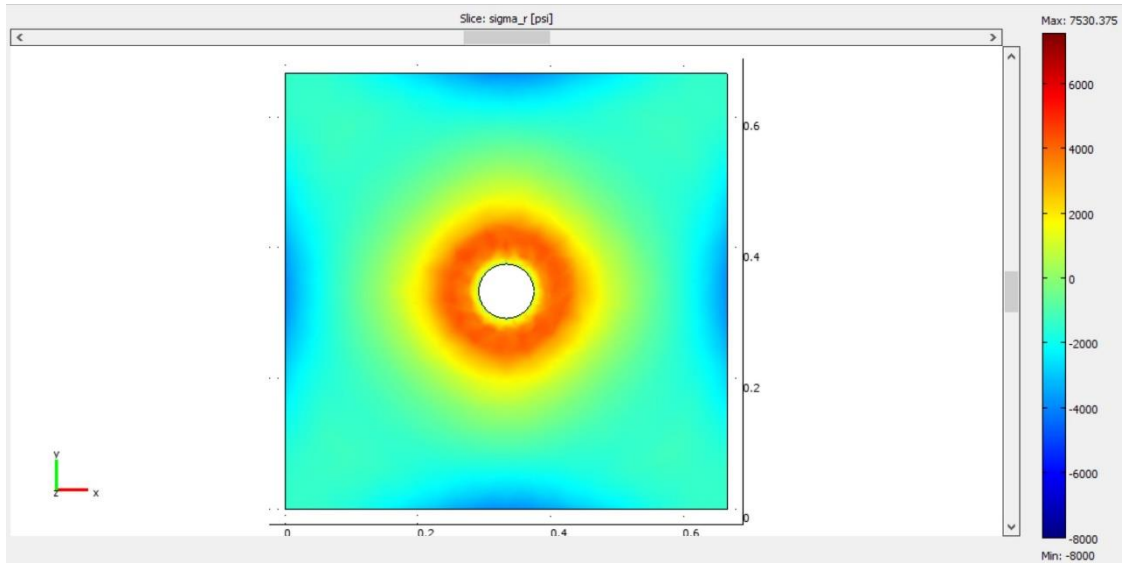


Figure 6.1.21 2D radial stress plot on XY-plane for unstressed and reservoir temperature (200 F) concrete block. The radial stress values concentrate around the wellbore circumference with equal distribution.

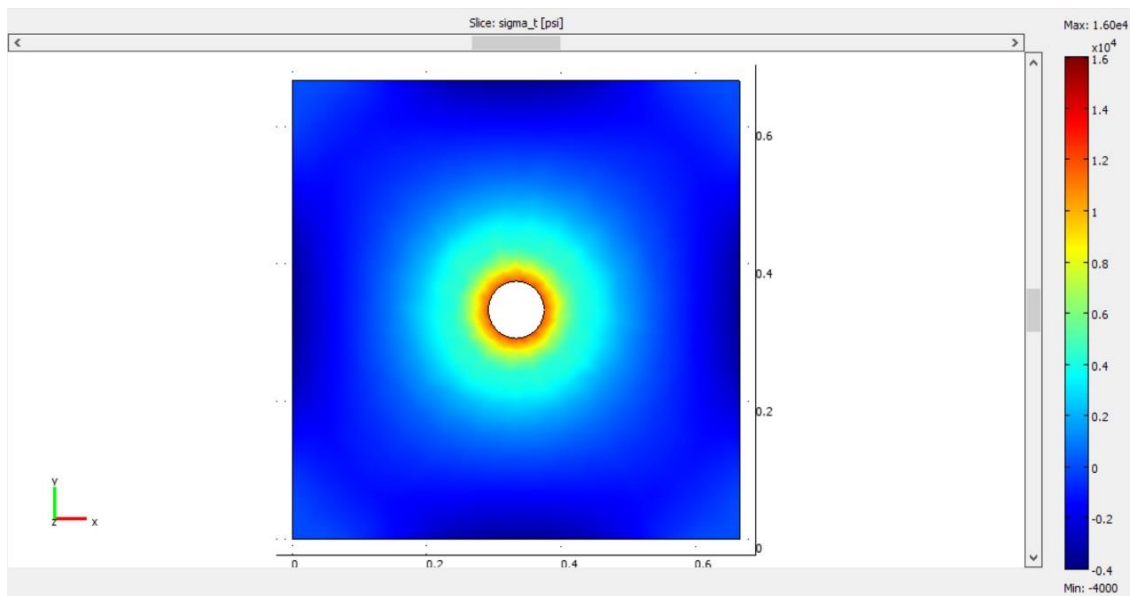


Figure 6.1.22 2D tangential stress plot on XY-plane for unstressed and room temperature (200 F) concrete block. The tangential stress values concentrate around the wellbore circumference with equal distribution.

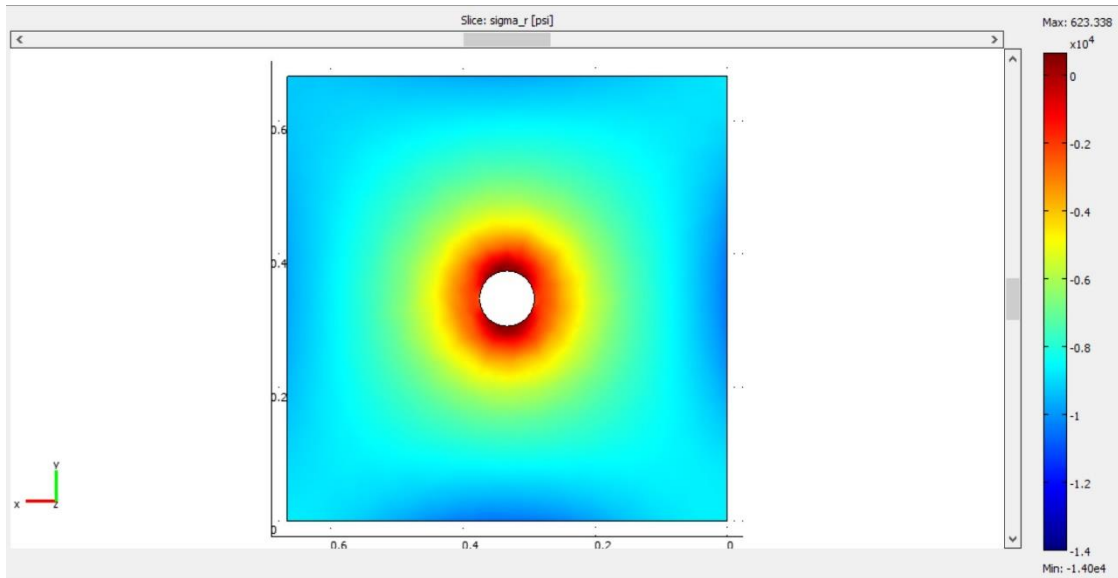


Figure 6.1.23 2D radial stress plot on XY-plane for concrete block under triaxial stresses at room temperature (70 °F). The radial stress values concentrate around the wellbore circumference, however, a lower radial magnitude is in the direction of maximum horizontal stress which is along the direction of fracture propagation.

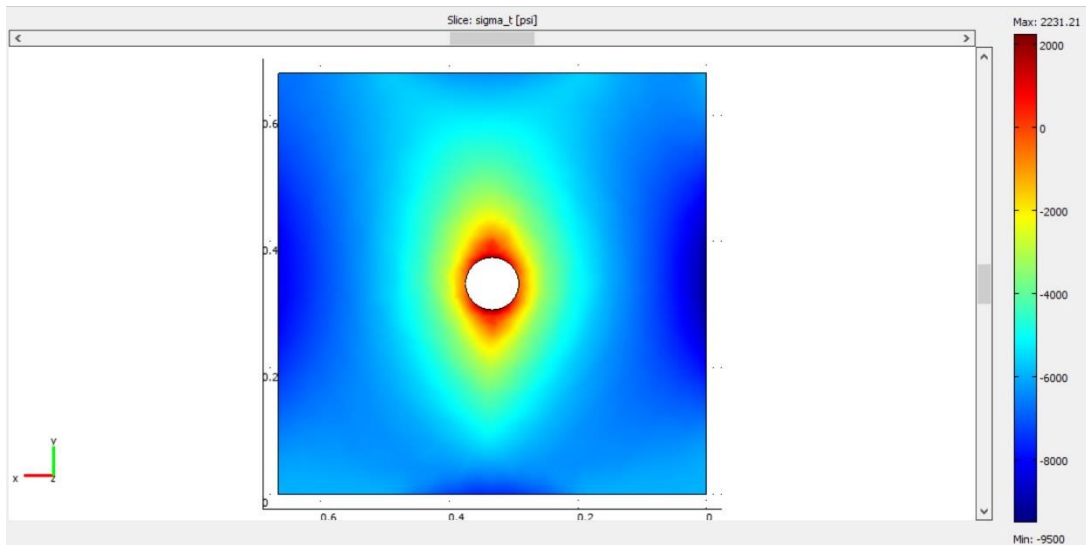


Figure 6.1.24 2D tangential stress plot on XY-plane for concrete block under triaxial stresses at room temperature (70 °F). The tangential stresses values concentrate around the wellbore circumference, however, a lower tangential magnitude is in the direction of maximum horizontal stress which is along the direction of fracture propagation.

The COMSOL program has a time-dependence feature that can be used to investigate the time-dependence of the stresses initiated as a result of temperature changes. Concrete

sample were tested using this feature when the sample was unstressed and the wellbore temperature was $-321\text{ }^{\circ}\text{F}$ and the sample temperature was $70\text{ }^{\circ}\text{F}$. The time frame for temperature increase was 20 minutes with one-second increments. **Figure 6.1.25a-d** are plots of the time-dependent variation of the temperature at 1, 5, 12, and 20 minutes, respectively. The plots are one-level slices in the XZ-plane. The temperature increases from the wellbore toward the outer boundary of the sample. **Figure 6.1.26a-d** are plots of the time-dependent variation of the radial stress responding to the changes in temperature at 1, 5, 12, and 20 minutes, respectively. The plots are one-level slices in the XY-plane. The radial stress starts to initiate at the wellbore and propagates towards the outer boundary of the concrete block.

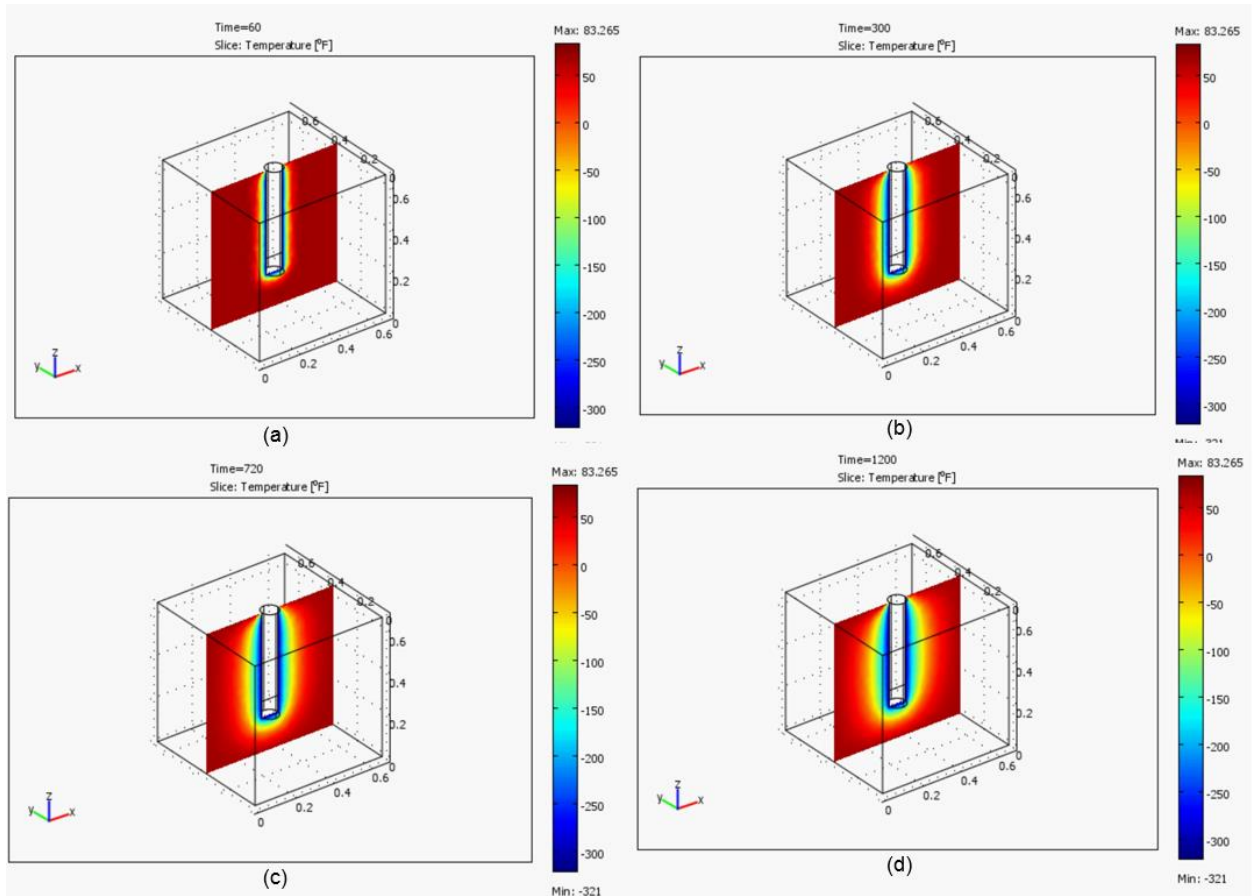


Figure 6.1.25 Time-dependent temperature of unstressed concrete sample with 6-inch wellbore. These slices in the XZ-plane plot the temperature distribution in $^{\circ}\text{F}$ with time.

Figure 6.1.25a shows the temperature in $^{\circ}\text{F}$ after 1 minutes; Figure 6.1.25b after 5 minutes; Figure 6.1.25c after 12 minutes; and Figure 6.1.25d after 20 minutes.

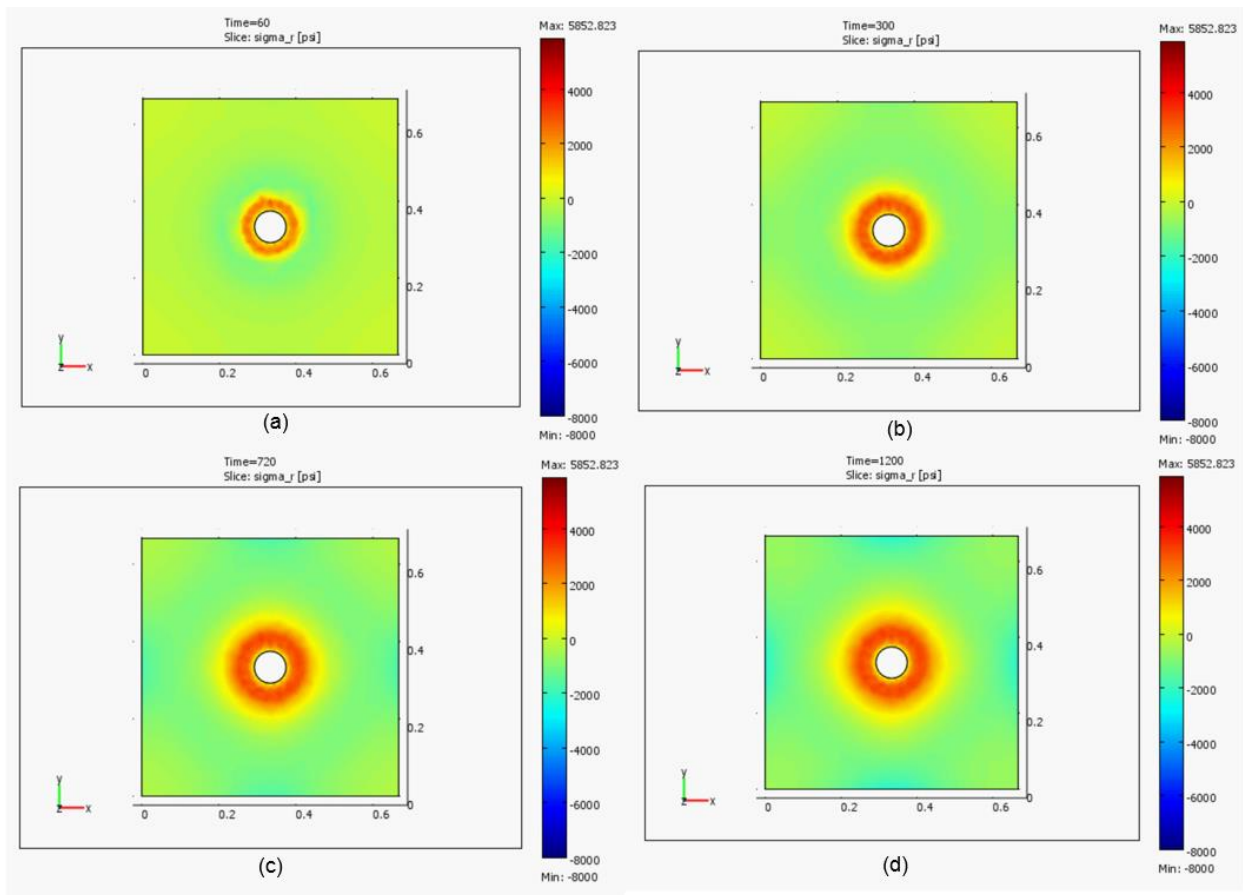


Figure 6.1.26 Time-dependent radial stress distribution of unstressed concrete sample with 6" wellbore. These slices in the XZ-plane show radial stress variation with time as a result of changing temperature. The radial stress changes from the wellbore towards the boundary. Figure 6.1.26a shows the radial stress in psi after 1 min; Figure 6.1.26b after 5 minutes; Figure 6.1.26c after 12 minutes; and Figure 6.1.26d after 20 minutes.

6.1.3.1.2 Concrete Sample with a 6-inch Cased Wellbore

The concrete sample with a 6-inch wellbore was cased with a 4-inch stainless steel tube at the top of the wellbore, leaving a 4-inch open hole section at the bottom. **Figure 6.1.27** shows the deformation and temperature in the YZ-plane when there is no stress loading applied and the outside boundary temperature is the room temperature. The temperature and displacement were both affected by introducing the stainless steel casing into the system. As we can see in this figure, the casing portion has higher shrinkage due to the reduction in the temperature introducing a weak area between the casing and the formation.

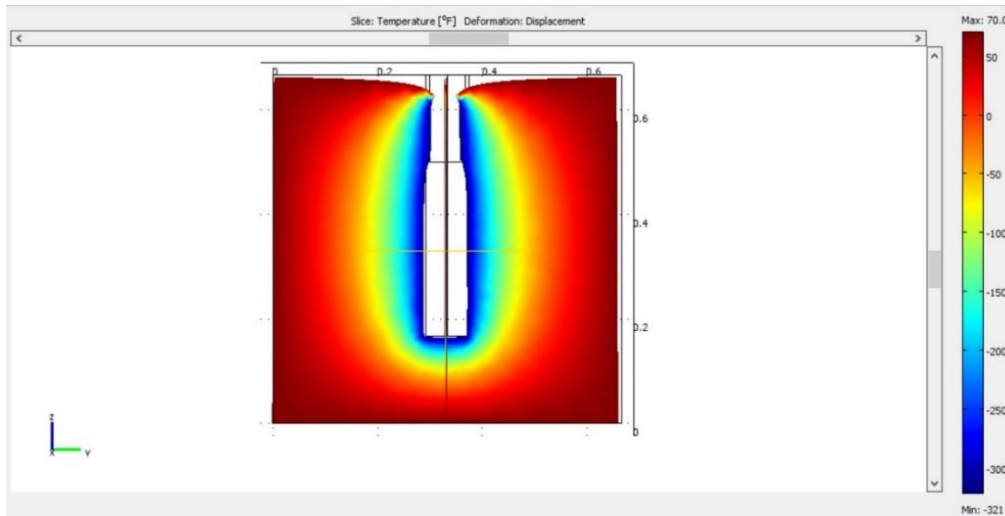


Figure 6.1.27 2D temperature and deformed shape plot for unstressed concrete block at room temperature (70 °F). More deformation is observed on the area attached to the casing at the top side of the block and reduces the diameter of the wellbore.

Figure 6.1.28 show the radial stress during the cryogenic treatment when the wellbore temperature is -321 °F, the concrete sample temperature is 70 °F, the sample has stainless steel casing, and no stresses are applied. This figure shows a one-level slice of the radial stress in psi with the slice taken in the XY-plane across the casing. The radial stress development is seen around the wellbore, and the magnitude is in the range of -345,733 to 33,027 psi. Since the stainless steel is present, it covers all the stress contrast, and it is hard to see any stress variation around the wellbore.

Therefore, \log_{10} stress is used to highlight the stress variations. **Figure 6.1.29** and **Figure 6.1.30** show the \log_{10} radial and tangential stresses, respectively, during the cryogenic treatment when the wellbore temperature is -321 °F, the concrete sample temperature is 70 °F with no stress loading applied. **Figure 6.1.29** shows a one-level slice of the \log_{10} radial stress with the slice taken in the YZ-plane and passing through the casing. The radial stress development is seen around the wellbore, and the magnitudes are in the range of 1.649 to 7.697. **Figure 6.1.30** shows a one-level slice of the \log_{10} tangential stress with the slice taken in the YZ-plane. The tangential stress development is seen around the wellbore, and the magnitudes are in the range of 2.142 to 7.449.

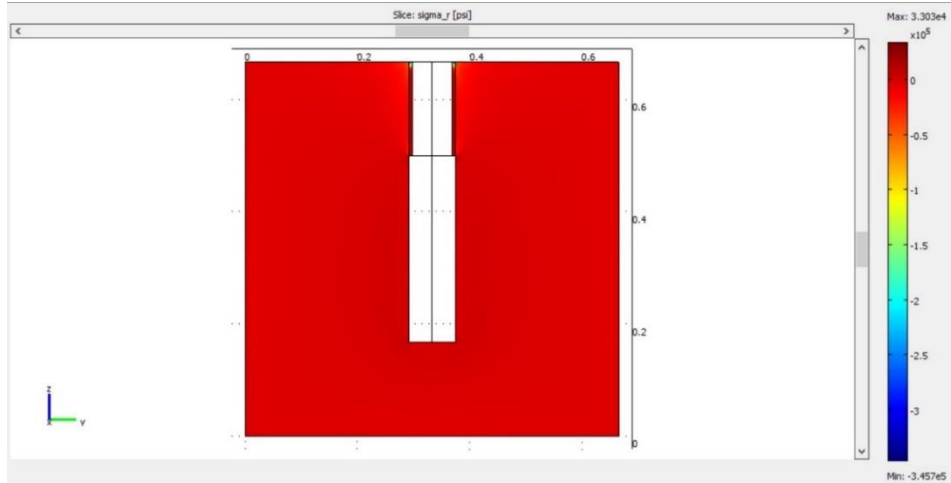


Figure 6.1.28 2D radial stress plot on YZ-plane for unstressed concrete block at room temperature (70 °F). Since the stainless steel is present, it covers all the stress contrast and it is hard to see any stress variation around the wellbore.

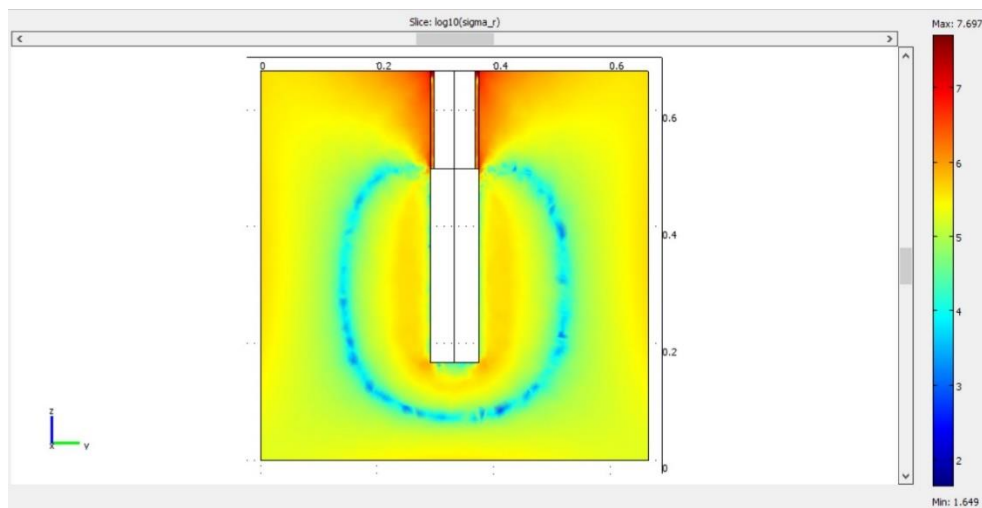


Figure 6.1.29 2D log₁₀ radial stress plot on YZ-plane for unstressed concrete block at room temperature (70 °F). The radial stress development is seen around the wellbore and the magnitudes are in the range of 1.649 to 7.697 (log₁₀ psi).

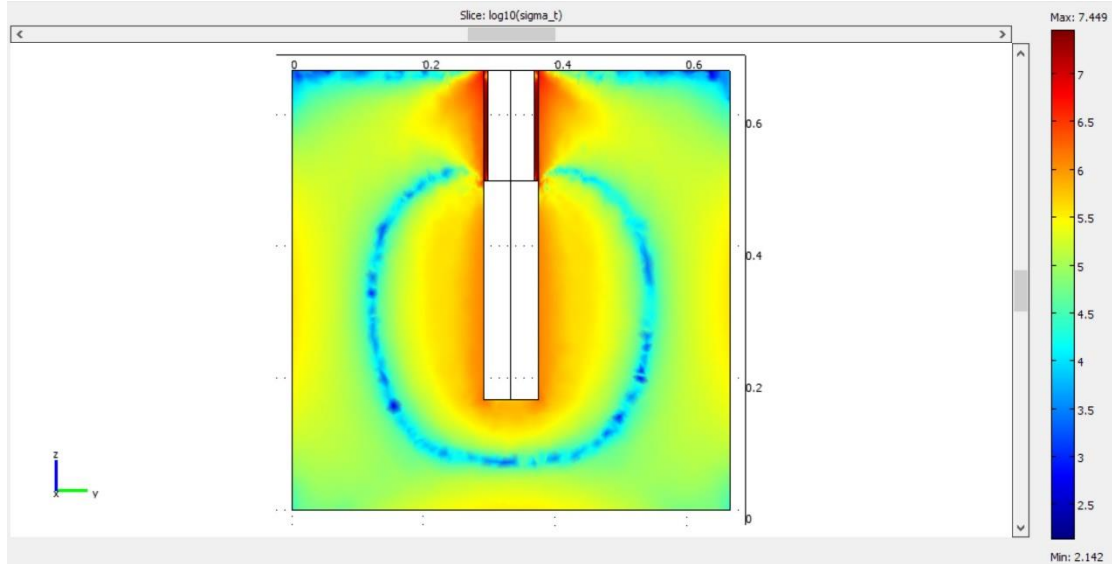


Figure 6.1.30 2D \log_{10} tangential stress plot on YZ-plane for unstressed concrete block at room temperature (70 °F). The tangential stress development is seen around the wellbore and the magnitudes are in the range of 2.142 to 7.449 (\log_{10} psi).

To see the effect of temperature, a line cross section plot of the radial stress is taken along the x-axis through the casing (**Figure 6.1.31**). **Figure 6.1.32** and **Figure 6.1.33** show the radial stress during the cryogenic treatment when the wellbore temperature is -321 °F and the concrete sample temperatures are 70 and 200 °F, respectively, and the sample has no stress loading applied. **Figure 6.1.32** shows a line cross section plot of the radial stress in psi, when the sample temperature is 70 °F, with the line taken in the x-axis and through the casing. The radial stress development is seen in the stainless steel casing, close to the wellbore, and the magnitudes are in the range of -15,000 to 16,000 psi. **Figure 6.1.33** shows a line cross section plot of the radial stress in psi, when the sample temperature is 200 °F, with the line taken in the x-axis and through the casing. The radial stress development is seen in the stainless steel casing, close to the wellbore, and the magnitudes are in the range of -14,000 to 17,000 psi. Clearly, the radial stress value increased by 1000 psi with increasing sample temperature, which results in increasing temperature gradient (ΔT , subtracting the wellbore temperature-LN₂ from the sample temperature).

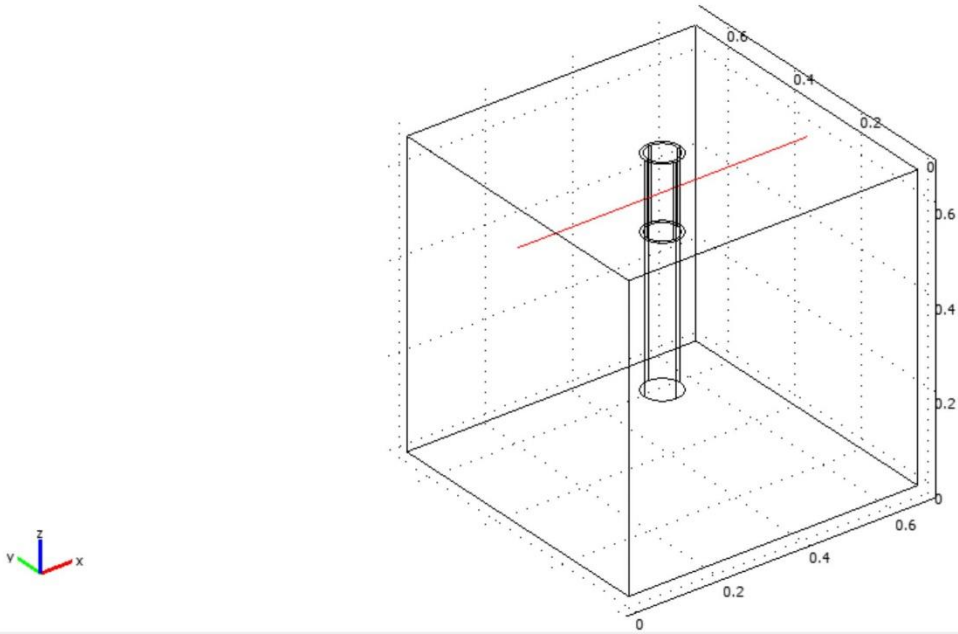


Figure 6.1.31 The red line is the line cross section along x-axis and passes through the stainless steel casing.

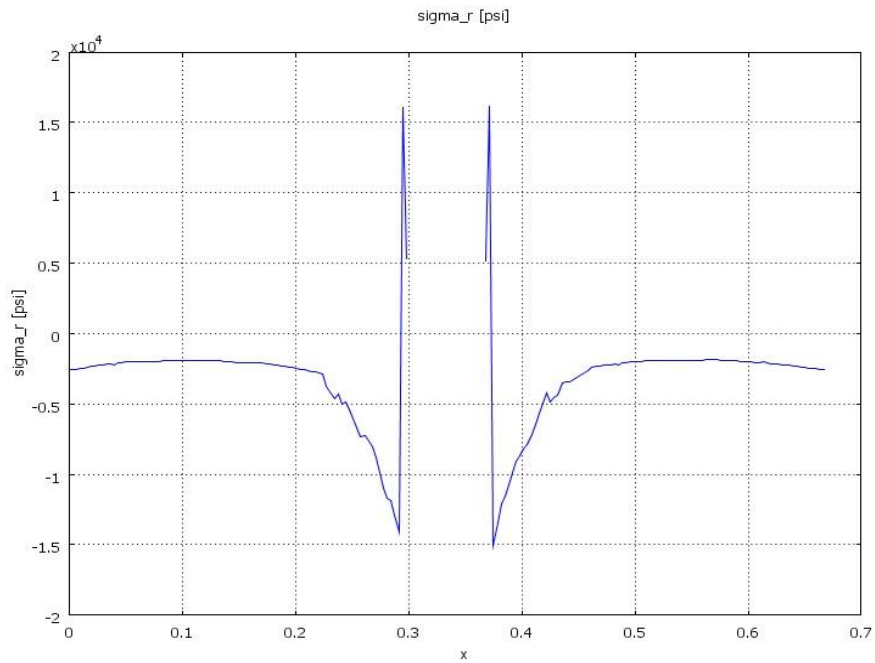


Figure 6.1.32 Plot showing the radial stress value along the line cross section on the x-axis from Figure 6.1.31.

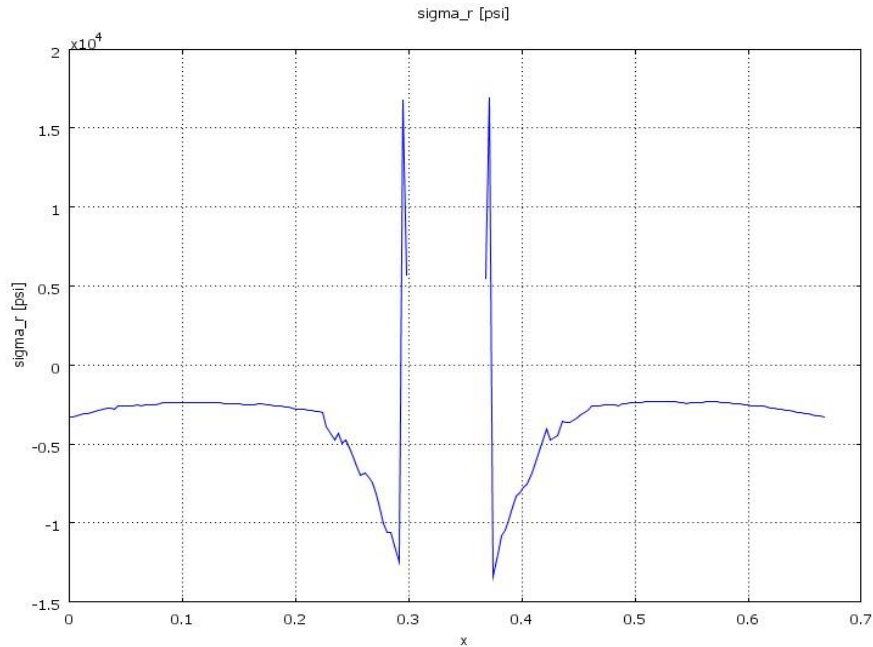


Figure 6.1.33 Plot showing the tangential stress value along the line cross section on the x-axis from Figure 6.1.31.

To mimic the laboratory conditions, the concrete sample with a 6-inch cased wellbore was triaxially stressed as follows: $x = 4000$ psi, $y = 6000$ psi, and $z = 8000$ psi. The sample temperature was 70 °F. **Figure 6.1.34** shows a one-level slice plot of the τ_{xy} shear stress in psi with the slice taken in the XY-plane for a concrete sample that was triaxially stressed at room temperature (70 °F). The shear stress development is seen inside the stainless steel casing and also around the wellbore next to the casing. Shear stress magnitudes are in the range of 0 to 81,550 psi in opposite directions across the wellbore of the concrete sample (compressional and tensional forces), and the shear stress around the wellbore next to the casing is in the range of 0 to 20,000 psi. **Figure 6.1.35** shows a one-level slice plot of the τ_{yz} shear stress in psi with the slice taken in the YZ-plane for a concrete sample that was triaxially stressed at room temperature (70 °F). The shear stress development is seen at the edge of the casing and the wellbore next to it. Shear stress magnitudes are in the range of 0 to 87,000 psi in opposite directions across the wellbore of the concrete sample (compressional and tensional forces).

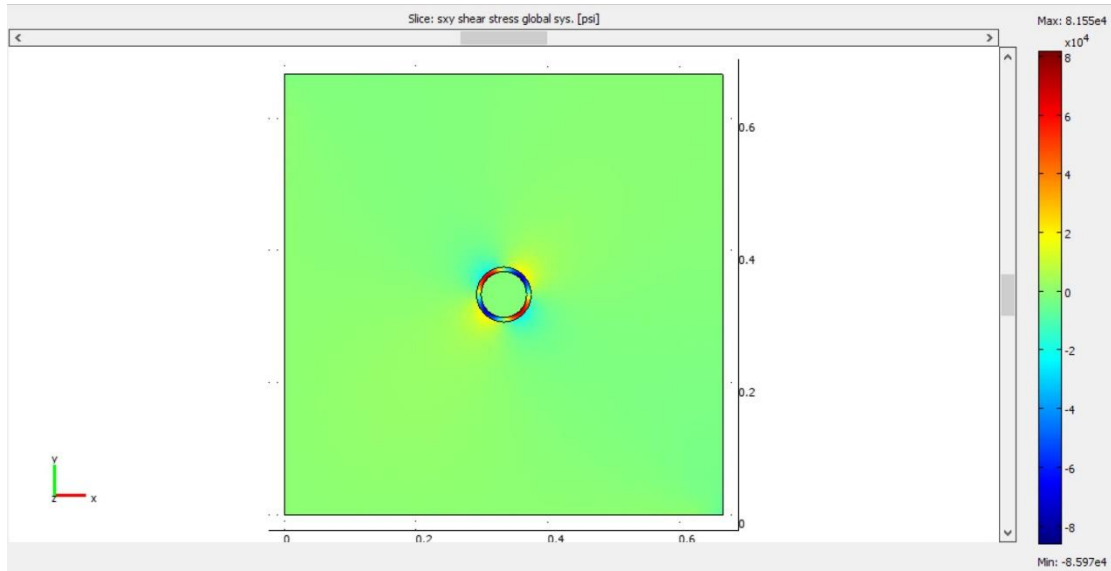


Figure 6.1.34 2D one-level slice plot of the τ_{xy} shear stress in psi with the slice taken in the XY-plane for a cased concrete sample that was triaxially stressed at room temperature (70 °F). Shear stress magnitudes are in the range of 0 to 81,550 psi in opposite direction across the wellbore of the concrete sample.

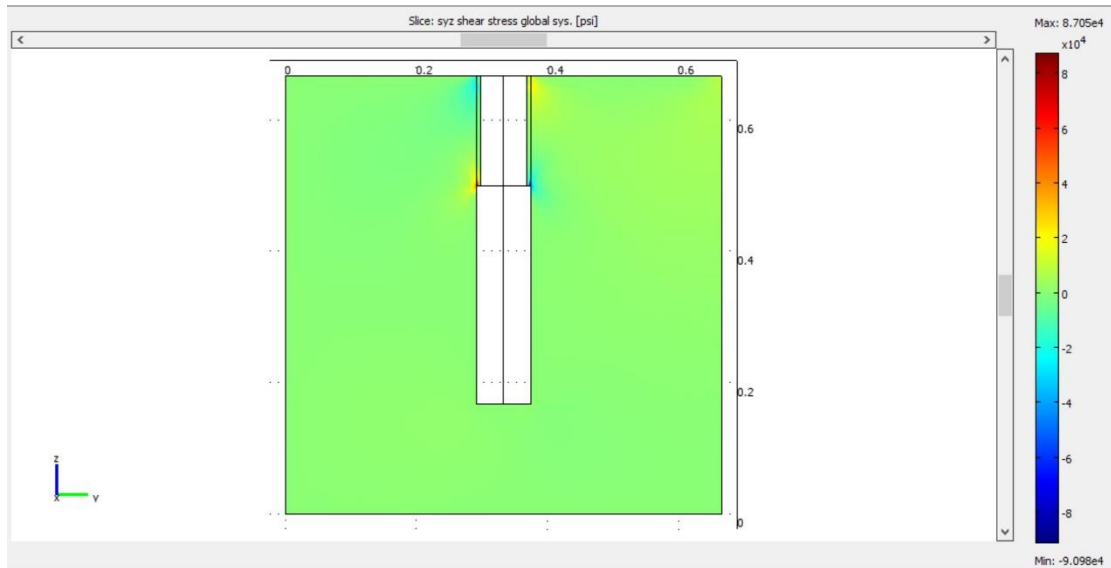


Figure 6.1.35 2D one-level slice plot of the τ_{yz} shear stress in psi with the slice taken in the YZ-plane for a cased concrete sample that was triaxially stressed at room temperature (70 °F). Shear stress magnitudes are in the range of 0 to 87,000 psi in the opposite direction across the wellbore of the concrete sample.

Figure 6.1.36 and **Figure 6.1.37** show the radial and tangential stresses, respectively, during the cryogenic treatment when the wellbore temperature is -321 °F, the concrete

sample temperature is 70 °F, and the sample was triaxially stressed as: $x = 4000$ psi, $y = 6000$ psi, and $z = 8000$ psi. **Figure 6.1.36** shows a one-level slice of the \log_{10} radial stress with the slice taken in the XY-plane. The radial stress development is seen around the wellbore and the magnitudes are in the range of 3.07 to 7.704 (\log_{10} psi). **Figure 6.1.37** shows a one-level slice of the \log_{10} tangential stress with the slice taken in the XY-plane. The tangential stress development is seen around the wellbore, and the magnitudes are in the range of 2.775 to 7.388 (\log_{10} psi). It seems the stresses around the casing distribute equally even though the system is under triaxial stresses. However, **Figure 6.1.38** and **Figure 6.1.39** show the radial and tangential stresses in the middle of the wellbore under the casing shoe, respectively, during the cryogenic treatment when the wellbore temperature is -321 °F, the concrete sample temperature is 70 °F, and the sample was triaxially stressed as: $x = 4000$ psi, $y = 6000$ psi, and $z = 8000$ psi. **Figure 6.1.38** shows a one-level slice of the radial stress in psi with the slice taken in the XY-plane. The radial stress development is seen around the wellbore, and the magnitudes are in the range of -10,050 to 10,050 psi. **Figure 6.1.39** shows a one-level slice of the tangential stress in psi with the slice taken in the XY-plane. The tangential stress development is seen around the wellbore, and the magnitudes are in the range of -10,000 to 10,000 psi. The lower radial and tangential magnitudes are in the direction of maximum horizontal stress which is the direction of fracture propagation.

Figure 6.1.40 and **Figure 6.1.41** show the \log_{10} radial and tangential stresses, respectively, during the cryogenic treatment when the wellbore temperature is -321 °F, the concrete sample temperature is 70 °F, and the sample was stressed triaxially as: $x = 4000$ psi, $y = 6000$ psi, and $z = 8000$ psi. **Figure 6.1.40** shows a one-level slice of the \log_{10} radial stress with the slice taken in the YZ-plane passing through the casing. The radial stress development is seen around the wellbore, and the magnitudes are in the range of 3.07 to 7.704 (\log_{10} psi). **Figure 6.1.41** shows a one-level slice of the \log_{10} tangential stress with the slice taken in the YZ-plane. The tangential stress development is seen around the wellbore and the magnitudes are in the range of 2.775 to 7.386 (\log_{10} psi).

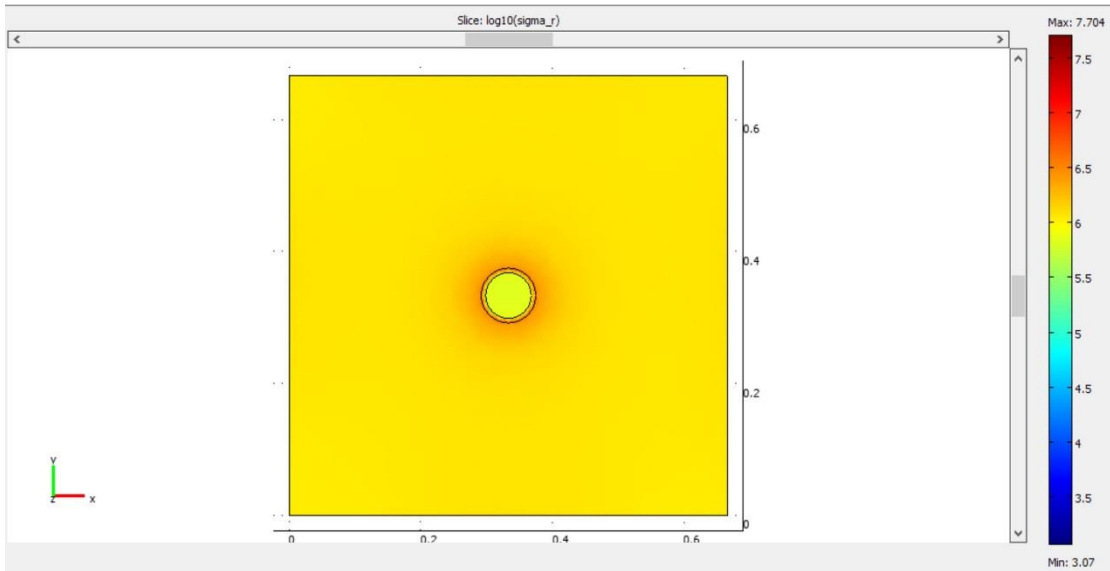


Figure 6.1.36 2D one-level slice plot of the \log_{10} radial stress with the slice taken in the XY-plane for a cased concrete sample that was triaxially stressed at room temperature (70 °F). The radial stress development is seen around the casing and wellbore, and the magnitudes are in the range of 3.07 to 7.704 (\log_{10} psi).

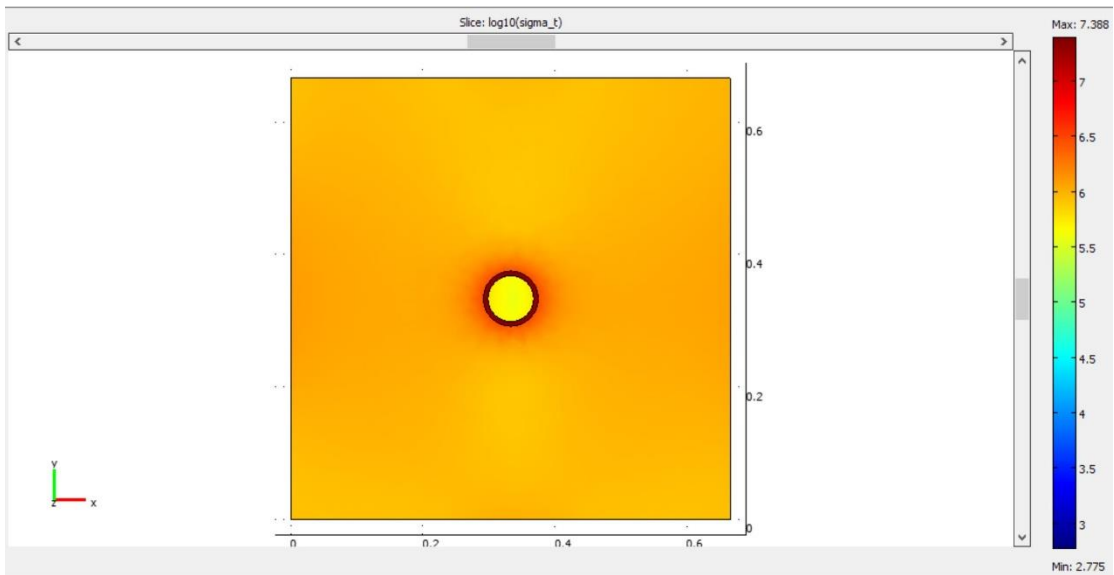


Figure 6.1.37 2D one-level slice plot of the \log_{10} tangential stress with the slice taken in the XY-plane for a cased concrete sample that was triaxially stressed at room temperature (70 °F). The radial stress development is seen around the casing and the wellbore, the magnitudes are in the range of 2.775 to 7.388 (\log_{10} psi).

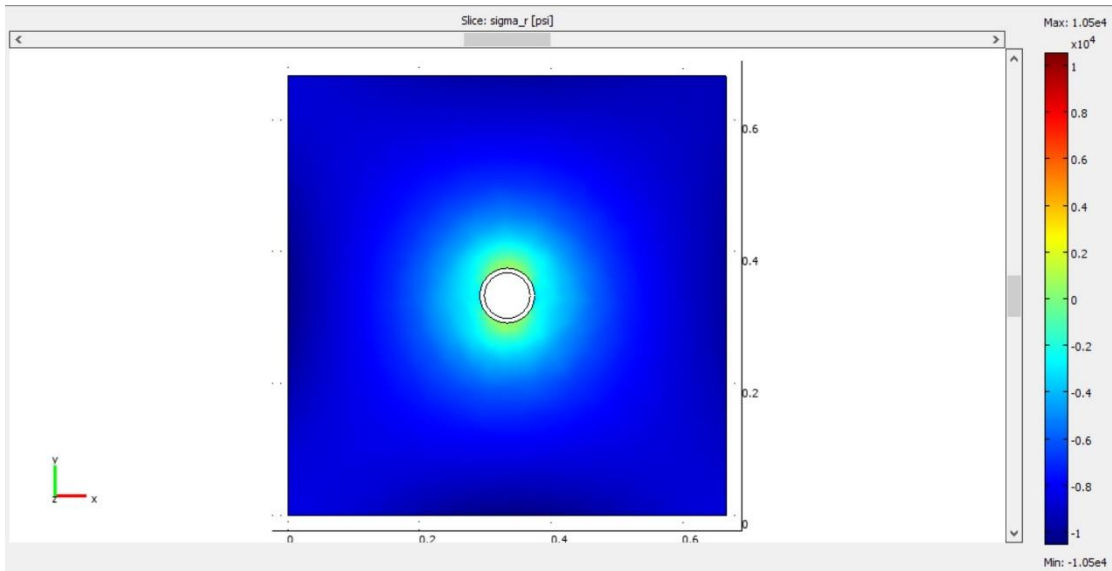


Figure 6.1.38 2D one-level slice of the radial stress in psi with the slice taken in the XY-plane in the open-hole part of the wellbore for a cased concrete sample that was triaxially stressed at room temperature (70 F). The radial stress development is seen around the wellbore, and the magnitudes are in the range of -10,050 to 10,050 psi.

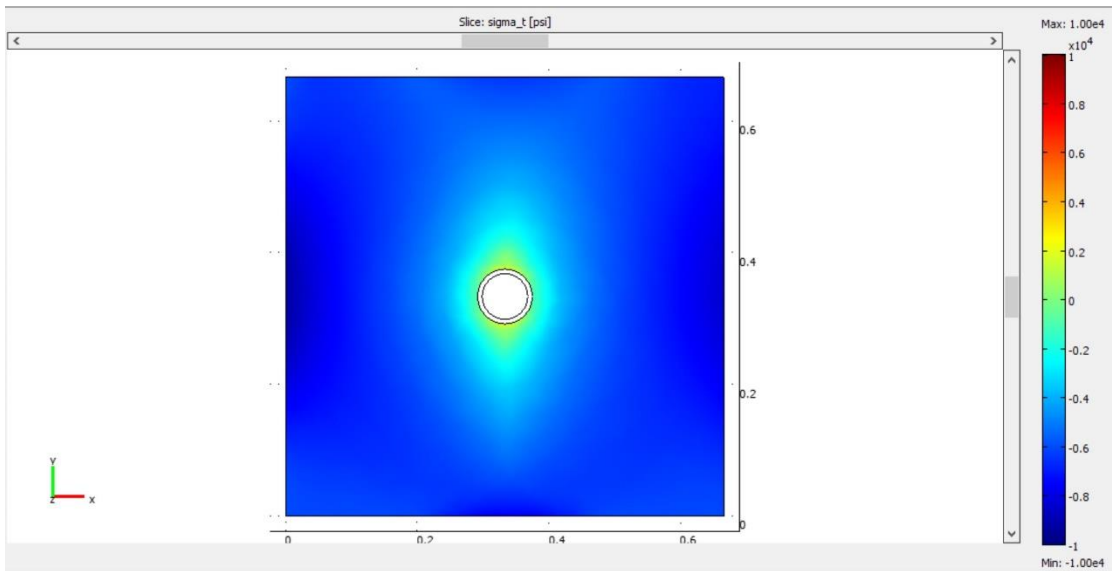


Figure 6.1.39 2D one-level slice of the tangential stress in psi with the slice taken in the XY-plane in the open-hole part of the wellbore for a cased concrete sample that was triaxially stressed at room temperature (70 F). The tangential stress development is seen around the wellbore, and the magnitudes are in the range of -10,000 to 10,000 psi.

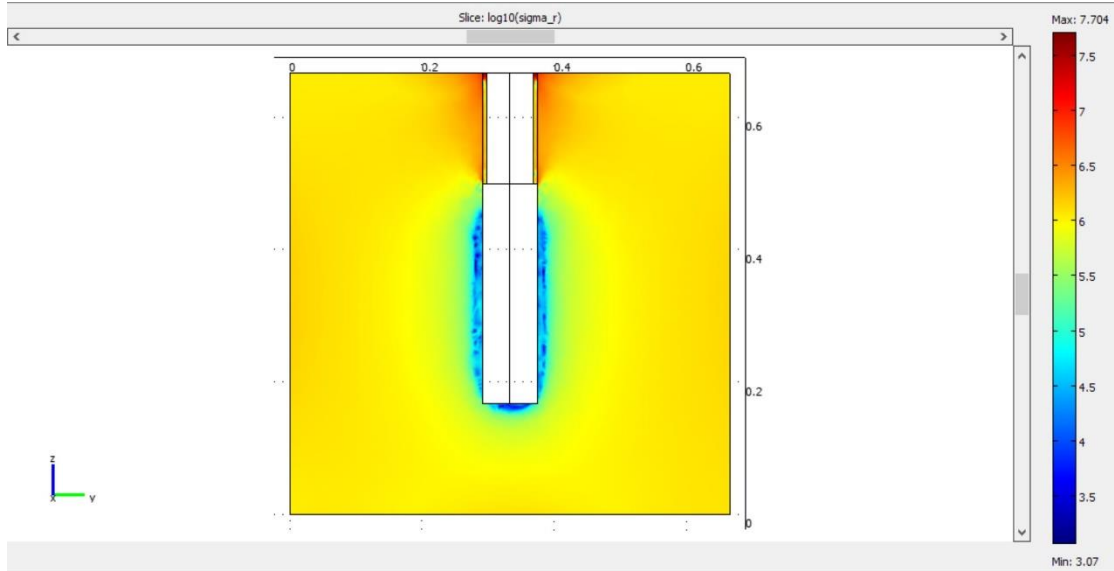


Figure 6.1.40 2D one-level slice of the \log_{10} radial stress with the slice taken in the YZ-plane pass through the casing for a cased concrete sample that was triaxially stressed at room temperature (70 °F). The radial stress development is seen around the wellbore and the magnitudes are in the range of 3.07 to 7.704 (\log_{10} psi).

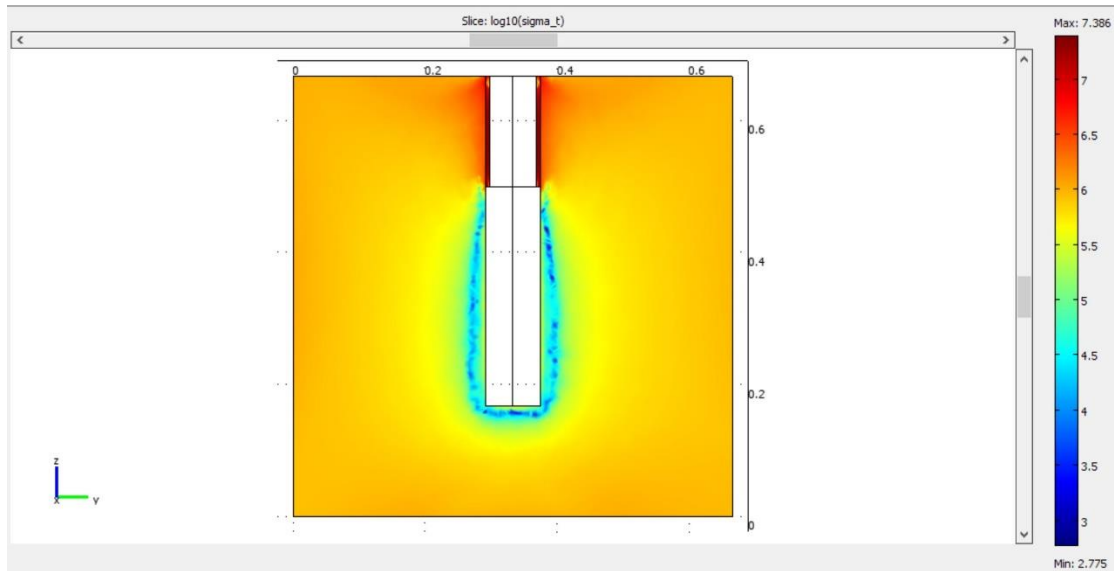


Figure 6.1.41 2D one-level slice of the \log_{10} tangential stress with the slice taken in the YZ-plane pass through the casing for a cased concrete sample that was triaxially stressed at room temperature (70 °F). The tangential stress development is seen around the wellbore and the magnitudes are in the range of 2.775 to 7.386 (\log_{10} psi).

6.1.3.1.3 Concrete Sample with an 8-inch Open Hole

In this section the results for concrete sample with an open hole penetrating 8 inches into the sample from the top to the bottom are provided. Different from the 6-inch wellbore, the shear stress results show that the stress contrast at the end of the 6-inch wellbore disappeared in the 8-inch wellbore. Also the temperature distribution behaves differently than the previous wellbore, in that it is distributed more evenly along the wellbore.

Figure 6.1.42 shows the temperature in the YZ-plane with deformation plot when the outside boundary temperature of the unstressed concrete is room temperature. The displacement is lower compared to the 6-inch wellbore sample. In this figure, the 8-inch wellbore has lower shrinkage than 6-inch wellbore due to the wellbore geometry.

Figure 6.1.43 shows a one-level slice plot of the τ_{yz} shear stress in psi with the slice taken in the YZ-plane for an unstressed concrete sample during the cryogenic treatment when the wellbore temperature is $-321\text{ }^{\circ}\text{F}$ and the sample temperature is $70\text{ }^{\circ}\text{F}$. The shear stress development is around the wellbore and is in the range of 0 to 1400 psi, in opposite directions across the wellbore (compressional and tensional forces). **Figure 6.1.44** shows the τ_{xy} shear stress of this sample in the range of 0 to 5300 psi.

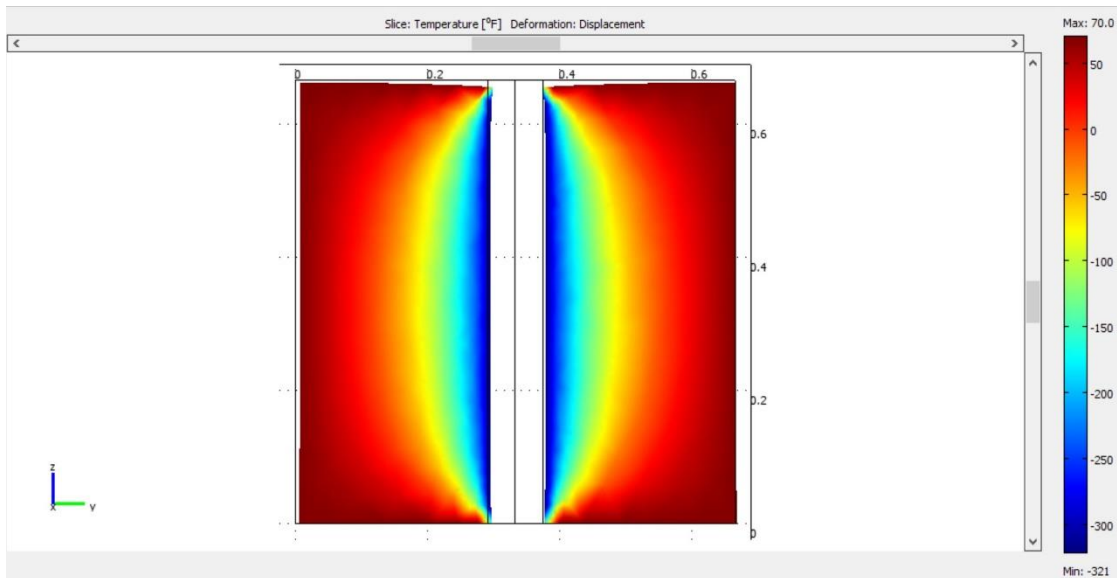


Figure 6.1.42 The temperature in the YZ-plane with deformation plot of unstressed concrete sample and the outside boundary temperature is the room temperature ($70\text{ }^{\circ}\text{F}$).

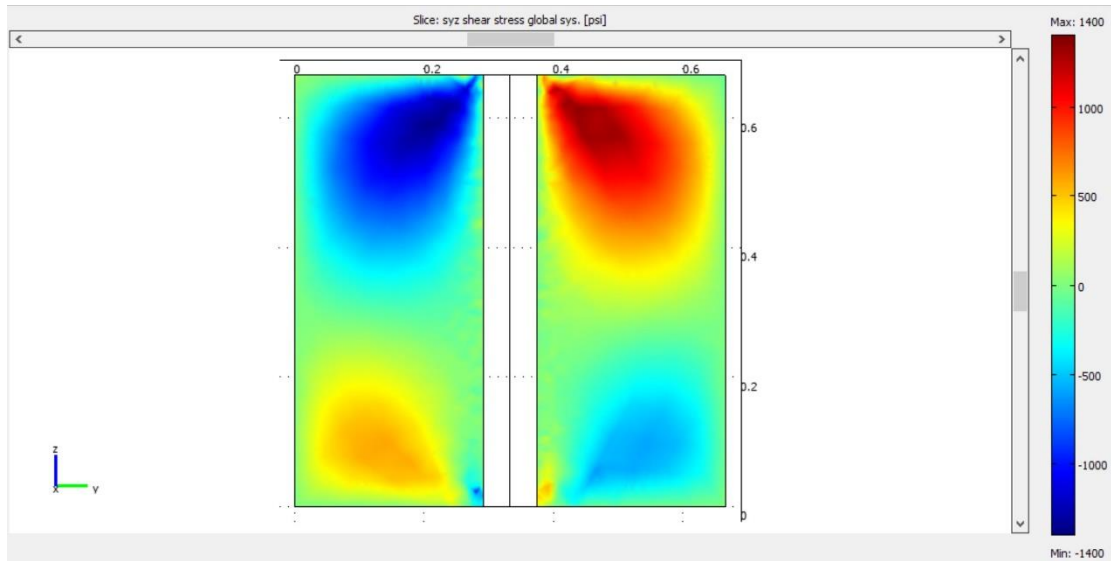


Figure 6.1.43 2D one-level slice plot of the τ_{yz} shear stress in psi with the slice taken in the YZ-plane for an unstressed concrete sample with the 8-inch wellbore during the cryogenic treatment when the wellbore temperature is $-321\text{ }^{\circ}\text{F}$ and the sample temperature is $70\text{ }^{\circ}\text{F}$. Shear stress magnitudes are in the range of 0 to 1400 psi, in the opposite directions across the wellbore (compressional and tensional forces).

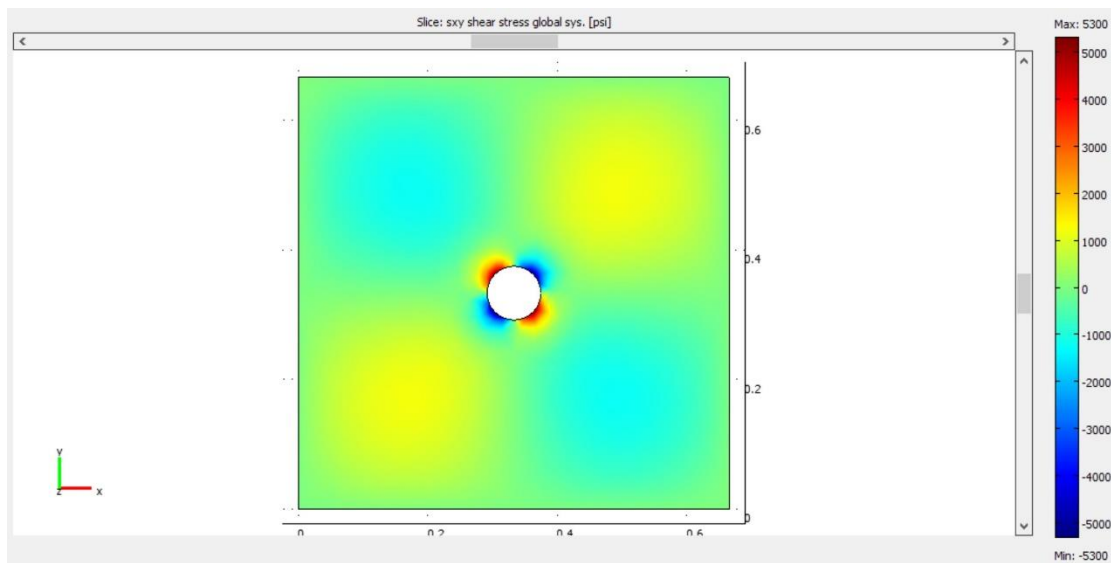


Figure 6.1.44 2D one-level slice plot of the τ_{xy} shear stress in psi with the slice taken in the XY-plane for an unstressed concrete sample with the 8-inch wellbore during the cryogenic treatment when the wellbore temperature is $-321\text{ }^{\circ}\text{F}$ and the sample temperature is $70\text{ }^{\circ}\text{F}$. Shear stress magnitudes are in the range of 0 to 5300 psi in opposite directions across the wellbore (compressional and tensional forces).

6.1.3.2 Sandstone Samples

In this section, the results and the observations for the homogeneous, cubic block models of sandstone, with 6-inch open and cased wellbores are presented.

6.1.3.2.1 Sandstone Sample with a 6-inch Open Hole

Figure 6.1.45 shows the temperature in $^{\circ}\text{F}$ with deformed shape in the YZ-plane when there are no external stresses applied and the outside boundary temperature is the room temperature (70°F). The block deformed inward toward the center of the sample causing the top part of the wellbore to be smaller and tighter than the rest of the wellbore. **Figure 6.1.46** shows the same block with a boundary temperature of 200°F . The block deformed inward toward the center. Comparing to the sandstone sample when its boundary temperature is the room temperature and the concrete case with the same conditions in **Figure 6.1.12**, there is not much change in its size and shape.

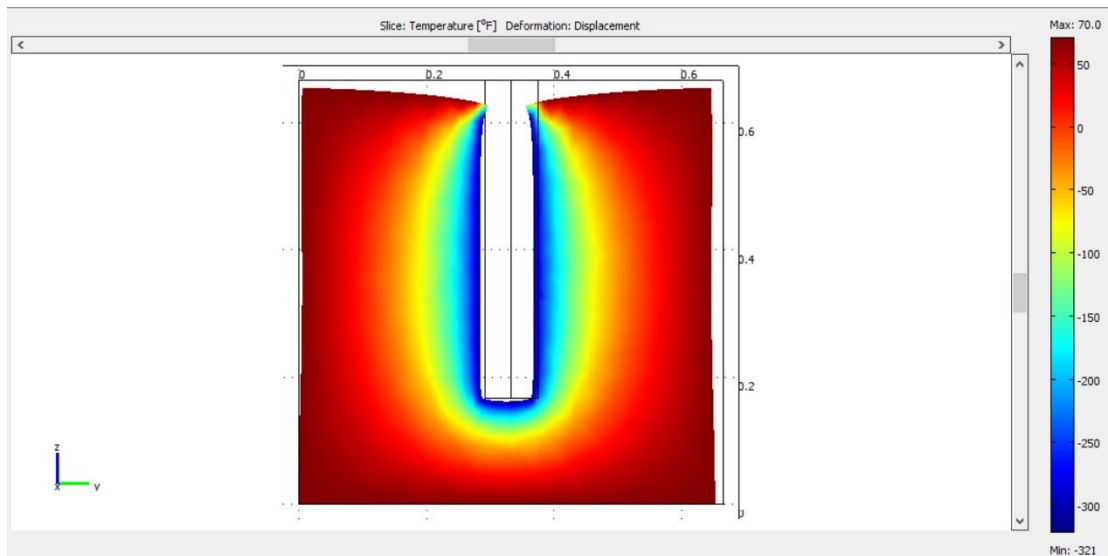


Figure 6.1.45 The temperature and deformation plot in the YZ-plane of an unstressed sandstone sample when the outside boundary temperature is the room temperature (70°F).

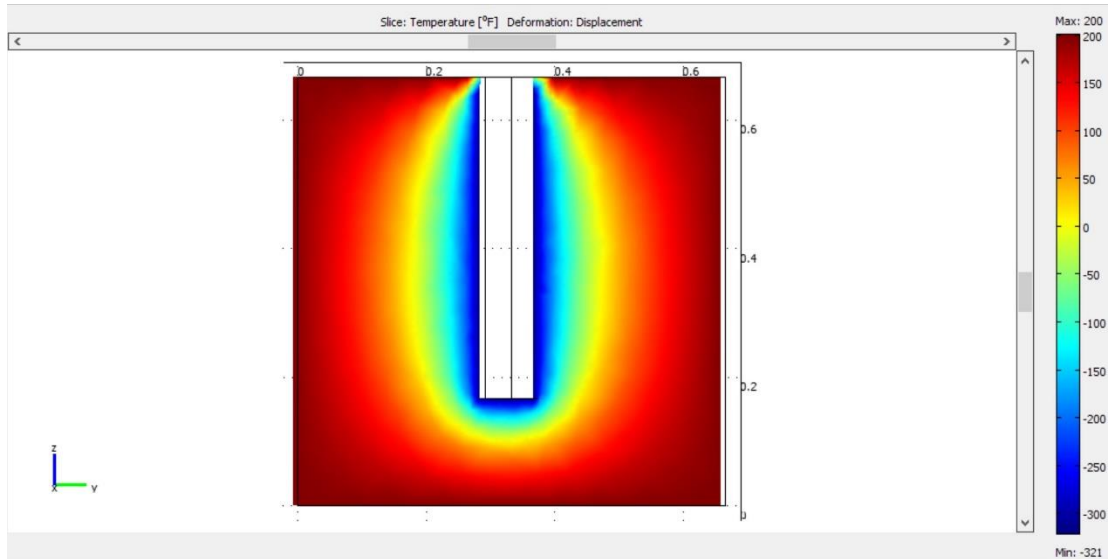


Figure 6.1.46 The temperature with deformation plot in the YZ-plane of an unstressed sandstone sample with the outside boundary temperature of 200 °F.

Figure 6.1.47 and **Figure 6.1.48** show a one-level slice plot of the τ_{xy} shear stress in psi with the slice taken in the XY-plane for the unstressed sandstone sample at 70 °F and 200 °F, respectively. The shear stress development is seen around the wellbore. Shear stress magnitudes are in the range of 0 to 8831 psi for the 70 °F case and 0 to 11,000 psi for the 200 °F case, both in opposite directions across the wellbore (compressional and tensional forces).

Figure 6.1.49 and **Figure 6.1.50** show a one-level slice plot of the τ_{xy} shear stress in psi with the slice taken in the XY-plane for a sandstone sample that was triaxially stressed ($x = 4000$ psi, $y = 6000$ psi, and $z = 8000$ psi) at 70 °F and 200 °F, respectively. The shear stress development is seen around the wellbore. The shear stress magnitudes are in the range of 0 to 4400 psi for 70 °F and 0 to 7200 psi for 200 °F, in the opposite directions across the wellbore of the sandstone sample (compressional and tensional forces).

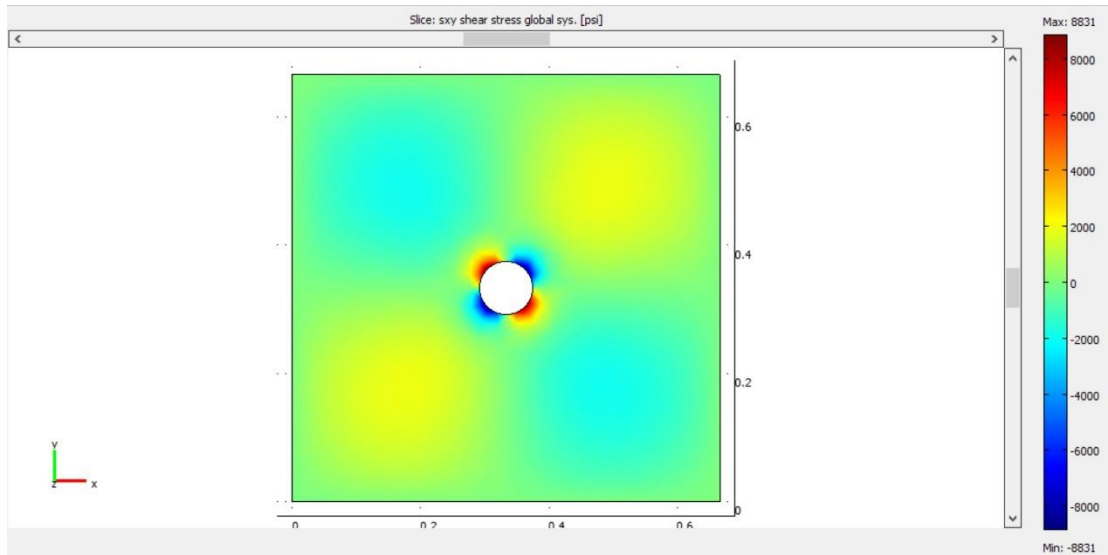


Figure 6.1.47 2D slice plot of the τ_{xy} shear stress in psi taken in the XY-plane for an unstressed sandstone sample at room temperature (70 °F). Shear stress magnitudes are in the range of 0 to 8831 psi in the opposite directions across the wellbore (compressional and tensional forces).

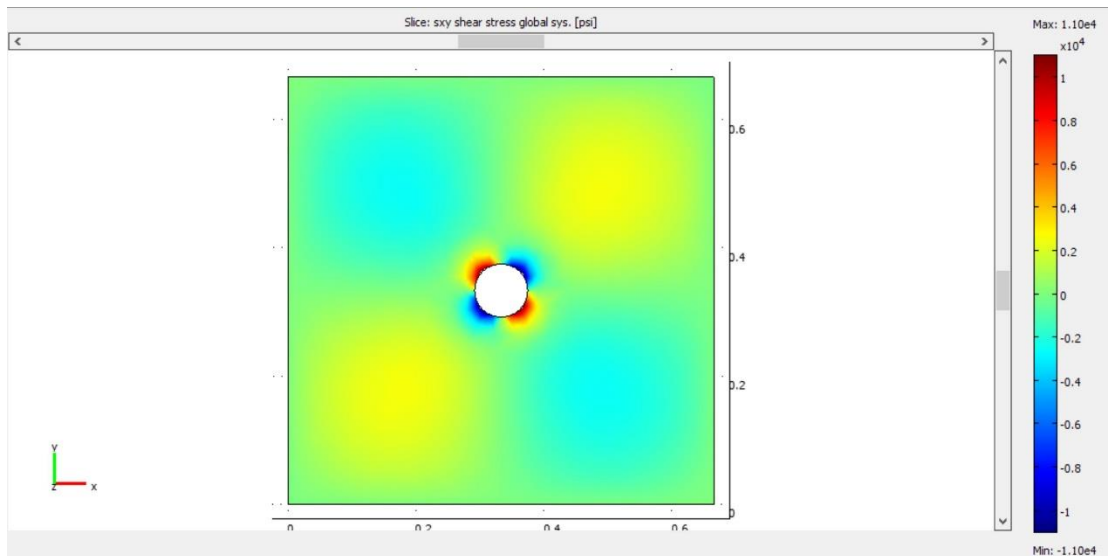


Figure 6.1.48 2D slice of the τ_{xy} shear stress in psi taken in the XY-plane for an unstressed sandstone sample at reservoir temperature (200 °F). Shear stress magnitudes are in the range of 0 to 11,000 psi in the opposite directions across the wellbore (compressional and tensional forces).

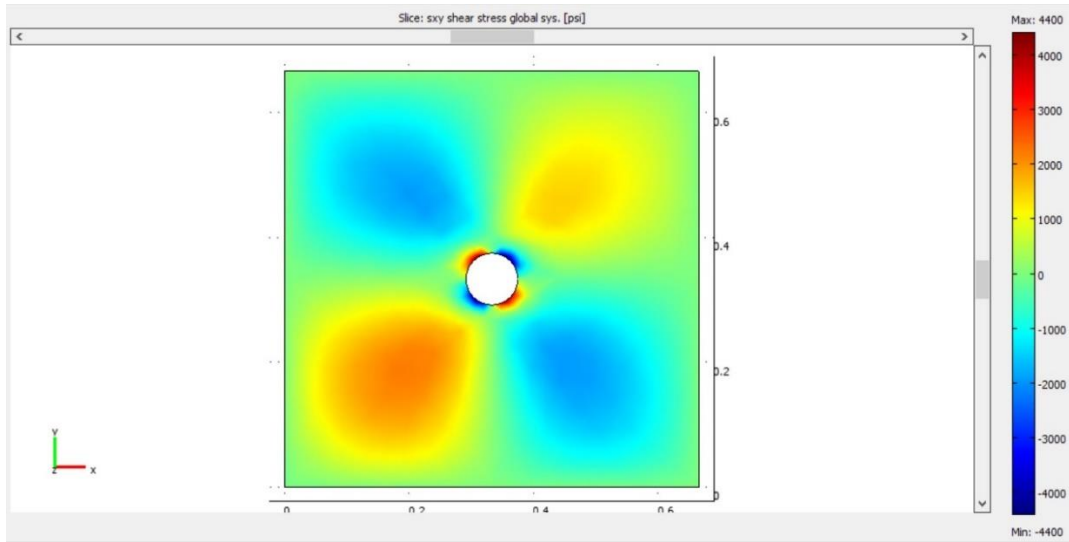


Figure 6.1.49 2D slice of the τ_{xy} shear stress in psi taken in the XY-plane for a sandstone sample that was triaxially stressed ($x = 4000$ psi, $y = 6000$ psi, and $z = 8000$ psi) at room temperature (70 °F). Shear stress magnitudes are in the range of 0 to 4400 psi in the opposite directions across the wellbore.

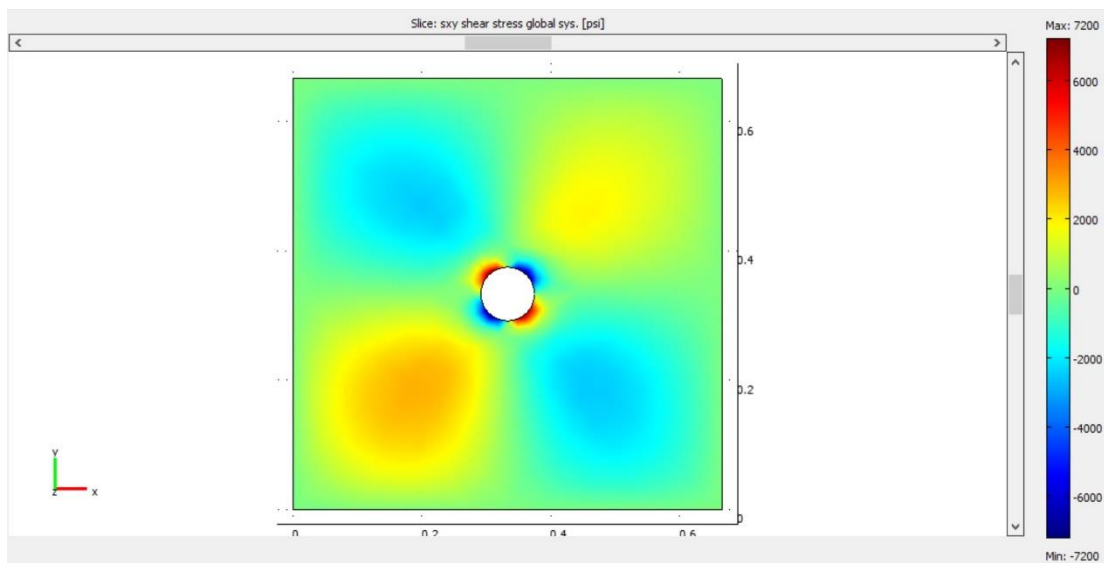


Figure 6.1.50 2D slice of the τ_{xy} shear stress in psi taken in the XY-plane for a sandstone sample that was triaxially stressed ($x = 4000$ psi, $y = 6000$ psi, and $z = 8000$ psi) at reservoir temperature (200 °F). Shear stress magnitudes are in the range of 0 to 7200 psi in the opposite directions across the wellbore.

Figure 6.1.51 and **Figure 6.1.52** show a one-level slice of the radial and tangential stresses in psi with the slice taken in the XY-plane for an unstressed sandstone sample during the cryogenic treatment when the wellbore temperature is -321 °F and the sample temperature

is 70 °F. **Figure 6.1.51** shows radial stress in the range of -10,000 to 9000 psi, **Figure 6.1.52** shows tangential stress in the range of -4230 to 17,100 psi.

Figure 6.1.53 and **Figure 6.1.54** are the same plots with the sandstone sample temperature at 200 °F. **Figure 6.1.53** shows radial stress in the range of -23,000 to 12,000 psi and **Figure 6.1.54** shows tangential stress in the range of -5600 to 22,000 psi. Clearly, the radial and tangential stresses increased with increasing sample temperature, due to increased temperature gradient (ΔT).

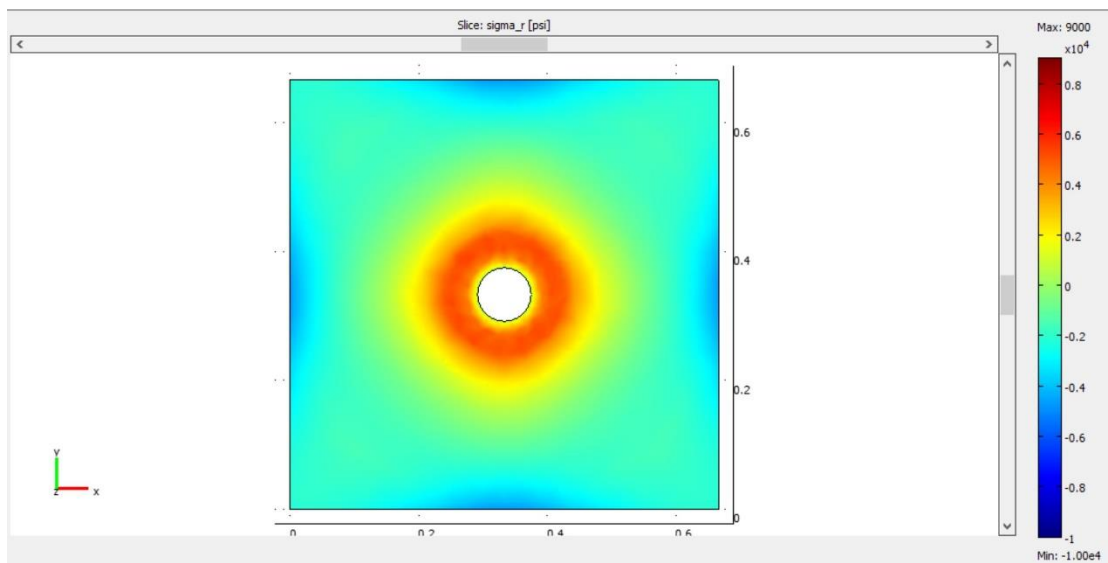


Figure 6.1.51 2D slice of radial stress in psi taken in the XY-plane for unstressed sandstone sample at room temperature. The radial stress development is seen around the wellbore, and the magnitudes are in the range of -10,000 to 9000 psi.

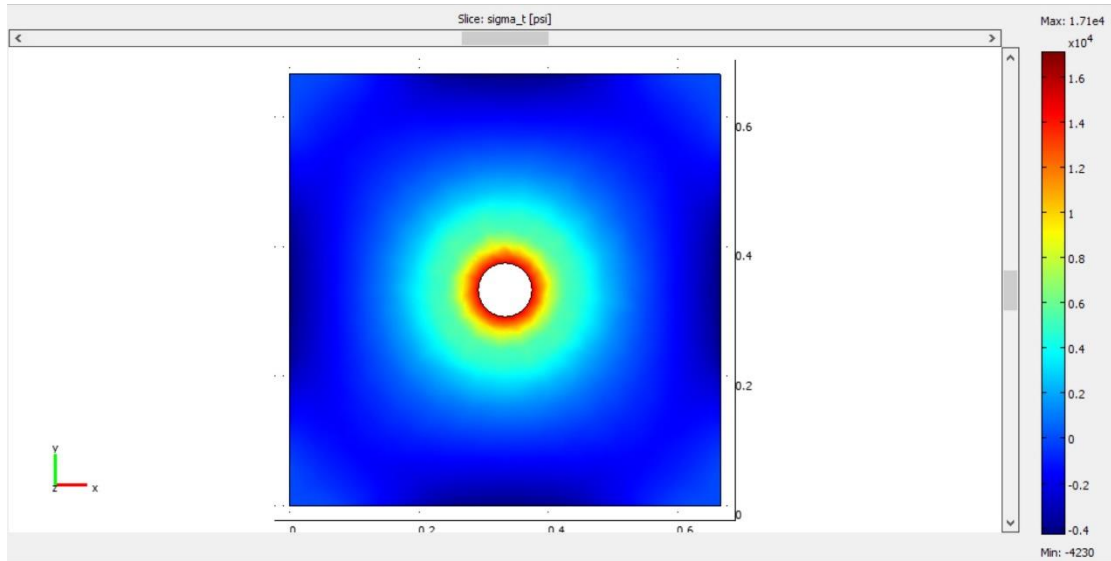


Figure 6.1.52 2D slice of tangential stress in psi taken in the XY-plane for an unstressed sandstone sample at room temperature. The radial stress development is seen around the wellbore, and the magnitudes are in the range of -4230 to 17,100 psi.

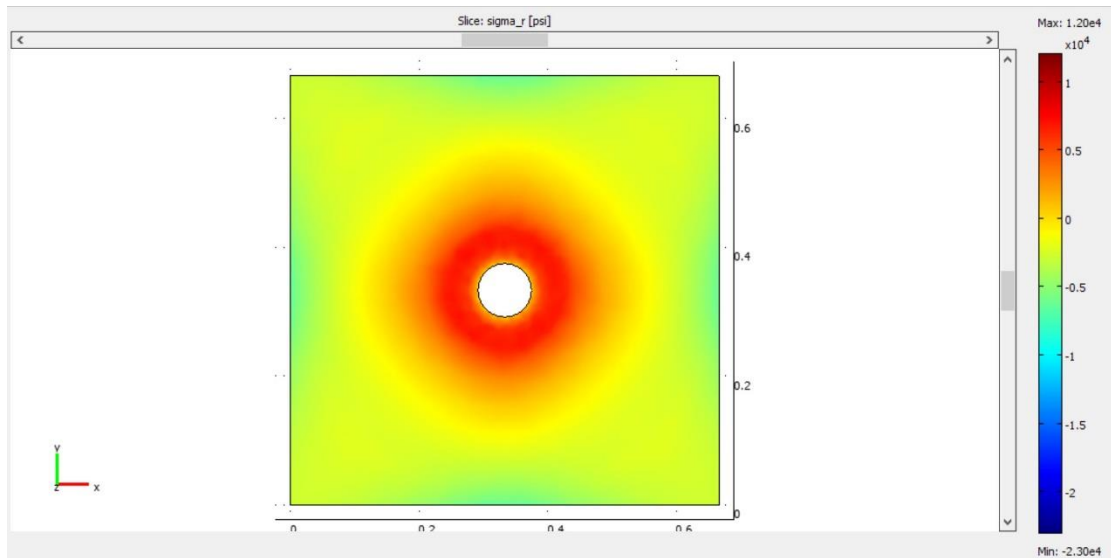


Figure 6.1.53 2D slice of radial stress in psi taken in the XY-plane for an unstressed sandstone sample at reservoir temperature (200 F). The radial stress development is seen around the wellbore, and the magnitudes are in the range of -23,000 to 12,000 psi.

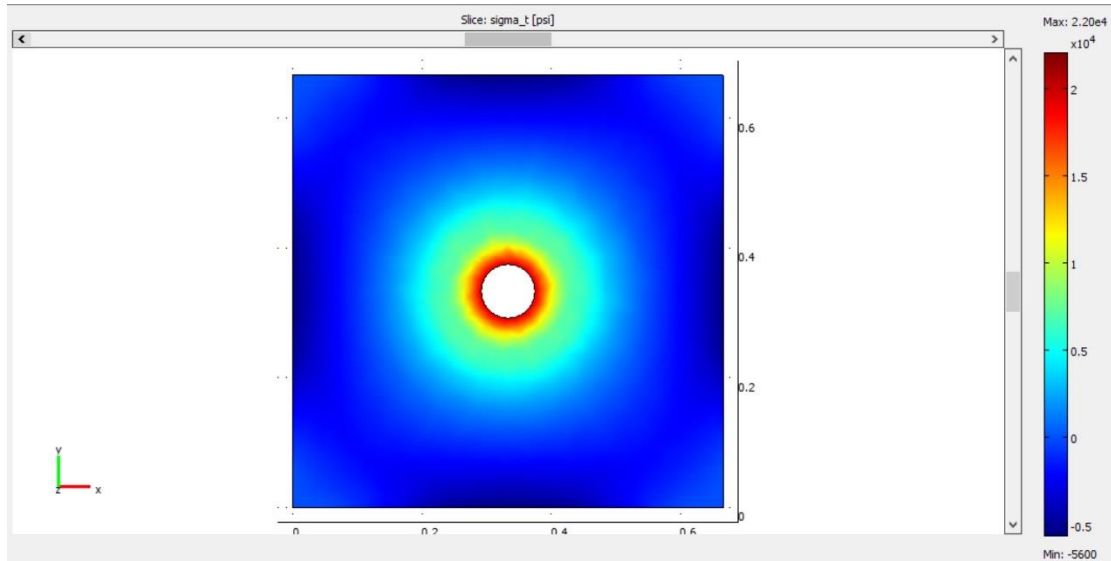


Figure 6.1.54 2D one-level slice of tangential stress in psi with the slice taken in the XY-plane for an unstressed sandstone sample at reservoir temperature (200 °F). The radial stress development is seen around the wellbore, and the magnitudes are in the range of -5600 to 22,000 psi.

To see the effect of loading stresses, **Figure 6.1.55** and **Figure 6.1.56** show the radial and tangential stresses, with the slice taken in the XY-plane, that have been created during the cryogenic treatment when the wellbore temperature is -321 °F, the sandstone sample temperature is 70 °F, and the sample was triaxially stressed ($x = 4000$ psi, $y = 6000$ psi, and $z = 8000$ psi). **Figure 6.1.55** shows radial stress of -26,500 to 3820 psi. **Figure 6.1.56** shows tangential stress of -11,500 to 8780 psi. The lower radial and tangential magnitudes are in the direction of maximum horizontal stress which is the direction of fracture propagation.

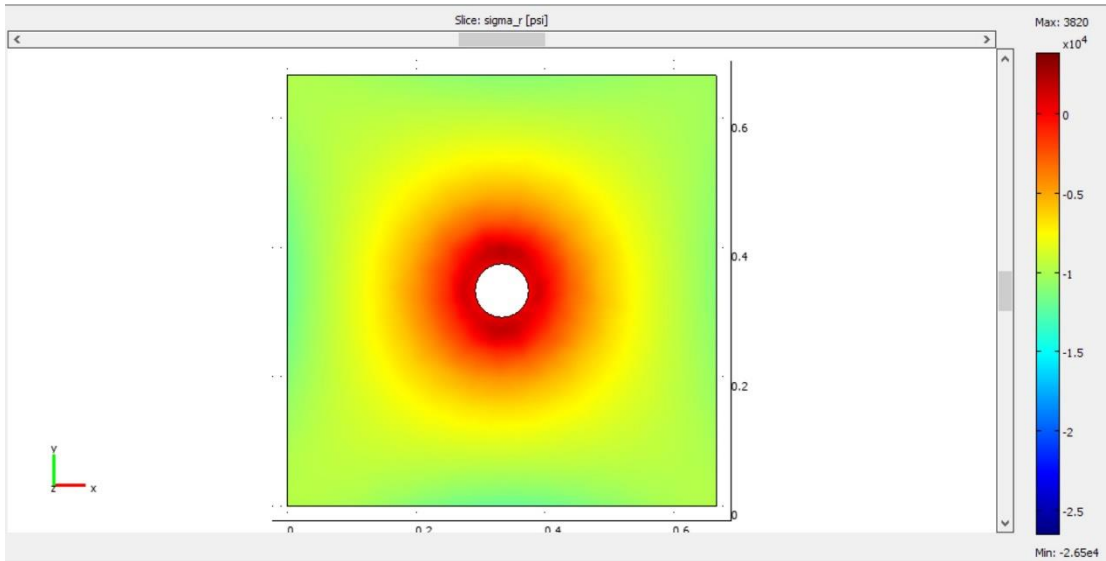


Figure 6.1.55 2D one-level slice of radial stress in psi with the slice taken in the XY-plane for triaxially stressed sandstone sample at room temperature (70 °F). The radial stress development is seen around the wellbore, and the magnitudes are in the range of -26,500 to 3820 psi.

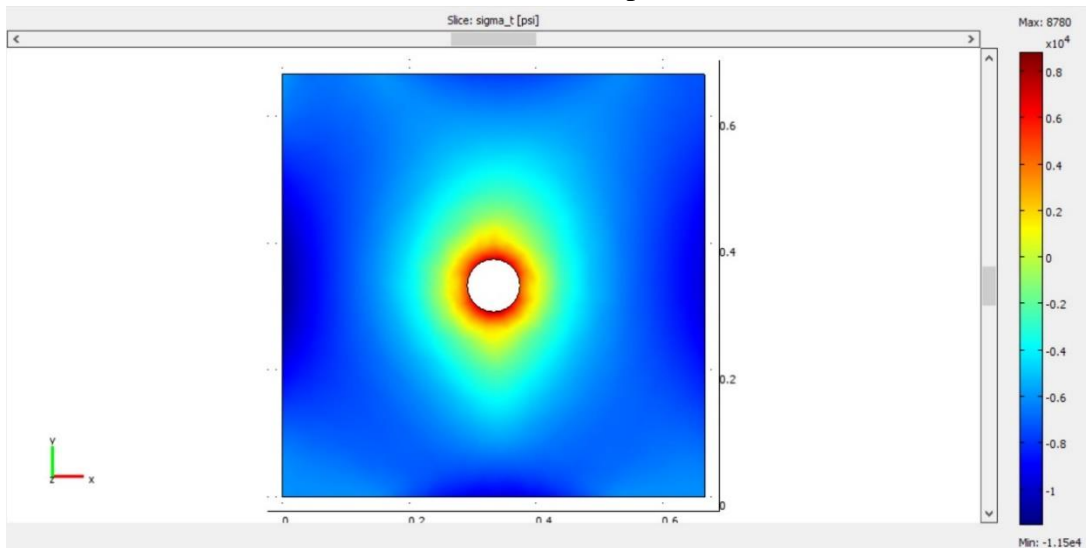


Figure 6.1.56 2D one-level slice of tangential stress in psi with the slice taken in the XY-plane for triaxially stressed sandstone sample at room temperature (70 °F). The tangential stress development is seen around the wellbore, and the magnitudes are in the range of -11,500 to 8780 psi.

6.1.3.2.2 Sandstone Sample with a 6-inch Cased Wellbore

To mimic the laboratory conditions, the sandstone sample with a 6-inch cased wellbore was placed under triaxial stresses ($x = 4000$ psi, $y = 6000$ psi, and $z = 8000$ psi). The sample

temperature was 70 °F. **Figure 6.1.57** shows a one-level slice plot of the τ_{xy} shear stress in psi with the slice taken in the XY-plane. The shear stress development is seen inside the stainless steel casing and also around the wellbore next to the casing. Shear stress magnitudes are in the range of 0 to 125,000 psi in the opposite directions across the wellbore. **Figure 6.1.58** shows the τ_{yz} shear stress in psi with the slice taken in the YZ-plane for this sample, the shear stress development is seen at the edge of the casing and the wellbore next to it. Shear stress magnitudes are in the range of 0 to 120,000 psi in opposite directions across the wellbore of the sandstone sample.

In **Figure 6.1.59** and **Figure 6.1.60**, the radial and tangential stresses in the XY plane can be seen developing around the wellbore in the range of 3.206 to 7.682 (\log_{10} psi) for radial and 2.775 to 7.388 (\log_{10} psi) for tangential. **Figure 6.1.61** and **Figure 6.1.62** show the \log_{10} radial and tangential stresses in the XY plane of the triaxially stressed sandstone sample, respectively. During the cryogenic treatment, the wellbore temperature is -321 °F and the sample temperature is 70 °F. It seems that the stresses around the casing distributed equally even though the sandstone was under triaxial stresses.

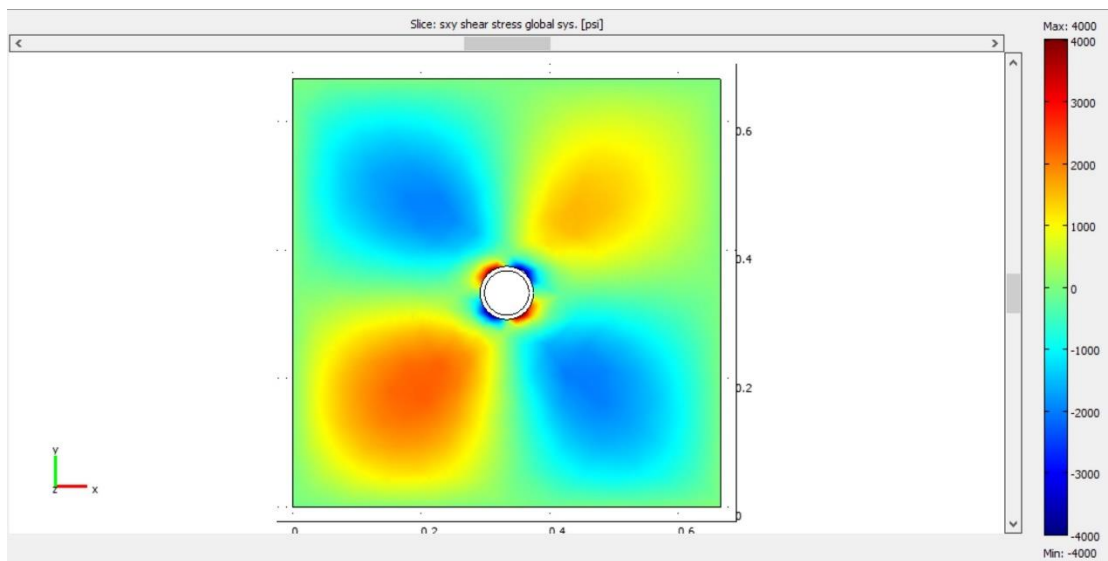


Figure 6.1.57 2D one-level slice plot of the τ_{xy} shear stress in psi taken in the XY-plane for a triaxially stressed sandstone sample at room temperature (70 °F). The shear stress development is seen inside the stainless steel casing and around the wellbore. Shear stress magnitudes are in the range of 0 to 125,000 psi in opposite directions across the wellbore.

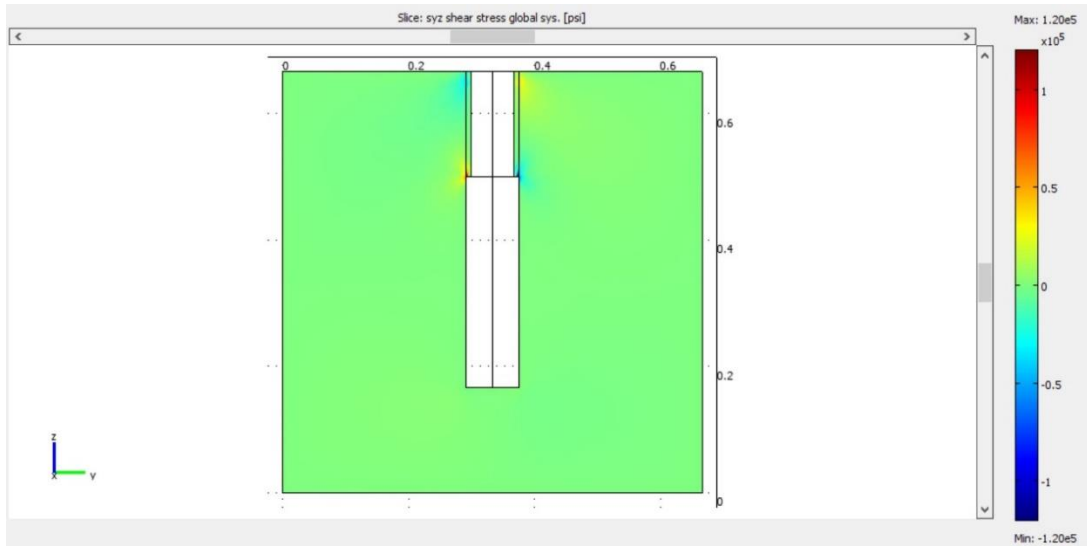


Figure 6.1.58 2D one-level slice plot of the τ_{yz} shear stress in psi with the slice taken in the YZ-plane for a sandstone sample that was triaxially stressed at room temperature (70 F). The shear stress development is seen at the edge of the casing and the wellbore. Shear stress magnitudes are in the range of 0 to 120,000 psi in opposite directions across the wellbore of the sandstone sample.

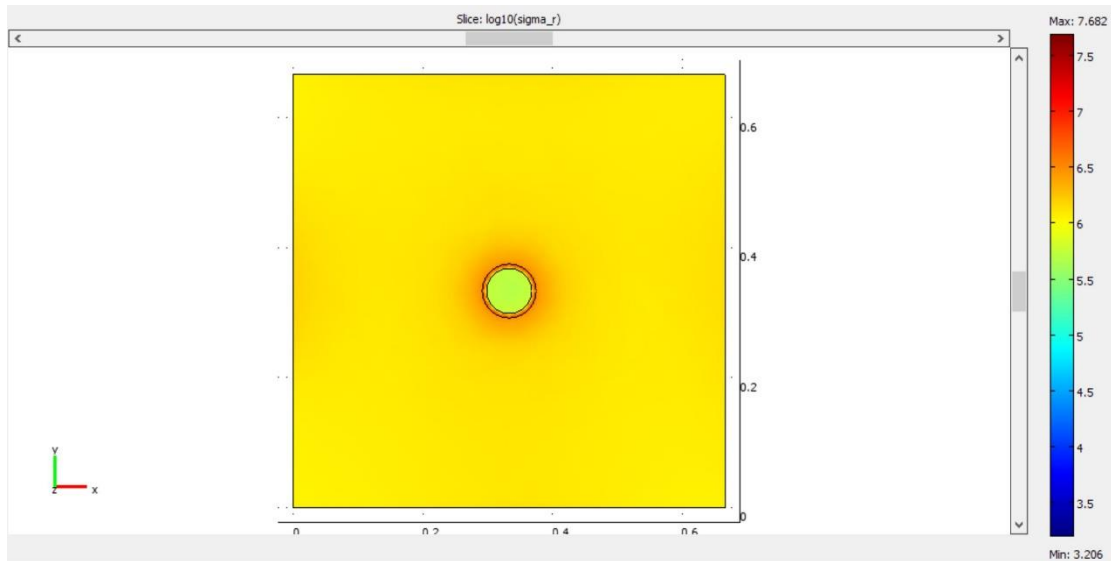


Figure 6.1.59 2D one-level slice of the \log_{10} radial stress with the slice taken in the XY-plane. The radial stress development is seen around the wellbore and the magnitudes are in the range of 3.206 to 7.682 (\log_{10} psi).

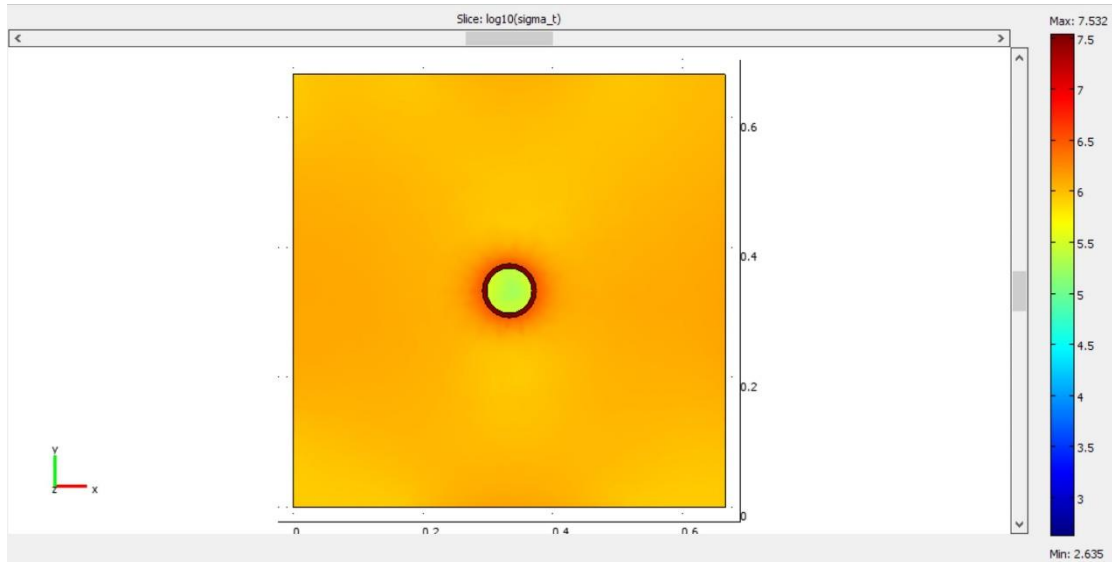


Figure 6.1.60 2D one-level slice of the \log_{10} tangential stress with the slice taken in the XY-plane. The tangential stress development is seen around the wellbore and the magnitudes are in the range of 2.775 to 7.388 (\log_{10} psi).

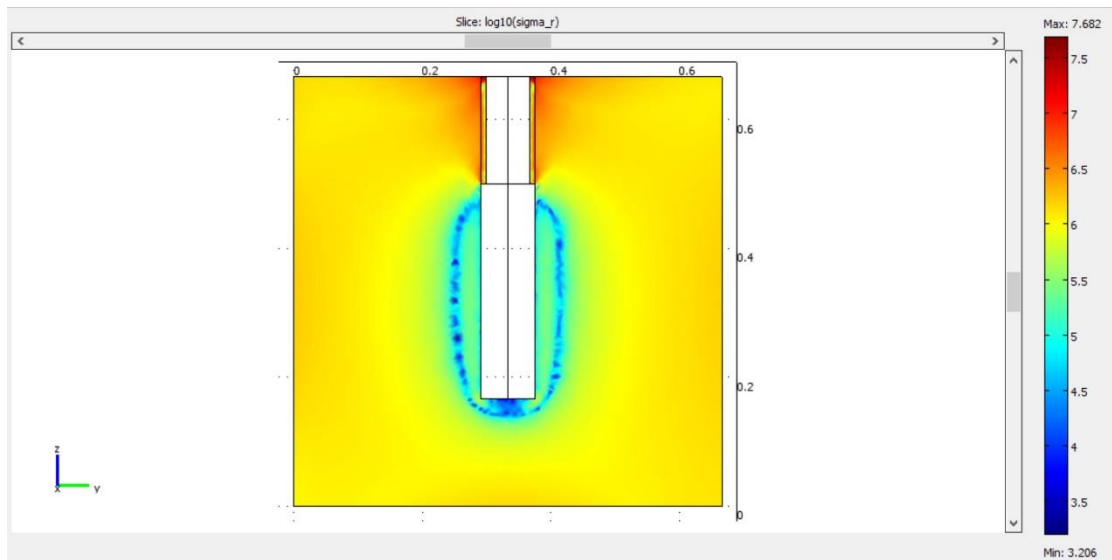


Figure 6.1.61 2D one-level slice of the \log_{10} radial stress with the slice taken in the YZ-plane pass through the casing. The radial stress development is seen around the wellbore, and the magnitudes are in the range of 3.206 to 7.682 (\log_{10} psi).

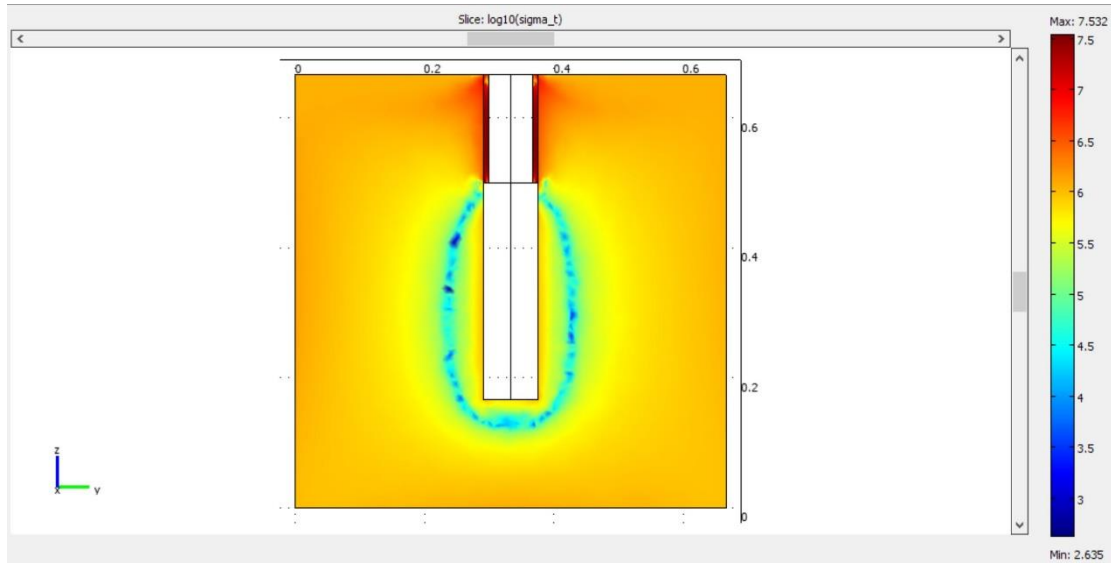


Figure 6.1.62 2D one-level slice of the \log_{10} tangential stress with the slice taken in the YZ-plane. The tangential stress development is seen around the wellbore, and the magnitudes are in the range of 2.635 to 7.532 (\log_{10} psi).

6.1.3.3 Shale Samples

In this section, the results and observations for the multi-layered heterogeneous, cubic block models of shale with 6-inch open and cased wellbores are presented.

6.1.3.3.1 Shale Sample with a 6-inch Open Hole

Figure 6.1.63 and **Figure 6.1.64** show the temperature in $^{\circ}\text{F}$ with deformed shape in the YZ-plane of an unstressed shale with the outside boundary temperature of 70°F and 200°F , respectively. It appears more deformation occurred at the lower temperature.

Figure 6.1.65 shows a one-level slice plot of the τ_{xy} shear stress in psi with the slice taken in the XY-plane for a shale sample at the bottom of the wellbore. The unstressed sample was treated at 70°F and shear stress development is seen around the wellbore ranging from 0 to 2100 psi in opposite directions across the wellbore (compressional and tensional forces). However, as you can see in **Figure 6.1.66**, the shear stress values change by layer. This figure shows a line cross section plot of the share stress in psi with the line taken in the z-axis and next to the wellbore. This pattern persists and increases in magnitude at 200°F (**Figure 6.1.67**).

Figure 6.1.68 shows the effect of applying the triaxial stresses. As with the previous cases the shear stress has different magnitudes for each layer but both the magnitude and directions of the stresses have changed.

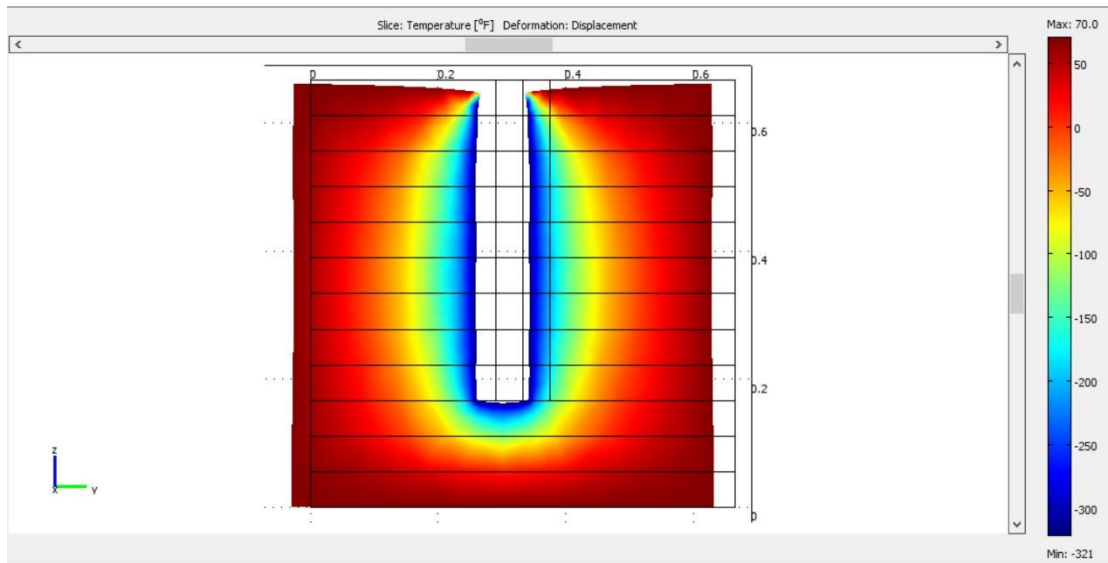


Figure 6.1.63 Temperature in $^{\circ}\text{F}$ with deformed shape in the YZ-plane for the unstressed multi-layered shale sample with the outside boundary temperature of 70 $^{\circ}\text{F}$.

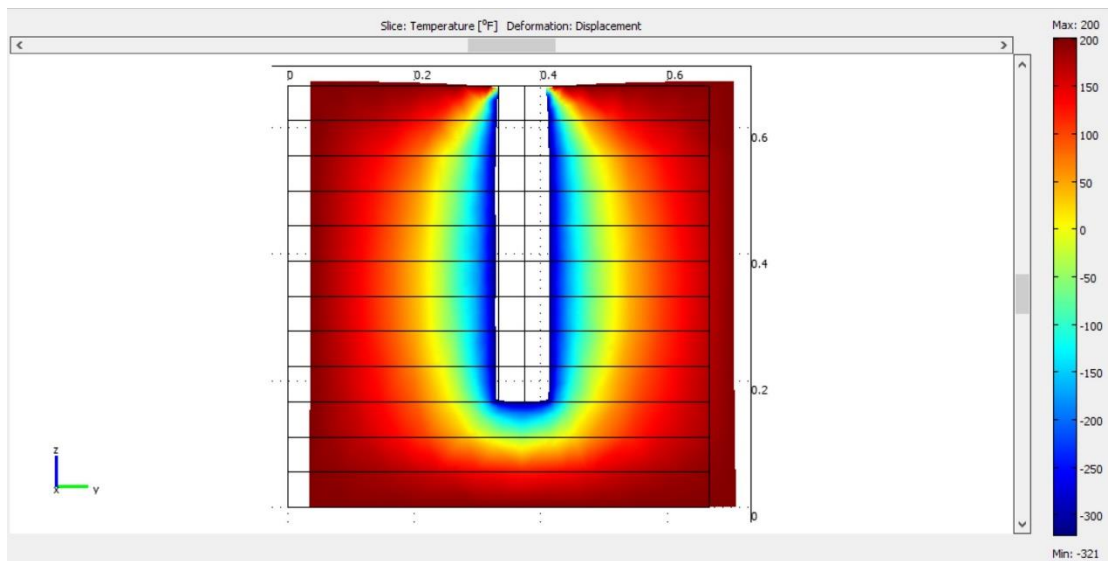


Figure 6.1.64 Temperature in $^{\circ}\text{F}$ with deformed shape in the YZ-plane for the unstressed shale and the outside boundary temperature is the reservoir temperature (200 $^{\circ}\text{F}$).

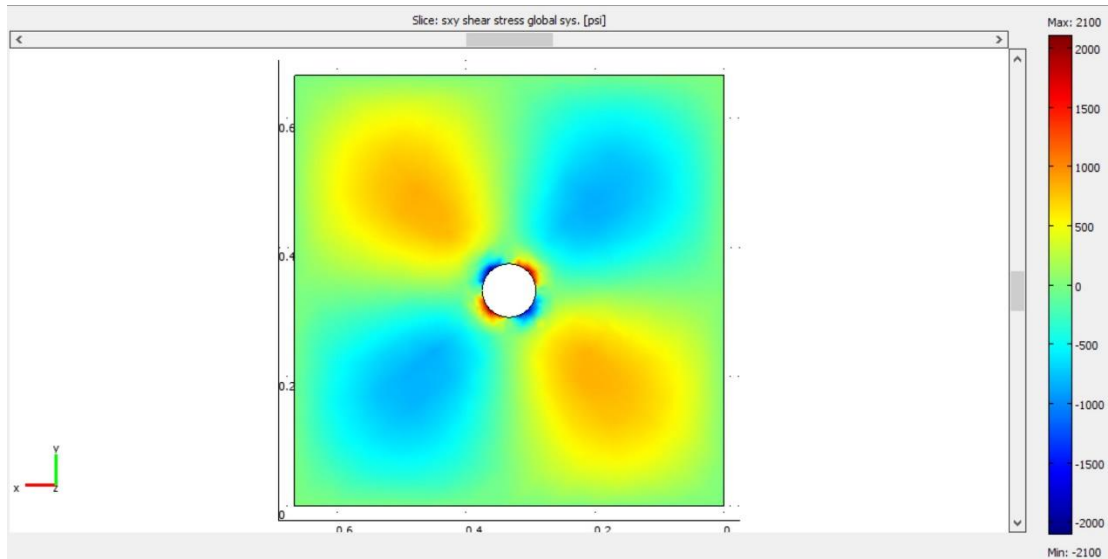


Figure 6.1.65 2D slice plot of the τ_{xy} shear stress in psi taken in the XY-plane for an unstressed shale sample at the bottom side of the wellbore at room temperature (70 $^{\circ}$ F). The shear stress development is seen around the wellbore. Shear stress magnitudes are in the range of 0 to 2100 psi in opposite directions across the wellbore.

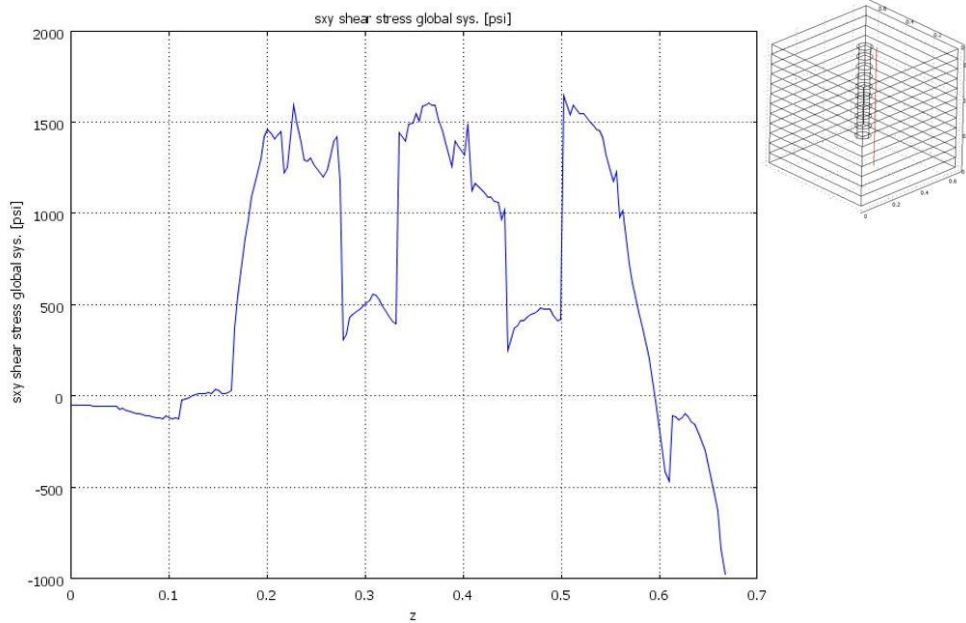


Figure 6.1.66 Line cross section plot of the τ_{xy} share stress in psi of the shale sample at 70 $^{\circ}$ F, with line taken in the z-axis (red line inside the block-top right illustration). The share stress development has different magnitudes for each layer.

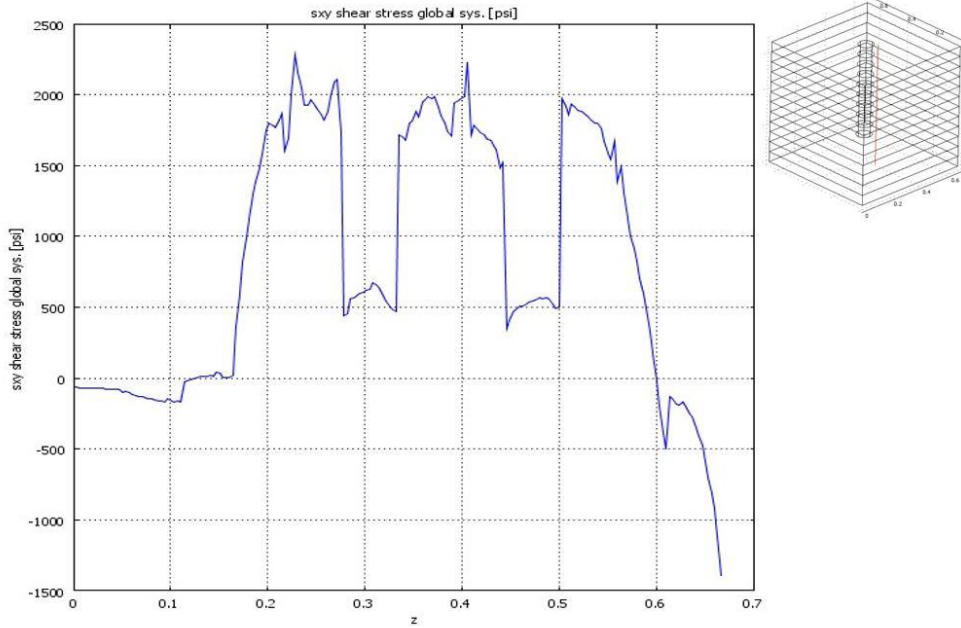


Figure 6.1.67 Line cross section plot of the τ_{xy} share stress in psi of the shale sample at 200 F, with line taken in the z-axis (red line inside the block-top right illustration). The share stress development has different magnitudes for each layer.

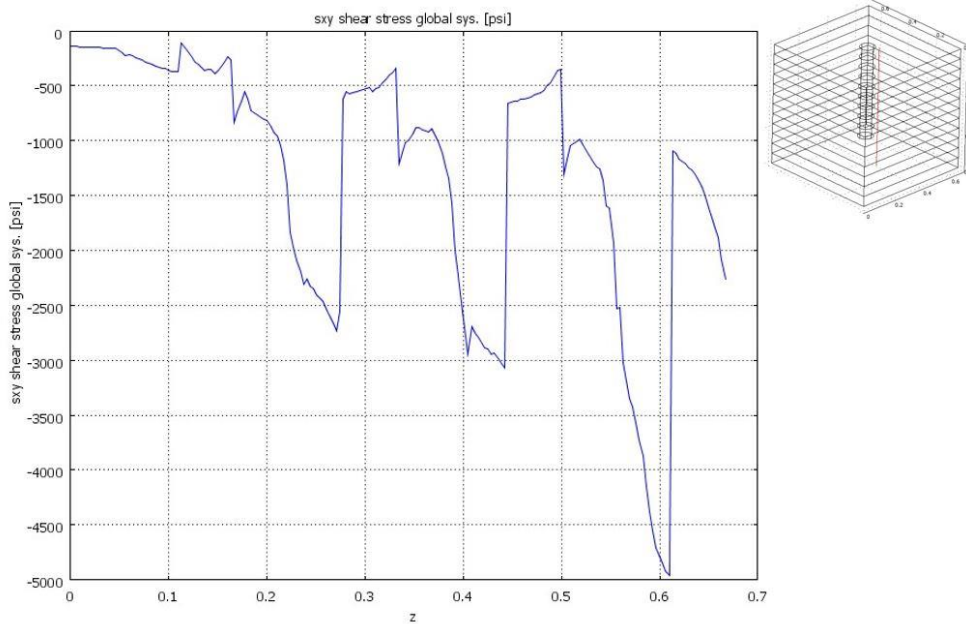


Figure 6.1.68 Line cross section plot of the τ_{xy} share stress in psi of the stressed shale block ($x = 4000$ psi, $y = 6000$ psi, and $z = 8000$ psi) at 70 F, the line is taken in the z-axis (red line inside the block-top right illustration). The shear stress development is seen around the wellbore, and its magnitudes are from 0 to 4900 psi in opposite directions across the wellbore. The shear stress has different magnitudes for each layer.

Figure 6.1.69 and **Figure 6.1.70** show YZ-plane slices of the radial and tangential stresses in psi when the wellbore temperature is -321 °F, the shale sample temperature is 70 °F, and there are no triaxial stresses applied. Radial stress ranges from -3197 to 2640 psi, and tangential stresses range from -1469 to 8470 psi. To see the effect of temperature, **Figure 6.1.71** shows the radial stress when the shale sample temperature is 200 °F. The radial stress increases (ranges from -3686 to 3413 psi) due to the increase in temperature gradient (ΔT).

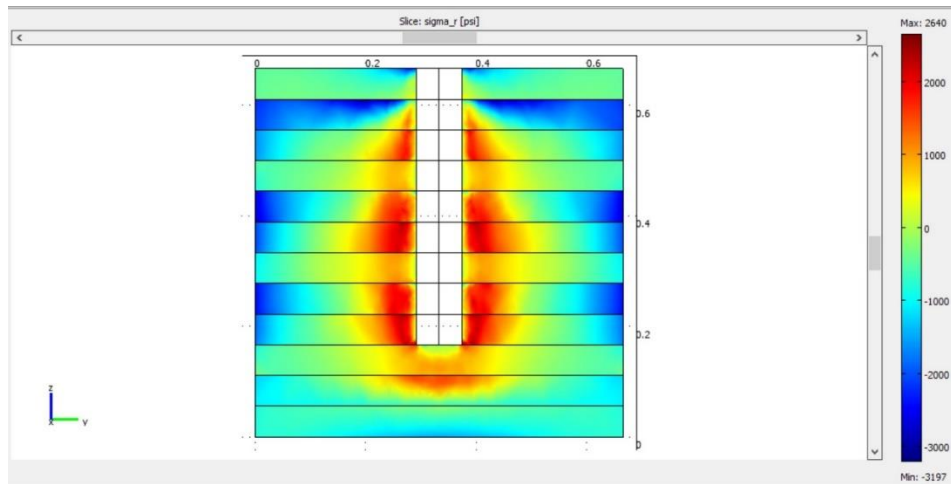


Figure 6.1.69 2D one-level slice of the radial stress in psi with the slice taken in the YZ-plane to show the variation in radial stress for each layer. The radial stress development is seen around the wellbore, and the magnitudes are in the range of -3197 to 2640 psi.

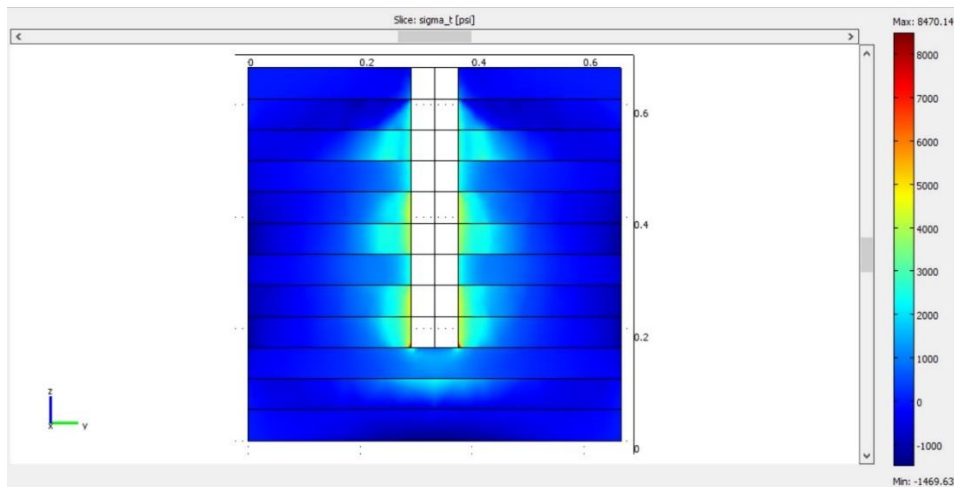


Figure 6.1.70 2D one-level slice of the tangential stress in psi with the slice taken in the YZ-plane. The tangential stress development is seen around the wellbore, and the magnitudes are in the range of -1469 to 8470 psi.

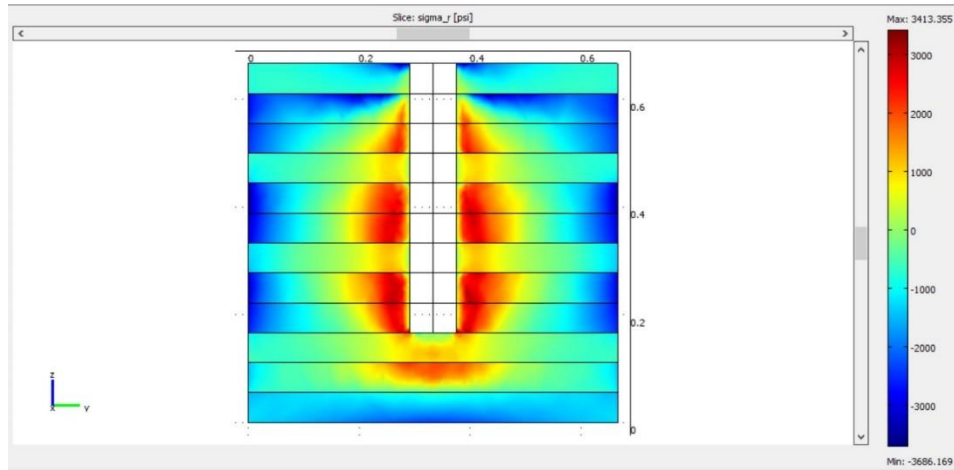


Figure 6.1.71 2D one-level slice of the radial stress in psi taken in the YZ-plane during the cryogenic treatment of the unstressed shale sample with the wellbore temperature of -321 °F and the boundary temperature of 200 °F. The radial stress development is seen around the wellbore, and the magnitudes are in the range of -3686 to 3413 psi.

To see the effect of loading stresses, **Figure 6.1.72** and **Figure 6.1.73** show the radial stress during the cryogenic treatment. Different views in YZ and XZ-planes are provided. **Figure 6.1.72** shows a one-level slice of the radial stress in psi with the slice taken in the YZ-plane. The magnitudes are in the range of -22,957 to 691 psi. **Figure 6.1.73** shows a slice taken in the XZ-plane. The lower radial and tangential stresses are in the direction of maximum horizontal stress which is along the direction of fracture propagation.

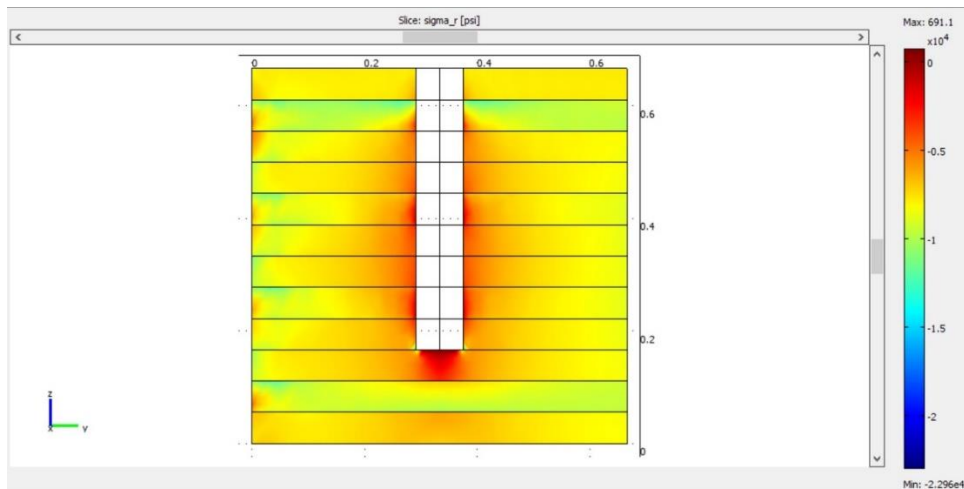


Figure 6.1.72 2D one-level slice of the radial stress in psi with the slice taken in the YZ-plane. The radial stress development is seen around the wellbore, and the magnitudes are in the range of -22,957 to 691 psi.

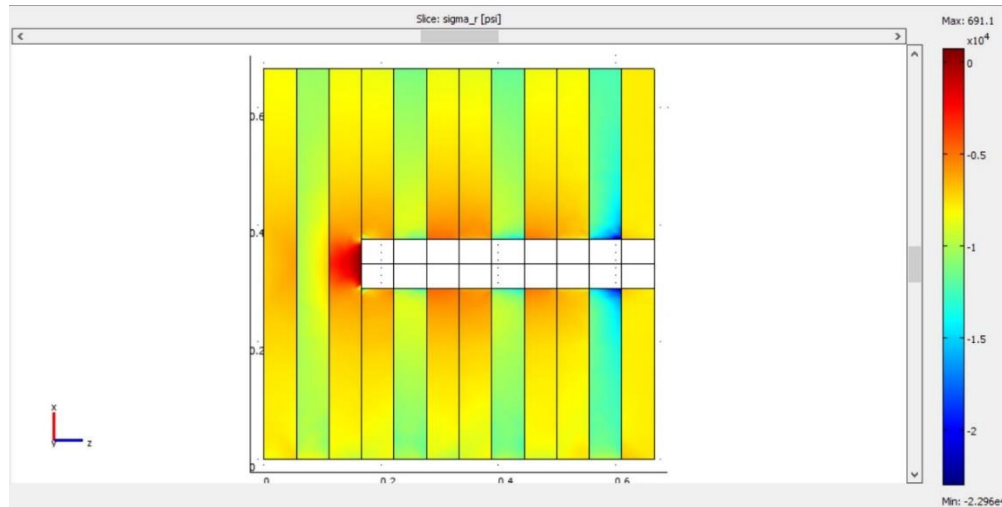


Figure 6.1.73 2D one-level slice of the radial stress in psi with the slice taken in the XZ-plane. The radial stress development is seen around the wellbore, and the magnitudes are in the range of -22,957 to 691 psi.

6.1.3.3.2 Shale Sample with a 6-inch Cased Wellbore

To mimic the laboratory conditions, the shale sample with a 6-inch cased wellbore was also modeled under triaxial stresses ($x = 4000$ psi, $y = 6000$ psi, and $z = 8000$ psi). The sample temperature is 70 F. **Figure 6.1.74** shows a one-level slice plot of the τ_{xy} shear stress in psi with the slice taken in the XY-plane. The shear stress development is seen inside the stainless steel casing and also around the wellbore next to the casing. Shear stress magnitudes are in the range of 0 to 93,000 psi in the opposite directions across the wellbore (compressional and tensional forces) and vary in each layer. **Figure 6.1.75** shows a slice taken in the YZ-plane. Shear stress magnitudes are in the range of 0 to 56,000 psi in the opposite directions across the wellbore of the shale sample.

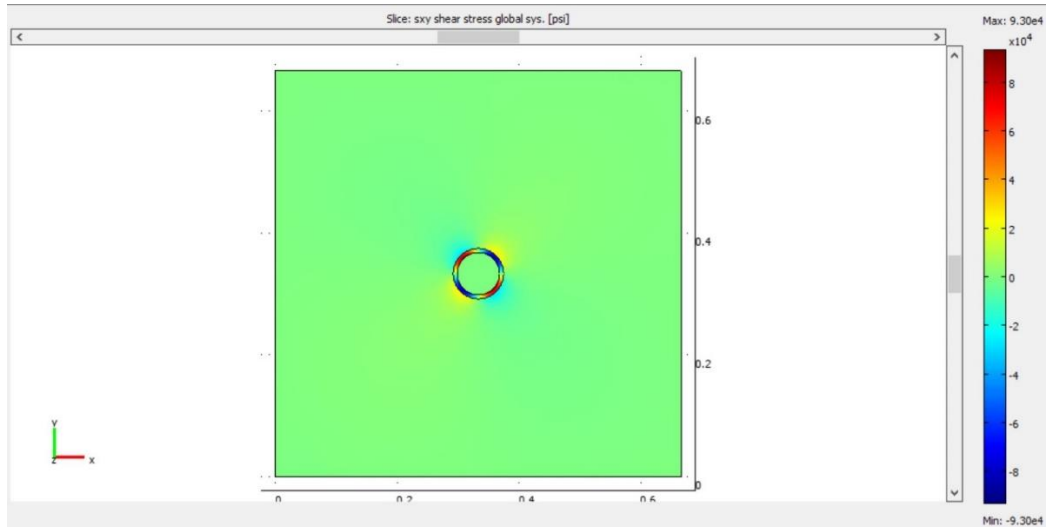


Figure 6.1.74 2D one-level slice plot of the τ_{xy} shear stress in psi with the slice taken in the XY-plane for a triaxially stressed shale sample at room temperature (70 °F). The shear stress development is seen inside the stainless steel casing and also around the wellbore next to the casing. Shear stress magnitudes are in the range of 0 to 93,000 psi in the opposite directions across the wellbore.

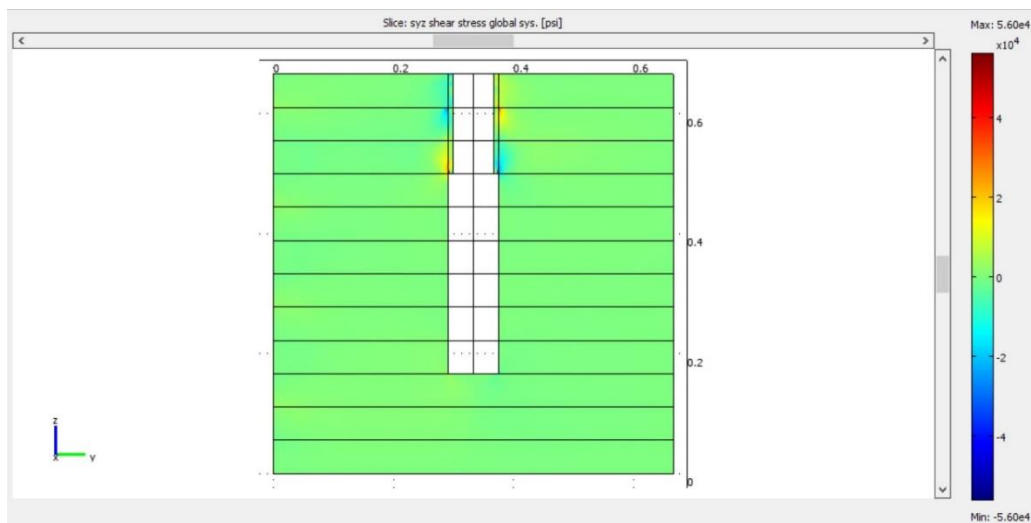
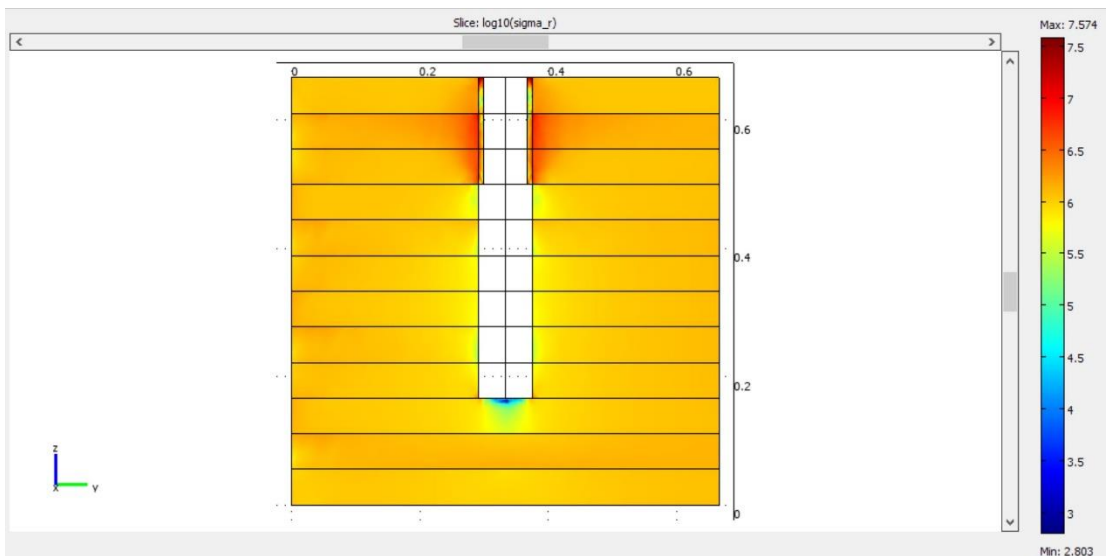


Figure 6.1.75 2D one-level slice plot of the τ_{yz} shear stress in psi with the slice taken in the YZ-plane for a triaxially stressed shale sample at room temperature (70 °F). The shear stress development is seen at the edge of the casing and between the first and second layers from the top around the wellbore. Shear stress magnitude are in the range of 0 to 56,000 psi in the opposite directions across the wellbore.

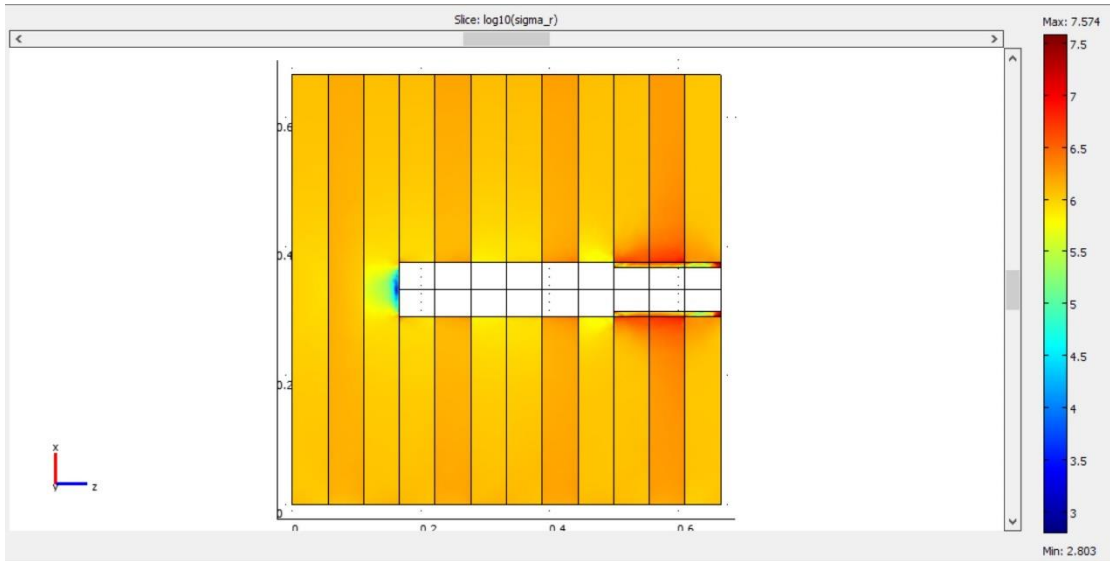
Figure 6.1.76 and **Figure 6.1.77** show the radial and tangential stresses, respectively, during the cryogenic treatment of a triaxially stressed shale block ($x = 4000$ psi, $y = 6000$

psi, and $z = 8000$ psi) when the wellbore temperature is -321 °F and the shale sample temperature is 70 °F. **Figure 6.1.76a** shows a one-level slice of the \log_{10} radial stress with the slice taken in the YZ-plane. **Figure 6.1.76b** shows a one-level slice of the \log_{10} radial stress with the slice taken in the XZ-plane. The radial stress development is seen around the wellbore, and the magnitudes are in the range of 2.803 to 7.574 (\log_{10} psi).

Figure 6.1.77a shows a one-level slice of the \log_{10} tangential stress with the slice taken in the YZ-plane. **Figure 6.1.77b** shows a one-level slice of the \log_{10} tangential stress with the slice taken in the XZ-plane. The tangential stress development is seen around the wellbore, and the magnitudes are in the range of 2.67 to 7.364 (\log_{10} psi). It seems the stresses around the casing distribute equally even though the block was under triaxial stresses.

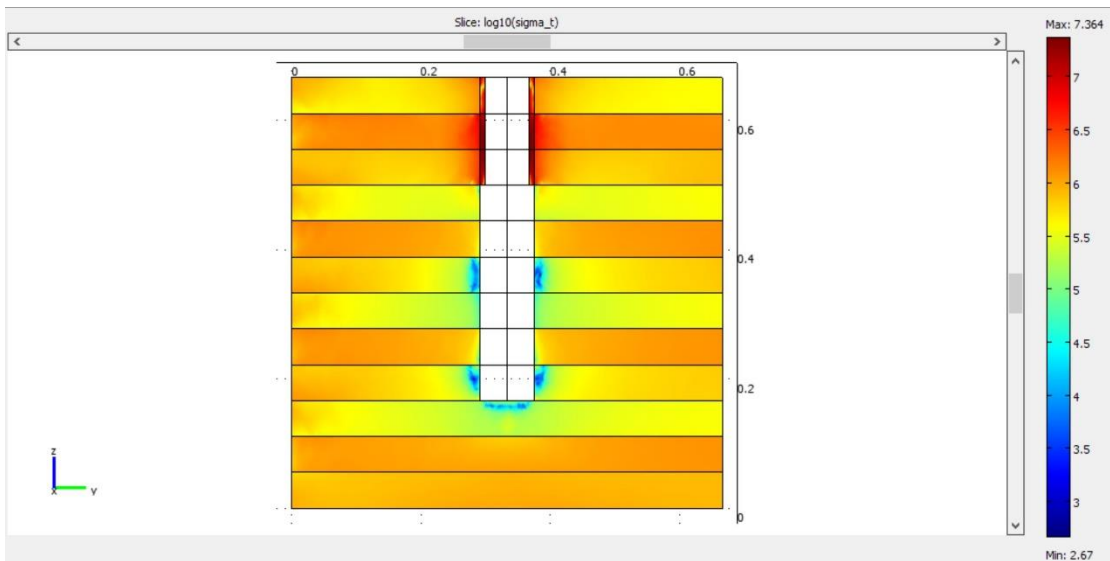


(a)

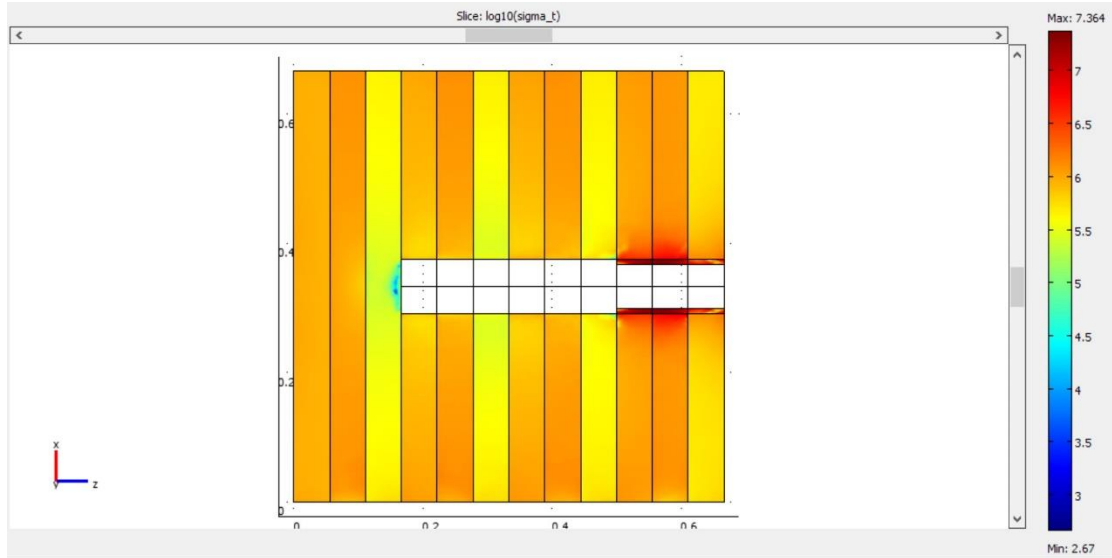


(b)

Figure 6.1.76 2D slice plots of radial stress during the cryogenic treatment of a triaxially stressed shale sample ($x = 4000$ psi, $y = 6000$ psi, and $z = 8000$ psi) when the wellbore temperature is -321 °F and the sample temperature is 70 °F. (a) shows a one-level slice of the \log_{10} radial stress with the slice taken in the YZ-plane. (b) shows a one-level slice of the \log_{10} radial stress with the slice taken in the XZ-plane. The radial stress develops around the wellbore with the magnitudes in the range of 2.803 to 7.574 (\log_{10} psi).



(a)



(b)

Figure 6.1.77 2D one-level slice plots of tangential stress during the cryogenic treatment of a triaxially stressed shale block ($x = 4000$ psi, $y = 6000$ psi, and $z = 8000$ psi) when the wellbore temperature is -321 °F and the shale sample temperature is 70 °F. (a) shows a one-level slice of the \log_{10} tangential stress with the slice taken in the YZ-plane. (b) shows a one-level slice if the \log_{10} tangential stress with slice taken in the XZ-plane. The magnitudes are in the range of 2.67 to 7.364 (\log_{10} psi).

6.2 Finite Difference Modeling

In this section, the theory and work flow of the simulation tool developed for this research are introduced. The objective for developing these tools is to evaluate the distribution and the effect of thermally induced fractures during cryogenic fracturing treatments. This simulation tool is modified from TOUGH2-EGS (Enhanced Geothermal System), which is a coupled geomechanical and reactive geochemical simulator for fluid and heat flows in an enhanced geothermal system (Xiong et al., 2013, Zhang et al., 2013). With the ability of TOUGH2-EGS and modification on fracture initiation and propagation, this simulation tool can simulate cryogenic fracturing processes and predict the distribution of fractures.

6.2.1 Theoretical Analysis

Cryogenic fracturing is a very complex process involving hydraulics, thermodynamics, and rock mechanics. In order to analyze this process, several assumptions have been made to

simplify the physics. In addition, heat transfer, thermal stresses, and failure criteria are addressed in this section.

6.2.1.1 Assumptions

In order to simplify the development of the simulation tool, several assumptions have been made:

1) For heat transfer, only heat conduction is considered, which means that both advection and radiation are neglected. In porous media, the contacting area between fluid and rock surfaces is very large per unit volume of fluid. This indicates that heat conduction plays a much more important role than advection and radiation during a short period of cryogenic treatment. In each grid block, the temperature of the rock matrix is assumed always the same as that of the fluid in the pore volume.

2) For fracturing processes, the stress change in the rock matrix includes thermal expansion or contraction due to the change in temperature, fluid pressure in pores, and external stress condition, as imposed by the hydraulic press and pistons in the experiment. The principal stress directions follow the loading direction in the triaxially stressed experiments.

3) The rock matrix is assumed to be homogeneous within each grid block. The heterogeneity of the sample is achieved by assigning different rock properties to different grid blocks.

4) For natural fractures, since they are very difficult to characterize, pre-existing natural fractures are neglected (Zhao et al. 2015). Only the fractures generated by the cryogenic treatment are considered and tracked.

6.2.1.2 Heat Transfer and Fluid Flow

The heat transfer and fluid flow model in the simulation tool is adapted from the TOUGH2-EGS simulator. The governing equation for mass and heat balance can be written in the form (Fakchroenphol et al. 2013, Zhang et al., 2015a, 2015b),

$$\frac{d}{dt} \int_{V_n} M^\kappa dV_n = \int_{\Gamma_n} F^\kappa \cdot \vec{n} d\Gamma_n + \int_{V_n} q^\kappa dV_n$$

Where:

$\kappa = 1, \dots, NK$ (total number of components);

$n = 1, \dots, NEL$ (total number of grid blocks);

V_n is an arbitrary subdomain of the system under study;

Γ_n is the closed surface by which the subdomain is bounded by;

M is the quantity representing mass or energy per volume;

F is mass or heat flux;

Q is sinks and sources;

\vec{n} is a normal vector on surface element $d\Gamma_n$ pointing inward into V_n .

6.2.1.3 Thermal Stress

Thermal stress is the stress change caused by temperature change within a solid material. It is the most important parameter when simulating the cryogenic fracturing process. The thermally induced stress can be integrated into the generalized stress-strain relation in a rock volume, as shown below:

$$\sigma_{kk} - Bi \times p_{pore} - \frac{E}{(1-2\nu)} [\alpha_L (T - T_0)] = \frac{E}{(1+\nu)} \varepsilon_{kk} + \frac{E\nu}{(1+\nu)(1-2\nu)} (\varepsilon_{xx} + \varepsilon_{yy} + \varepsilon_{zz})$$

Where:

σ is the normal stress;

ε is the strain;

Subscript kk is direction, which can be x, y and z;

Bi is the Biot number of the rock;

α_L is the linear thermal expansion of the rock;

E is the Young's modulus;

ν is the Poisson's ratio;

p_{pore} is the pore pressure;

T is the current temperature;

T_0 is the reference or the original temperature.

6.2.1.4 Failure Criteria

A failure criterion is used to judge the condition of rock fracturing. It gives the maximum strength of rock under certain stress conditions. Once the stress exceeds the maximum strength given by the failure criterion, the rock will break, in other words, be fractured. The current failure model used in this simulation tool is the Mogi-Coulomb Failure Criterion, which is first introduced by Al-Ajmi and Zimmerman (2006) and widely used in rock mechanics. The Mogi-Coulomb Failure Criterion has the following form:

$$\tau_{oct} = k + m\sigma_{oct}$$

Where:

τ_{oct} is the octahedral shear stress;

σ_{oct} is the octahedral normal stress.

The octahedral shear and normal stresses are defined as:

$$\tau_{oct} = \frac{1}{3} \sqrt{(\sigma_v - \sigma_H)^2 + (\sigma_v - \sigma_h)^2 + (\sigma_H - \sigma_h)^2}$$
$$\sigma_{oct} = \frac{1}{3} (\sigma_v + \sigma_H + \sigma_h)$$

In the above equations, k and m are constants that are usually obtained from fitting actual data; and σ_H is the maximum horizontal stress. The failure envelope from Mogi-Coulomb Failure Criterion is shown in **Figure 6.2.1**. Normally the stress conditions of rock make the calculated τ_{oct} and σ_{oct} fall into the blue area under the failure envelope. When the stress condition changes, i.e. due to cryogenic treatment, the calculated τ_{oct} and σ_{oct} may fall onto a point outside of the failure envelope, the rock would then be fractured. Mogi-Coulomb Failure Criterion is simple and easy to apply in simulation and has similar accuracy with other failure criteria when assuming that the physical properties of rock remain the same with temperature change.

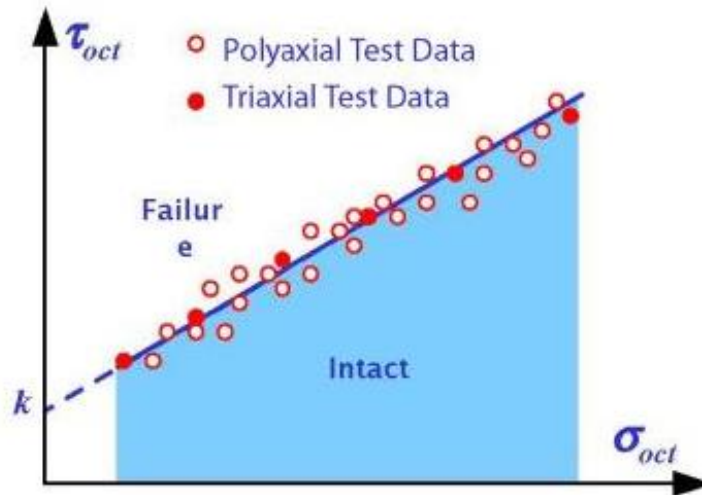


Figure 6.2.1 Failure envelope of Mogi-Coulomb Criterion (Aadnoy and Looyeh, 2011).

6.2.2 Problem Setup

The simulation tool simulates the cryogenic fracturing process using a control volume finite difference method. The basic geometry of the simulated well is the same as that in the experiment: the cryogenic fluid flows into a borehole and cools the wall. Then, the fluid will permeate through the porous medium through the inner borehole wall. The domain dimensions of the geometry are set as 8" × 8" × 8", identical to the dimensions of the samples used in the actual experiments.

6.2.2.1 Geometry

The details of this case are as follows. A 2.54 cm (1 inch) diameter borehole is centrally located on top surface extending 15.24 cm (6 inches) into the block. The upper 5.08 cm (2 inches) section of borehole will be cased, which means no fluid flow through this section into samples. **Figure 6.2.2** shows the schematic of geometry for modeling.

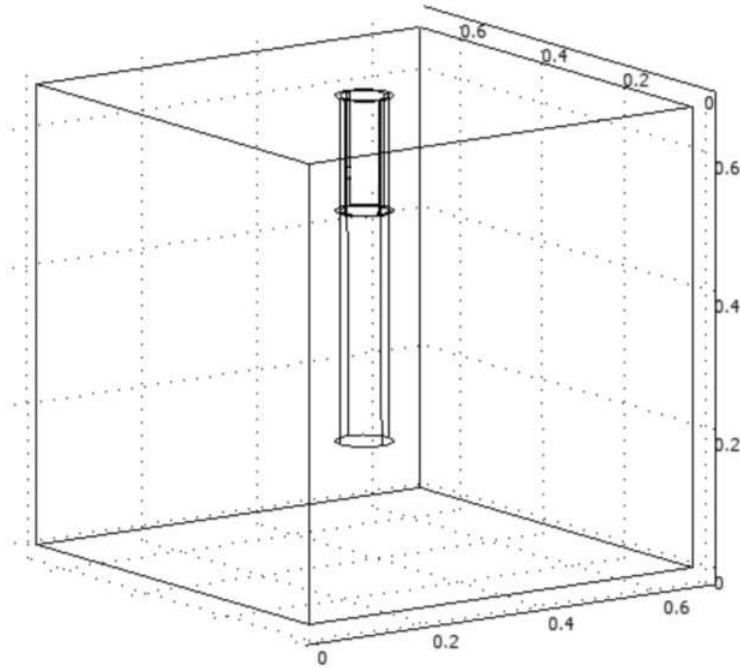


Figure 6.2.2 Schematic drawing for modeled geometry.

6.2.2.2 Boundary Conditions

The outer boundary, consisting of the six faces of the sandstone block, is exposed to ambient pressure and room temperature in the laboratory, which are 11.8 psia (81.4 KPa) and 66 °F (19 °C or 292 K) at Golden, Colorado. The initial sample temperature is also set at the room temperature, which is 66 °F (19 °C).

The stress condition is set the same as that in the experiment such that simulation and experimental results can be matched and compared.

For modeling, the thermal diffusivity of shale sample is set according to USGS (Robertson, 1988) as $8.00 \times 10^{-7} \text{ m}^2/\text{s}$. The constants from Mogi-Coulomb Criterion are set as $k = 230 \text{ psi}$ (1.59 MPa) and $m = 0.58$, which are fitted by experimental data from these four shale samples. And the permeability of fractured grids is set as 200 mD. All basic input parameters of the simulation can be found in **Table 6.4**.

Table 6.4 Input parameters for simulation

Properties	Value
Ambient pressure	11.8 psi (81.4 KPa)
Ambient temperature	66 °F (19 °C)
Rock density	2.38 g/cc
Permeability	1.05×10^{-3} mD
Permeability of fractured grid	200 mD
Porosity	8%
Rock compressibility	2×10^{-3} psi ⁻¹ (2.9×10^{-7} Pa)
Thermal diffusivity	8×10^{-7} m ² /s
Thermal expansion coefficient	2.7×10^{-5} °C
Specific heat	990 J/(kg·K)
Young's modulus	7.15×10^6 psi (4.93×10^4 Mpa)
Poisson's ratio	0.268
Mogi-Coulomb constant, k	230 psi (1.59 Mpa)
Mogi-Coulomb slope, m	0.58

6.2.2.3 Meshing

The meshing procedure, adapted from TOUGH2-EGS, is relatively simple. The samples are meshed into cubic cells with equal lengths in x-, y- and z-direction. Typically, a finer meshing with smaller cell size yields better resolution of the geometric features and more accurate results.

There are three types of grid blocks used in this simulation tool. The normal grid, which can be considered as the intact rock material, has the same properties with the measured rock properties. The fractured grid has larger permeability due to fractures induced by thermal shock in cryogenic treatment. The other properties remain the same with the normal grid. However, since fluid flow increases with higher permeability of grids, fractured grid blocks generally appear to be more thermally conductive. The third type of grid is the wellbore grid, which is set to have the same property with void space. If the center of a grid block falls within the borehole space, it is set as a wellbore grid.

6.2.2.4 Processing

The basic work flow of the simulation tool follows the original work flow of TOUGH2-EGS with modification on fractured grids judgement according to the Mogi-Coulomb Failure Criterion. The exact work flow is presented in **Figure 6.2.3**. At the beginning, the simulation tool reads the input file and initializes fluid, heat and stress variables. Then it builds Jacobian matrix for residual equations of fluid, heat, and stress, and then computes through an iteration process with the original thermal, hydraulic and mechanical modules. Once converged, the primary and secondary variables such as pressure, temperature, mass fraction and stress are updated with new values at current time step. Then the modified mechanical module solves for the octahedral stresses for each grid with the stress condition data. Next, these data are plugged into the Mogi-Coulomb Criterion. If the octahedral stresses of a grid indicate that it is fractured, this grid will be set as the fractured grid with higher permeability. After the judgement, the grid domain will be updated and the program continues to next time step until the maximum time step has been reached.

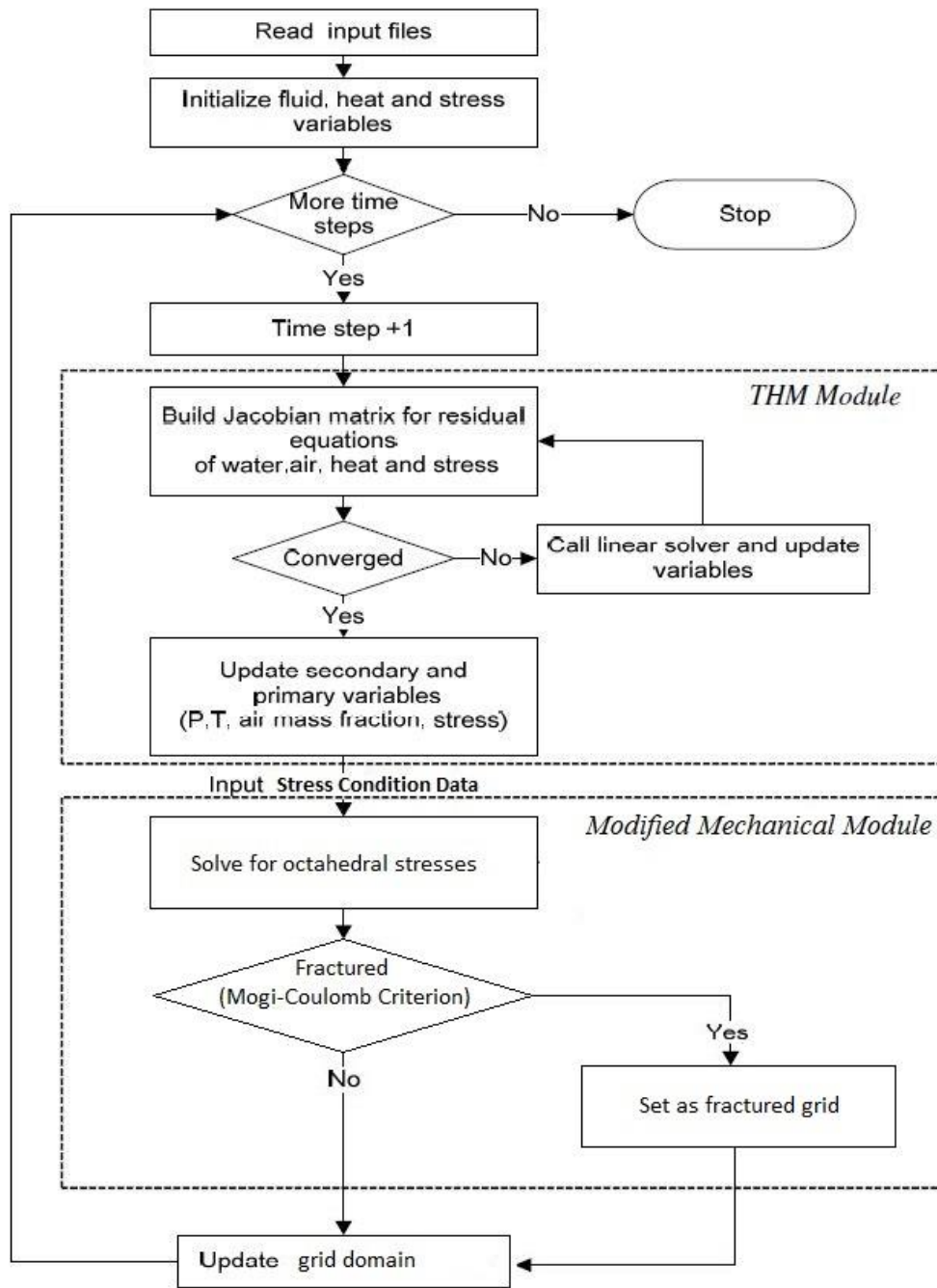


Figure 6.2.3 Work flow chart of the simulation tool.

6.2.3 Results

In this section, results of triaxially stressed tests and simulations for four shale samples through different treatment processes are presented and compared.

The four shale samples were treated with different cryogen injection pressure, treating time or cycles, and triaxial stress conditions. These conditions were varied to investigate the effect of different parameters on the final treatment results. The detailed experimental conditions and procedures are listed in **Table 6.5**.

Table 6.5 Experiment conditions for shale samples

Sample #	Stress condition (x-y-z)	Test procedure
Shale Sample 1	1000-1500-2000 (psi) 6.89-10.34-13.79 (MPa)	Flowing LN ₂ under low pressure (40 mins)
		3 cycles of LN ₂ under high pressure
Shale Sample 2	1000-3000-4000 (psi) 6.89-20.68-27.58 (MPa)	Flowing LN ₂ under high pressure (3 cycles)
		Flowing LN ₂ under high pressure (3 cycles)
Shale Sample 3	1000-1500-2000 (psi) 6.89-10.34-13.79 (MPa)	Flowing LN ₂ under low pressure (40 mins)
		Flowing LN ₂ under high pressure (fractured)
Shale Sample 4	1000-1500-2000 (psi) 6.89-10.34-13.79 (MPa)	Fractured by GN ₂

6.2.3.1 Shale Sample 1

Shale Sample 1 was treated with two cycles of liquid nitrogen under room temperature. The confining stress profile used for this sample is $x = 1000$ psi (6.89 MPa), $y = 1500$ psi (10.34 MPa), and $z = 2000$ psi (13.79 MPa). The first liquid nitrogen treatment is a low-pressure (about 15 psi or 0.1 MPa) circulation and lasts for 40 minutes. The second treatment includes three cycles of high-pressure liquid nitrogen injection with outlet partially open to provide opportunities for circulation while maintaining a back pressure.

The results of pressure decay tests before and after each treatment are shown in **Figure 6.2.4**. The average permeability matched from simulation for shale before the first cryogenic treatment is 1.30×10^{-3} mD, after the first treatment is 1.65×10^{-3} mD, and after the second treatment is 3.45×10^{-3} mD. The first round of low-pressure liquid nitrogen

circulation increases the average permeability of shale Sample 1 to 1.26 times to its original value. The second round of high-pressure liquid nitrogen treatment increases the permeability to 2.64 times of its original value.

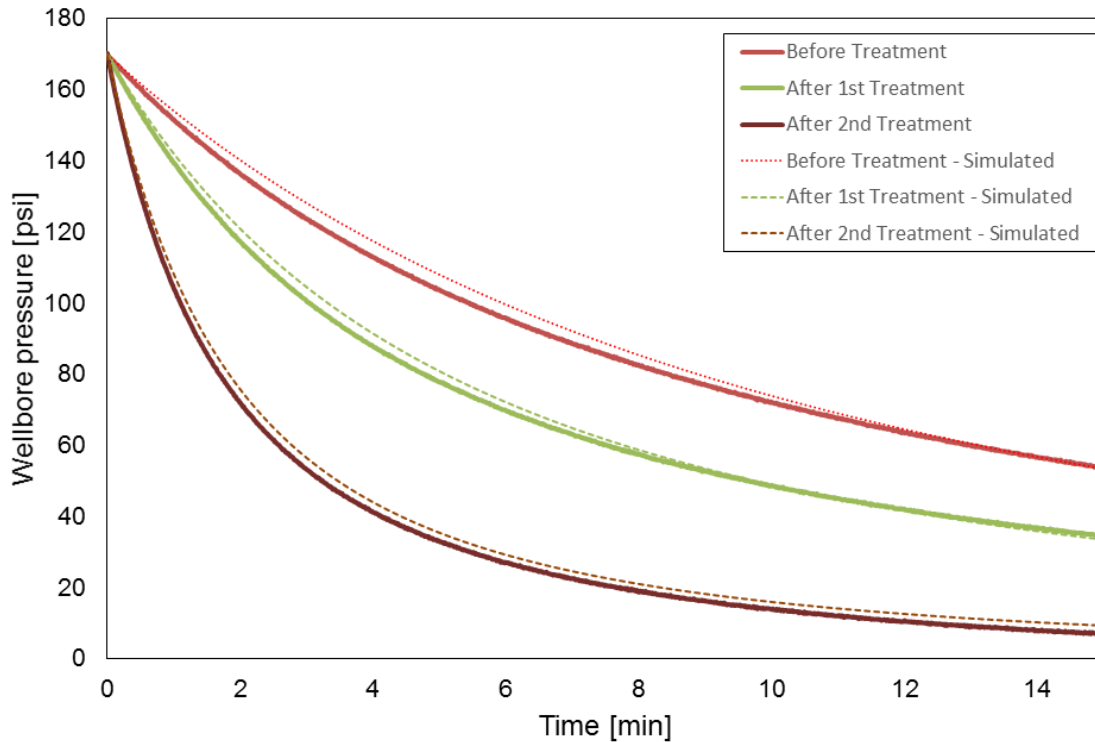


Figure 6.2.4 Pressure decay tests for shale Sample 1.

The simulation cases for shale Sample 1 include two situations. The first one is a low-pressure liquid nitrogen circulating through the borehole of the sample. The pressure used for injection is 15 psi (0.1 MPa) and the time for injection is 40 minutes (2400 seconds). The temperature distribution of shale Sample 1 after the first low-pressure liquid nitrogen treatment is shown in **Figure 6.2.5**. The fractured grids distribution is shown in **Figure 6.2.6**. The results show that although heat conduction is not affected by fractures, the increased fluid or gas flow in fractures results in directional temperature distribution inside shale Sample 1. The fracture half-length after first treatment is about 0.6 inch (1.52 cm) around wellbore in y direction.

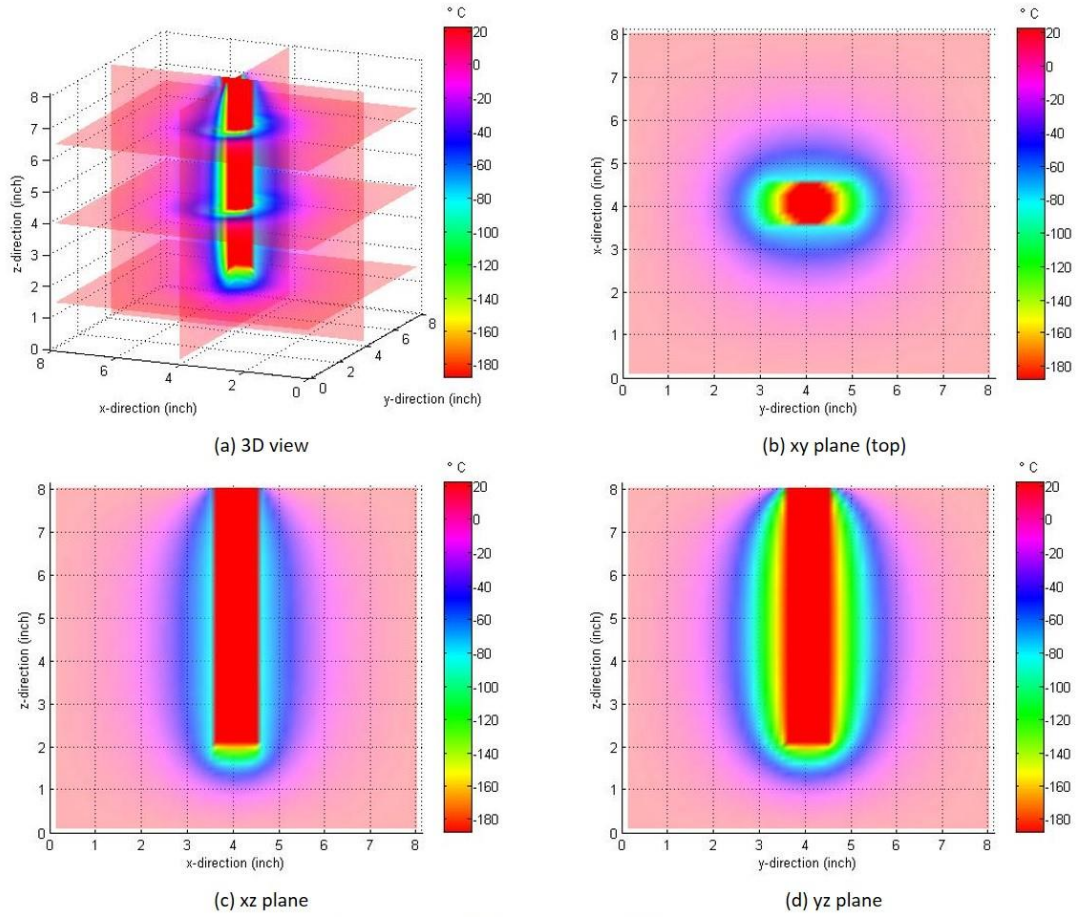


Figure 6.2.5 Temperature distribution in shale Sample 1 after the first cryogenic treatment.

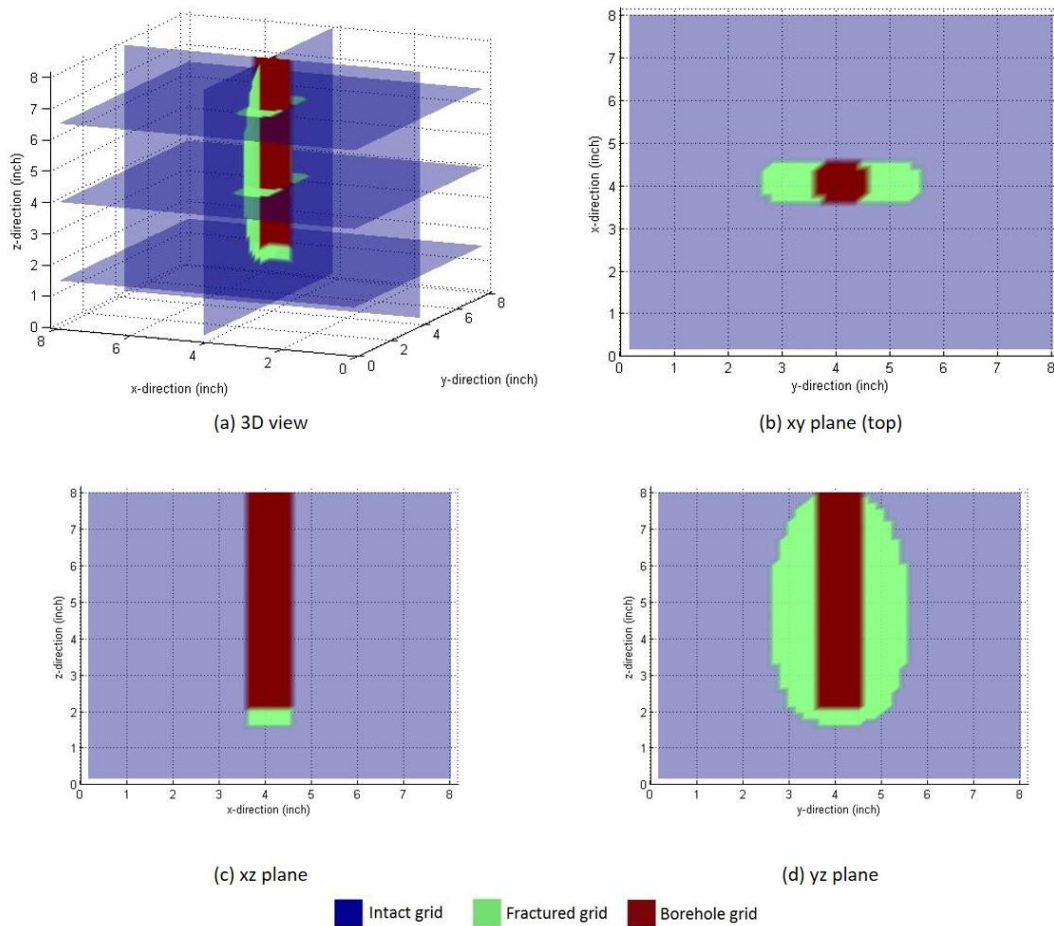


Figure 6.2.6 Fractured grids distribution in shale Sample 1 after the first treatment.

For the second test, the injection pressure is set as 450 psi (3.10 MPa) and time of injection for each cycle is 15 seconds, which is the approximate time for high pressure treatment in the experiment. After the injection, there is 10-minute relaxation for the sample to warm up. The pressure distribution in shale Sample 1 after the second high pressure LN₂ treatment is shown in **Figure 6.2.7**. The temperature distribution is shown in **Figure 6.2.8** and the fractured grids distribution is shown in **Figure 6.2.9**. The results show that the high pressure treatment extends the existing fracture grids to the direction perpendicular to the minimum horizontal stress direction. The fracture half-length after the second treatment increased to about 0.9 inch (2.29 cm) around the wellbore in y direction. The average permeability matched from simulation is 2.25×10^{-3} mD, which is 2.25 times of its original value.

Finally, the results of experiment and simulation for shale Sample 1 are compared side-by-side in **Table 6.6**. Clearly, the average permeability improvements from simulation are in reasonable agreement with those in the experiment.

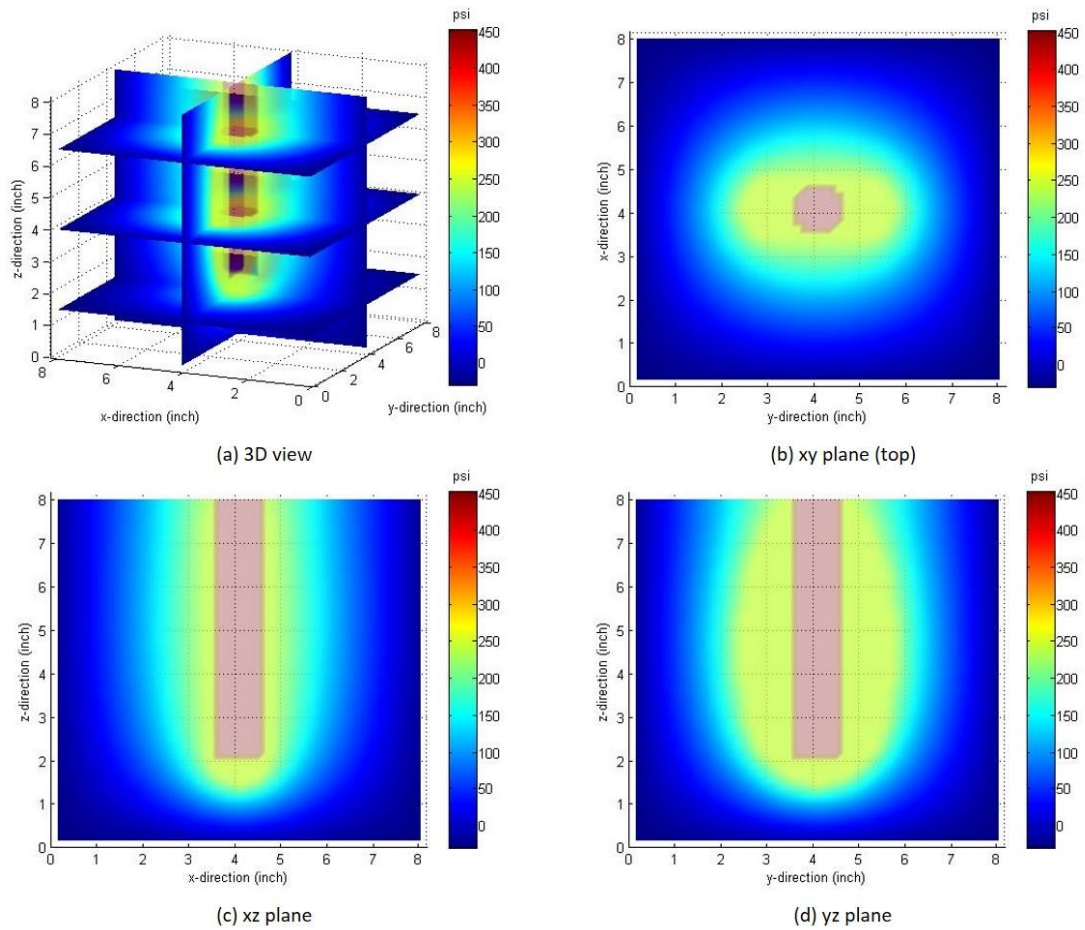


Figure 6.2.7 Pressure distribution in shale Sample 1 after the second cryogenic treatment.

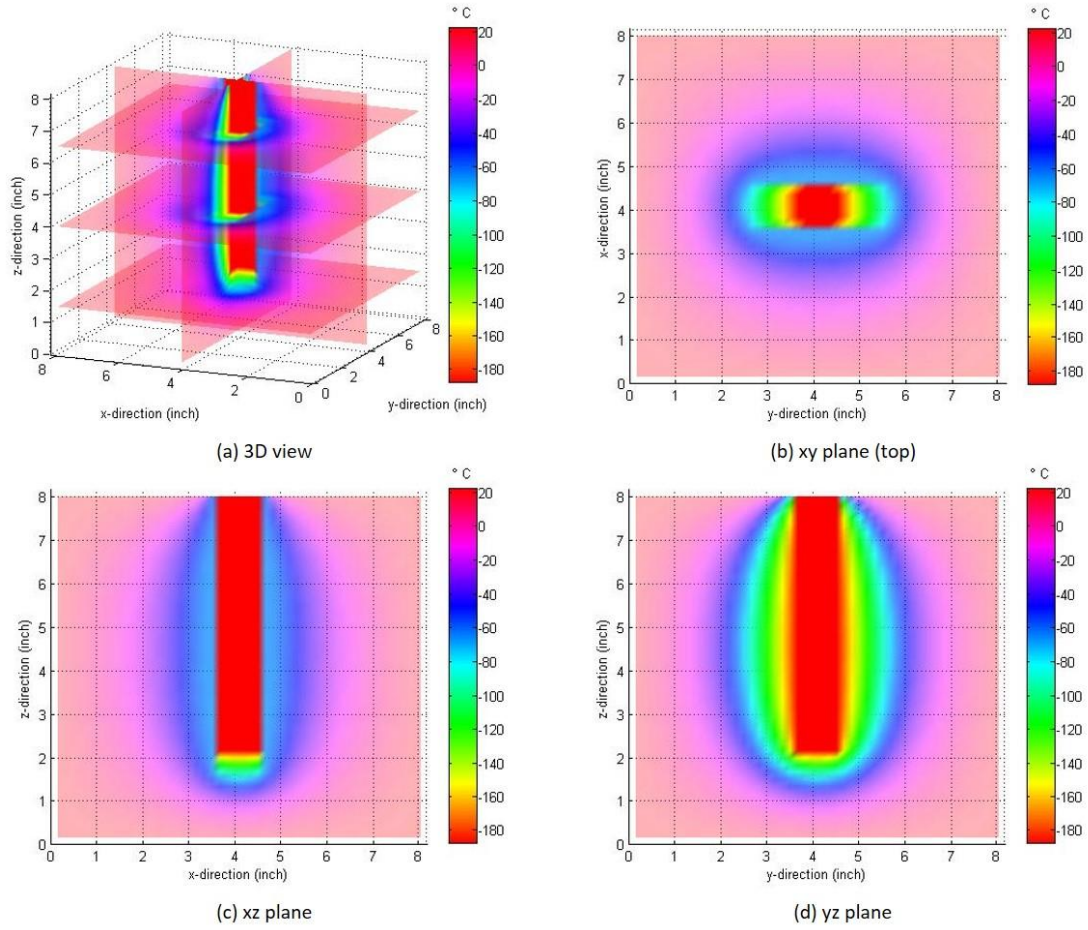


Figure 6.2.8 Temperature distribution in shale Sample 1 after the second cryogenic treatment.

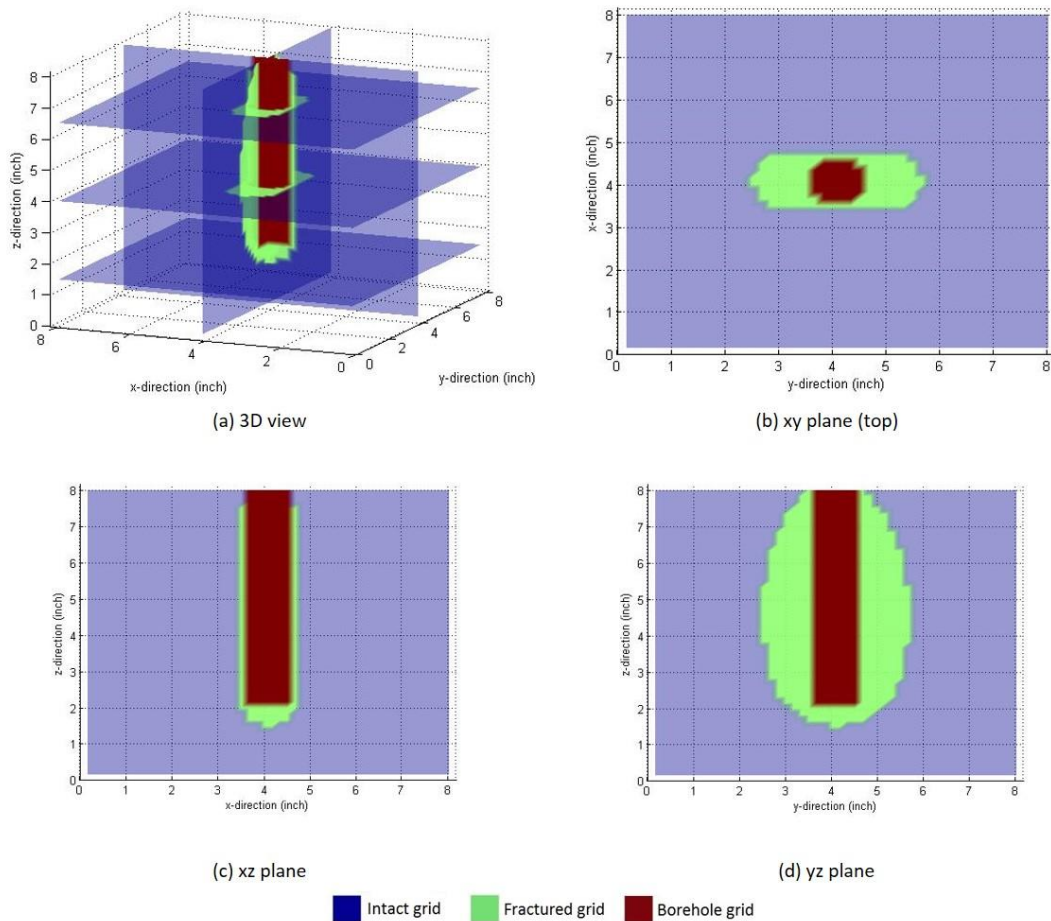


Figure 6.2.9 Fractured grids distribution in shale Sample 1 after the second treatment.

Table 6.6 Experimental and simulation results for shale Sample 1

Procedure	Experiment		Simulation		
	Average permeability	Improve ment	Average permeability	Improve ment	Fracture half-length
Before treatment	1.30×10^{-3} mD	1.00	1.00×10^{-3} mD	1.00	0
After low pressure circulation for 40 mins	1.65×10^{-3} mD	1.26	1.30×10^{-3} mD	1.30	0.6 inch (1.52 cm)
After 3 cycles of high pressure injection	3.45×10^{-3} mD	2.64	2.25×10^{-3} mD	2.25	0.9 inch (2.29 cm)

6.2.3.2 Shale Sample 2

Shale Sample 2 is treated twice with high-pressure liquid nitrogen under the room temperature. The confining stress profile used for this sample is 1000 psi (6.89 MPa) in x direction, 3000 psi (20.68 MPa) in y direction and 4000 psi (27.58 MPa) in z direction. Both treatments used a pressure of about 450 psi (3.10 MPa) and contained three cycles of liquid nitrogen injection.

The results of pressure decay tests before and after each treatment is shown in **Figure 6.2.10**. The average permeability matched from simulation for Shale 2 before the first cryogen treatment is 2.90×10^{-4} mD, after the first treatment is 1.25×10^{-3} mD, and after the second treatment is 2.90×10^{-3} mD. The first round of high-pressure liquid nitrogen treatment increases the average permeability of shale Sample 2 to 4.32 times to its original value. The second round of high pressure liquid nitrogen treatment increases the permeability to 10 times of its original value.

After the cryogenic treatment, shale Sample 2 is fractured by high pressure gas nitrogen. The section area of fracture plane shows a clear profile of cryogenic fractures induced by thermal shock, as shown in **Figure 6.2.11**. The cryogenic fracture profile shows a slight deviation in direction with pressure induced fracture. This observation may indicate that thermal shock could cause local stress re-orientation. The induced fracture half-length is 1.1 inches (2.79 cm) from borehole wall.

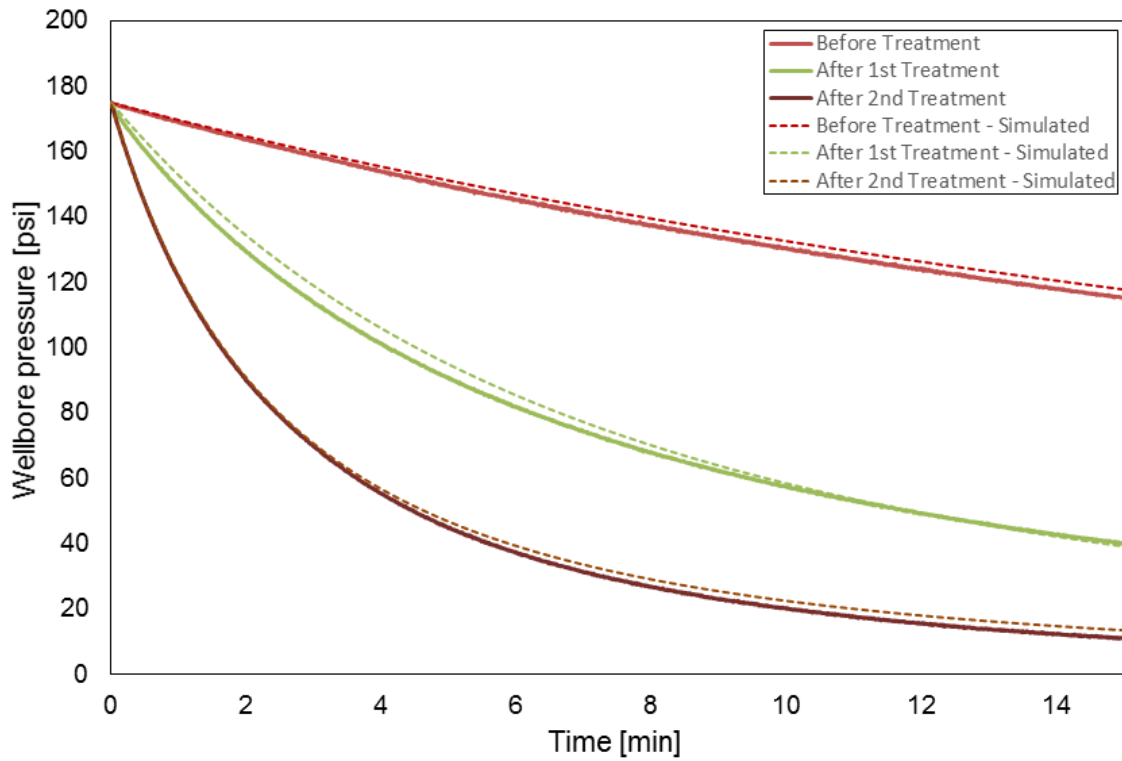


Figure 6.2.10 Pressure decay tests for shale Sample 2.

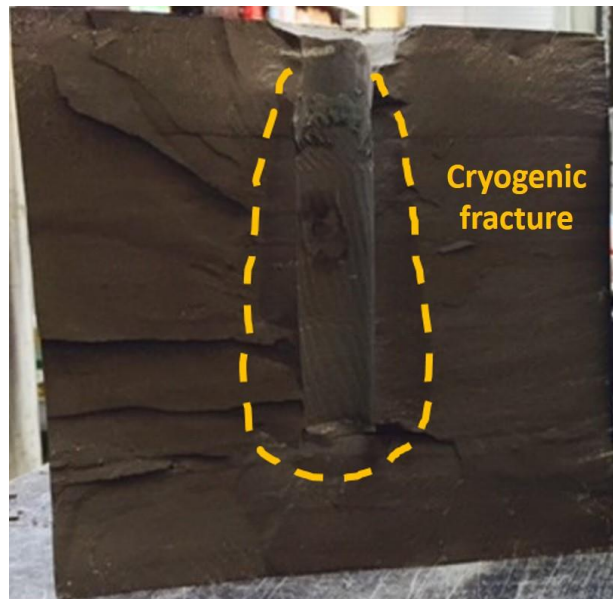


Figure 6.2.11 Fracture planes of shale Sample 2.

The simulation processes for shale Sample 2 include two rounds of cryogenic treatment, both of which are high pressure liquid nitrogen injections. For each round, the treatment procedures are the same with the second case for shale Sample 1 with higher contrast in

the triaxial stress anisotropy. High pressure liquid nitrogen is injected at 450 psi (3.10 MPa) for three cycles with 10-minute relaxation between each cycle. In addition, there is a sufficiently long period of time between the two rounds to simulate the warm up period for shale Sample 2.

After the first round, distributions of pressure, temperature and fractured grids are shown in **Figure 6.2.12**, **Figure 6.2.13**, and **Figure 6.2.14**, respectively. With a higher contrast in the triaxial stresses, fractured grids should be more distributed along the plane perpendicular to the minimum horizontal stress. However, the results show that although the number of fractured grids becomes larger, the distribution of fractured grids is more circular under high triaxial stress contrast. This may be related to the simple stress calculation function adapted in the simulation tool and the mesh used. Also, with a high contrast in the triaxial stresses, grids tend to be fractured more easily under lower pressure difference and smaller temperature change. Thus, there are more fractured grids generated outside the fracture plane. The fracture half-length after the first treatment is about 0.8 inch (2.03 cm) in y direction and 0.4 inch (1.02 cm) in x direction. The average permeability from matching with simulation is 3.80×10^{-3} mD, which is 3.80 times of its original value.

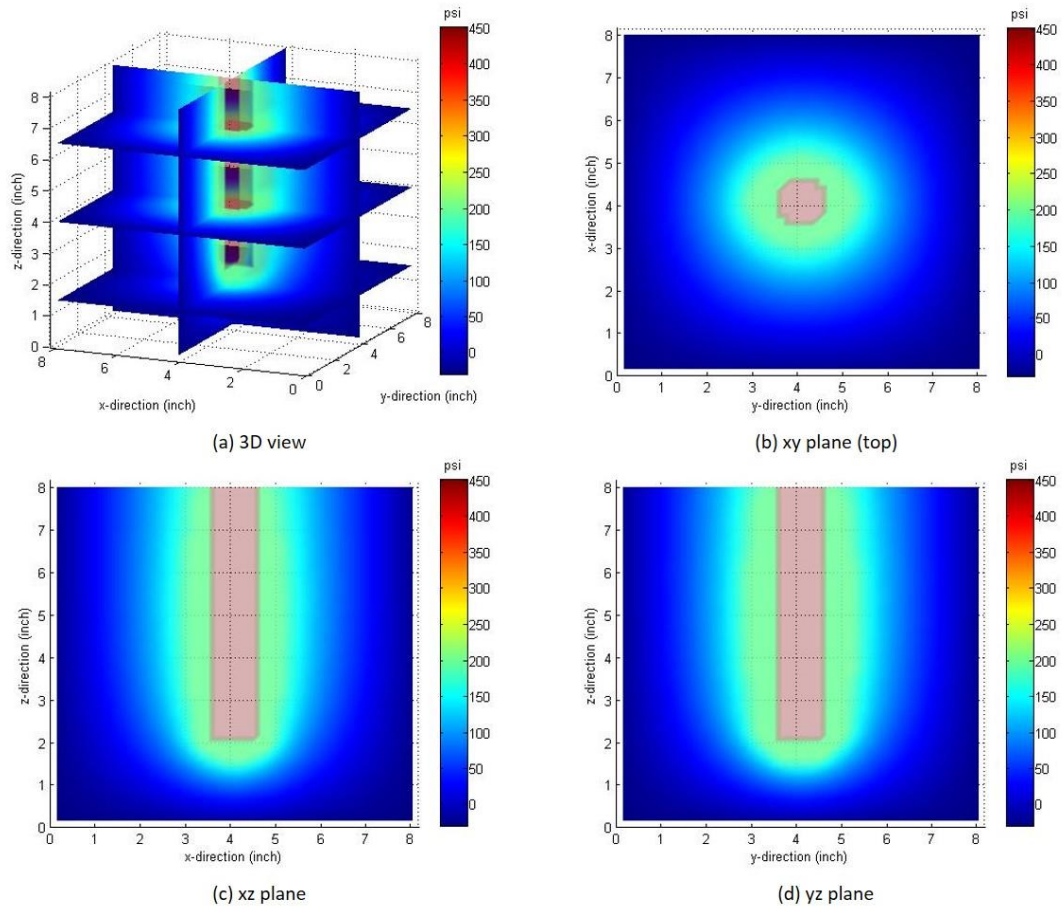


Figure 6.2.12 Pressure distribution in shale Sample 2 after the first high pressure cryogenic treatment.

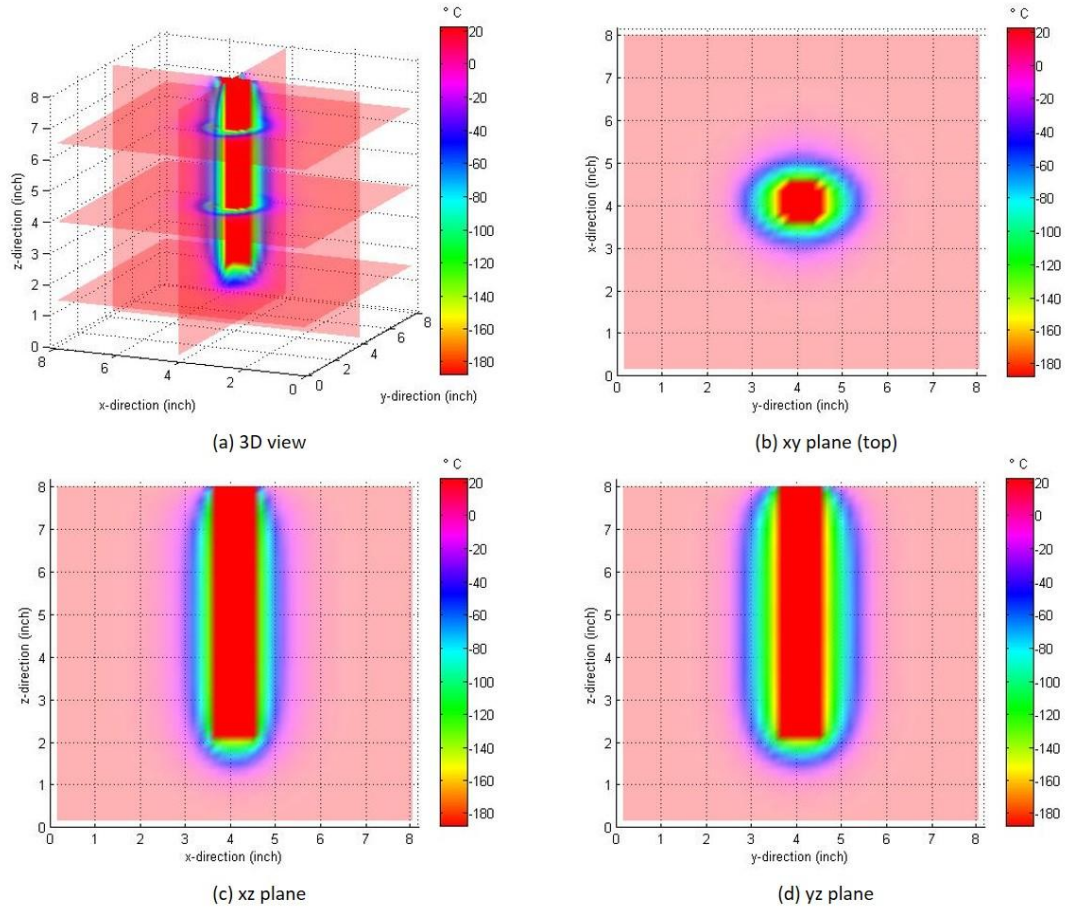


Figure 6.2.13 Temperature distribution in shale Sample 2 after the first high pressure cryogenic treatment.

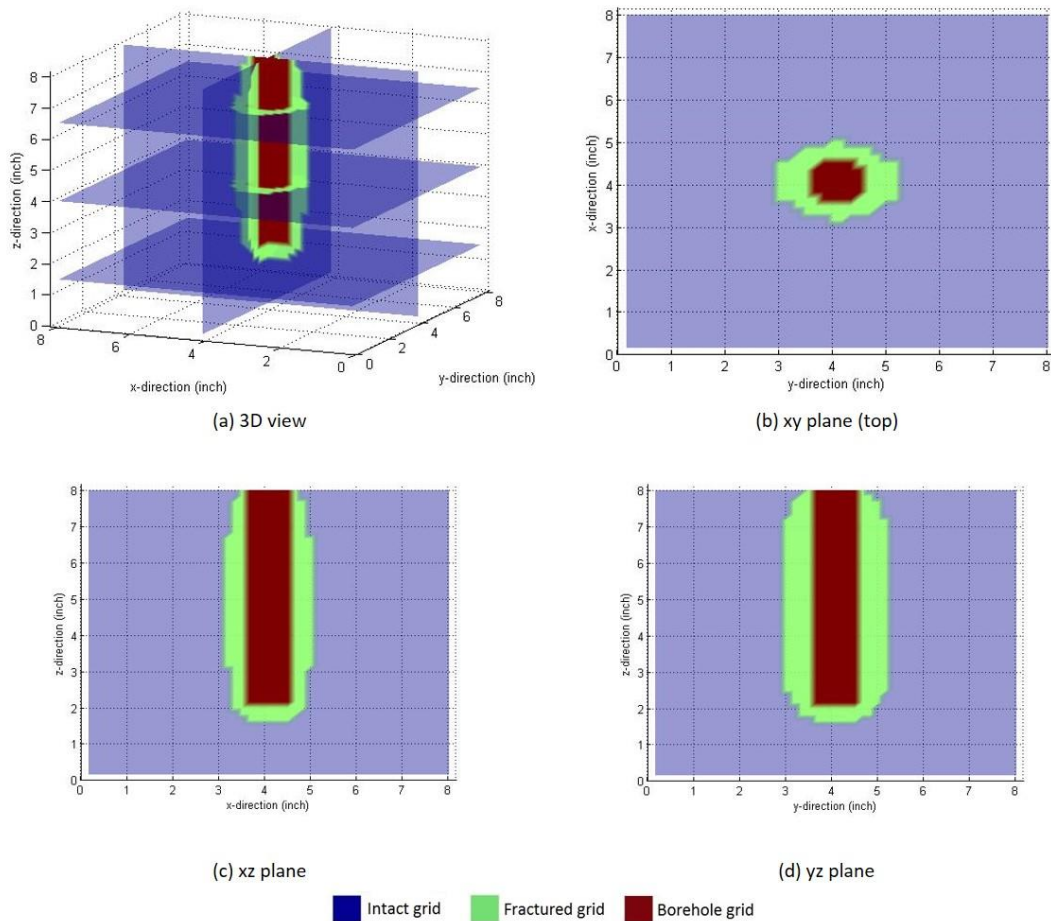


Figure 6.2.14 Fractured grids distribution in shale Sample 2 after the first high pressure cryogenic treatment.

For the second round, distributions of pressure, temperature and fractured grids are shown in **Figure 6.2.15**, **Figure 6.2.16**, and **Figure 6.2.17**, respectively. The fracture half-length after the second round of treatment is about 1.2 inch (3.05 cm) in y direction and 0.5 inch (1.27 cm) in x direction. The average permeability from simulation is 6.10×10^{-3} mD, which is 6.1 times of its original value. All experimental and simulation results for shale Sample 2 are shown in **Table 6.7**.

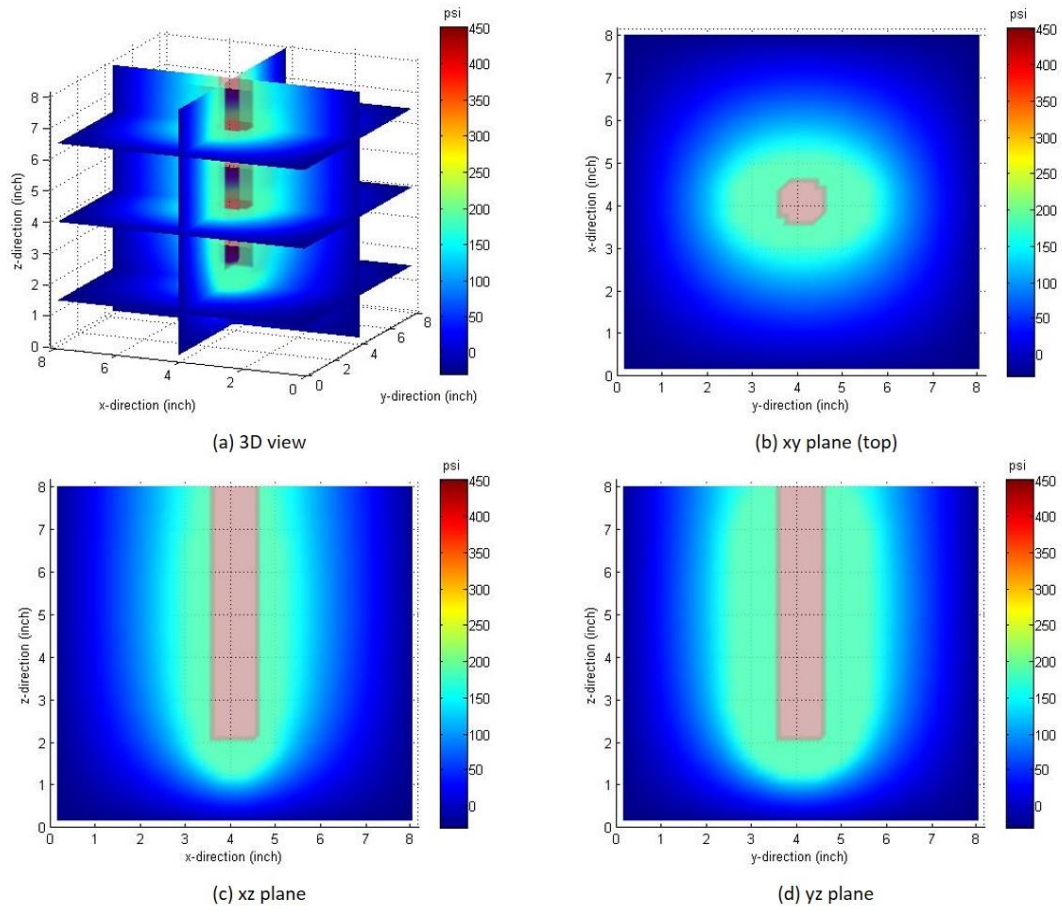


Figure 6.2.15 Pressure distribution in shale Sample 2 after the second round of cryogenic treatment.

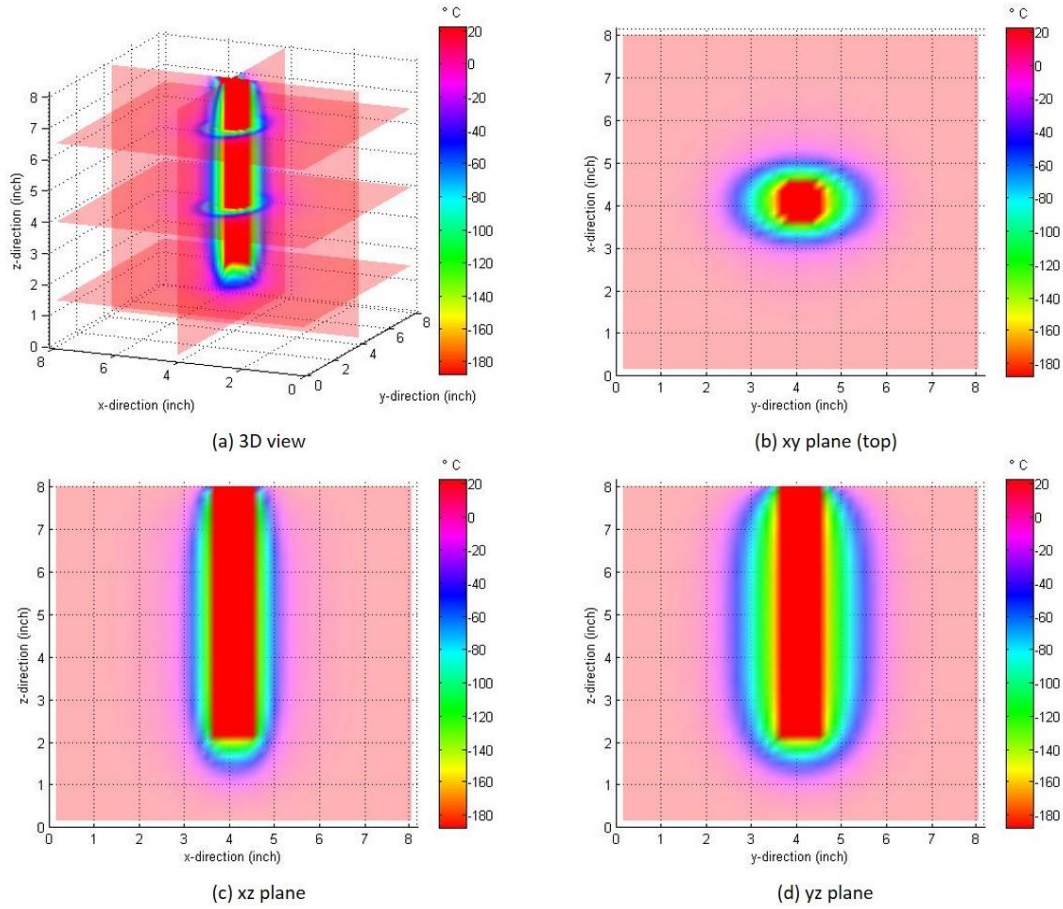


Figure 6.2.16 Temperature distribution in shale Sample 2 after the second round of cryogenic treatment.

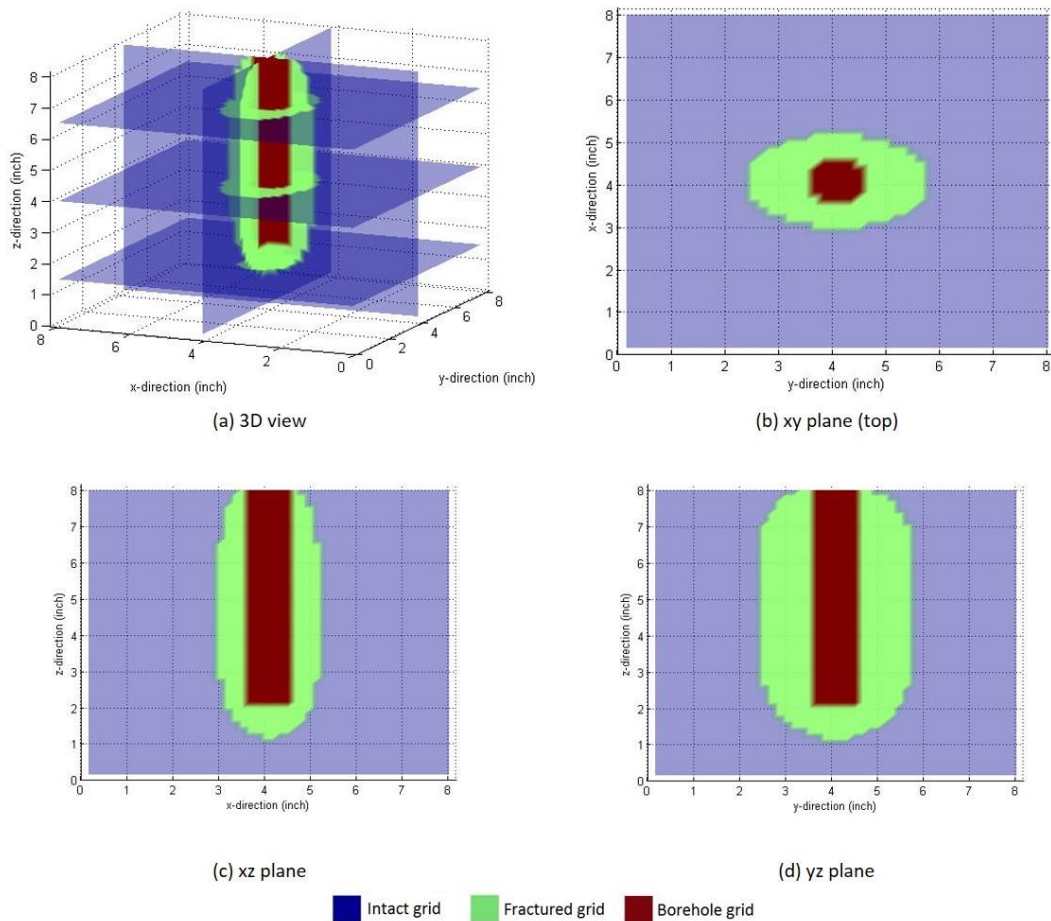


Figure 6.2.17 Fractured grids distribution in shale Sample 2 after the second round of cryogenic treatment.

Table 6.7 Experiment and simulation results for shale Sample 2

Procedure	Experiment		Simulation		
	Average permeability	Improve ment	Average permeability	Improve ment	Fracture half-length
Before treatment	2.90×10^{-4} mD	1	1.00×10^{-3} mD	1	0
After 1st round of 3 cycles of high pressure injection	1.25×10^{-3} mD	4.32	3.80×10^{-3} mD	3.8	0.8 inch (2.03 cm) in y 0.4 inch (1.02cm) in x
After 2nd round of 3 cycles of high pressure injection	2.90×10^{-3} mD	10	6.10×10^{-3} mD	6.1	1.2 inch (3.05 cm) in y 0.5 inch (1.27 cm) in x

6.2.3.3 Shale Sample 3

Shale Sample 3 was planned to be treated twice with liquid nitrogen under the room temperature following exactly the same procedures with shale Sample 1. The triaxial stresses used for this sample are 1000 psi (6.89 MPa) in x direction, 1500 psi (10.34 MPa) in y direction, and 2000 psi (13.79 MPa) in z direction. However, after the second cycle of low pressure liquid nitrogen treatment, shale sample 3 was fractured during the pressure build-up process of pressure decay test. The possible reasons for shale Sample 3 fractured at an early stage of treatment include pre-existing natural fractures, weak sedimentary layers, and induced defects during drilling of the wellbore.

The results of the pressure decay tests before and after the first treatment are shown in **Figure 6.2.18**. The average permeability from simulation for shale Sample 3 before the first cryogen treatment is 1.32×10^{-4} mD, and after the first treatment is 2.52×10^{-3} mD. The first round of low pressure liquid nitrogen circulation increases the average permeability of shale Sample 3 to 1.91 times of its original value.

Since testing conditions of shale Sample 3 is identical to those of shale Sample 1, no simulation is performed for shale Sample 3.

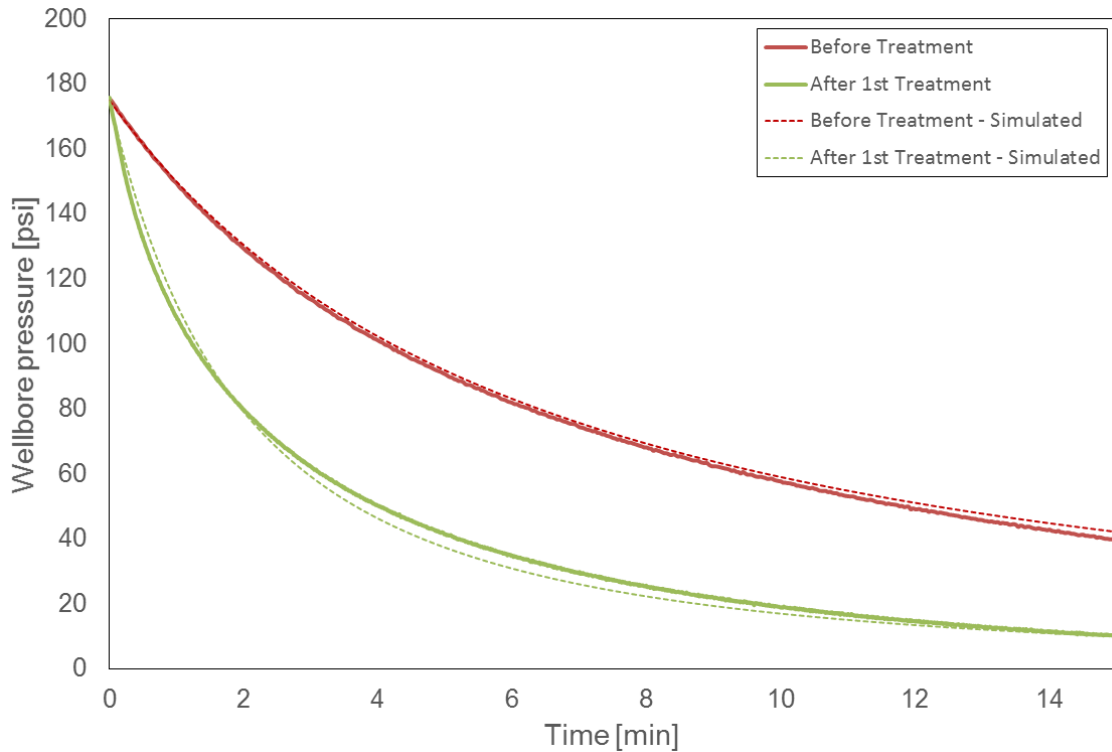


Figure 6.2.18 Pressure decay test for shale Sample 3.

6.2.3.4 Shale Sample 4

Shale Sample 4 is directly fractured by high pressure gas nitrogen to establish a reference for evaluation of cryogenic fracturing efficacy. The triaxial stresses used for this sample are 1000 psi (6.89 MPa) in x direction, 1500 psi (10.34 MPa) in y direction, and 2000 psi (13.79 MPa) in z direction. The breakdown pressure for shale Sample 4 is about 2460 psi (18.2 MPa), which is shown in **Figure 6.2.19**. **Figure 6.2.20** shows pictures of all faces of shale Sample 4 after fractured by high pressure gas nitrogen. An observation from the faces of shale Sample 4 is that the fracture is basically in YZ-plane (Faces 2 and 4, top and bottom in **Figure 6.2.20**), which is perpendicular to the direction of minimum horizontal stress.

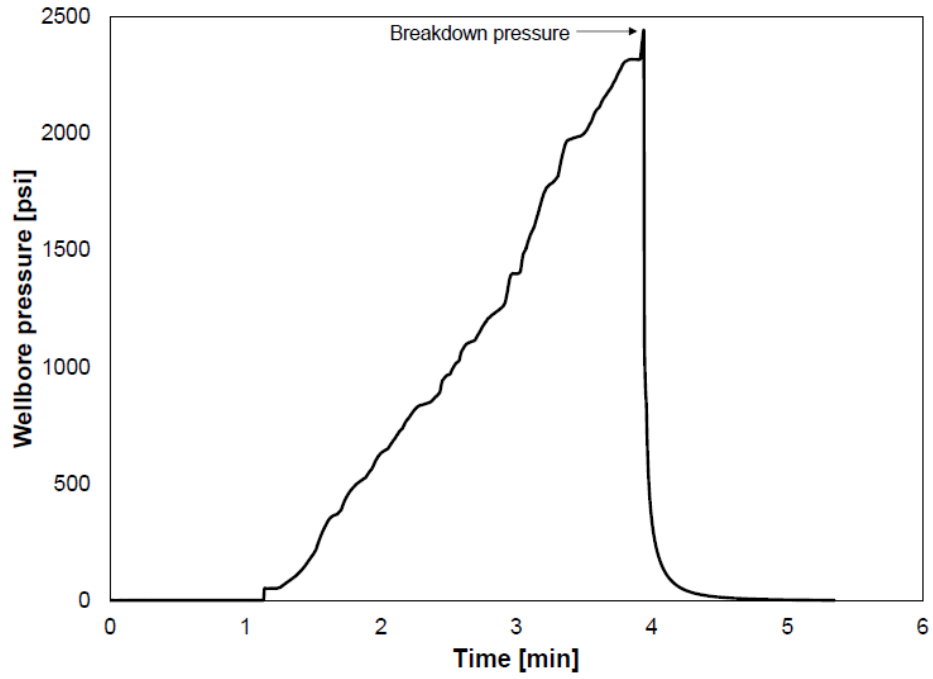


Figure 6.2.19 Breakdown pressure of shale Sample 4.

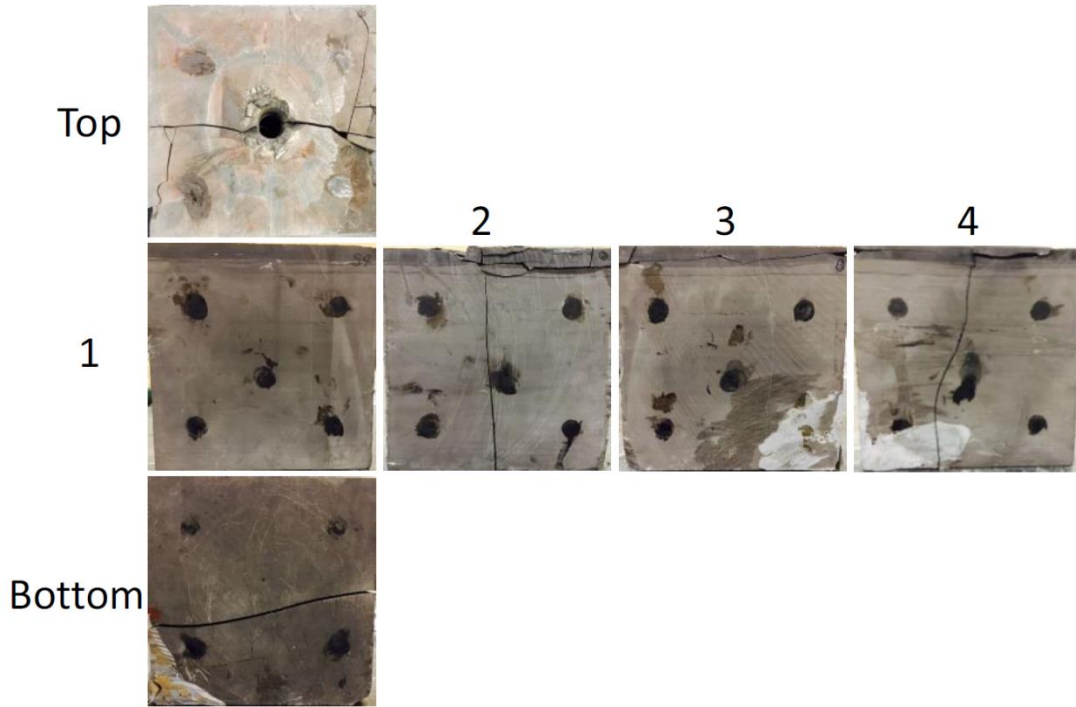


Figure 6.2.20 Faces of shale Sample 4 after high pressure gas fracturing.

A pressure only (i.e. no cryogen) simulation was run for shale Sample 4, which provides a fracture distribution as shown in **Figure 6.2.21**. Fractured grids for this case are mostly distributed in the YZ-plane, which agrees with the fracture description for shale Sample 4 mentioned above. Fractures induced by high pressure gas nitrogen have reached the top and bottom surfaces, causing most of gas leaking out to ambient environment through these grids. The breakdown pressure matched by Mogi-Coulomb Criterion using parameters in **Table 6.4** for this case is 2472 psi (17.1 MPa), which is very close to the actual breakdown pressure shown in **Figure 6.2.19**.

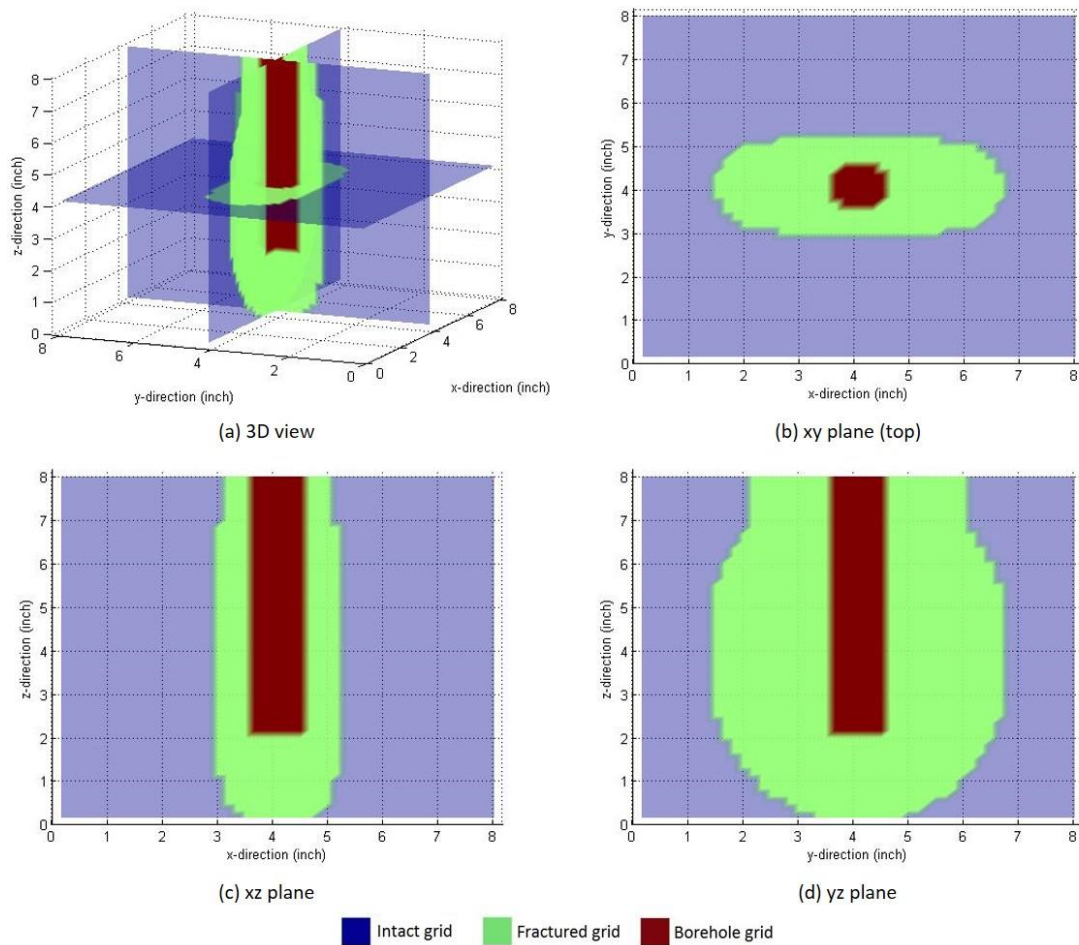


Figure 6.2.21 Fracture distribution in shale Sample 4.

6.3 Summary

We carried out finite element simulation for the unstressed and triaxially stressed rock block samples (concrete, sandstone, and shale) with a wellbore, and finite difference simulation of shale samples under different triaxial stresses treated with different cryogenic fracturing procedures.

If the cryogenically induced stress exceeds the combination of the triaxial stresses and the tensile strength of the formation, fractures will be initiated. Stress contrasts are seen around the wellbore for all samples and across the different layers for the multilayer shale samples. Compared to room temperature (70 °F), these contrasts have higher magnitudes when the sample is initially at reservoir temperature (200 °F). This higher temperature increases the value of temperature gradient, thus causing an increase in thermal stress. Higher shear stress magnitudes correspond to higher sample temperatures. However, when the sample is under triaxial stresses, the shear stress drops down by around 65% for both temperature cases. For the unstressed multilayer sample, there is not much difference between the values of the shear stresses when the temperature of these samples changed from room temperature to reservoir temperature. However, when the sample is under triaxial stresses, the shear stresses between layers increased. Corresponding to the laboratory results for shale Sample 3, this explains the planar fracture generated along one of the horizontal layer (**Figure 4.4.81** Face 1). The simulated values of radial and tangential stresses show that in the unstressed tests for all rock samples, the radial and tangential stress magnitudes distributed evenly around the wellbore circumference. This suggests that the fracture will initiate in unexpected directions, while for the stressed tests for all rock samples, the values of radial and tangential stresses are lower in the fracture propagating directions.

The simulated pressure decay tests show that with low pressure liquid nitrogen circulation treatment, shale samples obtained from Niobrara formation show a general 50% increment on average permeability for 8” cubic blocks. This also implies that circulation of cryogenic fluid in wellbore at low pressure can be applied as a near-wellbore formation damage treatment technique with very low cost and without any environmental concerns. For high

pressure treatment, effectiveness of injection pressure is demonstrated by comparing different shale samples undergoing various treatment procedures in both experiments and simulation. High injection pressure tends to enhance cryogenic fracturing efficacy in both fracturing speed and fracture conductivity. Liquid nitrogen treatments at high pressure for very short time achieve at least two times larger average permeability on 8” cubic shale blocks.

The influence of triaxial stress contrast observed in experiments is also demonstrated by the simulations. Higher contrast in confining stress aids cryogenic fracturing process. The improvement on average permeability on 8” cubic block under higher contrast triaxial stresses is significantly larger than those under lower contrast triaxial stresses.

Overall, simulation results from finite element and finite difference modeling reproduced the experimental observations and measurements for rock samples under either no stress or triaxial stress conditions, in terms of stress-strain, temperature, fluid pressure, and permeability profiles as well as fracture morphology.

7. Field Test Plan

7.1 Well Site

The site for our proposed small-scale field tests was inside the CEMEX Lyons Quarry Plant, which is located in the town of Lyon, Colorado (**Figure 7.1.1**). It is the same quarry where we collected the shale blocks used for the laboratory cryogenic fracturing tests. Based on our thorough review of the geological maps for undeveloped areas provided by the CEMEX quarry, we selected a site with geographic coordinates of (40°14'17.0" N, 105°13'34.0" W) for well drilling. This location for the wellbore group was selected such that all the wellbores have as similar vertical profiles and properties as possible. Specifically, the formation layers they penetrate are horizontal, and with 30 feet total depth, the soil layer should be thin and the last 6 feet of open-hole interval should be located in the middle of a thick layer.

The site is a shallowly buried Niobrara shale formation, which is an oil and gas producing formation in some regions in Colorado and other states. At this location (see **Figure 7.1.1**), 1-2 feet of the surface layer is soil, then about 10 feet down is the fourth ridge, below that it is 3-4 inter-ridge, which is the target formation with a thickness of about 32 feet. This accessible stratum is a good test targets for our project. The data for our site are derived from an exploration well 42.7_3RDEXPL a few meters to the east side. Our wellbores are at least 300 feet away from a nearby mining pit and a highway. The effects of mining section relaxation, blasting activities and traffic are negligible.

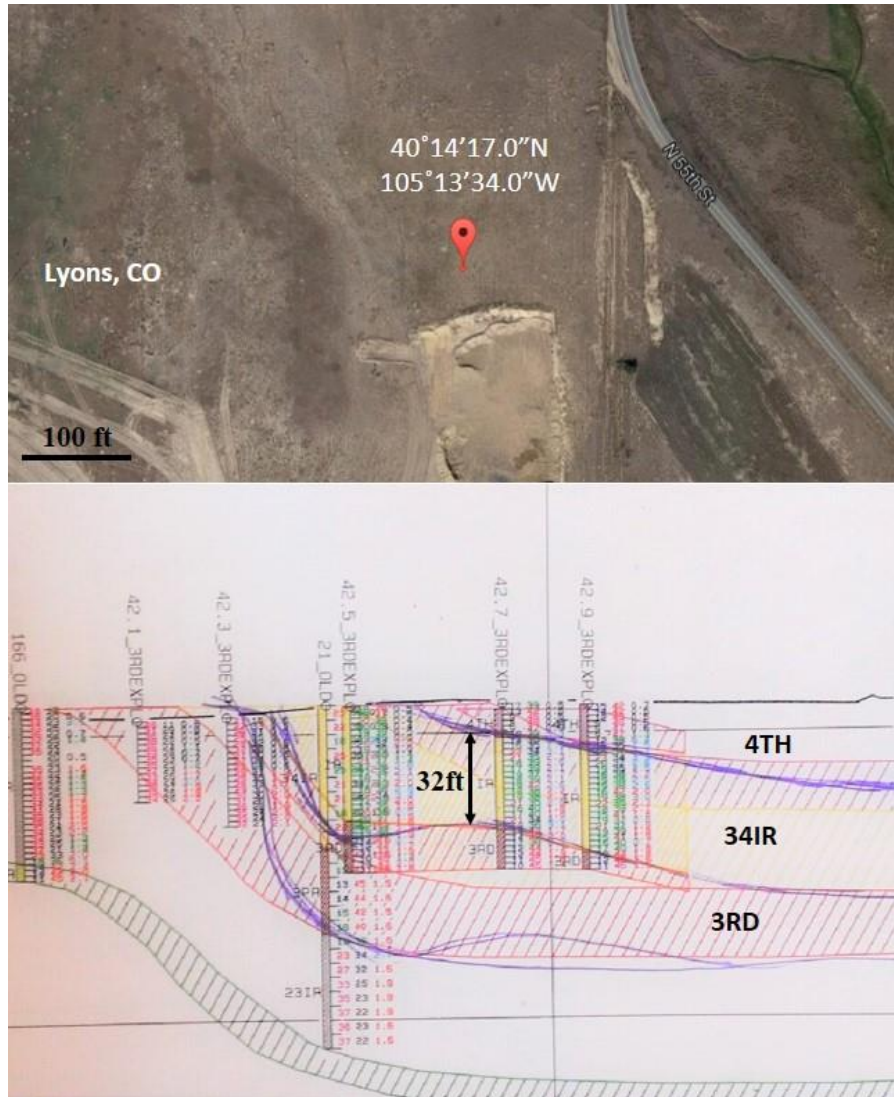


Figure 7.1.1 Well site location from Google Maps and corresponding east-west geological cross section provided by CEMEX. The cross section has the same length scale but a different depth scale.

7.2 Well Pattern

Multiple wellbores were to be drilled into the shallow Niobrara shale formation for cryogenic stimulation tests. A double five-spot square pattern was planned, as shown in **Figure 7.2.1**. This double five-spot pattern endows us with considerable degree of freedom in conducting sufficient comparative experiments and measurements. Wellbores 1 and 8 were to be stimulated first by circulating LN₂ into them at relatively low pressure (10-50 psi), 4 and 5 were to be treated in a way that depended on observations of wellbores 1 and

8 during stimulation. Corner wells 2, 3, 6, and 7 were to be tentatively used as observation wells for temperature monitoring, pressure decay tests, directional permeability tests and cross-hole sonic logging measurements.

As shown in **Figure 7.2.1**, the diameter of all 8 wellbores was to be 4 inches. Based on our heat transfer simulations for 1D and 2D radial wellbore geometries, the wellbore distance in diagonal directions was set as 5 feet (1.52m), which is the distance from the wellbore to the temperature front (0.0003 K) after a 10-hour circulation of LN₂. Therefore, we expect negligible temperature interference among the stimulation wells. The distance between wellbores 1 and 2 is 5 feet, and that between wellbores 2 and 3 is 7.6 ft. In total, this double 5-spot well pattern was to cover an area of about 117 square ft. Since this is a relatively small area, the Niobrara formation penetrated by the wellbores is expected to be reasonably homogeneous, which serves as a basis for treatment and measurement comparison.

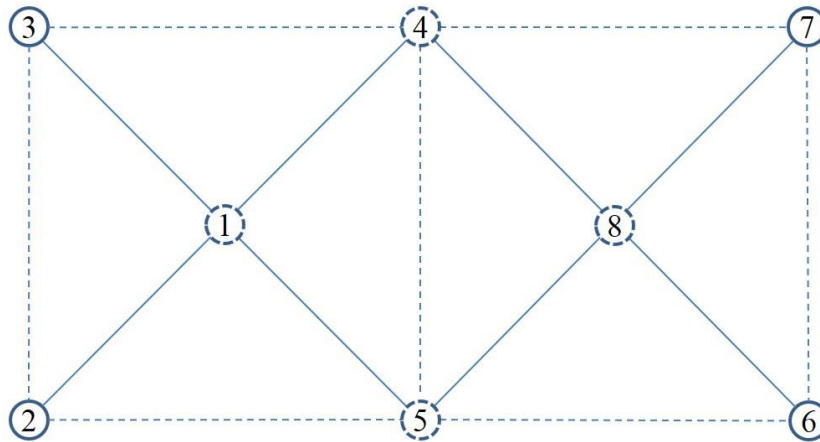


Figure 7.2.1 Double five-spot pattern for wellbore layout. Wellbores 1 and 8 were to be fractured with liquid nitrogen.

7.3 Drilling and Completion

Drilling was to be provided by the CEMEX quarry Plant. The drill bits are button-face percussion-type and provide fairly smooth wellbore surface. All wellbores in this double 5-spot pattern were to be uniformly drilled using the 4-inch bit. During drilling, it would have been possible to collect rock cuttings along depth to see stratigraphy and for laboratory characterization.

Figure 7.3.1 shows the vertical profile of wellbores 1, 8, 4, 5, which adopts a casing and a packer to isolate the 6-ft interval at the bottom for cryogenic stimulation and to protect the upper wellbore. The site has about 1-foot soil layer, about 10 ft of 4th ridge layer, with more intact 3-4 inter-ridge layer deeper in the profile. After drilling, we would have run a 24-ft long casing with an air-filled packer bladder at the end and welded flange on the top into the wellbore. Then the bladder would be filled with air, and on top of it, cement would be injected first to form a solid ring. Afterwards, with the support of the solid grout ring, the whole annulus would be grouted with well-mixed cement slurry. After 1-2 days' curing of the cement, the casing would be bonded tightly to the formation. The mock-ups of the packer and the PVC shoe for the casing are shown in **Figure 7.3.2**.

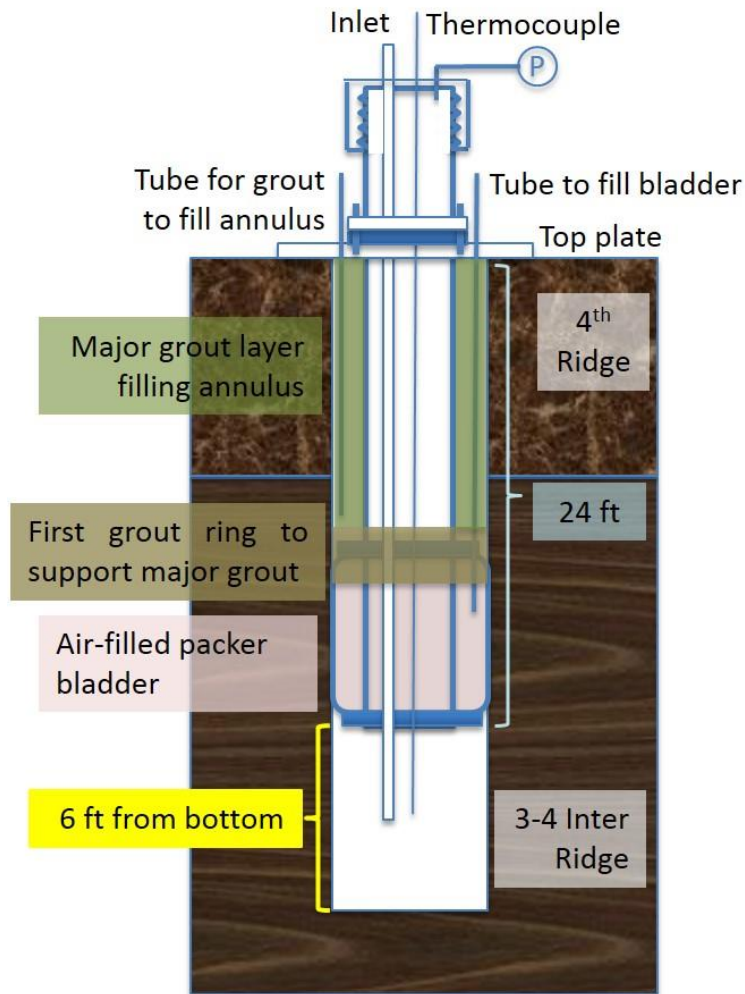


Figure 7.3.1 Wellbore vertical sketch.



Figure 7.3.2 Mock-ups of top cap assembly (left), pant-leg hydraulic packer (center back), and PVC shoe (right) for casing.

7.4 Wellhead Installation

As shown in **Figure 7.3.1**, a casing with OD of 4 inches was be cemented to stabilize the upper part of the borehole as well as to facilitate the installation of the wellhead. Removable wellheads were designed and mock-ups manufactured to facilitate the LN₂ and GN₂ injection. These would be connected to the casing head by flanges. Polytetrafluoroethylene film that can resist the cryogenic temperature would be used for flange sealing. Inlet tubing (0.75" ID) going through the wellhead was to reach into the open hole interval, a back pressure regulator would be installed to the outlet on the wellhead. Thermocouples would be directed to the bottom through a 0.25" tubing. **Figure 7.3.2** shows a top cap assembly (left object) manufactured for an injection well.

7.5 LN₂ Delivery System

Since stimulation zones are located at shallow depths (24-30 ft), it is possible to deliver LN₂ efficiently using delivery systems available commercially. Air Liquide was identified as being able to provide a portable LN₂ trailer with the highest pressure of 275 psi. Also, they can provide manifolds, fittings and pipes to connect the vessel to the wellhead. It is estimated that each wellbore would need about 500 gallons of LN₂, i.e. ideally it can be injected at 0.92 m/s (twice as much as that in laboratory) through the 0.75" inlet tubing for 2 hours. Thus, two wellbores will need 1000 gallons.

LN₂ would be delivered directly from the LN₂ vessel on the site, and gas N₂ would be delivered from a portable cylinder. It would be possible to inject LN₂ under almost ambient pressure and higher pressure.

7.6 Planned Experimental Procedure

Wellbores were to be characterized before, during, and after cryogenic stimulations for shale formation characteristics, fracturing monitoring, and data set comparison. At least center wellbores 1 and 8 would be fractured with LN₂, in which petrophysical measurements would be performed, including caliper, gamma ray, induction, density, neutron porosity, optical, and acoustic logs (six logs). Stimulation procedures of each wellbore might have varied depending on situations and needs.

7.6.1 Pre-Stimulation Wellbore Characterization

The well site was to be cleaned to make sure that the surface condition meets the needs of the operational activities. Immediately after drilling and before cryogenic stimulation, we planned to characterize the near-wellbore area as described below, which serves as the reference for post-stimulation comparison.

- Well logging of all eight wells, in wellbores 1, 8, 4, and 5, only the uncased interval (six logs);
- Geophysical tests (Cross-hole sonic logging) for wellbores 1, 8, 4, and 5;
- Pressure decay tests for wellbores 1, 8, 4, and 5;

- Gas injection from center wells to observation wellbores for directional permeability tests.

7.6.2 Cryogenic Stimulation

At least two wellbores (1 & 8) were selected for cryogenic stimulation; wellbores 4 & 5 could be stimulated as well. Wellbores 1 & 8 and 4 & 5 would have undergone different stimulation schemes based on practical operation and situation.

7.6.3 Post-Stimulation Well Characterization/Evaluation

The same geophysical measurements done for pre-stimulation characterization would have been performed after cryogenic stimulation for comparison.

7.7 Schedule

The water table is generally lower at the end of the dry season, which is from late September to early October in this area. Therefore, we targeted to perform the main cryogenic tests during those days. The total working days needed was estimated to be sixteen, i.e. approximately three weeks. Procurement of devices and equipment was initiated and discontinued at the request of RPSEA and NETL.

8. Conclusions and Recommendations

8.1 Conclusions

In this project numerous cryogenic fracturing tests were performed on acrylic, glass, concrete, sandstone, and shale samples. The effectiveness of cryogenic fracturing processes depended on the rock or material properties, water saturation, injection pressure, treatment time, number of treatment cycles, and triaxial stress conditions. For concrete, tensile strength variation was controlled by curing time and this strength variation was probably the most significant influence on breakdown pressure of all the metrics tested. For all materials tested, increased injection pressure and flow rate of LN₂ through the borehole significantly enhanced the rock breakdown process. In addition, water saturation, which can vary significantly in unconventional reservoirs due to connate water, and triaxial stress anisotropy also reduced breakdown pressure.

To visualize the fracturing process, both glass blocks and acrylic cylinders were subjected to cryogenic treatment. Crack patterns in acrylic blocks were dominated by a horizontal (borehole perpendicular), planar, radial propagation. These cracks were most likely created due to the cylindrical geometry of the block and the borehole which causes thermal contraction to be greater in the longitudinal direction. The circumferential thermal contraction also generates vertical (borehole parallel) cracks, though they are smaller and fewer than the horizontal fractures. Glass block samples were tested under confining stresses. When uniaxial stress was applied, fractures formed parallel to the borehole and propagated in the direction of the maximum principal stress. Under higher triaxial stresses, the fractures generated were much less extensive because cryogenic tension has to overcome both compressional stresses and tensile strength of the glass before fracturing.

Cryogenic treatments of concrete, sandstone, and shale samples all show reduction in breakdown pressure of gas fracturing. Analyses of tests on concrete and shale samples confirm that liquid nitrogen stimulation reduces breakdown pressures by generating fractures inside the rock blocks. Multiple cycles of treatments in shale samples demonstrate

that greater permeability enhancement can be achieved after each cycle, indicating that each LN₂ treatment cycle not only creates new fractures, but also widens the existing ones. In addition, as temperature returned to ambient, the fractures narrowed, as is evidenced by a decrease in permeability. Compared with concrete and shale, sandstone samples did not show obvious enhancement in permeability after each LN₂ treatment cycle, due to very high original permeability. It appears that existing natural fractures may have diminished the impacts of cryogenic fracturing.

For cryogenic treatment under triaxial stresses with low horizontal stress contrast, fractures propagated along or between the maximum and minimum horizontal stress directions. For higher horizontal stress contrasts, the fracture always propagated as expected, perpendicular to the minimum horizontal stress. For a shale sample treated with LN₂, the fracture planes diverted from the wellbore with a 12° angle then returned to the direction of expected fracture opening, whereas an untreated shale sample under triaxial stresses the fracture did not divert around the wellbore, but rather formed a sharp straight fracture from the wellbore to the edge of the sample.

The Leidenfrost effect, when an insulating gas layer develops between the rock and the LN₂, was minimized by increasing the flowing pressure of the LN₂ during the cryogenic treatment. During this project, we developed an increased understanding of the Leidenfrost effect in rock-LN₂ systems to enable more effective design of laboratory experiments. This knowledge will be important when applying this technology to field conditions, and will save time and volume of the LN₂ used in cryogenic stimulation.

To visualize fractures in rock, the energies and currents of CT scan have been optimized for capturing specific features of cryogenic fractures, and proper operating parameters for fracture detection in shale samples were determined. Optimized parameters enable us to detect fractures down to 50 μm-wide apertures. These significant improvements have enabled the X-Ray CT scan to perform better characterization of the fracture morphology in glass and shale samples. In addition, the combination of PET and CT scanning techniques was utilized to identify fractures that were not seen by X-ray CT. Synchrotron

X-ray micro tomography was attempted to identify fractures, but the sample size was too large to obtain reasonable images.

Numerical simulation results from finite element modeling and finite difference modeling corroborated the physics of cryogenic fracturing by successfully reproducing laboratory experimental results, in terms of temperature distribution, strain generation, fracture morphology, and permeability enhancements. Finite element simulation was completed for both unstressed and stressed samples for concrete, sandstone, and shale samples. In unstressed samples, radial and tangential stresses are distributed evenly around the wellbore circumference, which causes fractures to initiate in unexpected directions. In stressed tests, radial and tangential stresses are lower in the direction of fracture propagation (perpendicular to the minimum horizontal stress direction). Simulated pressure decay tests by finite difference modeling showed low pressure liquid nitrogen can be applied as a near-wellbore formation damage treatment technique. Higher pressure injection enhances both fracturing speed and fracture conductivity. The finite difference simulation also demonstrated the influence of triaxial stress contrast observed in experiments, i.e. high contrast in triaxial stresses is favorable for cryogenic fracturing. Overall, the developed numerical models are able to match experimental results and will be useful for prediction of cryogenic fracturing applications.

No water was used for fracturing in the cryogenic stimulation experiments, which completely avoids the formation damage and environmental concerns caused by water-based fracturing fluids. Damage-free stimulated reservoir volume can provide low-resistant fracture networks that will increase the effective oil and gas drainage area. In addition, zero flowback is expected after cryogenic fracturing in field, thereby stimulated wells are directly ready to be put into production. Another advantage is that flowback treatment and disposal are not needed for cryogenic fracturing wells. Thus, time and money are saved in terms of zero water usage, no water storage pits and tanks, faster development pace, and larger reservoir drainage area, etc.

8.2 Recommendations

8.2.1 Field Tests

Based on our findings on lab-scale tests, shallow well pilot tests/field tests of cryogenic stimulation using LN₂ are highly recommended for the next step, considering the reservoir conditions are difficult to replicate in the lab. A meso-scale field cryogenic stimulation plan was prepared based on our laboratory observations and measurements, numerical simulation analyses, as well as geological examination of the Niobrara shale formation near Lyons, Colorado.

8.2.2 Larger Scale Laboratory Tests

Laboratory tests have shown significant permeability enhancement resulting from cryogenic fracturing of up to 8" × 8" × 8" samples. Thermal gradients, fracture generation and distribution, and the magnitude of permeability enhancement with cryogenic stimulation will vary with the size of samples. It is therefore recommended that large-scale laboratory tests, preferably on 1-meter cubic concrete and/or concrete/shale samples, would be essential for testing LN₂ delivery methods and useful monitoring tools for implementation at the field-scale.

8.2.3 Further Testing of Tight Sandstone

The rocks used for cryogenic fracturing experiments completed in this project included acrylic, glass, concrete, sandstone, and shale samples. Results of tests on regular sandstone have generated important questions, including how permeability (allowing the movement of cold gas ahead of the thermal front) and rock structure affect the sharpness of the thermal gradient and fracturing processes. Also, the effect of pore-space distribution on heat transfer and fracturing is not clearly understood. As an important production rock in many unconventional oil and gas reservoirs, tight sandstone samples need to be tested in the laboratory to see the potential of cryogenic stimulation in enhancing the matrix permeability.

8.2.4 Permeability Enhancement by Cryogenic Seed Fractures

Studies in glass cubes and shale blocks have shown that seed fractures created by thermal shock can be extended via other means (in our studies pneumatically, perhaps hydraulically in the field). Because cryogenically generated seed fractures are strongly influenced by processes that are radial with respect to the borehole, and less by the local pre-cryogenic stress field, these fractures may create or connect networks differently than fractures generated by pressure alone. Because one of our goals is to reduce water use in fracturing, if cryogenic seed fractures produce access to other fracture networks, the overall consumption of water may be reduced over time.

8.2.5 Development of Proppants for Cryogenically Induced Fractures

During our experiments, cryogenic fractures partially closed as temperature returned to ambient, implicating that proppants or other supporting materials are needed to be placed to keep fractures open to maintain conductivity during or after a cryogenic stimulation treatment. Finding appropriate proppants (e.g. ultralight weight proppants) for use with LN₂ treatments will be a challenge, owing to low liquid viscosity and vaporization of LN₂. However, for cryogenic fracturing used to provide seed fractures, subsequent fracturing techniques and proppants introduction methods could be used.

8.2.6 Improvement of LN₂ Delivery System

It was observed that LN₂ damaged the epoxy cementing the annulus between the casing and borehole, thus special LN₂ delivery system is required to protect the casing and cement sheath of the wells (fiberglass tubing). Also, the Leidenfrost effect must be taken into consideration when planning and implementing the injection strategy. The LN₂ must be actively flowing against the formation so a vapor cushion does not form and insulate the formation from the cryogenic temperatures.

8.2.7 Improvement in Cryogenically Induced Fracture Detection Techniques

Many of the cryogenic fractures are too small to be observed, thus more development of microscopy and fluorescence techniques are necessary for detailed characterization of

cryogenic fractures. Understanding how these fractures impact fluid flow and subsequent fracturing is important.

REFERENCES

- Aadnoy, B. and Looyeh, R., 2011. Petroleum rock mechanics: drilling operations and well design, Gulf Professional Publishing.
- Al-Ajmi, A. M. and Zimmerman, R. W., 2006. Stability analysis of vertical boreholes using the Mogi-Coulomb failure criterion, *International Journal of Rock Mechanics and Mining Sciences* 43(8), 1200-1211.
- Bergosh, J. L., Marks, T. R., and Mitkus, A. F., 1985. New core analysis techniques for naturally fractured reservoirs. SPE-13653-MS.
- Browning, J., Horton, W. & Hartman, H., 1965. Recent advances in flame jet working of minerals, in *Annual Symposium on Rock Mechanics*, Pennsylvania State University.
- Brannon, H. D., 2010. Hydraulic fracturing materials: application trends and consideration, SPE distinguished lecture.
- Canyon technical service, 2016. <http://wwwtest.canyontech.ca/Products-and-Services/Service-Lines>.
- Cracknell, R.F., Nicholson, D., Tennison, S. R. and Bromhead, J., 1996. Adsorption and selectivity of carbon dioxide with methane and nitrogen in slit-shaped carbonaceous micropores: simulation and experiment. *Adsorption*, 2(3),193-203.
- Cuderman, J. F., 1982. Multiple fracturing experiments-propellant and borehole considerations. SPE 10845.
- Cuderman, J. F., 1986. Effects of wellbore liquids in propellant-based fracturing. SPE 86-0562.
- Department of Energy, USA. 2009. Modern shale gas development in the United States: A primer.
- Detienne, J., Creusot, M., Kessler, N., Sahuquet, B. and Bergerot, J. L., 1998. Thermally induced fractures: A field-proven analytical model, *SPE Reservoir Evaluation & Engineering*, 1(01), 30-35. SPE 30777.

- Enick, R.M. and Ammer, J., 1998. A literature review of attempts to increase the viscosity of dense carbon dioxide. Website of the National Energy Technology Laboratory.
- Erdogan, F. and Sih, G. C., 1963, On the crack extension in plates under plane loading and transverse shear, *Journal of Basic Engineering*, 85(4), 519-525.
- Fakcharoenphol, P., Xiong, Y., Hu, L., Winterfeld, P., Xu, T. and Wu, Y.S., 2013. TOUGH2-EGS: A coupled geomechanical and reactive geochemical simulator for fluid and heat flow in enhanced geothermal systems, Petroleum Engineering Department Colorado School of Mines, 1500 Illinois Street Golden, CO 80401 USA.
- Fenghour, A., Wakeham, W. A. and Vesovic, V., 1998. The viscosity of carbon dioxide, *Journal of Physical and Chemical Reference Data*, 27(1), 31-44.
- Freeman, E. R., Abel, J. C., Kim, C. M. and Heinrich, C., 1983. A stimulation technique using only nitrogen. *Journal of Petroleum Technology*, 35(12), 2165-2174. SPE 10129.
- Germanovich, L. N., 2012, November. Thermal spalling of rock, in ICF 9-Sydney, Australia-1997.
- Ghabezloo, S. and Sulem, J., 2009. Stress dependent thermal pressurization of a fluid-saturated rock, *Rock Mechanics and Rock Engineering*, 42(1), 2009, 1-24.
- Gottschling, J.C., Royce, T.N. and Shuck, L.Z., 1985. Nitrogen gas and sand: a new technique for stimulation of Devonian shale. *Journal of Petroleum Engineering*, 37(5), 901-907. SPE 12313.
- Grundmann, S. R., Rodvelt, G. D., Dials, G. A. and Allen, R. E., 1998. Cryogenic nitrogen as a hydraulic fracturing fluid in the devonian shale, in SPE Eastern Regional Meeting, Society of Petroleum Engineers. SPE 51067.
- Gupta, D. V. S. and Bobier, D. M., 1998. The history and success of liquid CO₂ and CO₂/N₂ fracturing system, SPE 40016.
- Gupta, D. V. S., Leshchynshyn, T. T. and Hlidek, B. T., 2005. Surfactant gel foam/emulsions: history and field application in the western Canadian sedimentary basin. SPE 97211.

Hayes, T. D., Halldorson, B., Horner, P., Ewing, J., Werline, J. R. and Severin, B. F., 2014. Mechanical vapor recompression for the treatment of shale-gas flowback water, Oil and Gas Facility, 3(4), 54-62. SPE 170247.

Heins, R. W. and Friz, T. O., 1967. The effect of low temperature on some physical properties of rock, in Drilling and Rock Mechanics Conference, Society of Petroleum Engineers. SPE 1714.

Hernandez, J.M., Fernandez, C.T. and Scianca, N. M., 1994. Methanol as fracture fluid in gas wells. SPE 27007.

Huebner, K.H., Dewhurst, D.L., Smith, D.E. and Byrom, T.G., 2001. The finite element method for engineers, 4th edition. New York: John Wiley and Sons;

Hutton, D.V. 2004. Fundamentals of finite element analysis, first edition. McGraw Hill.

Inada, Y., Kinoshita, N., Ebisawa, A. and Gomi, S., 1997. Strength and deformation characteristics of rocks after undergoing thermal hysteresis of high and low temperatures, International Journal of Rock Mechanics and Mining Sciences, 34 (3), 140.e1-e14.

Inada, Y. and Yokota, K., 1984. Some studies of low temperature rock strength, International Journal of Rock Mechanics and Mining Sciences & Geomechanics Abstracts, 21, 145-153.

Jaeger, J. C., Cook, N. G. and Zimmerman, R., 2009. Fundamentals of rock mechanics, John Wiley & Sons.

Kendrick, D. E., Puskar, M. P., Schlotterbeck, S. T., 2005. Ultralight weight proppants: a field study in the big sandy field of eastern kentucky, in SPE Eastern Regional Meeting, Society of Petroleum Engineers. SPE 98006.

King, S. R., 1983. Liquid CO₂ for the stimulation of low-permeability reservoirs, in SPE/DOE Low Permeability Gas Reservoirs Symposium, Society of Petroleum Engineers. SPE 11616.

Kothare, S., 2012. Economics and applicability of nitrogen for fracking. Air Products and Chemicals. Inc.

- Law, B. E., 2002. Basin-centered gas systems. *AAPG Bulletin*, 86 (11): 1891-1919.
- LeBlanc, D., Martel, T., Graves, D., Tudor, E. and Lestz, R., 2011. Application of propane (LPG) based hydraulic fracturing in the McCully gas field, New Brunswick, Canada. *SPE* 144093.
- Luo, Z., Bryant, S. L., 2010. Influence of thermo-elastic stress on CO₂ injection induced fractures during storage, in *SPE International Conference on CO₂ Capture Storage and Utilization*, Society of Petroleum Engineers. *SPE* 139719.
- McDaniel, B., Grundmann, S. R., Kendrick, W. D., Wilson, D. R. and Jordan, S. W., 1998. Field applications of cryogenic nitrogen as a hydraulic-fracturing fluid, *Journal of petroleum technology* 50(3), 38-39.
- Middleton, R. S., Carey, J. W., Currier, R. P., et al. 2015. Shale gas and non-aqueous fracturing fluids: opportunities and challenges for supercritical CO₂. *Applied Energy*, 147, 500-509.
- Miller, J. S. and Johansen, R. T., 1976. Fracturing oil shale with explosives for in situ recovery. *Advances in Chemistry Series*, 151.
- Olson, J. E. and Pollard, D. D., 1991. The initiation and growth of en echelon veins, *Journal of Structural Geology*, 13(5), 595-608.
- Page, J. C. and Miskimins, J. L., 2009. A comparison of hydraulic and propellant fracture propagation in a shale gas reservoir, *Journal of Canadian Petroleum Technology*, 48(5), 26-30.
- Pranter, M. J., Vargas, M. F. and Davis, T. L., 2008. Characterization and 3D reservoir modelling of fluvial sandstones of the Williams Fork Formation, Rulison field, Piceance basin, Colorado, USA. *Journal of Geophysics and Engineering*, 5(2), 158-172.
- Preston, F., 1926. The spalling of bricks, *Journal of the American Ceramic Society* 9(10), 654-658.
- Preston, F. and White, H., 1934. Observations on spalling, *Journal of the American Ceramic Society*, 17(1-12), 137-144.

- Robertson, E.C., 1988. Thermal Properties of Rock, USGS.
- Rogala, A., Krzysiek, J., Bernaciak, M. and Hupka, J., 2013. Non-aqueous fracturing technologies for shale gas recovery. 49(1), 313-322.
- Rudenko, N. and Schubnikow, L., 1934. The viscosity of liquid nitrogen, carbon monoxide, argon and oxygen as a function of temperature, NASA Technical Translation (1968).
- Schmidt, R. A., Warpinski, N. R. and Cooper, P. W., 1980. In situ evaluation of several tailored-pulse well-shooting concepts. SPE 8934.
- Steward, D. B., 2013. George P. Mitchell and the Barnett shale, Journal of Petroleum Technology, 65(11), 58-68.
- Stosur, J. J., 1977. Approaches to extracting potentially recoverable hydrocarbons, International Journal of Energy Research, 1(2), 99-114.
- Suehiro, Y. Nakajima, M., Yamada, K. and Uematsu, M., 1996. Critical parameters of $\{x\text{CO}_2 + (1-x)\text{CHF}_3\}$ for $x = (1.0000, 0.7496, 0.5013, \text{ and } 0.2522)$. The Journal of Chemical Thermodynamics, 28(10), 1153-1164.
- Sun, Y., 2014. Impact of slickwater fracturing fluid compositions on the petrophysical properties of shale and tight sand. PhD dissertation.
- Thompson, J.E., McBain, C., Gregory, G. and Gerbrandt, D., 1992. New continuous-mix process for gelling anhydrous methanol minimizes hazards. Journal of Petroleum Technology, 44(7), 832-839.
- Tutor, E.H, Nevison, G. W., Allen, S. and Pike, B., 2009. Case study of a novel hydraulic fracturing method that maximizes effective hydraulic fracture length. SPE 124480.
- Wu, Y-S., Chen, Z., Kazemi, H., Yin, X., Pruess, K., Oldenburg, C., Winterfeld, P., Zhang, R., 2014. Simulation of Coupled Processes of Flow, Transport, and Storage of CO₂ in Saline Aquifers, Tech. rep., Trustees of The Colorado School of Mines.
- Xiong, Y., Fakcharoenphol, P., Winterfeld, P.H., Zhang, R. and Wu, Y-S., 2013. Coupled geomechanical and reactive geochemical model for fluid and heat flow: Application for

enhanced geothermal reservoir, in SPE Reservoir Characterization and Simulation Conference and Exhibition, 16-18 September, Abu Dhabi, UAE, SPE 165982.

Zhang, R., 2013. Numerical Simulation of Thermal Hydrological Mechanical Chemical Processes during CO₂ Geological Sequestration, PhD thesis, Colorado School of Mines.

Zhang, R., Winterfeld, P.H., Yin, X., Xiong, Y. and Wu, Y-S., 2015a. Sequentially coupled THMC model for CO₂ geological sequestration into a 2D heterogeneous saline aquifer, *Journal of Natural Gas Science and Engineering*, 27, 579-615.

Zhang, R., Xiong, Y., Winterfeld, P.H., Yin, X. and Wu, Y-S., 2015b. A novel computational framework for thermal-hydrological-mechanical-chemical processes of CO₂ geological sequestration into a layered saline aquifer and a naturally fractured enhanced geothermal system, *Greenhouse Gases: Science and Technology*.

Zhang, R., Wu, Y-S. and Fakcharoenphol, P., 2014. Non-Darcy displacement in linear composite and radial aquifer during CO₂ sequestration, *International Journal of Oil, Gas and Coal Technology*, 7(3), 244-262.

Zhang, R., Yin, X., Winterfeld, P.H. and Wu, Y-S., 2012a. A fully coupled model of nonisothermal multiphase flow, geomechanics, and chemistry during CO₂ sequestration in brine aquifers, *Proceedings of the TOUGH Symposium*, 838-848.

Zhang, R., Yin, X., Wu, Y-S. and Winterfeld, P.H., 2012b. A fully coupled model of nonisothermal multiphase flow, solute transport and reactive chemistry in porous media, in SPE Annual Technical Conference and Exhibition, 8-10 October, San Antonio, Texas, USA. SPE 159380.

Zhang, R., Yin, X., Winterfeld, P.H. and Wu, Y-S., 2016. A fully coupled thermal-hydrological-mechanical-chemical model for CO₂ geological sequestration, *Journal of Natural Gas Science and Engineering*, 28, 280-304.

Zhao, X., Rui, Z., Liao, X. and Zhang, R., 2015a. The qualitative and quantitative fracture evaluation methodology in shale gas reservoir, *Journal of Natural Gas Science and Engineering*, 27, 486-495.

Zhou, X., Aydin, A., Liu, F. and Pollard, D. D., 2010. Numerical modeling of secondary thermal fractures in hot dry geothermal reservoirs, Proceedings in Thirty-Fifth Work-shop on Geothermal Reservoir Engineering Stanford University, Stanford, California.

Zoback, M. D., 2007. Reservoir geomechanics: Earth stress and rock mechanics applied to exploration, production and wellbore stability.

APPENDIX A: Master and PhD Theses

Two Masters and one Ph.D. graduated from Petroleum Engineering Department at Colorado School of Mines, Golden, Colorado, with their research focusing on development of non-contaminating cryogenic fracturing technology for shale and tight reservoirs.

1. Taylor W. Patterson, 2015. Laboratory study of cryogenic fracturing of concrete samples, Master thesis.
2. Bowen Yao, 2015. Experimental study and numerical modeling of cryogenic fracturing process on laboratory-scale rock and concrete samples, Master thesis.
3. Naif B. Alqahtani, 2015. Experimental study and finite element modeling of cryogenic fracturing in unconventional reservoirs, PhD thesis.

APPENDIX B: Presentations / Posters / Publications

During this project, we have prepared the following poster, presentations, and publications:

1. Cha, M., Yin, X., Kneafsey, T. J., Johanson, B., Alqahtani, N., and Miskimins, J., Patterson, T., and Wu, Y.S. Cryogenic fracturing for reservoir stimulation-Laboratory studies. *Journal of Petroleum Science and Engineering*. 2014.
2. Cha, M., Yin, X., Kneafsey, T., Wu, Y.S., Alqahtani, N., Patterson, T., Yao, B., and Miskimins, J. Studying Cryogenic Fracturing Process and Fracture Morphology using Transparent Specimens, presented at the 2014 AGU Fall Meeting, San Francisco.
3. Kneafsey, T.J., S. Nakagawa, Y. Wu, S. Mukhopadhyay, Laboratory Visualization Experiments of Temperature-induced Fractures Around a Borehole (Cryogenic Fracturing) in Shale and Analogue Rock Samples, presented at the 2014 AGU Fall Meeting, San Francisco.
4. Edmiston, J, R. Martin-Short, S. Nakagawa, T. Kneafsey, Cryogenic Fracturing: Laboratory Visualization Experiments and Numerical Simulations Using Peridynamics, presented at the 2015 AGU Fall Meeting, San Francisco.
5. Alqahtani, N. B., Cha, M., Yao, B., Yin, X., Kneafsey, T.J., Wang, L., Wu, Y.-S., and Miskimins, J. L. Cryogenic fracturing of rock specimens under true triaxial confining stresses. *SPE EUROPEC 2016*. Vienna, Austria. May 30-June 2, 2016.
6. Cha, M., Alqahtani, N. B., Yao, B., Yin, X., Kneafsey, T. J., and Wu, Y.-S. Development of laboratory system for cryogenic rock fracturing study. *1st International Conference on Energy Geotechnics ICEGT 2016*. Kiel, Germany. August 29-31, 2016.
7. Cha, M., Alqahtani, N.B., Yao, B., Wang, L., Yin, X., Kneafsey, T.J., and Wu, Y.-S. Cryogenic Fracturing Process and Fracture Morphology using Transparent Specimens. *1st International Conference on Energy Geotechnics ICEGT 2016*. Kiel, Germany. August 29-31, 2016.
8. Wang, L., Yao B., Cha, M., Alqahtani, N., Kneafsey, T., Miskimins, J., Yin, X., Wu, Y.-S. Waterless fracturing technologies for unconventional reservoirs: opportunities and challenges for liquid nitrogen, accepted by *Journal of Natural Gas Science and Engineering*, 2016.

APPENDIX C: Participating Researchers / Students

Colorado School of Mines:

- Yu-Shu Wu, Professor, Petroleum Engineering
- Xiaolong Yin, Associate Professor, Petroleum Engineering
- Jennifer L. Miskimins, Associate Professor, Petroleum Engineering
- Lei Wang, Post-doctoral researcher, Petroleum Engineering
- Naif Alqahtani, PhD Student (Graduated), Petroleum Engineering
- Bowen Yao, MS Student (Graduated), Petroleum Engineering
- Taylor Patterson, MS Student (Graduated), Petroleum Engineering
- Brent Johanson, MS Student (Graduated), Petroleum Engineering

Texas A&M University:

- Minsu Cha, Assistant Professor, Civil and Environmental Engineering

Lawrence Berkeley National Laboratory:

- Timothy J. Kneafsey, Staff Scientist
- Seiji Nakagawa, Scientist
- Sumit Mukopadhyay, Scientist
- Jil T. Geller, Scientist
- Rohit Salve, Staff Scientist
- Sharon Borglin, Principal Science and Engineering Associate
- Paul Cook, Principal Science and Engineering Associate
- Alejandro Morales, Mechanical Technician
- Robin Lopez, Research Associate
- John Edmiston, Post-doctoral researcher
- Robert Short-Martin, Research Associate

Pioneer Natural Resources:

- Shannon Osterhout
- Bryant Morris